Detailed Assessment of Thermochemistry, Material Response, and Radiation Modeling for Hypersonic Air Flows

by

Lt Col Nicholas Carter, USAF

B.S., The United States Air Force Academy, 2010

S.M., The Massachusetts Institute of Technology, 2012

A thesis submitted to the

Faculty of the Graduate School of the

University of Colorado in partial fulfillment

of the requirement for the degree of

Doctor of Philosophy

Department of Aerospace Engineering Sciences

2025

Committee Members:

Iain D. Boyd, Chair

Hisham K. Ali

Matthew J. Conway

Alireza Doostan

Robyn L. Macdonald

Carter, Nicholas A. (Ph.D., Aerospace Engineering Sciences)

Detailed Assessment of Thermochemistry, Material Response, and Radiation Modeling for Hypersonic Air Flows

Thesis directed by Prof. Iain D. Boyd

In hypersonic flows around a vehicle, strong bow shock waves rapidly convert kinetic energy into internal energy. These rapid energy conversions and increased temperatures lead to many processes, including internal energy excitation, dissociation, exchange, ionization, and gas-surface interactions. Each of these processes can occur at rates similar to the rate of fluid motion. Therefore, in the cases of rapid compression and expansion present in hypersonic flow, these similar rates lead to flows that are in states of both thermodynamic and chemical nonequilibrium. The high-fidelity simulation of these hypersonic flows around vehicles requires a comprehensive multidisciplinary analysis of these phenomena. Vehicle scale computational fluid dynamics (CFD) analyses of hypersonic flows incorporate computationally tractable models that rely upon numerous semi-empirical parameters. Many of these parameters are obtained from experiment under a relatively narrow range of conditions. The uncertainty associated with these parameters can greatly affect important end results, known as quantities of interest (QoIs). For many hypersonic flow analyses, QoIs that drive vehicle design include predictions for vehicle heating, communications and remote observation.

In this thesis, high-fidelity hypersonic flow, material response, and radiation models are assessed for the purposes of quantifying the effects of rate processes on plasma formation and vehicle and gas radiation in nonequilibrium flows. Suborbital, weakly-ionized conditions are specifically chosen for study, as many of the parameters used in these models were validated under hyperbolic reentry conditions with greater levels of ionization. The relatively less energetic flow conditions present in this study are of increased interest for both civil and defense applications.

The tools, theories, and models utilized in this work are first described in detail. In addition to the models described, global sensitivity analyses and uncertainty quantification (GSA/UQ) methods and novel

finite rate surface chemistry (FRSC) ablation models are also depicted. To better inform parameter effects on various QoIs, case studies and conditions used in this study are also explained.

Next, a comprehensive literature review of 612 gas-phase reaction rate coefficients, energy relaxation parameters, FRSC coefficients, and collision induced excitation and quenching rate coefficients is conducted. For each parameter, experimental, numerical, theoretical and aggregate studies of these parameters were investigated to obtain variance bounds used in the case studies in this work. Qualitative and quantitative trends in these uncertain parameters are also compared with previous hypersonic GSA/UQ studies, where any significant differences are explained. The accumulated data, analysis and relative uncertainty bounds from multiple source types in this chapter provide a significant contribution to the hypersonic flow community. Relationships between uncertain input parameters and other QoIs can be used beyond the case studies in this work.

Gas-phase kinetic rate parameter effects on plasma formation in suborbital flow conditions are then investigated using GSA/UQ analyses. These conditions included velocities at 5, 7, and 9 km/s and at an altitude of 60 km. Results from these analyses are first compared with previous 1D shock GSA/UQ studies at the stagnation line. For 5 and 7 km/s, the main sensitivities on electron density in the 2D model come from associative ionization and dissociative recombination of N and O atoms, plus direct oxygen dissociation and the Zel'dovich mechanism. These trends match 1D results, but differ near the shock and wall. Such differences arise from the 1D shock discontinuity assumption, the inviscid assumption of the 1D model, and the incorporation of 2D plasma catalytic wall boundaries. For 9 km/s, the stagnation line first depends on associative ionization generating O_2^+, followed by charge the exchange reaction $O_2^+ + N \rightleftharpoons N^+ + O_2$ and Zeldovich-driven nitrogen dissociation. Unlike in 1D, electron impact ionization is absent in the 2D domain due to influences of the wall boundaries. These differences underscore how two-dimensional viscous and boundary effects steer post-shock plasma evolution—highlighting where 1D assumptions may not apply for higher fidelity vehicle-scale applications. Flowfield sensitivities and uncertainties were also examined via streamtraces of uncertainty bounds and sensitivity metrics. For 5 and 7 km/s, the largest electron density uncertainties appear near the stagnation line and body, driven mainly by $N + O \rightleftharpoons NO^+ +$

e^- after peak electron number density near the strong shock at the nose. Further downstream, weaker shocks increase vibrational-translational (VT) relaxation processes that drive O_2 dissociation's impact on eventual plasma formation. At 7 and 9 km/s, added complexity and variance from charge exchange reactions occur near the vehicle shoulder and surface due to flow expansion complicating ionization pathways.

Gas infrared (IR) radiation uncertainty in ablative flow around the nose of a slender hypersonic reentry vehicle is then analyzed. These analyses include the propagation and allocation of uncertainty from 195 gas-phase reaction rate parameters and QoIs involving integrated spectral radiance across multiple IR bands. Using the IRV-2's first trajectory point as a test case; methods were used to reduce uncertainty through a multi-grid convergence study with automated coupled flow/solid mesh movements and shock tailoring. Results on nominal grids covering flow temperatures, species densities, and radiance compare uncoupled flow with coupled flow-material responses. Surrogate model coefficients from 500 evaluations using sparse regression were compared for sensitivity metric convergence. The analysis highlights the second Zel'dovich mechanism and NO dissociation as major contributors to gas IR radiance uncertainty, while CN and CO exchange reactions additionally affected near and mid-IR regions. Uncertainty-scaled sensitivities further emphasized NO, N_2, and O_2 dissociation reaction rate parameters near the vehicle nose and shoulder regions.

FRSC models are then developed and evaluated. The models incorporate additional parameters by using surface kinetics and boundary layer edge mass conductance with four-dimensional (4D) tables used to generate nondimensional carbon flux values. This shifts most preprocessing to the 4D tables, enabling more efficient and stable carbon ablation surface updates in the tightly coupled flow and material response models. Comparisons were made between the FRSC model, the equilibrium surface chemistry (CEA2) model, and experiments under subsonic to hypersonic conditions. The FRSC models better match experiments at lower temperatures, where CEA2 overpredicts normalized carbon mass flux, though both models overpredict above 3,000 K. A global sensitivity analysis at atmospheric conditions identified the O_2 oxidation reaction probability and sublimation mass flux rate as the main contributors to normalized

carbon mass flux uncertainty below and above 1,800 K, respectively. Baseline comparisons at IRV-2's initial trajectory highlight significant differences in ablation mass flux and surface recession between FRSC and CEA2 models, while disparities in near-surface CO, C, and CN densities diminished at higher temperatures as CO diffusion limits are reached.

Finally, all parameters reviewed previously are implemented in a final case study for the entire IRV-2 vehicle over multiple trajectory points. These scenarios examine parameter effects on surface temperature, gas and vehicle body IR radiation. These GSA/UQ studies evaluate 612 uncertain parameters' influence on 200 wall-normal LOSs over two trajectory points, two radiance types, and four IR bands totaling 3,200 QoIs. Results consistently highlight the critical role of nitrogen dissociation and recombination via Zel'dovich exchange. For vehicle body included radiance, these reactions influenced surface temperature and thus grey-body radiation. Gas only radiance, these reaction rate coefficients directly affect N_2 and NO concentrations across all bands. Additionally, NO dissociation and recombination with atomic oxygen and nitrogen partners were identified as major contributors, indirectly impacting N_2 populations and directly affecting wall temperature for gas-only and vehicle body radiance scenarios, respectively. The study also reveals that in certain areas of the flow, an increased number of small magnitude variance contributors are present. These locations and flight conditions are characterized with low uncertainty, limited parameter sparsity, and potential radiation code numerical instabilities. In downstream areas with vehicle body radiance QoIs, low uncertainty leads to numerous small variance contributions. Conversely, approximately 1–3% of LOS evaluations near the nose and shoulder experience state population balance convergence failures, which NEQAIR addresses by iterating multiple solution algorithms before defaulting to a Boltzmann distribution. Furthermore, differences between trajectory points were noted. Lower trajectory points displayed amplified effects from FRSC and collisional excitation/quenching rates. These sensitivities affect IR radiation via their influence on carbon mass flux and collision induced excitation rates, driving complex state population dynamics at the nose/shoulder and downstream regions, respectively.

Each of the reviews and case studies present in this thesis provide value for both hypersonic vehicle modeling and experimental design. The GSA/UQ results not only identify the parameters that most influence specific QoIs, but also provide a clear roadmap for enhancing computational models and system designs. By quantifying uncertainty propagation in complex hypersonic flow, material response and radiative models, this work enables engineers to focus on reducing uncertainty in key parameters that impact flow ionization, wall temperatures and IR radiance. This can ultimately lead to more robust thermal protection systems and improved remote observations of ablative vehicles under weakly ionized conditions. This targeted approach also aids in the design of sensor and diagnostic systems by pinpointing critical spatial and spectral regions where measurement resources can be optimized, such as calibrating instruments to capture data in specific IR bands. These outcomes offer insights into computational efficiency and model refinement by revealing areas where parameter sparsity assumptions break down, suggesting the need for increased model complexity or enhanced numerical schemes. The analyses highlight sensitive parameters filtered by their influence on ionization and IR radiance across various conditions and locations, and they point to specific regions, e.g., near the IRV-2 shoulder, where increased parameter interaction effects are present. Overall, these findings guide both simulation improvements and the strategic deployment of computational resources, thereby narrowing uncertainties and setting the stage for further investigations and refinements in future studies.

Dedication

For God, my family, and my country.

Acknowledgements

I would like to first acknowledge Professor Iain Boyd for both his mentorship and support over the past 32 months. Prof. Boyd's guidance was invaluable, especially when advising the proper scope of the research conducted and providing a 60 km view of the monumental challenges and complexity surrounding hypersonic flow simulation. His ability to steer my efforts and provide resources for further inquiry to best facilitate meaningful contributions to the aerospace community were extremely helpful and I could not have developed to this point without his leadership. I also wish to thank Prof. Hisham Ali, Dr. Matthew Conway, Prof. Alireza Doostan, and Prof. Robyn L. Macdonald for serving on my committee. Your feedback and guidance for my research was greatly appreciated.

I would also like to thank the members of NGPDL and NSI for their support and help throughout this process. In particular, I would like to acknowledge Dr. Tim Aiken, Dr. Chris Roseman, and Dr. Ross Chaudhry for hours of guidance, thoughtful conversations, and great banter. Your input on numerous topics greatly helped facilitate a smoother transition from a decade of flying airplanes to navigating an accelerated aerospace PhD process. I also want to thank Dr. Tommy Kava, Dr. Jens Rataczak, Dr. Jenny Horing, Kal Monroe, Mitch Wall, and Tomaz Remec for their insightful conversations that made this work possible. In spite of over a decade difference in age, you all made me feel welcome within the lab area from day one.

From other organizations, I want to thank Dr. Brianne Williams from the Aerospace Corporation, Dr. Tom West from NASA, Dr. Jeffrey Engerer from Sandia National Laboratory, Dr. Jesse Streicher from Stanford, and Brigadier General Douglas Wickert and Colonel James Gresham from the U.S. Air Force. Your help throughout this process was instrumental in enabling and focusing my research with a variety of perspectives and backgrounds.

I want express immense gratitude to my family for their unwavering support throughout this process. To my dad Major (Ret.) Robin Carter, mom Dr. Becky Carter, and sister Jennifer, thank you for your sacrifice and guidance throughout my life. Your dedication to selfless service has always been an inspiration. To my in-laws Mr. Keith Lerew and Mrs. Debbie Lerew, thank you so much for your support

and help throughout this process as well. To my daughters Rayla and Alaura, you are the reason why I conducted this intellectual journey. Your growth throughout these years is inspirational and I can't wait to see you continue to develop into exceptional young women. Most importantly to my wife Kim, thank you so much for all of your steadfast support throughout my life. Ever since first meeting you freshman year in high school, I knew how lucky I was to have you in my life. When looking at our 22 years together, these 2.67 may appear short, but your sacrifice during this time is definitely not lost on me. Thank you.

This research was enabled by the USAFA Faculty pipeline for officers in the U.S. Air Force. This work utilized the Blanca condo computing resource at the University of Colorado Boulder. Blanca is jointly funded by computing users and the University of Colorado Boulder. This work also utilized the Alpine high-performance computing resource at the University of Colorado Boulder. Alpine is jointly funded by the University of Colorado Boulder, the University of Colorado Anschutz, Colorado State University, and the National Science Foundation (award 2201538).

Contents

Chapter

Tables

Figures

Chapter 1

Introduction

1.1 Hypersonic Vehicles, Remote Observation and Defense

Hypersonic vehicles are generally defined as objects traveling at velocities over five times the speed of sound. The design of these vehicles is primarily driven by flow conditions characterized by high temperatures and multiple thermochemical processes. This kinetic to thermal and internal energy conversion occurs as the flow passes through a strong shock wave and slows significantly [1,2]. Figure 1.1 depicts an example of the hypersonic flow around the nose of a slender vehicle travelling at 7 km/s and an altitude of 60 km. At these conditions, the vehicle is travelling at over 20 times the speed of sound and temperatures of the flow between the bow shock and the vehicle increase to tens of thousands of degrees Kelvin. These temperatures are high enough to vary the chemistry of the air, form plasma, and affect the heat transferred to the vehicle surface. The range of hypersonic conditions varies significantly and are dictated by mission requirements for a particular vehicle. This large scope makes defense against hypersonic weapons a daunting task; where remote observation, identification, and countering actions vary significantly depending on the vehicle flight conditions along a trajectory.

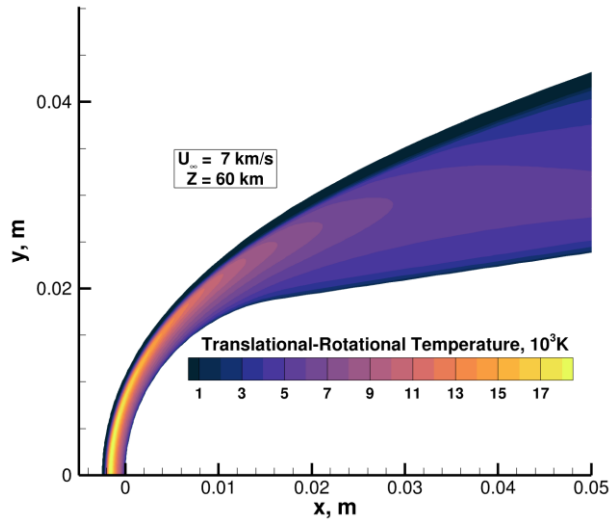

Figure 1.1: Example of a bow shock wave and temperature flowfield around the nose tip of a slender hypersonic vehicle.

Factors that influence remote observation of these vehicles also vary significantly due to the wide range of conditions present. Hypersonic vehicle remote observation metrics for both civil and defense applications include a wide range of spectral resolutions and wavelengths. Major electromagnetic (EM) categories for remote observation of hypersonic vehicles include ultraviolet (UV), infrared (IR) and radio frequency (RF) bands. Each band has its advantages and disadvantages when detecting and identifying hypersonic vehicles via their respective EM fingerprint based on trajectory conditions [3–17].

For air defense applications, many multispectral remote sensors are used simultaneously to provide situational awareness when tracking potential threats. These Integrated Air Defense Systems (IADS) are utilized in a layered manner, where core functions like detection, identification, threat evaluation, and potential engagement are coordinated between multiple military and intelligence entities from multiple countries. Figure 1.2 shows a simplified defense depiction of a Glide Phase Interceptor (GPI) IADS concept, where a suite of sensors first detects, identifies and tracks a potential threat while a countermeasure is employed through a set of communications channels leading to eventual threat neutralization [18]. Defense success against potential hypersonic threats greatly depends upon the speed at which this detection, identification, threat evaluation, and potential engagement process occurs within the IADS.

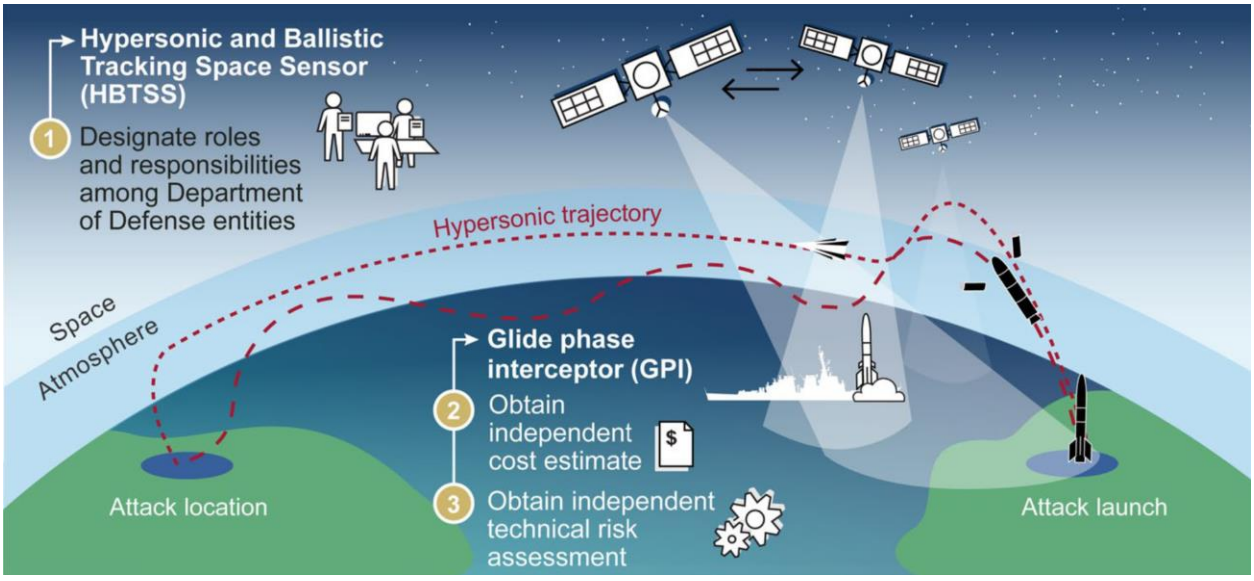

Figure 1.2: Glide Phase Interceptor (GPI) Integrated Air Defense Systems (IADS) incorporation framework [18].

Over the past decade, there has been increased interest in the simulation and testing of hypersonic vehicles for defense applications. Fiscal year 2025 hypersonic missile Department of Defense (DoD) budgets allocate over $1.6 billion for testing critical technology areas, including long range hypersonic attack cruise missile (HACM) and GPI weapons development [19]. Figure 1.3 illustrates general hypersonic vehicle categories and their respective aerospace environments. Each of these general vehicle types involve a wide range of conditions over their trajectories that greatly affect vehicle design. Traditional ballistic missiles include more predictable paths, wherein detection, identification and tracking of various flight phases have been optimized over decades. In contrast, hypersonic cruise missiles like HACM include vehicles with propulsive systems, relatively lower velocities, and lower altitudes. These higher density conditions drive vehicle design primarily through material heating constraints but also allow for greater maneuverability depending on the application. Aeroballistic and boost-glide systems include higher altitude trajectories that allow for greater velocities while maintaining enough control authority for maneuverability. Additionally, the relatively lower altitudes in terminal phases of these trajectories allow for terrain masking from ground-based sensors due to the Earth's curvature. This combination of capabilities make successful defense of these vehicle types a significant challenge.

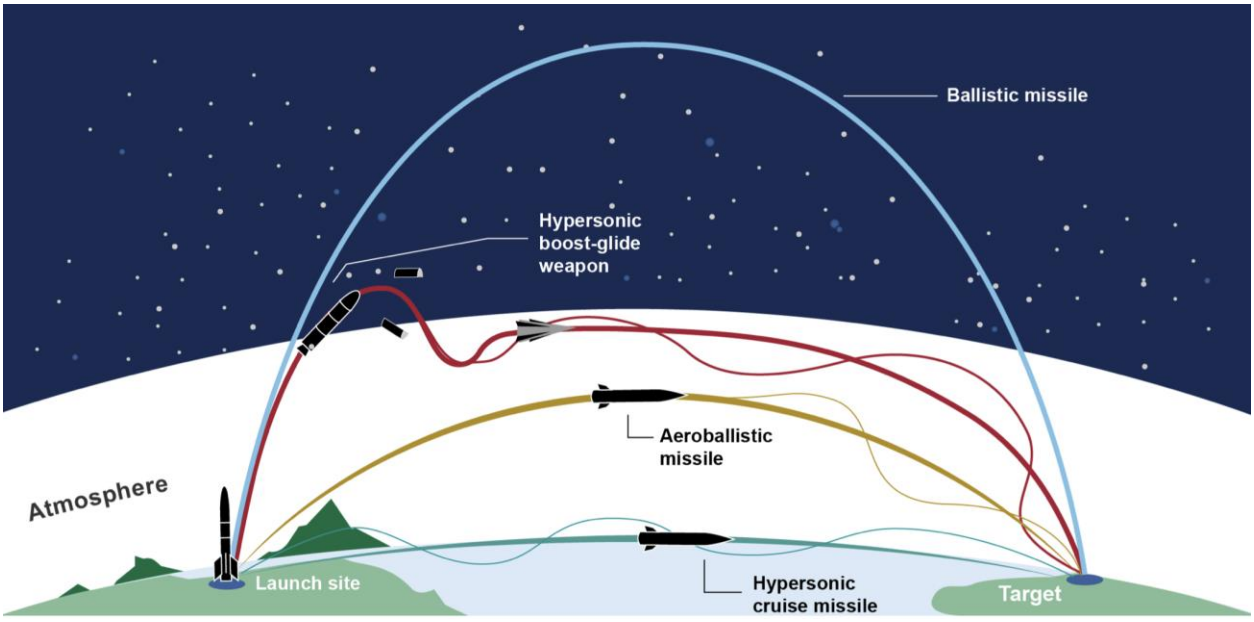

Figure 1.3: General hypersonic missile categories and general environments [19].

Example velocities, altitudes and overall trajectories are compared for various vehicle types in Figure 1.4. The characteristics of remote observation greatly depend upon both heating of the vehicle and the air between the vehicle and the bow shock. Figure 1.4(a) also depicts regions where various processes occur in the flow surrounding and at the surface of hypersonic vehicles. These processes are further defined in Section 1.2. The 10% and 90% values for each process range signify region bounds where the effects of these processes become significant [1,20–22]. Many of the hypersonic vehicle trajectories experience multiple of these different processes. Air-breathing and other low altitude propulsive hypersonic experimental vehicles (orange) experience maximum velocities below 5 km/s, where varying degrees of species excitation and oxygen dissociation occur. In contrast, reentry vehicles like those of the Apollo missions (purple) experience velocities greater than 11 km/s, where a significant fraction of the flow dissociates and ionizes throughout the trajectory. Lifting body hypersonic vehicles like the space shuttle (green) also allow for slowing during reentry at higher altitudes to better manage heating and force design variables.

In-between these vehicle types are typical ballistic (yellow) and boost glide (blue) vehicle trajectories. These involve velocities between 5 to 7 km/s, where nitrogen dissociation and a small fraction of ionization occurs. For these slender vehicles, this ‘weakly ionized’ flow consists of a plasma that typically makes up less than 2% of flow species and includes a mixture of free electrons and ions such as NO^+, O_2^+, and N_2^+. These plasma species have implications for RF applications including communication, remote observation and tracking; where plasma density and frequency around the vehicle affect how inbound EM waves absorb, emit, reflect and scatter around the vehicle and its wake [23–25].

Additionally, thermal protection systems (TPSs) for these vehicles can include surface cooling through ablative processes, where controlled removal of material occurs to manage and dissipate heat generated during reentry. Both these ablative products and air species formed from various chemical reactions present in the highly reactive flow leave specific observation characteristics within UV and IR bands. The magnitudes of these spectral patterns depend upon the density of different atoms, molecules, ions and electrons (defined as species in this work), the underlying internal energy states of the species, as

well as the temperatures of both the vehicle body and the flow surrounding the vehicle. Figure 1.4(b) depicts the specific conditions investigated in this thesis, where ablative and weakly-ionized flows occur. Specifics on this work's scope and outline are found in Section 1.3. The next section will provide context for accurately simulating the main hypersonic flow processes shown in Figure 1.4(a) and their relation to vehicle observation for defense applications.

a)

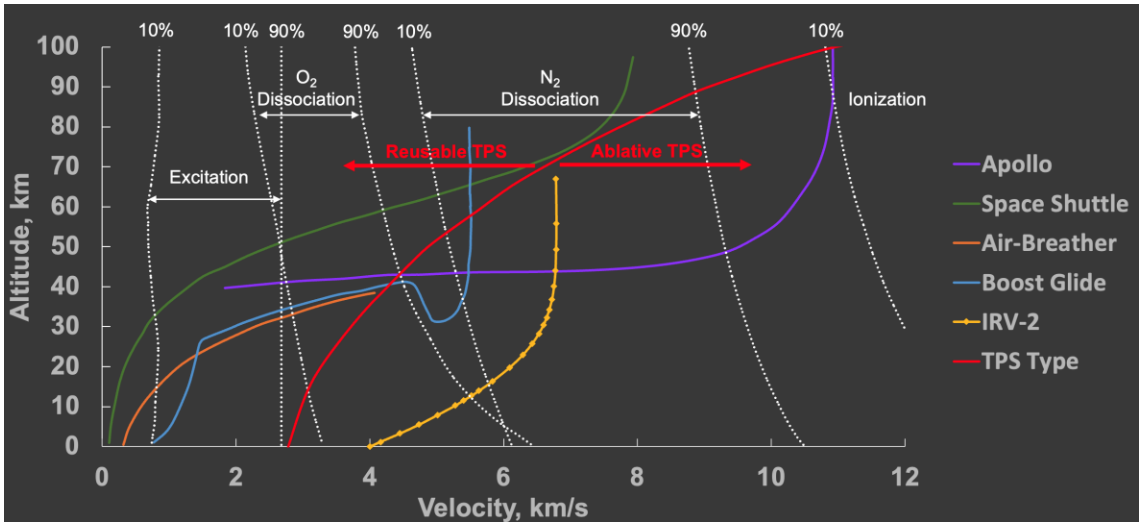

b)

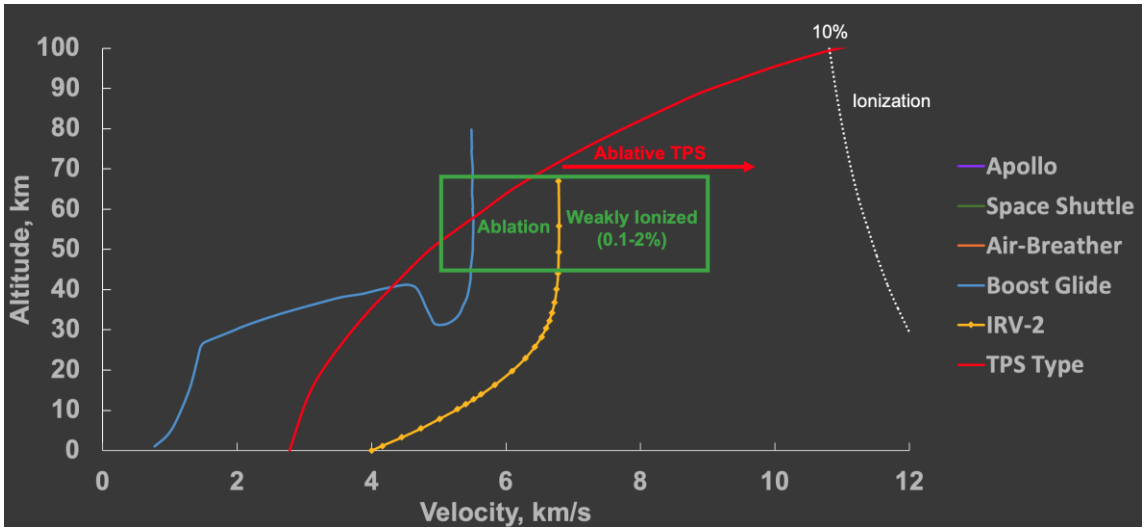

Figure 1.4: Example hypersonic vehicle trajectories a) in relation to various flow processes and b) emphasizing the conditions for ablative, weakly ionized flows around boost glide and aeroballistic vehicles.

1.2 Nonequilibrium Hypersonic Flow, Material Response, and Radiative Processes

The challenges involved with the high-fidelity simulation of nonequilibrium hypersonic flows, associated material response and subsequent radiation are myriad. The highly coupled influences of multiple subdisciplines, length scales, and levels of fidelity make accurate modeling and simulation of both the flow and vehicle computationally expensive and subject to many uncertain inputs. Additionally, the wide range of hypersonic flow conditions make for additional modeling challenges, wherein semiempirical model inputs are derived from a narrow range of conditions.

Hypersonic flows around vehicles are generally characterized by a strong bow shock marked by a rapid kinetic to thermal and subsequent internal energy transfer. Coupling between concurrent processes of thermal and chemical relaxation increase modeling complexity as the energetic chemical species transfer energy to internal excitation and endothermic chemical reactions. The length scales of these processes are often similar to the bulk advection rates of the flow, which necessitates accounting for both thermal and chemical nonequilibrium rate effects for multiple energy modes and chemical species. Many hypersonic flow simulations incorporate thermochemical models that approximate the coupled relationship between various thermal energy modes in the form of multiple energy conservation equations. These multi-temperature models characterize the energy modes with different temperatures to approximate thermal nonequilibrium. Typically, an assumed combination of the temperatures associated with these energy modes acts as a controlling temperature for chemical reaction rates. Boltzmann statistics are also utilized to describe the internal state populations of the gas particles for the different energy modes [1,2].

Additionally, options in hypersonic flow simulations further incorporate surface boundary conditions, including choices for varying levels of wall species recombination, wall temperature relations, as well as TPS processes [26–38]. In analyses involving ablative TPSs, flow and material response coupling requires information transfer between the flow and material response parameters that further lead to increased computational expense and numerical instabilities under certain conditions. Species added to the flow in ablation and pyrolysis processes are then included for accurate coupling, which further increases the number of chemical reactions and thermal relaxation parameters involved in high-fidelity hypersonic

flow solvers. This coupling affects flow composition, internal energy distributions and transport parameters that in turn affect energy and mass balances at the vehicle surface.

Further complication in modeling hypersonic flow environments involves processes of radiative energy transfer. Although convective and conductive heat transfer inclusion is of great importance for hypersonic vehicle design, radiative heating and remote observation QoIs play roles in thermal management and detection applications as well. Unlike the former energy transfer mechanisms, EM radiation is especially difficult to simulate as it does not require a medium to travel through and is considered a long-range phenomenon. Emitted energy in the form of photons travel distances that can range from 10^{-10} m to 10^{10} m prior to interaction with other particles, where complex processes like absorption, stimulated emission, spontaneous emission, and scattering can occur. Furthermore, modeling these processes via energy conservation cannot be applied over infinitesimal volumes, but must instead be calculated over the entire considered volume. Therefore, while conductance and convection rely upon four independent variables of space and time with linear temperature dependence, radiation involves an integral equation with up to seven independent variables: radiation frequency, space, time, and coordinates related to photon direction [39,40]. The particle-wave duality of EM radiation allows for classification of radiation types based EM waves or energy parcels (photons). Classification of frequencies of the EM waves are shown in Figure 1.5, where ranges can be described by wavelength, frequency, or wave number related to one another via

$$\nu = \frac{c}{\lambda} = c\eta \tag{1}$$

where ν, λ, η, and c are the EM frequency, wavelength, wave number and speed of light, respectively. The wave or photon energy transmitted follows the relation

$$\epsilon = h\nu \tag{2}$$

where h is Planck's constant. Many hypersonic studies have investigated the simulation and validation of radiative heat transfer in the UV, visible and near IR spectrums. For studies involving higher energy flows, radiative heat transfer simulations can also be coupled with CFD governing energy modes [1,3,13,41–50].

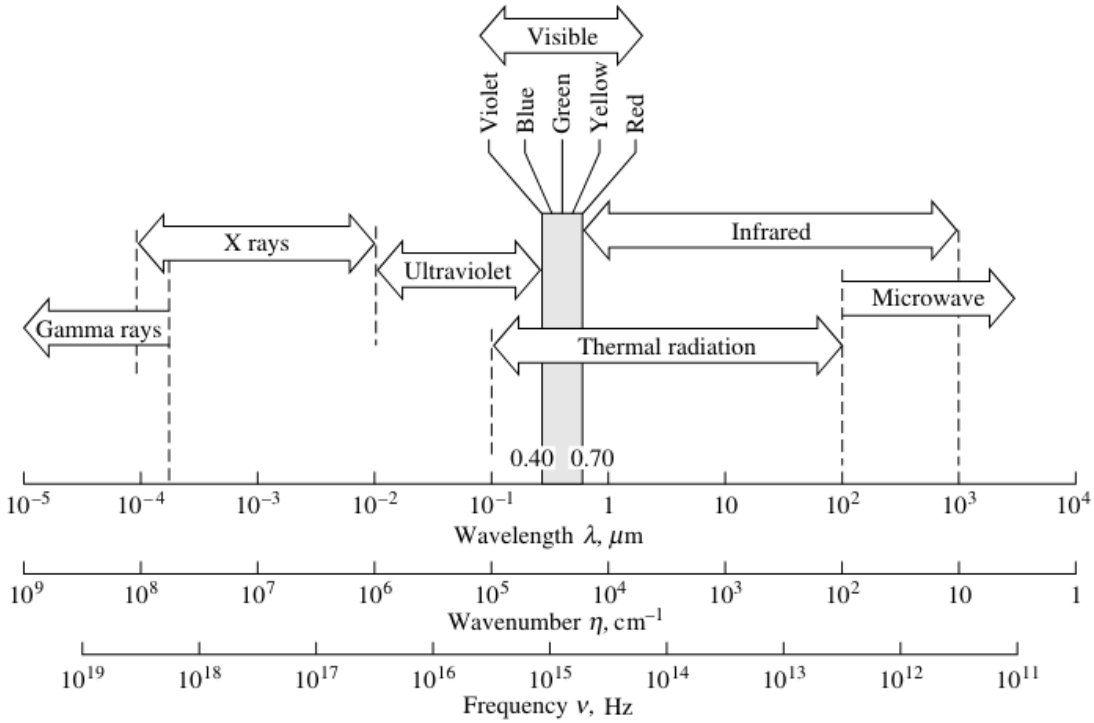

Figure 1.5: Electromagnetic wave spectrum in a vacuum adapted from Modest [39].

Considerable effort has been undertaken in the past two decades from NASA and others to reduce uncertainty and increase reliability of hypersonic vehicle design by improving the simulation of these highly coupled subdisciplines under various reentry conditions for different planetary atmospheres [2,45,47,48,51–59]. However, although many experimental and simulation campaigns within these hypersonic flow regimes focus on refining fundamental physics behind these complex processes, many rely upon experimental parameter fitting and assumptions that make vehicle scale modeling and full trajectory simulation computationally tractable. Furthermore, input parameters and models developed at these higher velocities may not necessarily translate well to weakly ionized flow conditions. Many of the parameters

involved in hypersonic flow, material response and radiation are therefore extensively reviewed in this work to ultimately provide insight for QoIs related to various applications.

1.3 Dissertation Scope and Outline

Due to increased interest in hypersonic defense, this dissertation focuses on furthering the accuracy of threat detection for IADS. The approach taken in this work begins with the incorporation and assessment of high-fidelity models used to approximate flows around hypersonic vehicles under conditions from 5 to 9 km/s and altitudes from 50 to 60 km. At these weakly ionized conditions, there have yet to be significant campaigns dedicated to the validation of both ionization and radiative QoIs for these multiple models. Additionally, the experimental and computational data used in the semiempirical relations within these models introduce uncertainties based on a relatively narrow range of conditions. A concerted effort is therefore undertaken in this thesis to characterize variability in these model input parameters and use these data to ascertain overall ionization and radiation QoI uncertainties under suborbital flight conditions. Furthermore, techniques are utilized to apportion the uncertainty of these QoIs while accounting for highly nonlinear influences from these parameters. To this date, no major studies have extensively quantified the input parameter variance or the propagated uncertainty and uncertainty apportionment of these parameters on ionization and radiation under these conditions for the entire flowfield around a slender hypersonic vehicle. This thesis incorporates a series of case studies and model developments that build upon one another to further extend model capabilities and more accurately quantify remote observation predictions.

This work consists of eight chapters, where the first provides context for the research efforts involved while highlighting knowledge gaps that this work attempts to fill. Chapter 2 provides a detailed depiction of the tools, theory and case study implementation processes. This includes a comprehensive review of previously developed hypersonic flow, material response, and radiation models, including major input parameters that drive QoI uncertainties. Additionally, theory behind a novel FRSC model is provided along with GSA/UQ software and methods. Chapter 3 provides a comprehensive literature review of all input parameter uncertainties used in assessing these models as well as thorough explanations of parameter

subcategories. These parameter groups include rates involving thermochemical gas-phase reactions, internal energy relaxation, excitation and quenching, and surface-phase reactions.

Chapters 4 to 7 include the main case studies and results of this work. Chapter 4 focuses on modeling and uncertainty apportionment and propagation of thermochemical reaction rate and energy relaxation parameters for 11 species air for ionization QoIs around a slender vehicle body under weakly ionized conditions. This includes comparisons to previous one-dimensional shock tube models along the stagnation line as well as ionization GSA/UQ results throughout an entire two-dimensional, axisymmetric flowfield. Chapter 5 analyzes gas-phase thermochemical reaction rate parameters' influence on flowfield IR radiation involving 11 air and 9 ablative carbon species at the nose of the aeroballistic IRV-2 vehicle. Chapter 6 evaluates the FRSC models developed in this work and includes comparisons to theory and experiment. Additionally, this chapter includes GSA/UQ analyses, ablation recession, and flowfield air and carbon species results between models for multiple IRV-2 trajectory points. Chapter 7 focuses on multiple scenarios involving all parameters reviewed in Chapter 3 and assesses their relative influence on IR radiation around the entire IRV-2 vehicle at multiple trajectory points. This chapter is a culmination of assessing how thermochemical gas, surface, energy relaxation, internal energy excitation and quenching rates affect IR radiation from the IRV-2 vehicle. Chapter 8 then provides a summary of completed work, the major contributions to the research field, and recommendations for future efforts.

Chapter 2

Tools, Theory, and Implementation

2.1 Introduction

To properly assess thermochemistry, material response, and radiation modeling of thermochemical nonequilibrium hypersonic air flows, a background of the theories and tools utilized is required. This chapter incorporates formal definitions, derivations and assumptions for the theory incorporated within each modeling framework, focusing on areas where uncertain input parameters (usually incorporated within semiempirical relations) are used within this work for uncertainty propagation to various QoIs. The subsections include a detailed explanation of the hypersonic flow and material response codes LeMANS-MOPAR-MD, a novel FRSC material response model, the nonequilibrium air radiation code NEQAIR, and GSA/UQ software Dakota and UQLab. Additionally, a subsection explaining the case studies involved in the assessments of the various processes within these codes is provided.

2.2 Hypersonic Flow: LeMANS

Flow simulations described in this study employ the LeMANS CFD software initially developed at the University of Michigan for simulating hypersonic reacting flows. NASA's hypersonic CFD codes DPLR [60] and LAURA [61] have both benchmarked LeMANS. Furthermore, LeMANS has undergone validation under diverse hypersonic conditions, such as those encountered in the Apollo, Fire II, and RAMC flight missions [36,62,63].

LeMANS stands as a parallel, multidimensional software engineered to solve the Navier–Stokes equations with second-order spatial precision and is adaptable to structured or unstructured grids. Embedded within LeMANS are the Park two-temperature (2T) and Modified Marrone-Treanor (MMT) models. Thermochemical nonequilibrium is accounted for by employing a continuum approximation for flow modeling. The software couples Navier–Stokes equations with models for thermodynamic and transport properties, integrating spatial and temporal differential equations through the finite volume

method. Flux calculation across cell faces involves a modified Steger–Warming flux vector splitting scheme for inviscid components and a central scheme for viscous fluxes. Viscous stresses are depicted under Newtonian flow and Stokes's hypothesis. Species mass diffusion fluxes follow a modified Fick's law, while heat fluxes are modeled according to Fourier's law. Transport properties are determined using Wilke's mixing rule with Blottner's curve fits for viscosity and Eucken's relation for thermal conductivity.

The differential form of the governing equations utilized in LeMANS follow that of Equations 3-4, where a system of multi-species continuity, three momentum, and two energy equations are discretized and iterated until a sufficient residual convergence throughout the flow domain.

$$\frac{\partial \boldsymbol{Q}}{\partial t} + \nabla \cdot (\boldsymbol{F} - \boldsymbol{F_d}) = \boldsymbol{S_{c,v}} \tag{3}$$

$$\boldsymbol{Q} = \begin{Bmatrix} \rho \boldsymbol{Y}^T \\ \rho \boldsymbol{u}^T \\ E_t \\ E_{ve} \end{Bmatrix}, \qquad \boldsymbol{F} = \begin{Bmatrix} \rho \boldsymbol{Y}^T \boldsymbol{u} \\ \rho \boldsymbol{u}^T \boldsymbol{u} + \boldsymbol{I}p \\ (E_t + p\boldsymbol{u}) \\ E_{ve}\boldsymbol{u} \end{Bmatrix}, \qquad \boldsymbol{F_d} = \begin{Bmatrix} -\boldsymbol{J} \\ \boldsymbol{\tau} \\ \boldsymbol{u\tau} - (\boldsymbol{q_{tr}} + \boldsymbol{q_{ve}}) - (\boldsymbol{h}^T \boldsymbol{J}) \\ -\boldsymbol{q_{ve}} - (\boldsymbol{e_{ve}^T J}) \end{Bmatrix}, \qquad \boldsymbol{S_{c,v}} = \begin{Bmatrix} \dot{\boldsymbol{w}}^T \\ \boldsymbol{0}^T \\ 0 \\ \dot{\boldsymbol{w}}_{ve} \end{Bmatrix} \tag{4}$$

The majority of the analyses in this work involve quantifying the effects of parameter uncertainties on source terms involved the governing equations for LeMANS. The source terms in the species conservation equations in Equation 5 and 6 are represented by $\dot{w}_{1,\dots,n_s}$, where n_s represents the number of species. The α and β terms in Equation 6 represent stoichiometric coefficients for each j reactants or products within each k reactions. These chemical reaction source terms are a function of forward and reverse kinetic rates k_{f_k} and k_{r_k} for each of the k reactions.

$$S_{c,v} = \left\{ \dot{w}_1 \dots \dot{w}_{n_s} \; 0 \; 0 \; 0 \; 0 \; \dot{w}_v \right\}^T \tag{5}$$

$$\dot{w}_{1,\dots,n_s} = M_{1,\dots,n_s} \sum_k \left(\beta_{s_k} - \alpha_{s_k}\right) \left[10^3 k_{f_k} \Pi_j \left(10^{-3} \frac{\rho_j}{M_j} \right)^{\alpha_{j_k}} - 10^3 k_{r_k} \Pi_j \left(10^{-3} \frac{\rho_j}{M_j} \right)^{\beta_{j_k}} \right] \tag{6}$$

These reaction rates address thermochemical nonequilibrium through the 2T thermochemical model, where chemical reactions are integrated into species continuity equations' source terms. The 2T model employs two temperatures, representing translational and rotational (T_{tr}) and vibrational and electron-electronic (T_{ve}) energy modes that regulate forward reaction rates using the generalized Arrhenius

expressions and the controlling temperature T_a defined in Equations 7 and 8. For forward reactions, values of n in Equation 8 are 0.7 for dissociation reactions, 1.0 for neutral exchange, charge exchange and associative ionization reactions, and 0.0 for electron impact dissociation and ionization reactions following previous analyses [54,64]. Reverse reaction rates are calculated via Equations 9-12 using equilibrium constants calculated from Gibb's free energy minimization and NASA Lewis Research Center curve fits for enthalpy and entropy [65,66]. For reverse reactions, n values in Equation 8 are 1.0 for charge exchange and dissociation reactions involving heavy particles, and 0.0 for electron impact ionization, electron impact dissociation, and associative ionization reactions.

$$k_{f_k} = C_{f_k} T_a^{\eta_{f_k}} \exp\left(-\frac{\theta_{f_k}}{T_a}\right) \tag{7}$$

$$T_a = T_{tr}^{n} T_{ve}^{1-n} \tag{8}$$

$$k_{r_k} = \frac{k_{f_k}}{K_{eq_k}} \tag{9}$$

$$k_{eq_k} = \left(\frac{p_0}{R_u T_{tr}}\right)^{\sum_s \left(\beta_{s_k} - \alpha_{s_k}\right)} \exp\left[-\sum_s \left(\beta_{s_k} - \alpha_{s_k}\right)\left[\left(\frac{h_{s_k}}{R_u T} - \frac{s_{s_k}}{R_u}\right)\right]\right] \tag{10}$$

$$\frac{h_{s_k}}{R_u T} = -\frac{a_{1,s}}{T^2} + a_{2,s}\frac{\log(T)}{T} + a_{3,s} + a_{4,s}\frac{T}{2} + a_{5,s}\frac{T^2}{3} + a_{6,2}\frac{T^3}{4} + a_{7,s}\frac{T^4}{5} + a_{8,s} + \frac{a_{9,s}}{T} \tag{11}$$

$$\frac{s_{s_k}}{R_u} = -\frac{a_{1,s}}{2T^2} - \frac{a_{2,s}}{T} + a_{3,s}\log(T) + a_{5,s}\frac{T^2}{2} + a_{6,s}\frac{T^3}{3} + a_{7,s}\frac{T^4}{5} + a_{8,s}\log(T) + a_{10,s} \tag{12}$$

The vibrational energy source terms are defined by Equation 13, where S_{epg} approximates electron pressure gradient induced work done on electrons by the electric field, S_{c-v} is the chemical reaction driven vibrational-electron-electronic energy change, S_{h-e} is the energy exchange between heavy particles and electrons, S_{e-i} is the energy removed from electrons during impact ionization reactions, and S_{t-v} is the energy exchange between translational-rotational and vibrational-electron-electronic modes.

$$\dot{w}_{ve} = S_{epg} + S_{c-v} + S_{h-e} + S_{e-i} + S_{t-v} \tag{13}$$

$$S_{epg} = -p_e \vec{\nabla} \cdot \vec{u} \tag{14}$$

The reaction driven vibrational energy added or removed during dissociation or recombination is modeled with either non-preferential or preferential treatment as seen in Equations 15-16, where D_s', $e_{el,s}$, $e_{ve,s}$, α, and D_s represent molecular dissociation or recombination driven energy change, electron energy, vibrational-electronic energy, dissociation potential fraction multiplier, and molecular dissociation potential, respectively. For this work, a non-preferential treatment is used, where molecules are created or destroyed at the average vibrational energy.

$$S_{c-v} = \sum_s \dot{w}_s \left(D_s' + e_{el,s}\right) \tag{15}$$

$$D_s' = \begin{cases} e_{ve,s} & \text{nonpreferential} \\ \alpha D_s & \text{preferential} \end{cases} \tag{16}$$

The energy transfer between heavy particles and electrons is modeled using Equations 17 and 18, where σ_{er} is the collision cross section between electrons and heavy particles [67].

$$S_{h-e} = 3R_u \rho_e (T_{tr} - T_{ve}) \sqrt{\frac{8R_u T_{ve}}{\pi M_e}} \sum_{s \neq e} \frac{\rho_s N_a}{M_s^2} \sigma_{er} \tag{17}$$

$$\sigma_{er} = \begin{cases} 2x10^{-19} & \text{electron} - \text{neutral collisions} \\ \dfrac{8\pi}{27} \dfrac{e^4}{k_B^2 T_e^2} \ln\left[1 + \dfrac{9 k_B^3 T_e^3}{4\pi n_e e^6}\right] & \text{electron} - \text{ion collisions} \end{cases} \tag{18}$$

The free electron impact ionization (EII) translational energy transfer during the EII process is defined by Equation 19, where I_s and α_{EII} are the first ionization energy of the species and average energy transferred as a fraction of I_s (usually set to 0.3), respectively [62–64].

$$S_{e-i} = \alpha_{EII} \left(\dot{w}_{N,EII} M_N I_N + \dot{w}_{O,EII} M_O I_O\right) \tag{19}$$

Lastly, the vibrational-translational relaxation model in Equations 20-25 follows a molar-averaged Landau-Teller inter-species relaxation time (τ_{sr}) using fits from Millikan and White. This formulation also includes high temperature relaxation correction factors from Park (τ_{ps}). Approximations are made in Equation 20 by Gnoffo et al. to obtain a relation that reduces the number of species-dependent parameters [1,67–70].

$$S_{t-v} = \sum_s \rho_s \frac{e_{vs}^* - e_{vs}}{\tau_s} \approx \frac{\rho C_{v_{ve}}}{\tau} (T_{tr} - T_{ve}) \tag{20}$$

$$\tau = \frac{\sum_{s=mol.} \frac{\rho_s}{M_s}}{\sum_{s=mol.} \frac{\rho_s}{M_s \tau_s}} \tag{21}$$

$$\tau_{ps} = \frac{1}{\sigma_s c_s n_s} = \frac{1}{\left[3x10^{-21}\left(\frac{5x10^4}{T_{tr}}\right)^2\right]\sqrt{\frac{8R_u T_{tr}}{\pi M_s}}\, n_s} \tag{22}$$

$$\langle \tau_s \rangle = \frac{\sum_r X_r}{\sum_r X_r / \tau_{sr}} \tag{23}$$

$$\tau_{sr} = \frac{101325}{p} \exp\left[A_{sr}\left(T_{tr}^{-\frac{1}{3}} - B_{sr}\right) - 18.42\right] \tag{24}$$

$$\begin{aligned} A_{sr} &= 1.16x10^{-3}\mu_{sr}^{\frac{1}{2}}\theta_{v_s}^{\frac{4}{3}} \\ B_{sr} &= 0.015\,\mu_{sr}^{\frac{1}{4}} \\ \mu_{sr} &= \frac{M_s M_r}{M_s + M_r} \end{aligned} \tag{25}$$

Baseline and uncertainty bounds for gas phase chemistry forward rate coefficients k_{f_k} for dissociation, neutral exchange, associative ionization, charge exchange and electron impact ionization reactions are depicted in Table A1. Baseline and uncertainty bounds for Landau-Teller inter-species relaxation times τ_{vt}, collision cross section between electrons and heavy particles σ_{er}, and average energy transferred as a fraction of first ionization energy α_{EII} are in Table A2.

2.3 Material Response: MOPAR-MD

The material response solver in this study MOPAR-MD is a tightly coupled flow-solid boundary update routine used with LeMANS that is capable of simulating two-dimensional and axisymmetric ablation and pyrolysis with material recession based on equilibrium surface energy balance relations or FRSC [29,71,72]. Time integration is with a first-order implicit method, with spatial discretization on an unstructured grid using second-order control volume finite element methods. Equations 26-29 represent the integral forms of the governing equations used, including solid and gas continuity, mixture energy, and momentum (Forchheimer's law), respectively.

$$\frac{d}{dt}\int_{cv}\rho_s dV - \int_{cs}\rho_s v_{cs}\, dS - \int_{cv}\dot{m}_s'''dV \;\; = 0 \tag{26}$$

$$\frac{d}{dt}\int_{cv}\phi\rho_g dV - \int_{cs}\phi\rho_g v_{cs}\, dS \; + \int_{cs}\phi\rho_g v_g dS - \int_{cv}\dot{m}_g'''dV = 0 \tag{27}$$

$$\frac{d}{dt}\int_{cv}\rho E\, dV - \int_{cs}\rho h v_{cs}\, dS + \int_{cs}\phi\rho_g h_g v_g\, dS + \int_{cs}\dot{q}''dA = 0 \tag{28}$$

$$\frac{\partial p}{\partial x} = \frac{\mu}{K}\phi v_g(1+Fo) \quad Fo = \frac{\beta K\rho\phi v_g}{\mu} \tag{29}$$

Mesh deformation, energy, solid phase, and gas-phase continuity equations are solved iteratively at each time step.

Fluid-solid coupling is conducted between LeMANS and MOPAR-MD by discretizing a time solution over which the material is responding into a number of discrete time steps. At each time step, a steady state flowfield solution is obtained from the flow solver, where flow boundary conditions are passed to the material response solver wall boundary. Using these new boundary conditions, the material response solver performs a transient analysis of the aforementioned surface mass and energy balances using the previous time step material response solution. The respective boundary solution values at different time points are then linearly interpolated. For all energy balance methods, mesh movements are calculated based upon the converged material response solution at each time step. This work uses and compares an ablating wall-heat flux surface energy balance via carbon-air equilibrium surface chemistry "extended" B' tables to determine ablating species blowing rates that are passed back to the flow solver. An example of the coupling process is outlined by Cross and Boyd (2019) in Figure 2.1, where a sufficiently converged LeMANS flowfield passes pressure, heat flux and recovery enthalpy at the wall to MOPAR [27]. Equations 26-29 are numerically solved to convergence with a nested mesh movement algorithm and the computed wall temperature, mass blowing flux rate, wall boundary locations, and wall species mass fractions are passed back to LeMANS.

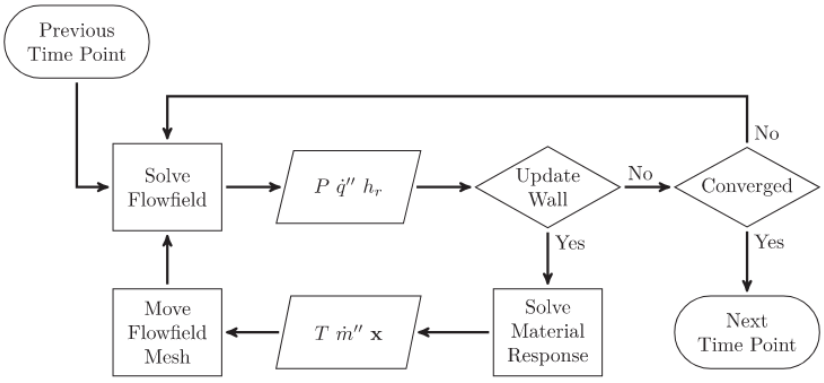

Figure 2.1: Flow and material response converged conjugate solution for LeMANS-MOPAR-MD adapted from [27].

The material response solver is called when three criteria are met. The first criterion is a defined minimum number of iterations required, ensuring that the flow has enough time to respond to updated wall conditions. The second is defined in Equation 30 as $\epsilon_{\dot{q}''}$:

$$\max\left(100\left|\frac{\dot{q}''^{\,n}_{j\in N}-\dot{q}''^{\,n-1}_{j\in N}}{\dot{q}''^{\,n-1}_{j\in N}}\right|\right)<\epsilon_{\dot{q}''} \tag{30}$$

This criterion ensures that MOPAR-MD is not called until the maximum percent difference in heat flux $\dot{q}''$ along all N wall points between the current and previous LeMANS iteration n is below the $\epsilon_{\dot{q}''}$ threshold. The last criterion:

$$\left|\frac{\dot{q}''^{\,n}_{RMS}-\dot{q}''^{\,n_{MR}}_{RMS}}{\dot{q}''^{\,n-1}_{RMS}}\right|\geq\epsilon_{\dot{q}''_{RMS}},\qquad \dot{q}''_{RMS}=\sqrt{\frac{1}{N}\sum_{j}^{N}\dot{q}''^{\,2}_{j}} \tag{31}$$

ensures that MOPAR-MD is not called if the difference in root mean square (RMS) of heat flux along all N wall points since last MOPAR-MD call iteration n_{MR} is below $\epsilon_{\dot{q}''_{RMS}}$. Unless otherwise stated, the minimum number of iterations required prior to a MOPAR call in this work is one, while $\epsilon_{\dot{q}''}=0.01\%$ and $\epsilon_{\dot{q}''_{RMS}}=1.0\%$.

The equilibrium surface thermochemistry "extended" B' tables are generated in this work by automating the Chemical Equilibrium Applications (CEA2) tool with a carbon-air gaseous mixture and a solid carbon (graphite) surface [73]. Following Candler (2012), the mass flux of carbon gas from the surface,

$$-\rho_w D_{c,w} \nabla Y_c|_w + Y_{c,w}\dot{m}_c'' = \dot{m}_c'' \tag{32}$$

provides a way to enforce mass conservation on a moving surface. $Y_{c,w}$ represents the total mass fraction of gaseous carbon at the wall. The normalized char blowing rate B_c' can then be estimated via

$$B_c' = \frac{\dot{m}_c''}{\rho_e u_e St_m} \approx \frac{\dot{m}_c''}{\rho_e u_e C_H} = \frac{Y_{c,w}}{1 - Y_{c,w}} = \frac{Y_{c,w}}{Y_{a,w}} \tag{33}$$

where $\dot{m}_c''$, $\rho_e u_e St_m$, $\rho_e u_e C_H$, $Y_{c,w}$, and $Y_{a,w}$ represent the gaseous carbon mass flux blowing rate, mass and enthalpy conductance, and gaseous carbon and air mass fractions, respectively. Equation 33 assumes that heat and mass transfer coefficients are equal ($St_m = C_H$) with unity Prandtl and Lewis numbers and a constant specific heat [74].

To produce the "extended" B' tables, the carbon-air gaseous mixture input into CEA2 is increased iteratively until saturation, i.e., when condensed carbon solids appear in the mixture. This process produces a distribution of carbon-air species for a given temperature and pressure combination as depicted in Figure 2.2 and Figure 2.3. The species mass fractions and specific enthalpies are interpolated from the B' tables and are used to estimate the enthalpy conductance via

$$\rho_e u_e C_H = \frac{\dot{q}_{FS}''}{h_r - h_w} \tag{34}$$

where the recovery enthalpy h_r is assumed to be equal to the flow solver stagnation enthalpy. An iterative procedure is used to estimate $\rho_e u_e C_H$ as wall enthalpy h_w is a function of the B' tables and is therefore a function of $\rho_e u_e C_H$.

Examining Figure 2.2, it is clear that below 3,200 K, the majority of the mixture is composed of nitrogen, carbon dioxide and carbon monoxide. Additionally, at these lower temperatures it is apparent that there are two carbon mass fraction plateaus from 300-1,000 K and 1,000-3,200 K, respectively. These are a function of assuming a saturated carbon-gaseous flow in equilibrium. This leads to a state for a given pressure and temperature where all oxidation reactions at the surface happen without resistance, i.e., oxidation reactions from atomic and molecular oxygen are only limited by mass conductance. As a result, utilizing these B'_C tables generally overpredicts normalized carbon blowing rates and associated recession for these lower temperature ranges. At temperatures above 3,200 K, multiple carbon-air species' mass fractions increase, with C_3 being a major constituent above approximately 3,500 K. In this region, carbon rich sublimation becomes dominant as vapor pressure differences drive the transition of carbon directly from solid to gas [1]. Figure 2.3 follows similar trends for different pressures and temperatures. These values, along with the species mass fractions and specific enthalpies, are what this work utilizes for equilibrium surface chemistry ablation.

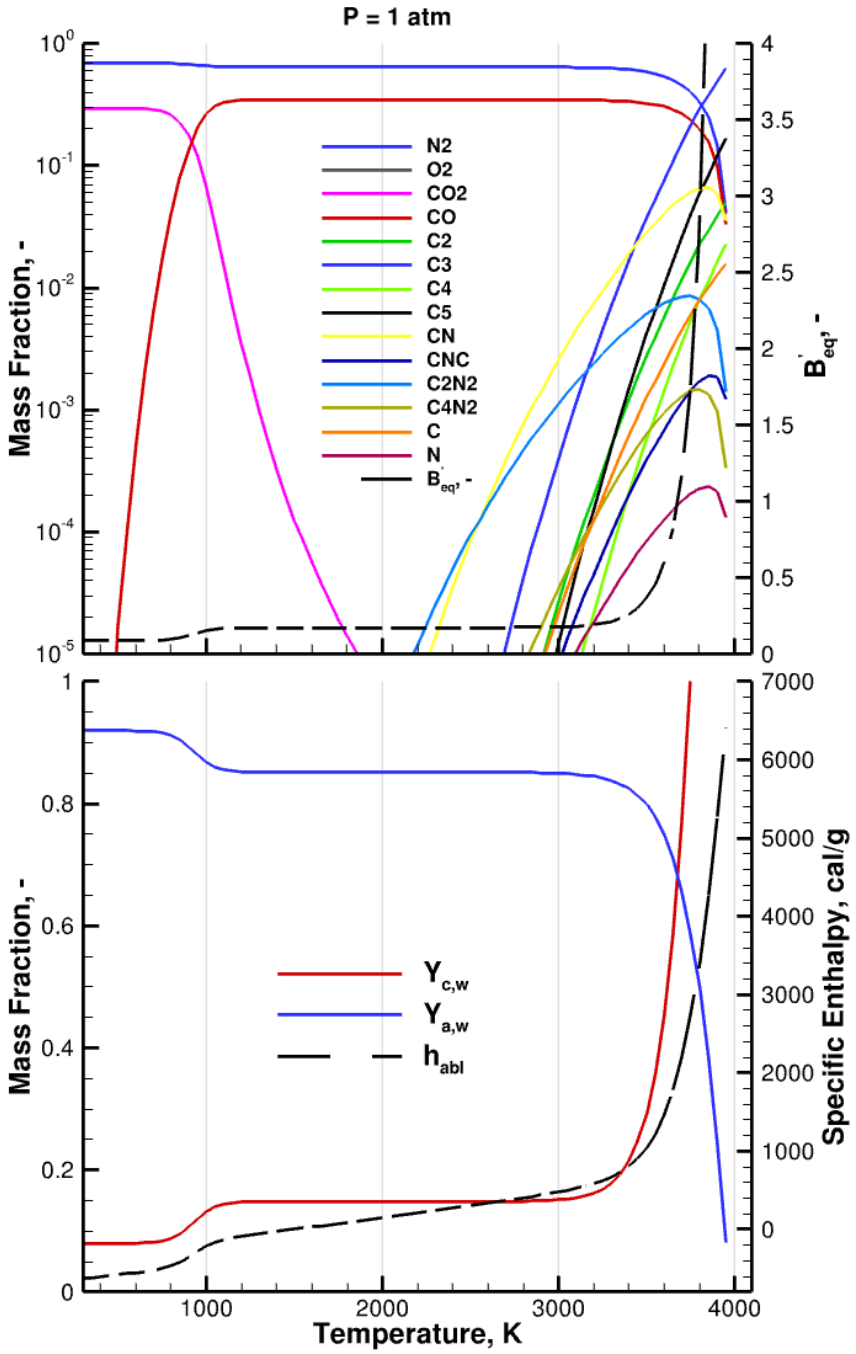

Figure 2.2: Equilibrium surface chemistry using CEA2 for a carbon-air mixture at 1 atm.

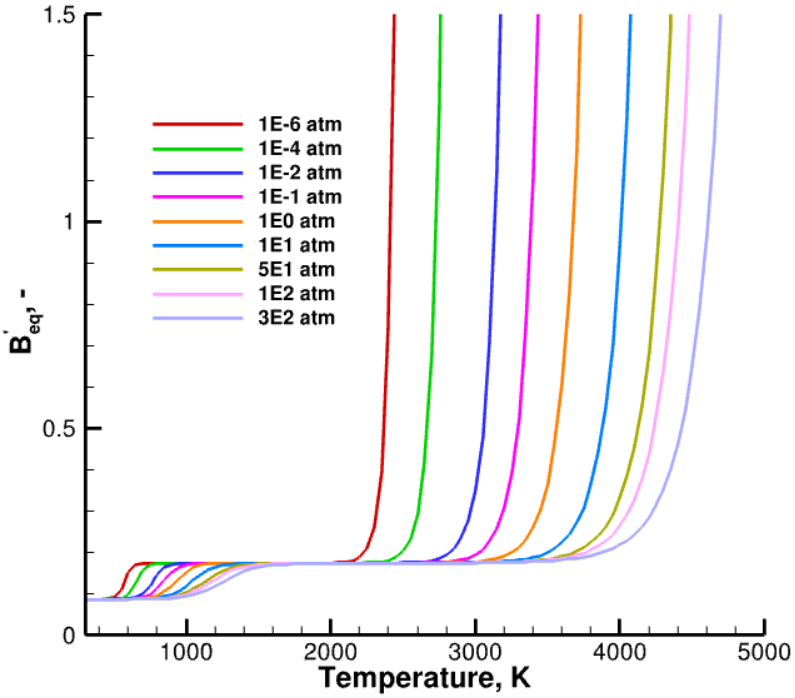

Figure 2.3: Normalized carbon mass flux rate equilibrium surface chemistry tables.

2.4 Finite Rate Surface Chemistry Model

2.4.1 Background

Although equilibrium surface chemistry models tend to overpredict ablation at various conditions, their primary advantages are inherent stability and efficiency when incorporated into high-fidelity hypersonic flow modelling. Starting in the 1960s, researchers focused on leveraging these benefits by using lookup tables similar to B'_C that incorporated finite rate ablation phenomena for lifted-entry applications that include oxidation and sublimation surface reaction processes. Models from Welsh (1963) and Scala and Gilbert (1965) include the use of equilibrium gas-phase thermochemistry and finite rate oxidation that predefine chemical kinetics and mass conductance models independently. The mass conductance in these frameworks follows that of the normalization factor in Equation 33 and redefined as

$$\rho_e h_m = \rho_e u_e St_m \tag{35}$$

where h_m is the mass-transfer coefficient. Scala and Gilbert (1965), Miller and Sutton (1966), and Metzger et al. (1967) all utilize modelling frameworks that incorporate a "resistances in series" analogy, whereby ATJ graphite ablation flux rates are dependent upon FRSC and mass diffusion resistances approximated by simple circuit analysis [75–79]. An example of this relation is depicted as

$$\dot{m}_c'' = \left[\frac{1}{\dot{m}_R''^2} + \frac{1}{\dot{m}_D''^2}\right]^{-1/2} \tag{36}$$

where $\dot{m}_R''$ and $\dot{m}_D''$ are the FRSC and diffusion limited mass flux rates, respectively. Although these models incorporate finite rate ablation thermochemistry phenomena, the approximate carbon mass flux rates are restricted to a single case. Other models including the Multicomponent Ablation Thermochemistry (MAT) utilize surface 'pseudo elements' that react via kinetically controlled mechanisms to build B_C' tables, but these approximations too require independent mass conductance and surface kinetics approximations tied to each experiment. More recent models like those of Zhluktov and Abe (1999), Poovathingal et al. (2017), Swaminathan-Gopalan et al. (2018) and Prata (2022) incorporate more complex reaction mechanisms derived from beam experiments [2,26,28,80,81]. Although more accurate at predicting recession, these models require more intrusive integration into tightly coupled hypersonic flow/material response models and are subject to stability and computational expense challenges.

A novel model is created in this work to leverage the simplicity and robustness of normalized carbon blowing flux rate lookup tables while incorporating finite rate processes. The heart of this model relies upon incorporating a variant of the Damköhler number, a dimensionless parameter that relates chemical reaction rates to transport phenomena rates. The following conventions are used for defining the Damköhler number,

$$Da = \frac{\bar{k}_{O_n}}{h_m} = \frac{\bar{k}_{O_n}}{u_e St_m} \tag{37}$$

$$\overline{Da}_{\rho_e} = \frac{Da}{\rho_e} = \frac{\bar{k}_{O_n}}{\rho_e u_e St_m} \left[\frac{m^3}{kg}\right] \tag{38}$$

where Da is the unitless Damköhler number defined by oxidizer FRSC rate $\bar{k}_{O_n}$ normalized by the mass transfer coefficient h_m. $\overline{Da}_{\rho_e}$is normalized by the boundary layer edge density to relate FRSC kinetics to mass conductance [82]. The remainder of this work will use the term Damköhler number to define $\overline{Da}_{\rho_e}$. Ultimately, this ratio will enable the formation of generalized tabulated B'_C tables for a given surface chemistry model without the need for extensive integration into complex and often proprietary hypersonic source codes. The following sections outline the development of the novel ablation model that incorporates a generalized tabular lookup scheme for normalized carbon blowing rates while allowing for multiple finite rate chemistry effects. Chapter 6 further includes this model's parameter variations for uncertainty quantification, benchmarking and verification as well as comparisons with experimental results at different flow conditions.

2.4.2 Oxidation FRSC Only

The regimes involved in the finite rate oxidation ablation model for a graphite carbon surface are depicted in Figure 2.4. At each regime are state variables including concentrations $\tilde{C}$ and mass fractions $\tilde{K}$ related by,

$$\tilde{C} = \rho\tilde{K} \tag{39}$$

where the subscripts e, w, and s represent the boundary layer edge, near wall layer and surface regimes, respectively. Oxidizer mass diffusion $\tilde{J}''_{diff,O_n}$ and gas surface kinetics flux $\tilde{J}''_{diff,O_n}$represent the mass change between regimes per area per time, while the inverse of mass conductance $\rho_e h_m$ and oxidizer FRSC coefficient $\bar{k}_{O_n}$ represent resistance terms for this mass transfer. The potential drivers for diffusion and surface kinetics are mass fractions $\tilde{K}$ and concentration differences $\tilde{C}$, respectively. The simple circuit analysis on the right of Figure 2.4 is analogous to Ohm's law, where the current, voltage and resistances are represented by the mass flux rates, mass fractions or concentration differences, and the mass conductance and finite rate kinetics, respectively. Mass continuity (Kirchhoff's current law by analogy)

relates $\tilde{J}''_{diff,O_n} = \tilde{J}''_{GSI,O_n}$ which allows for calculation of the overall mass transfer of the system as a sum of resistances in series.

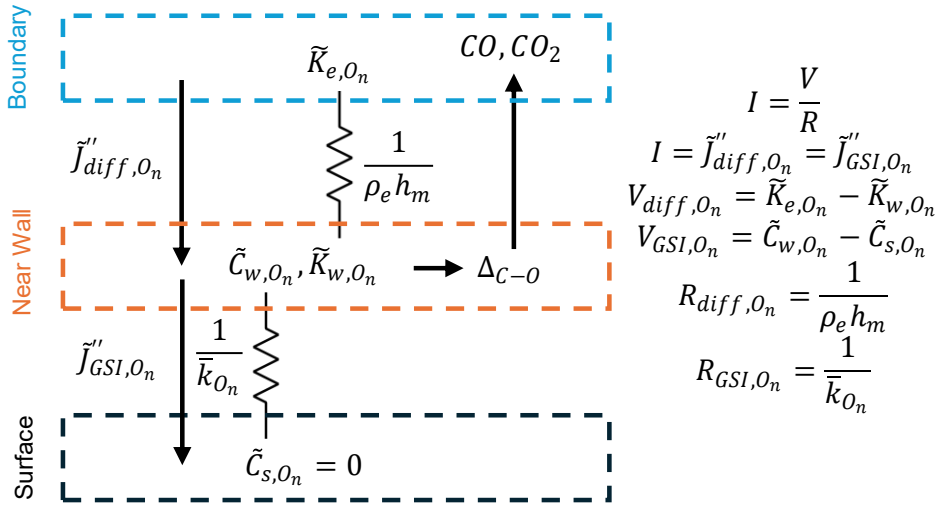

Figure 2.4: Oxidation only finite rate surface chemistry circuit analogy.

In its current form, the model surface regime consists of a uniform, smooth ATJ graphite thermal protection system layer where oxidation occurs. Activation site fidelity as well as finite rate adsorption/desorption, Eley-Rideal, and Langmuir-Hinshelwood reactions are currently not considered. The surface is also assumed to be oxygen starved with an oxidizer concentration $\tilde{C}_{s,O_n} = 0\ kg/m^3$ and the molar mass of the wall is set to 10% greater than that of molecular oxygen [76]. The near wall combustion layer indicates where ablative products react within the boundary layer. This model assumes that all gaseous chemical reactions in this localized region occur in equilibrium following the reactions and equilibrium constants

$$\begin{aligned} O_2(g) &\overset{1}{\rightleftharpoons} 2O(g) \\ 2CO_2 &\overset{2}{\rightleftharpoons} 2CO(g) + O_2(g) \\ CO_2(g) &\overset{3}{\rightleftharpoons} CO(g) + O(g) \end{aligned} \tag{40}$$

$$K_{p,1} = \frac{P_O^2}{P_{O_2}}$$
$$K_{p,2} = \frac{P_{CO}^2 P_{O_2}}{P_{CO_2}^2} \quad (41)$$
$$K_{p,3} = \frac{P_{CO} P_O}{P_{CO_2}}$$

where P represents the partial pressures of the gas constituents including O_2, O, CO_2, and CO. Equilibrium constants as a function of temperature are sourced from JANAF equilibrium tables [83]. The Δ_{C-O} term represents the wall gas carbon to oxygen stoichiometric ratio that determines carbon species apportionment to the boundary layer edge. Lastly, the boundary layer edge regime represents the area where the gaseous phase constituents and associated flux rates are passed to LeMANS. The current assumption for this regime is that the edge oxidizer mass fraction follows that of standard atmosphere molecular oxygen ($\widetilde{K}_{e,O_n} = 0.233$). Wall regime pressure P_w, temperature T_w and Damköhler number $\overline{Da}_{\rho_e}$ are utilized with oxidizer mass flux rate continuity $\dot{m}''_{O_n}$ to form

$$\rho_w = \frac{P_w M_w}{R_u T_w} \quad (42)$$

$$\dot{m}''_{O_n} = \tilde{J}''_{diff,O_n} = \frac{\widetilde{K}_{e,O_n} - \widetilde{K}_{w,O_n}}{\frac{1}{\rho_e h_m}} = \tilde{J}''_{GSI,O_n} = \frac{\tilde{C}_{w,O_n} - \tilde{C}_{s,O_n}}{\frac{1}{\bar{k}_{O_n}}} \quad (43)$$

$$\widetilde{K}_{w,O_n} = \frac{\widetilde{K}_{e,O_n}}{1 + \frac{\bar{k}_{O_n}}{\rho_e h_m}\rho_w} = \frac{\widetilde{K}_{e,O_n}}{1 + \rho_w \overline{Da}_{\rho_e}} \quad (44)$$

where the near wall layer oxidizer mass fraction $\widetilde{K}_{w,O_n}$ is used with the relations

$$\widetilde{K}_{w,O_n} = \frac{P_O}{P_w}\frac{M_O}{M_w} + \frac{P_O}{P_w}\frac{M_O}{M_w} \quad (45)$$

and the definition of $K_{p,1}$ in Equation 41 to obtain the oxidizer constituent partial pressures via

$$P_O = \frac{-\frac{M_O}{M_w P_w} + \sqrt{\left(\frac{M_O}{M_w P_w}\right)^2 - 4\left(\frac{M_{O_2}}{M_w K_{p,1} P_w}\right)\left(-K_{w,O_n}\right)}}{\frac{2M_{O_2}}{M_w K_{p,1} P_w}} \tag{46}$$

$$P_{O_2} = \frac{P_O^2}{K_{p,1}} \tag{47}$$

The stoichiometric ratio of carbon to oxygen can then be determined from the equilibrium constants in Equation 41 and these partial pressures using

$$\Delta_{C-O} = \frac{P_{CO_2} + P_{CO}}{2P_{CO_2} + P_{CO}} \frac{M_C}{M_O} = \frac{1+\delta}{2+\delta} \frac{M_C}{M_O}, \qquad \delta = \frac{P_{CO}}{P_{CO_2}} = \frac{P_O K_{p,2}}{P_{O_2} K_{p,3}} \tag{48}$$

where δ represents the molar ratio of carbon monoxide to carbon dioxide. Once this ratio is known, the carbon mass flux can be calculated following

$$\dot{m}''_{O_n} = \bar{k}_{O_n} \rho_w \widetilde{K}_{w,O_n} = \frac{\bar{k}_{O_n} \rho_w \widetilde{K}_{e,O_n}}{1 + \frac{\bar{k}_{O_n}}{\rho_e h_m} \rho_w} = \frac{\rho_e u_e St_m \widetilde{K}_{e,O_n}}{1 + \frac{1}{\rho_w} \frac{\rho_e u_e St_m}{\bar{k}_{O_n}}} \tag{49}$$

$$\Gamma = \frac{1}{1 + \left(\rho_w \overline{Da}_{\rho_e}\right)^{-1}} \tag{50}$$

$$\dot{m}''_C = \Delta_{C-O} \dot{m}''_{O_n} = \Delta_{C-O} \rho_e u_e St_m \Gamma \widetilde{K}_{e,O_n} \tag{51}$$

where Γ is a fraction between 0 and 1 that represents the chemical resistance as a function of aggregate density at the wall regime and the Damköhler number. Finally, the B'_C value for a given wall temperature, pressure and Damköhler number is found via

$$B'_C = \frac{\dot{m}''_C}{\rho_e u_e St_m} = \frac{\Delta_{C-O} \dot{m}''_{O_n}}{\rho_e u_e St_m} = \Delta_{C-O} \frac{1}{1 + \left(\rho_w \overline{Da}_{\rho_e}\right)^{-1}} \widetilde{K}_{e,O_n} = \Delta_{C-O} \Gamma \widetilde{K}_{e,O_n} \tag{52}$$

indicating a simple relation that includes finite rate surface chemistry effects without the need to embed surface kinetics or mass conductance models.

Model trends are depicted in Figure 2.5 at atmospheric pressure. The dark blue, light blue, and yellow regions in the B' figure (top right) represents the wall temperatures and Damköhler values where the normalized carbon mass flux rate is limited by surface kinetics, CO_2 diffusion plateau, and CO diffusion plateau, respectively. The decrease in Γ to near unity drives the majority of the reduction in B'_C as the kinetic rates are at the same scale as mass conductance. The other surveyed parameters also follow expected trends, where Δ_{C-O} and oxygen dissociation fraction are mainly a function of temperature, and the oxygen wall mass fraction and partial pressures are a function of kinetic rates for a given pressure and mass conductance. The B'_C CO plateau is not obtained until temperatures greater than 2,000 K, which does not well estimate experimental values at these conditions until there is relatively large mass conductance. Additionally, there is no sublimation present at higher temperatures as seen in the literature (see Chapter 6). These last two observations motivate the inclusion of sublimation processes into the model. The following two sections outline incorporating sublimation under oxygen rich and oxygen rich conditions.

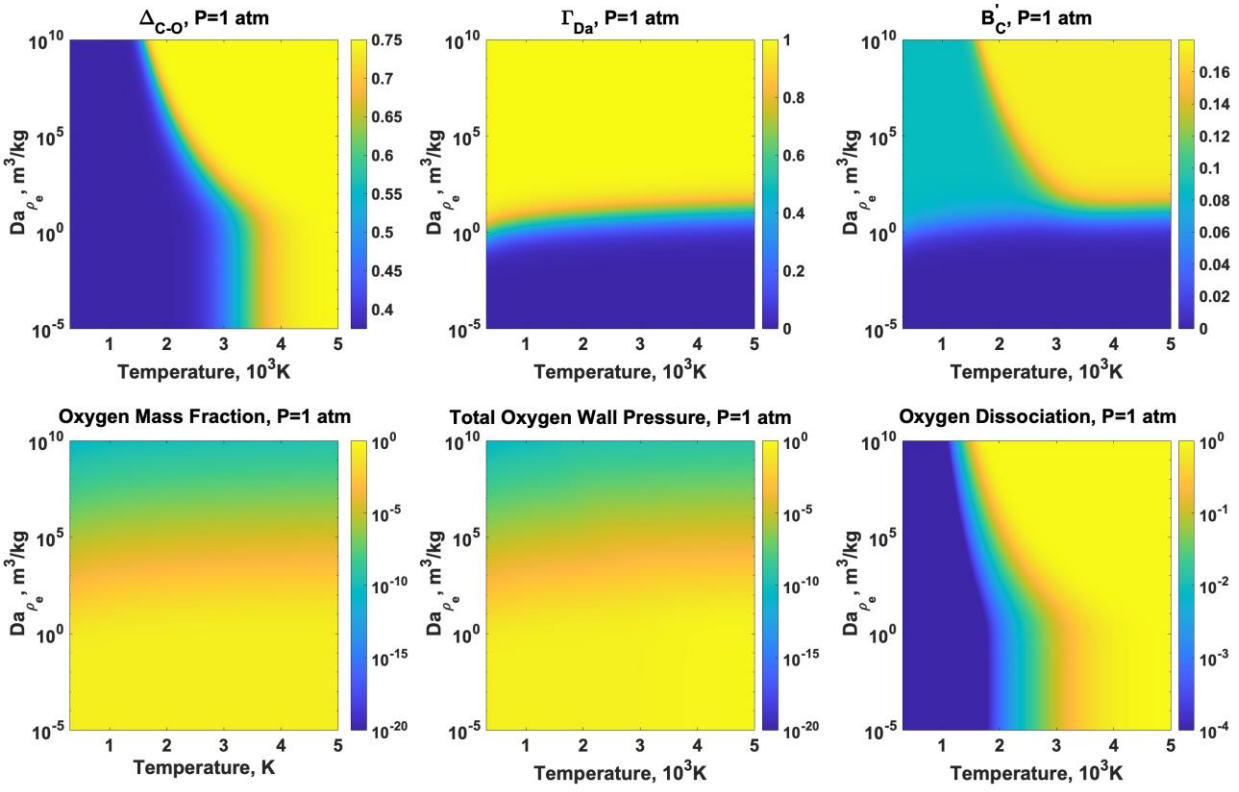

Figure 2.5: Oxidation only FRSC results at 1 atm

2.4.3 Oxidation and Sublimation FRSC: Oxygen Rich Case

A similar process is undertaken for determining B'_C values while including surface sublimation rate processes. Figure 2.6 depicts the same regimes as the oxidation-only model while including the direct sublimation from the graphite surface given a resistance to sublimation as the inverse of the sublimation kinetic rate coefficient $\bar{k}_{sub,C}$, the a carbon concentration driving potential $\tilde{C}_{s,C} - \tilde{C}_{w,C}$, and sublimation mass flux rate $\tilde{J}''_{sub,C}$. The concentration of carbon at the near wall layer is assumed to be negligible.

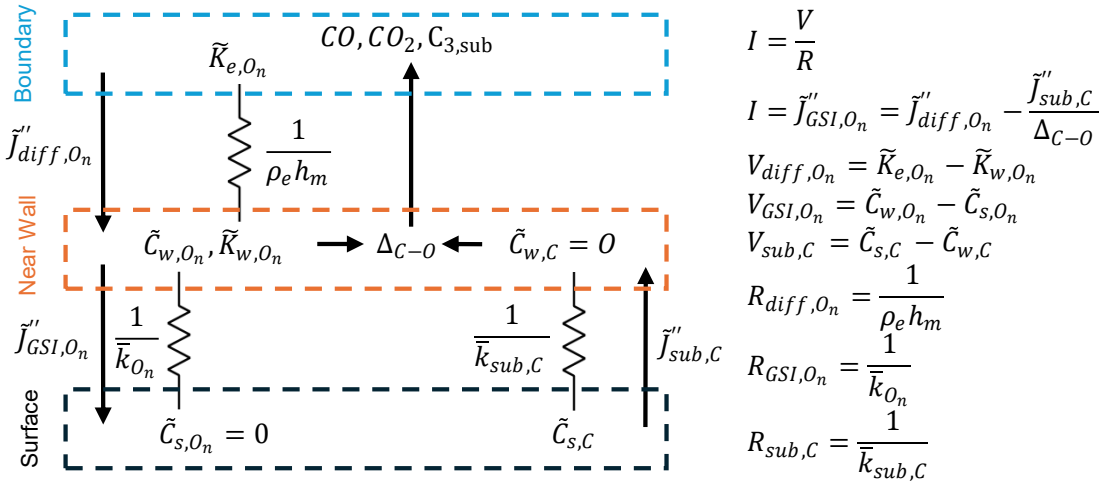

Figure 2.6: Oxidation and sublimation finite rate surface chemistry, oxygen rich case circuit analogy.

The mass flux rate continuity of oxidizer enforces

$$\dot{m}''_{O_n} = \tilde{J}''_{GSI,O_n} - \frac{\tilde{J}''_{sub,C}}{\Delta_{C-O}} = \frac{\tilde{C}_{w,O_n} - \tilde{C}_{s,O_n}}{\frac{1}{\bar{k}_{O_n}}} = \frac{\tilde{K}_{e,O_n} - \tilde{K}_{w,O_n}}{\frac{1}{\rho_e h_m}} - \frac{1}{\Delta_{C-O}} \frac{\tilde{C}_{s,C} - \tilde{C}_{w,C}}{\frac{1}{\bar{k}_{sub,C}}} \tag{53}$$

and leads to an expression for the oxidizer concentration at the wall

$$\bar{k}_{sub,C} \tilde{C}_{s,C} = \rho_e u_e St_m B'_{C,sub+}$$

$$\tilde{K}_{w,O_n} = \left(\frac{1}{1 + \overline{Da}_{\rho_e} \rho_w} \right) \left(\tilde{K}_{e,O_n} - \frac{B'_{C,sub+}}{\Delta_{C-O}} \right), \qquad B'_{C,sub+} = \frac{\bar{k}_{sub,C} \tilde{C}_{s,C}}{\rho_e u_e St_m} = \frac{\dot{m}''_{C,sub+}}{\rho_e u_e St_m} \tag{54}$$

where $B'_{C,sub+}$ represents the mass conductance normalized mass flux rate of sublimated carbon. Equation 41, Equation 45, and Equation 54 are then used to evaluate the partial pressures P_{O_2} and P_O via

$$\widetilde{K}_{w,O_n} = \left(\frac{1}{1+\overline{Da}_{\rho_e}\rho_w}\right)\left(\widetilde{K}_{e,O_n} - \frac{B'_{C,sub+}}{\Delta_{C-O}}\right) = \frac{P_{O_2}}{P_w}\frac{M_{O_2}}{M_w} + \frac{P_O}{P_w}\frac{M_O}{M_w} \tag{55}$$

$$\Delta_{C-O} = \frac{1+\delta}{2+\delta}\frac{M_C}{M_O} = \frac{1+\dfrac{P_O}{P_{O_2}}\dfrac{K_{p,2}}{K_{p,3}}}{2+\dfrac{P_O}{P_{O_2}}\dfrac{K_{p,2}}{K_{p,3}}}\frac{M_C}{M_O} = \frac{1+\dfrac{\sqrt{P_{O_2}K_{p,1}}}{P_{O_2}}\dfrac{K_{p,2}}{K_{p,3}}}{2+\dfrac{\sqrt{P_{O_2}K_{p,1}}}{P_{O_2}}\dfrac{K_{p,2}}{K_{p,3}}}\frac{M_C}{M_O} \tag{56}$$

where solving for P_{O_2} in Equations 55 and 56 yields the cubic relation

$$\begin{gathered} X = \sqrt{P_{O_2}} \\ 0 = AX^3 + BX^2 + CX + D \\ A = \frac{M_{O_2}}{M_w P_w} \\ B = \frac{\sqrt{K_{p,1}}}{M_w P_w}\left(\frac{M_{O_2}K_{p,2}}{K_{p,3}} + M_O\right) \\ C = \frac{M_O K_{p,2}K_{p,1}}{M_w P_w K_{p,3}} + \frac{2M_O B'_{C,sub+}}{M_C\left(1+\overline{Da}_{\rho_e}\rho_w\right)} - \frac{\widetilde{K}_{e,O_n}}{1+\overline{Da}_{\rho_e}\rho_w} \\ D = \frac{K_{p,2}\sqrt{K_{p,1}}}{K_{p,3}\left(1+\overline{Da}_{\rho_e}\rho_w\right)}\left(\frac{M_O}{M_C}B'_{C,sub+} - \widetilde{K}_{e,O_n}\right) \end{gathered} \tag{57}$$

After solving Equation 57, P_{O_2}, P_O, and Δ_{C-O} are found via the definition of $K_{p,1}$ in Equation 41 and Equation 56. The mass flux rate of carbon is then found as the summation of oxidation and sublimation flux rates

$$\dot{m}''_c = \Delta_{C-O}\dot{m}''_{O_n} + \tilde{J}''_{sub} = \Delta_{C-O}\bar{k}_{O_n}\rho_w\widetilde{K}_{w,O_n} + \rho_e h_m B'_{c,sub+} = \frac{\Delta_{C-O}\rho_e h_m}{1+\left(\rho_w\overline{Da}_{\rho_e}\right)^{-1}}\widetilde{K}_{e,O_n} + \frac{\rho_e h_m B'_{C,sub+}}{1+\rho_w\overline{Da}_{\rho_e}} \tag{58}$$

and the B'_C value is finally determined

$$B'_C = \frac{\dot{m}''_c}{\rho_e u_e St_m} = \Delta_{C-O}\left[\frac{1}{1+\left(\rho_w\overline{Da}_{\rho_e}\right)^{-1}} + \frac{1}{1+\rho_w\overline{Da}_{\rho_e}}\frac{B'_{c,sub+}}{\Delta_{C-O}\widetilde{K}_{e,O_n}}\right]\widetilde{K}_{e,O_n} \tag{59}$$

where the term in brackets represents the combined effects of oxidation and sublimation rate limiters.

Including the effects of sublimation into the model results in a transition to the CO plateau at temperatures below 2,000 K at atmospheric pressure and a mass conductance of 1.0 $kgm^{-2}s^{-2}$ as seen in Figure 2.8. As the wall temperature increases for a given Damköhler number, pressure and mass conductance, the sublimation contributions increase until the $CO\ B'$ plateau at 0.175. Although sublimation in the model contributes to carbon mass flux rate at lower temperatures, this does not include sublimation effects from carbon vapor pressure at temperatures above 3,000 K. The next section attempts to model this carbon rich environment after obtaining the $CO\ B'_C$ plateau.

2.4.4 Oxidation and Sublimation FRSC: Carbon Rich Case

The carbon rich oxidation and sublimation ATJ graphite ablation model in Figure 2.7 is applied after the B' values reach the $CO\ B'_C$ plateau of 0.175.

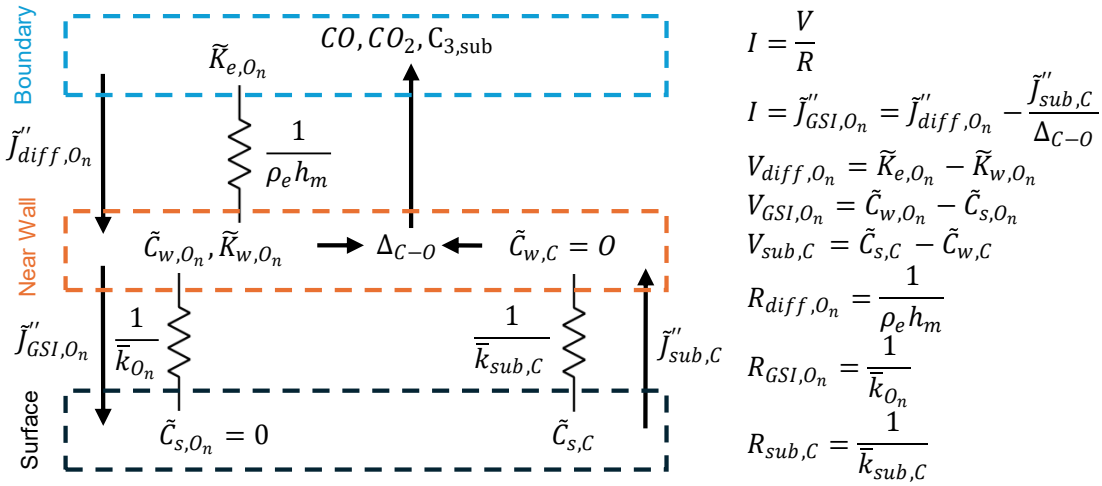

Figure 2.7: Oxidation and sublimation finite rate surface chemistry, carbon rich case circuit analogy.

A similar process to the oxygen rich case is employed, where oxidizer and carbon mass flux rate balances are utilized. The oxidizer mass flux continuity balance

$$\dot{m}''_{O_n} = \tilde{J}_{diff,O_n} = \frac{\widetilde{K}_{e,O_n} - \widetilde{K}_{w,O_n}}{\frac{1}{\rho_e h_m}} = \frac{\tilde{J}_{diff,C}}{\Delta_{C-O}} - \frac{\tilde{J}_{sub,C}}{\Delta_{C-O}} = \frac{1}{\Delta_{C-O}}\left(\frac{\tilde{C}_{s,C} - \tilde{C}_{w,C}}{\frac{1}{\bar{k}_{sub,C}}} - \frac{\widetilde{K}_{w,C} - \widetilde{K}_{e,C}}{\frac{1}{\rho_e h_m}}\right) \quad (60)$$

is used to find the carbon mass fraction at the wall

$$\widetilde{K}_{w,C} = \frac{\bar{k}_{sub,C}\rho_w \widetilde{K}_{s,C} - \Delta_{C-O}\rho_e h_m \widetilde{K}_{e,O_n}}{\bar{k}_{sub,C}\rho_w + \rho_e h_m} \tag{61}$$

Equation 61 is then used along with the carbon mass flux continuity to obtain

$$\begin{gathered}\dot{m}_C'' = \rho_e h_m \widetilde{K}_{w,C} + \Delta_{C-O}\rho_e h_m \widetilde{K}_{e,O_n} = \rho_e h_m \frac{\bar{k}_{sub,C}\rho_w \widetilde{K}_{s,C} - \Delta_{C-O}\rho_e h_m \widetilde{K}_{e,O_n}}{\bar{k}_{sub,C}\rho_w + \rho_e h_m} + \Delta_{C-O}\rho_e h_m \widetilde{K}_{e,O_n} \\ \dot{m}_C'' = \frac{\rho_e h_m \widetilde{K}_{s,C} + \Delta_{C-O}\rho_e h_m \widetilde{K}_{e,O_n}}{1 + \frac{\rho_e h_m}{\bar{k}_{sub}\rho_w}}\end{gathered} \tag{62}$$

where the saturation mass fraction of carbon vapor under equilibrium conditions $\widetilde{K}_{s,C}$ is estimated via

$$\widetilde{K}_{s,C} = \frac{M_{C_3} P_{sat}}{M_{total} P_w} \tag{63}$$

$$M_{total} = M_{C_3}\widetilde{K}_{s,C} + M_w\left(1 - \widetilde{K}_{s,C}\right) \tag{64}$$

to obtain

$$\widetilde{K}_{s,C} = \frac{-M_w + \sqrt{M_w + \frac{4P_{sat}M_{C_3}}{P_w}\left(M_{C_3} - M_w\right)}}{2\left(M_{C_3} - M_w\right)} \tag{65}$$

Finally, the normalized carbon mass flux rate is defined as

$$B_C' = \frac{\dot{m}_C''}{\rho_e u_e St_m} = \frac{\widetilde{K}_{s,C} + \Delta_{C-O}\widetilde{K}_{e,O_n}}{1 + \frac{\rho_e h_m}{\bar{k}_{sub}\rho_w}} = \frac{\widetilde{K}_{s,C} + \Delta_{C-O}\widetilde{K}_{e,O_n}}{1 + \left(\rho_w \overline{Da}_{sub,\rho_e}\right)^{-1}} \tag{66}$$

where the vapor pressure driven sublimation Damköhler number is defined as

$$\overline{Da}_{sub,\rho_e} = \frac{\bar{k}_{sub,C}}{\rho_e u_e St_m} = \frac{B'_{C,sub+}}{\rho_w \widetilde{K}_{s,C}} \tag{67}$$

The major assumptions with this carbon rich regime are that the mass fraction of oxidizer at the wall and C_3 at the boundary layer edge are negligible. The latter assumption is shown in Section 6.4 to be the main

explanation for under prediction of B_C' values when compared with equilibrium and experimental values. These comparisons, as well as model implementation in the context of LeMANS-MOPAR are found within Chapter 6. Baseline and uncertainty bounds for oxidation and sublimation rate coefficient parameters are also depicted in Section 6.2 and Table A7.

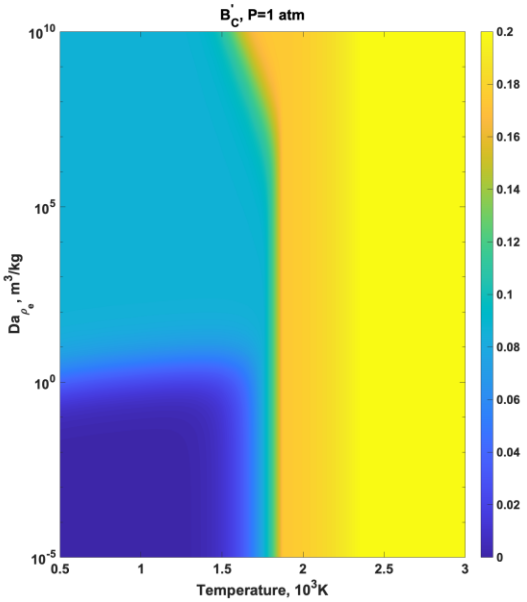

Figure 2.8: Oxidation and sublimation results at 1 atm and 1 kgm^{-2}s^{-1}.

2.5 Radiation: NEQAIR

NASA's Nonequilibrium and Equilibrium Radiative Transport and Spectra Program (NEQAIR) code version 15.3 utilized in this work is a high-resolution, spectral "line-by-line" solver that calculates emission and absorption of atomic and molecular electronic and infrared band systems [44,84,85]. NEQAIR solves radiative transport along discretized lines of sight (LOSs) and requires temperature and species number density data, with boundary conditions specified at the start and end of each LOS. In addition to bound-bound radiation for atomic systems N, O, C, and N^+, NEQAIR can also estimates bound-free and free-free continuum radiation for N, O, and C. Excited electronic state populations are calculated via Boltzmann or non-Boltzmann distributions using electronic temperatures (T_{ve} for the two-temperature models in this work). Non-Boltzmann distribution solutions are utilized in this work and incorporate variations of quasi-

steady state (QSS) assumptions, i.e., that excited electronic state population rate changes are much less than the net excitation/quenching rates between energy levels. The implementation of the QSS assumption impacts the electronic state-specific master equation,

$$\frac{dn_i}{dt} = \sum_j \left[\left(k_{ji}^M n_M + k_{ji}^{el} n_e + B_{ji}\int \phi_{ji}(\lambda) I(\lambda) d\lambda\right) n_j - \left(k_{ij}^M n_M + k_{ij}^{el} n_e + B_{ij}\int \phi_{ij}(\lambda) I(\lambda) d\lambda\right) n_i\right] + \sum_{j>i} A_{ji} n_j - \sum_{i>j} A_{ij} n_i + \sum_k r_k^i - r_{-k}^i n_i \tag{68}$$

where the first summation term represents the net population change due to collisional and stimulated radiative processes, the second and third summations represent the net population change from spontaneous emission, and the fourth summation term represents the net population change from state specific reactions [1,86]. This balance can be organized into the matrix form below,

$$(\boldsymbol{M}_{coll} + \boldsymbol{M}_{rad} + \boldsymbol{M}_{chem})\boldsymbol{n} - \boldsymbol{b} = \frac{d\boldsymbol{n}}{dt} - \nabla \cdot \boldsymbol{J} + \boldsymbol{r}_{k \notin QSS} + \boldsymbol{r}_{k \in QSS} \approx \alpha_{flux}\boldsymbol{n} \tag{69}$$

$$\boldsymbol{n} \approx \left(\boldsymbol{M} - \alpha_{flux}\boldsymbol{I}\right)^{-1} - \boldsymbol{b} \tag{70}$$

where the left-hand side of Equation 69 terms $\boldsymbol{M}_{coll}$, $\boldsymbol{M}_{rad}$, $\boldsymbol{M}_{chem}$, $\boldsymbol{n}$, and $\boldsymbol{b}$ represent collisional, radiative, and chemical excitation rate matrices; species population vector, and external reaction population rates of change. In the ideal case, the right-hand side of Equation 69 would equal zero. However, temporal, diffusion and convection, and state specific chemical rate differences between the LEMANS-MOPAR and NEQAIR can have similar magnitudes to the left-hand side under certain conditions. The terms $\frac{d\boldsymbol{n}}{dt}$, $\nabla \cdot \boldsymbol{J}$, and $\boldsymbol{r}$ represent these effects, respectively. NEQAIR can handle these differences with various assumptions, the most stable of which is invoking a flux limiting term α_{flux} such that the state population rate of change of a given species is proportional to the state population. The α_{flux} term is iterated to enforce species state continuity along the LOS. Other methods for solving the master equation include temporal and chemical rate limited assumptions in a similar manner. These methods and their numerical stability are shown to be significant in later case studies (see Chapter 7).

Heavy particle collisional quenching rate terms k_{ij}^{M} in Equation 68 are further defined by categories of atom and molecule collision partners. Rate coefficients for the collision induced excitation of atoms with heavy-particles (HP-CIE) is hard coded within NEQAIR following Lemal et al. (2016) [87],

$$k_{ij}^{M,atom} = \sigma_0 \sqrt{\frac{8k_B^3 T_{tr}^3}{\pi\mu}} \frac{E_1\left(\frac{E_j - E_i}{k_B T_{tr}}\right)}{E_j - E_i} \tag{71}$$

where $\sigma_0 = 1.210^{-19} cm^2$, μ is the reduced mass and the first-order exponential integral E_1 is a function of $(E_j - E_i)/(k_B T_{tr})$ assuming a Maxwellian energy distribution of heavy-particles. Rate coefficients for the collisional quenching of molecules with heavy particles are calculated via

$$k_{ij}^{M,molec} = k_{q,0} \sqrt{\frac{T_{tr}}{300}} exp(-\theta_{hp}/T_{tr}) \tag{72}$$

where $k_{q,0}$ and θ_{hp} represent quenching rates for various molecule-heavy state transitions and the characteristic excitation temperature for heavy particle collision quenching, respectively. Baseline and uncertainty intervals for $k_{q,0}$ used in this work are depicted in Table A5. Atom electron collision induced excitation (E-CIE) rate coefficients are estimated via

$$k_{ij}^{el,atom} = C_{el} \left(\frac{T_{el}}{10{,}000}\right)^{\eta_{el}} \exp\left(-\frac{E_{th}}{k_B T_{ve}}\right) \tag{73}$$

where C_{el} and η_{el} for a given electronic state pair are fit to average thermal energy delineated cross sections from NIST and Huo et. al. (2015) [66,88]. Baseline and uncertainty bounds for C_{el}, η_{el}, and E_{th} (in units of cm^{-1}) used in this work are listed in Table A3 and Table A4 for atomic oxygen and nitrogen, respectively. Molecule E-CIE rate coefficients are estimated based on Park (1990) following

$$
\begin{gathered}
k_{ij}^{el,molec} = \left[\sum_{v,v'} S_{vv'} q_{vv'} exp\left(-\frac{E_v}{T_{ve}}\right)\right] / Q_{vr} \\
S_{vv'} = 5.47x10^{-11} n_e \sqrt{T_{ve}} exp\left(-\frac{\Delta E_{ve}}{T_{ve}}\right) I \\
I = \int_0^\infty (2J)^2 exp\left[-\left(\frac{B_e' - B_e}{T_{ve}} + \frac{B_e}{T_{tr}}\right) J^2\right] \left(C + B\frac{B_e' - B_e}{T_{ve}} J^2\right) dJ \\
C = \frac{\Delta E_{ve}}{T_{ve}} B + A
\end{gathered}
\tag{74}
$$

where A and B are constants of integration that have been updated from Park's formulation to be dependent upon T_{ve} through a cross section dependence,

$$
\begin{gathered}
A = \int_0^\infty \frac{\sigma(\xi T_{ve})}{\pi a_0^2} \exp(-\xi)\, \xi d\xi \\
B = \int_0^\infty \frac{\sigma(\xi T_{ve})}{\pi a_0^2} \exp(-\xi)\, d\xi
\end{gathered}
\tag{75}
$$

where the cross sections depend upon electron energy [1,89]. Baseline and uncertainty bounds for cross sections at various energies $\sigma(\xi T_{ve})$ used in this work are listed in Table A6.

Absorption and stimulated emission terms within the first summation term of Equation 68 incorporate a local self-absorbance approximation known as the escape factor. This parameter physically represents the probability that an emitted photon from a point along the LOS is absorbed within a characteristic distance. For this work, the local approximation characteristic length is set to $1.0x10^{-2}$ m. In previous nonequilibrium radiation validation experiments, developers of NEQAIR recommend that the characteristic length be the same order of magnitude as the shock-standoff distance [59,84,90]. The effect of this characteristic distance on IR radiance is depicted in Figure 2.9 for the first trajectory point of the IRV-2 vehicle reentry described in Chapters 4 and 7. The figure consists of three plots, with the top showing the spectral and integrated radiance values for baseline and ±1 order of magnitude characteristic distances over the wavelength domains depicted in Figure 5.3. The percent differences between scenarios for both spectral radiance and radiance are depicted in the middle and bottom plots, respectively. The majority of the local sensitivities reside in the IR-A and IR-B regions, and are a function of O and N line features. Spectral radiance and radiance percent difference values peak for ±2 orders of magnitude at 0.86% and

0.02%, respectively. These insensitive results are due to the optically thin conditions for the IRV-2 vehicle, where the probability of self-absorbance along the LOS is small enough where order of magnitude distance changes do not have large effects. Other nonequilibrium factor sensitivity studies using the High-Temperature Aerothermodynamic Radiation (HARA) code also found similar first order sensitivity results in optically thin environments [48]. The case studies in this work, therefore, will utilize a constant d value in their assessments.

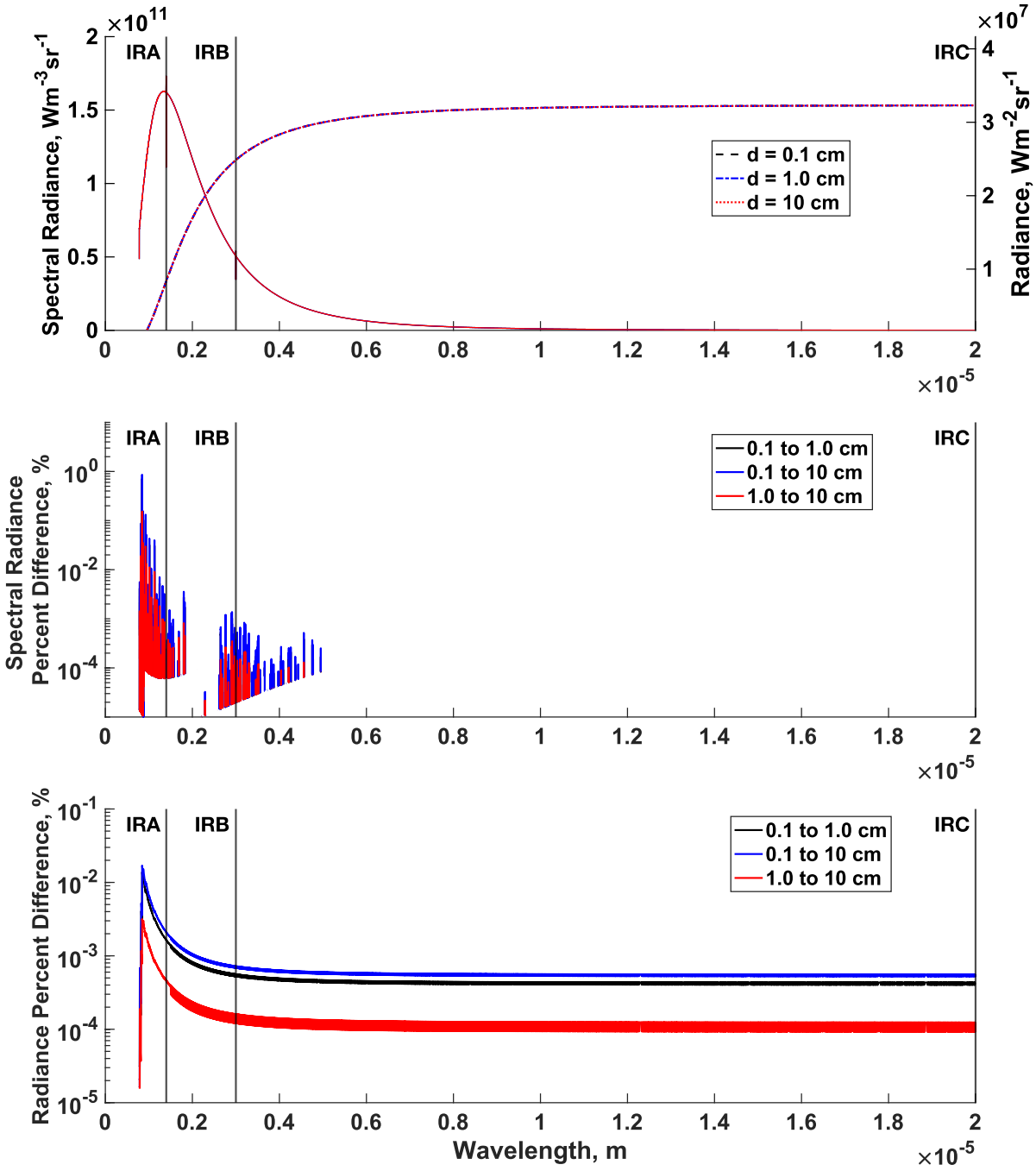

Figure 2.9: Escape factor characteristic length effects on stagnation line radiance at TP01 for the IRV-2 vehicle.

The absorption and stimulated emission rates are estimated with this local approximation following the third and sixth terms in the first summation in Equation 68,

$$k_{ab}^{ij} = B_{ji}\int \phi_{ji}(\lambda)I(\lambda)d\lambda = \int \frac{4\pi}{hc}\frac{\epsilon^{ji}(\lambda)}{\frac{N_j}{N_i} - \frac{\sigma^{ji}(\lambda)}{\alpha^{ij}(\lambda)}}\left[1 - \exp\left(-\alpha^{ij}(\lambda)N_i d\right)\right]d\lambda \tag{76}$$

in units of s^{-1}, where ϵ, σ, α, and d represent the emission, stimulated emission, and absorption coefficients, and characteristic absorption distance, respectively. The $\exp\left(-\alpha^{ij}(\lambda)N_i d\right)$ term represents the escape factor absorbance from the participating medium.

Spontaneous emission rates (the second and third summation terms in Equation 68) are estimated from state specific emission spectrum databases and follow

$$k_{em}^{ji} = \int \frac{4\pi\lambda}{hc}\epsilon^{ji}(\lambda)d\lambda \tag{77}$$

in units of s^{-1}. These rates reflect the balance of transition probabilities for spontaneous emission to and from different electronic states.

Lastly, the reaction term in Equation 68 represents electronic state population changes due to state-specific reactions. For molecules, these include pre-dissociation, heavy particle dissociation as a proportion of total dissociation rate, and electron impact dissociation from cross section data. For this work, two-temperature model gas phase reaction rate coefficients within LeMANS-MOPAR-MD are passed into NEQAIR's molecular excitation database files where applicable (EXCITE_MOLE_NEW.dat). Table 2.1 lists molecular reactions used in this work that are included in NEQAIR databases, whether parameters for each reaction are state specific or two-temperature based, and whether parameter values are sourced from NEQAIR or LeMANS-MOPAR-MD. Default NEQAIR refers to values that are available in an input file but have not been changed while hard-coded NEQAIR cannot be changed without recompiling the software.

Table 2.1: NEQAIR molecule reactions included in QSS Non-Boltzmann master equation.

Reaction	Rate type*	Source
$N_2^+ + e^- \rightleftharpoons N(^4S) + N^+(^3P) + e^-$	State specific (cross sections)	Default NEQAIR
N_2^+ Predissociation	State specific	Default NEQAIR
$N_2^+ + M \rightleftharpoons N + N^+ + M$	2T (M = atom or molecule specific)	LeMANS-MOPAR-MD (assume same rates as N_2 dissociation)
$N_2 + e^- \rightleftharpoons 2N(^4S) + e^-$	State specific (cross sections)	Default NEQAIR
N_2 Predissociation	State specific	Default NEQAIR
$N_2 + M \rightleftharpoons 2N + M$	2T (M = atom or molecule specific)	LeMANS-MOPAR-MD
$NO + e^- \rightleftharpoons N(^4S) + O(^3P) + e^-$	State specific (cross sections)	Default NEQAIR
NO Predissociation	State specific	Default NEQAIR
$NO + M \rightleftharpoons N + O + M$	2T (M = atom or molecule specific)	LeMANS-MOPAR-MD
$O_2 + e^- \rightleftharpoons 2O(^3P) + e^-$	State specific (cross sections)	Default NEQAIR
O_2 Predissociation	State specific	Default NEQAIR
$O_2 + M \rightleftharpoons 2O + M$	2T (M = atom or molecule specific)	LeMANS-MOPAR-MD
$CN + e^- \rightleftharpoons C(^3P) + N(^4S) + e^-$	State specific (cross sections)	Default NEQAIR
CN Predissociation	State specific	Default NEQAIR
$CN + M \rightleftharpoons C + N + M$	2T (M = atom or molecule specific)	LeMANS-MOPAR-MD
$CO + e^- \rightleftharpoons C(^4S) + O(^4S) + e^-$	State specific (cross sections)	Default NEQAIR
CO Predissociation	State specific	Default NEQAIR
$CO + M \rightleftharpoons C + O + M$	2T (M = atom)	Default NEQAIR
$CO + M \rightleftharpoons C + O + M$	2T (M = molecule)	LeMANS-MOPAR-MD
$N_2 + O \rightleftharpoons NO + N$	2T	Hard-coded NEQAIR
$O_2 + N \rightleftharpoons NO + O$	2T	Hard-coded NEQAIR
$CO + O \rightleftharpoons O_2 + C$	2T	Hard-coded NEQAIR
$CN + C \rightleftharpoons C_2 + N$	2T	Hard-coded NEQAIR
$C + N_2 \rightleftharpoons CN + N$	2T	Hard-coded NEQAIR
$N_2 + N^+ \rightleftharpoons N_2^+ + N$	2T	Hard-coded NEQAIR
$N + O \rightleftharpoons NO^+ + e^-$	2T	Hard-coded NEQAIR
$N + N \rightleftharpoons N_2^+ + e^-$	2T	Hard-coded NEQAIR
$O + O \rightleftharpoons O_2^+ + e^-$	2T	Hard-coded NEQAIR

*2T – Two-temperature

2.6 Uncertainty Quantification: Dakota and UQLab

The GSA/UQ analyses performed in this work utilize Sandia National Laboratories' Dakota software [91,92]. Dakota acts as a "black box" wrapper tool with an extensive library of optimization and uncertainty analysis capabilities. This generalized and flexible framework enables the integration of multiple computationally expensive codes with GSA/UQ algorithms necessary for the meta-analyses conducted in this work. Modified configurations of Dakota used in this work are displayed in each subsequent case study summarized in Section 2.7, where embarrassingly parallel processes start with Dakota running on a small allocation of resources to then generate multiple evaluations in a batch of synchronous evaluations. Each evaluation starts with a vector of uncertain parameters sampled by Dakota that are then preprocessed by a custom driver file. This driver file then places parameters into respective input files for expensive hypersonic flow, material response and radiation codes. Evaluation drivers then submit and self-monitor supercomputer job statuses on CU Boulder's Blanca and Alpine clusters. Once the expensive codes are complete within an evaluation batch, results are post-processed and stored. As evaluations complete, the first of the next batch is initiated and so on until all evaluations are complete. GSA and UQ metrics are then calculated and output by Dakota. All simulations are submitted over all compatible resources on the supercomputer cluster, allowing for simulations to compute as resources become available. Additionally, MATLAB toolbox and add-on UQLab is used to compute and compare multiple regression and cross-validation algorithms not available in Dakota [93,94]. Matrices of input parameters and output QoIs are taken from Dakota once all evaluations are complete and are used within this software for additional post-processing of GSA/UQ metrics.

2.6.1 Polynomial Chaos Expansions and Global Sensitivity

Many of the previous hypersonic flow GSA/UQ studies utilize polynomial chaos expansions (PCEs) for determining sensitivity and uncertainty metrics between uncertain input parameters and output QoIs. These studies usually involve many uncertain parameters as PCE methods can allow for obtaining converged metrics with fewer evaluations when compared to statistical sampling methods [47,48,54–

56,64,95–99]. Equation 78 defines the basic form of a PCE, where $\boldsymbol{R}$ represents the response function, α_i are the PCE basis function coefficients, $\boldsymbol{\Psi}_i$ are polynomial basis functions, and $\boldsymbol{\xi}$ are normalized uncertain parameters. In practice, this relationship is approximated by truncating the polynomial to N_P basis polynomial expansion terms to allow for the formation of a surrogate model approximation via estimating α_i for each of the terms. Equation 79 describes how the number of uncertain parameters n and the PCE order p affect the total number of terms for a complete expansion, N_t. The r term represents the oversampling ratio, where a value of unity represents a total order set for a given PCE surrogate [91]. Although fewer evaluations are required than for traditional statistical sampling, the rapid growth of the number of terms (and thus number of evaluations) required for constructing total order PCE surrogates usually makes evaluating many uncertain parameters computationally intractable for hypersonic simulation.

$$\boldsymbol{R} = \sum_{i=0}^{\infty} \alpha_i \boldsymbol{\Psi}_{\mathrm{i}}(\boldsymbol{\xi}) \approx \boldsymbol{R}^{PC} = \sum_{i=0}^{N_P} \alpha_i \boldsymbol{\Psi}_{\mathrm{i}}(\boldsymbol{\xi}) \tag{78}$$

$$N_t = N_P + 1 = r\frac{(n+p)!}{n!\,p!} \tag{79}$$

Global sensitivity analysis metrics in this study utilize the decomposition of variance via the calculation of Sobol' indices. Equation 80 represents the total variance in terms of a PCE as well as decomposed into partial variances following [100,101]. The orthonormal basis functions used in this study are Legendre polynomials in accordance with the Askey scheme for uniform sampling with uncertainty variables normalized to a support range $[-1,1]$ [102]. Each individual contributing variance term in this decomposition is defined generally in Equation 81 as a summation of the set of coefficient and basis polynomial term combinations for a given parameter. Each partial variance contribution of a particular parameter can be further related as a ratio of total variance (the main Sobol' index) in Equation 82. The summation of the partial Sobol' indices that include a particular parameter k in Equation 83 is the resulting GSA metric used in this study. This metric describes how much the variance in each individual uncertain

parameter contributes to overall QoI uncertainty while accounting for nonlinear correlations from other parameters on the QoI.

$$D_T = \sum_{i=1}^{N_P} a_i^2 \langle \Psi_i^2(\boldsymbol{\xi}) \rangle = \sum_{i=1}^{n} D_i + \sum_{1 \le i < j \le n}^{n-1} D_{i,j} + \sum_{1 \le i < j < k \le n}^{n-2} D_{i,j,k} + \cdots + D_{1,2,\ldots,n} \tag{80}$$

$$D_{i_1,\ldots,i_s} = \sum_{\beta \in \{i_1,\ldots,i_s\}} \alpha_\beta^2 \langle \Psi_\beta^2(\boldsymbol{\xi}) \rangle, \qquad 1 \le i_1 < \cdots < i_s \le n \tag{81}$$

$$S_{i_1,\ldots,i_s} = \frac{D_{i_1,\ldots i_s}}{D_T} \tag{82}$$

$$S_{T_i} = \sum_{\mathcal{L}_i} \frac{D_{i_1,\ldots,i_s}}{D_T}, \qquad \mathcal{L}_i = \{(i_1, \ldots, i_s) : \exists\, k, 1 \le k \le s, i_k = i\} \tag{83}$$

2.6.2 Nonintrusive Point-Collocation

The studies involving NIPC methods utilize a collocation approach to solve for the basis coefficients $\boldsymbol{\alpha}$ from the relation in Equation 84. The basis polynomials $\boldsymbol{\Psi}$ is a $N_s \times N_P$ matrix of multivariate polynomial terms $\Psi_{0 \ldots N_P}$ evaluated for array $\boldsymbol{\xi}$ of a particular evaluation out to N_s evaluations, $\boldsymbol{\alpha}$ is a coefficient array for each N_P basis polynomial terms, and $\boldsymbol{R^{PC}}$ is the QoI response array for each N_s sample [91,103,104]. Multiple methods in Dakota are available for solving this relationship via spectral projection (numerical integration based on random sampling, tensor-product quadrature, Smolyak sparse grids or cubature methods) or linear regression methods. Classical orthogonal multivariate basis polynomials are generated using the Askey scheme based on the assumed continuous probability distributions for the uncertain parameters being sampled for the evaluations. This work utilizes ordinary least squares (OLS) regression with an oversampling ratio $r = 2$ for overdetermined systems (Chapter 4) or various sparse regression techniques for underdetermined systems (Chapters 5 and 7) to approximate the basis polynomial coefficients for a given system [93,103].

$$\boldsymbol{R^{PC} = \Psi\alpha}$$

$$\begin{pmatrix} R^{PC}(\xi_1) \\ R^{PC}(\xi_2) \\ \vdots \\ R^{PC}(\xi_{N_S}) \end{pmatrix} = \begin{pmatrix} \Psi_0(\xi_1) & \Psi_1(\xi_1) & \cdots & \Psi_{\mathrm{N_P}}(\xi_1) \\ \Psi_0(\xi_2) & \Psi_1(\xi_2) & \cdots & \Psi_{N_P}(\xi_2) \\ \vdots & \vdots & \ddots & \vdots \\ \Psi_0(\xi_{N_S}) & \Psi_1(\xi_{N_S}) & \cdots & \Psi_{N_P}(\xi_{N_s}) \end{pmatrix} \begin{pmatrix} \alpha_0 \\ \alpha_1 \\ \vdots \\ \alpha_{N_P} \end{pmatrix} \tag{84}$$

2.6.3 Baseline, PCE Derived and Propagated Mean and Variance Metrics

Baseline QoIs are obtained for each case study and flow condition using a baseline set of parameters. Approximate QoI mean and variance values for a given field location can be directly found from Ψ_0 and D_T for the regressed PCE, respectively. However, these moments alone do not incorporate 'off-design' samples, and the uncertainties associated with the QoI surrogate model. Therefore, Monte Carlo sampling of each PCE is conducted with 10^6 samples to generate mean and 95% confidence intervals for each PCE and QoI for comparison. These metrics provide a location-specific context for where the relative Sobol' indices influence the largest uncertainty bounds throughout the flowfield.

2.7 Case Study Implementations

Chapters 4, 5, and 7 represent three case studies with detailed assessments of how gas phase, material response and radiation parameters affect plasma formation and radiative observation of a vehicle under weakly ionized flow conditions. An incremental approach is utilized, where each case study builds upon previous findings to better characterize parameters' influences on multiple QoIs. Table 2.2 lists the case studies in this work, including the flight conditions, assessed uncertain parameters, incorporated models and affected QoIs. To provide context for the case studies, Chapters 3 and 6 introduce literature reviews and FRSC model assessments, respectively.

Table 2.2: Case studies, uncertain parameters, and quantities of interest for the assessment of hypersonic flow, material response and radiation models

Case Study	Conditions	Uncertain Parameters	Incorporated Models	QoIs
IRV-2 Nose (11 Species)	60 km 5, 7, and 9 km/s	47 reaction rate coefficients 11 relaxation parameters	LeMANS	Electron number density (entire flowfield)
IRV-2 Nose (20 Species)	TP01: 56 km, 6.8 km/s, 4.25 s	195 reaction rate coefficients	LeMANS-MOPAR (B'_C Equilibrium)	PM IR radiance (LOSs)

			NEQAIR	
IRV-2 Full Body (20 Species)	TP01: 56 km, 6.8 km/s, 4.25 s TP02: 49 km, 6.8 km/s, 6.75 s	195 reaction rate coefficients 11 relaxation parameters 3 FRSC rate coefficients 290 E-CIE coefficients (Atoms) 61 HP-CIE coefficients (Molecules) 52 E-CIE cross sections (Molecules)	LeMANS-MOPAR (B_C' FRSC) NEQAIR	Total and PM IR radiance (LOSs)

2.8 Summary

This chapter outlined the background, theory and assumptions for each assessed model while focusing on uncertain input parameters evaluated within case studies in this work. A detailed description of the hypersonic flow code LeMANS, material response integrated code LeMANS-MOPAR-MD, the novel FRSC model, the nonequilibrium air radiation code NEQAIR, and the uncertainty quantification software Dakota and UQLab is provided. Additionally, details on the case studies involved in this thesis are defined and act a framework for model assessments under various conditions and scenarios.

Chapter 3

Literature Reviews and Uncertain Parameter Determinations

3.1 Introduction

The following chapter provides context for previous detailed assessments of hypersonic flow models while also including baseline, upper and lower bounds for a multitude of uncertain input parameters for the models explained in Chapter 2. The GSA/UQ review includes a wide range of hypersonic flow conditions, geometries, parameters, quantities of interest, and GSA/UQ methods and metrics that help provide motivation for the case studies examined in this work. The thermochemical gas, energy relaxation, excitation/deexcitation, and surface chemistry rate parameters reviewed provide a history of the experimental and computational methods involved in their estimation since the 1960's and a quantitative review of their relative uncertainties used throughout this work.

3.2 Hypersonic Flow Global Sensitivity and Uncertainty Analyses

Hypersonic flow global sensitivity analysis and uncertainty quantification involves methodological assumptions to help improve scientific discovery and engineering application. These approaches enhance models by revealing unforeseen system characteristics, pinpointing conceptual errors, or detecting coding flaws. Additionally, researchers can refine resource distribution by focusing on areas that minimize measurement uncertainty in key parameters identified [105,106]. Previous hypersonic flow GSA/UQ studies vary factors including parameter uncertainty bounds, parameter probability distributions as well as sampling methods for producing parameter inputs and QoI outputs. These QoIs traditionally focus on a limited number of flow parameters and conditions.

Table 3.1 describes multiple hypersonic sensitivity and uncertainty analyses, including parameters, assumed parameter probability distributions, as well as sampling and GSA/UQ methods and metrics [47,48,54–56,64,95–98,107–110]. The vast majority of studies include either 0D reactor/1D shock or 2D axisymmetric geometries that examine gas phase chemical kinetics parameters in the form of Arrhenius

preexponential constants that are Latin hypercube sampled (LHS) from log-uniform probability distributions between chosen bounds. GSA/UQ methods and metrics vary, where less expensive simulations often use Monte Carlo methods, while more costly simulations typically rely on PCE methods. Those PCE methods with a higher number of parameters utilize a nonintrusive point collocation (NIPC) approach, allowing for the investigation of many parameters with fewer simulation evaluations than traditional Monte Carlo sampling methods for a given GSA/UQ metric convergence level.

Additionally, the flow conditions for these studies include velocities from 5 to over 10 km/s, with gaseous compositions ranging from a few to over 20 species. This review organizes two general categories for studies prior to 2024: suborbital (5-8 km/s) and hyperbolic (>10 km/s) reentry conditions. The former category assessments focus on GSA/UQ metrics for major dissociated air species number densities (N, O, and NO) [95,98,108,109] as well as aerodynamic coefficients and surface temperatures [97,111]. These computational campaigns usually compliment experiments at relatively lower velocities and temperatures consistent with processes that do not include significant ionization. The latter category, mainly conducted by NASA computational studies, includes flight conditions consistent with relatively faster reentry, where processes including significant ionization and radiative heat flux occur [47,48,54–56,96,107,110]. More recent computational assessment studies now include analyses in the 5-9 km/s 'weakly-ionized' flow regimes, focusing on gaseous kinetics rate parameters' effects on pathways leading to plasma formation [64,99,112–115]. This regime is of particular interest for obtaining GSA/UQ metrics for various QoIs because the majority of the empirically derived rate coefficients were obtained for flow conditions that do not cover this range. Moreover, these flight conditions are consistent with that of the reentry phase of boost glide and aeroballistic hypersonic vehicles.

The model and parameter assessments in this work and summarized in Table 2.2 therefore address a lack of knowledge in the literature on both the uncertain parameter bounds as well as their influence on key QoIs for communication and defense purposes in this flight regime, i.e., plasma formation and vehicle observation. Additionally, effects of highly coupled material response and excitation/deexcitation processes and their associated input parameter uncertainties are also incorporated for these QoIs and flow conditions.

Table 3.1: Various hypersonic sensitivity and uncertainty studies.

Study	Model Type	Parameters		Samples	GSA Method	Metric(s)	QoI(s)
		Categories	Number Type Distribution*				
Bose et al. (2006) [107]	2D Axisym	Arrhenius prefactors V-Tr relaxation times El-Tr relaxation times	130 PR	3000	Monte Carlo	Propagated Uncertainty	Radiative heat flux
Strand & Goldstein (2011) [108]	0D Reactor (DSMC)	Arrhenius prefactors Temperature-viscosity exponents VHS reference collision diameters Rotational/vibrational collision number	10 PR ULB	960	Monte Carlo	Local QoI Gradients	Translational Temperature NO number density
Johnston & Kleb (2012) [52]	1D Lines of Sight	Atomic line oscillator strengths Atomic-line Stark broadening widths Atomic photoionization cross sections Ion photo-detachment cross sections Molecular band oscillator strengths Electron-impact excitation rates	11,905 PR U	11,905	Cauchy deviates (Monte Carlo)	Propagated Uncertainty	Radiative heat flux
Han & Hosder (2012) [95]	2D Axisym	Freestream velocity Unsteady velocity-inlet boundary condition Turbulent viscosity coefficient	3 PR U	1000	NIPC	Sobol' Indices	Pressure and skin friction coefficients
Strand & Goldstein (2013) [109]	1D Sock (DSMC)	Arrhenius prefactors	17 PR U	5600	Monte Carlo	Pearson correlation, Mutual information	NO density
West et al. (2014) [96]	2D Axisym	Arrhenius prefactors Heavy-particle impact excitation rates Electron-impact excitation rates Molecular band processes	93 LHC U	20	NIPC Local Gradients	Local QoI Gradients, Global Approximation	Radiative heat flux
West & Hosder (2015) [55]	2D Axisym	Arrhenius prefactors Heavy-particle impact excitation rates Electron-impact excitation rates Molecular band processes	93 LHC U, G	156	NIPC Sparse (BP)	Sobol' Indices	Radiative heat flux
West et al. (2016) [56]	2D Axisym	Arrhenius prefactors Heavy-particle impact excitation rates Electron-impact excitation rates Molecular band processes	79 LHC U	500	NIPC Sparse (BP)	Sobol' Indices	Radiative heat flux

West et al. (2017) [47]	2D Axisym	Arrhenius prefactors Heavy-particle impact excitation rates Electron-impact excitation rates Molecular band processes Atomic N & O lines	388 LHC U	100	NIPC Sparse (BP)	Sobol' Indices	Radiative heat flux
Higdon et al. (2018) [110]	1D Shock (DSMC)	Arrhenius prefactors	53 LHC U, G	1920	Monte Carlo	Pearson correlation, Mutual information	Translational Temperature Electron number density N, O number density
Johnston et al. (2019) [48]	2D Axisym	Arrhenius prefactors Molecular band oscillator strength Escape factor distance Non-Boltzmann rates	29 N/A UL	100	NIPC Sparse (BP)	Sobol' Indices	Radiative heat flux
Holloway & Boyd (2022) [97]	2D Axisym	Arrhenius prefactors	5 LHC U	83	PCE Sparse Quadrature	Sobol' Indices	Surface pressure Surface heat transfer Drag Surface temperature
Kuppa et al. (2022) [98]	1D Shock	Arrhenius prefactors Heat addition	9 LHC LU	2000	NIPC Sparse (LAR)	Sobol' Indices	O, NO mole fractions
Aiken & Boyd (2023) [99]	1D Shock	Arrhenius prefactors V-Tr relaxation times El-Tr relaxation times	578 LHC LU	1000	NIPC Sparse (SPGL1)	Sobol' Indices	Electron number density
West & Johnston (2023) [54]	2D Axisym	Arrhenius prefactors Finite rate surface reaction rates Wall roughness height Turbulent Schmidt number Collision integrals Heats of formation	329 LHC U	50	NIPC Sparse (LAR and BP)	Sobol' Indices	Convective heat transfer
Aiken & Boyd (2024) [64]	1D Shock 0D Reactor	Arrhenius prefactors V-Tr relaxation times El-Tr relaxation El-impact excitation	58 LHC LU	3540	NIPC (OLS)	Sobol' Indices	Electron number density
Carter & Boyd (2024) [114]	2D Axisym	Arrhenius prefactors	195 LHC LU	500	NIPC Sparse (LAR, LASSO, OMP, BP, BCS)	Sobol' Indices	Infrared radiance

Rataczak et al. (2024) [116]	2D Axisym	Arrhenius prefactors V-Tr relaxation times Transport property cross sections Freestream CH_4 mass fraction	248 LHC LU	200, 300	NIPC Sparse (LAR)	Sobol' Indices	Radiative heat flux
Aiken et. al. (2025) [113]	1D Shock	Arrhenius prefactors V-Tr relaxation times El-Tr relaxation El-impact excitation	866 LHC LU	3600	NIPC Sparse (SPGL1)	Sobol' Indices	Maximum electron number density
Carter et. al. (2025) [115]	2D Axisym	Arrhenius prefactors V-Tr relaxation times El-Tr relaxation El-impact excitation	58 LHC LU	3540	NIPC (OLS)	Sobol' Indices	Electron number density (entire flowfield)

*PR – Pseudo Random, LHC – Latin Hypercube, LU – Log-Uniform, U – Uniform, G – Gaussian, ULB – Upper/Lower Bounds

3.3 Thermochemical Gas Rates

A literature review of 195 forward thermochemical kinetics parameters involving 11 air and 9 carbon species is conducted and includes values of modified Arrhenius form from experiments, meta-studies, as well as numerical and theoretical analyses. An exhaustive review on these parameters is required to more accurately depict the relationship between input parameter variance and associated GSA/UQ metrics for specified QoIs. Upper and lower uncertainty bounds are also provided from these reviews and from previous studies in each sub-section. Sections 3.3.1 through 3.3.5 are categorized by dissociation, neutral exchange, associative ionization, charge exchange, and electron impact ionization reactions, respectively.

Extensive literature review results are shown in Appendices A and B, where each reaction contains references, controlling temperature exponents, forward modified Arrhenius reaction rate equations with coefficient parameters, and uncertainty bound multipliers from a baseline study. Previous study uncertainty bounds for each parameter are also depicted in Appendix C. Each reaction lists uncertainty bounds quantified in previous GSA/UQ studies and contains references to experimental, numerical and meta-studies as compared to the bounds estimated from this work's literature review denoted by the superscript symbols † and §, respectively. Bounds for each reaction are chosen to cover all of the studies' reaction rates over the minimum to maximum temperature ranges with the exception of outliers. These are defined as reaction rates greater than an order of magnitude from all other studies for a given temperature range or sources omitted based on recommendations from other parameter meta-analyses. For those reactions with only one source, the uncertainty bounds are assumed to be an order of magnitude. Those reaction studies whose rates are converted from backward reaction rates utilize equilibrium constants calculated from Gibb's free energy minimization and NASA Lewis Research Center curve fits for enthalpy and entropy. Other methods include utilizing curve fits from Park, Kim, Gupta, or Kang with activation energies from baseline forward reaction rate studies [1,62,65,66,117–119]. The former method is utilized in this work (Equations 10-12) for converting reverse reaction rate coefficients from equilibrium constants (Equation 9). Differences between the former and latter methods are within the uncertainty bounds for the involved

temperature range. Where studies are digitized from raw data or backwards rate converted, log-linear and non-linear regression methods of the modified Arrhenius coefficients are compared for given activation energies and found to be well within uncertainty bounds for each reaction.

3.3.1 Dissociation

The dissociation reaction uncertainty bounds from experiments, numerical and meta-studies as well as this work's literature review are depicted in Table C1. Third body dissociation partners are explicitly stated by study when multiple are reported for a given reaction type. Most uncertainty bound ranges in the current work agree well with previous studies. Exceptions to this include nitrogen dissociation from electron collisions, where bounds are found to be multiple orders of magnitude between studies spanning 2,000-20,000 K. This wide range in rate coefficients is due to variations in vibrational and electronic states of nitrogen over wide temperature ranges and measurement uncertainties [89,120]. This is especially evident when comparing ground states of nitrogen to the weighted population rates from Bourdon & Vervisch, Teulet et al. and Yu et al. with a variance of over three orders of magnitude as seen in Figure B1(c) [121–123]. Arguments for and against the inclusion of weighted excited states within the calculation of rate coefficients were provided by multiple authors. Bourdon & Vervisch contended that rates by Park "led to strong dissociation of the flow which was in total disagreement with experiment" and found better agreement when $N_2(v = 0)$ was used for the global reaction [121]. However, as seen in Figure B1(c), the conditions for their investigation mainly focused on comparisons below 10,000 K, while other studies include higher temperature ranges. Yu et. al. (2001) provides a comparison between various energy distribution assumption effects on aggregate rate coefficients using cross section data from Majeed and Strickland and made comparisons to Sharma and Gillespie (1991) [123,124]. The authors found a large influence of excited vibrational levels on dissociation rates that matched the multiple order of magnitude differences seen in Figure B1(c). Cruden and Brandis (2017) made further refinements for electron impact dissociation of nitrogen using the molecular QSS balance depicted in Section 2.5 and cross sections recommended by Itikawa (2006) [89,125]. Using this detailed balance framework in NEQAIR, rate

coefficients with a higher Arrhenius slope were obtained with magnitudes between $N_2(v = 0)$ and vibrational energy incorporated studies. To remain consistent with NEQAIR and to better represent the effects of vibrational excitation at higher temperatures, the following case studies in this work incorporate rate coefficients with uncertainty bounds that span all studies which include internal excitation.

Additionally, NCO dissociation reaction uncertainty ranges in Figure B8 are also wider based on lower bounds due to measurements made by Mertens & Hanson and meta study suggestions by Baulch et al. (2005). Most earlier studies utilized C_2N_2 decomposition resulting in larger error limits when compared to utilizing HNCO decomposition and updated NCO absorption coefficients [126,127]. The resulting bounds that span three orders of magnitude are considered conservative and are chosen to incorporate the uncertainty involved with a lack of other studies using this newer HNCO decomposition technique.

3.3.2 Neutral Exchange

The neutral exchange reactions exhibited similar agreement with previous study uncertainty bounds as seen in Table C2. Many of these reactions' forward rates (particularly carbon species) have few references, making bound determinations difficult. Exchange reactions involving carbon of note include $C_3 + C \rightleftharpoons C_2 + C_2$, $CN + CO_2 \rightleftharpoons CO + NCO$, and $NCO + O \rightleftharpoons CN + O_2$. The first reaction rate bounds in Figure B13 do not include estimates by Park (2001) because the Arrhenius estimate relied upon a range of values from other reactions, leading to over four orders of magnitude lower values [119,128]. The second reaction in Figure B19 includes influences of experiment type on reaction rate coefficient estimates. Three studies included open flame [129] and laser-induced fluorescence [130–132] methods that estimated significantly higher rate coefficients for high and low temperature ranges when compared to shock tube experiments [132,133], respectively. Only the shock tube experiments, and their associated uncertainties are included in the current case studies. The last reaction in Figure B22 includes bounds that are most influenced by Tsang (1992) and Zhao et al. (2019), where equilibrium constant conversions from reverse reactions as well as branching ratio uncertainty from the competing reaction $NCO + O \rightleftharpoons CO + NO$ leads to uncertainties greater than a factor of 20 above 1,000 K [134,135].

Additionally, a considerable number of studies have been conducted for determining temperature reaction rate coefficients for nitrogen dissociation via the Zel'dovich mechanism reactions as seen in Figure B15 and Figure B16. These reactions' relative variance contributions to plasma formation and vehicle observation is denoted in the case studies in Chapters 4, 5, and 7. The second of these reactions ($O_2 + N \rightleftharpoons NO + N$) exhibits wider variation at low temperatures and is largely a function of measurement technique. The computational analyses of this reaction by Bose and Candler lies in the middle of the rate sources across all temperature ranges and is used as the baseline [136].

3.3.3 Associative Ionization

Previous GSA/UQ studies involving associative ionization bounded their rates by an order of magnitude with the exception of $N + N \rightleftharpoons N_2^+ + e^-$ [54]. Table C3 shows good agreement with the literature review, with all bounds within an order of magnitude from their respective baselines. Few references were found for atomic carbon and oxygen associative ionization to produce CO^+, with uncertainty bounds encompassing rates estimated by Park (1994) and Boyd and Josyula (2022) [137,138]. Park's estimate set the rate equal to NO^+ associative ionization while accounting for a different activation energy. Boyd and Josyula utilized cross sections proposed by Le Padellec and weighted Boltzmann fractions of reactants for each state specific reaction to obtain an overall reaction rate [139]. Similar numerical studies that account for these states for associative ionization air atoms produce an equilibrium Arrhenius approximation that agreed with the majority of studies at higher temperatures [138,140].

3.3.4 Charge Exchange

The majority of charge exchange reactions in Table C4 show smaller uncertainty bound multipliers when compared to the order of magnitude estimates of West and Gokcen [47,54,141]. Almost all exchange reaction studies are derived from converted exothermic rates stemming from low temperature ionosphere reaction experiments via processes defined by Park [1]. The $N_2 + O_2^+$ exchange reaction is used as an example for this process, starting with fitting c and q in the endothermic rate coefficients following

$$\kappa = c\left(\frac{E_{th}/k_B}{300}\right)^q \tag{85}$$

where thermal energy

$$E_{th} = \frac{1}{2}mw^2 \tag{86}$$

is determined by the mass and average velocity of each particle. The fits in Figure 3.1 include references for which there are only results at 300 K, where Park states to fit with q values of zero. Park also states that the rise in energy states at higher temperatures should be omitted to better approximate the majority ground states of the constituents in this fitting process. The Park approximation is also shown in this figure by converting from the endothermic reaction rate Arrhenius formulation for comparison purposes. The exothermic rates are then approximated using

$$k_r = 4\pi\int_0^\infty \kappa f(w)w^2 dw = \frac{2c}{\sqrt{\pi}}\left(\frac{T}{300}\right)^q \Gamma\left(\mathrm{q}+\frac{3}{2}\right) \tag{87}$$

where $f(w)$ and Γ represent the Maxwellian velocity distribution and gamma functions, respectively. An example of these translated endothermic reaction rates are depicted in Figure 3.2. From there, the endothermic rates are translated into exothermic rates via temperature dependent equilibrium constants and Equation 9. Examples of variations in the equilibrium constants are shown in Figure 3.3. As previously stated, equilibrium constants determined via Gibbs free energy minimization are utilized for all reverse reaction rate calculations, which closely matches Park values in the example. Other equilibrium constant fit approximations from Kim or Dunn and Kang can vary significantly from Park / Gibbs free energy minimization depending on the reaction and are therefore not used [117,142]. Finally, the end result endothermic charge exchange reaction is reported. An example of these end results is depicted in Figure 3.4, where Park's forward reaction rate coefficients are compared with each individual reference that Park utilized to obtain an uncertainty bound range. For many of the references and in this example, experiments with measurements at only 300 K that are then converted have values significantly higher than those at multiple temperatures. This makes sense because assuming the same exothermic rates over all thermal

kinetic energies will lead to significantly larger endothermic rates. However, even with these variations, the majority of the charge exchange reaction uncertainty bounds remain within an order of magnitude.

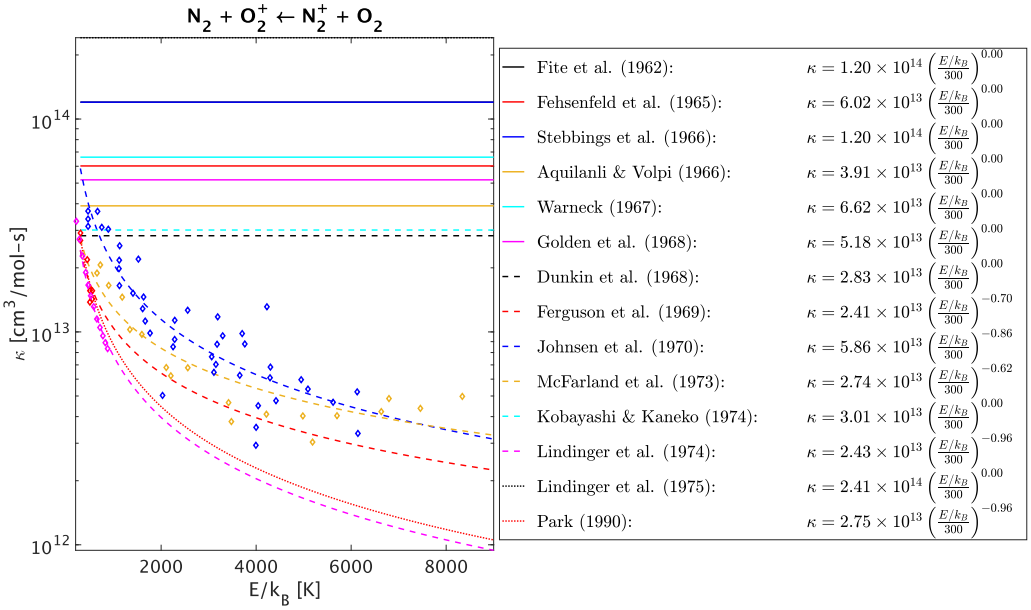

Figure 3.1: Exothermic charge exchange energy fit example following Park (1990).

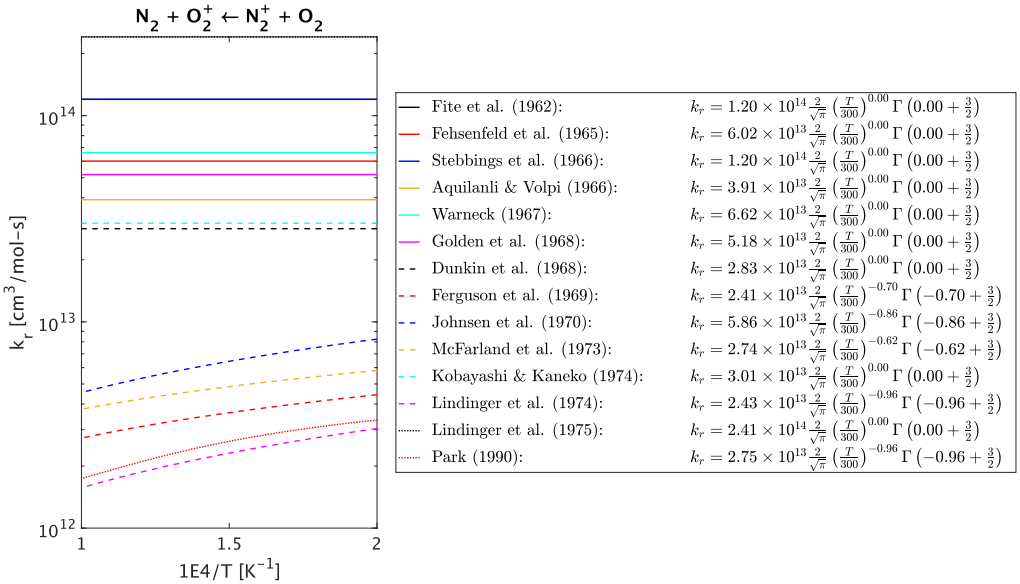

Figure 3.2: Exothermic charge exchange reaction rate coefficients example following Park (1990).

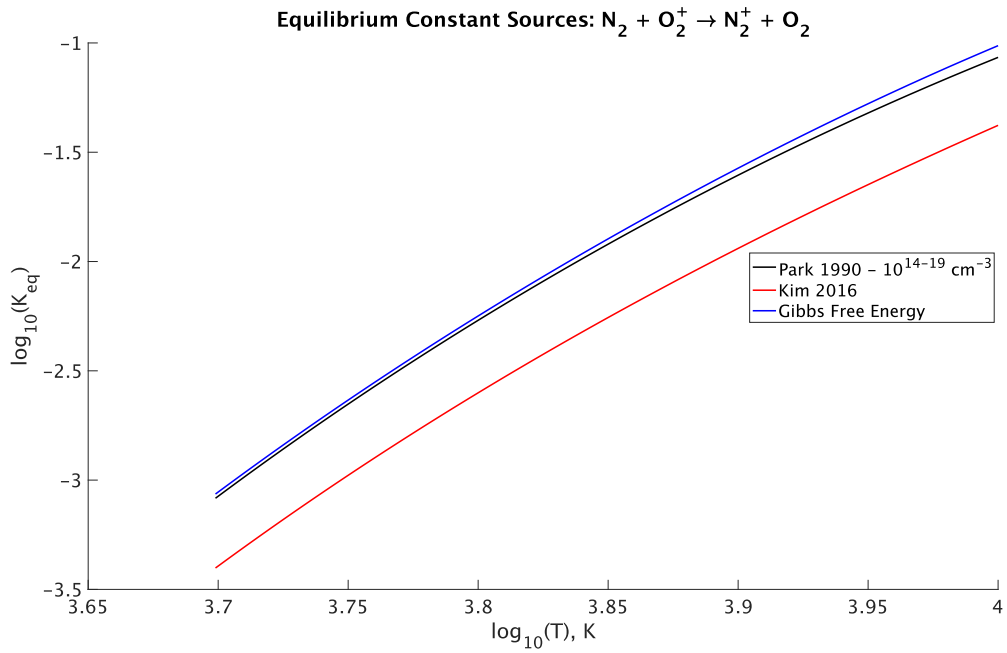

Figure 3.3: Exothermic charge exchange reaction rate equilibrium constant example following Park (1990).

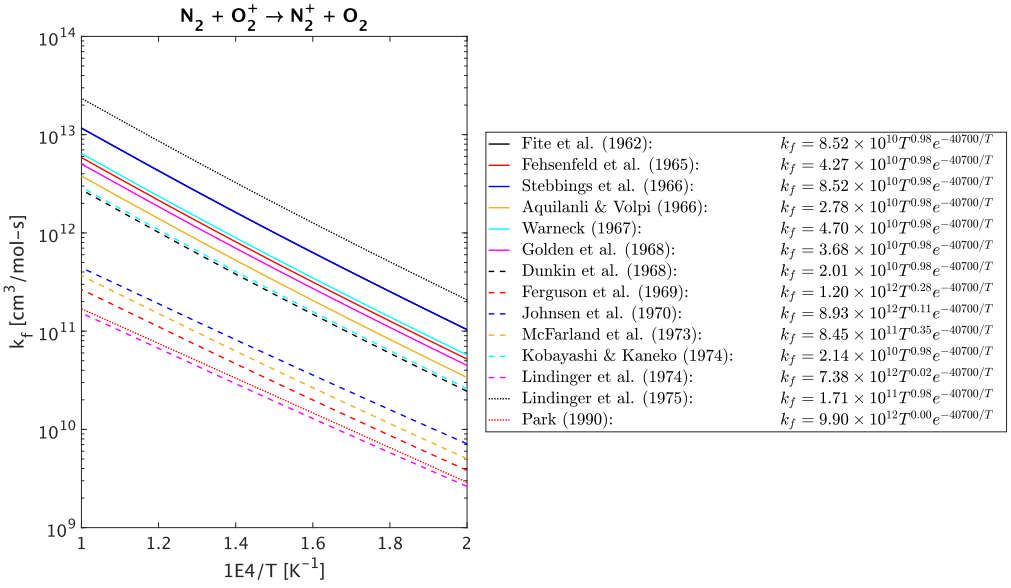

Figure 3.4: Endothermic charge exchange reaction rate coefficients example following Park (1990).

Exceptions include $NO^+ + N \rightleftharpoons O^+ + N_2$, shown in Figure B34, where uncertainty bounds span multiple orders of magnitude and differences from Park's forward rates are larger by a factor of 300. Additional references are accumulated for this particular reaction for comparison using the similar exothermic to endothermic reaction conversion process for comparison with that of Park. All endothermic reaction conversions for this reaction, including experiments in the late 1990's, are found to be significantly higher than those reported by Park [143,144]. Although Park did not explicitly state which references he includes, by undergoing the reverse rate calculation process for each reference, it appears for most reactions that data with exothermic temperatures greater than 300 K are converted. Few studies and reactions besides Park provide endothermic reaction rates and are mainly concentrated in the $N_2 + N^+$ and $O_2^+ + O$ reactions [89,117,123,145–148].

3.3.5 Electron Impact Ionization

All electron impact ionization uncertainty bounds are larger than previous GSA/UQ studies. Table C5 shows up to two orders of magnitude uncertainty ranges in the literature. For atomic nitrogen and oxygen, variations in Arrhenius plot slopes account for a large portion of this variation at temperature above 10,000 K and less than 6,000 K. Notable outliers include Losev (1994) and Bird (1987), where rate values were multiple orders of magnitude lower than the uncertainty bound ranges across all temperatures. These larger uncertainty bounds will most likely have a larger influence on plasma formation than the order of magnitude bounds introduced in the case study in Chapter 4.

3.4 Relaxation Energy Exchange Parameters

Various relaxation exchange parameter baselines and bounds used within the LeMANS hypersonic flow code are surveyed from multiple aggregate sources and displayed in Table A2. Vibrational-translational (VT) relaxation time baselines are taken from modified Millikan and White curve fits for all 11 or 20 species combinations, where applicable. The VT energy exchange parameters for combinations of $N_2, O_2, N,$ and O collision pairs also include relative uncertainty bounds [64,149–152]. The VT upper and lower uncertainty bounds for each of these collision pairs were applied as a multiplicative factor to the VT

relaxation time τ_{VT} calculations. Similar processes were conducted for heavy particle-electron energy exchange, where order of magnitude uncertainty bound parameters are applied as direct multiplier factors. The electron impact ionization average energy transferred as a fraction of first ionization energy (α_{EII}) variance ranges are directly input into the relations derived by Gnoffo et. al. [64,70,153].

3.5 Excitation and Quenching Rates

Baseline and uncertainty bounds for excitation and quenching rate parameters are used to assess how variance impacts NEQAIR based QoIs defined in Table 2.2. Each of these parameters reflect transitions that may not be applicable for the wavelength range of the QoIs directly. However, as seen in Chapter 7, many transition rate sensitivities produce differences in electronic state populations that eventually lead to radiative transitions for wavelength ranges outside of the original transition. These additional collisional transition rates are also included to accommodate future GSA/UQ metric investigations over multiple spectral ranges.

3.5.1 Atomic Electron Impact Excitation

Baseline and uncertainty bound multipliers for atomic electron impact excitation rate coefficients for oxygen and nitrogen are depicted in Table A3 and Table A4. These rates are a combinations of cross section data from NIST and Huo et. al. fit to Equation 73. This parameter set includes order of magnitude uncertainty bounds from previous GSA/UQ analyses by West, Johnston, and Kleb [47,52,66,84,88,89,154]. Uncertainty bound level combinations both N and O include $l > 1$ and $u \leq 22$ or 19, equating to 165 and 125 rate parameters, respectively.

3.5.2 Molecular Electron Impact Excitation

Molecular electron impact excitation rate approximations follow Equations 74 and 75, where baseline cross sections and uncertainty bounds for N_2^+, N_2, NO, O_2, and CO are depicted in Table A6. Uncertainty bound multiplier intervals from other GSA/UQ studies are included where applicable. Order of magnitude bounds are utilized where there are a lack of data beyond the baselines. Each of the uncertainty bound multipliers are applied directly to each cross section at each energy level in the NEQAIR input files

to ensure constant propagation through to the calculated rates. All terms in Equations 74 and 75 are combined to ensure that the uncertainty bound multipliers (treated as constants for each evaluation) are distributed through each term to act effectively as a multiplier for rate coefficient approximations.

3.5.3 Molecular Heavy Particle Impact Quenching

Molecular heavy particle impact quenching rate baselines and uncertainty multipliers defined by Equation 72 are depicted in Table A5. A similar process is conducted for uncertainty bound multipliers, where an order of magnitude is chosen for each transition where there is a lack of data beyond baseline values [47]. Quenching rate baselines for various collision partner and transition combinations are included for $N_2^+, N_2, NO, CN,$ and CO. Rates for all other transitions and collision partners for each molecule are depicted as "Others."

3.6 Finite Rate Surface Chemistry Rates

ATJ carbon-carbon graphite O and O_2 oxidation reaction parameter baselines and uncertainty bounds follow Equations 95 and 96. Each baseline rate equation is fit to experimental data by Park (1976) in Figure B48 and Figure B49 and is listed in Table A7 [77,155–168]. The uncertainty bounds are chosen to encapsulate all reaction probability data while maintaining the baseline fit parameters throughout the temperature range. Although it has been shown that oxidation rate coefficients do not follow a simplified Arrhenius form, this work focuses on incorporating the rate constant variance as part of its scope with the new implementation framework described in Section 2.4 [26,33,80,81].

Sublimation rate parameters of C_3 follow a similar process, where a simplified input model incorporates Equations 97 and 98 and baseline and bound multipliers listed in Table A7 [1,169–171]. These bounds are determined from a review of a range of carbon vaporization coefficients for C_3 and are defined as the ratio of the evaporation rate measured to the theoretical maximum rate defined by the Knudsen-Langmuir relation (Equation 98). Park provides a theoretical estimate for the sticking coefficient from a surface equilibrium balance ratio while assuming spherical kinetics with a unity absorption vibrational partition function

$$\left(\frac{N_g}{N_a}\right)_E = \sqrt{\frac{T}{\theta_r}}\sqrt{\frac{2\pi m k_B T}{h^2}}\exp\left(-\frac{D_A}{k_B T}\right), \quad N_g = \frac{p_E}{k_B T} \tag{88}$$

where N_g, N_a, θ_r, D_A, p_E are the gas and absorbed number densities at equilibrium, the rotational constant of the molecule, the absorption potential, and the vapor pressure at equilibrium. Park utilized this equilibrium balance to show that the evaporation coefficient can be approximated by $\sqrt{\theta_r/T}$. This approximation relates absorption and evaporation balance as a function of the molecules' ability to rotate at the surface. In the case of C_3, vaporization coefficient values on the order of 0.01 are found to reflect this rotational hindrance [1].

3.7 Discussion and Summary

Examining parameter inputs for the hypersonic flow, material response and radiation models is critical in their detailed assessment. This includes estimating baseline and uncertainty bounds from multiple source types and conditions where available. Experimental, numerical, theoretical and aggregate studies of these parameters were investigated to obtain variance bounds used in the case studies in this work. Additionally, these bounds were compared with previous GSA/UQ analyses, where select parameters in this review varied significantly. As seen later in this work, the variations in these bounds can have a significant effect on various QoIs under similar weakly ionized hypersonic flow conditions.

The accumulated data, analysis and relative uncertainty bounds from multiple source types in this chapter provide a significant contribution to the hypersonic flow community, wherein relationships between uncertain input parameters and other QoIs can be used beyond the case studies and QoIs in this work. For certain parameters, myriad data are accumulated to provide assumed probability density functions other than uniform. This could include multivariate distributions for temperature and rate coefficients while accounting for uncertainty within each data source. For those parameters with large uncertainty bounds that are driven by few sources, these accumulated data provide a means for pinpointing data that either warrants experimental replication or possible exclusion. For these cases, caution should be taken to ensure undue decreased uncertainty is not placed on parameters without proper justification. For cases where parameters

include sources that require significant raw data post-processing, i.e., temperature extrapolation, equilibrium constant based reverse reaction calculations, and reaction channel uncertainties, increased uncertainty bounds could be implemented [113].

For those parameters where little to no bounds were classified based on experimental data beyond baseline references, this review helps clarify where further parameter investigation could be warranted for certain QoIs. Specifically, although one or two order of magnitude uncertainty bounds for excitation and quenching rates could be deemed conservative based on past expertise, under certain conditions and QoI choices, further reviews of more informed uncertainties could help better estimate sensitivities and propagated uncertainties. For the purposes of this work, those additional parameter investigations are considered out of scope and are recommended as future work in Section 8.3.

Chapter 4

Plasma Formation

Portions of this chapter have been included in the ***AIAA SciTech 2025 Forum*** [113]. *Reproduced with the permission of the American Institute of Aeronautics and Astronautics.*

4.1 Introduction

This chapter focuses on the first case study in Table 2.2 and involves a continuation of the GSA/UQ methods and flight conditions utilized by Aiken & Boyd (2024) [64] with a 1D inviscid space-marching two-temperature solver applied to 2D viscous axisymmetric flows around a representative vehicle. Similarities and differences between these models' GSA/UQ metrics are made while also investigating the spatial variations of these metrics in a 2D axisymmetric domain. To this date, no surveyed studies have included GSA/UQ metrics for QoIs that span the entire flowfield around a hypersonic vehicle under weakly-ionized, thermochemical nonequilibrium conditions. Further trends involved with plasma formation uncertainty due to uncertain parameter and spatial variances are therefore investigated.

Both the previous GSA/UQ plasma formation studies and this work utilize 11 species air chemistry models with freestream molar fractions corresponding to the standard atmosphere values of molecular nitrogen and oxygen. To best balance accuracy and computational cost, several plasma constituent case studies are investigated at 7 km/s as seen in Table 4.1. For 7, 9, and 11 species air, the freestream air constituents include only molecular nitrogen and oxygen. For 14 species air, Ar, Ar^+, and CO_2 species were included, along with various dissociation, exchange, and ionization reactions. A comparison of the electron number densities along the stagnation line at 7 km/s and 60 km is made in Figure 4.1. Under these conditions, it is clear that 7 and 9 species air underpredict the maximum plasma formed in this region when compared to 11 species. However, 14 species air and included freestream molar fractions for Ar and CO_2 do not significantly affect electron number density at appreciable values. The percent differences between 11 and 14 species air plasma formation is approximately 2% at regions of maximum n_e formation along

the stagnation line. Therefore, this work will include only the freestream molar fractions, ions, and reactions within the 11 species case. The following section further delineates these reactions and other parameters involved.

Table 4.1: Plasma species cases, neutral and plasma constituents, and total reactions

Case	Neutral Species*	Plasma Species	Total Reactions	Reaction Refs.
7 Species	N_2 (0.79), O_2 (0.21) NO, N, O	NO^+, e^-	22	
9 Species	N_2 (0.79), O_2 (0.21) NO, N, O	NO^+, N_2^+, O_2^+, e^-	34	[64,172]
11 Species	N_2 (0.79), O_2 (0.21) NO, N, O	NO^+, N_2^+, O_2^+, N^+, O^+, e^-	47	
14 Species	N_2 (0.78), O_2 (0.21), Ar (0.0096), CO_2 (0.0004), NO, N, O	NO^+, N_2^+, O_2^+, N^+, O^+, Ar^+, e^-	59	[64,172–177]

*Numbers in parentheses indicate freestream molar fractions

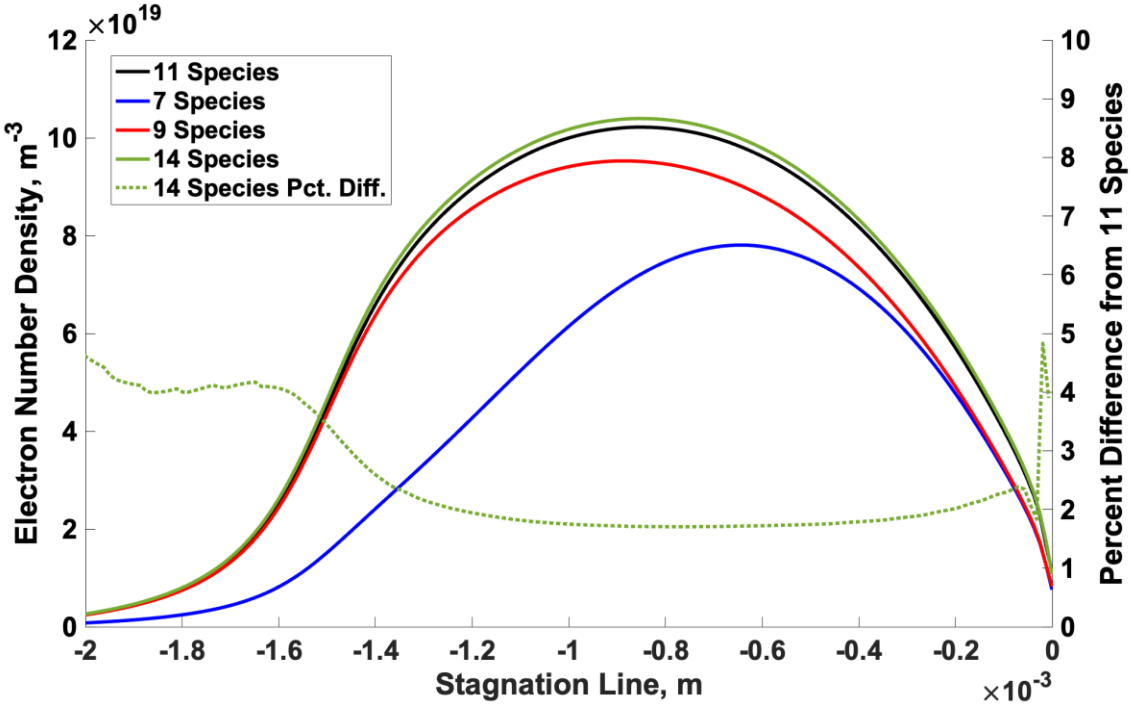

Figure 4.1: Electron number densities along the stagnation line for various plasma species and reaction sets at 7 km/s, 60 km

4.2 Methodology and Implementation

4.2.1 Uncertain Parameters

Uncertain parameters baseline definitions and uncertainty bounds that vary from those reviewed in Chapter 3 are defined in Table 4.2. These parameters and bounds are identical to those in Aiken and Boyd (2024) to facilitate comparison of geometry and model effects on GSA/UQ metrics while controlling input conditions [64]. The first 47 parameters include forward gas phase chemical reaction rate coefficients k_f in standard Arrhenius form. The sampled uncertainty bounds are applied as multiplicative factors to the preexponential terms of the Arrhenius expression. Reaction baselines are from Park 1993 [172] with the exception of reactions 32 and 45. Baseline and uncertainty bound references from West et al. (2023) are also listed for these reaction parameters [54]. Parameters 48-55 involve a survey of values utilizing the Millikan and White semiempirical correlations conducted by Aiken and Boyd for uncertainty bounds [64]. Baselines calculated using expressions for A_{sr} and B_{sr} in Millikan and White are then multiplied by the sampled values [69]. Parameters 56-57 are similarly sampled from bounds and multiply the baseline σ_{er} values in Equation 18. Lastly, parameter 58 uses an α_{EII} baseline value of 0.3 and multiplier values ensuring a range of 0.1 to 1.0.

Table 4.2: Uncertain parameters, baselines, and multiplier bounds.

No	Identifier	Baseline parameter	Units	Bounds	Refs.
1	$N_2 + N \rightleftharpoons 2N + N$	$k_f = 3.00x10^{22}T_a^{-1.60}\exp(-113{,}200/T_a)$		$U(0.2, 3.0)$	
2	$N_2 + O \rightleftharpoons 2N + O$	$k_f = 3.00x10^{22}T_a^{-1.60}\exp(-113{,}200/T_a)$		$U(0.2, 3.0)$	
3	$N_2 + N_2 \rightleftharpoons 2N + N_2$	$k_f = 7.00x10^{21}T_a^{-1.60}\exp(-113{,}200/T_a)$		$U(0.5, 4.0)$	
4	$N_2 + O_2 \rightleftharpoons 2N + O_2$	$k_f = 7.00x10^{21}T_a^{-1.60}\exp(-113{,}200/T_a)$		$U(0.5, 4.0)$	
5	$N_2 + NO \rightleftharpoons 2N + NO$	$k_f = 7.00x10^{21}T_a^{-1.60}\exp(-113{,}200/T_a)$		$U(0.5, 4.0)$	
6	$N_2 + N^+ \rightleftharpoons 2N + N^+$	$k_f = 3.00x10^{22}T_a^{-1.60}\exp(-113{,}200/T_a)$		$U(0.2, 3.0)$	
7	$N_2 + O^+ \rightleftharpoons 2N + O^+$	$k_f = 3.00x10^{22}T_a^{-1.60}\exp(-113{,}200/T_a)$		$U(0.2, 3.0)$	
8	$N_2 + N_2^+ \rightleftharpoons 2N + N_2^+$	$k_f = 7.00x10^{21}T_a^{-1.60}\exp(-113{,}200/T_a)$	cm^3 mol^{-1} s^{-1}	$U(0.5, 4.0)$	[1,54,64,119, 137,172]
9	$N_2 + O_2^+ \rightleftharpoons 2N + O_2^+$	$k_f = 7.00x10^{21}T_a^{-1.60}\exp(-113{,}200/T_a)$		$U(0.5, 4.0)$	
10	$N_2 + NO^+ \rightleftharpoons 2N + NO^+$	$k_f = 7.00x10^{21}T_a^{-1.60}\exp(-113{,}200/T_a)$		$U(0.5, 4.0)$	
11	$O_2 + N \rightleftharpoons 2O + N$	$k_f = 1.00x10^{22}T_a^{-1.50}\exp(-59{,}500/T_a)$		$U(0.3, 1.3)$	
12	$O_2 + O \rightleftharpoons 2O + O$	$k_f = 1.00x10^{22}T_a^{-1.50}\exp(-59{,}500/T_a)$		$U(0.3, 1.3)$	
13	$O_2 + N_2 \rightleftharpoons 2O + N_2$	$k_f = 2.00x10^{21}T_a^{-1.50}\exp(-59{,}500/T_a)$		$U(0.3, 1.3)$	
14	$O_2 + O_2 \rightleftharpoons 2O + O_2$	$k_f = 2.00x10^{21}T_a^{-1.50}\exp(-59{,}500/T_a)$		$U(0.3, 1.3)$	
15	$O_2 + NO \rightleftharpoons 2O + NO$	$k_f = 2.00x10^{21}T_a^{-1.50}\exp(-59{,}500/T_a)$		$U(0.3, 1.3)$	
16	$O_2 + N^+ \rightleftharpoons 2O + N^+$	$k_f = 1.00x10^{22}T_a^{-1.50}\exp(-59{,}500/T_a)$		$U(0.3, 1.3)$	
17	$O_2 + O^+ \rightleftharpoons 2O + O^+$	$k_f = 1.00x10^{22}T_a^{-1.50}\exp(-59{,}500/T_a)$		$U(0.3, 1.3)$	

18	$O_2 + N_2^+ \rightleftharpoons 2O + N_2^+$	$k_f = 2.00x10^{21}T_a^{-1.50}\exp(-59{,}500/T_a)$		$U(0.3, 1.3)$	
19	$O_2 + O_2^+ \rightleftharpoons 2O + O_2^+$	$k_f = 2.00x10^{21}T_a^{-1.50}\exp(-59{,}500/T_a)$		$U(0.3, 1.3)$	
20	$O_2 + NO^+ \rightleftharpoons 2O + NO^+$	$k_f = 2.00x10^{21}T_a^{-1.50}\exp(-59{,}500/T_a)$		$U(0.3, 1.3$	
21	$NO + N \rightleftharpoons N + O + N$	$k_f = 4.57x10^{17}T_a^{0.00}\exp(-75{,}500/T_a)$		$U(0.3, 1.3)$	
22	$NO + O \rightleftharpoons N + O + O$	$k_f = 4.57x10^{17}T_a^{0.00}\exp(-75{,}500/T_a)$		$U(0.2, 2.5)$	
23	$NO + N_2 \rightleftharpoons N + O + N_2$	$k_f = 2.08x10^{16}T_a^{0.00}\exp(-75{,}500/T_a)$		$U(0.2, 2.5)$	
24	$NO + O_2 \rightleftharpoons N + O + O2$	$k_f = 2.08x10^{16}T_a^{0.00}\exp(-75{,}500/T_a)$		$U(0.2, 2.5)$	
25	$NO + NO \rightleftharpoons N + O + NO$	$k_f = 4.57x10^{17}T_a^{0.00}\exp(-75{,}500/T_a)$		$U(0.2, 2.5)$	
26	$NO + N^+ \rightleftharpoons N + O + N^+$	$k_f = 4.57x10^{17}T_a^{0.00}\exp(-75{,}500/T_a)$		$U(0.2, 2.5)$	
27	$NO + O^+ \rightleftharpoons N + O + O^+$	$k_f = 4.57x10^{17}T_a^{0.00}\exp(-75{,}500/T_a)$		$U(0.2, 2.5)$	
28	$NO + N_2^+ \rightleftharpoons N + O + N_2^+$	$k_f = 2.08x10^{16}T_a^{0.00}\exp(-75{,}500/T_a)$		$U(0.2, 2.5)$	
29	$NO + O_2^+ \rightleftharpoons N + O + O_2^+$	$k_f = 2.08x10^{16}T_a^{0.00}\exp(-75{,}500/T_a)$		$U(0.2, 2.5)$	
30	$NO + NO^+ \rightleftharpoons N + O + NO^+$	$k_f = 4.57x10^{17}T_a^{0.00}\exp(-75{,}500/T_a)$		$U(0.2, 2.5)$	
31	$N_2 + O \rightleftharpoons NO + N$	$k_f = 6.00x10^{13}T_a^{0.10}\exp(-38{,}000/T_a)$	cm^3 mol^{-1} s^{-1}	$U(0.4, 1.3)$	[54,64,128]
32	$O_2 + N \rightleftharpoons NO + O$	$k_f = 2.49x10^{09}T_a^{1.18}\exp(-4{,}010/T_a)$		$U(0.1, 10)$	[54,64,136]
33	$N + O \rightleftharpoons NO^+ + e^-$	$k_f = 8.80x10^{8}T_a^{1.00}\exp(-31{,}900/T_a)$	cm^3 mol^{-1} s^{-1}	$U(0.1, 10)$	
34	$N + N \rightleftharpoons N_2^+ + e^-$	$k_f = 4.40x10^{07}T_a^{1.50}\exp(-67{,}500/T_a)$		$U(0.3, 1.3)$	[54,64,172]
35	$O + O \rightleftharpoons O_2^+ + e^-$	$k_f = 7.10x10^{02}T_a^{2.70}\exp(-80{,}600/T_a)$		$U(0.1, 10)$	
36	$N_2 + O_2^+ \rightleftharpoons N_2^+ + O_2$	$k_f = 9.90x10^{12}T_a^{0.00}\exp(-40{,}700/T_a)$		$U(0.1, 10)$	
37	$NO^+ + N \rightleftharpoons O^+ + N_2$	$k_f = 3.40x10^{13}T_a^{-1.08}\exp(-12{,}800/T_a)$		$U(0.1, 10)$	
38	$NO^+ + O \rightleftharpoons N^+ + O_2$	$k_f = 1.00x10^{12}T_a^{0.50}\exp(-77{,}200/T_a)$		$U(0.1, 10)$	
39	$NO^+ + O_2 \rightleftharpoons O_2^+ + NO$	$k_f = 2.40x10^{13}T_a^{0.41}\exp(-32{,}600/T_a)$	cm^3	$U(0.1, 10)$	
40	$NO^+ + N \rightleftharpoons N_2^+ + O$	$k_f = 7.20x10^{13}T_a^{0.00}\exp(-35{,}500/T_a)$	mol^{-1} s^{-1}	$U(0.1, 10)$	[1,54,64,172]
41	$O_2^+ + N \rightleftharpoons N^+ + O_2$	$k_f = 8.70x10^{13}T_a^{0.14}\exp(-28{,}600/T_a)$		$U(0.1, 10)$	
42	$O^+ + NO \rightleftharpoons N^+ + O_2$	$k_f = 1.40x10^{05}T_a^{1.90}\exp(-26{,}600/T_a)$		$U(0.1, 10)$	
43	$NO^+ + O \rightleftharpoons O_2^+ + N$	$k_f = 7.20x10^{12}T_a^{0.29}\exp(-48{,}600/T_a)$		$U(0.1, 10)$	
44	$O^+ + N_2 \rightleftharpoons N_2^+ + O$	$k_f = 9.10x10^{11}T_a^{0.36}\exp(-22{,}800/T_a)$		$U(0.1, 10)$	
45	$N_2 + e^- \rightleftharpoons 2N + e^-$	$k_f = 6.00x10^{03}T_a^{2.60}\exp(-113{,}200/T_a)$	cm^3 mol^{-1} s^{-1}	$U(0.1, 10)$	[54,64,121]
46	$N + e^- \rightleftharpoons N^+ + e^- + e^-$	$k_f = 2.50x10^{34}T_a^{-3.82}\exp(-168{,}600/T_a)$	cm^3 mol^{-1} s^{-1}	$U(0.5, 2.0)$	[1,54,64,172, 178]
47	$O + e^- \rightleftharpoons O^+ + e^- + e^-$	$k_f = 3.90x10^{33}T_a^{-3.78}\exp(-158{,}500/T_a)$		$U(0.4, 3.0)$	
48	$\boldsymbol{\tau}_{vt}$, $N_2 + N_2$	$\tau_{sr} = \frac{101{,}325}{p}\exp\left[A_{sr}\left(T_{tr}^{-\frac{1}{3}} - B_{sr}\right) - 18.42\right]$ $A_{sr} = 1.16x10^{-3}\mu_{sr}^{\frac{1}{2}}\theta_{v_s}^{\frac{4}{3}}$ $B_{sr} = 0.015\,\mu_{sr}^{\frac{1}{4}}$ $\mu_{sr} = \frac{M_s M_r}{M_s + M_r}$	s	$U(0.3, 1.5)$	[64,149]
49	$\boldsymbol{\tau}_{vt}$, $N_2 + N$			$U(0.5, 2.0)$	[64,149]
50	$\boldsymbol{\tau}_{vt}$, $N_2 + O_2$			$U(0.1, 10)$	[64,150]
51	$\boldsymbol{\tau}_{vt}$, $N_2 + O$			$U(0.1, 10)$	[64,150]
52	$\boldsymbol{\tau}_{vt}$, $O_2 + O_2$			$U(0.5, 2.0)$	[64,151]
53	$\boldsymbol{\tau}_{vt}$, $O_2 + O$			$U(0.5, 4.0)$	[64,150,152]
54	$\boldsymbol{\tau}_{vt}$, $O_2 + N_2$			$U(0.1, 5.0)$	[64,150]
55	$\boldsymbol{\tau}_{vt}$, $O_2 + N$			$U(0.3, 2.0)$	[64,150]
56	$\boldsymbol{\sigma}_{er}$, N	S_{h-e} $= 3R_u\rho_e(T_{tr} - T_{ve})\sqrt{\frac{8R_uT_{ve}}{\pi M_e}}\sum_{s\neq e}\frac{\rho_s N_a}{M_s^2}\sigma_{er}$	m^2	$U(0.1, 10)$	[54,64]
57	$\boldsymbol{\sigma}_{er}$, O			$U(0.1, 10)$	
58	$\boldsymbol{\alpha}_{EII}$	$S_{e-i} = 0.3\left(\dot{w}_{N,EII}M_N I_N + \dot{w}_{O,EII}M_O I_O\right)$	-	$U(0.3, 3.3)$	[64,70,153]

4.2.2 Grid Refinement and Tailoring

An example of a baseline computational grid and geometry used in the case study are depicted in Figure 4.2(a). The IRV-2 vehicle body is approximated as a sphere-biconic geometry with a nose radius of 0.0195 m and total length of 1.386 m. For this study, the geometry represents the first 0.15 m from nose tip of the IRV-2 flight vehicle [71,114,179]. A grid refinement study is conducted to decrease epistemic uncertainty for the electron number density QoIs. Coarse, baseline, and fine grids defined in Table 4.3 are evaluated at 5, 7, and 9 km/s at 60 km. Each refinement study starts from the original grids and is shock-tailored three times. Each shock alignment routine is called after flow residuals converge to a plateau value. Shock detection is set to 95% of the freestream Mach number value and allows for 10% of the wall-normal cells to be placed upstream of the detected shock region. An example of a shock-tailored grid is depicted in Figure 4.2(b). More details on the shock alignment processes in LeMANS and LeMANS-MOPAR-MD can be found in Section 5.3.1 and references [71,114,180]. After shock tailoring for each grid and condition, percent differences in the electron number density QoIs are determined throughout the flowfield by interpolating and comparing values from coarse to baseline and baseline to fine grids as seen in the 7 km/s example in Figure 4.3. The larger percent differences in plasma formation between grids resides predominantly outside the shock layer or further downstream away from the body. The baseline grid is chosen for each flight condition with a maximum percent difference less than 2% throughout all considered flow conditions.

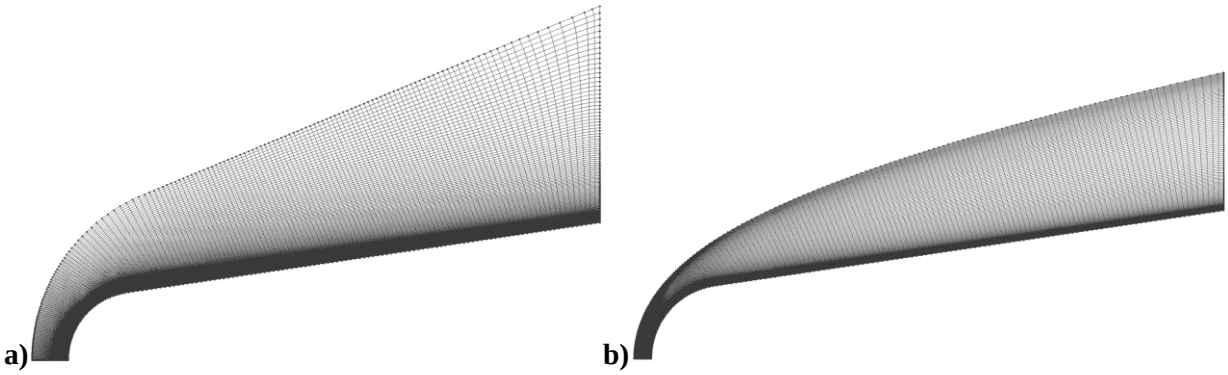

Figure 4.2: Baseline (a) original and (b) 3 times shock-aligned domains at 7 km/s, 60 km

Table 4.3 Grid refinement study at 7 km/s, 60 km

Grid descriptor	Coarse	Baseline	Fine
Grid type		Two-dimensional structured	
Streamwise nodes	97	176	200
Wall normal nodes	88	194	250
Cells	8,352	33,775	49,551
Shock alignments	3	3	3
Maximum plateaued residual	4.77×10^{-12}	1.10×10^{-12}	6.39×10^{-13}
Local y^+	0.16-0.18	0.13-0.18	0.09-0.68
Wall boundary condition 1		Isothermal at 1,000 K	
Wall boundary condition 2		Plasma catalytic (Forced ion recombination)	
Uncoupled cost (core-hours)	101	1,862	2,136

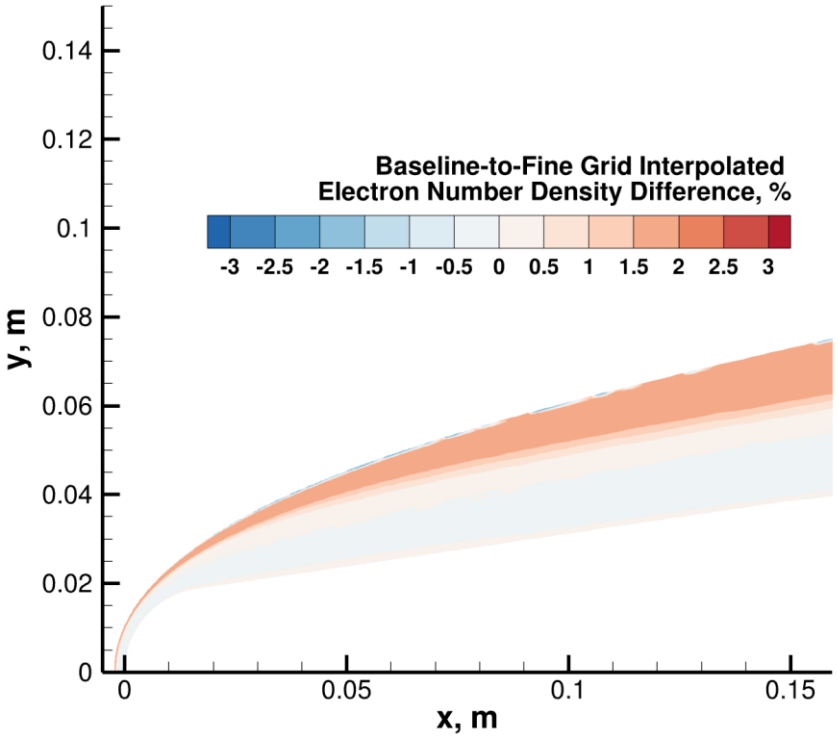

Figure 4.3: Grid refinement study on electron number density percent change at 7 km/s, 60 km.

4.2.3 Dakota and UQLab Implementation

The customized configuration of Dakota employed in this study is depicted in Figure 4.4, initiating with an embarrassingly parallel process where Dakota runs on a small resource allocation to synchronously generate a batch of M evaluations. Each evaluation begins with a set of uncertain parameters sampled by Dakota, which are then preprocessed by a custom driver file to populate respective input files for LeMANS.

Evaluation drivers subsequently submit and autonomously monitor job statuses on CU Boulder's Alpine cluster. Once a LeMANS simulation (including three shock alignments) concludes for an evaluation, the results are post-processed and stored. Subsequent evaluations, starting with M+1, are initiated sequentially until all evaluations are completed. GSA and UQ metrics are then computed and output by Dakota. All simulations are submitted in parallel in this fashion in the largest batch amounts allowed ($M = 1{,}000$) and are executed as resources become available. After completion of all specified evaluations, sampled parameters and QoIs are post processed both with Dakota and in UQlab for sensitivity and uncertainty metric comparisons.

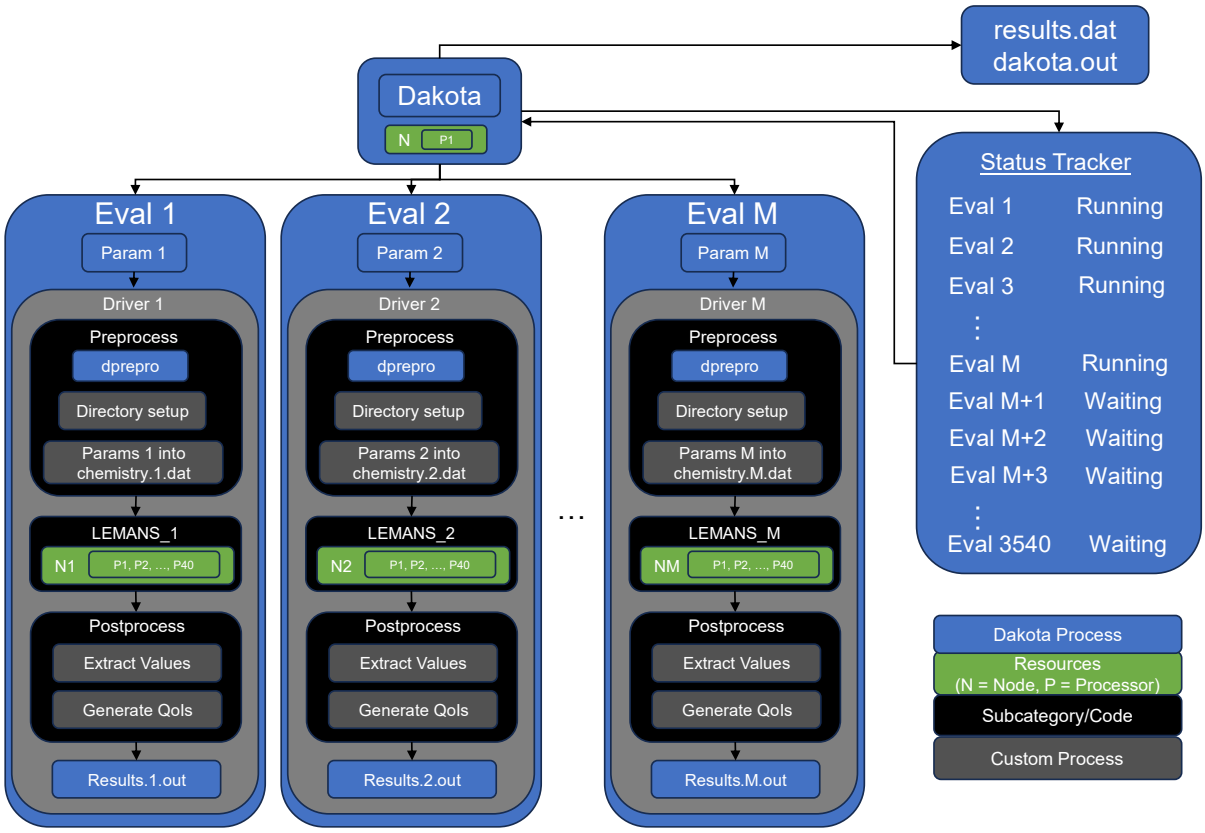

Figure 4.4: Integration of LeMANS into Dakota meta-parallel framework.

4.2.4 Baseline, PCE Derived and Propagated Mean and Variance Metrics

Electron number densities are obtained at each flow condition using the baseline set of parameters in Table 4.2. Once PCE coefficients are approximated, electron number density mean and variance values

for a given field location can be directly found from Ψ_0 and D_T in Equations 78 and 81, respectively. However, these moments alone do not incorporate the effects of 'off-design' samples and therefore, do not account for uncertainties associated with potential overfitting the QoI surrogate model. Therefore, Monte Carlo sampling of each PCE is conducted with 10^6 samples to generate mean and 95% confidence intervals for each PCE/QoI. These metrics provide a location-specific context for where the relative Sobol' indices influence the largest uncertainty bounds throughout the flowfield.

4.2.5 GSA/UQ Implementation and QoI Determination

For each evaluation, Dakota is used following Figure 4.4 to generate 58 parameters via Latin hypercube sampling from uniform uncertainty intervals in Table 4.2 that are first transformed into logarithmic space and normalized to the interval $[-1,1]$. Legendre polynomials are then created from these joint-uniform distributions to populate the $\mathbf{\Psi}$ matrix. Following Equation 79, second order ($p = 2$) PCEs are used with the 58 parameters and an oversampling ratio of 2 for a total of 3,540 evaluations.

After all evaluations are complete, electron number densities at each CFD node-centered grid point for a given evaluation ($N_{QoIs} = 193x175 = 33{,}775$ grid points) are bilinearly interpolated to the baseline grid as depicted in Figure 4.5. This figure conveys a conceptual example of three shock aligned grids as a function of input parameters (ξ_1, ξ_2, ξ_{N_s}) and the baseline grid (ξ_{BL}). Electron number densities throughout the flowfields of each evaluation are interpolated to the baseline grid location for each respective point. For evaluations and locations where extrapolation is required, nearest neighbor interpolation is utilized. This is considered sufficient as these locations have near freestream values outside of the shock layer for the respective grids. After interpolating all electron number density values, OLS regression is conducted on the resulting matrix equation in Figure 4.5 and a PCE is built at all N_{QoIs} grid locations. Each PCE's coefficients are then used to obtain total Sobol' indices and PCE's are evaluated 10^6 times via Monte Carlo sampling to obtain means and uncertainty bounds at each location. Streamlines are then produced to facilitate 2D spatially varying visualization and interpretation of GSA/UQ metrics throughout the flowfield.

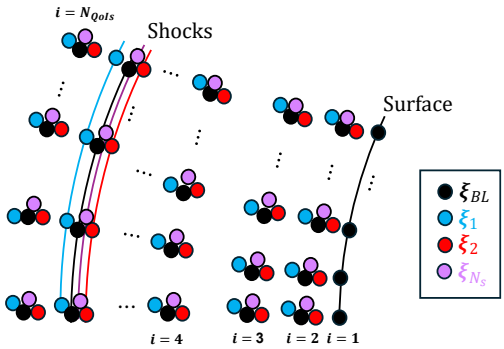

$$\begin{pmatrix} \boldsymbol{R}_i(x_i(\xi_1), y_i(\xi_1), \xi_1) \xrightarrow{\text{interp}} \boldsymbol{R}_i(x_i(\xi_{BL}), y_i(\xi_{BL}), \xi_1) \\ \boldsymbol{R}_i(x_i(\xi_2), y_i(\xi_2), \xi_2) \xrightarrow{\text{interp}} \boldsymbol{R}_i(x_i(\xi_{BL}), y_i(\xi_{BL}), \xi_2) \\ \vdots \\ \boldsymbol{R}_i(x_i(\xi_{N_S}), y_i(\xi_{N_S}), \xi_{N_S}) \xrightarrow{\text{interp}} \boldsymbol{R}_i(x_i(\xi_{BL}), y_i(\xi_{BL}), \xi_{N_S}) \end{pmatrix} = \begin{pmatrix} \Psi_{i,0}(\xi_1) & \Psi_{i,1}(\xi_1) & \cdots & \Psi_{i,N_P}(\xi_1) \\ \Psi_{i,0}(\xi_2) & \Psi_{i,1}(\xi_2) & \cdots & \Psi_{i,N_P}(\xi_2) \\ \vdots & \vdots & \ddots & \vdots \\ \Psi_{i,0}(\xi_{N_S}) & \Psi_{i,1}(\xi_{N_S}) & \cdots & \Psi_{i,N_P}(\xi_{N_S}) \end{pmatrix} \begin{pmatrix} \alpha_{i,0} \\ \alpha_{i,1} \\ \vdots \\ \alpha_{i,N_P} \end{pmatrix} : 1 \leq i \leq N_{QoIs}$$

Figure 4.5: Conceptual example of electron number density QoI field interpolation to the baseline (BL) grid. Evaluation 1, 2, and N_S grids are shown as examples for depicting the interpolation process for all QoIs.

4.3 Results and Discussion

4.3.1 1D MTCR and 2D Axisymmetric CFD Plasma

Previous 1D inviscid simulations of 11 species reactive 2T flows were conducted by Aiken & Boyd [64] with freestream and post-shock flow conditions outlined in Table 4.4. Rankine–Hugoniot relations are used to calculate these post-shock conditions assuming constant vibrational-electron-electronic energy across the shock. This 1D space-marching post-shock inviscid flow solver includes GSA/UQ analyses for these flow conditions over a distance range out to 0.10 m downstream of the shock. For the purposes of comparison, identical parameter baselines, uncertainty bounds with Latin hypercube sampling of lognormal distributions, oversampling ratio, PCE order, and NIPC OLS regression are used in this case study's GSA/UQ analyses. Due to the computational domain differences in this solver, comparisons are made for metrics between the first 2.5×10^{-3} m downstream of the shock in the 1D flow and the shock aligned stagnation lines for the 2D axisymmetric flow. At 60 km, the diffuse nature of the shock in the 2D model over a finite distance leads to a somewhat arbitrary choice for the shock location when compared to the instantaneous discontinuity present in the 1D model. To help facilitate spatial comparison between models,

approximate shock locations are depicted in Figure 4.6. The approximate shock location is defined for each flight condition based on where the flow Mach number transitions from supersonic to subsonic along the stagnation line (vertical red dashed lines in the figure). Translational-rotational and vibrational-electron-electronic temperatures are also depicted for reference between flight conditions. These locations are also depicted in the GSA/UQ figures for the comparison purposes.

Table 4.4 1D Post-shock conditions at 60 km (T_∞ = 247.0 K, P_∞ = 22.0 Pa) from Aiken & Boyd [64].

	Normal Shock Velocity		
Condition	5 km/s	7 km/s	9 km/s
P, Pa	6,422	12,590	20,820
T_{tr}, K	12,280	23,850	39,270
T_{ve}, K	247.0	247.0	247.0
X_{O_2}, -	0.21	0.21	0.21
X_{N_2}, -	0.79	0.79	0.79

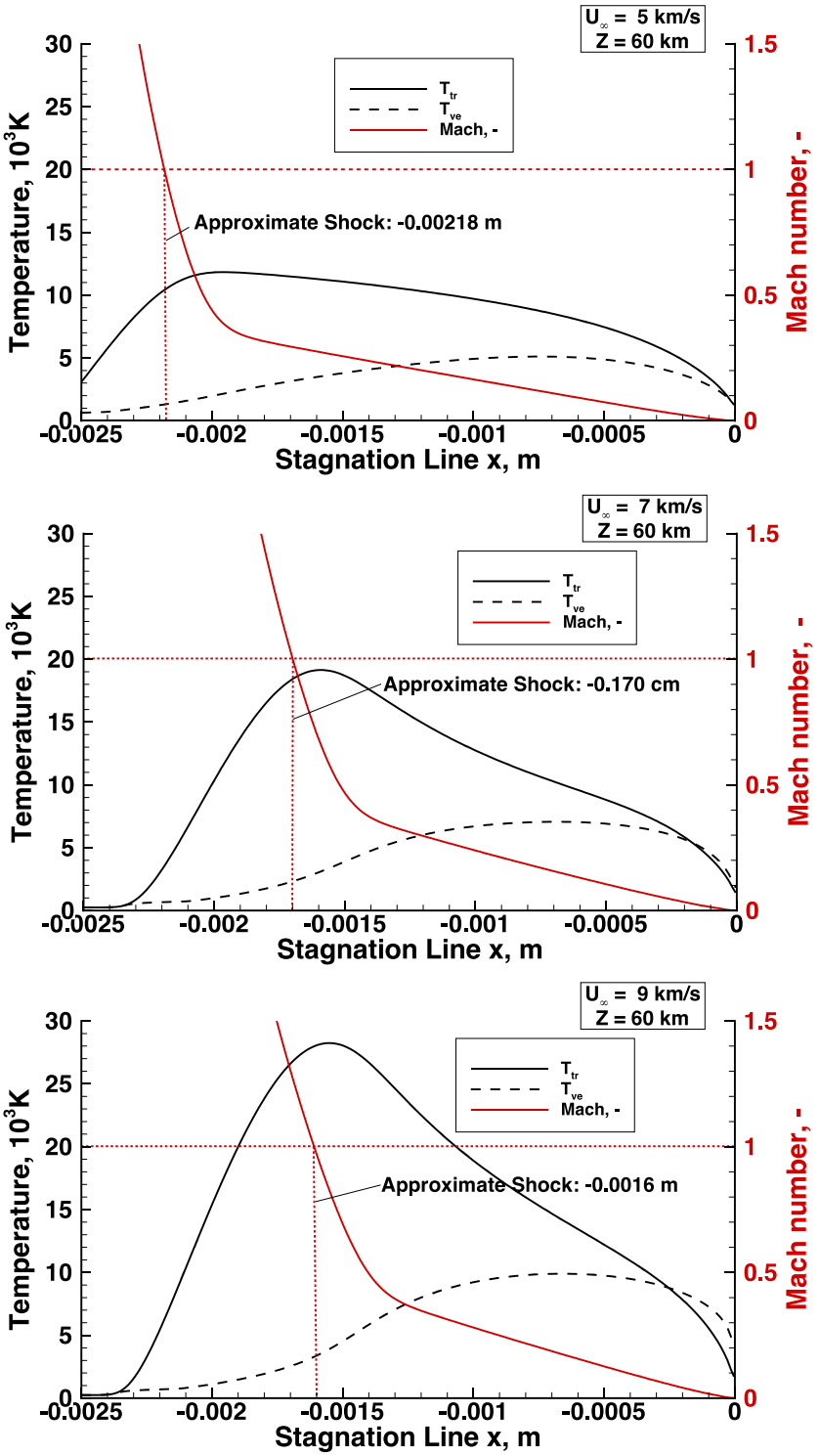

Figure 4.6: LeMANS 2D axisymmetric diffuse shock location estimation for comparison with 1D model results.

Baseline ionized species mole fraction comparisons are displayed in Figure 4.7 and are used to provide context for plasma formation and associated GSA/UQ metrics. Each of the rows depicts the 5, 7, and 9 km/s flow conditions for the columns representing 1D and 2D axisymmetric simulations, respectively. Mole fraction trends follow similar patterns across all conditions with the exception of the formation of O_2^+ near the shock at 5 km/s. The dissipation of energy through including viscous and associated transport terms accounts for a lower O_2^+ fraction at a given distance near the shock. Decreases in ion and electron mole fractions further downstream in the 2D model are explained by surface boundary conditions, i.e., isothermal temperature of 1,000 K and ion forced recombination (defined as "plasma catalytic" in this work) at the wall. These additional differences lead to flow compression near the wall in the 2D model and thus, cause earlier recombination of the ionized species than would be present solely based on the return to equilibrium conditions without the presence of a vehicle surface. Maximum electron number densities for each velocity condition follow similar relative increases between models. Electron number density maximums for the 1D model occur at approximately $3.0\text{x}10^{-3}$, $1.0\text{x}10^{-3}$ and $2.0\text{x}10^{-3}$ m downstream of the shock for 5, 7 and 9 km/s, respectively. The 9 km/s maximum electron number density distance increases due to electron impact ionization reactions occurring further downstream in the flow. Assuming the shock occurs at a unity Mach number value along the stagnation line, the 2D model electron number density maximums occur at approximately $1.5\text{x}10^{-3}$, $4.0\text{x}10^{-4}$, and $3.0\text{x}10^{-4}$ m downstream of the approximate shock for 5, 7 and 9 km/s, respectively. These maximum locations occur sooner in the 2D model due to the same wall influences on net ion recombination.

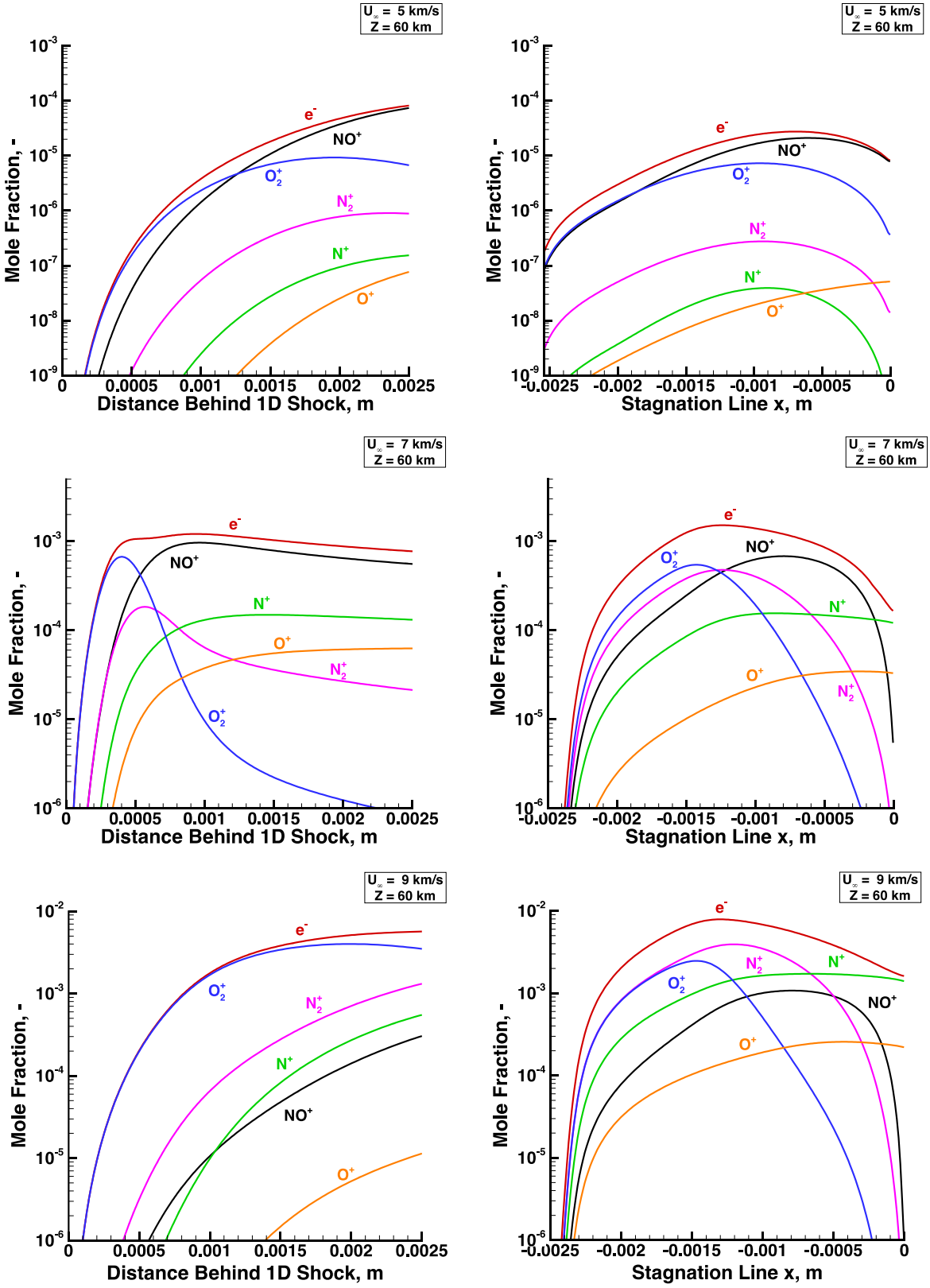

Figure 4.7: Mole fraction comparisons between 1D (left) and baseline 2D axisymmetric stagnation line (right).

Quantified uncertainty and sensitivity metrics in the form of Sobol' indices are also compared in Figure 4.8 between 1D post-shock and 2D axisymmetric flow along the stagnation line at 5 km/s, 60 km. The magnitude of peak ionization in the 1D model is a factor of 4 greater than that of the 2D stagnation line peak. This is mainly due to relatively lower post-shock maximum temperatures along the stagnation line due to fractions of the overall energy being accounted for in additional viscous terms as well as relief effects from adding additional dimensionality. The uncertainties follow similar trends with the peak uncertainty magnitudes for both models occurring near the maximum plateau. Wall boundary condition effects for the 2D model are observed in both the rapid decrease in electron number density upper bounds as well as an increase in uncertainty within $1.0\text{x}10^{-4}$ m from the stagnation point.

The inclusion of many more parameters with Sobol' indices less than 0.025 (grey lines) in the 2D model indicates higher complexity and more nonlinear interactions within the flow. This difference can be attributed to both the influences of accounting for viscous terms and dimensionality effects including interpolation between shock aligned meshes to the baseline mesh. The largest contributors to n_e variance, i.e., $N + O \rightleftharpoons NO^+ + e^-$, $O + O \rightleftharpoons O_2^+ + e^-$, and $O_2 + N_2 \rightleftharpoons 2O + N_2$, are similar for both models between $1.0\text{x}10^{-3}$ and $3.0\text{x}10^{-3}$ m behind the shock in the 1D case. These major variance contributors to n_e uncertainty are explained by the relative influences of those reactions that are limiting factors for the populations of N and O. Categorized source terms for N, O, and NO^+ are depicted in Figure 4.9 and illustrate where along the 2D stagnation line reaction types affect the pathway to plasma formation at 5 km/s. In the middle region where peak ionization occurs, the rate limiting step, i.e., associative ionization of NO^+, dominates. Up to $1.0\text{x}10^{-3}$ m behind the shock in the 1D model, O_2^+ formation and vibrational relaxation time parameters involving N_2 and O_2 have higher sensitivities, indicating a more complex mixture of variance contributions shortly after the Rankine-Hugoniot enforced instantaneous temperature increase from freestream conditions to over 12,000 K.

At greater than $3.0\text{x}10^{-3}$ m post shock in the 1D model, the most sensitive parameters decrease as NO^+ variance contributions increase. For the 2D stagnation line, wall effects including a rapid increase in

density and pressure lead to a net recombining region within $5x10^{-4}$ m from the wall as seen in Figure 4.9. Although compressed into a smaller region, similar increased variance influences from the nitrogen generating reactions (particularly through Zeldovich exchange) is observed in this recombination region as compared to the 1D model [64]. These boundary condition effects lead to earlier dissociative recombination to form N and O, as well as the recombination of neutral atoms for a given distance. These effects also lead to a much more rapid level-off of the baseline electron number density as compared with the 1D flow model. The sensitivity differences between these models show the effects of the 1D discontinuity (Rankine-Hugoniot relations) and inviscid assumptions for the same reacting flow chemical model.

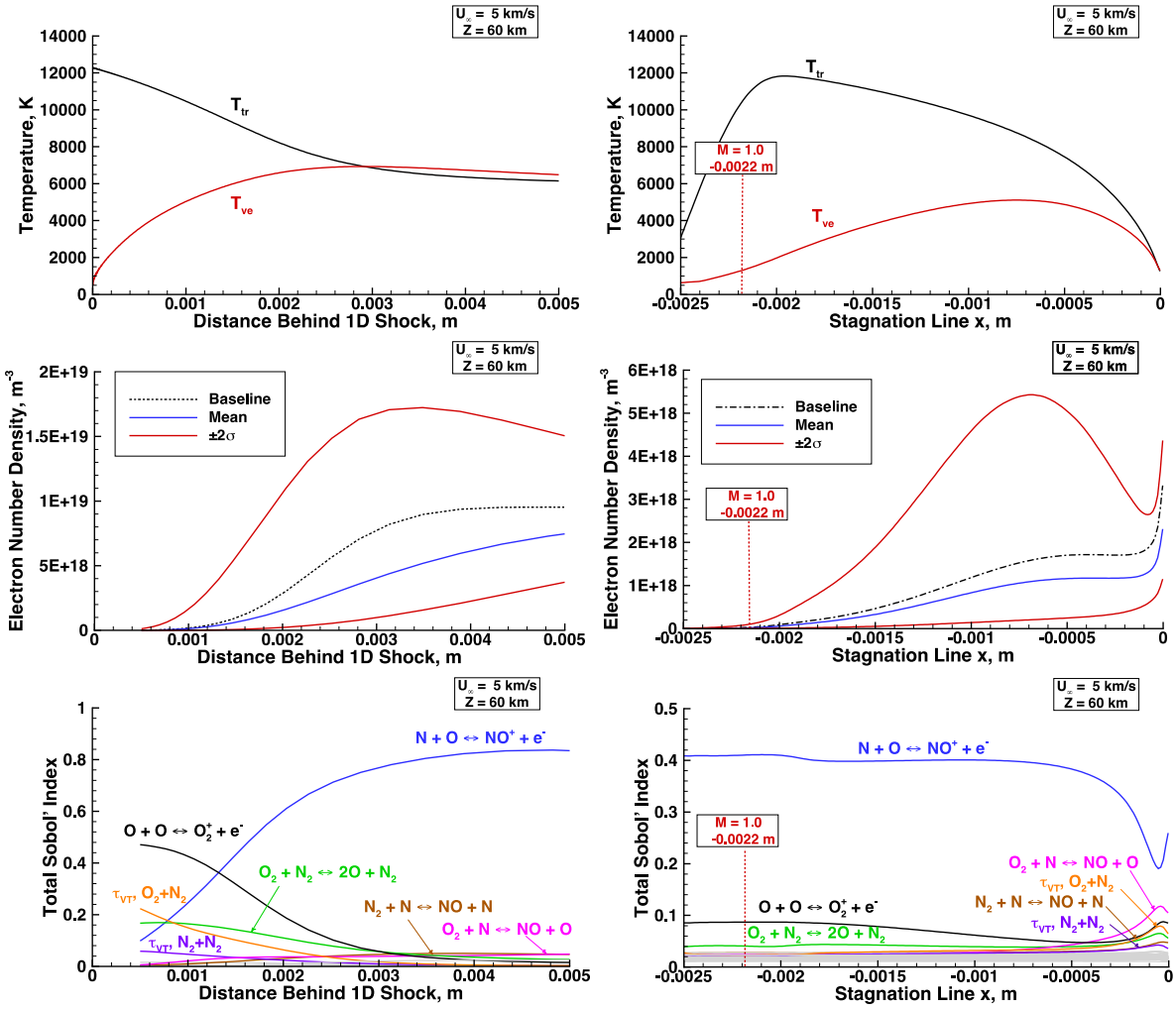

Figure 4.8: Uncertainty and sensitivity comparisons between 1D (left) and 2D axisymmetric stagnation line (right) at 5 km/s, 60 km.

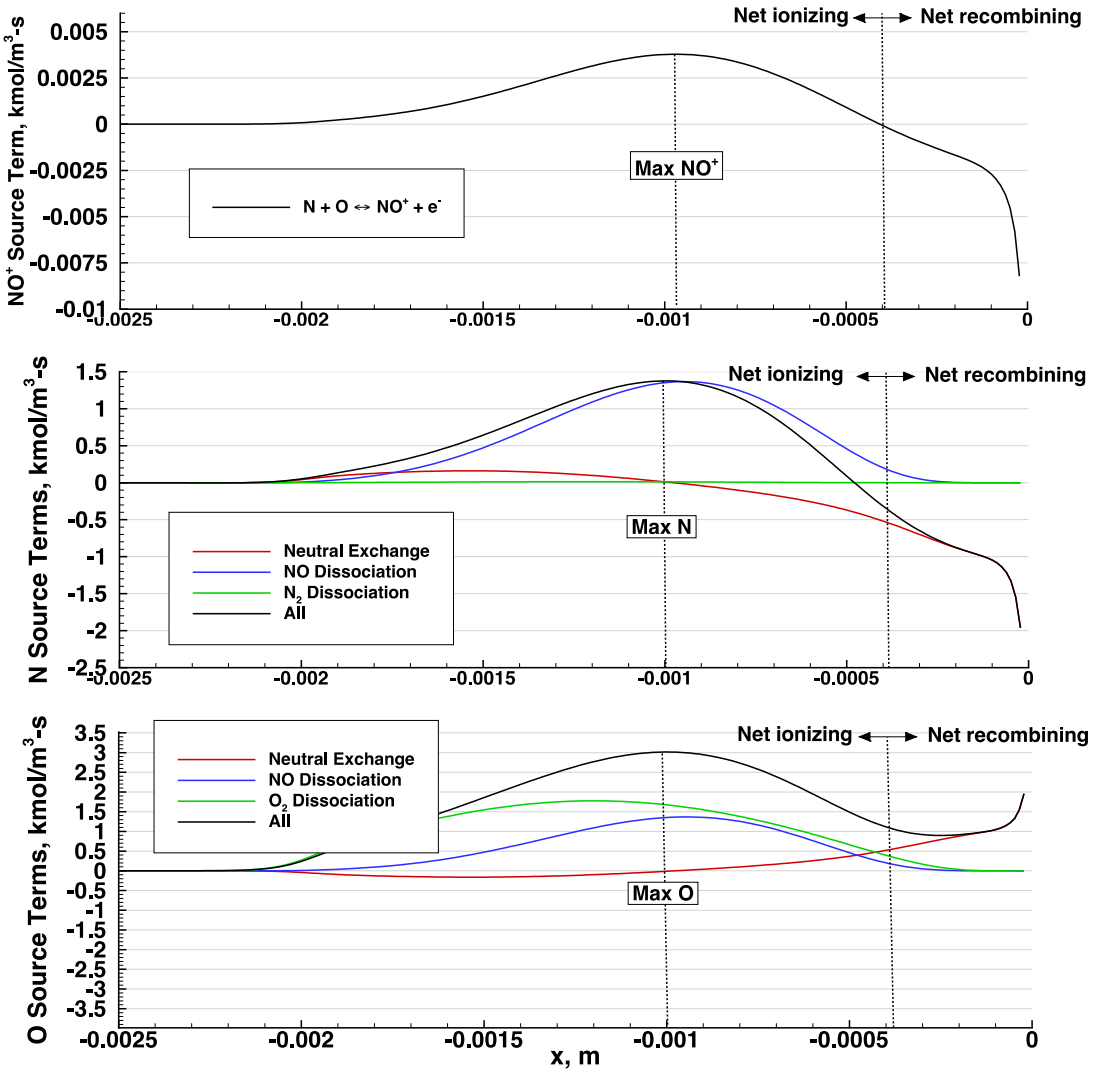

Figure 4.9: Dominant source terms for *N*, *O*, and NO^+ along the stagnation line at 5 km/s, 60 km.

Similar quantified uncertainty and sensitivity comparisons are made for 7 km/s in Figure 4.10. Unlike at slower conditions, the more defined shock layer of the 2D model yields similar electron number density peaks, where the 1D model is a factor of 1.2 greater for the baseline parameter set. Additionally, uncertainty bounds follow similar trends and values except near the shock. The larger uncertainty bounds for the 1D model between 1.0×10^{-3} and 5.0×10^{-3} m post shock are a function of the rapid increase in temperature over a short distance influencing a larger dependence on uncertainty from the parameters. The more gradual controlling temperature increase in the 2D model yields smaller uncertainty bounds for a

given distance along the stagnation line. A similar trend of decreasing electron number density occurs within 5.0x10^{-4} m from the wall followed by a rapid increase within 1.0x10^{-4} m of the wall in the 2D model.

A greater number of significant parameter variance influences are experienced at 7 km/s when compared to 5 km/s, particularly for Zeldovich exchange reaction parameters involved in nitrogen atom formation. Additionally, more defined shock influences on GSA/UQ metrics are seen at ~2.2x10^{-3} m from the vehicle surface. The major parameter contributions to n_e uncertainty are associative ionization reactions to form O_2^+ followed by NO^+ along both 1D and 2D stagnation lines. The NO^+ sensitivity peaks at the maximum n_e formation for both models. The second Zeldovich reaction to form NO is more sensitive outside the shock and is followed by similarly low values with a slight increase along the stagnation line. This increase, as well as an increase in first Zeldovich reaction and charge exchange reaction $O_2^+ + N \rightleftharpoons N^+ + O_2$ sensitivities are experienced after peak n_e in the 2D model as the flow compresses between 1.0x10^{-3} and 2.0x10^{-4} m from the stagnation point. These relative increases and the decrease in NO^+ variance contributions are explained by comparing the relative mole fraction of N^+ in the bottom right of Figure 4.7. As the relative fraction of N^+ ions increases in this region, variance of reaction parameters that contribute to pathways that involve N^+ exert a greater effect on n_e variance. In contrast, the 1D ion mole fractions do not experience significant changes over a similar length scale as seen in the bottom left of Figure 4.7. Overall, GSA/UQ metric differences of the 2D model are mainly present near the diffuse shock and wall influenced regions.

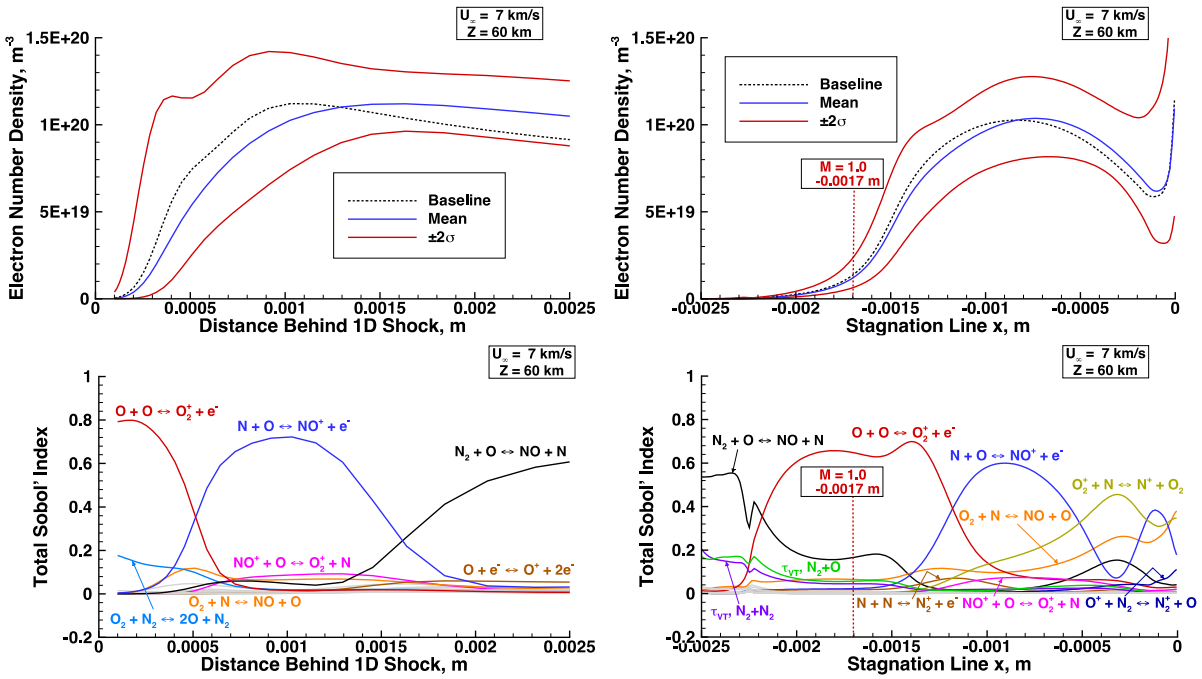

Figure 4.10: Uncertainty and sensitivity comparisons between 1D (left) and 2D axisymmetric stagnation line (right) at 7 km/s, 60 km.

The maximum electron number density at 9 km/s for the 1D model within the first $2.5x10^{-3}$ m of the shock is a factor of 3 larger than that of the 2D model. Similar effects associated with the models' frameworks account for these differences, including higher dimension relief effects and the inclusion of viscous flux terms in the 2D model. The maximum uncertainty range for the 1D model is approximately $7.0x10^{21}$ m^{-3} and occurs near the maximum electron number density location. The 2D model maximum uncertainty range is $1.1x10^{21}$ m^{-3} and occurs closer to the wall. The difference between models can be explained by examining the bottom row of Figure 4.7. First, O_2^+ formed via associative ionization is present in both models closer to the shock, but the 2D model includes a larger relative fraction of N_2^+ ions, leading to a larger importance for N formation via Zeldovich exchange nitrogen dissociation as the limiting set of reactions for N_2^+ formation via associative ionization. The reason for lower O_2^+ fractions follows that of the slower flow conditions. Second, because the 2D model experiences slower energy transfer from kinetic to thermal and internal forms, reaction pathways experienced in the 1D model over a similar distance post-shock (including electron impact ionization) do not have enough time or space to occur prior to

encountering wall influences. The factor of 6.3 larger maximum uncertainty bounds in the 1D case is therefore explained by the larger variance contributions from electron impact ionization seen in Figure 4.11.

The Sobol' index plots follow these trends in Figure 4.11, where electron impact ionization with atomic nitrogen dominates the larger uncertainty bounds in the 1D model while the 2D model sensitivities appear to lag behind until the estimated shock location at -1.6x10^{-3} m along the stagnation line. This relative shift in sensitivities leads to similar variance contribution trends after this location, where O_2^+ associative ionization is followed by exchange reaction of O_2^+ and second Zeldovich mechanism up until approximately 5.0x10^{-4} m from the wall in the 2D model. These comparisons are of particular importance for identifying reactions that most influence plasma formation while accounting also for viscous flow, dimensional relief, and vehicle shape effects.

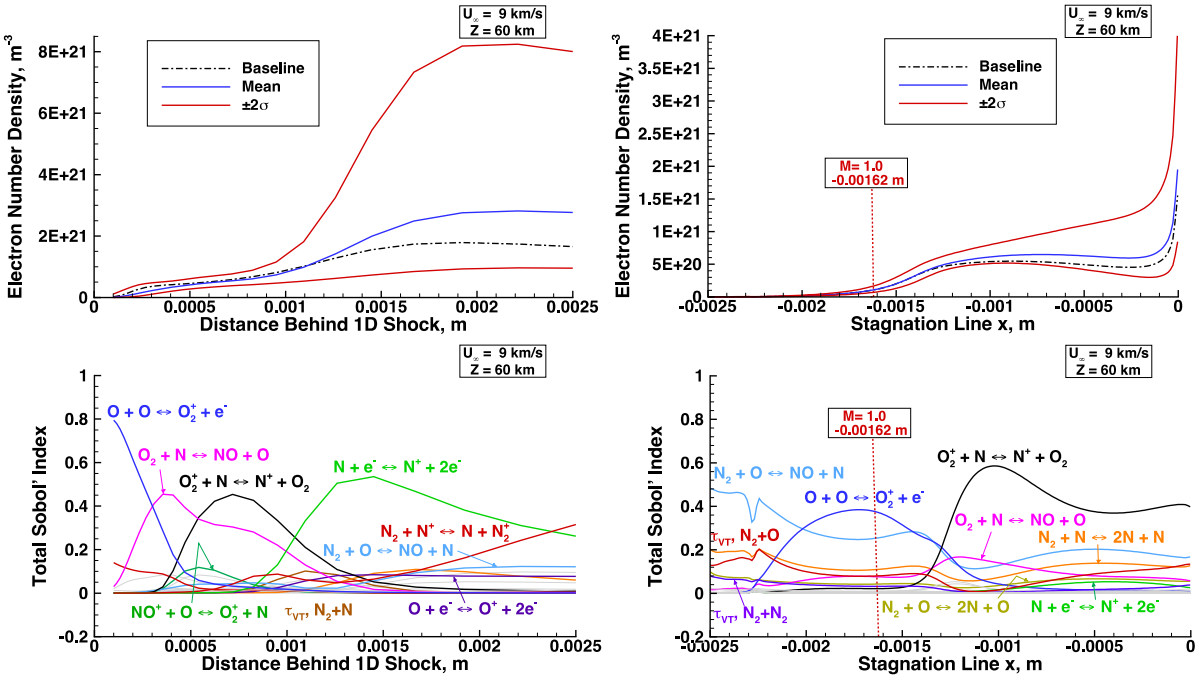

Figure 4.11: Uncertainty and sensitivity comparisons between 1D (left) and 2D axisymmetric stagnation line (right) at 9km/s, 60 km.

4.3.2 Field Sensitivity and Uncertainty Results

Interest in the uncertainty of plasma formation as a function of spatial location and associated relative global sensitivity variance fractions has led to GSA/UQ analyses for QoIs across the entire flowfield

domain. To help visualize the spatial trends across the axisymmetric flowfield, select streamtraces are extracted. Along each streamtrace, the baseline electron number density as well as the Monte Carlo sampled means, 95% confidence intervals, and total Sobol' indices for each QoI are depicted.

Select streamtraces are depicted as the rows in Figure 4.12 for the 5 km/s condition. The seed locations for these traces are chosen to represent the general trend in plasma formation, uncertainty in that formation, and the apportionment of each parameter's variance on that uncertainty as a function of location in the flowfield. The left column shows the streamtrace location within the flowfield, where streamtraces 3, 6 and 9 are located progressively closer to the stagnation line and the vehicle body. Streamtrace 3 represents flow across a diffuse shock case with lower electron number densities. Plasma formation along this trace is gradual with increasing uncertainty further downstream. The largest uncertainty contributions in this region are from associative ionization of atomic nitrogen and oxygen to form NO^+. Before n_e rises to a relatively appreciable amount while crossing the diffuse shock, the variance in relaxation time for the dissociation of O_2 with partner N_2 $(\tau_{VT}, O_2 - N_2)$ contributes to over 27% of electron number density variance. As previously stated, this localized sensitivity is expected near the shock as O_2 dissociation to produce oxygen atoms is a precursor to the associative ionization induced production of NO^+ and O_2^+ [23,99]. A 24% contribution to uncertainty from NO^+ production occurs in the post shock region and decreases to 21% further downstream. Uncertainty within the second Zeldovich reaction, oxygen dissociation with partner nitrogen and associative ionization to produce O_2^+ show similar sensitivities characterizing 3-6% of total uncertainty contributions. It is important to note that the largest uncertainty region along this streamtrace occurs furthest away from the shock as n_e increases.

Streamtrace 6 at 5 km/s represents a midpoint seed in the flowfield, where a stronger shock and higher n_e lead to a profile along the streamline characterized by a sharp spike in plasma formation and increased uncertainty bounds followed by a recombination region with lower relative uncertainties. An increasingly localized region of oxygen dissociation sensitivity is present crossing a stronger shock, followed by a similar, but more pronounced decrease in sensitivity for associative ionization to produce

NO^+ further downstream. This difference as well as increased sensitivity for the second Zeldovich and oxygen dissociation reactions is ultimately caused by the dissociative recombination into N and O species further downstream. This return to chemical equilibrium occurs after rapid associative ionization gives way to recombination as vibrational relaxation and dissociation cause the temperature to decrease.

Streamtrace 9 follows similar n_e uncertainty trends with increased magnitudes and a larger range near a nearly normal shock. The majority of the contributions to the large uncertainty in this region of maximum local electron number density ($y \approx 1.0x10^{-2}$ m) consist of associative ionization to produce NO^+ and O_2^+ with 26% and 6.2% overall uncertainty fractions, respectively. The larger overshoot of electron production through associative ionization leads to more rapid recombination with a similar distribution of parameter sensitivities as in the other streamtraces.

Sobol' index fields for the top five most sensitive parameters at 5 km/s are depicted in Figure 4.13. These provide a more complete context for those parameters with the largest n_e uncertainty contributions as a function of spatial location in the flow. The largest contributor throughout the post-shock region of the flowfield is associative ionization of atomic nitrogen and oxygen to form NO^+. Lower sensitivity values for this reaction occur further downstream near the shock and surface. Looking at the other variance contributors, except for O_2^+ formation, the largest Sobol' index locations correspond to lower variance contributions for $N + O \rightleftharpoons NO^+ + e^-$. For τ_{VT,O_2-N_2}, rate limiting occurs in the weaker, diffuse shock regions further downstream where a relatively longer amount of time and space is required for vibrational relaxation and O_2 dissociation. Electron number density in this region is limited by vibrational-translational energy exchange, the first step in electron formation due to its role in facilitating atomic oxygen production, which is then followed by associative ionization with atomic nitrogen to produce NO^+. For the second Zeldovich reaction and oxygen dissociation with partner nitrogen, larger sensitivities occur further downstream away from the shock region, where N and O concentrations affect the dissociative recombination of electrons with NO^+. Lastly, $O + O \rightleftharpoons O_2^+ + e^-$ follows a similar, albeit less pronounced sensitivity trend to NO^+production rates in the post-shock region near the nose.

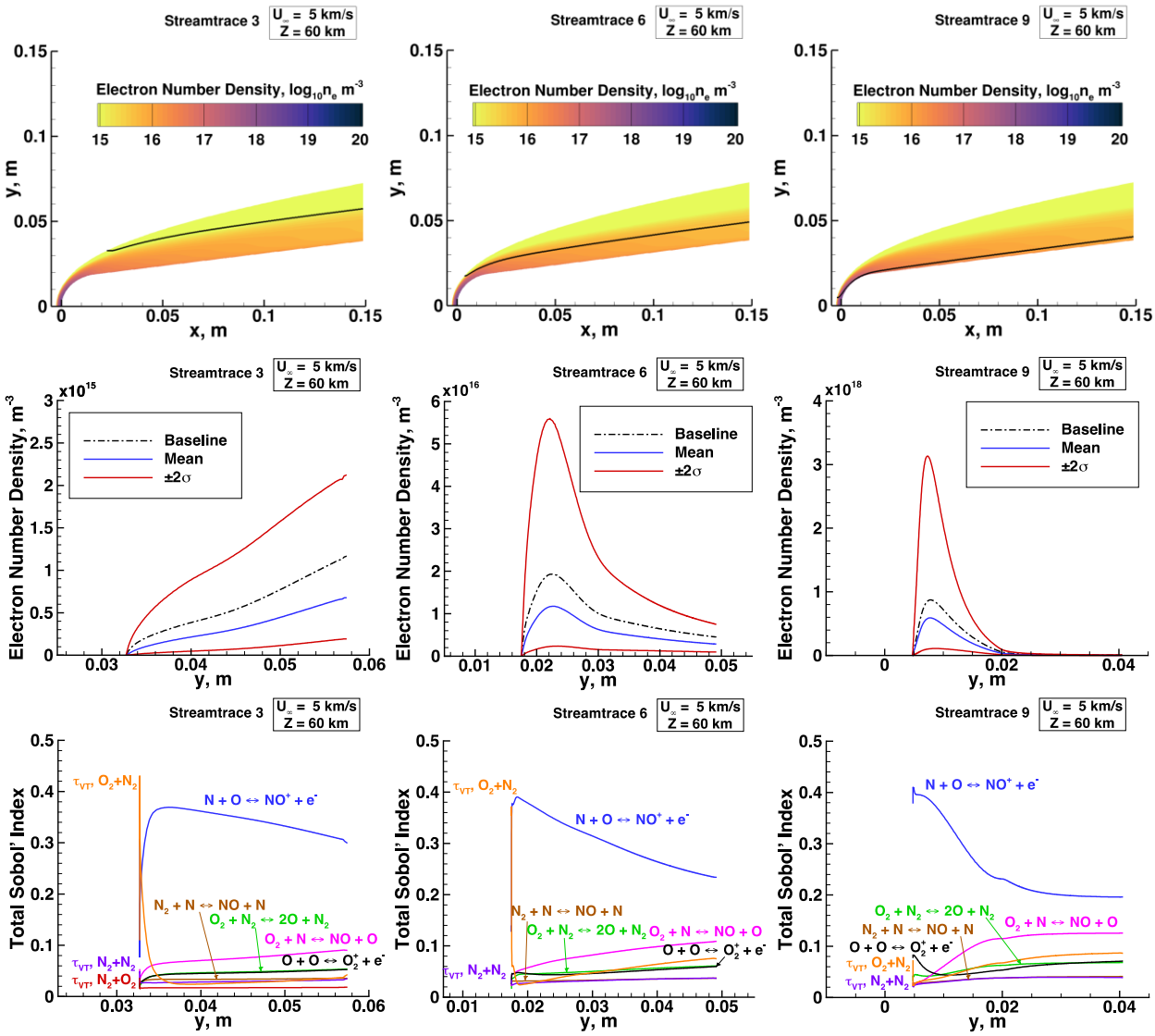

Figure 4.12: 2D axisymmetric electron number density field, select streamtraces, and associated uncertainties and global sensitivities at 5 km/s, 60 km.

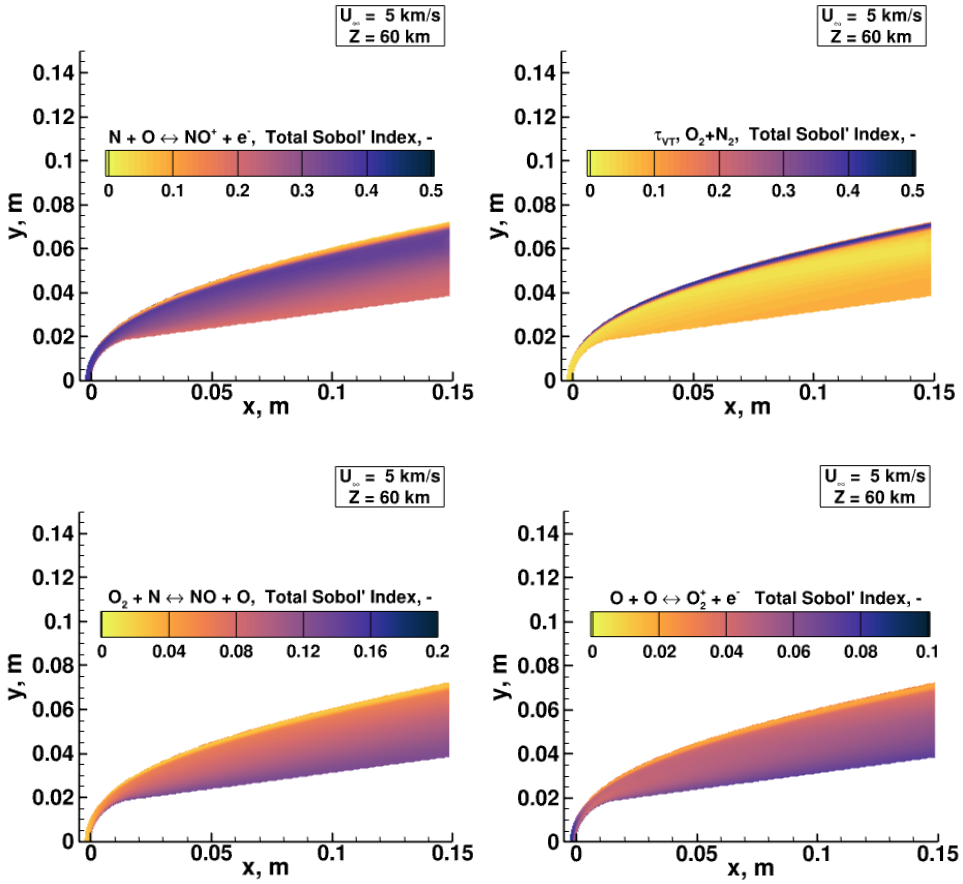

Figure 4.13: Highest parameter variance contributions to electron number density uncertainty flowfields at 5 km/s, 60 km.

Similar streamtrace and field analyses are conducted at 7 km/s and are depicted in Figure 4.14. An expected stronger bow shock and larger associated electron number densities ($\sim 10^{15}$ to 10^{21} m^{-3}) are depicted in the left column of the figure. Electron number density spatial variations, uncertainty bounds, as well as dominating variance contributions from associative ionization to form NO^+ are similar to those at 5 km/s in regions downstream of the shock. However, significant increased complexity in parameter variance contributions is experienced crossing the bow shock for all streamtraces. In this region, dominant parameters include those involved with vibrational-translational relaxation times for both nitrogen and oxygen, Zeldovich pathways as well as NO dissociation. Additionally, increased spatial variation in dominant sensitivities is seen as the streamlines turn around the vehicle. This qualitative observation is

explained by the initial compression passing the shock, followed by a second body-induced compression and then further expansion as the streamtraces turn parallel to the vehicle downstream.

For streamtrace 3 at 7 km/s, vibrational-translational relaxation and NO dissociation are most sensitive crossing the relatively weaker shock, while dissociative recombination from NO^+ dominates downstream where the majority of n_e uncertainty exists. Streamtrace 6 depicts stronger shocks with increased local variance contributions. Similar to 5 km/s, associative ionization to form O_2^+ and $O_2 + N \rightleftharpoons NO + O$ sensitivities increase in the immediate post-shock region. In contrast to 5 km/s, variance contributions from charge exchange reactions at 7 km/s become relatively more pronounced as the flow turns around the vehicle shoulder. Streamtrace 9 near the boundary layer includes more variance contributions from charge exchange reactions as these reactions play an important role in enforcing the plasma catalytic boundary condition at the surface.

The field Sobol' indices in Figure 4.15 include additional major variance contributors that depend more upon spatial location for 7 km/s. Associative ionization of N and O to form NO^+ is still the dominant variance contributor throughout the flow, but sections immediately post-shock near the stagnation line as well as around the shoulder of the vehicle give way to other variance contributors. These sensitivities include Zeldovich and charge exchange reactions that are associated with the recompression and expansion of the flow as it moves around the vehicle. Lastly, the region crossing the shock further downstream includes increased sensitivities from oxygen and nitrogen vibrational relaxation and NO dissociation parameters. These follow similar trends and explanations to that of the 5 km/s sensitivity field results.

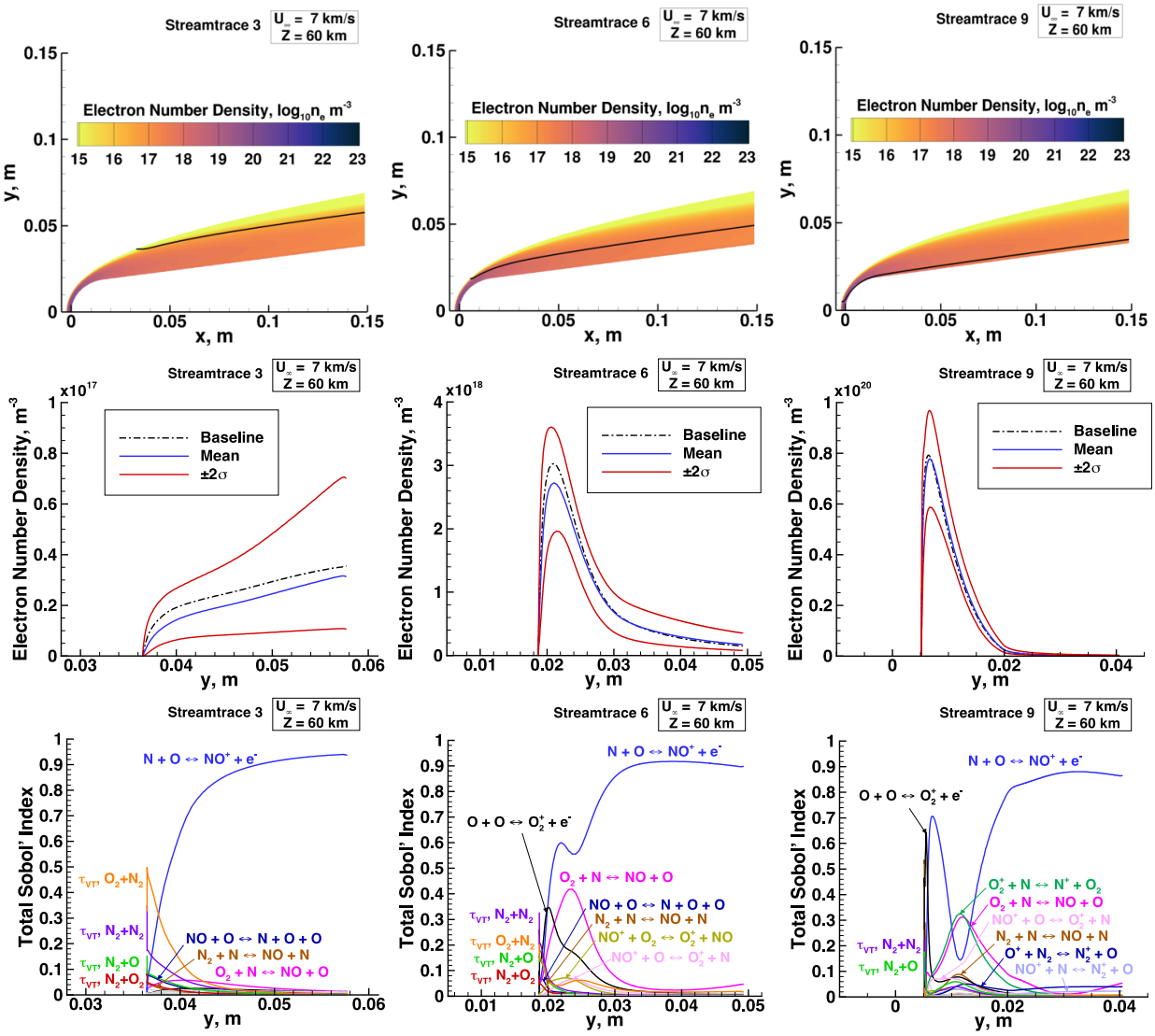

Figure 4.14: 2D axisymmetric electron number density field, select streamtraces, and associated uncertainties and global sensitivities at 7 km/s, 60 km.

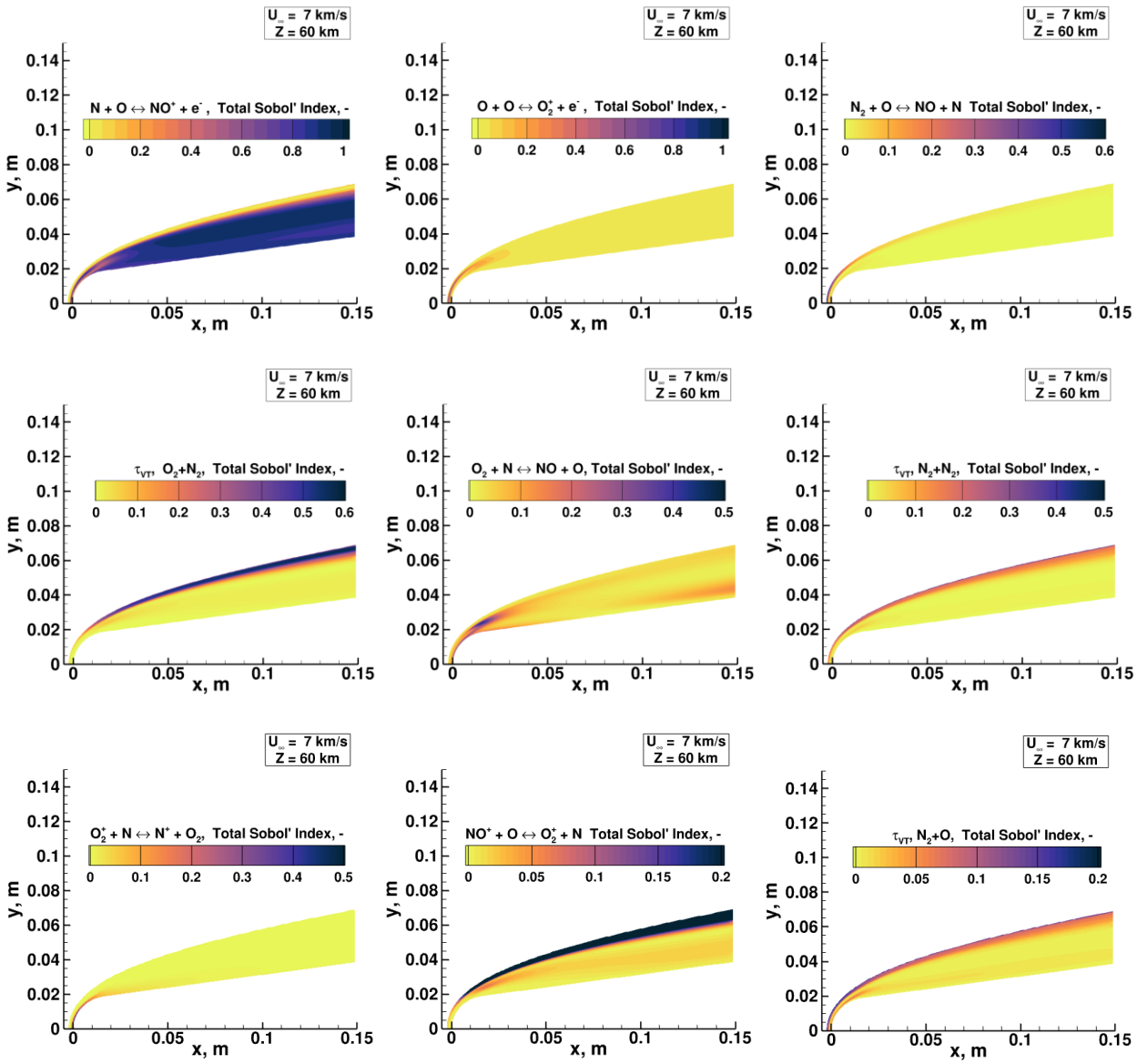

Figure 4.15: Highest parameter variance contributions to electron number density uncertainty flowfields at 7 km/s, 60 km.

Streamtraces for 9 km/s, electron number density uncertainty bounds, and Sobol' indices are depicted in Figure 4.16. The baseline, mean and 95% confidence intervals follow similar trends to that of 7 km/s with maximum values ranging between 10^{16} to 10^{21} m^{-3} throughout the flowfield. Streamtrace 3 shows a similar increase in n_e magnitude and uncertainty range moving further downstream. Similar to 7

km/s, streamtraces 6 and 9 for 9 km/s show peaks in n_e magnitude and uncertainty bounds shortly after crossing the bow shock followed by a decrease moving downstream.

Streamtrace 3 variance contributions to n_e uncertainty remain similar to that of 7 km/s, where uncertainty in nitrogen and oxygen dissociation parameters contribute most crossing the weak shock followed by NO^+ dissociative recombination dominance as n_e begins to plateau further downstream. Streamtrace 6 variance contributions exhibit similar complexities at 7 km/s near the shoulder of the vehicle, with greater Sobol' indices for the first Zeldovich reaction crossing the shock followed by a more pronounced increase, decrease and then increase in Sobol' indices for the NO^+ associative ionization reaction. Within the dip region at the shoulder, the second Zeldovich and O_2^+ associative ionization reactions increase in variance contributions. These two observations for Streamtrace 6 make sense because for the similar streamtrace locations, a higher freestream velocity, subsequent compressed post-shock region and higher relative plasma formation all accentuate the variation in Sobol' indices during compression and expansion at the shock and around the vehicle shoulder. Variance contributions for streamtrace 9 are significantly different than those at slower speeds. Variance contributions from NO^+ associative ionization are significantly less and are instead comprised of O_2^+ charge exchange to N^+, O_2^+ associative ionization and first Zeldovich reaction contributions near the strong shock. Explanations for these major contributors are similar to those detailed at the stagnation line in the lower right sections of Figure 4.7 and Figure 4.10, where the importance of associative ionization reactions to produce ion molecules gives way to charge exchange reactions (particularly for those that influence N^+ production). As a precursor to this charge exchange, atomic nitrogen production via the Zeldovich mechanism understandably also remains influential to plasma formation in this region both prior and after peak n_e along the streamline.

The largest field variance contributions to n_e at 9 km/s are depicted in Figure 4.17. These parameter contributions still include associative ionization reactions in certain flowfield locations; however, nitrogen dissociation and charge exchange influences increase near the vehicle surface when compared to slower freestream velocities. Relaxation time parameters have similar influences in the weaker shock regions

further downstream for reasons previously discussed. Overall, the pathways that most influence n_e formation at 5 and 7 km/s for the majority of the flowfield no longer apply at 9 km/s, where nitrogen dissociation and subsequent charge exchange influences extend into larger portions of the flowfield.

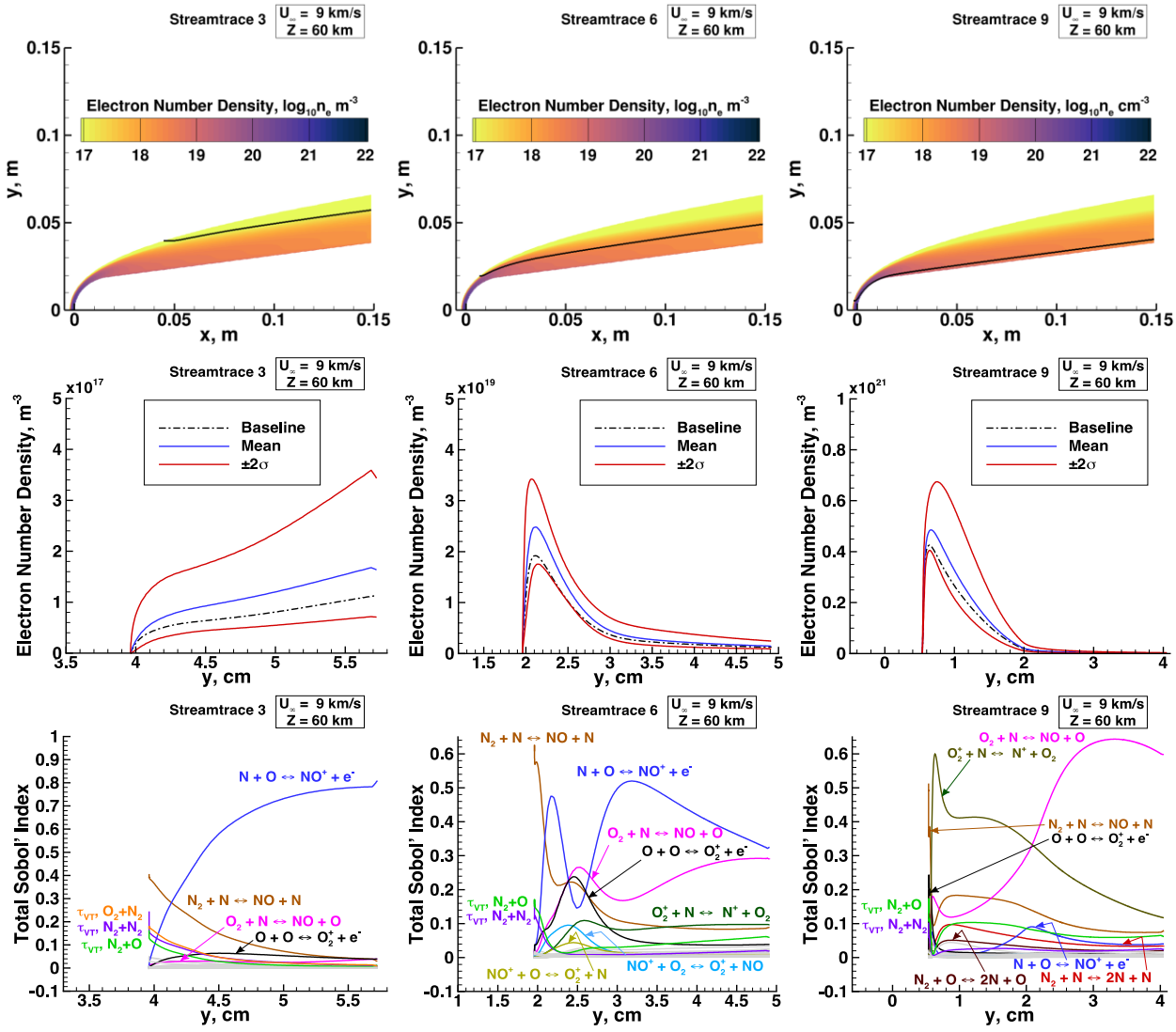

Figure 4.16: 2D axisymmetric electron number density field, select streamtraces, and associated uncertainties and global sensitivities at 9 km/s, 60 km.

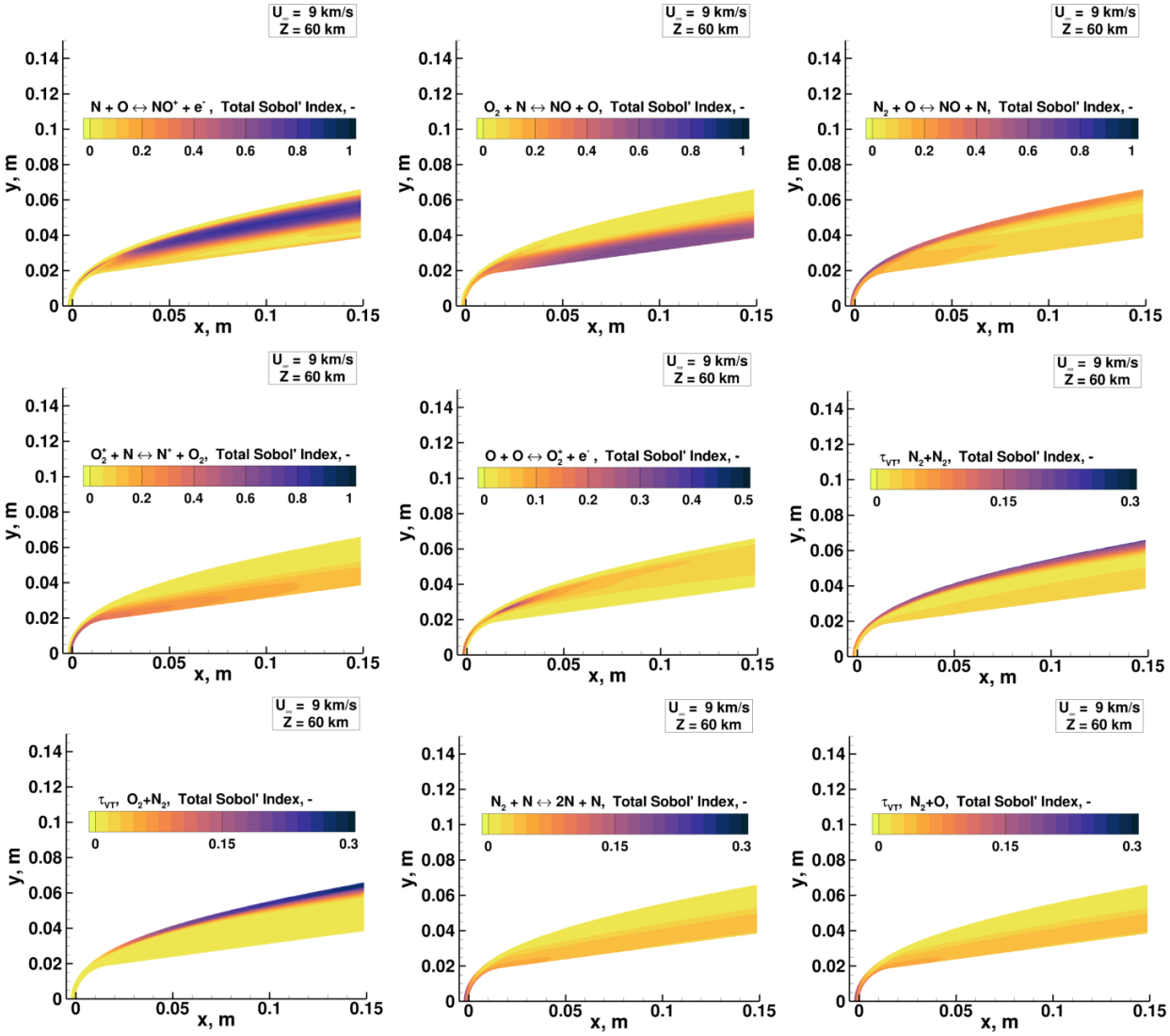

Figure 4.17: Highest parameter variance contributions to electron number density uncertainty flowfields at 9 km/s, 60 km.

Table 4.5 summarizes the 2D axisymmetric field n_e sensitivity trends for all freestream velocities at 60 km. All prominent locations are defined by general wall normal (pre/post-shock and wall) and streamwise (nose, shoulder, downstream) location combinations. Taken in context with the overall uncertainty bounds from Figure 4.12, Figure 4.14 and Figure 4.16, the parameters with the highest Sobol' indices near the nose and shoulder of the vehicle encompass the largest scaled variance contributions since n_e uncertainty is also the largest in these regions.

Table 4.5 Summary of electron number density field sensitivities.

Parameter	5 km/s, 60 km		7 km/s, 60 km		9 km/s, 60 km	
	Sobol' Index Maximum	Prominent Location(s)*	Sobol' Index Maximum	Prominent Location(s)*	Sobol' Index Maximum	Prominent Location(s)*
$N + O \leftrightarrow NO^+ + e^-$	0.40	PS, A	0.95	PS, N/DS	0.81	PS, SH/DS
$O + O \leftrightarrow O_2^+ + e^-$	0.10	PS, N; W, DS	0.62	PS, N	0.39	PS, N/SH
$\tau_{VT}, O_2 + N_2$	0.43	PS, DS	0.58	PS, DS	0.28	PS, DS
$O_2 + N \leftrightarrow NO + O$	0.15	W, DS	0.43	PS/W, SH	0.64	W, SH/DS
$N_2 + O \leftrightarrow NO + N$			0.55	PS, N	0.63	PS, N/SH
$\tau_{VT}, N_2 + N_2$			0.36	PS, A	0.28	PS, A
$O_2^+ + N \leftrightarrow N^+ + O_2$			0.46	W, N/SH	0.62	W, N/SH
$\tau_{VT}, N_2 + O$			0.18	PS, A; W, N	0.22	PS, A; W, N
$N_2 + N \leftrightarrow 2N + N$					0.22	PS, N; W, N/SH

*Wall normal location: PS = pre/post-shock, W = wall
Streamwise location: N = Nose, SH = shoulder, DS = downstream, A = all

4.4 Discussion and Summary

This case study integrated simulations with advanced sensitivity analysis and uncertainty quantification techniques to compare and contrast 2D axisymmetric plasma formation sensitivity and uncertainty metrics from previous 1D post-shock studies. Nonintrusive point collocation with polynomial chaos expansions was used to construct surrogate models for each CFD point within the flowfield around a spherical nose-cone representation of IRV-2 nose tip. A point collocation oversampling ratio of 2 was applied for freestream flow conditions of 5, 7 and 9 km/s at 60 km, resulting in 3,540 simulations per condition to evaluate 33,775 electron number density quantities of interest in the domain. For each simulation, input bounds for multiple parameters were Latin hypercube sampled in log-space for building the surrogates.

For 5 and 7 km/s, major reaction rate sensitivities on electron number density for the 2D model along the stagnation line are associative ionization and dissociative recombination of N and O. Moreover,

reactions producing N and O via direct dissociation of oxygen and Zel'dovich mechanism contribute significantly to variance. These trends align with sensitivities observed in 1D model analyses. Differences in these sensitivities between the models occurred near the shock (smaller contributions to n_e variance from the associative ionization to form O_2^+) and near the wall (smaller contributions to $n_e$variance from the associative ionization to form NO^+). These differences stem from the 1D model's assumption of a shock discontinuity and the 2D model's inclusion of plasma catalytic wall boundary conditions.

For 9 km/s, the sensitivities at the stagnation line follow an initial dependence on associative ionization to produce O_2^+ followed by charge exchange reaction $O_2^+ + N \rightleftharpoons N^+ + O_2$ and Zeldovich mechanism reactions for nitrogen dissociation. Electron impact ionization reaction sensitivities exhibited in the 1D model were not present along the 2D stagnation line due to the wall influences affecting flow conditions prior to their development. Considering electron number density uncertainties in the post-shock region, these sensitivity differences highlight how two-dimensional viscous effects and surface boundary conditions shape plasma evolution in axisymmetric nonequilibrium flow at the stagnation line. Additionally, these comparisons highlight where certain assumptions within an inviscid 1D flow can lead to different sensitivity and uncertainty conclusions that might not be valid when applied to higher fidelity vehicle applications.

Flowfield domain sensitivity and propagated uncertainty trends were also investigated using select streamtraces and flowfield Sobol' index diagrams. For 5 and 7 km/s, streamtraces nearest to the stagnation line and body exhibited the largest electron number density uncertainties, with the maximum variance contributions from $N + O \rightleftharpoons NO^+ + e^-$ occurring at the strong shock just after peak n_e values near the nose of the vehicle. At shock transition locations further away from the nose, the weaker shocks led to increased variance contributions to n_e uncertainty from vibrational relaxation times affecting O_2 dissociation. These were attributed to relatively lower temperature increases making vibrational-translational energy exchange rates the limiting factor influencing electron number density magnitudes near the weaker shock regions further downstream from the vehicle nose. At 7 and 9 km/s, increased complexity

and relative variance contributions from charge exchange reactions occurs near the vehicle shoulder and surface.

The results in this section have several implications on the study of plasma formation in weakly-ionized flow regimes. First, the comparisons between 1D inviscid and 2D axisymmetric models demonstrated that higher-fidelity, multi-dimensional simulations capture critical phenomena (e.g., shock diffusion, multidimensional energy relief, and wall boundary effects) that lower fidelity models may not capture. These case studies not only identified where these phenomena affect simulated electron number densities at baseline conditions, but also showed their effect on relative uncertainty bounds and variance contributions to those bounds. This is of particular interest for flows around slender suborbital vehicles like the IRV-2, where shorter shock standoff distances lead to less space along the stagnation line when compared to certain shock tube experiments and simulations. These effects are especially pronounced at 9 km/s, where the influence of the 2D model and vehicle geometry results in significant discrepancies in predicted plasma formation and associated uncertainty. These differences arise due to the limited space behind the diffuse shock, preventing the full development of pathway dependencies observed in the 1D model before experiencing wall boundary influences.

Second, the multidimensional uncertainty bounds and associated variance contribution fields provide insight into how variations in thermochemistry and energy exchange semiempirical relations affect plasma formation throughout the flowfield. Specifically, spatial variations in electron number density, uncertainty bounds, and variance contributions to those bounds depict significant thermochemical complexity as the flow expands around the shoulder region of the vehicle at 7 and 9 km/s. These findings have critical implications for vehicle design and experimental studies on plasma formation around slender vehicles. Subfields such as vehicle observation analysis, communications blackout, and magnetohydrodynamics can leverage these results or apply similar methods to refine uncertainty assessments for location-specific design goals [23,24].

Overall, the results in this case study can directly inform experimental and computational efforts whose aim is to improve ionization models. The depicted GSA/UQ metrics provide absolute uncertainty

bounds and a set of reactions whose further study will most affect plasma formation at various flow conditions and locations around slender vehicles.

Chapter 5

IRV-2 Infrared Radiation: Nose

The contents of this chapter have been included in the ***Journal of Thermophysics and Heat Transfer*** [181]. *Reproduced with the permission of the American Institute of Aeronautics and Astronautics.*

5.1 Introduction

Simulating hypersonic flow environments over a vehicle of interest provides several unique challenges across multiple disciplines. The inherent complexity involved with accurately modeling flow phenomena around hypersonic platforms often includes many uncertain inputs that rely upon relatively few experimental data obtained from a narrow range of flow conditions in ground and flight tests. Many of these data are required to relax assumptions involving the thermochemical equilibrium states of gaseous mixtures that no longer apply under certain hypersonic flight conditions. Moreover, conditions involving aerothermochemistry effects on governing flow equations, including molecular excitation, dissociation, relaxation, ionization, and fluid surface interactions, further add to model complexity and computational expense. While first principle reaction models including computational quantum chemistry and state-to-state methods are being employed to address the lack of experimental data, these techniques often require extensive computational resources for even the most basic of reaction pathways. As a result, a significant level of uncertainty persists under more widely employed and computationally tractable methods where multiple hundreds of reactions are involved [2,31,97,182].

The limited availability of experimental data and the significant uncertainty associated with various input parameters across a broad spectrum of hypersonic flight conditions make it imperative to employ formal GSA/UQ. These statistical techniques assess how changes in input parameters contribute to the overall variability of QoIs and determine the extent to which each parameter influences the uncertainty of QoIs. Subsequently, measures can be implemented to gather additional information through experimental data or employ more precise modeling methods to address simulation uncertainties. These methodologies

also serve to improve models by uncovering unexpected system features, identifying conceptual inaccuracies, or detecting coding errors. Furthermore, experimentalists can optimize resource allocation by targeting areas that reduce measurement uncertainty in the identified critical parameters [105,106].

To these ends, this case study provides a framework for conducting GSA/UQ for 195 chemical reaction rate parameters to identify those reactions that most influence overall uncertainty for participating medium (PM) radiance in the IR spectrum as observed along LOSs emanating from the vehicle surface to the inflow boundary. The methods employed in this case study reflect and build upon previous GSA/UQ studies involving chemical kinetics in nonequilibrium hypersonic flow conditions [47,54,99,107,110]. Section 5.2 provides background on the various methods and assumptions involved in simulations utilized in each GSA/UQ evaluation. Section 5.3 depicts results from each of these methodologies on a nominal parameter set to verify each subsequent code for a given GSA/UQ evaluation. Section 5.4 provides GSA/UQ results for all parameter sets on various QoIs. Section 5.5 describes conclusions inferred from these results.

5.2 Methodology and Implementation

The GSA/UQ case study utilizes Sandia National Laboratories' Dakota software [91,183]. Dakota acts as a "black box" wrapper tool with an extensive library of optimization and uncertainty analysis capabilities. This generalized and flexible methodology enables the integration of multiple computationally expensive codes with GSA/UQ algorithms necessary for the meta-analyses conducted in this work. The modified configuration of Dakota used in this work is displayed in Figure 5.1, where a meta-parallel process starts with Dakota running on a small allocation of resources to then generate multiple evaluations in a batch of M asynchronous evaluations. Each evaluation starts with a vector of uncertain parameters sampled by Dakota that are then preprocessed by a custom driver file which places parameters into respective input files for LeMANS-MOPAR-MD. Evaluation drivers then submit and self-monitor supercomputer job statuses on CU Boulder's Blanca clusters. After flow-material response simulation completion, each evaluation submits and monitors NEQAIR simulations for multiple LOSs. Once LeMANS-MOPAR-MD

and NEQAIR are complete for an evaluation, results are post-processed and stored. After the first of the evaluations completes, evaluation $M + 1$ is initiated and so on until all F evaluations are completed. GSA and UQ metrics are then calculated and output by Dakota. All simulations are submitted as low priority preemptible jobs over all compatible resources on supercomputer clusters, allowing for simulations to compute as resources become available.

Additionally, MATLAB toolbox and add-on UQLab is used to compute and compare multiple sparse regression and cross-validation algorithms not available in Dakota [93]. Matrices of input parameters and output QoIs are taken from Dakota once all evaluations are complete and are used within this software for additional post-processing of GSA/UQ metrics. See Section 5.4 for Dakota and UQLab inputs and GSA/UQ options.

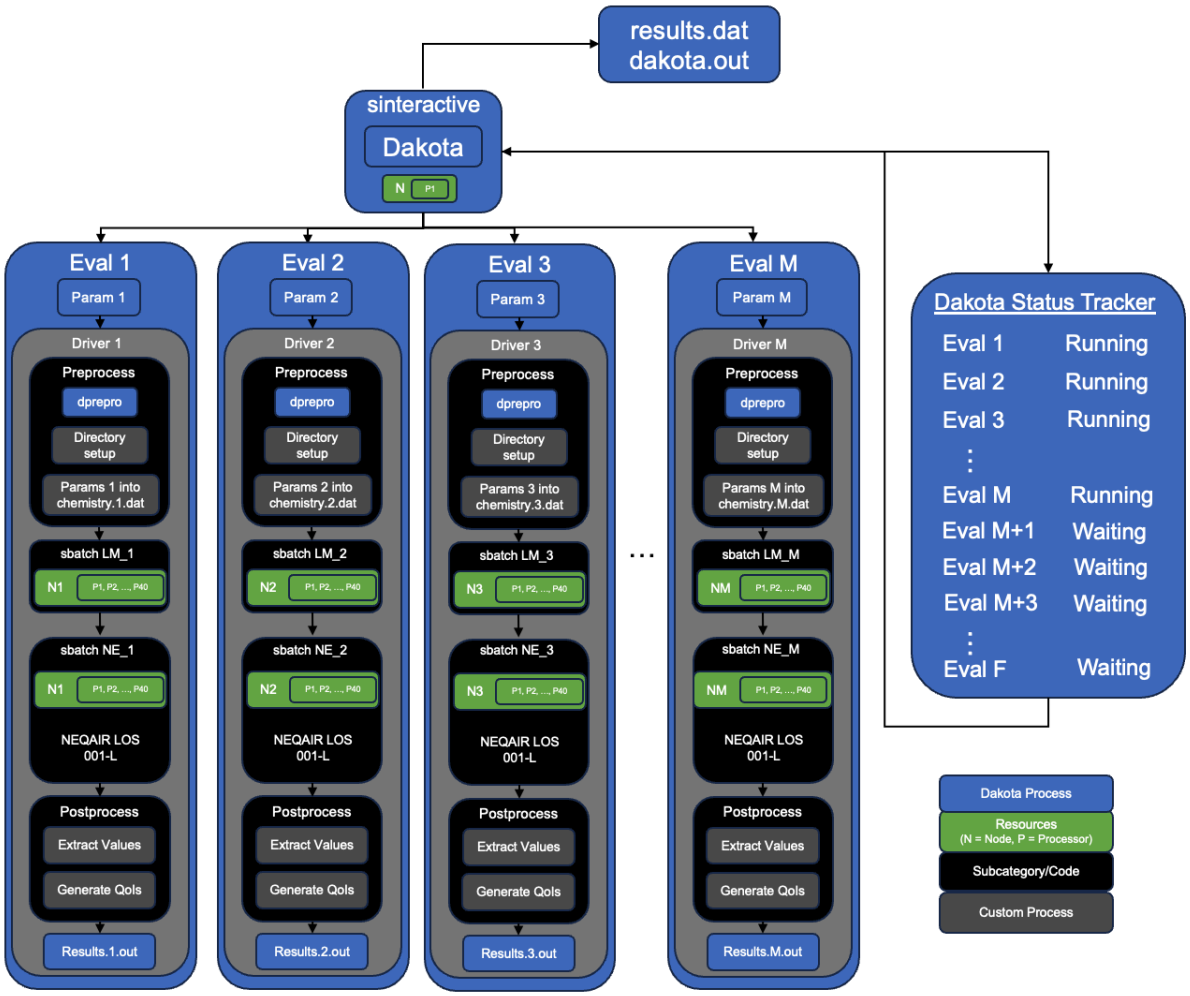

Figure 5.1: Embarrassingly parallel integration framework of LeMANS-MOPAR-MD (LM) and NEQAIR (NE) within Dakota.

5.3 Baseline Results

Baseline results for this work include sections outlining a systematic attempt at decreasing epistemic (or reducible) uncertainty (Section 5.3.1), initial uncoupled baseline results without ablation (Section 5.3.2), coupled baseline results (Section 5.3.3), and baseline radiance results (Section 5.3.4). All sections focus on the IRV-2 case study with vehicle dimensions and grid outlines depicted in Figure 5.2. Due to computational expense, the geometry for this work encompasses the nose tip of the IRV-2 vehicle. Total vehicle geometry flow evaluations at various trajectory points are provided in Chapter 7. Table 5.1

provides the first four trajectory point conditions for the IRV-2 reentry, including freestream inflow boundary conditions. For this case study, the ablation occurring at the first trajectory point (bold) is analyzed.

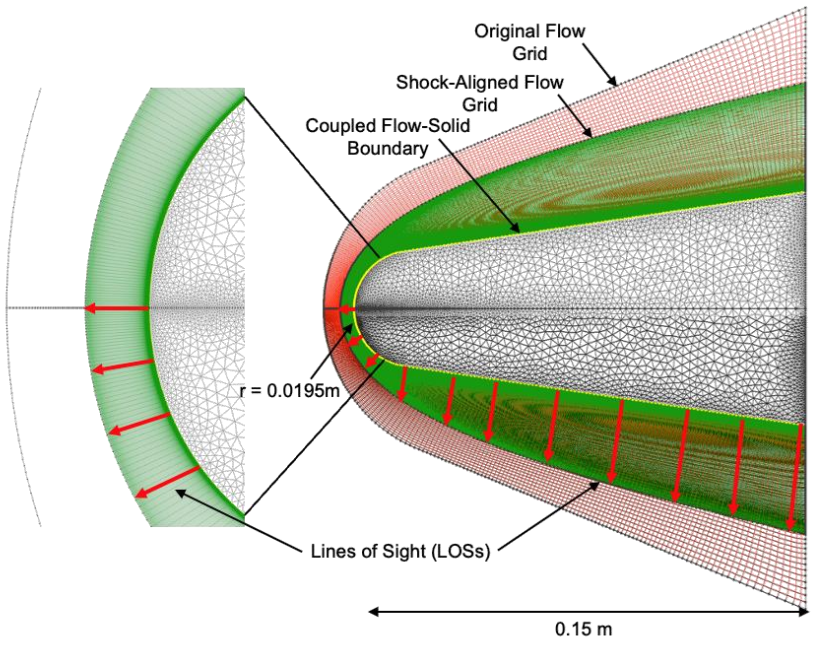

Figure 5.2: IRV-2 Nose tip baseline original and tailored flow, solid grids, and example radiance lines of sight.

Table 5.1: IRV-2 initial trajectory conditions.

Trajectory point	0	**1**	2	3
Reentry time, s	0	**4.25**	6.75	8.75
Mach, -	22	**21**	21	21
Altitude, km	66.7	**55.8**	49.3	44.0
Velocity, km/s	6.78	**6.79**	6.78	6.77
Temperature, K	227.8	**258.0**	270.7	261.4
Air Density, kg/m^3	$1.25\text{x}10^{-4}$	$\mathbf{5.05\text{x}10^{-4}}$	$1.13\text{x}10^{-3}$	$2.26\text{x}10^{-3}$
N_2 Density, kg/m^3 (76.7%)	$9.59\text{x}10^{-5}$	$\mathbf{3.87\text{x}10^{-4}}$	$8.67\text{x}10^{-4}$	$1.73\text{x}10^{-3}$
O_2 Density, kg/m^3 (23.3%)	$2.91\text{x}10^{-5}$	$\mathbf{1.18\text{x}10^{-4}}$	$2.63\text{x}10^{-4}$	$5.26\text{x}10^{-4}$

5.3.1 Flow, Solid, and Spectral Grid Tailoring and Convergence

In an effort to reduce epistemic uncertainty prior to the GSA/UQ analysis, a multi-grid convergence study is conducted. This process involves assessing multiple resolutions for the flow, solid and spectral radiance grids. Table 5.2 defines these resolutions as coarse, baseline, and fine for each of the grids. Each grid resolution roughly doubles grid densities starting from coarse to fine. For each of the CFD grid

resolutions, multiple automated shock alignments (grid tailoring) are conducted starting from a larger domain that encompasses the shock. Figure 5.3 portrays an example starting flow domain (S0) and three subsequent automated shock alignments (S1 to S3). For this study, automated shock tailoring options are chosen to detect where the flow velocity magnitude equals 95% of the freestream Mach number along each wall normal line moving from the wall outwards. The mesh is then shifted to allow for 10% of the cells to be in the freestream normal to the detected shock without having to reconstruct new grid points. User defined options also allow for a fraction of the cells inside the shock and wall boundary to be normal to their respective boundaries. Inside of these fractions, the grid points are connected via Bezier curves to complete the aligned grids. The flow mesh shock alignment routine is also called after each solid surface mesh movement due to ablation in a coupled simulation. This allows for updated shock tailoring to capture flow changes coupled to each material response.

The QoI investigated for the grid convergence study includes the PM radiance over the IRV-2 vehicle from the IR regions defined in Table 5.3 [184]. The percent difference in the QoIs between grid resolutions decreases from a maximum of 191% between coarse and baseline to a maximum 5.62% between baseline and fine with an overall computational cost (core-hour) increase of 46.2%. The percent differences in QoIs between grids for each IR region along the vehicle are also depicted in Figure 5.4. Based on these results, the GSA/UQ analyses in this study use the baseline grids when balancing reduced epistemic uncertainty and computational cost. The following sections outline results from these baseline grids for each respective models.

Table 5.2: Multi-grid convergence study.

Type	Grid descriptor	Coarse	Baseline	Fine
Flow	Grid type	Two-dimensional structured		
	Streamwise nodes	97	176	200
	Wall normal nodes	88	194	250
	Cells	8,352	33,775	49,551
	Shock alignments	3	3	3
	Maximum uncoupled plateaued residual	$4.77\text{x}10^{-12}$	$1.10\text{x}10^{-12}$	$6.39\text{x}10^{-13}$
	Local y^+	0.16-0.18	0.13-0.18	0.09-0.68
	Uncoupled cost (core-hours)	101	1,862	2,136
Solid	Grid type	Two-dimensional unstructured		
	Cells	2,111	6,034	15,671
	Interior wall spacing, m	$4\text{x}10^{-4}$	$2.45\text{x}10^{-4}$	$1.40\text{x}10^{-4}$
	Maximum coupled plateaued residual	$1.70\text{x}10^{-12}$	$3.93\text{x}10^{-13}$	$2.08\text{x}10^{-12}$
	Coupled cost (core-hours)	73	532	969
Spectral	Grid type	One-dimensional (LOS and spectral grids)		
	LOS grid points	97	176	200
	IR-A spectral grid points	155,001	310,001	620,001
	IR-B spectral grid points	400,001	800,001	1,600,001
	IR-C spectral grid points	425,001	850,001	1,700,001
	Wall Normal LOSs	96	175	250
	Cost per LOS (core-hours)	0.6	1.5	3.12
Maximum Difference Across QoIs	IR-A	-	191%	5.62%
	IR-B	-	181%	2.78%
	IR-C	-	19.3%	1.80%
	IR-Total	-	179%	3.21%

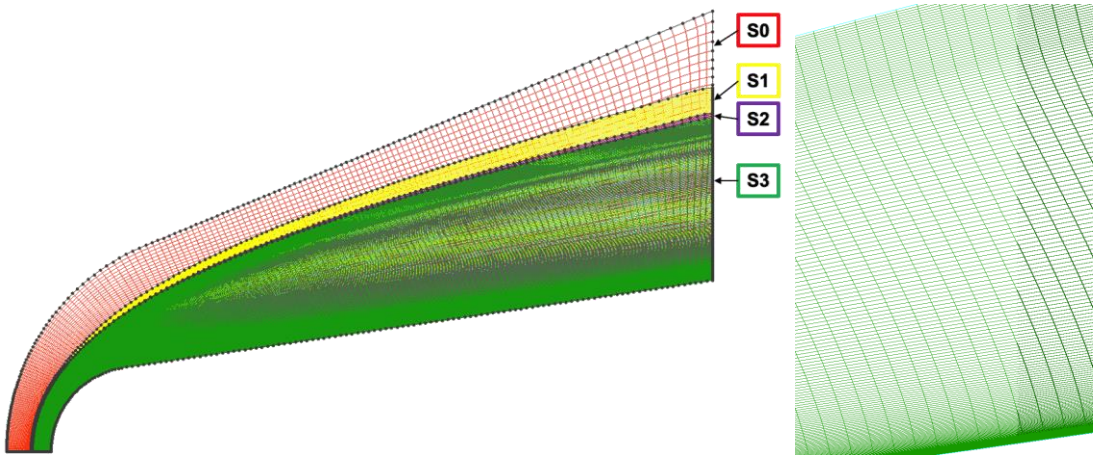

Figure 5.3: Automated shock alignment/mesh tailoring example. Multiple shock alignments (left) and individual grid showing wall and shock normal alignment cells with Bezier curves in-between (right).

Table 5.3: Infrared wavelength region definitions.

Radiation Designation			Wavelength, $x10^{-6}$ m
Infrared Radiation	Near IR	IR-A	0.78-1.40
		IR-B	1.40-3.00
	Mid IR	IR-C	3.00-5.00
	Far IR		5.00-20.0

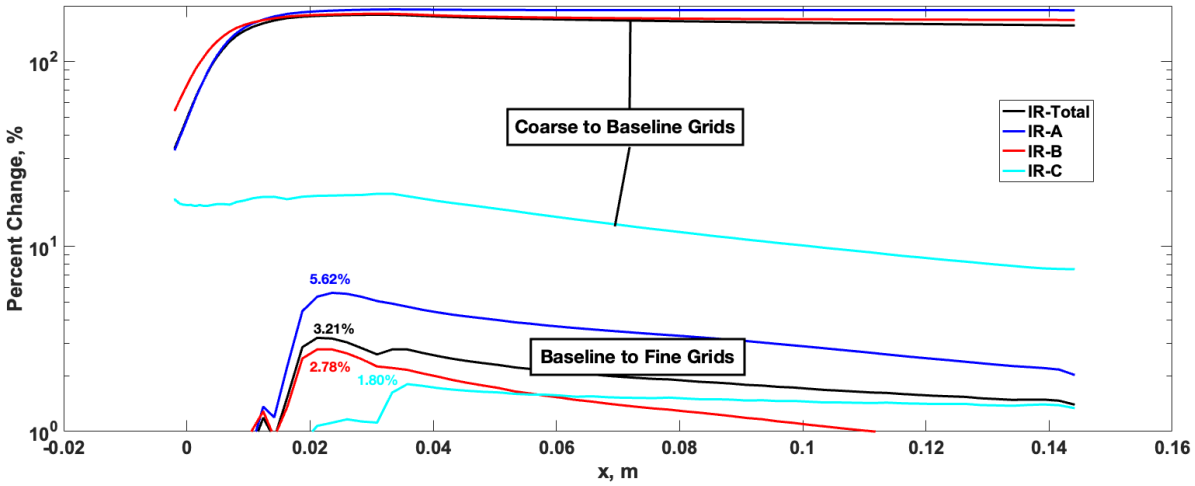

Figure 5.4: Multi-grid QoI convergence.

5.3.2 Initial Flow Solution

To initiate a coupled flow-material response solution at the first trajectory point, a flow solution must be generated to act as an initial condition. The following results portray the initial flow solution after three shock alignments for the baseline flow grid at trajectory point 1 (TP01) for the IRV-2. The baseline flow solution is converged in this manner to help facilitate the GSA/UQ analysis by restarting from this solution for all coupled evaluations with varying uncertain parameters. Figure 5.5 depicts the Mach number and translational-rotational temperature profiles over the front portion of the IRV-2 domain. Shock alignment parameters are chosen to ensure 10% of the domain cells emanating outward from the wall remains within the freestream. This buffer ensures that the shock location remains within the domain when the coupled simulations restart from the nominal uncoupled solution and parameters are changed during each evaluation of the sensitivity analysis. Figure 5.6 displays the uncoupled flow stagnation line temperatures and species number densities for the 11 non-carbon species air. The translational-rotational

and vibrational-electronic temperatures portray an expected high degree of thermal nonequilibrium where the isothermal wall temperature boundary condition of 1,000 K obtains local thermal equilibrium at the surface. Similarly, the species number densities illustrate wall boundary condition effects near the vehicle surface with atomic oxygen and nitrogen number densities increasing. Similar trends for ionized species at 6 to 7 km/s are displayed, with NO^+ as the dominant ion until the stagnation point. A noncatalytic wall boundary is chosen for the uncoupled solution to help facilitate numerical stability when a mass balance is used for the wall boundary condition with the coupled solutions.

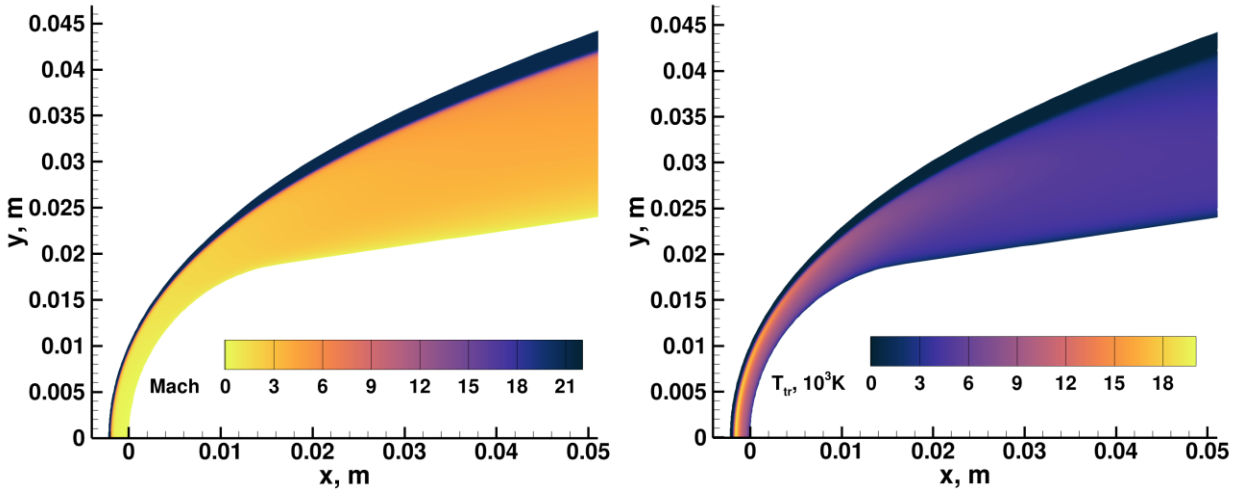

Figure 5.5: Uncoupled flow Mach number (left) and translational-rotational temperature (right) profiles at IRV-2 TP01 (M=21, 56 km).

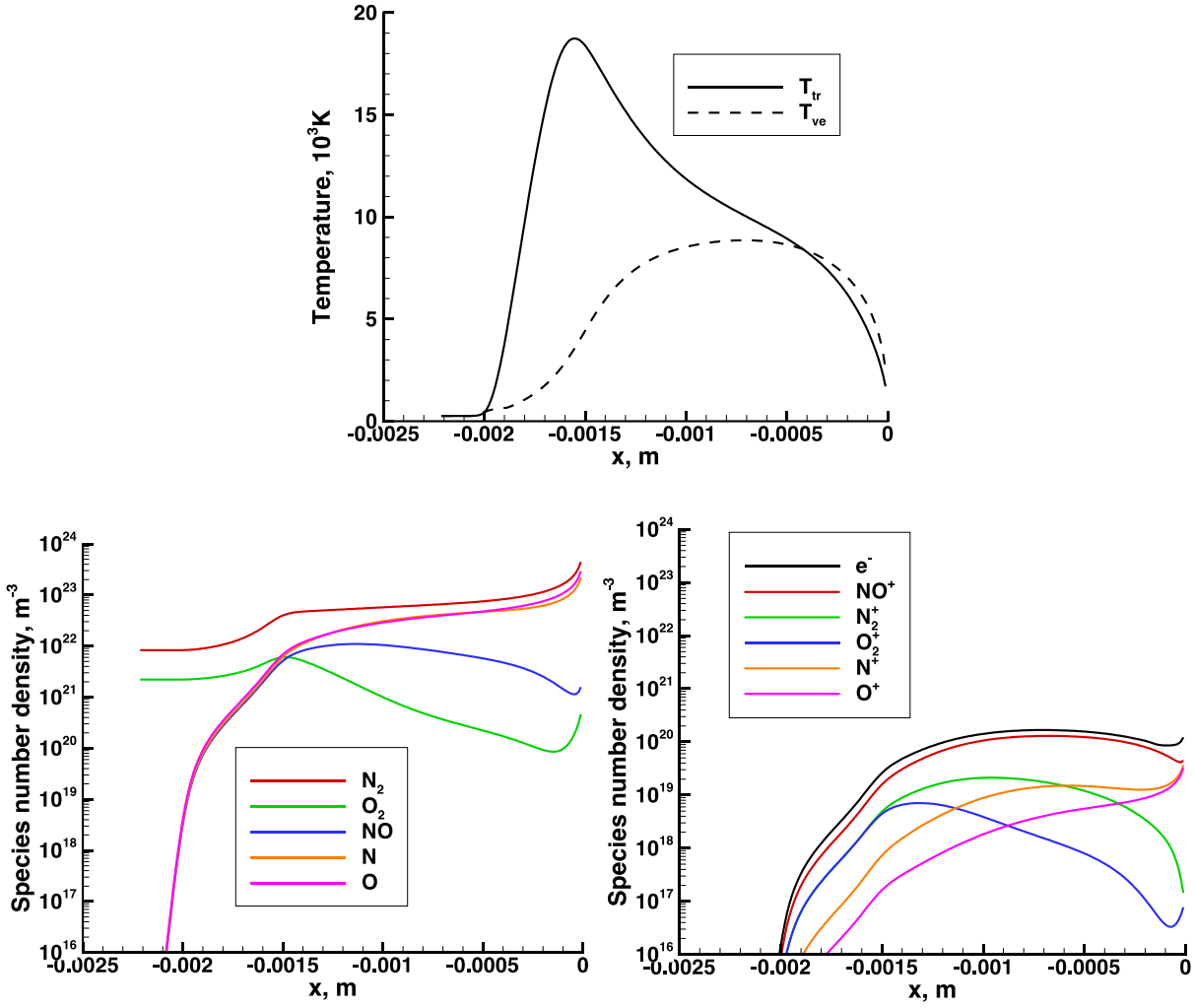

Figure 5.6: Uncoupled flow temperature (top) and species number density stagnation line profiles (bottom) at IRV-2 trajectory point 1 (6.8 km/s, 56 km).

5.3.3 Coupled Material Response Solution

The baseline coupled solution results are depicted in Figure 5.8 and Figure 5.9. In the coupled case, flowfield shock alignments occur after each material response update and surface mesh movement. The freestream fraction of flow domain cells after shock alignments in this baseline case is 5%. Both material response and flow-initiated mesh movements are called when the maximum change in wall heat flux between two flow iterations decreases below 1% (see Equation 30). Figure 5.7 illustrates an example of the convergence of both surface recession and subsequent inflow boundary via shock tailoring. In this example

4 calls to MOPAR-MD are made after sufficient wall heat flux convergence, where surface recession is determined at each call followed by a flow shock alignment in LeMANS to move the inflow boundary. As the information passes between the flow and material response codes updates at each successive MOPAR-MD call, both boundaries converge to an overall mesh.

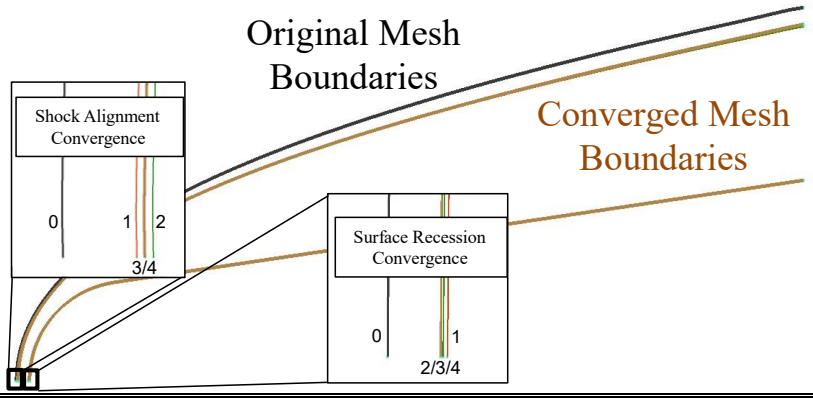

Material Response Surface Movement and Shock Alignment Number	ΔInflow Boundary, mm	ΔSurface Boundary, mm
1	0.302	0.116
2	0.055	8.12×10^{-3}
3	0.028	3.99×10^{-3}
4	2.60×10^{-3}	6.38×10^{-4}

Figure 5.7: Coupled flow-material response shock and surface mesh movement convergence example.

Updates from MOPAR-MD continues until the change in the root mean square of the surface heat flux since the last material response call decreases below 1% (see Equation 31) [27]. After this point, material response calls cease and the flow is converged until a residual plateau tolerance is met. The plateau tolerance is defined by comparing the average of the L_2 norm of the residuals over the previous 12 iterations and comparing the value to the L_2 norm 12 iteration average 1,000 iterations ago. If the past L_2 average value is less than the current and the flow maximum residual is less than 10^{-10}, the coupled flow simulation terminates.

Similar trends are depicted for Mach number and translational-rotational temperature profiles with most differences located near the stagnation line where the majority of recession occurs. There is a similar trend to the temperature profiles as in the uncoupled case with the exception of a higher wall temperature

after the mass and energy balances from the material response wall boundary influences the flow solution. Both uncoupled and coupled species number densities follow similar trends for the neutral non-carbon species. Neutral-carbon species follow trends seen in previous equilibrium ablation studies, where CO dominates from diffusion limited oxidation corresponding to wall temperatures near 2,300 K. CN experiences a local increase near the wall, while CO_2 and NCO experience local minimums resulting from primarily neutral carbon-air exchange reactions. Lastly, the non-carbon charged species number densities follow similar trends as the uncoupled simulation. Charged carbon species follow their neutral counterparts with the exception of CO^+ having a local maximum near the wall.

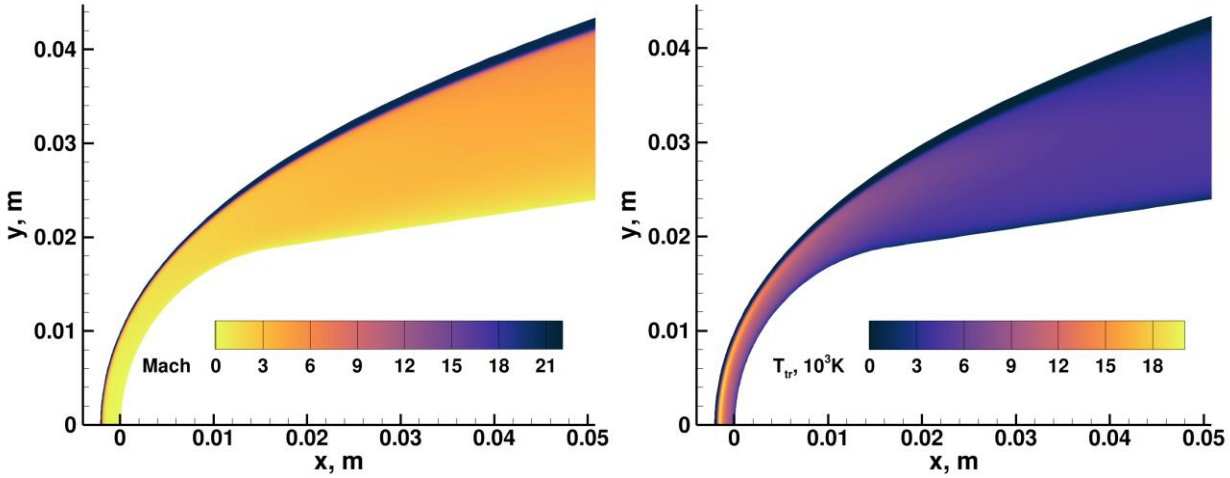

Figure 5.8: Coupled flow Material Response Mach (a) and translational-rotational temperature (b) profiles at IRV-2 trajectory point 1 (M=21, 56 km).

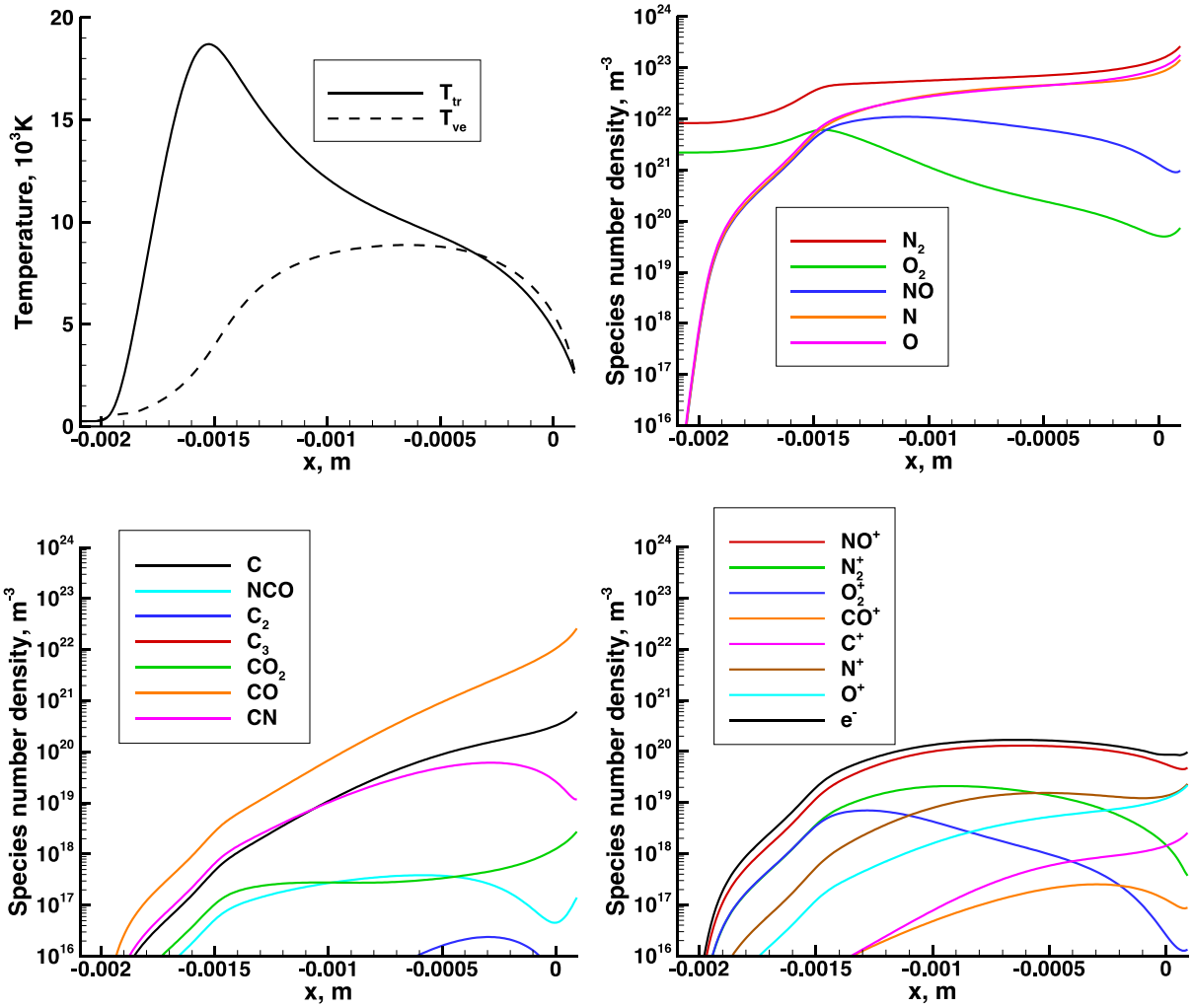

Figure 5.9: Coupled flow temperature (a) and species number density stagnation line profiles at IRV-2 trajectory point 1 (Neutral (b), carbon neutral (c), and ionized (d) species).

5.3.4 NEQAIR Radiance

Baseline NEQAIR radiance results include the construction of multiple LOSs emanating from the vehicle wall to just outside of the shock where the vibrational-electronic temperature decreases below 500 K. The geometries of these LOSs are depicted as black lines in Figure 5.10. The streamwise distance increases between LOSs are identical to the wall and flow CFD grid streamwise spacings. Each line consists of 176 points with flow values interpolated from the CFD flow grid. Position, two-temperature and 20 species number density values are then passed to NEQAIR to obtain aggregate radiance values. While many studies investigate radiative heat flux calculations toward the body at speeds typical of reentry (>8 km/s),

this study investigates radiance values calculated from the perspective of an observer at the end of each LOS near the inflow domain boundary at velocities near 7 km/s. Boundary conditions are therefore set with the initial and final line points of each LOS as both black body. This ensures the inclusion of black body radiation emanating from the initial point and absorbance for the observer at the final point. These boundaries are denoted by brown and green lines, respectively in Figure 5.10. For the sensitivity study, only PM radiances are compared as a QoI. A non-Boltzmann state population is assumed with approximated local escape factors with a characteristic length of 1.0×10^{-2} m. Default NEQAIR database molecular and atomic excitation rates in Appendix A are used. All relevant NEQAIR database species bands are included, and each IR region defined in Table 5.3 is discretized in accordance with that of the baseline spectral grid scenario in Figure 5.11 depicts representative baseline scanned PM spectral radiances (solid lines) and integrated radiances (dashed lines) for contributing species bands in the stagnation (a), shoulder (b) and downstream (c) regions along the vehicle body. For all locations, the individual species contributions superimpose nearly linearly to the species total radiance. For the stagnation LOS, the IR-A region represents the majority of the IR radiance. Nitrogen and CN are the dominant radiators in this location. For the shoulder LOS, the majority of radiance is also in the IR-A band for the same major radiative species with the exception of an increased relative contribution for NO and CO in the IR-B and IR-C bands. For the downstream LOS, the majority of radiance is in the IR-B and IR-C bands, where NO and CO dominates, followed by CN in the IR-A region. These trends are useful as a means for explaining species specific contributions to variance and uncertainty in later sections.

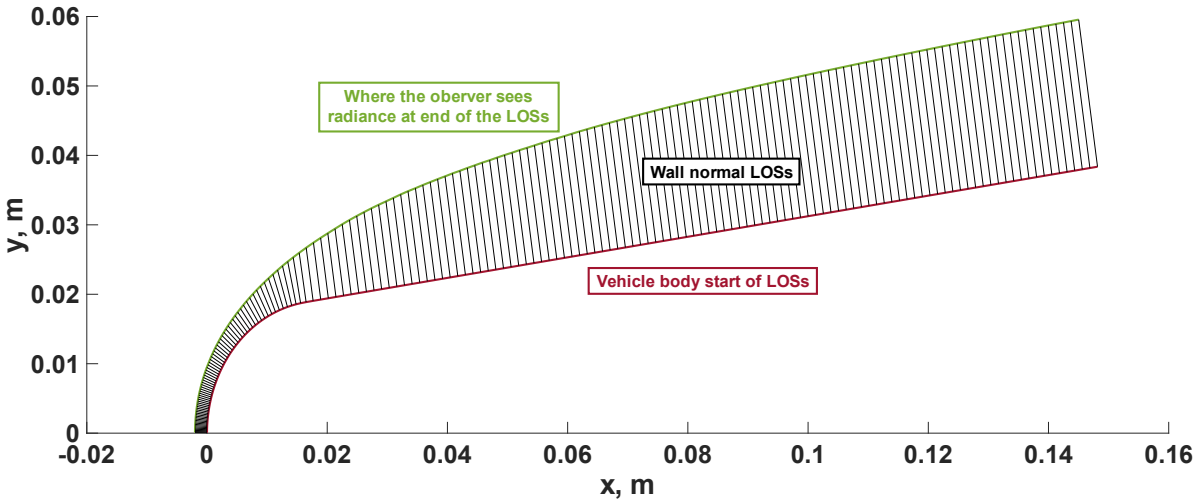

Figure 5.10: IRV-2 Nose geometry and wall normal lines of sight (LOSs).

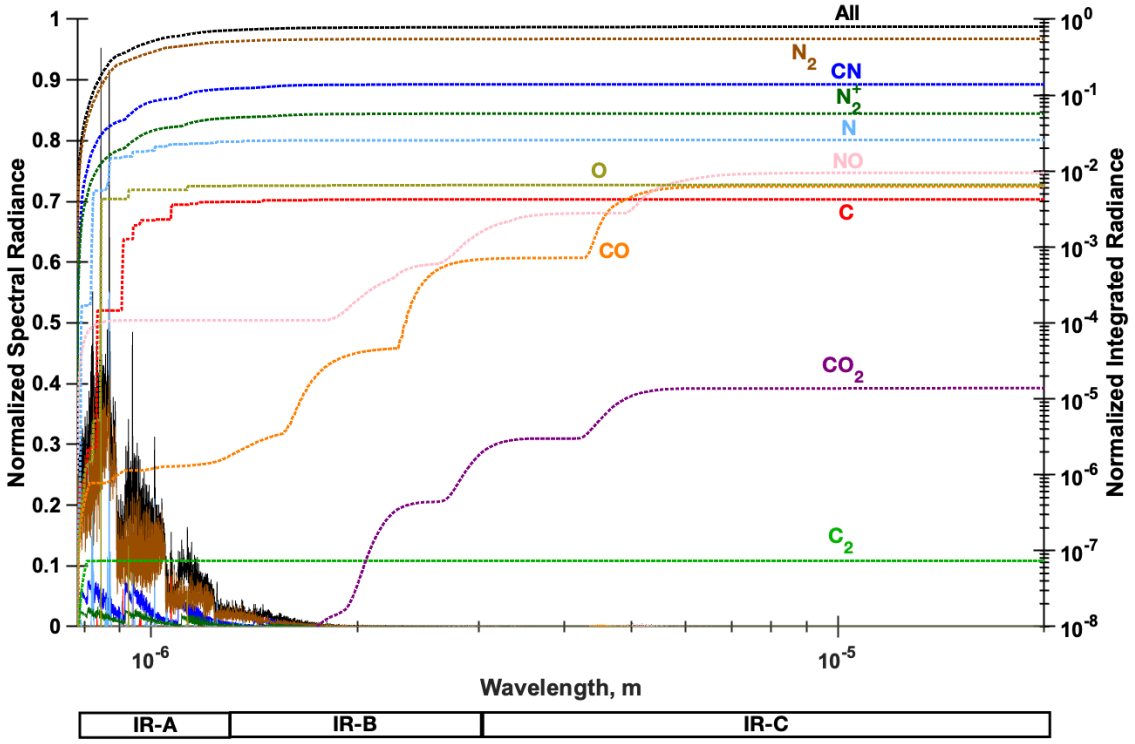
All
N2
CN
N2+
N
NO
O
C
CO
CO2
C2
Normalized Spectral Radiance
Normalized Integrated Radiance
Wavelength, m
IR-A
IR-B
IR-C

a)

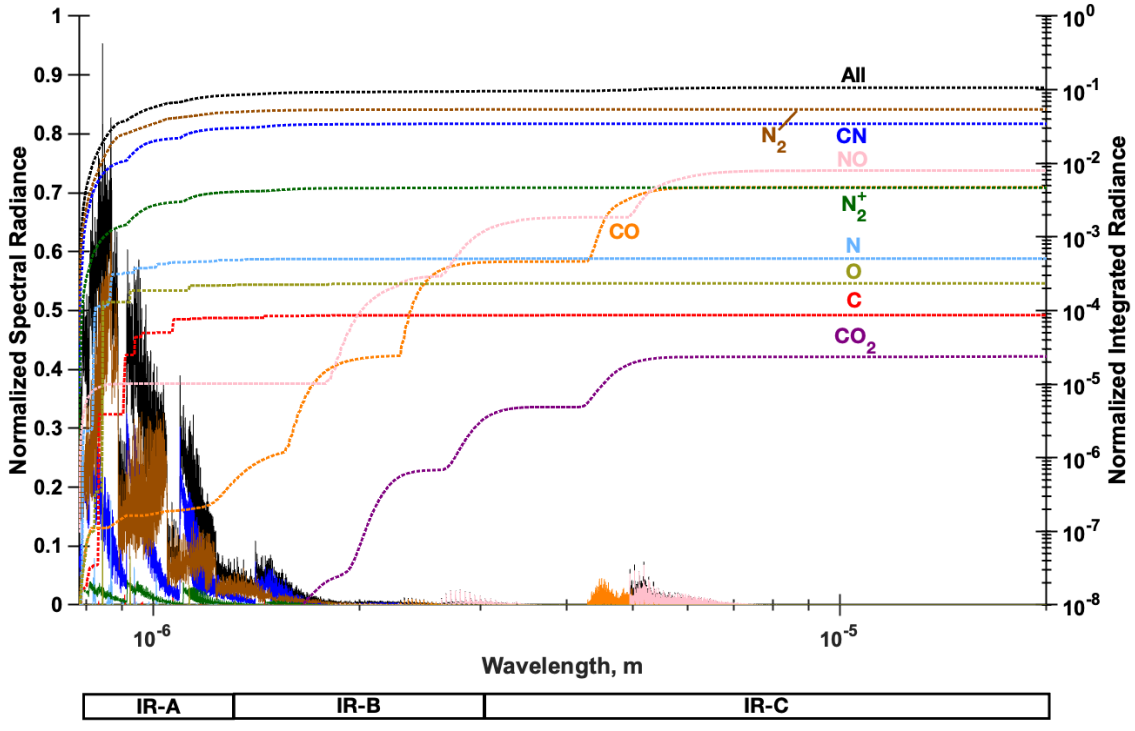
All
N2
CN
NO
N2+
CO
N
O
C
CO2
Normalized Spectral Radiance
Normalized Integrated Radiance
Wavelength, m
IR-A
IR-B
IR-C

b)

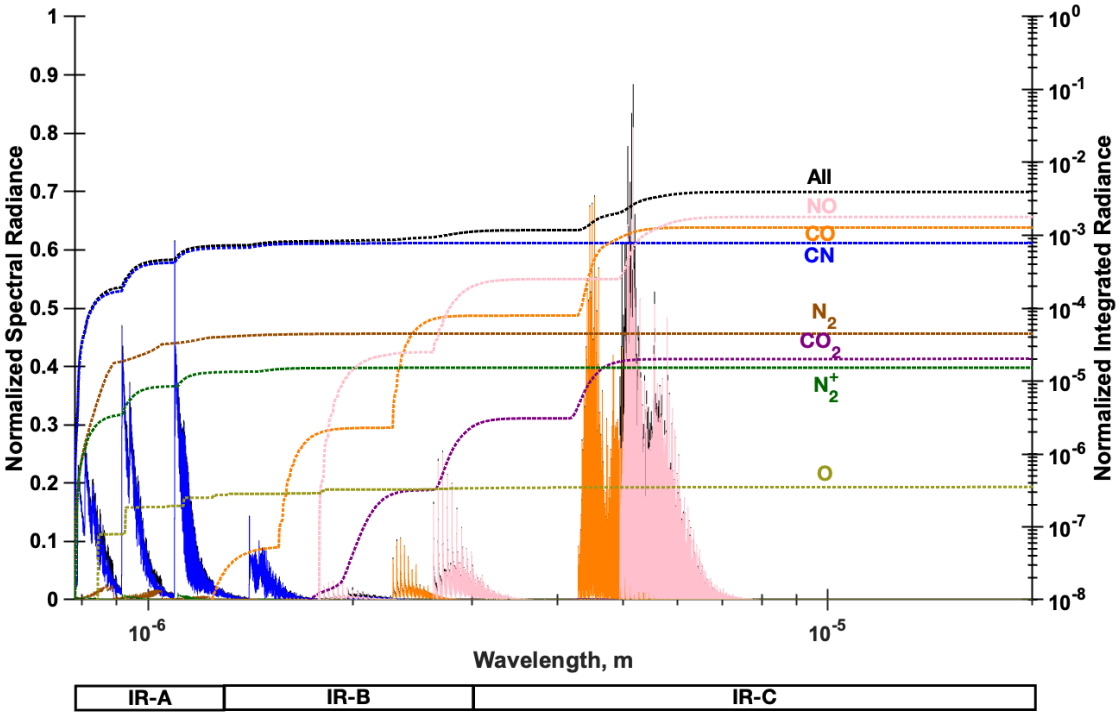

c)

Figure 5.11: Baseline PM Spectral radiance: (a) Stagnation LOS, (b) Shoulder LOS, and (c) Downstream LOS.

5.4 Global Sensitivity Analysis and Uncertainty Quantification Results

The GSA/UQ process for this study expands upon similar techniques and procedures from that of West et al. and Aiken and Boyd, among others [47,54,64,99]. These methods involve using software like Dakota to sample uncertain model parameters from predefined distributions, input these parameters into the CFD and radiation simulations and extract various QoIs for a given evaluation.

Input parameters are sampled via Latin hypercube methods assuming log-uniform continuous distributions. Legendre PCEs are utilized in this study following the Askey scheme of continuous hyper-geometric polynomials. These coefficients are then approximated to replicate inputs to outputs via spectral projection or regression [91]. Following [54,64,99], this investigation uses a 2nd order PCE expansion and 195 input parameters which would require 19,306 evaluations for a total order PCE with a unity

oversampling ratio. Although this is less than what would be required for GSA using traditional Monte Carlo sampling methods, this total order set is not computationally tractable for our analyses.

To address this "curse of dimensionality" limitation, highly underdetermined systems can leverage the assumption of sparsity in the PCE coefficient set to decrease the number of required evaluations while maintaining stochastic surrogate model prediction accuracy. Multiple sparse regression point collocation methods have been developed to try and identify coefficients $\boldsymbol{\alpha}$ in Equation 78 with the largest influence and drive as many as others possible to near zero or zero [91,93]. A part of this study compares how sparse regression algorithms balance between surrogate model accuracy (bias) and complexity (variance) as well as sensitivity metric convergence rates while including the effects of cross-validation. The sparse regression algorithms investigated are Orthogonal Matching Pursuit (OMP), Least Angle Regression (LARS), Least Absolute Shrinkage and Selection Operator (LASSO), Basis pursuit (BP), Subspace Pursuit (SP) and Bayesian Compressive Sensing (BCS). All regression methods attempt to replicate the relation in Equation 84, where $\boldsymbol{\Psi}$ is a $N_s \times N_P$ matrix of multivariate polynomials evaluated for array $\boldsymbol{\xi}$ of a particular evaluation out to N_s evaluations, $\boldsymbol{\alpha}$ is a coefficient array, and $\boldsymbol{R^{PC}}$ is the QoI or response array.

The following describes each of the sparse regression methods investigated. The OMP method involves a heuristic method to find an approximation for Equation 89.

$$\boldsymbol{\alpha} = \arg\min \|\boldsymbol{\alpha}\|_{\ell_0} \text{ such that } \left\|\boldsymbol{\Psi\alpha} - \boldsymbol{R^{PC}}\right\|_{\ell_2} \leq \epsilon \tag{89}$$

This method builds approximations of the coefficient vector as a linear combination of a subset of active columns of $\boldsymbol{\Psi}$. Active sets are added by testing columns, where at each iteration, inactive columns that have the highest inner product with the current residual are added. This effectively allows for 'greedily' building only those coefficients that have the most impact on the input-output relationships while maintaining under a residual threshold ϵ [185]. Like OMP, LARS builds a set of active columns by including columns with largest inner products with current residuals. However, as seen in Equation 90, LARS also solves a penalized least squares problem at each step along an equiangular direction with respect to the active set [186].

$$\boldsymbol{\alpha} = \arg\min \left\| \boldsymbol{\Psi\alpha} - \boldsymbol{R^{PC}} \right\|_{\ell_2}^2 \text{ such that } \|\boldsymbol{\alpha}\|_{\ell_1} \leq \tau \tag{90}$$

LARS does not allow columns to leave the active set, but by relaxing this constraint, the algorithm produced is equivalent to the LASSO solution [187]. The BP algorithm follows that of Equation 91, where the ℓ_1 norm is minimized subject to the noise term ϵ.

$$\boldsymbol{\alpha} = \arg\min \|\boldsymbol{\alpha}\|_{\ell_1} \text{ such that } \|\boldsymbol{\Psi\alpha} - \boldsymbol{R}\|_{\ell_2} \leq \epsilon \tag{91}$$

In this case study, ϵ is set to zero for BP regression following [99]. The SP method takes K elements of $\boldsymbol{\alpha}$ and iteratively conducts least model correlated K regressors, performs least squares regression on subsets while removing regressors with the smallest coefficient magnitudes until convergence [188]. Lastly, BCS follows a Bayesian framework termed Fast Laplace by Babacan et al., wherein likelihood, prior, and auxiliary parameters are chosen to enforce coefficient sparsity. This is achieved by maintaining a vector of coefficient variances where if a variance is zero, then the associated coefficient must be zero. At each iteration, a regressor is chosen to be added, deleted, or reassessed (re-estimate variance) as determined by an updated evaluation of an analytical objective function that is a function of random variables with distributions parametrized by noise variance hyperparameters [189].

5.4.1 Uncertain Parameters

An original literature review is conducted on the 195 reaction rates in this case study following the Arrhenius form in Equations 7 and 8. Baseline parameter values and references are divided by dissociation, exchange, and ionization reactions and are depicted in Table 5.4, Table 5.5, and Table 5.6, respectively [1,47,48,54,89,114,123,127,128,132,134,136–138,140,190–209]. Additionally, references that have uncertainty estimates are also listed with uncertainty bound multipliers U_f applied to the nominal reaction rates. These bounds are informed from multiple nonequilibrium hypersonic flow GSA/UQ studies. In this work, 195 parameters C_f are Latin Hypercube sampled from a log-uniform distribution with bounds set by U_f. These baseline and uncertainty bound multipliers are different from those in the appendices because the extensive literature review had yet to be completed. These results, therefore provide a comparison of the

effects of the baseline and uncertainty bound differences for the 195 gas phase thermochemical rate coefficient parameters in Table A1 the TP01 radiance results in Chapter 7.

Table 5.4: Baseline (BL) dissociation reaction parameters and uncertainty bound (UB) multipliers.

No.	Reaction	Third Body, M	C_f, cm^3 $mol^{-1}sec^{-1}$	η_f	θ_f, K	Controlling Temperature T_a Exponents (T_{tr}, T_{ve})	Uncertainty Multipliers U_f	BL and UB References
1-20	$N_2 + M \rightleftharpoons 2N + M$	N_2, O_2, NO, NCO, C_2, C_3, CO_2, CO, CN, NO^+, N_2^+, O_2^+, CO^+	7.00×10^{21}	-1.60	113,200	0.7, 0.3	0.5, 4.0	[1,54]
		N, O, C, N^+, O^+, C^+	3.01×10^{22}				0.2, 3.0	
		e^-	1.20×10^{7}	2.69		0.0, 1.0	0.1, 10	[54,89]
21-39	$O_2 + M \rightleftharpoons 2O + M$	N_2, O_2, NO, NCO, C_2, C_3, CO_2, CO, CN, NO^+, N_2^+, O_2^+, CO^+	2.00×10^{21}	-1.50	59,500	0.7, 0.3	0.3, 1.3	[54,190]
		N, O, C, N^+, O^+, C^+	1.00×10^{22}					
40-58	$NO + M \rightleftharpoons N + O + M$	N_2, O_2, NCO, C_2, C_3, CO, CN, N_2^+, O_2^+, CO^+	5.00×10^{15}	0.00	75,500	0.7, 0.3	0.2, 2.5	[54,191]
		NO, N, O, C, CO_2, NO^+, N^+, O^+, C^+	7.98×10^{21}	-1.50				[54,192]
59-77	$C_2 + M \rightleftharpoons 2C + M$	All	9.68×10^{22}	-2.00	71,000	0.5, 0.5	0.1, 10	[54,193]
78-96	$CN + M \rightleftharpoons C + N + M$	All	6.00×10^{15}	-0.40	71,000	0.5, 0.5	0.3, 1.9	[54]
97-115	$CO + M \rightleftharpoons C + O + M$	N_2, O_2, NO, NCO, C_2, C_3, CO_2, CO, CN, NO^+, N_2^+, O_2^+, CO^+	1.20×10^{21}	-1.00	129,000	0.5, 0.5	0.25, 1.5	[54,194]
		N, O, C, N^+, O^+, C^+	3.40×10^{20}					[54,137]
116-134	$CO_2 + M \rightleftharpoons O + CO + M$	N_2, O_2, NO, NCO, C_2, C_3, CO_2, CO, CN, NO^+, N_2^+, O_2^+, CO^+	7.47×10^{12}	0.50	52,321	0.5, 0.5	0.1, 10	[47,54]
		N, O, C, N^+, O^+, C^+	1.38×10^{22}	-1.50	63,275			[54,195]
135-153	$NCO + M \rightleftharpoons C + O + M$	All	3.10×10^{16}	-0.50	24,000	0.5, 0.5	0.4, 1.6	[127,196]

Table 5.5: Baseline (BL) neutral exchange reaction parameters and uncertainty bound (UB) multipliers.

Number	Reaction	C_f, cm^3/mol/sec	η_f	θ_f, K	Controlling Temperature T_a Exponents (T_{tr}, T_{ve})	Uncertainty Multipliers U_f	BL and UB References
154	$N_2 + C \rightleftharpoons CN + N$	5.24×10^{13}	0.00	22,600	1.0, 0.0	0.5, 1.5	[54,127]
155	$CN + O \rightleftharpoons NO + C$	3.23×10^{13}	0.00	13,720	1.0, 0.0	0.1, 10	[54,197]
156	$CO + N \rightleftharpoons NO + C$	1.10×10^{14}	0.07	53,500	1.0, 0.0	0.1, 10	[54,128]
157	$CO + O \rightleftharpoons C + O_2$	9.10×10^{10}	0.59	69,200	1.0, 0.0	0.1, 10	[54,198]
158	$C_3 + C \rightleftharpoons C_2 + C_2$	6.00×10^{11}	1.07	16,500	1.0, 0.0	0.1, 10	[54,128]
159	$C_2 + N_2 \rightleftharpoons CN + CN$	8.80×10^{14}	0.13	25,100	1.0, 0.0	0.5, 150	[54,128]
160	$N_2 + O \rightleftharpoons NO + N$	2.97×10^{10}	0.98	37,890	1.0, 0.0	0.4, 1.3	[54,199]
161	$O_2 + N \rightleftharpoons NO + O$	2.49×10^{09}	1.18	4,005	1.0, 0.0	0.1, 10	[54,136]
162	$CN + C \rightleftharpoons C_2 + N$	3.00×10^{14}	0.00	18,120	1.0, 0.0	0.5, 3.0	[48,200]
163	$CN + CO \rightleftharpoons C + NCO$	1.50×10^{16}	-0.49	65,800	1.0, 0.0	0.1, 10	[201]
164	$CN + CO_2 \rightleftharpoons CO + NCO$	3.68×10^{6}	2.16	13,470	1.0, 0.0	0.1, 10	[132]
165	$CN + NO \rightleftharpoons N + NCO$	9.64×10^{13}	0.00	21,170	1.0, 0.0	0.5, 2.0	[134,202]
166	$CN + O \rightleftharpoons CO + N$	1.02×10^{13}	0.00	0	1.0, 0.0	0.8, 2.3	[203]
167	$CN + O_2 \rightleftharpoons O + NCO$	6.60×10^{12}	0.00	200	1.0, 0.0	0.1, 10	[204]
168	$CO_2 + O \rightleftharpoons CO + O_2$	2.71×10^{14}	0.00	33,800	1.0, 0.0	0.1, 10	[54,205]
169	$N+CO_2 \rightleftharpoons NO + CO$	1.93×10^{11}	0.00	1,710	1.0, 0.0	0.1, 10	[206]
170	$NCO + N \rightleftharpoons N_2 + CO$	1.39×10^{14}	-0.25	0	1.0, 0.0	0.3, 3.2	[127]
171	$NCO + NO \rightleftharpoons N_2 + CO_2$	5.68×10^{18}	-1.98	450	1.0, 0.0	0.7, 1.3	[203,207]
172	$NCO + O \rightleftharpoons NO + CO$	2.59×10^{16}	-1.14	0	1.0, 0.0	0.4, 2.3	[203,208]
173	$NCO + O_2 \rightleftharpoons NO + CO_2$	1.32×10^{10}	0.00	0	1.0, 0.0	0.1, 10	[208]

Table 5.6: Baseline (BL) ionization reaction parameters and uncertainty bound (UB) multipliers.

Number	Reaction	C_f, cm^3/mol/sec	η_f	θ_f, K	Controlling Temperature T_a Exponents (T_{tr}, T_{ve}/T_e)	Uncertainty Multipliers U_f	BL and UB References
174	$C + O \rightleftharpoons CO^+ + e^-$	$2.05\text{x}10^{10}$	0.60	34,990	1.0, 0.0	0.1, 10	[54,114]
175	$N + O \rightleftharpoons NO^+ + e^-$	$1.93\text{x}10^{9}$	0.79	31,900	1.0, 0.0	0.1, 10	[54,140]
176	$N + N \rightleftharpoons N_2^+ + e^-$	$1.20\text{x}10^{16}$	-0.69	72,750	1.0, 0.0	0.3, 1.3	[54,138]
177	$O + O \rightleftharpoons O_2^+ + e^-$	$1.82\text{x}10^{10}$	0.68	80,600	1.0, 0.0	0.1, 10	[54,138]
178	$N_2 + O_2^+ \rightleftharpoons N_2^+ + O_2$	$9.90\text{x}10^{12}$	0.00	40,700	1.0, 0.0	0.1, 10	[1,54]
179	$NO^+ + N \rightleftharpoons O^+ + N_2$	$3.40\text{x}10^{13}$	-1.08	12,800	1.0, 0.0	0.1, 10	
180	$NO^+ + O \rightleftharpoons N^+ + O_2$	$1.00\text{x}10^{12}$	0.50	77,200	1.0, 0.0	0.1, 10	
181	$NO^+ + O_2 \rightleftharpoons O_2^+ + NO$	$2.40\text{x}10^{13}$	0.41	3,2600	1.0, 0.0	0.1, 10	
182	$NO^+ + N \rightleftharpoons N_2^+ + O$	$7.20\text{x}10^{13}$	0.00	35,500	1.0, 0.0	0.1, 10	
183	$O_2^+ + N \rightleftharpoons N^+ + O_2$	$8.70\text{x}10^{13}$	0.14	28,600	1.0, 0.0	0.1, 10	
184	$NO + O^+ \rightleftharpoons N^+ + O_2$	$1.40\text{x}10^{5}$	1.90	26,600	1.0, 0.0	0.1, 10	
185	$NO^+ + O \rightleftharpoons O_2^+ + N$	$7.20\text{x}10^{12}$	0.29	48,600	1.0, 0.0	0.1, 10	
186	$O^+ + N_2 \rightleftharpoons N_2^+ + O$	$9.10\text{x}10^{11}$	0.36	22,800	1.0, 0.0	0.1, 10	
187	$NO^+ + C \rightleftharpoons NO + C^+$	$1.00\text{x}10^{13}$	0.00	23,200	1.0, 0.0	0.1, 10	[54,137]
188	$O_2 + C^+ \rightleftharpoons O_2^+ + C$	$1.00\text{x}10^{13}$	0.00	9,400	1.0, 0.0	0.1, 10	
189	$CO + C^+ \rightleftharpoons CO^+ + C$	$1.00\text{x}10^{13}$	0.00	31,400	1.0, 0.0	0.1, 10	
190	$N_2 + C^+ \rightleftharpoons N_2^+ + C$	$1.11\text{x}10^{14}$	-0.11	50,000	1.0, 0.0	0.1, 10	[54,193]
191	$N_2 + N^+ \rightleftharpoons N_2^+ + N$	$1.00\text{x}10^{12}$	0.50	12,200	1.0, 0.0	0.1, 10	[54,123]
192	$O_2^+ + O \rightleftharpoons O^+ + O_2$	$4.00\text{x}10^{12}$	-0.09	18,000	1.0, 0.0	0.1, 10	[1,54]
193	$C + e^- \rightleftharpoons C^+ + 2e^-$	$3.70\text{x}10^{31}$	-3.00	130,720	0.0, 1.0	0.1, 10	[54,137]
194	$N + e^- \rightleftharpoons N^+ + 2e^-$	$2.50\text{x}10^{34}$	-3.82	168,200	0.0, 1.0	0.5, 2.0	[54,209]
195	$O + e^- \rightleftharpoons O^+ + 2e^-$	$3.90\text{x}10^{33}$	-3.78	158,500	0.0, 1.0	0.4, 3.0	[1,54]

5.4.2 Quantities of Interest

QoIs in this study involve PM radiance values along LOSs emanating from the vehicle body outwards toward an observer at the end of each LOS. For the GSA, integrated IR-A, IR-B, IR-C, and IR-Total PM radiance are followed as QoIs. Figure 5.12 shows baseline IR PM radiances along the IRV-2 vehicle nose at trajectory point 1. Each radiance point location corresponds to the end of each LOS (green line in Figure 5.10). As expected, peak total LOS radiance values occur along the stagnation line that ends at an axial distance $x = -2.0\text{x}10^{-3}$ m from the non-recessed nose tip datum. IR-A and IR-B radiance decrease rapidly from the stagnation LOS, where IR-C radiance overtakes each at $7.0\text{x}10^{-3}$ m and $2.2\text{x}10^{-2}$ m, respectively. This axial distance defined region is described as the "shoulder" region throughout the rest of this work. Axial distance values less and greater than this region are termed "nose" and "downstream" regions, respectively. The shoulder to downstream is dominated by IR-C radiance as temperatures and net chemical reaction rates decrease.

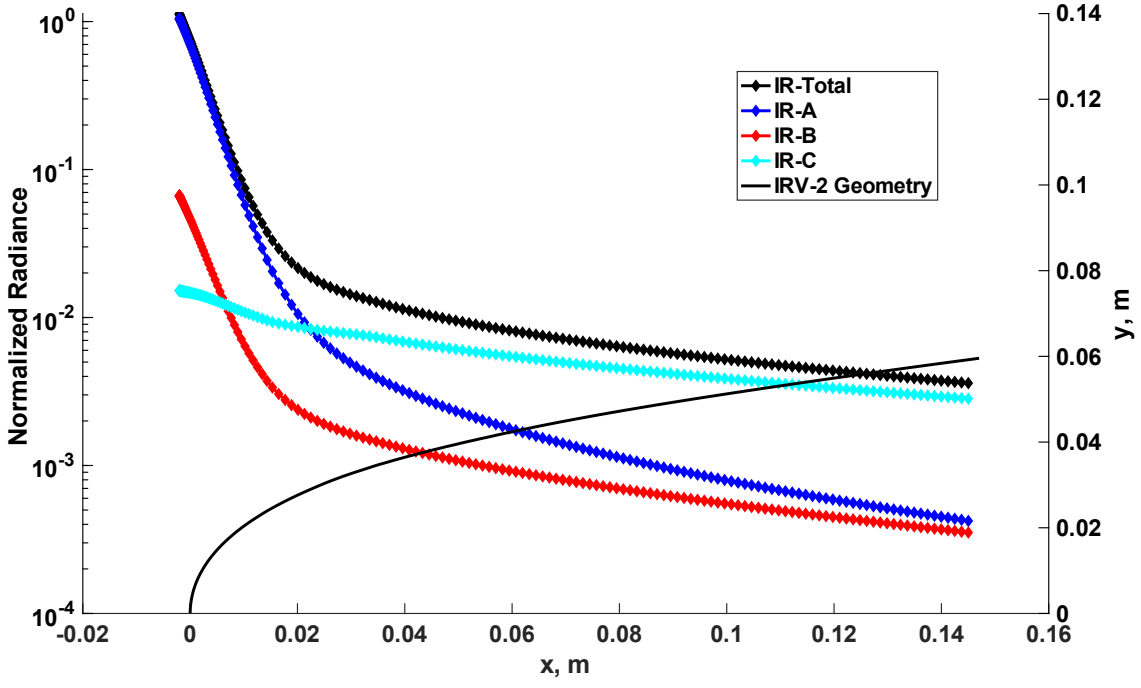

Figure 5.12: Baseline PM IR radiance QoIs along the IRV-2 vehicle.

5.4.3 Global Sensitivity Metric Convergence

To better quantify global sensitivities, Sobol' indices are used to estimate how each parameter contributes to overall QoI variance. This metric stems from the decomposition of total variance depicted in Equation 80, where the first and remaining righthand side terms represent single parameter and interaction effects, respectively. The total Sobol' index in Equation 83 represents both main and interaction variance fractions and effectively represents a way to quantify how much input uncertainty of a given parameter affects overall output variance.

Sensitivity convergence metrics are measured based on the maximum and mean changes in Sobol' indices for each IR PM band along the vehicle body in a manner similar to [99]. Equations 92 and 93 represent the maximum and mean change in Sobol' indices between i and $i-1$ Dakota sample batches for each j parameters for all k QoIs.

$$|\Delta S_T|_{max,QoIs} = \max_{k \in QoIs} \left(\sum_{j=1}^{n} \left| S_{T,i,j} - S_{T,i-1,j} \right| \right)_k \tag{92}$$

$$|\Delta S_T|_{mean,QoIs} = \operatorname*{mean}_{k \in QoIs} \left(\frac{1}{n} \sum_{j=1}^{n} \left| S_{T,i,j} - S_{T,i-1,j} \right| \right)_k \tag{93}$$

Figure 5.13 illustrates these convergence metrics as a function of evaluation batch size and sparse regression algorithm. LARS, BP, LASSO, and BCS methods experience similar maximum Sobol' convergences ranging between 0.1-1.0% at 500 Dakota evaluations. In contrast, OMP and SP method Sobol' index convergences plateau between 2-5%. These convergence results agree with similar sparse regression meta studies for small experimental design and large parameter sets [93,210].

Figure 5.14 depicts the total Sobol' indices for total IR PM radiance at the stagnation LOS calculated using various sparse regression methods for estimating PCE coefficients at increasing batches of evaluation inputs and outputs. These figures both portray the differences in methods as well as the relative emergence of reactions with higher sensitivity metrics for a given evaluation batch. All sparse regression methods for this particular QoI provide similar trends, where the first Zeldovich reaction rate coefficient

emerges as the dominant contributor to PM IR radiance variance. Cross-validation (CV) methods are also employed to balance surrogate model accuracy with complexity. For each batch, the SPGL1 algorithm for BP and LASSO sweeps through multiple regressions to provide the minimum noise tolerances ϵ and τ for a specified model prediction accuracy of 10^{-4} [211]. Similarly, the LAR, OMP, and SP algorithms sweep through multiple regressions to minimize leave-one-out CV errors [94]. The BCS method uses traditional 10-fold CV error methods for each batch. Each of these CV methods have the benefits of balancing model complexity and 'off-design' accuracy at the cost of overall metric convergence rates when compared to previous GSA/UQ studies. Similar trends exist for other PM IR radiance QoIs at different locations along the IRV-2 vehicle nose.

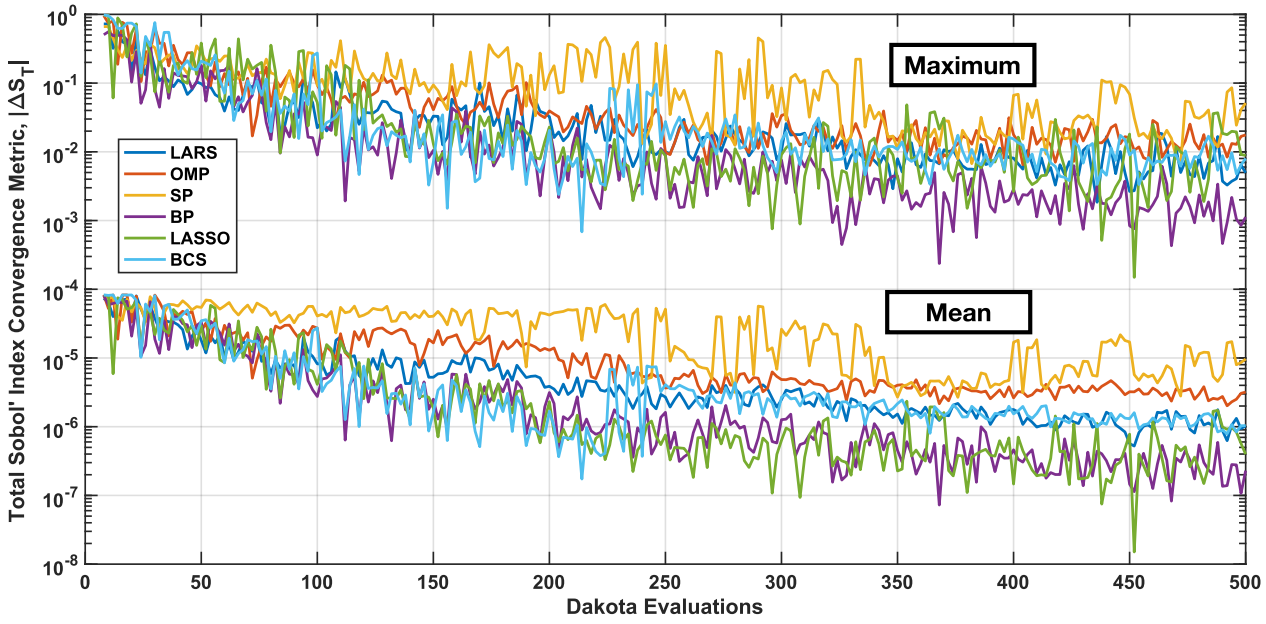

Figure 5.13: Total IR PM radiance sensitivity metric convergence across the IRV-2 vehicle.

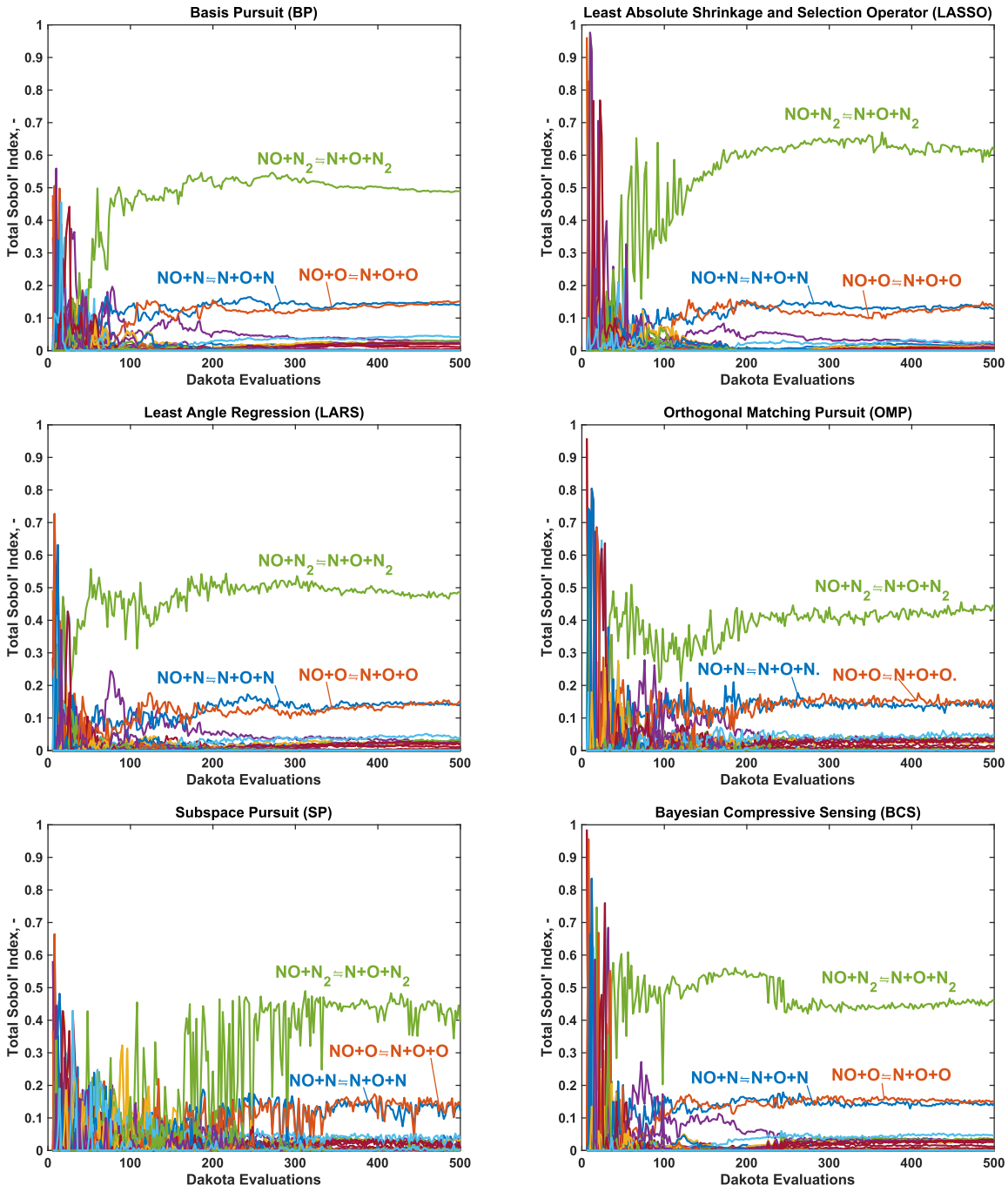

Figure 5.14: Stagnation line total PM IR radiance total Sobol' index convergence by evaluations and sparse regression approximation.

5.4.4 Global Sensitivity Metric and Uncertainty Propagation Results and Discussion

Sensitivity and uncertainty results for PM IR radiance along the IRV-2 nose are depicted in Figure 5.15. Subfigures (a) to (d) represent IR-A (0.78-1.4 μm), IR-B (1.4-3.0 μm), IR-C (3.0-20.0 μm) and IR-T

(0.78-20.0 μm) spectral band ranges, respectively. The first row of each subfigure depicts normalized radiance results for the 500 samples, the mean and propagated 95% confidence interval bounds (red). The middle row of each subfigure depicts the parameter variance contributions in the form of Sobol' indices. The bottom row of each subfigure scales the Sobol' indices by the normalized 95% confidence interval bounds. The scaled Sobol' indices are plotted in a stacked area chart to show the relative percentages each parameter contributes to the uncertainty bounds at each point along the IRV-2 vehicle. This scaling provides context on where the parameter variance contributions most affect absolute QoI uncertainty over the IRV-2 vehicle nose [64]. For both Sobol' indices and uncertainty scaled Sobol' indices, an 'All Others' category is defined as the sum of parameters whose variance or scaled variance contributions integrated remains less than 2% over the QoI range. All results in these subfigures are second order polynomial chaos expansions with coefficients estimated using the SPGL1 BP algorithm.

The first rows of Figure 5.15(a-d) show the radiance profiles for propagated mean and 95% confidence intervals, as well as the 500 evaluations. Uncertainty propagation involves evaluating 10^6 Monte Carlo samples for each PCE for all wavelength regions and LOS locations. The majority of PM IR radiance uncertainty is experienced near the nose tip of the vehicle with the exception of IR-C, where the uncertainty fraction is relatively constant along the vehicle. IR-A, IR-B, IR-C, and IR-T each experiences a maximum propagated uncertainty range of +46/-32%, +40/-34%, +28%/-24% and +45%/-39% from the mean at the stagnation LOS, respectively. Normalized uncertainty bounds decrease significantly after reaching the shoulder of the vehicle for all spectral ranges except IR-C.

The second rows of Figure 5.15(a-d) depict PM IR Sobol' indices. For all spectral bands, the vast majority of reaction rate parameters whose Sobol' index values contribute less than 2% of integrated variance across the QoI range (grey lines). The IR-A sensitivities in Figure 5.15(a) vary the most spatially when compared to other spectral ranges. The beginning of the nose region is most sensitive to NO dissociation through collisions with N_2, O and N. NO dissociation rate sensitivities from these partners are followed by NO dissociation via the second Zel'dovich mechanism reaction and O_2 dissociation rates with partners O and N at the beginning of the shoulder region. $CN + O$ exchange to form NO reaction rate

sensitivity rapidly increases from the center of the nose region to peak at the end of the nose region. $CO + N$ and $CN + O$ to form CO reaction rate variance contributions steadily increase in the downstream region. One overarching observation from these reaction rates is that all involve the production or destruction of N_2, O, N, and CN prior to the downstream region. These species all exhibit strong radiance proportions in the near IR region as shown on the left side of Figure 5.11(a) [1,212]. As temperatures cool in the downstream region, the relatively slower carbon exchange CO, NO and CN reaction rate sensitivities increase as the other net reaction rates settle into a chemically frozen state. These sensitivities correspond to the dominant radiator CN in the IR-A region of Figure 5.11(c). These results are most relevant to developing sensors tuned to the near IR spectrum involving ablative carbon remote observations. Additionally, the results further downstream better represent the frozen chemical states experienced in the wake of ablative hypersonic vehicle.

IR-B and IR-C sensitivities in Figure 5.15(b, c) follow similar trends in the nose region as IR-A, where nitrogen dissociation pathways dominate. IR-B has a lower contribution to uncertainty from O_2 dissociation and $CN + O$ exchange in the nose region when compared to IR-A. The downstream region sensitivities for IR-B and IR-C are dominated by the second Zel'dovich mechanism and are primarily due to fundamental and overtone vibrational excitation and emission from NO populations. Figure 5.11(c) shows the importance of NO as a radiator especially in the IR-C region.

Total IR sensitivities in Figure 5.15(d) follow similar trends as a combination of its subcomponent band sensitivities, where NO dissociation in the nose section, oxygen dissociation and $CN + O$ exchange in the shoulder region, and second Zel'dovich reaction in the downstream region contribute most to overall IR radiance variance. The NO dissociation and second Zel'dovich mechanism sensitivities most influence populations of N_2 and CN near the nose and NO, CO, and CN further aft along the vehicle LOSs.

The link between NO dissociation variance contributions to total IR PM radiance at the stagnation line is depicted in Figure 5.16(a,b), where total PM IR radiance is depicted in black. Nitrogen comprises the majority (68.8%) of this radiance in the form of HP-CIE and E-CIE influences. Figure 5.16 also depicts

chemical reaction source terms for NO and N_2 along the line of sight, respectively. The majority of NO dissociation variance contributions seen near the stagnation point of Figure 5.15(d) stem from the nonequilibrium chemical interplay between direct NO dissociation to form atomic nitrogen (red line in Figure 5.16(a)), which in-turn limits the production of N_2 via the backwards rate exchange reaction (blue line in Figure 5.16(b)). Interestingly, this limiting exchange between NO destruction and N_2 production also occurs near the inflection point of the radiance slope in these figures (~7.5×10^{-3} m along the LOS). This region along the LOS is also where the reverse of the first Zel'dovich reaction (N_2 source production) condition occurs and where the atomic nitrogen population can meaningfully affect the net source term for nitrogen removal or production via this reaction.

Lastly, sensitivities scaled by normalized radiance bounds are depicted in the bottom rows of Figure 5.15(a-d). For all wavelength bands, the majority of scaled sensitivities resides within the nose and shoulder region of the IRV-2 vehicle. The scaled sensitivities in each band display the importance of NO, O_2, and N_2 dissociation on IR radiance in these locations. This makes sense as the scaled sensitivities accentuate the higher energy sections of the flow where most dissociation occurs. This region experiences the highest temperatures and species number densities, making relative changes in those values from gas phase kinetics more impactful. Although the dissociation reaction scaled variance contributions dominate in this region for all wavelength bands, it is important to note that sensitivities involving other reaction categories and species further downstream would better represent the variance contributors to IR radiance present in the wake of a vehicle. These reactions and species, particularly for ablative products, have been shown to significantly influence integrated LOS vehicle remote observation in the wake [213].

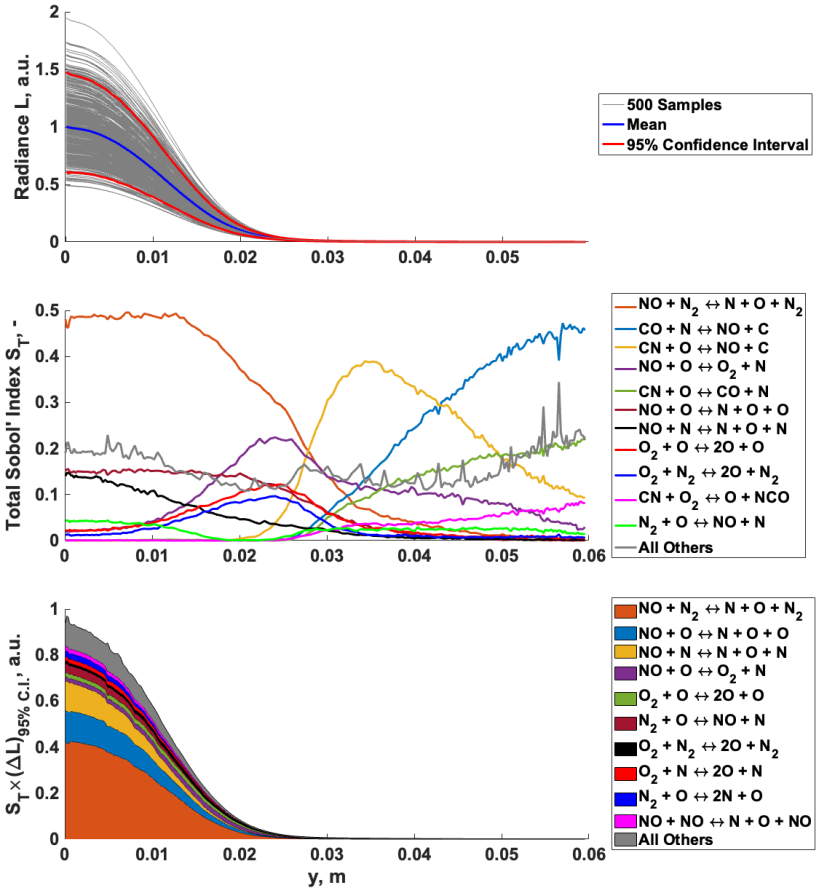
Radiance L, a.u.
500 Samples
Mean
95% Confidence Interval
Total Sobol' Index S_T, -
$NO + N_2 \leftrightarrow N + O + N_2$
$CO + N \leftrightarrow NO + C$
$CN + O \leftrightarrow NO + C$
$NO + O \leftrightarrow O_2 + N$
$CN + O \leftrightarrow CO + N$
$NO + O \leftrightarrow N + O + O$
$NO + N \leftrightarrow N + O + N$
$O_2 + O \leftrightarrow 2O + O$
$O_2 + N_2 \leftrightarrow 2O + N_2$
$CN + O_2 \leftrightarrow O + NCO$
$N_2 + O \leftrightarrow NO + N$
All Others
$S_T \times (\Delta L)_{95\%\ c.i.}$, a.u.
$NO + N_2 \leftrightarrow N + O + N_2$
$NO + O \leftrightarrow N + O + O$
$NO + N \leftrightarrow N + O + N$
$NO + O \leftrightarrow O_2 + N$
$O_2 + O \leftrightarrow 2O + O$
$N_2 + O \leftrightarrow NO + N$
$O_2 + N_2 \leftrightarrow 2O + N_2$
$O_2 + N \leftrightarrow 2O + N$
$N_2 + O \leftrightarrow 2N + O$
$NO + NO \leftrightarrow N + O + NO$
All Others
y, m

a)

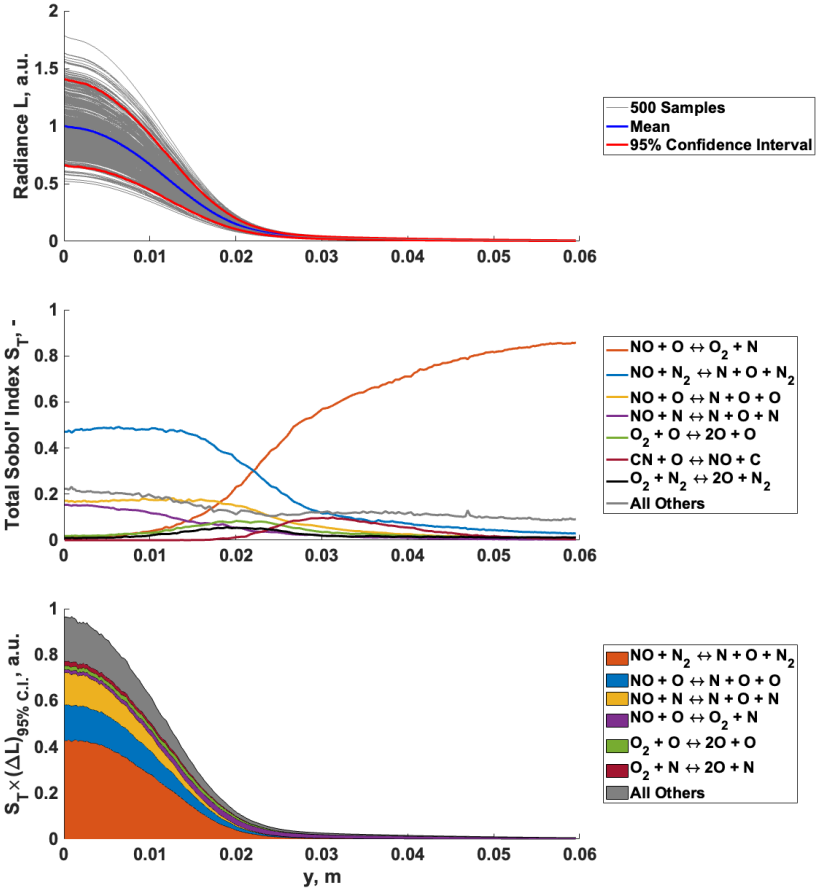
Radiance L, a.u.
500 Samples
Mean
95% Confidence Interval
Total Sobol' Index S_T, -
$NO + O \leftrightarrow O_2 + N$
$NO + N_2 \leftrightarrow N + O + N_2$
$NO + O \leftrightarrow N + O + O$
$NO + N \leftrightarrow N + O + N$
$O_2 + O \leftrightarrow 2O + O$
$CN + O \leftrightarrow NO + C$
$O_2 + N_2 \leftrightarrow 2O + N_2$
All Others
$S_T \times (\Delta L)_{95\%\ c.i.}$, a.u.
$NO + N_2 \leftrightarrow N + O + N_2$
$NO + O \leftrightarrow N + O + O$
$NO + N \leftrightarrow N + O + N$
$NO + O \leftrightarrow O_2 + N$
$O_2 + O \leftrightarrow 2O + O$
$O_2 + N \leftrightarrow 2O + N$
All Others
y, m

b)

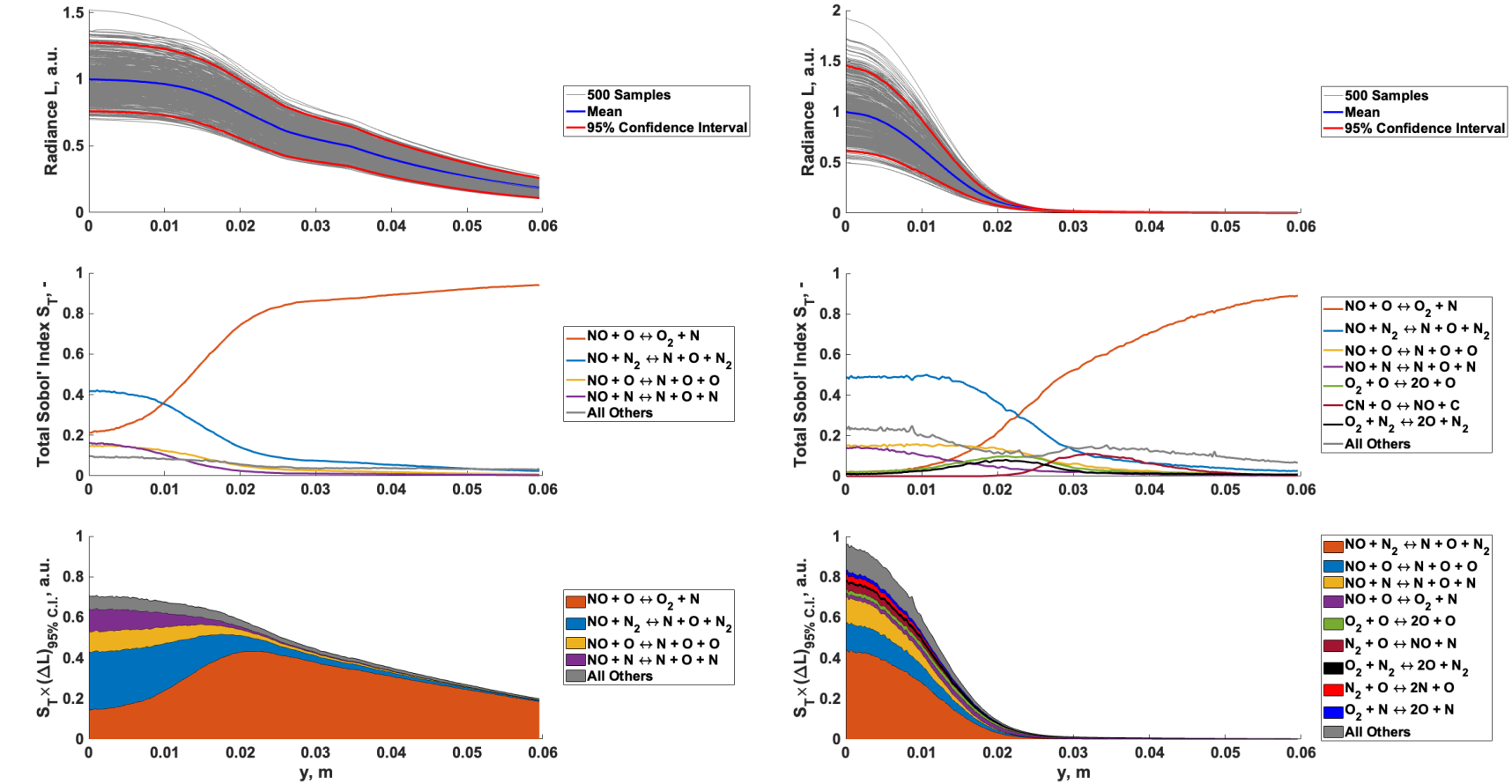

Figure 5.15: Normalized uncertainty bounds, Sobol' indices, and scaled Sobol' indices for PM (a) IR-A (0.78-1.4 μm), (b) IR-B (1.4-3.0 μm), (c) IR-C (3.0-20.0 μm) and (d) IR-T (0.78-20.0 μm) bands. 'All others' category defined as less than 2% variance or scaled variance contribution integrated over the QoI range.

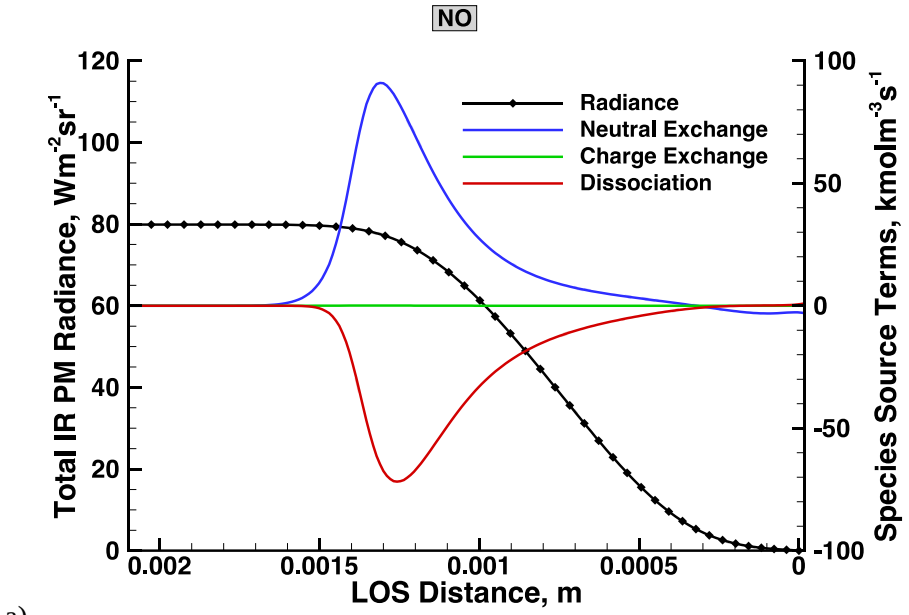

a)

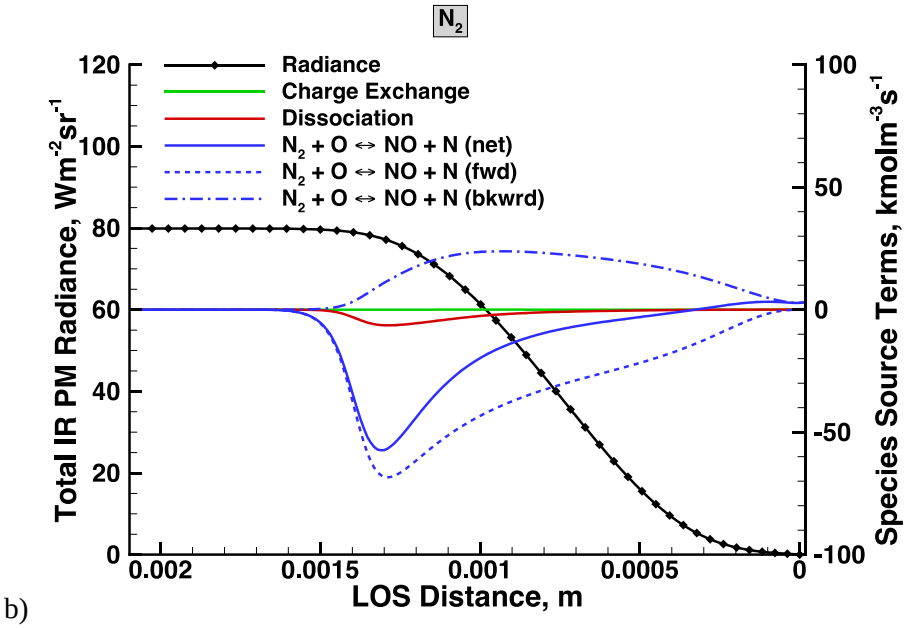

b)

Figure 5.16: Nitrogen and total IR PM radiance and NO and N_2 chemical reaction source terms along the stagnation line of sight.

5.5 Discussion and Summary

This work provides methods and results involving GSA/UQ of 195 thermochemical kinetics forward reaction rate parameters on PM IR radiance QoIs using surrogate model methods. The IRV-2 vehicle's first trajectory point was used as a test case to determine methods for decreasing reducible

uncertainty through a multi-grid convergence study with automated and coupled flow/solid mesh movement and shock tailoring. Uncoupled flow and coupled flow-material response results are provided on a nominal set of grids including flow temperatures, species number densities, and radiance values. A review of input parameters was conducted to inform both nominal values, bounding multipliers, and distribution choices in a GSA. Approximated surrogate model PCE coefficients from various sparse regression algorithms using 500 multi-model evaluations were compared for sensitivity metric convergence. Sensitivity analysis and uncertainty quantification results indicate the importance of Zel'dovich exchange and dissociation of NO reaction chemical kinetics uncertainties as major contributors to overall PM IR radiance uncertainty. The near and mid IR regions experienced additional PM radiance sensitivity contributions from CN and CO exchange reactions with atomic oxygen and nitrogen. Uncertainty bound scaled sensitivities were also investigated and show greater emphasis on NO, N_2, and O_2 dissociation near the nose and shoulder of the vehicle.

By integrating global GSA/UQ techniques, this case study identifies which thermochemical reaction rate uncertainties most affect predicted PM IR radiance. The targeted insights direct future efforts toward improving experimental measurements and reaction rate data where they are most influential to radiance QoIs. With the clear identification of the most influential reactions on IR radiance uncertainty, this study provides a roadmap for experimentalists to enable more effective resource allocation by focusing on the critical parameters that govern overall simulation uncertainty. Moreover, this work demonstrates how multi-grid convergence studies, automated shock alignment, and coupled flow-material response simulations can be used to reduce epistemic uncertainties in complex hypersonic flow environments. These methodologies increase the fidelity of simulations while managing computational expense, thereby enabling more reliable predictions of thermal and radiative behavior during reentry. Additionally, the identification of near IR spectral regions dominated by species NO, CN, and CO can inform the design of specialized sensors. Such sensors could be tuned to detect specific radiative wavelengths, aiding in in-flight diagnostics, tracking and identification of hypersonic vehicles. This also informs location of interest ranges in more localized regions around vehicles for ground testing campaigns. Lastly, the methodologies

developed in this chapter offer a scalable and computationally efficient pathway to extend high-fidelity simulations to full-vehicle analyses and diverse flight conditions. The use of surrogate models and sparse regression techniques enables researchers to maintain accuracy while managing the computational burden of high dimension uncertainty quantification studies. These advances can be directly applied to optimize design cycles, reduce experimental costs, and ultimately improve the predictive capabilities of simulation frameworks used in the aerospace industry.

However, the limitations of this case study, particularly the lack of detailed parameter bound reviews, freestream condition change effects, finite rate surface chemistry processes, radiation excitation/de-excitation rate change effects, and incorporating the entire IRV-2 vehicle body all warrant further investigation. Extensions of this work are therefore depicted in Chapter 7, which include the analyses of lower trajectory points involving the entire vehicle to quantify sensitivity and uncertainty metrics where greater heating and subsequent ablation occurs. Additional parameter uncertainties following a more extensive literature review are included and involve surface chemistry as well as atomic and molecular excitation rates over the entire IRV-2 geometry. The next chapter involves the evaluation of the finite rate surface chemistry models whose rates are eventually used in the GSA/UQ analyses in Chapter 7.

Chapter 6

Finite Rate Surface Chemistry Results

6.1 Introduction

This chapter explores a novel FRSC model framework and includes input parameters estimations, implementation methods, theoretical and experimental comparisons, and sensitivity and uncertainty quantification studies. The results from these examined methods are then implemented in the full IRV-2 body sensitivity analyses in Chapter 7.

6.2 Parameter Determination

The primary parameters defining the FRSC model include oxidation and sublimation rates. As seen in Section 6.3, many oxidation surface kinetics and sublimation models can be utilized within the FRSC model. The Park oxidation model is chosen as it has been well-studied and established in the hypersonic CFD community. Other higher fidelity models incorporating additional surface chemistry phenomena can be implemented using this FRSC framework but are considered out of the scope of this work.

The Park oxidation surface chemistry rates are determined by the reaction probability parameters for the reactions

$$\begin{aligned} \mathrm{C(s)} + \mathrm{O_2(a)} &\overset{\epsilon_{O_2}}{\rightharpoonup} \mathrm{CO(a)} + \mathrm{O(a)} \\ \mathrm{C(s)} + \mathrm{O(a)} &\overset{\epsilon_{O}}{\rightharpoonup} \mathrm{CO(a)} \rightharpoonup \mathrm{CO(g)} \end{aligned} \tag{94}$$

where ϵ_{O_2} and ϵ_O are the respective reaction probabilities. These reaction probabilities were fit in an effort to capture ablation phenomena in low density environments with dissociated oxygen mixtures. Reactions forming CO_2 and those involving nitrogen species were not included as they are comparatively slower [162]. The reaction probabilities were fit to multiple data with the following relations:

$$k_O(T_w) = \epsilon_O F_O = 0.63 exp\left(-\frac{1160}{T_w}\right) P_O \sqrt{\frac{8 k_B T_w}{\pi M_O}} \tag{95}$$

$$k_{O_2}(T_w) = \epsilon_{O_2} F_{O_2} = \frac{1.43x10^{-3} + 0.01exp\left(-\frac{1450}{T_w}\right)}{1 + 2x10^{-4}exp\left(-\frac{13000}{T_w}\right)} P_{O_2} \sqrt{\frac{8k_B T_w}{\pi M_{O_2}}} \tag{96}$$

where F_O and F_{O_2} represent the mean thermal speed of molecular and atomic oxygen, respectively. It is important to note that more recent models incorporating surface coverage for the formation of CO from atomic oxygen do not predict an Arrhenius relationship between reaction probability and temperature as well as direct scaling with incoming flux. Instead, a local maximum with increasing temperature is usually predicted with a peak that is moderately pressure dependent [26,28]. For the purposes of this work, the Arrhenius relation for CO formation from atomic oxygen of Park is utilized and with uncertainty bounds that incorporate the wide range of reaction probabilities, temperatures and pressures.

To estimate the sublimation flux rates, the Clausius-Clapeyron saturation pressure model for C_3 is utilized,

$$\begin{gathered} P_{sat} = P_1 \exp\left[-\frac{E}{R_u}\left(\frac{1}{T_w} - \frac{1}{T_1}\right)\right] \\ P_1 = 100kPa, \qquad T_1 = 3{,}915K, \qquad E = 175\frac{kJ}{mol} \end{gathered} \tag{97}$$

while the Knudsen-Langmuir relation is used to estimate C_3 mass flux from the surface,

$$\begin{gathered} \dot{m}''_{C,sub+} = \rho_e u_e St_m B'_{C,sub+} = \bar{k}_{sub,C} \tilde{C}_{s,C} = \frac{\alpha P_{sat} M_{C_3}}{\sqrt{2\pi M_{C_3} R_u T_w}} \\ \alpha = 0.03 \end{gathered} \tag{98}$$

where the vaporization coefficient α is taken from C_3 vaporization experiments [1,169–171].

6.3 Implementation Methodology

The implementation procedure for utilizing the Damköhler based lookup tables is portrayed in Figure 6.1. The first step in this process involves building a four-dimensional (4D) table of independent parameters $T_w, P_w, \overline{Da}_{\rho_e}$, and $B'_{C,sub+}$ with associated dependent variables B'_C and $\widehat{K}_O$. For a given wall pressure, temperature and mass conductance, oxidation and sublimation kinetic rate parameters defined in Section 6.2 are then used as inputs for determining both the Damköhler number and oxygen dissociation fraction

$\widehat{K}_O$. These values are obtained through an iterative process where $\widehat{K}_O$ is obtained from 4D table interpolation that depends upon $\overline{Da}_{\rho_e}$. A new $\overline{Da}_{\rho_e}$ value is then obtained using the relation

$$\overline{Da}_{\rho_e} = \frac{\bar{k}_{O_n}}{\rho_e u_e St_m} = \widehat{K}_O \frac{\bar{k}_O}{\rho_e u_e St_m} + (1 - K_O) \frac{\bar{k}_{O_2}}{\rho_e u_e St_m} \tag{99}$$

where the oxidizer kinetics contributions are weighted by dissociation fraction. The process then repeats until a convergence threshold for both parameters is met. Mass conductance is provided by the flow solver and is used to determine $B'_{C,sub+}$. Finally, the converged $\overline{Da}_{\rho_e}$ and $B'_{C,sub+}$ values along with wall temperature and pressure are used to obtain B'_C via 4D table interpolation.

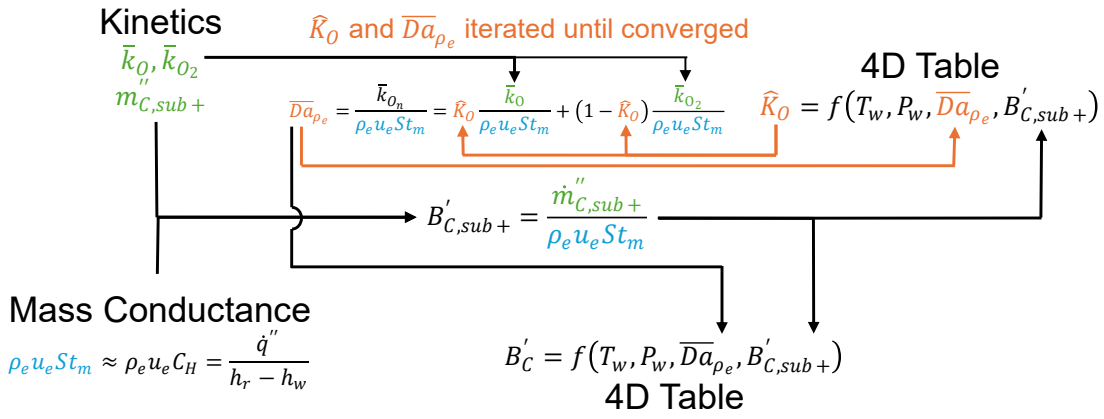

Figure 6.1: Implementation methodology for tabulated FRSC integration

6.4 Comparisons with Theory and Experiment

To better establish confidence in the FRSC model and its implementation, comparisons are made between the equilibrium surface chemistry and experimental results. The first results compared are the mass fractions of the near wall gas constituents calculated from the following

$$
\begin{gathered}
Y_O = \frac{m_O}{m_{total}} = \left(\frac{m_O + m_{O_2}}{m_{total}}\right)\left(\frac{m_o}{m_O + m_{O_2}}\right) = \widetilde{K}_{w,O_n}\widehat{K}_O \\
Y_{O_2} = \widetilde{K}_{w,O_n}\left(1 - \widehat{K}_O\right) \\
Y_{CO_n} = \widetilde{K}_{e,O_n} - \widetilde{K}_{w,O_n} \\
Y_{CO_2} = \frac{Y_{CO_n}}{1 + \delta\frac{M_{CO}}{M_{CO_2}}} \\
Y_{CO} = Y_{CO_n} - Y_{CO_2} \\
Y_{N_2} = 1 - \left(Y_{O_2} + Y_O + Y_{CO_2} + Y_{CO}\right)
\end{gathered}
\tag{100}
$$

and near wall specific enthalpy

$$
h_w = \sum_i Y_i \left[\int_{T_{ref}}^{T_w} C_{p_i}(T)dT + \Delta H_{f_i}^{\circ}\right] \tag{101}
$$

where the reference enthalpy difference from reference temperature and formation enthalpies are sourced from JANAF equilibrium tables [83]. Figure 6.3 depicts mass fractions and normalized carbon blowing rate as a function of wall temperature under conditions experienced by the IRV-2 vehicle at the first trajectory point. Comparing to Figure 2.2, the FRSC model predicts a significant increase in temperature before an appreciable amount of carbon blowing occurs. The initial presence of CO_2 followed by CO is more gradual as the surface rate kinetics prevents the blowing rates from reaching respective diffusion plateaus until wall temperatures of 1,500 K and 2,300 K, respectively. Oxygen dissociation and subsequent conversion to CO is also suppressed until above 2,000 K under these conditions. For the purposes of this study, the sublimated C_3 is assumed to react to form CO based on weighted molar fractions calculated from the partial pressure relations in Section 2.4. The individual contributions to normalized carbon mass blowing rate are also provided, showing that oxidation via molecular oxygen and direct carbon sublimation account for the majority of B_C' from 1,000 K to 2000 K, while oxidation via atomic oxygen increases the share of B_C' above 2,200 K. Temperatures above the diffusion limit of CO are demarcated by switching to the equilibrium surface chemistry. Traditional equilibrium tables are chosen for this region because the IRV-2 vehicle surface temperatures do not reach these levels during the flight trajectory and the carbon rich FRSC model in its current form does not match experimental results as well under these conditions.

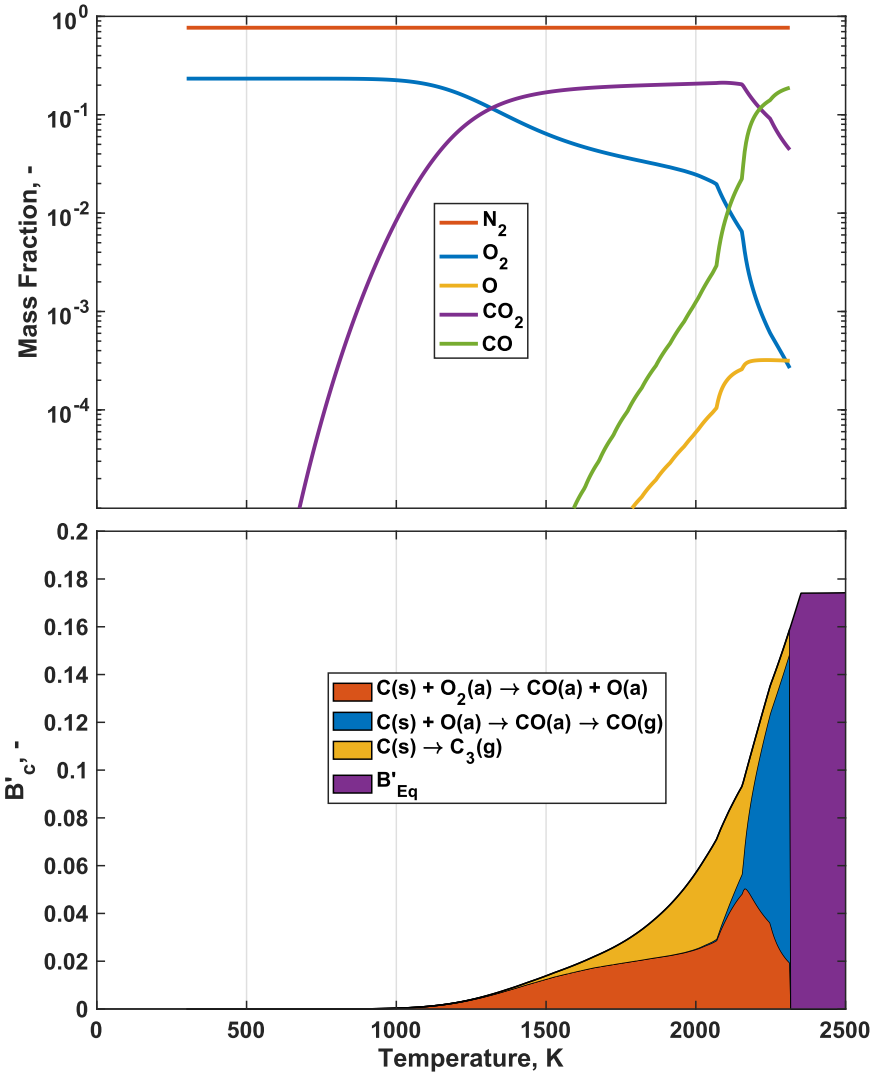

Figure 6.2: Near wall species mass fractions and graphite ablation sources at 0.223 atm, 0.229 kgm^{-2}s^{-1}.

The FRSC and equilibrium models are compared to various synthetic ATJ graphite carbon ablation experiments under subsonic and supersonic/hypersonic conditions in Figure 6.3, Figure 6.4, and Figure 6.5 [76–79,160,161,168,171,214–216]. For all experiments, normalized carbon mass blowing rates are compared at different wall pressures and temperatures. FRSC comparisons are made over a range of mass conductance and pressure values while equilibrium comparisons are dependent upon wall pressure for a given temperature range. For both subsonic and supersonic conditions at all pressures, the equilibrium model overpredicts B'_C compared to both FRSC model and experimental data below approximately 1,000

K and 1,500 K, respectively. This is an expected outcome as the equilibrium model assumes mass conductance as the only limit to oxidation. At subsonic conditions, FRSC model mass conductance values are 2 to 3 orders of magnitude less than those under supersonic and hypersonic conditions. For given temperatures, pressures, and oxidation and sublimation kinetic rates, boundary layer edge conditions at higher velocities will increase the relative mass conductance and decrease B_C'. In addition to capturing the effects of mass conductance, oxidation kinetics and sublimation kinetics, the FRSC model also incorporates the effects of relatively higher pressures under subsonic conditions. This can be seen in the solid blue line in Figure 6.3 between 700 K and 1,200 K as compared with the experimental observations (blue diamonds) from Welsh & Chung (1963) at atmospheric conditions [76]. As temperatures increase beyond this point, sublimation kinetics influences increase and pressure influences on B_C' become indistinguishable. This pressure dependence occurs at lower temperatures because the higher-pressure conditions at the wall correspond to higher incident oxidizer flux rates leading to higher normalized carbon mass flux rates that reach a diffusion limited CO_2 product plateau. Equations 95 and 96 depict this relationship as a proportional increase in molecular and atomic oxygen partial pressures driving faster relative finite rate oxidation kinetics. As more carbon is ablated through sublimation at higher temperatures (exponential temperature dependence in Equations 97 and 98), pressure dependence decreases as the $B_{c,sub+}'$ term begins to dominate in Equation 59. For subsonic conditions, only a few experimental results were acquired above 2,500 K that do not exhibit vapor pressure driven sublimation. The FRSC model does follow the equilibrium model in this carbon diffusion region, although at higher B_c' values for a given pressure and temperature. This FRSC overprediction is consistent with other FRSC and equilibrium models that incorporate a range of carbon species beyond C_3 [33,38,75,161,170,217].

Supersonic condition comparisons follow similar B_C' overpredictions of the equilibrium model, while the majority of the experimental data reside at higher temperatures, pressures and mass conductance values. Figure 6.4 depicts the FRSC models as compared to experiments. Similar trends exist at these conditions and compare well with the data points under conditions ranging from 0.1 atm to 1.0 atm and 0.5

$kgm^{-2}s^{-1}$ to 1.02 $kgm^{-2}s^{-1}$ at below 3,000 K. These values all reside within the ranges along the IRV-2 vehicle surface at various trajectory points as seen in Chapters 5 and 7. Similar to subsonic conditions, the FRSC model predicts larger ablation rates in the carbon diffusion region above approximately 3,000 K when compared to the CEA2 model. Both models overpredict the data from Lundell and Dickey and Maahs which is consistent with previous equilibrium models [160,161]. For the purposes of this work, the IRV-2 vehicle trajectory cases do not reach surface temperature conditions higher than 3,000 K.

Experiments that replicated conditions for space shuttle reentry were also compared in Figure 6.5 for multiple pressure and mass conductance conditions. The FRSC model compared favorably to these conditions, where four curves follow a similar trend to the experimental data at low temperatures. The previously mentioned finite rate model MAT (shown in dashed lines) is used to also compare with the data. The MAT model shows higher sensitivity to pressure variations when compared with the FRSC model at low temperatures, indicating that oxidation finite rate influences have higher influences in this region. Overall, these data and model comparisons provide confidence in the FRSC model used in this work.

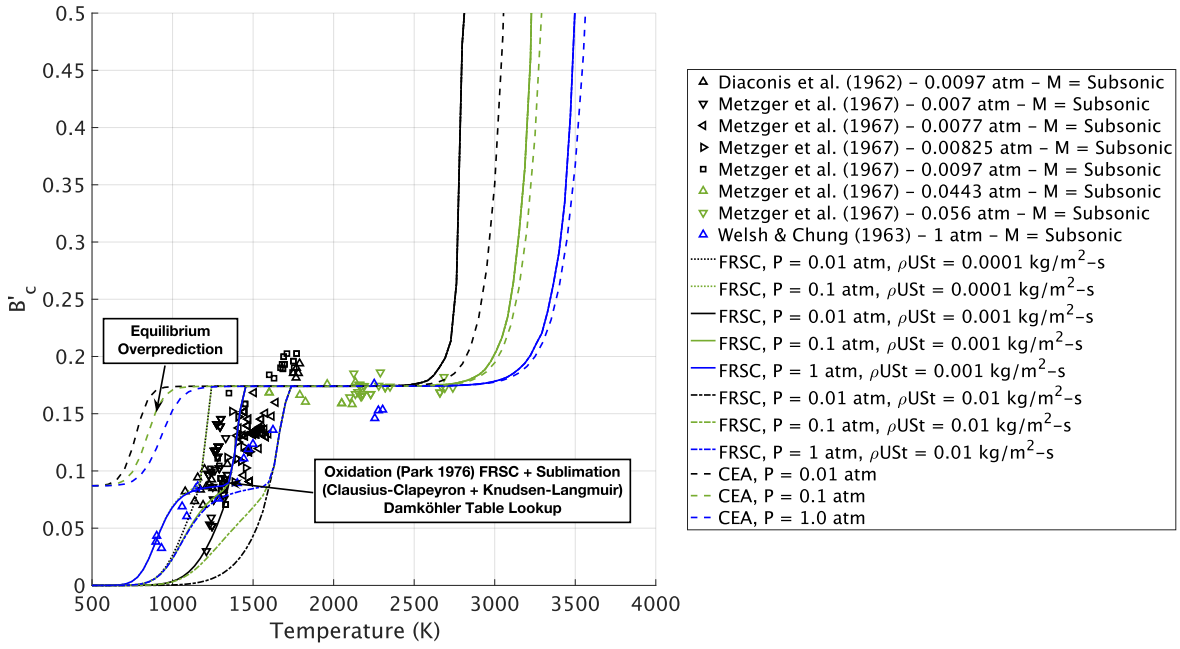

Figure 6.3: Experimental comparisons to equilibrium (CEA) and FRSC models at subsonic flow conditions.

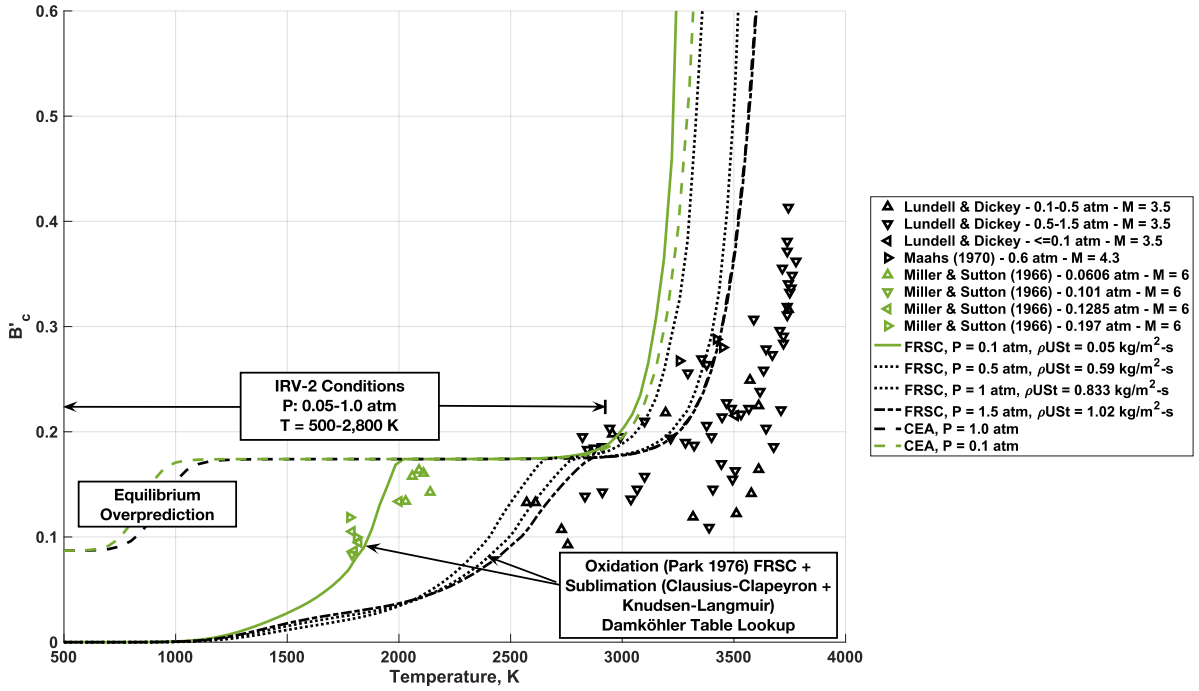

Figure 6.4: Experimental comparisons to equilibrium (CEA) and FRSC models at supersonic/hypersonic flow conditions

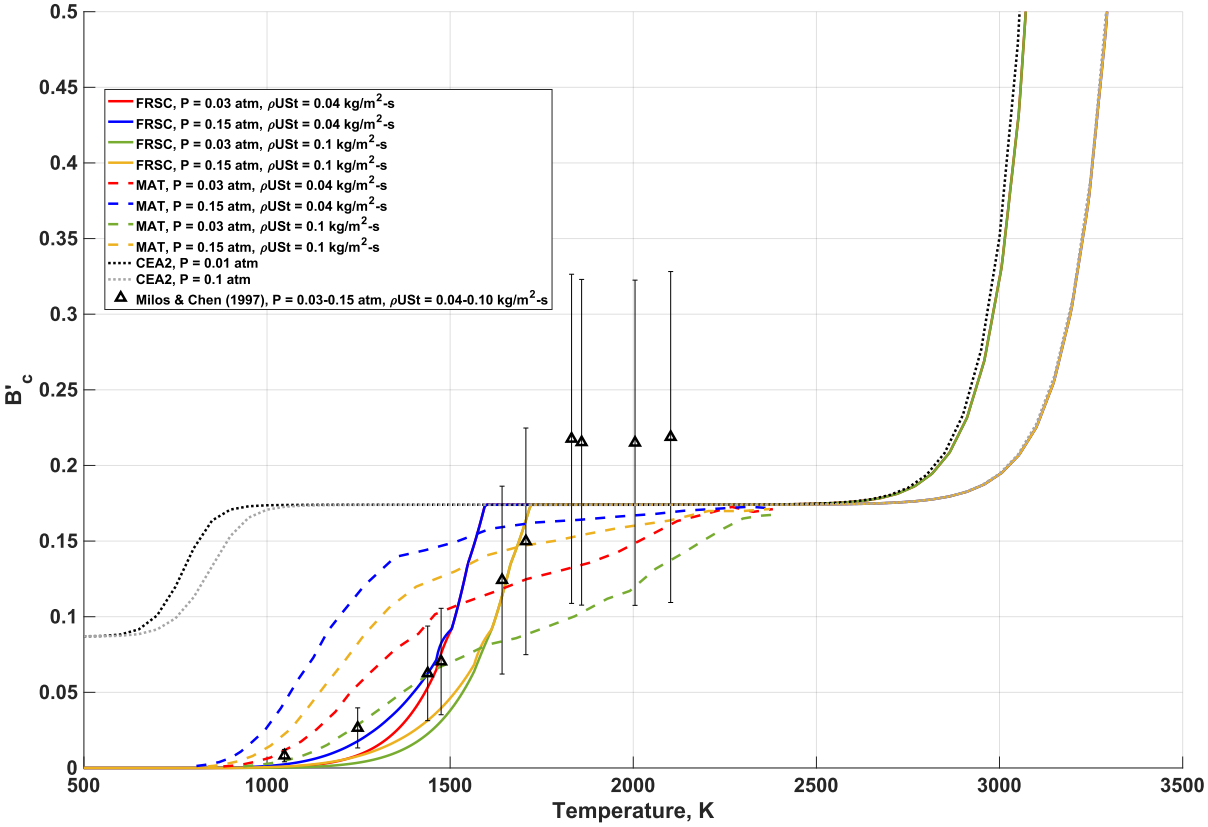

Figure 6.5: Experimental comparisons to equilibrium (CEA) and FRSC models at conditions replicating space shuttle reentry

6.5 Global Sensitivity Analysis and Uncertainty Quantification

A global sensitivity and uncertainty quantification analysis is conducted to better understand how variance contributions of the FRSC model kinetics parameters affect the normalized carbon mass flux rate at a given pressure, mass conductance and temperature range. A similar framework for PCE analyses as in Chapter 4 is utilized, where 300 evaluations sampled three FRSC kinetics parameters from uniform distribution bounds depicted at the bottom of Figure 6.6. PCEs are then constructed at each temperature using the previous point collocation and OLS regression processes with an oversampling ratio of 30. These bounds are determined from literature reviews in Table A7. The top subplot in Figure 6.6 depicts 300 samples, baseline, mean, and Monte Carlo PCE propagated 95% confidence intervals for B_c' QoIs for increasing temperatures at atmospheric pressure. There are two evident plateaus for CO_2 and CO diffusion present, where the lower CO_2 plateau is reached at lower temperatures for larger oxidation probabilities. This makes sense as the kinetics barriers to oxidation processes are lessened with these increased probabilities in a similar manner to when oxidizer partial pressures are increased in Figure 6.3. The larger CO plateau is reached sooner for larger sublimation flux rates. Uncertainty bound maximums for these conditions occur at approximately 1,300 K and 2,300 K, respectively. The middle subplot depicts the Sobol' indices over the same temperature range. The oxidation probability variance from the reaction involving O_2 most contributes to B_C' uncertainty up to 1,800 K, while mass flux sublimation rate contributes most from 1,800 K to 3,200 K. Above this range, the model reverts to the CEA2 data where kinetics parameters are not incorporated. The variance contributions scaled by relative uncertainty bounds are depicted in the bottom subplot of Figure 6.6. This both depicts the peaks of uncertainty bounds for B_C' previously mentioned while also attributing the relative variance contributions of the kinetics parameters. The uncertainty bound contributions for O_2 oxidation reaction probability at lower temperature represents approximately half of the uncertainty for sublimation rate kinetics at higher temperatures. These findings contribute to better understanding for how kinetics rate parameters will affect the amount of ablation products introduced into the flow from the high temperatures at the stagnation region to the lower

temperatures moving further aft along the shoulder of the vehicle. As surface temperatures increase along the trajectory, these results also predict a growing importance for the sublimation kinetics assumptions including the role of accommodation coefficient uncertainties.

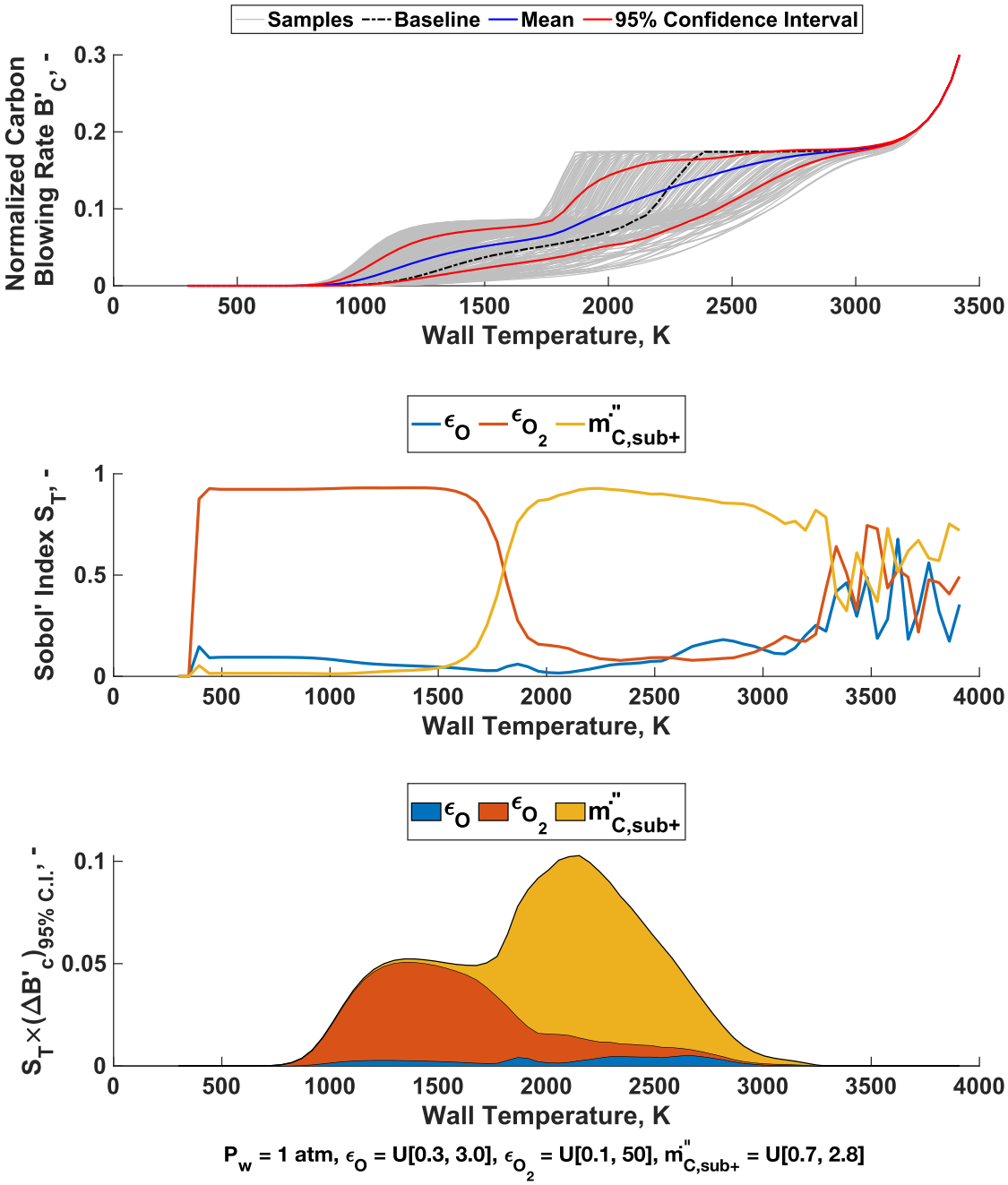

Figure 6.6: Global sensitivity and uncertainty results of the FRSC model.

6.6 Recession and Gas Phase Chemistry Comparisons

Finite rate and equilibrium surface chemistry lookup tables are compared in this section and include influences on surface and flow properties over multiple trajectory points. IRV-2 surface heat flux, temperature, ablation mass flux and recession changes are compared in Figure 6.7. All comparisons utilize the baseline flow and surface chemistry parameter sets outlined in Chapter 7 and Table A1, Table A2, and Table A7. Heat flux variations are minimal between surface models, with the majority of changes occurring at the first trajectory point near the stagnation point. Surface temperature changes are also minimal, with a maximum change between models at TP02 with a 14.7% difference at the stagnation point. Ablation mass flux differences are significantly different at TP01, where lower surface temperatures lead to half of the blowing rate at the stagnation point. TP02 and TP03 mass fluxes are nearly indistinguishable between models at the stagnation point until further aft along the vehicle body. This is explained by the relative surface temperature and the B'_C predictions prior to the diffusion limited CO oxidation plateau. At temperatures lower than 2,300 K in the FRSC model, B'_C values do not reach the 0.175 plateau and therefore, differ from the equilibrium model that is diffusion limited above 1,000 K. This can be shown by identifying what y values equate to 2,300 K for the TP02 and TP03 FRSC model results in the surface temperature plot (0.010 and 0.016 m, respectively). Looking at the ablation mass flux plot, these y values are where the FRSC and CEA2 models differ as the surface temperature decreases further. This 2,300 K temperature value is also where the plateau occurs for the baseline parameter set in the top chart of Figure 6.6. These trends are also evident in the recession figure, where CEA2 surface recession is much greater than FRSC for all trajectory points.

Comparisons with the ABRES Shape Change Code (ASCC) are also made, where the dots represent the surface location at the stagnation point [218]. Initial recession at TP01 for the ASCC model better matches the equilibrium model, while recession at TP02 and TP03 lies between the FRSC and equilibrium models. Wiebenga (2014) compared a 5 species coupled LeMANS-MOPAR-MD with equilibrium surface

chemistry and found similar differences [34]. As with these 20 species models, surface and flowfield chemistry model inputs, as well as material properties all contribute to the recession differences observed with ASCC. These chemical model variations along with coupled mesh movements between surface and shock all contribute and motivate the implementation of the sensitivity analyses and uncertainty propagation studies in Chapter 7.

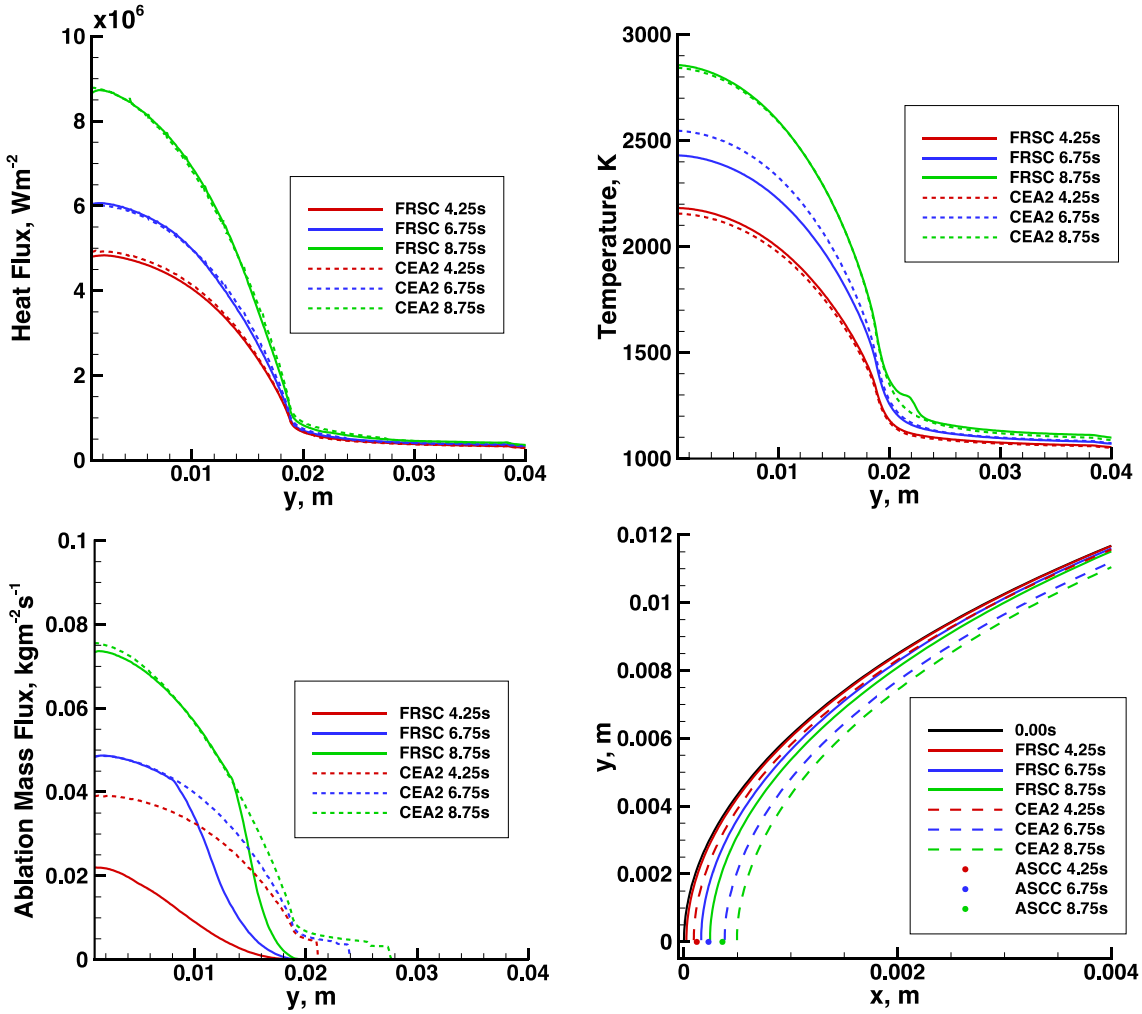

Figure 6.7: Baseline parameter set IRV-2 surface property comparisons between equilibrium and FRSC models.

Similar comparisons are made for flowfield results as seen in Figure 6.8 and Figure 6.9. Flow translational-rotational temperatures in the first figure do not vary significantly throughout the flowfield for

given trajectory points. However, an expected reduction in the shock standoff distance and increased surface recession are both evident between TP01 and TP02. Surface temperature maximums also increase between the trajectory points, with only slight variations between models. The temperatures and species mole fractions at the stagnation line in the second figure show a similar trend, where differences between surface model type more effect spatial location than variable differences. Notable exceptions are the major ablative product CO, C and CN, where all TP01 CEA2 values are significantly larger fractions of the 20 species. This increase in carbon species mole fractions does not occur at TP02 because the relatively higher surface temperatures in the FRSC model leads to B'_C values that are limited by the CO diffusion plateau. As long as the surface temperature of the IRV-2 remains between approximately 2,300 K and 3,000 K, this ablation plateau makes parameter differences between CEA2 and FRSC models virtually indistinguishable at a given trajectory point, even though the accumulated effect of different ablation amounts from TP01 at lower temperatures are evident.

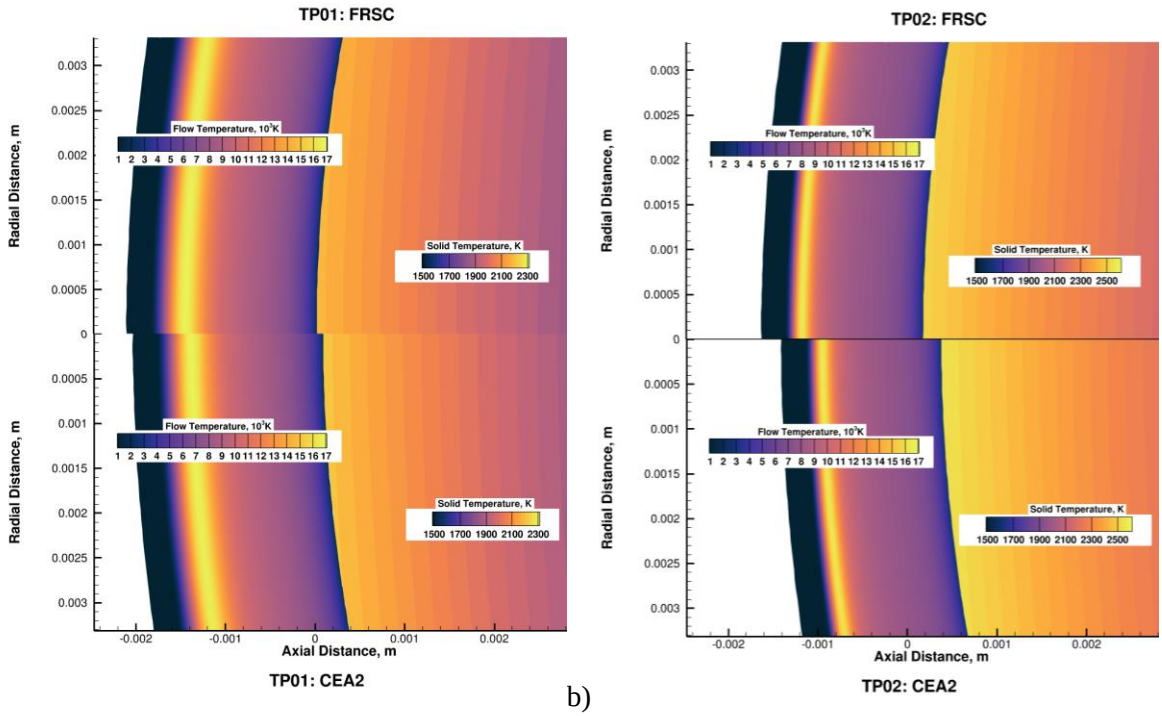

a) b)

Figure 6.8: Baseline parameter set flow translational-rotational and solid temperatures for (a) TP01 (Z = 55.8 km, U_∞ = 6.79 km/s, t = 4.25 s) and (b) TP02 (Z = 49.3 km, U_∞ = 6.78 km/s, t = 6.75 s).

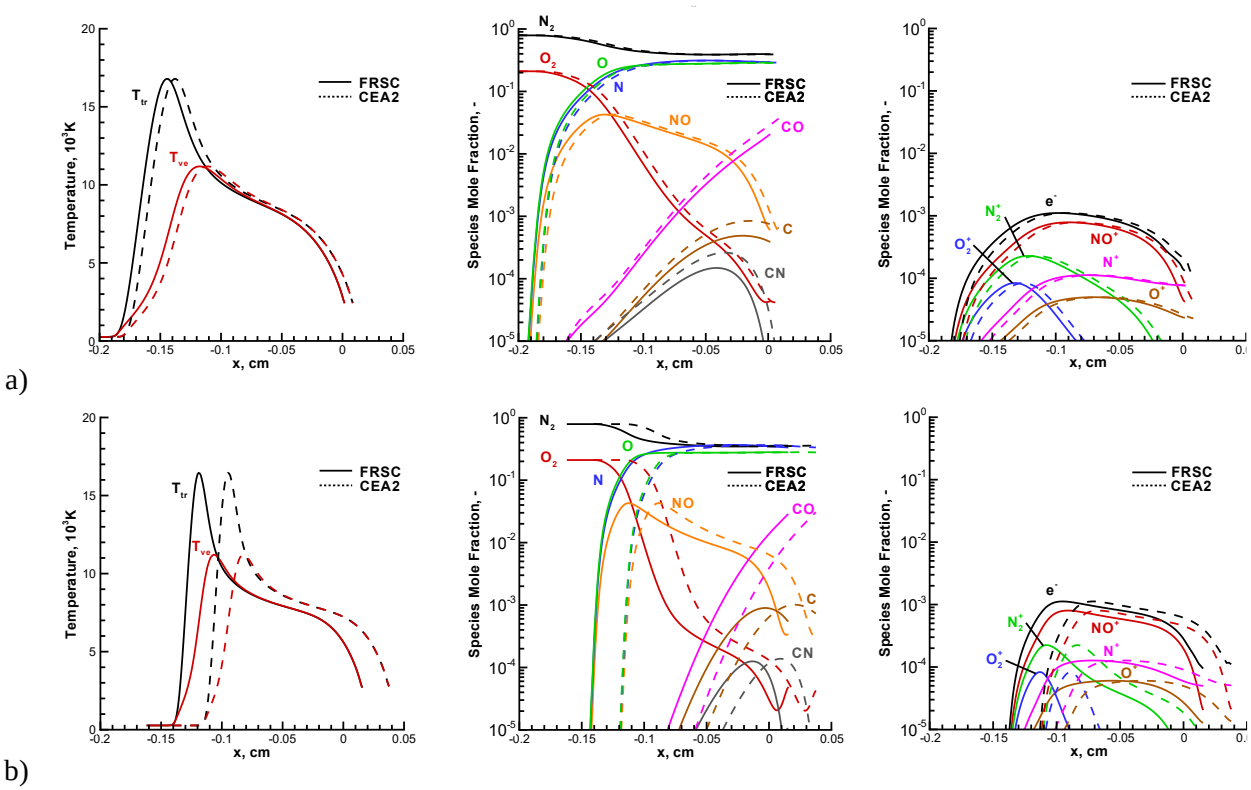

Figure 6.9: Baseline parameter set finite rate surface chemistry and equilibrium stagnation line temperatures and species mole fraction comparisons for (a) TP01 (Z = 55.8 km, U_∞ = 6.79 km/s, t = 4.25 s) and (b) TP02 (Z = 49.3 km, U_∞ = 6.78 km/s, t = 6.75 s).

The propagated effects of FRSC and CEA2 chemistry models on baseline IR radiance values at TP01 are depicted in Figure 6.10. As expected, surface chemistry effects are negligible between models except near the stagnation line, where surface temperature differences affect hard body radiation from the vehicle. The differences in blowing rate subsequent boundary layer cooling effects on wall temperature in this region leading to a 4.5% greater radiance values for the CEA2 model. Although this change is minimal for TP01 for the baseline values, the variation in FRSC parameters and their impact on B_C' values can vary overall radiance values significantly as seen in the Chapter 7.

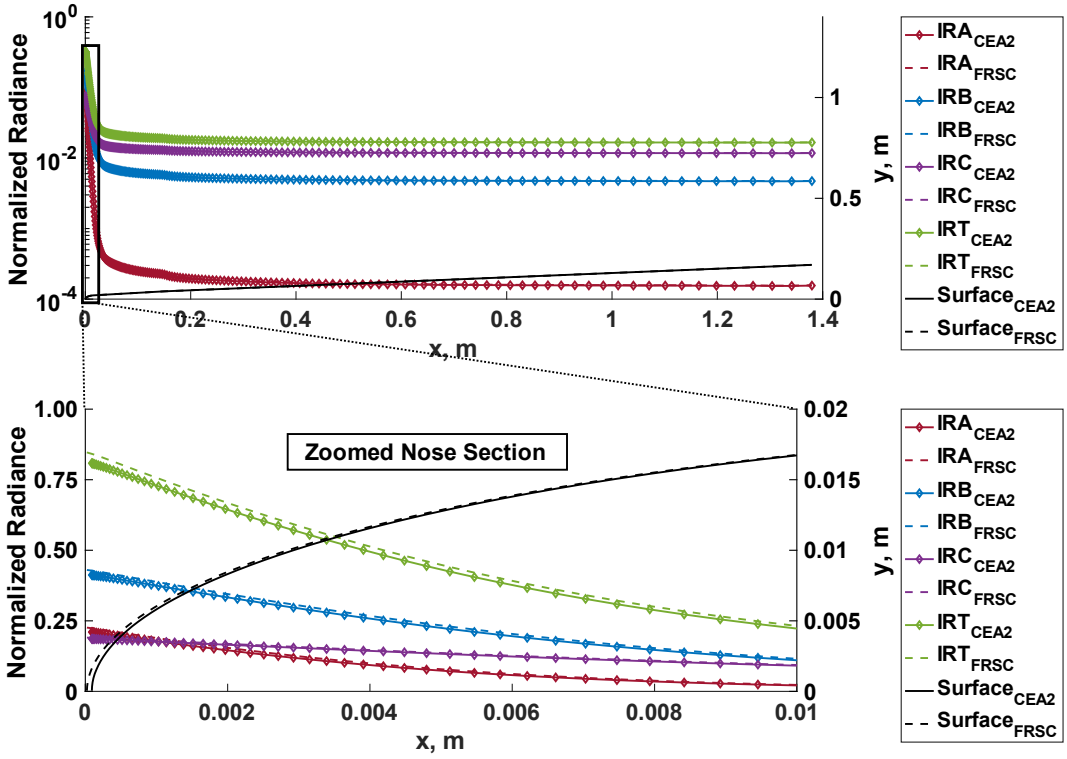

Figure 6.10: Baseline parameter set finite rate surface chemistry and equilibrium radiance comparisons for the TP01 (Z = 55.8 km, U_∞ = 6.79 km/s, t = 4.25 s).

6.7 Discussion and Summary

This chapter introduced the major uncertain surface kinetics parameters, including basic models approximating oxidation and sublimation processes. The methodology for parameter implementation within the FRSC model's framework was explained, wherein the surface kinetics rates along with boundary layer edge mass conductance were utilized with 4D $T_w, P_w, \overline{Da}_{\rho_e}$, and $B'_{C,sub+}$ based tables to generate B'_C values. This process offloads the majority of compute time for FRSC process integration to the initial 4D tables, allowing for more efficient and stable computation of carbon ablation vehicle surface updates in a tightly coupled flow-material response algorithm.

Comparisons of the new FRSC model were then made between the equilibrium CEA2 model and experiments, including subsonic and supersonic/hypersonic flow ground test conditions. The FRSC model

was determined to better approximate experiment at lower temperatures, where CEA2 overpredicts B_C' compared to ATJ carbon ablation experiments. However, both FRSC and CEA2 models tend to overpredict experiments above 3,000 K. A global sensitivity and uncertainty analysis was conducted for the uncertain surface kinetics parameters at atmospheric conditions. Reaction probability for oxidation of O_2 and sublimation mass flux rate kinetics were the major variance contributors to B_C' uncertainty for below and above 1,800 K, respectively. Sublimation mass flux rate encompasses more than double the uncertainty bounds for B_C' in the higher temperature region under atmospheric conditions. Baseline parameter set comparisons were made between finite rate surface and equilibrium chemistry sets for IRV-2 initial trajectory points. Surface parameter differences were identified, where ablation mass fluxes and surface recession were found to be most significantly impacted between models. Coupled flow parameter differences were distinguishable between surface models for ablative flow products near the surface, including CO, C, and CN at TP01. At further trajectory points with higher surface temperatures, differences between surface models decreased as CO diffusion limits were reached.

Overall, this chapter implemented and assessed a novel finite rate surface chemistry framework that directly addresses the limitations of equilibrium models in predicting carbon ablation phenomena during hypersonic flight. By explicitly accounting for finite rate oxidation and sublimation kinetics, the developed FRSC model provides a relatively higher fidelity portrayal of the complex interplay between surface reactions and the dynamic flow environment. This refined approach not only improves the accuracy of ablation predictions when compared to experiment but also offers deeper insights into the mechanisms that govern the thermal and chemical behavior of carbon-based materials under extreme conditions.

A key innovation in this work is the integration of four-dimensional lookup tables for molecular oxygen dissociation fraction K_O and nondimensional Damköhler number $\overline{Da}_{\rho_e}$ that capture the dependencies of reaction rates on wall temperature, pressure, mass conductance, and associated kinetic parameters. This efficient implementation methodology dramatically reduces computational overhead while maintaining a high degree of fidelity in simulating surface processes. The iterative convergence of

these parameters within a coupled flow–material response algorithm ensures that the FRSC model can be seamlessly incorporated into broader simulation frameworks used for designing thermal protection systems, making it a useful computational framework.

The detailed sensitivity and uncertainty quantification analyses presented in this chapter are particularly impactful. By applying polynomial chaos expansions to a selected set of kinetic parameters, the study identifies the oxidation probability for atomic oxygen and the sublimation mass flux rate as the dominant sources of uncertainty in the predicted carbon mass blowing rate. These findings not only pinpoint critical areas for experimental refinement over a wide temperature range, but also provide a clear roadmap for reducing uncertainties in future ablation simulations, ultimately leading to more reliable predictive models.

Comparative studies with both theoretical equilibrium models and experimental data underscore the practical advantages of the FRSC approach. The FRSC model's ability to better match experimental observations, especially in the low-to-moderate temperature regimes, highlights its potential for improving the design and analysis of hypersonic vehicles. For researchers and practitioners in the finite rate surface chemistry and material response communities, this work offers an enhanced framework that can be used to validate new material formulations and to optimize the performance of ablation-resistant TPSs under realistic operational conditions. By bridging the gap between detailed surface chemical kinetics and large-scale computational simulations, this research opens new avenues for interdisciplinary collaboration and paves the way for more accurate, efficient, and robust designs.

Chapter 7

IRV-2 Infrared Radiation: Full Vehicle

7.1 Introduction

This chapter builds upon the case study in Chapter 5, where uncertain input parameters' impact on IR radiance emanating from LOSs along IRV-2 vehicle nose are assessed. Changes and increased capabilities from the previous case study GSA/UQ analyses include:

- Modeling of the IRV-2 including the entire vehicle geometry and multiple materials, wherein the nose tip (first 0.15 m) and downstream sections consist of ATJ graphite and aluminum alloy 6061, respectively.
- 195 two-temperature gas phase forward chemical reaction rate coefficient baselines and uncertainty bounds are updated to those in Table A1 and are sourced from extensive literature reviews outlined in Section 3.3, Appendix B, and Appendix C.
- 11 vibrational-translational, electron-heavy particle, and electron impact ionization translational energy transfer baseline and uncertainty multiplier interval parameters depicted in Table A2 are included.
- 403 NEQAIR input parameter baselines and uncertainty bounds are added. These parameters include 290 O and N atom E-CIE rate coefficients outlined in Table A3 and Table A4, 61 N_2^+, N_2, NO, CN, and CO molecular HP-CIE and quenching rate coefficients outlined in Table A5, and 52 N_2^+, N_2, NO, O_2, CN, and CO molecular E-CIE rate coefficients outlined in Table A6.
- The novel FRSC model developed in Section 2.4 and assessed in Chapter 6 is utilized within LeMANS-MOPAR-MD. Three oxidation and sublimation baseline and uncertainty bound rate parameters in Table A7 are included.

- 3,200 QoIs are investigated. These include black body and PM (BB+PM) and PM only IR radiance estimates for 200 LOSs, four IR spectral ranges defined in Table 5.3, and two IRV-2 trajectory points outlined in Table 2.2 and Table 5.1.

The following sections include methods used to reduce epistemic uncertainty, baseline flow, material response, and radiation results, and GSA/UQ results for the case study scenarios.

7.2 Methodology and Implementation

The methods used to obtain GSA/UQ metrics across multiple trajectory points include using similar processes to those in Chapter 5. Figure 7.1 depicts the embarrassingly parallel flow for obtaining multiple trajectory point sensitivity and uncertainty metrics from parameter and QoI sets. Dakota is used again as a GSA/UQ wrapper tool with various input options. These options include specifying a second degree PCE, a random sampling method of uncertain input parameters, log-uniform distributed parameter lower bound, baseline, and upper bounds, and defining the various IR radiance field QoIs along the IRV-2. The sampling method of the input parameters is changed from Latin Hypercube methods due to evidence from multiple works from Hampton and Doostan that have found better PCE coefficient regression convergence for high-dimensional PCEs [219–221]. With these inputs and providing F collocation points, Dakota generates the input parameter sets and initiates multiple custom driver files in a parallel fashion.

Each driver copies template directories, preprocesses the sampled parameters into respective input files, runs and monitors multiple codes, and postprocesses results. Each template directory contains necessary input files common to each code that do not vary with parameter sets. For each trajectory point, a LeMANS-MOPAR-MD template directory contains a converged baseline restart file to greatly reduce compute time for each evaluation. This method accounts for the propagation of parameter sets from previous trajectory points while investigating the changes in GSA/UQ metrics at different flight conditions. Once directories and input parameters are preprocessed, the FRSC code is ran following Figure 6.1 to then provide FRSC informed B_C' tables that are then used as inputs for LeMANS-MOPAR-MD (LM). Converged LM results are then used as inputs for a postprocessing code Post-LeMANS (PL). This set of

functions takes in field data and generates multiple wall-normal LOSs that are then read into NEQAIR (NE). Once all radiance results for each LOS are obtained and postprocessed, QoIs are then sent to Dakota, and the next evaluation $M + 1$ is conducted. After all F evaluations are complete, the parameter sets and QoIs are input into the UQLab software suite for tracking convergence and generating GSA/UQ results.

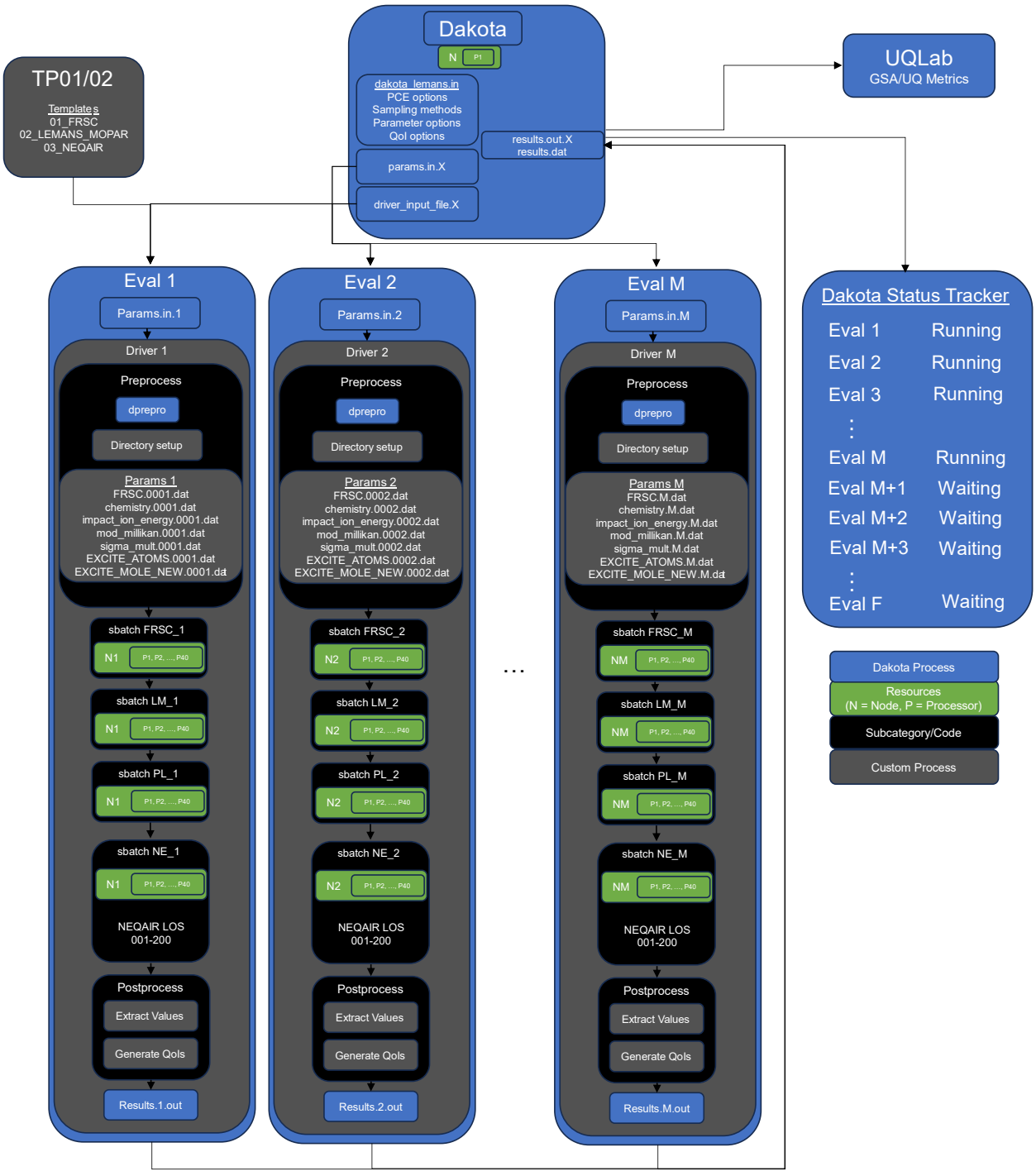

Figure 7.1: Embarrassingly parallel multi-trajectory point integration framework of Finite Rate Surface Chemistry model (FRSC), LeMANS-MOPAR (LM), Post-LeMANS (PL), and NEQAIR (NE) codes within Dakota.

7.3 Baseline Results

The baseline flow, material response and radiation results within this case study include the entire IRV-2 geometry at the first and second trajectory points (TP01/TP02) using the baseline parameters outlined in Appendix A.

7.3.1 Flow, Solid, and Spectral Grid Tailoring and Convergence

A similar process to Section 5.3.1 is used to reduce epistemic uncertainty for this case study. coarse, baseline, and fine flow, solid, and spectral grid sizes are defined in Table 7.1. An initial uncoupled flow is converged and shock aligned three times for each grid resolution in LeMANS. The restart files for these simulations act as a starting solution for each LeMANS-MOPAR grid. Where applicable, coarse and fine grids are a factor of two from the baseline to capture the combined effects of multiple grid resolutions on radiance QoIs. Figure 7.2 plots the interpolated coarse-to-baseline (CB) and baseline-to-fine (BF) percent differences in radiance QoIs along 200 wall-normal LOSs distributed across the entire IRV-2 vehicle following the streamwise spacing of the CFD grid. The maximum percent differences over all QoIs are 13.0% at 0.012m and 1.64% at 0.008m for the CB and BF grid combinations, respectively. This region is characterized as the "shoulder" of the vehicle and has been shown in previous case studies to be a complex region of thermochemical and radiative nonequilibrium where flow expansion occurs [115]. The vehicle shoulder is also a region of interest for the GSA/UQ results in Section 7.4. Spectrally, the largest percent change occurs within the IR-A (near IR) band. This is also where the majority of variance contributions occur in the various scenarios of this case study.

Table 7.1: Multi-grid convergence study for TP01.

Type	Grid descriptor	Coarse	Baseline	Fine
Flow	Grid type	Two-dimensional structured		
	Wall normal nodes	100	150	200
	Streamwise nodes	299	599	1,199
	Cells	29,502	89,102	238,402
	Shock alignments	3	3	3
	Maximum uncoupled plateaued residual	$5.87\text{x}10^{-13}$	$1.63\text{x}10^{-12}$	$6.72\text{x}10^{-13}$
	Local y^+	0.03-0.61	0.27-0.71	0.01-0.05
Solid	Grid type	Two-dimensional unstructured		
	Cells	3,566	9,442	22,393
	Interior wall spacing, m	$2.00\text{x}10^{-4}$	$1.00\text{x}10^{-4}$	$5.00\text{x}10^{-5}$

	Maximum coupled plateaued residual	3.38×10^{-12}	1.04×10^{-11}	1.33×10^{-11}
Spectral	Grid type	One-dimensional (LOS and spectral grids)		
	LOS grid points	100	150	200
	IR-A spectral grid points	155,001	310,001	620,001
	IR-B spectral grid points	400,001	800,001	1,600,001
	IR-C spectral grid points	425,001	850,001	1,700,001
	Wall Normal LOSs	100	200	400
Maximum Difference Across QoIs	IR-A	-	13.0%	1.64%
	IR-B	-	7.44%	0.94%
	IR-C	-	3.87%	0.85%
	IR-Total	-	6.21%	0.49%

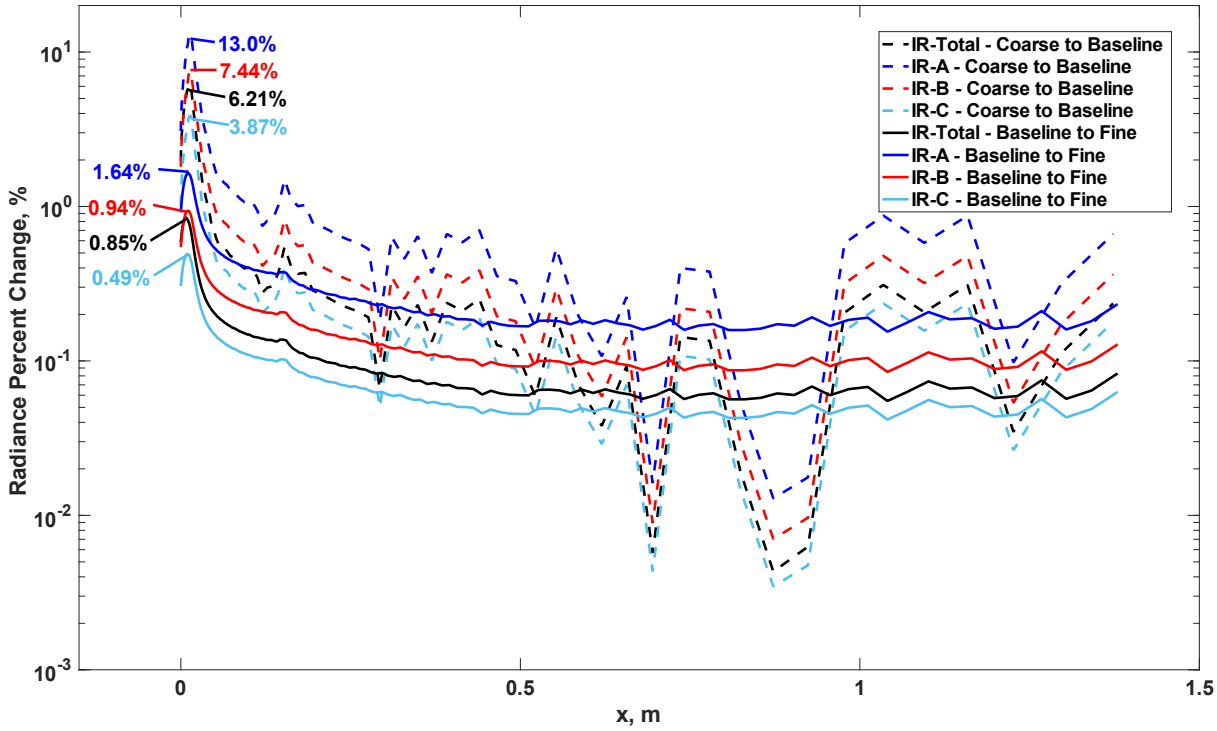

Figure 7.2: Black body and PM IR radiance multi-grid convergence along the IRV-2 vehicle body at TP01.

In addition to QoI evaluations, converged electron number density values are compared between flow and solid grids to ensure spanwise grid sensitivities are minimal. These results are depicted in Figure 7.3, where Figure 7.3(a) and (b) show the baseline and BF percent differences over the entire IRV-2 vehicle, respectively. The BF percent differences are all below 2.5 percent and reside mainly outside of the baseline bow shock, where the interpolated shock aligned grids most affect the small differences in electron number densities. Due to both these QoIs and field results, the baseline grid sets are chosen as they are the best balance between accuracy and computational cost per evaluation.

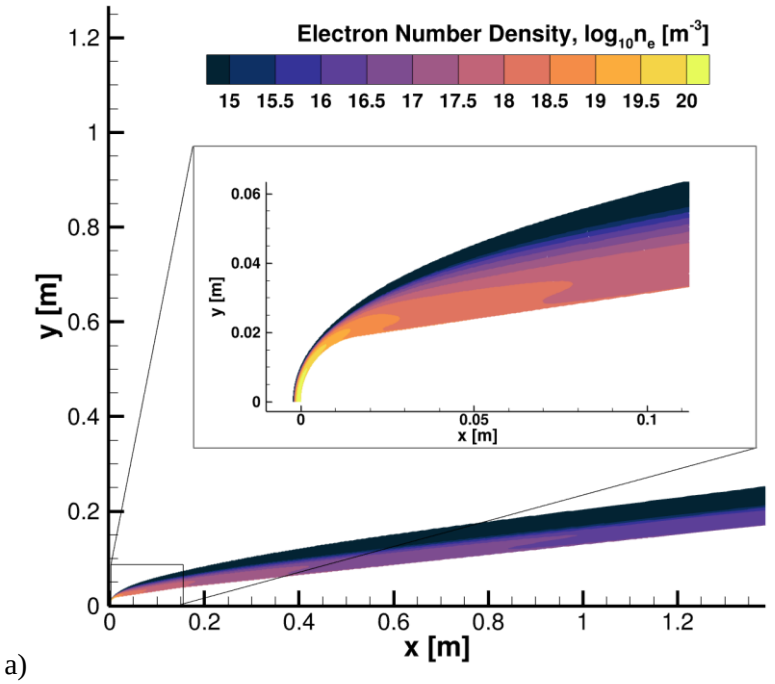

a)

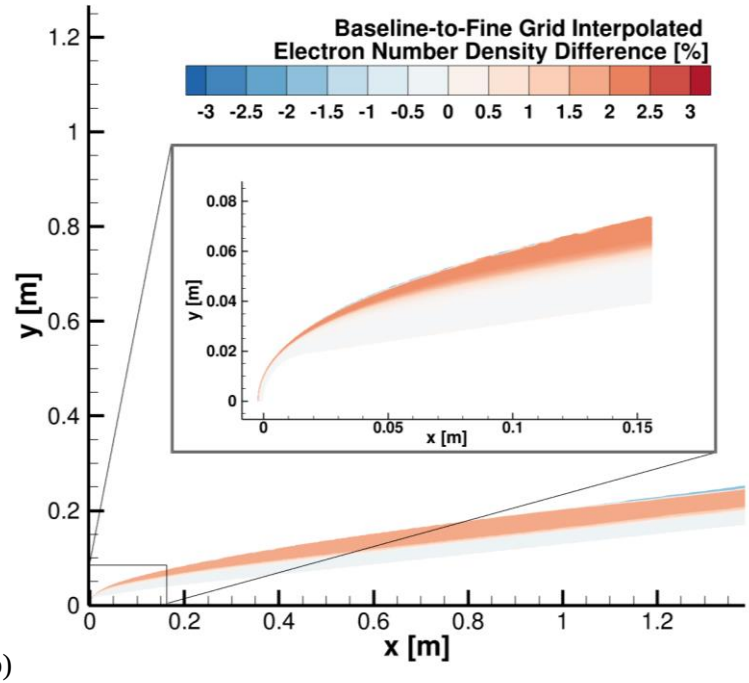

b)

Figure 7.3: (a) Electron number density and (b) grid convergence percent differences for the IRV-2 for TP01.

7.3.2 Flowfield

Baseline flowfield results for the first and second IRV-2 trajectory points are depicted in Figure 7.4. These flowfield parameters include Mach number, electron number density and carbon monoxide number density. The Mach number flowfield profiles appear similar between trajectories, while the zoomed portions show shock standoff distances of 0.0018 m and 0.0013 m for TP01 and TP02, respectively. Electron number density maximum values increase by a factor of 2.3: $1.79\text{x}10^{20}$ m^{-3} to $4.10\text{x}10^{20}$ m^{-3} for TP01 and TP02, respectively. Increased plasma formation is expected as the ballistic trajectory and slender body of the IRV-2 leads to little deceleration while the increased air density leads to an increase in temperatures behind the shock (see Figure 6.9). Similarly, the maximum field values for CO increased by a factor of 2.8: $1.43\text{x}10^{22}$ m^{-3} and $4.06\text{x}10^{22}$ m^{-3} for TP01 and TP02, respectively. The main reason for this increase is due to increased FRSC carbon ablation mass flux rates due to higher wall temperatures and pressures (see Figure 6.7). The GSA/UQ results in Section 7.4.3 reflect increased ablation and collisional excitation influences on IR radiation due to this density increase. These trends follow similar slender reentry vehicle studies involving weakly ionized plasmas with and without ablation [23,115,181].

7.3.3 Trajectory Point 1

For TP01, three baseline LOSs were taken from a video of all 200 LOSs to depict how changes in temperatures and species number densities affect both the PM spectral and integrated radiance along the IRV-2 vehicle. Figure 7.5 depicts the stagnation LOS and displays the maximum temperatures and species number densities in the flow. These inputs are similar to those depicted in Figure 5.9, but now include differences that stem from a different baseline gas phase chemical parameter set as well as the incorporation of the FRSC ablation model. As previously stated in Section 5.4.1, the previous chemical gas phase parameter baseline and uncertainty bound sets do not reflect the literature reviews conducted in this work. These rate changes and ablation model changes lead to lower overall translational and higher vibrational temperatures for this LOS with similar total LOS distances. Note that the LOS distances in these figures include both the converged recession point starting and the corresponding shock ending locations (see

Figure 5.7). These lower translational and higher vibrational-electron-electronic temperatures in this chapter reflect shorter relative relaxation times as well as differences in various air species dissociation and exchange rate coefficient baselines. The converged flow and material response neutral air species number densities are similar with the exception of NO values in the immediate post-shock region, where the values in this chapter exhibit a slower rise due to lower the relative control temperatures. Both neutral carbon and ionized species number densities follow similar trends and values as the previous parameter baselines. The notable exception is NO^+ and N^+ near the wall, where values with the new parameter set baselines yield number densities greater than NO^+ in the boundary layer. This difference is most likely attributed to the $NO^+ + O \rightleftharpoons N^+ + O_2$ charge exchange reaction, where the previous forward rate coefficients from Park (1993) [172] are over an order of magnitude lower than those of Dunn & Kang (1973) [117] and others. The higher rate values are chosen as the baseline in this case study as they better reflect the center of the rate coefficients for all references and temperatures in Figure B35. PM radiance trends are also similar when compared with Figure 5.11(a) with the exception of lower N_2 and higher N and O values in the near IR. Additionally, the overall integrated PM radiance in this case study is a factor of two larger than that of Chapter 5 . These differences are explained by higher stagnation line T_{ve}values post-shock leading to larger radiation contributions from N_2, N, and O rovibrational and atomic lines in the more energetic IR-A band.

Shoulder and downstream LOS comparisons will remain within this case study as these do not reflect the same locations as the IRV-2 nose only locations in Figure 5.11(b, c). Figure 7.6 depicts the shoulder region baseline inputs and results. In this region, the two temperatures equilibrate to a maximum of 7,000 K in the flow. All species number densities have decreased significantly from the stagnation point as the flow expands around the shoulder, leading to lower overall densities. CO, C, CN, and CO_2 species remain in appreciable relative number densities throughout the flow. Ionized species are now dominated by NO^+ in a similar manner to the 5 km/s and 7 km/s 11-species field plasma results in Chapter 4, where NO^+ is replaced by other ions as the primary charged species in the shoulder region. Excitation of N_2 and subsequent radiation still dominate the shoulder region, with notable increases in contributions from CO

and NO in the lower-energy IR-B and IR-C bands. This is similar to the trends observed in previous case studies, where major IR radiators tend to absorb and emit in these bands further downstream. The underlying reason is that species such as N_2, N, and O require sufficient time and space to become excited via collisional and radiative processes and subsequently emit photons, which can then be absorbed in the lower energy fundamental and overtone rovibrational bands of NO, CO, CN, and CO_2.

In Figure 7.7, the downstream LOS maximum equilibrium temperatures peak at 5,000 K and drop sharply to freestream conditions near the weaker bow shock. N number density populations decrease significantly compared to other neutral air species, while NO species number densities remain similar to the shoulder values near the vehicle surface. This is explained by the recombination processes for atomic nitrogen via Zel'dovich exchange processes that decrease atomic nitrogen and increase NO. The left side of Figure 7.8 shows the source term contributions for NO and N along the downstream LOS by reaction categories. Neutral exchange reactions (particularly the Zel'dovich exchange reactions $N_2 + O \rightleftharpoons NO + N$ and $O_2 + N \rightleftharpoons NO + O$) dominate near the vehicle surface with NO and N first net forming and then net declining due to the respective Zel'dovich reactions. All carbon neutral species decrease multiple orders of magnitude from the vehicle shoulder, but CO_2 decreases much less rapidly when compared to C and CN. This is due to an exchange reaction between CO and O_2 that produces CO_2 near the vehicle surface as seen in CO and CO_2 source term contributions on the right side of Figure 7.8. Ionized species continue to decrease from the shoulder as well, with NO^+ constituting the remainder of the plasma constituents. Both spectral and integrated radiance is now dominated by contributions of NO, CO and CO_2 rovibrational features (both fundamental vibration and overtones) in the IR-B/C bands, and N_2 in the IR-A band.

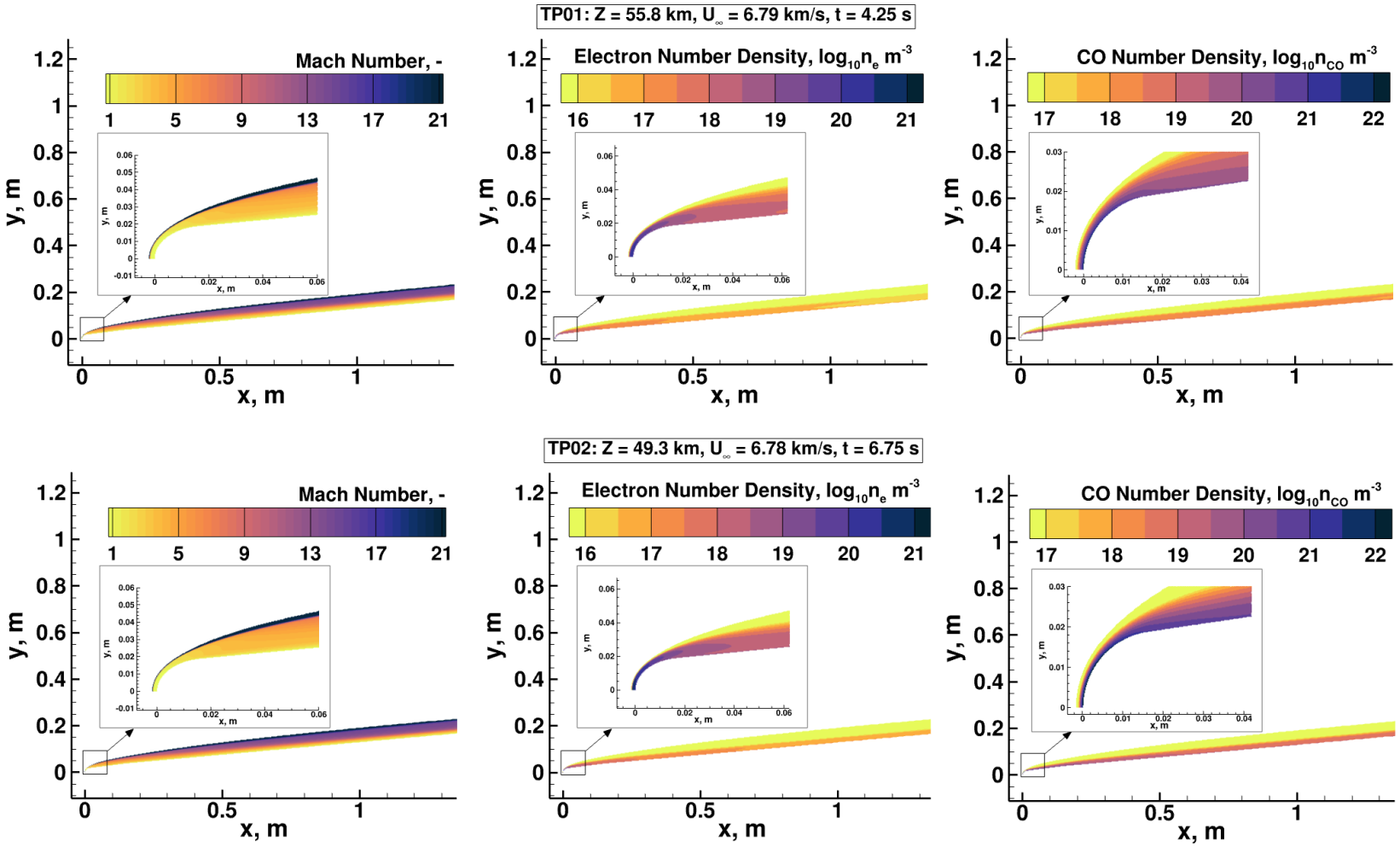

Figure 7.4: Select baseline flowfield properties around the IRV-2 vehicle at TP01 and TP02.

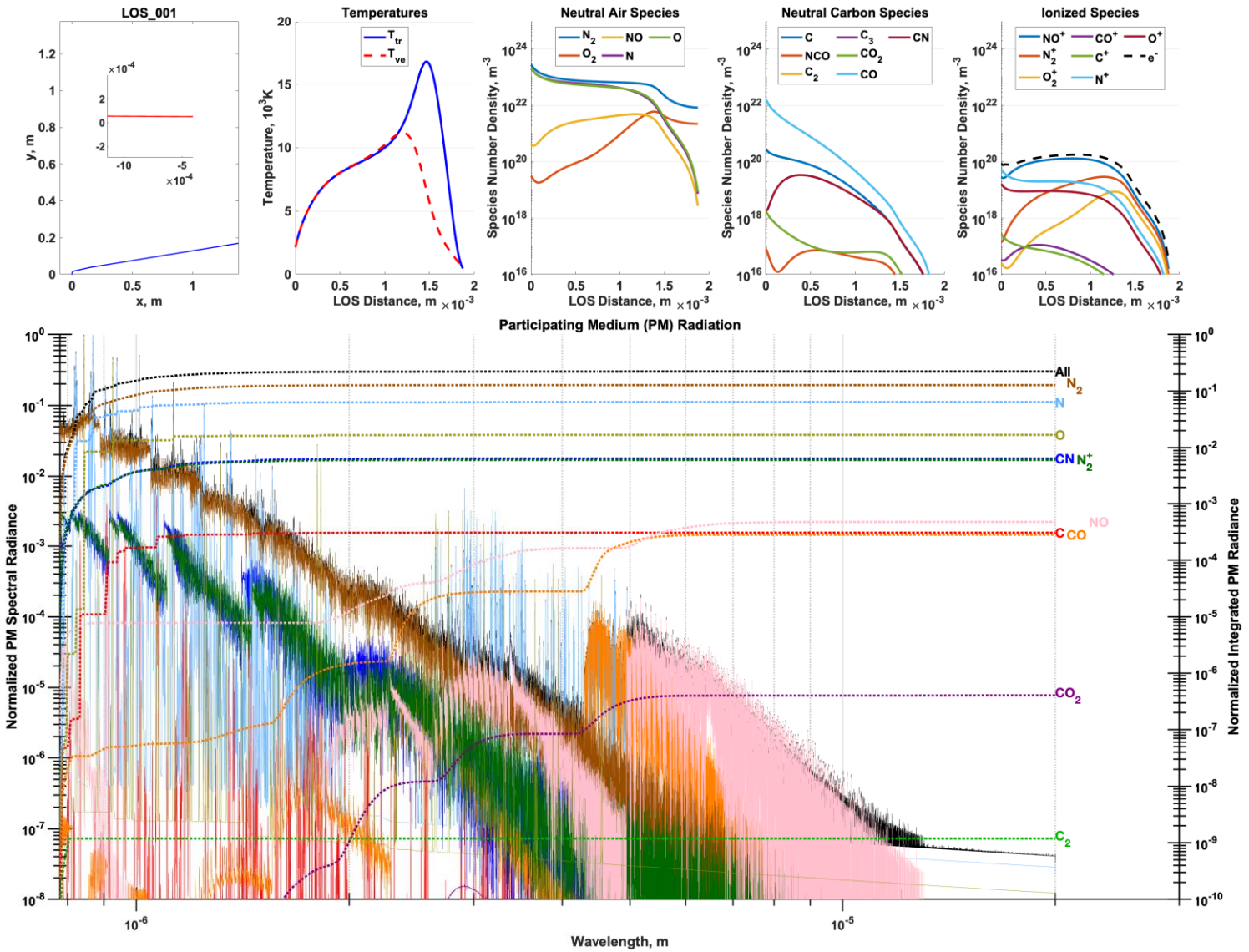

Figure 7.5: TP01 stagnation LOS: vehicle (blue) and inset LOS (red) geometries, LOS Ttr and Tve temperatures, LOS species number densities, and PM only spcectral and integrated radiances for various species.

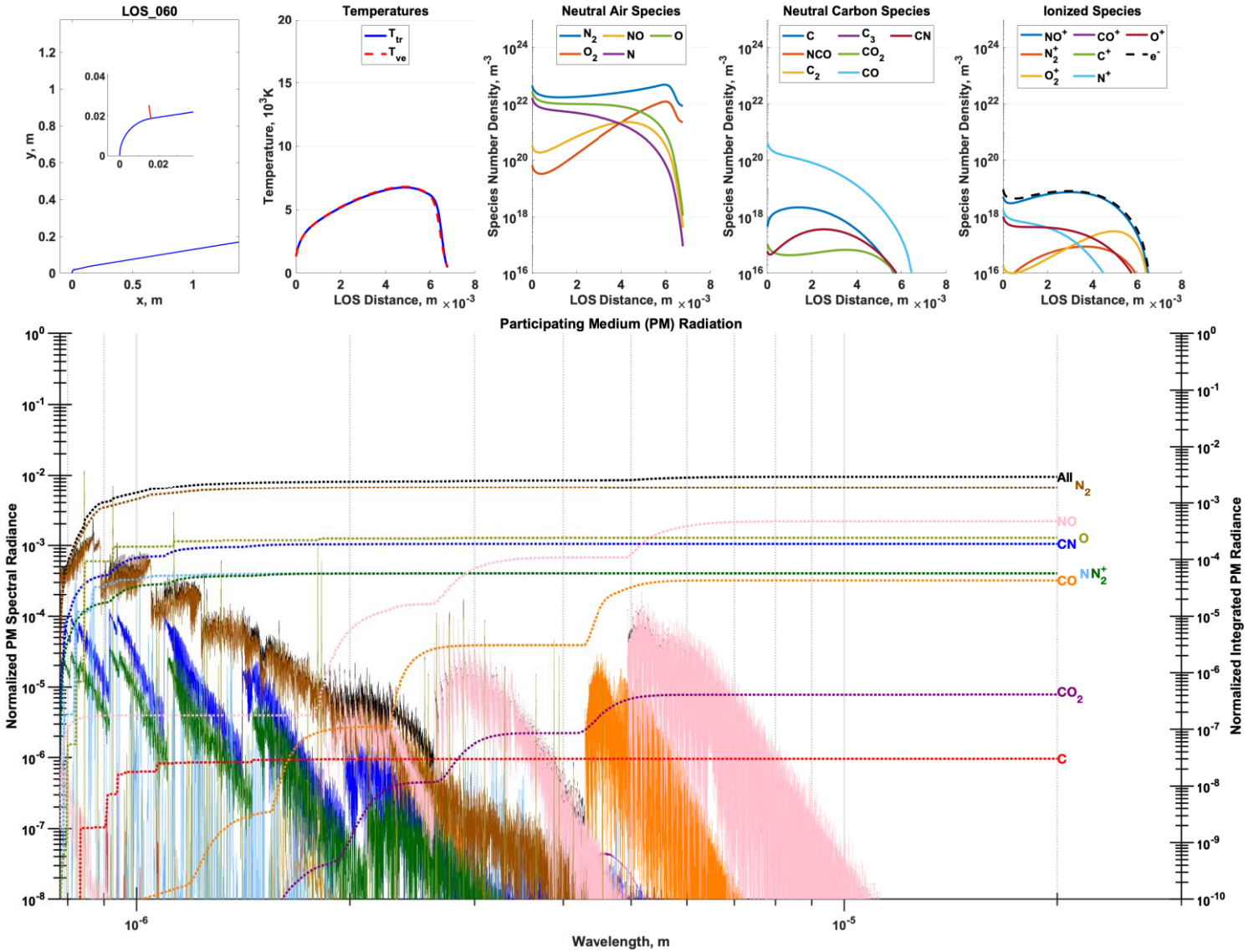

Figure 7.6: TP01 shoulder LOS: vehicle (blue) and inset LOS (red) geometries, LOS Ttr and Tve temperatures, LOS species number densities, and PM only spectral and integrated radiances for various species.

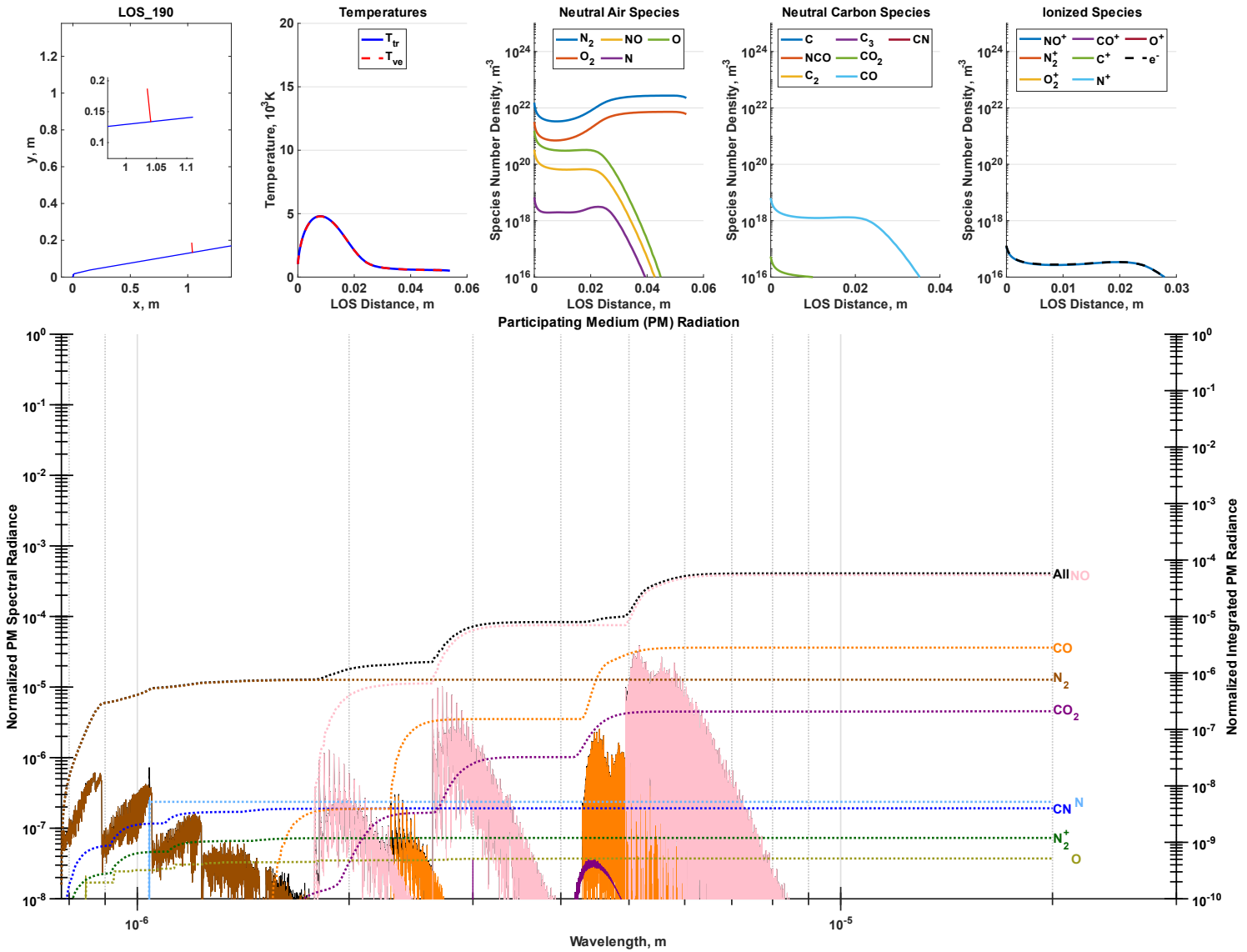

Figure 7.7: TP01 downstream LOS: vehicle (blue) and inset LOS (red) geometries, LOS Ttr and Tve temperatures, LOS species number densities, and PM only spectral and integrated radiances for various species.

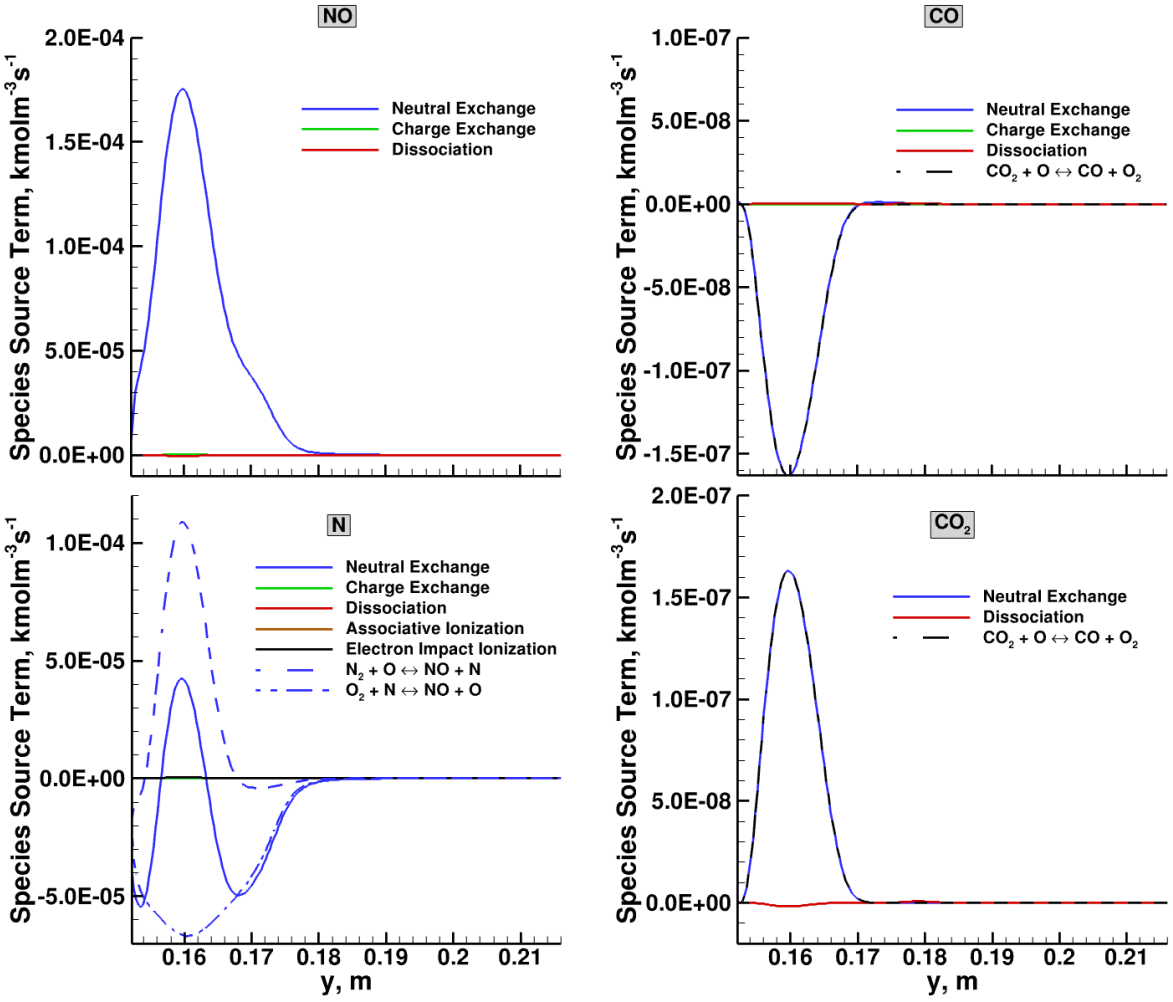

Figure 7.8: Downstream LOS nitric oxide, atomic nitrogen, carbon monoxide, and carbon dioxide source terms.

7.3.4 Trajectory Point 2

Three baseline LOS results are depicted for TP02 at similar locations as TP01 – stagnation, shoulder and downstream regions – in Figure 7.9, Figure 7.10, and Figure 7.11, respectively. For the stagnation region, TP02 temperature peaks are slightly larger with more compressed LOS and thermal nonequilibrium region distances that are $3x10^{-4}$ m and $4x10^{-4}$ m shorter, respectively. These differences are primarily a function of density differences between trajectory points. Neutral air species number densities exhibit similar trends with higher values corresponding to the lower altitude. Significantly higher neutral

carbon number densities, particularly CO, follow the ablation product trends in both Section 6.6 and Figure 7.4. Ionized species number densities increase as well between trajectory points with a slightly faster decrease in N_2^+ and O_2^+ in the post-shock region related to faster charge exchange as well as higher ionized carbon specie number densities related to the increased ablation. Overall integrated radiance increases by 30% and consists of spectral radiance increases primarily from N_2, N, CO, and CO_2.

For the shoulder LOS, temperatures did not change significantly between trajectory points and LOS distance decreases slightly for TP02. Neutral air species NO and O_2 number densities increase near the shock and decrease significantly near the vehicle surface, indicating increased levels of N_2 and O_2 dissociation in the region. Increases in neutral carbon species number densities for CO, C, and CO_2 are present and follow the progression of exchange reactions further downstream from the nose. For ionized species, O^+ and N^+values are relatively higher than TP01, where N^+remains the dominating species near the wall. Radiance for TP02 is 19% higher with major spectral contribution increases from N_2, NO, and CO. These results are consistent with the species neutral air and carbon number density increases at the shock and vehicle surface.

Lastly, the downstream LOS for TP02 exhibits a nearly identical temperature profile as TP01. Higher neutral air species number densities near the surface are present with a decrease in N, O, and NO sooner along the LOS, indicating a narrower bow shock consistent with the lower altitude and similar vehicle velocity. Significantly higher densities of ablative products CO and CO_2 are present near the vehicle surface and follow a similar distribution. Ionized species number densities are nearly indistinguishable between trajectory points.

Ultimately, these baseline flow, material response, and radiation results along three major regions of the vehicle and at different trajectory points provide context for the sensitivity and uncertainty analyses conducted in Section 7.4. Specifically, converged nonequilibrium PM radiation solutions highly depend upon gas composition. In contrast, BB+PM radiation solutions are primarily influenced by surface temperatures. Figure 7.12 depicts trajectory point, black body, and PM aggregate radiance differences along

the vehicle body. Figure 7.12(a/c) and (b/d) depict BB+PM versus PM only radiation, while Figure 7.12(a/b) and (c/d) portray TP01 and TP02, respectively. For both trajectory points, the vast majority (>99%) of the radiation along the vehicle is comprised of BB radiance and that is proportional to the surface temperature T_w^4. Moreover, the BB+PM radiance at the nose is dominated by the IR-B band, with a rapid decline along the vehicle shoulder as seen in the zoomed subplots of Figure 7.12(a/b), where IR-C radiance begins to dominate at $x > 0.014$ m and $x > 0.016$ m, respectively. In contrast, PM only radiance at the nose is mostly comprised of IR-A radiance due to N_2, O, and N transitions as seen previously. The zoomed subplots in Figure 7.12(c/d) show an even distribution of radiances between bands with contributions from multiple species until $x > 0.025$ m and $x > 0.021$ m, respectively. As will be shown in later sections, this region is characterized by high degrees of chemical and radiative nonequilibrium in an expanding flow. In the downstream region ($x > 0.04$ m), IR-C radiance dominates as well due to influences of major rovibrational IR radiators NO, CO, and CO_2. Lastly, peak radiance differences between trajectory points are significant, with TP02 stagnation point radiances greater by a factor of 2.00 and 1.30 for BB+PM and PM only radiance, respectively. These increases primarily stem from post-shock density and gas temperature increases leading to increased collisional excitation and ablation.

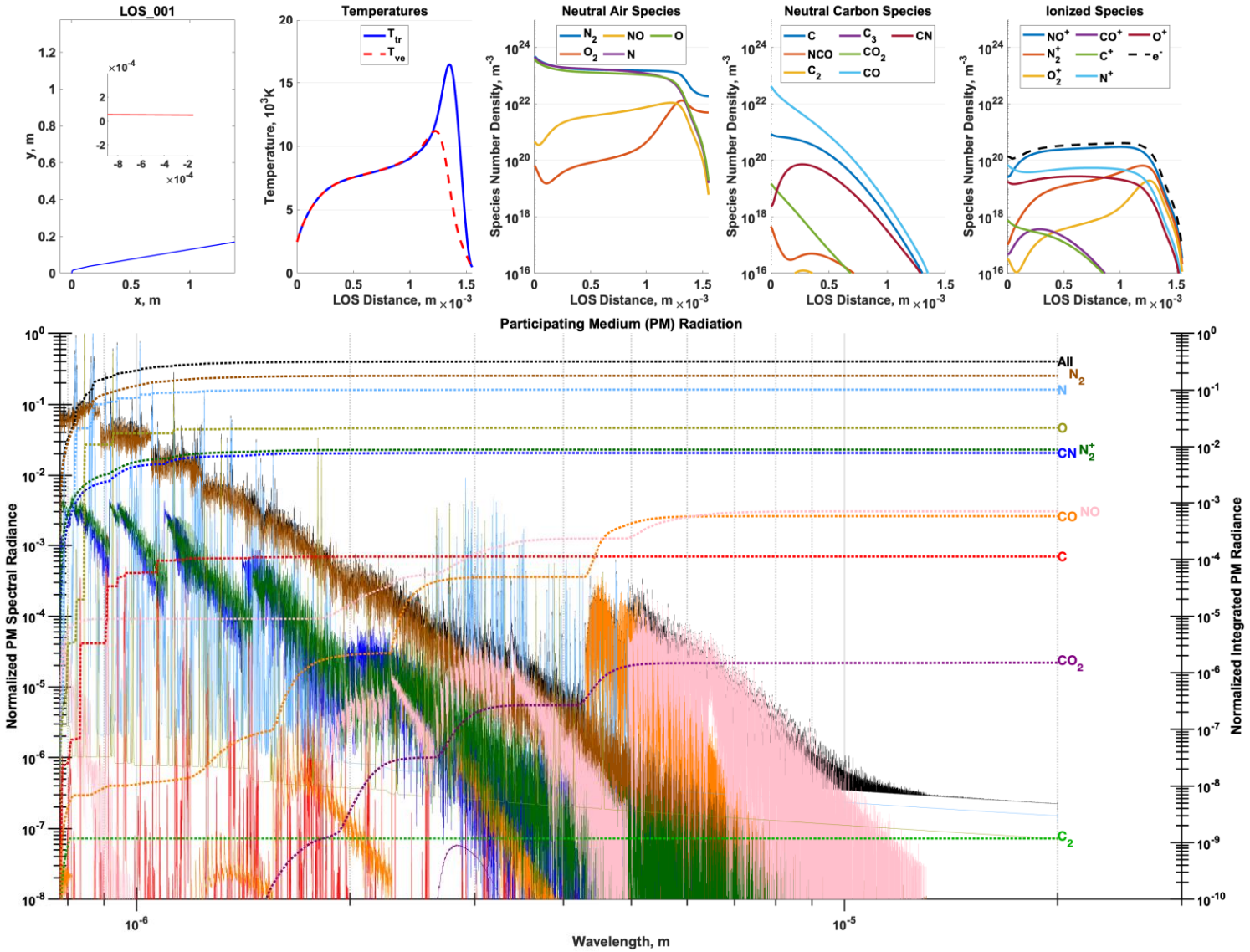

Figure 7.9: TP02 near stagnation LOS: vehicle (blue) and inset LOS (red) geometries, LOS T_{tr} and T_{ve} temperatures, LOS species number densities, and PM only spectral and integrated radiances for various species.

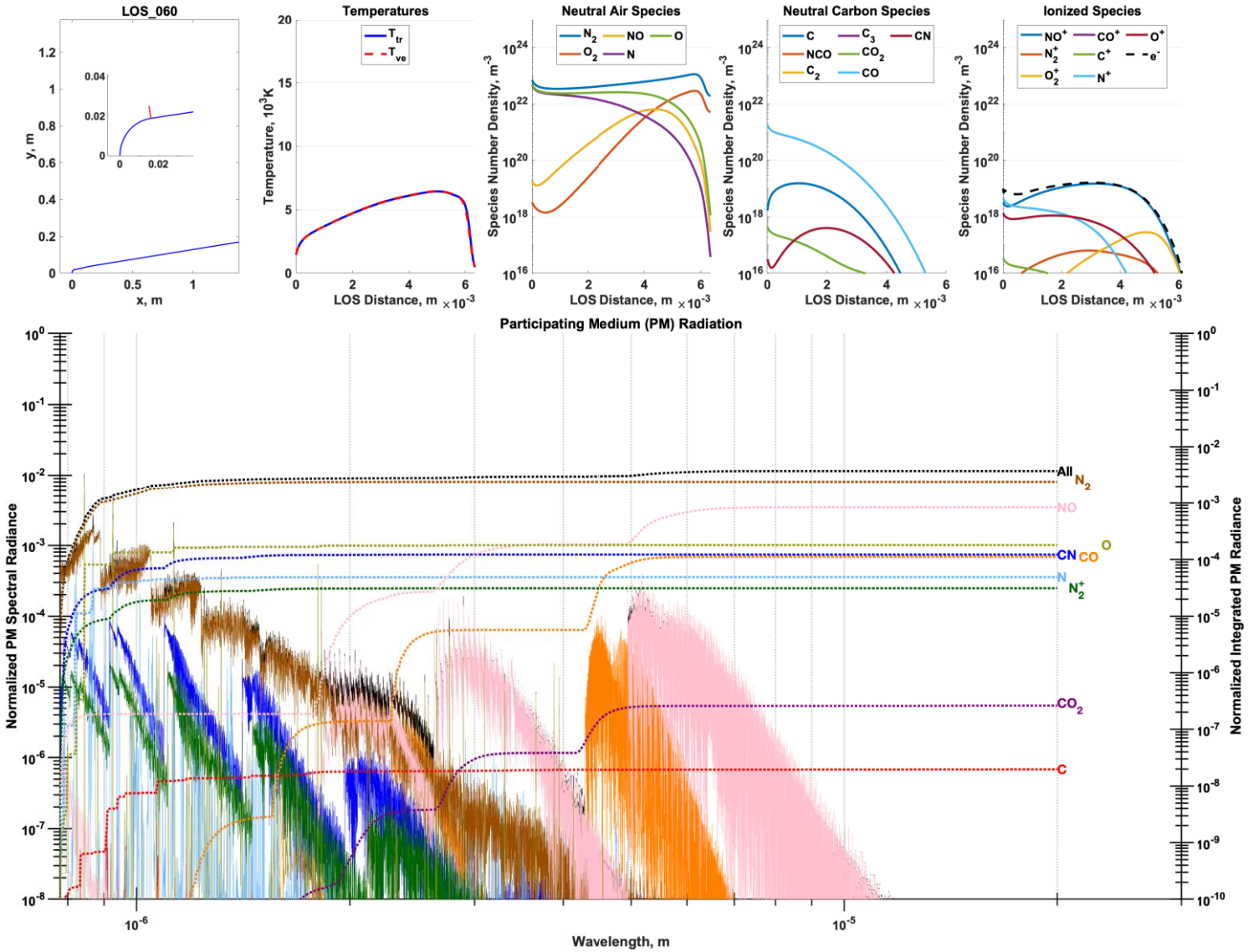

Figure 7.10: TP02 shoulder LOS: vehicle (blue) and inset LOS (red) geometries, LOS T_{tr} and T_{ve} temperatures, LOS species number densities, and PM only spectral and integrated radiances for various species.

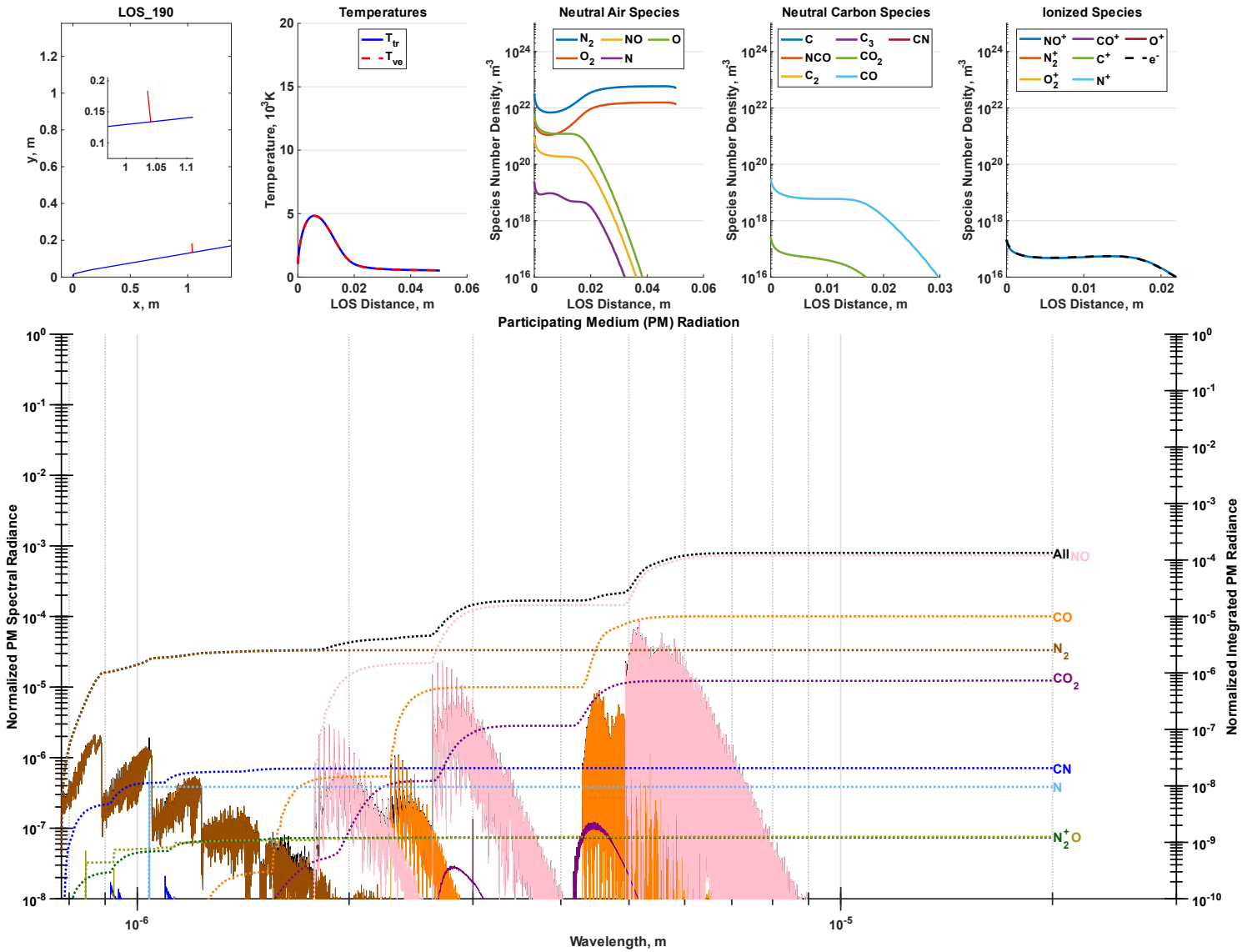

Figure 7.11: TP02 downstream LOS: vehicle (blue) and inset LOS (red) geometries, LOS T_{tr} and T_{ve} temperatures, LOS species number densities, and PM only spectral and integrated radiances for various species.

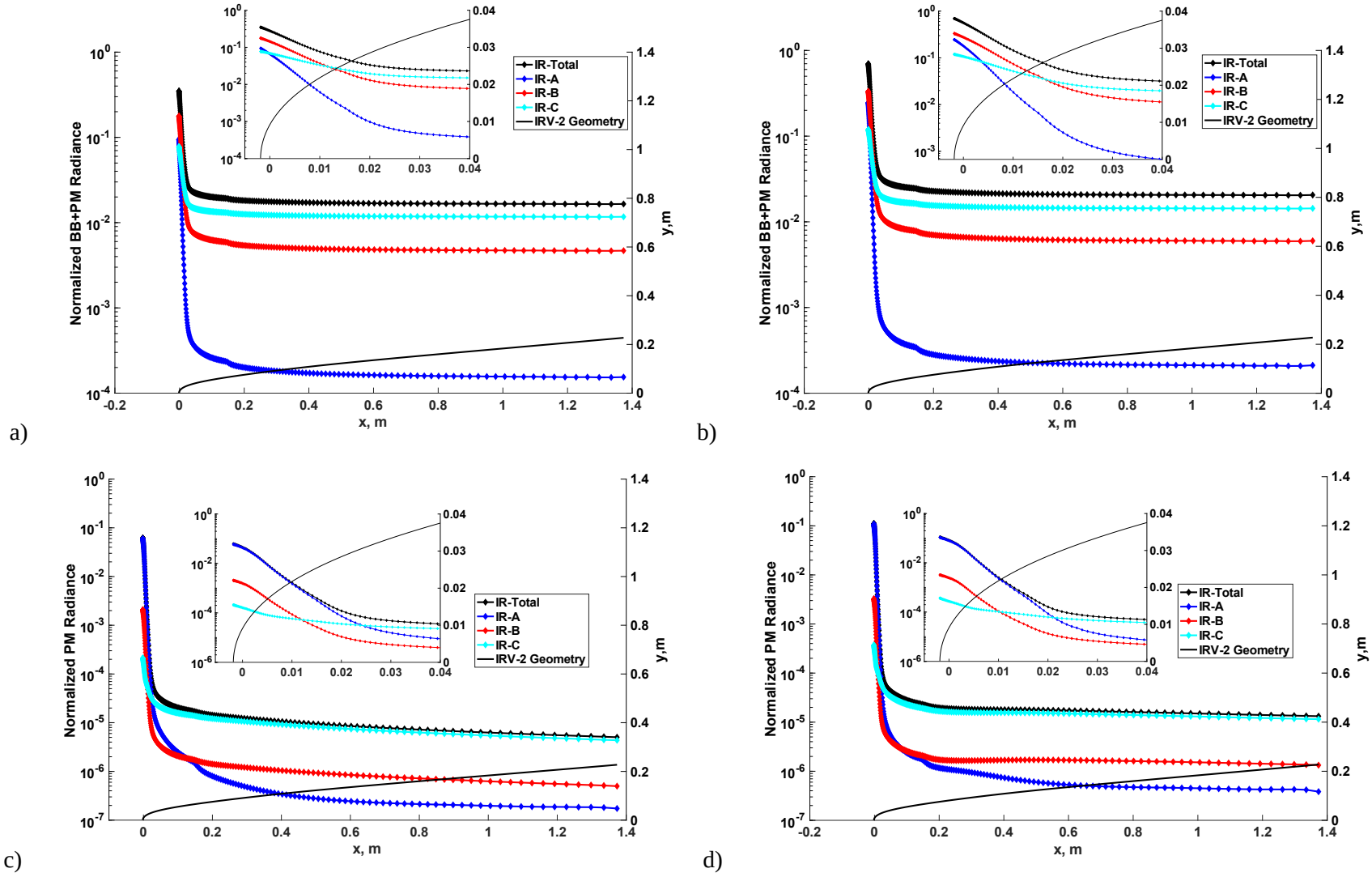

Figure 7.12: Baseline IR radiance (a) TP01 BB + PM, (b) TP02 BB + PM, (c) TP01 PM only, and (d) TP02 PM only.

7.4 Sensitivity Analysis and Uncertainty Quantification Results

The following section provides overall GSA/UQ results for those scenarios depicted in Table 7.2. Uncertain input parameters include 612 baseline values and uncertainty bounds reviewed in Chapter 3 outlined in Appendix A. Steps are taken to ensure sample GSA metric convergence in Section 7.4.1. Sections 7.4.2 and 7.4.3 provide sensitivity and propagated uncertainty results for 200 wall-normal LOSs moving aft along the vehicle for each wavelength band, radiance type, and trajectory combination totaling 3,200 QoIs. For each QoI, 10^6 Monte Carlo samples of each PCE are computed to produce 95% confidence intervals. Parameter total Sobol' indices for each QoI are directly computed from respective PCE coefficients. Sobol' indices that contribute to greater than or equal to 5% of overall variance over a trajectory point, radiance type, and band category (200 QoIs) are plotted. Uncertainty bound scaled Sobol' indices are also provided, where parameters that contribute less than 5% to radiance are aggregated as an 'All Others' variance contribution category. All radiance QoI results are normalized by the baseline stagnation point radiances in Section 7.3 for each respective trajectory point, radiance type, and band category.

Table 7.2: IRV-2 full body case study GSA/UQ parameters, conditions, and QoIs.

Case Study	Uncertain Parameters	Parameter Number	Conditions	Radiance Type	Bands	QoIs (LOSs)
IRV-2 Full Body 20 Species	Gas reaction rate coefficients Relaxation parameters FRSC reaction rate coefficients E-CIE rate coefficients (Atoms) HP-CIE rate coefficients (Molecules) E-CIE cross sections (Molecules)	195 11 3 290 61 52	TP01 56 km, 6.8 km/s 4.25 s	BB + PM	IR-A	200
					IR-B	200
					IR-C	200
					IR-T	200
				PM Only	IR-A	200
					IR-B	200
					IR-C	200
					IR-T	200
			TP02 49 km, 6.8 km/s 6.75 s	BB + PM	IR-A	200
					IR-B	200
					IR-C	200
					IR-T	200
				PM Only	IR-A	200
					IR-B	200
					IR-C	200
					IR-T	200

7.4.1 GSA/UQ Convergence Results

The highly underdetermined point collocation systems within these GSA/UQ analyses require a sufficient number of samples to ensure converged metrics. Dakota evaluation batches are used to with the sparse regression algorithm SPGL1 to approximate the underdetermined system of PCE coefficients using the NIPC approach in Section 2.6.2. A similar approach to Section 5.4.3 is used, where maximum and mean Sobol' index changes for each trajectory point and radiance type QoI. In this case study, the QoI sets defined in Equations 92 and 93 represent four total aggregated combinations of 800 QoIs (200 LOSs × 4 IR bands). These convergence metrics are conservative in that they provide the maximum and mean changes in global sensitivity metrics between samples for all parameters and QoIs in the defined subcategories. Following Equation 79, a complete second order PCE expansion would require 188,191 evaluations with a unity oversampling ratio. 300 Dakota evaluations (an oversampling ratio $r = 1.59x10^{-3}$) are found to reduce maximum Sobol' index batch change $|\Delta S_T|_{max}$ values of 0.0090±0.0071, 0.0111±0.0062, 0.0012±0.0092, and 0.0198±0.0134 over the last 25 sample batches for TP01 BB+PM, TP01 PM only, TP02 BB+PM, and TP02 PM only categories, respectively. These values are consistent with previous aggregate radiance QoI convergence rates and are within tolerances set by hypersonic flow GSA/UQ studies outlined in Section 3.2 [54,99,113,114,116,180].

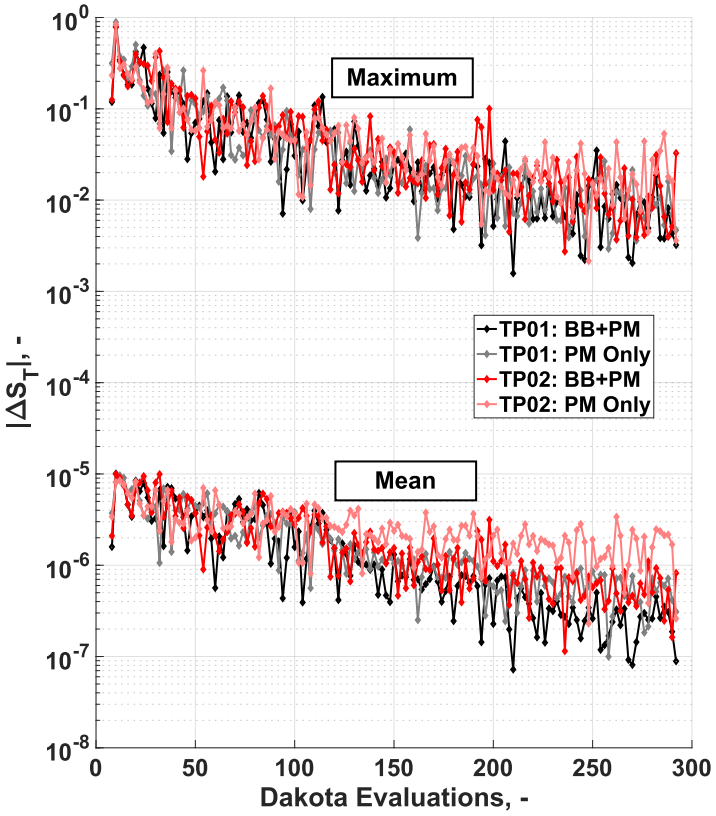

Figure 7.13: Maximum and mean Sobol' index convergence metrics for each 200 LOS x 4 IR Band = 800 QoIs for a given trajectory point and radiance type category.

7.4.2 Trajectory Point 1: Black Body and Participating Medium Radiation GSA/UQ Results

Uncertainty quantification and sensitivity analysis results for TP01 include radiance profiles along the vehicle body normalized by respective stagnation point radiances. Confidence intervals are included from 10^6 Monte Carlo evaluations for each of the 200 PCE surrogate models. Relative bound uncertainties are also depicted and defined as the absolute difference in confidence interval bounds normalized by the mean radiance for each LOS location. Total Sobol' indices are also calculated directly from PCE coefficients and include those parameters that contribute to at least five percent of overall variance for the 200 LOSs. Normalized confidence interval bounds are also used to scale the Sobol' indices to the uncertainty in the QoIs along the IRV-2. Figure 7.14 depicts the TP01 GSA/UQ results for BB+PM radiance broken down by IR bands defined in Table 5.3. For all IR bands, BB+PM radiance from the 612 parameter

variances account for a maximum of 7.4% relative uncertainty localized primarily within the IR-B bands at the vehicle shoulder. These spectral and spatial locations for maximum uncertainty make sense because black body radiation peaks within the IR-B bands for the wall temperatures near the nose and shoulder of the vehicle (see Figure 6.7 and Figure 7.12(b)). Wien's displacement law shown in Equation 102 predicts the peak black body spectral radiance wavelength at approximately 1.5 μm for a 2,000 K surface temperature which resides within the IR-B band. Other general trends include major variance contributions from gas rate constants involving N_2 dissociation via Zel'dovich exchange mechanisms as well as direct NO dissociation at the vehicle nose. These sensitivities follow reactions whose variance most influence surface temperature QoIs as seen in Figure 7.15. This connection makes sense near the vehicle nose and shoulder where wall temperatures are most elevated. Moreover, Planck's Law for grey and black bodies and the integrated radiance form in Equations 103 and 104 show the previously mentioned T_w^4 dependence. For the purposes of this case study, emissivity ϵ of ATJ carbon was treated as a constant grey body efficiency of 85%. With over 99% black body radiance in these locations, those parameters whose variance most influence wall temperature uncertainty also therefore most influence BB+PM radiance. These surface temperature dependencies also explain the little variation in parameter variance contributions between IR bands. Additionally, relative radiance uncertainty as both surface and gas temperatures cool downstream decreases to near zero. In this region, a lack of sparsity in the variance contributions becomes apparent as the "All Others" category dominates contributions to the remaining QoI uncertainties. Nitrogen dissociation via Zel'dovich exchange draws energy from the flow in the form of endothermic reactions at the nose region. Similarly, NO dissociation further provides additional energy decreases. Figure 7.16 depicts species mole fractions, temperatures, and the net reaction rates for those reactions most sensitive to wall temperature at the stagnation line. As expected, shortly after the temperature rise crossing the shock, nitrogen dissociation is driven primarily by the Zel'dovich mechanism reactions shortly after an increase in O formation, drawing energy from the flow. A similar, less reactive process occurs with the direct dissociation of NO with partner N. Moreover, the reverse process of $N_2 + O \rightleftharpoons NO + N$ near the wall

increases energy into the flow and thus, increases the local temperature near the surface. This nitrogen recombination and subsequent energy release is the primary driver for variance in wall temperature and by extension, the BB+PM radiance over all IR bands at TP01.

$$\lambda_{peak} = \frac{2989 \mu m K}{T_w} \tag{102}$$

$$B_\lambda(\epsilon, \lambda, T_w) = \epsilon \frac{2hc^2}{\lambda^5} \frac{1}{e^{\frac{hc}{\lambda k_B T_w}} - 1} \ \ Wm^{-3}sr^{-1} \tag{103}$$

$$L(T_w) = \int_0^\infty B_\lambda(\epsilon, \lambda, T_w) d\lambda = \frac{2\epsilon\pi^4 k_B^4}{15h^3c^2} T_w^4 \ \ Wm^{-2}sr^{-1} \tag{104}$$

As temperatures cool around the vehicle surface at the shoulder, NO and O_2 dissociation with partner O show increased variance contributions for both surface temperature and BB+PM radiance at all IR bands. This follows similar wall temperature dependencies found in other sensitivity analyses at slower velocity flow, where the primary energy changes in the flow propagating to the surface are due to oxygen dissociation and recombination near the shock and boundary layer, respectively [97,111]. Lastly, sensitivities for all IR bands become less sparse as wall temperature influences from the flow decrease further downstream. Therefore, a larger number of small variance contributors (the "All Others" category) dominate this region as relative wall temperature and uncertainty drops below 1%. Looking at the downstream LOS in Figure 7.7, this makes sense as the equilibrium temperature does not increase above 5,000 K and net recombination of O_2 decreases significantly.

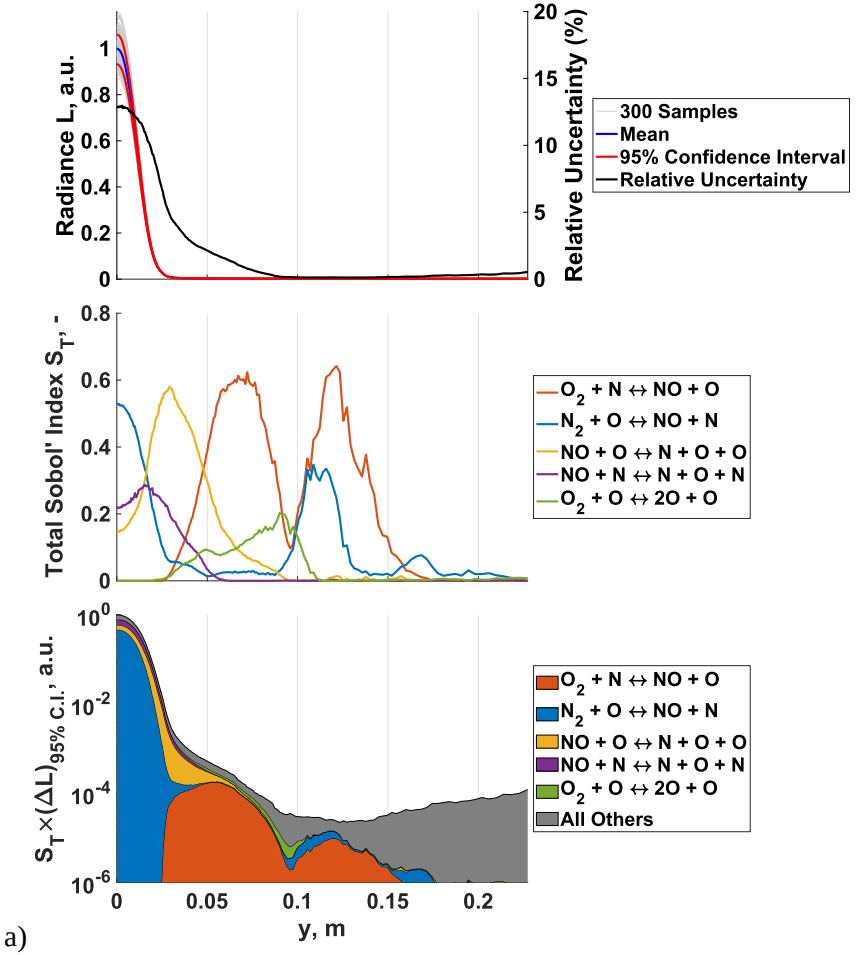
Radiance L, a.u.
Relative Uncertainty (%)
300 Samples
Mean
95% Confidence Interval
Relative Uncertainty
Total Sobol' Index S_T, -
$O_2 + N \leftrightarrow NO + O$
$N_2 + O \leftrightarrow NO + N$
$NO + O \leftrightarrow N + O + O$
$NO + N \leftrightarrow N + O + N$
$O_2 + O \leftrightarrow 2O + O$
$S_T \times (\Delta L)_{95\%\ c.l.}$, a.u.
All Others
y, m

a)

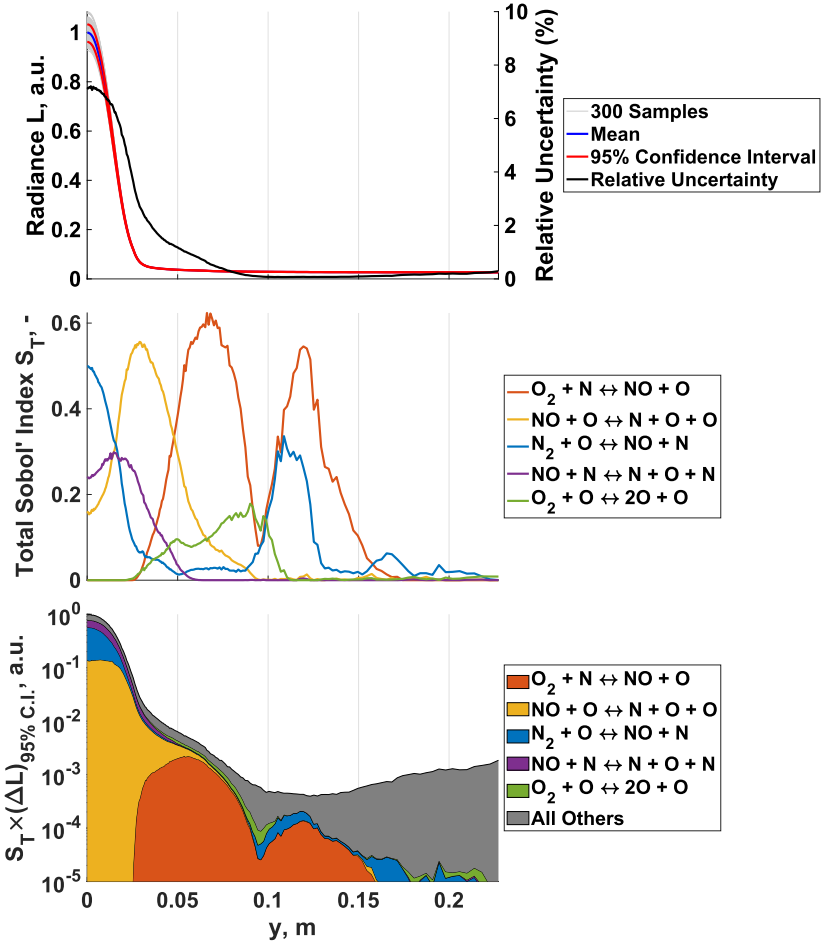
Radiance L, a.u.
Relative Uncertainty (%)
300 Samples
Mean
95% Confidence Interval
Relative Uncertainty
Total Sobol' Index S_T, -
$O_2 + N \leftrightarrow NO + O$
$NO + O \leftrightarrow N + O + O$
$N_2 + O \leftrightarrow NO + N$
$NO + N \leftrightarrow N + O + N$
$O_2 + O \leftrightarrow 2O + O$
$S_T \times (\Delta L)_{95\%\ c.l.}$, a.u.
All Others
y, m

b)

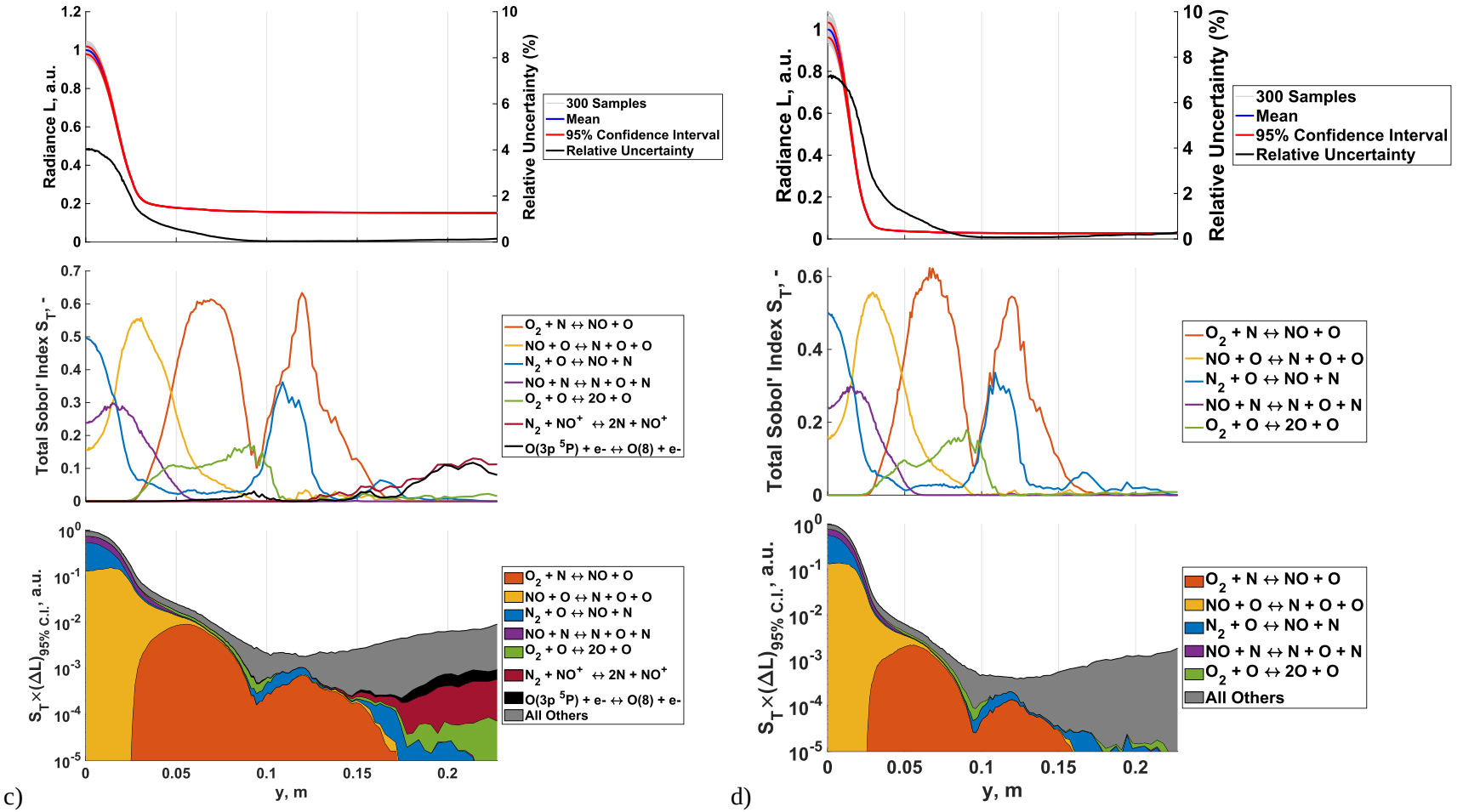

Figure 7.14: TP01 normalized uncertainty bounds, Sobol' indices, and scaled Sobol' indices for BB and PM (a) IR-A (0.78-1.4 μm), (b) IR-B (1.4-3.0 μm), (c) IR-C (3.0-20.0 μm) and (d) IR-T (0.78-20.0 μm) bands. 'All others' category defined as less than 5% variance or scaled variance contribution integrated over the QoI range.

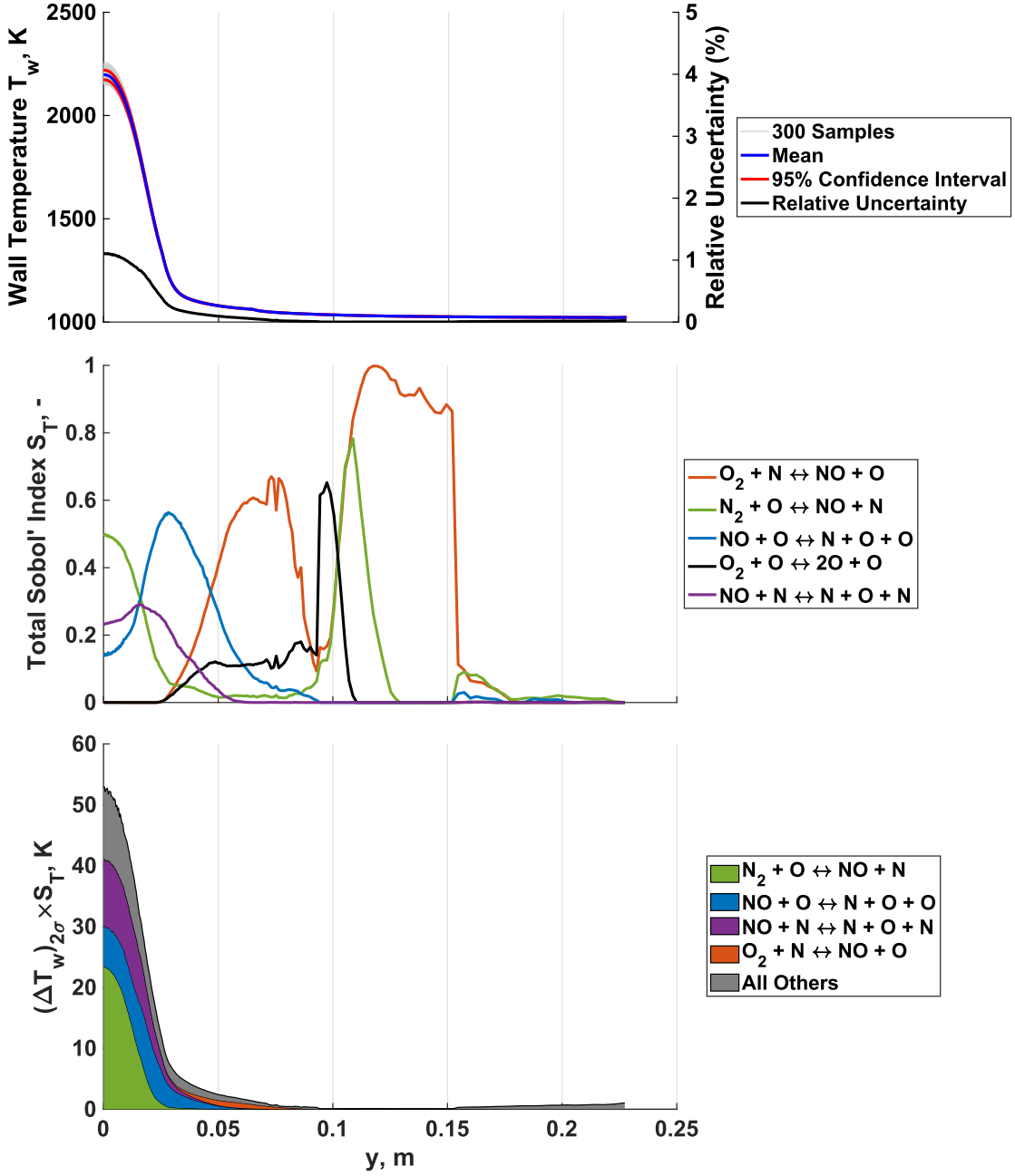

Figure 7.15: TP01 wall temperature uncertainty and global sensitivity results.

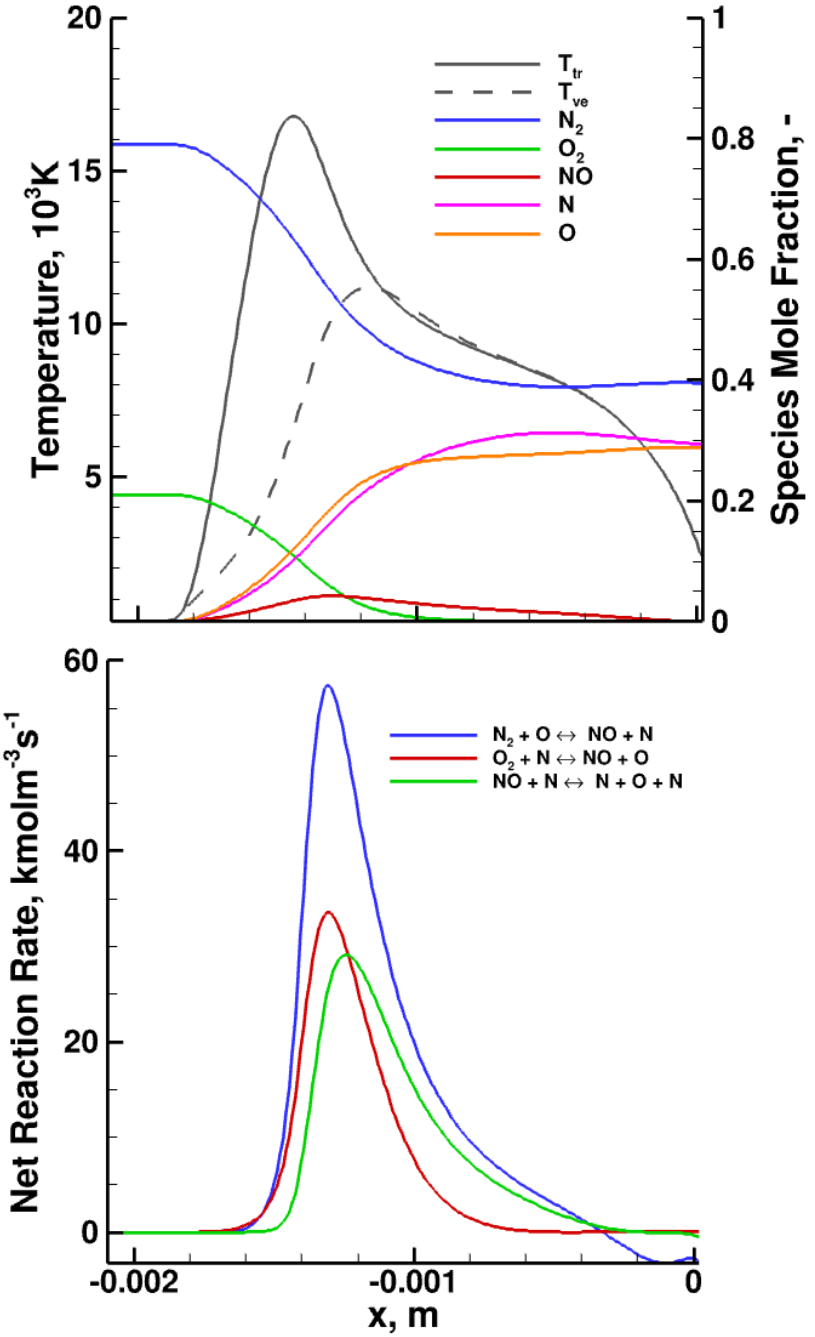

Figure 7.16: TP01 stagnation line temperatures, species mole fractions, and major wall temperature variance contributing reaction rates.

PM radiance GSA/UQ results for each TP01 IR band are depicted in Figure 7.17. For all IR bands, relative PM radiance uncertainties increase to over 110% at the shoulder region. This makes sense as many of the parameters have greater influences on integrated PM radiance. Additionally, all PM IR band

sensitivities for TP01 at the vehicle nose include the Zel'dovich mechanism reactions. This is explained by the dominance of spectral and integrated PM radiance for N_2, O, N shown in Figure 7.5 over the majority of wavelengths. The reactions that most influences the number densities of these species as well as the temperatures at the nose are $N_2 + O \rightleftharpoons NO + N$ and $O_2 + N \rightleftharpoons NO + O$ in this region.

For IR-A, relative PM radiance uncertainty begins to increase rapidly around the vehicle shoulder. Variance contributions involving oxygen dissociation and nitrogen quenching through heavy particle collisions increase as the number of nonzero variance contributors increases. This increased variance complexity trend is found for all PM radiance in this region, where the flow is characterized by expanding, cooling, and chemical nonequilibrium. Slightly further downstream, variance contributions from parameters involving ablative species including finite rate sublimation and exchange reaction with CN and CO dominate. Referencing Figure 7.6, the proportion of CN and CO PM IR-A radiance increases in this region. The direct sublimation of carbon into the flow leads to increases in CO and subsequent exchange reactions determine CN concentrations. Variations in these carbon pathways directly influence the amounts of CO and CN and therefore influence PM IR-A radiance. As temperatures cool further, reactions involving the recombination of nitrogen exchange and subsequent collisional quenching increase in sensitivity.

HP-CIE and quenching rate sensitivities in the downstream region are explained in Figure 7.18. LOS 190 is first shown in the top subplot in the downstream region. Temperatures and total PM radiance profiles are depicted in the next subplot. A particular LOS point is chosen where the maximum radiance change occurs (point 108 in this case) that also coincides with the maximum temperatures along the LOS. Degeneracy normalized state populations and rates of change of state populations at this LOS point are depicted in the bottom two subplots. Major collisional and radiative processes for the electronic state QSS balance in Equation 68 are categorized by E-CIE and HP-CIE as well as radiative (Rad.) categories. The radiative rates include the net of both stimulated and spontaneous emission and absorption rates. Other rate categories including external reaction excitation included in the QSS balance are not shown for clarity. At this LOS point, QSS populations are larger than a Boltzmann distribution, indicating radiative

nonequilibrium due to collisional and radiative rate processes. Particularly, higher energy populations are excited primarily by HP-CIE (yellow triangles), while subsequent emission transfers out of state populations. The yellow triangle in the bottom subplot at an energy level near $6.0\ \mathrm{m}^{-1}$ represents the $N_2(B)$ state while the ground state $N_2(X)$ is at $0.0\ \mathrm{m}^{-1}$. At this LOS point representing maximum PM radiance change, the population rate decrease in $N_2(X)$ due to HP-CIE and corresponding rate increase in $N_2(B)$ lead to a corresponding decrease in the $N_2(B)$ population due to radiative emission. Of all the higher energy state population rate transfers from HP-CIE to radiation, $N_2(B)$ has the largest gap in population rates. Therefore, changes in the HP-CIE rates from $N_2\ (X)$ to $N_2(B)$ with various collisional partners have the greatest influence on PM radiance in the IR-A band along LOSs further downstream.

IR-B PM radiance uncertainty bounds and global sensitivities in Figure 7.17(b) follow similar trends along the vehicle, with Zel'dovich reactions dominating at the nose and downstream regions. O_2 and NO dissociation, carbon sublimation, CO/CN exchange, and N_2 HP-CIE parameters depict a lower degree of increased variance contributions at the shoulder when compared to IR-A PM radiance. IR-C PM radiance GSA/UQ results in Figure 7.17(c) show less major variance contributors primarily involving N_2 and NO dissociation/recombination as well as carbon sublimation rates at the shoulder affecting CO and CO_2 number densities. Figure 7.7 shows the larger contributions of these species to radiance in the IR-C band, with N_2 dissociation via Zel'dovich reactions indirectly affecting NO formation.

Overall TP01 IR PM radiance GSA/UQ results in Figure 7.17(d) follow the combined effects of all band uncertainties and sensitivities. A peak relative uncertainty of 105% occurs immediately following the shoulder region and is comprised primarily of variance contributions from nitrogen recombination rate coefficients. The range of parameters involved with PM only radiance for TP01 along the IRV-2 indicate sensitivities that range from gas phase dissociation and exchange rate coefficients of neutral air and carbon species to FRSC and internal electronic state rate parameters. These PM only radiance GSA/UQ results highlight the importance of both spatial and spectral location on uncertainty and subsequent parameter contributions to that uncertainty.

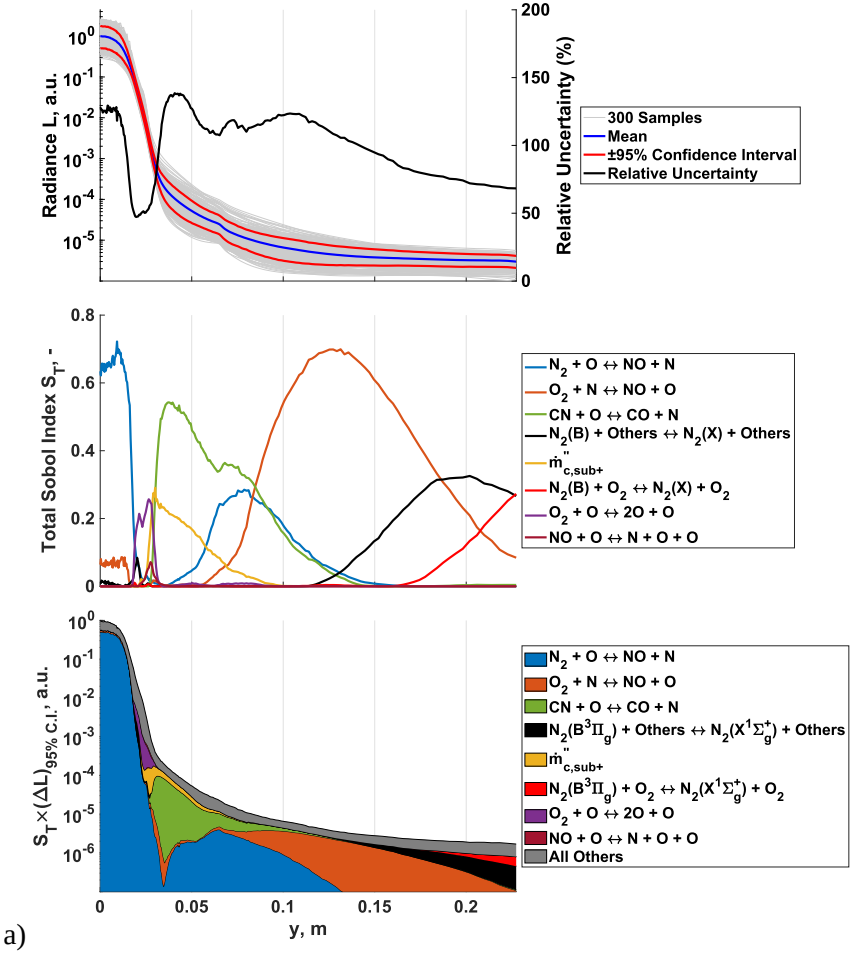
Radiance L, a.u.
Relative Uncertainty (%)
300 Samples
Mean
±95% Confidence Interval
Relative Uncertainty
Total Sobol Index S_T, -
$N_2 + O \leftrightarrow NO + N$
$O_2 + N \leftrightarrow NO + O$
$CN + O \leftrightarrow CO + N$
$N_2(B) + Others \leftrightarrow N_2(X) + Others$
$\dot{m}''_{c,sub+}$
$N_2(B) + O_2 \leftrightarrow N_2(X) + O_2$
$O_2 + O \leftrightarrow 2O + O$
$NO + O \leftrightarrow N + O + O$
$S_T \times (\Delta L)_{95\%\ c.l.}$, a.u.
$N_2(B^3\Pi_g) + Others \leftrightarrow N_2(X^1\Sigma_g^+) + Others$
$N_2(B^3\Pi_g) + O_2 \leftrightarrow N_2(X^1\Sigma_g^+) + O_2$
All Others
y, m

a)

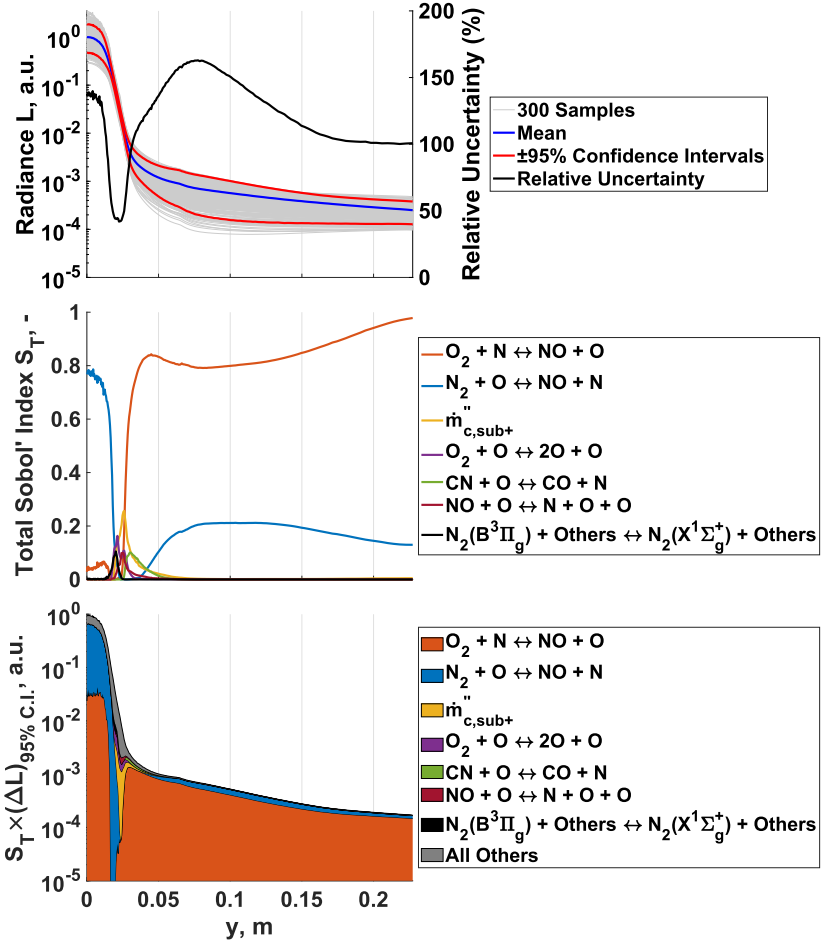
Radiance L, a.u.
Relative Uncertainty (%)
300 Samples
Mean
±95% Confidence Intervals
Relative Uncertainty
Total Sobol' Index S_T, -
$O_2 + N \leftrightarrow NO + O$
$N_2 + O \leftrightarrow NO + N$
$\dot{m}''_{c,sub+}$
$O_2 + O \leftrightarrow 2O + O$
$CN + O \leftrightarrow CO + N$
$NO + O \leftrightarrow N + O + O$
$N_2(B^3\Pi_g) + Others \leftrightarrow N_2(X^1\Sigma_g^+) + Others$
$S_T \times (\Delta L)_{95\%\ c.l.}$, a.u.
All Others
y, m

b)

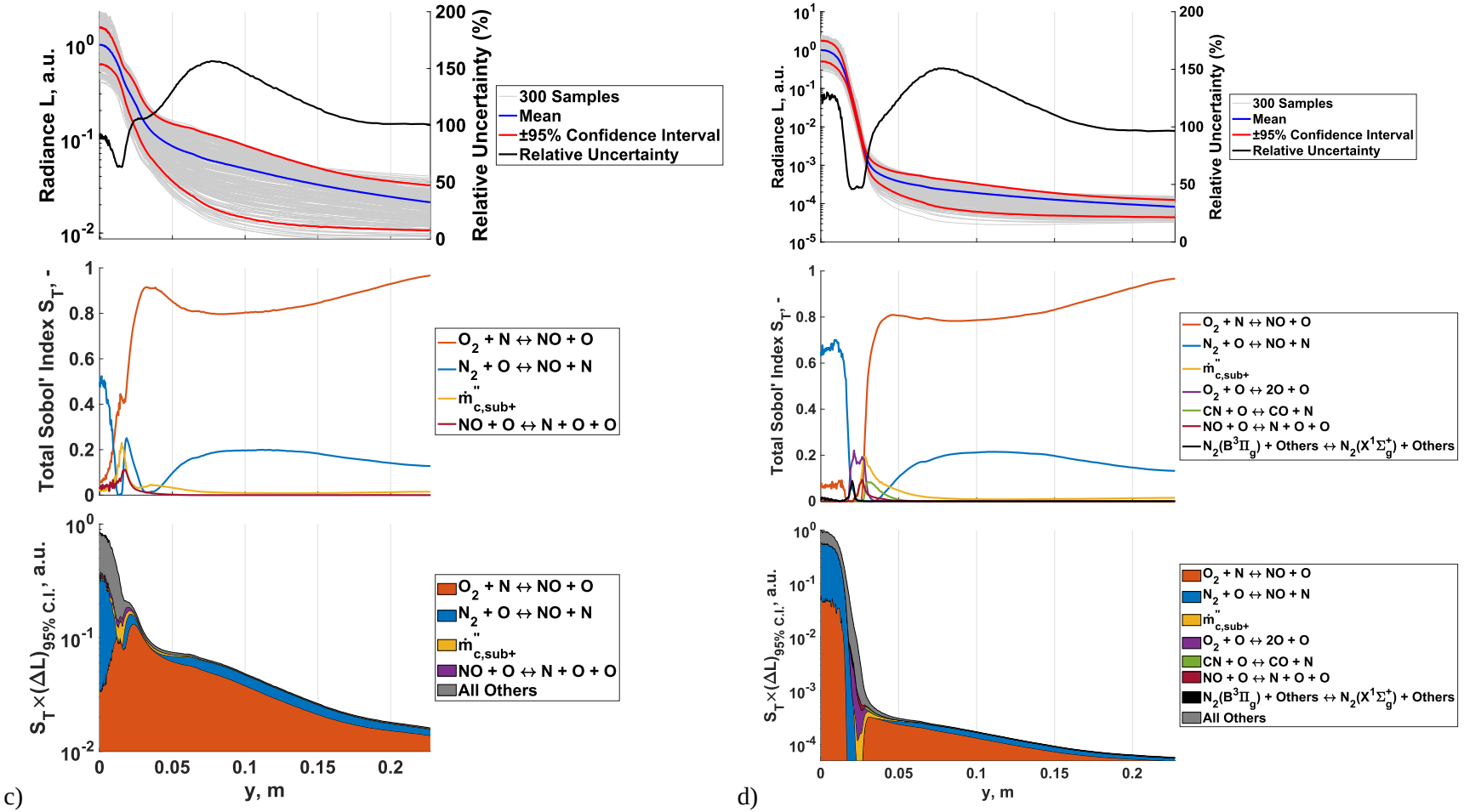

Figure 7.17: TP01 Normalized uncertainty bounds, Sobol' indices, and scaled Sobol' indices for PM only (a) IR-A (0.78-1.4 μm), (b) IR-B (1.4-3.0 μm), (c) IR-C (3.0-20.0 μm) and (d) IR-T (0.78-20.0 μm) bands. 'All others' category defined as less than 5% variance or scaled variance contribution integrated over the QoI range.

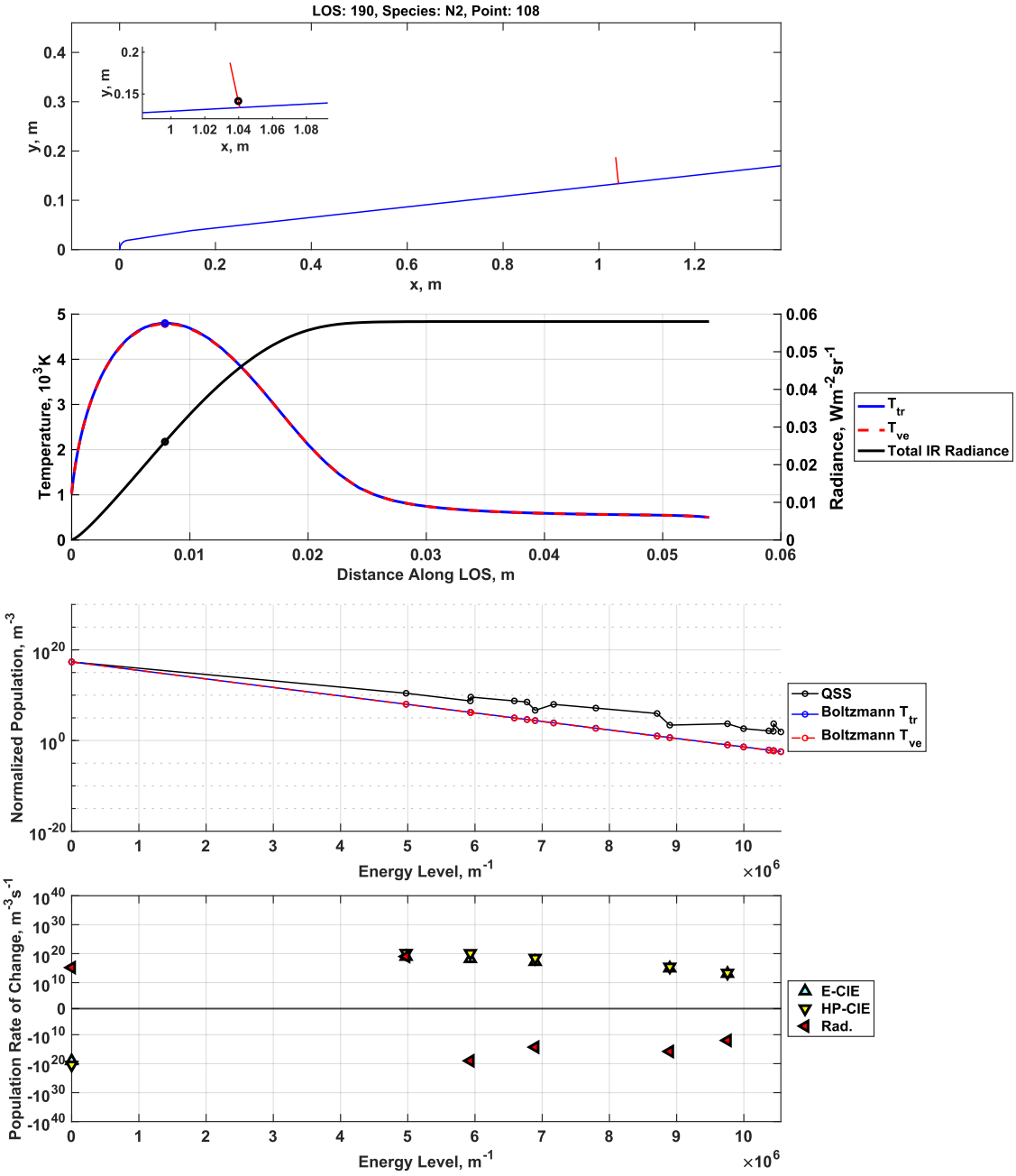

Figure 7.18: Downstream LOS geometry, temperatures, PM radiance, nitrogen QSS and Boltzmann electronic state populations, and electronic state population rates of change at LOS point 108.

7.4.3 Trajectory Point 2: Black Body and Participating Medium Radiation GSA/UQ Results

Uncertainty quantification and sensitivity analysis results for TP02 follow a similar procedure shown in Figure 7.1, where template directories shown in the upper left of the figure incorporate baseline

LeMANS-MOPAR-MD converged solution flow and material restart files from TP01. The same sampled FRSC, LeMANS-MOPAR-MD, and NEQAIR parameter sets are utilized for the 300 evaluations to ensure uncertainty propagation from the start of the IRV-2 trajectory. Both BB+PM and PM only IR radiance GSA/UQ results are depicted for comparison at a lower altitude in the IRV-2 ballistic trajectory.

Figure 7.19 depicts BB+PM IR radiance GSA/UQ results for the various IR bands. Maximum relative uncertainty values of 8.7% occur at a similar location to TP01 along the vehicle shoulder. However, this maximum uncertainty occurs in the IR-A band as surface temperatures have increased to over 2,300 K (see solid blue FRSC baselines temperature values in Figure 6.7). Using Equation 102, this equates to peak grey body spectral radiance at approximately 1.3 μm; well within the IR-A band. Additionally, sublimation rate sensitivities are now present near the nose for all bands. This is explained by more than double the ablation mass flux in the stagnation region as seen in Figure 6.7. A similar lack of change in sensitivities between IR bands and near zero uncertainty further downstream along the vehicle are present in the TP02 BB+PM radiance GSA/UQ results. Nitrogen dissociation via Zel'dovich exchange variance contributions still dominate in the nose region, while NO and O_2 dissociation rate influences have moved further downstream to the shoulder and beyond. E-CIE rate parameters for N and N_2 transitions contribute to greater than 5% of overall variance in the downstream region but are considered inconsequential as the relative uncertainty in this region is less than 0.05%.

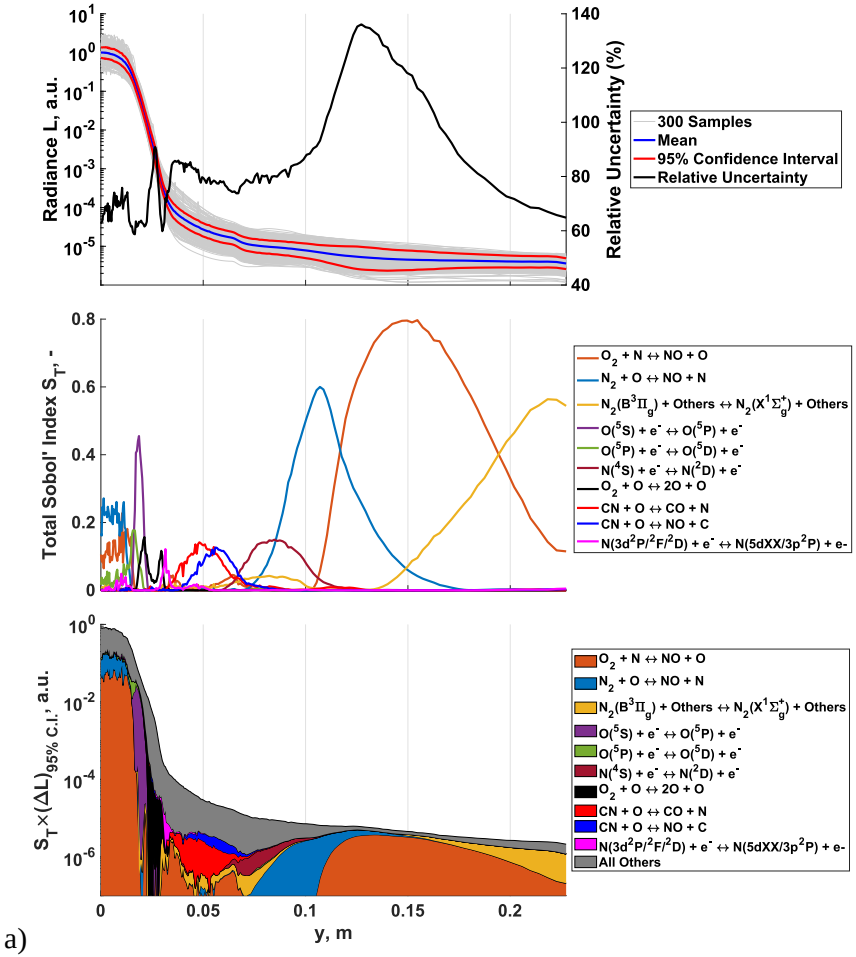
Radiance L, a.u.
Relative Uncertainty (%)
300 Samples
Mean
95% Confidence Interval
Relative Uncertainty
Total Sobol' Index S_T, -
$O_2 + N \leftrightarrow NO + O$
$N_2 + O \leftrightarrow NO + N$
$N_2(B^3\Pi_g) + Others \leftrightarrow N_2(X^1\Sigma_g^+) + Others$
$O(^5S) + e^- \leftrightarrow O(^5P) + e^-$
$O(^5P) + e^- \leftrightarrow O(^5D) + e^-$
$N(^4S) + e^- \leftrightarrow N(^2D) + e^-$
$O_2 + O \leftrightarrow 2O + O$
$CN + O \leftrightarrow CO + N$
$CN + O \leftrightarrow NO + C$
$N(3d^2P/^2F/^2D) + e^- \leftrightarrow N(5dXX/3p^2P) + e-$
$S_T \times (\Delta L)_{95\%\ c.i.}$, a.u.
All Others
y, m

a)

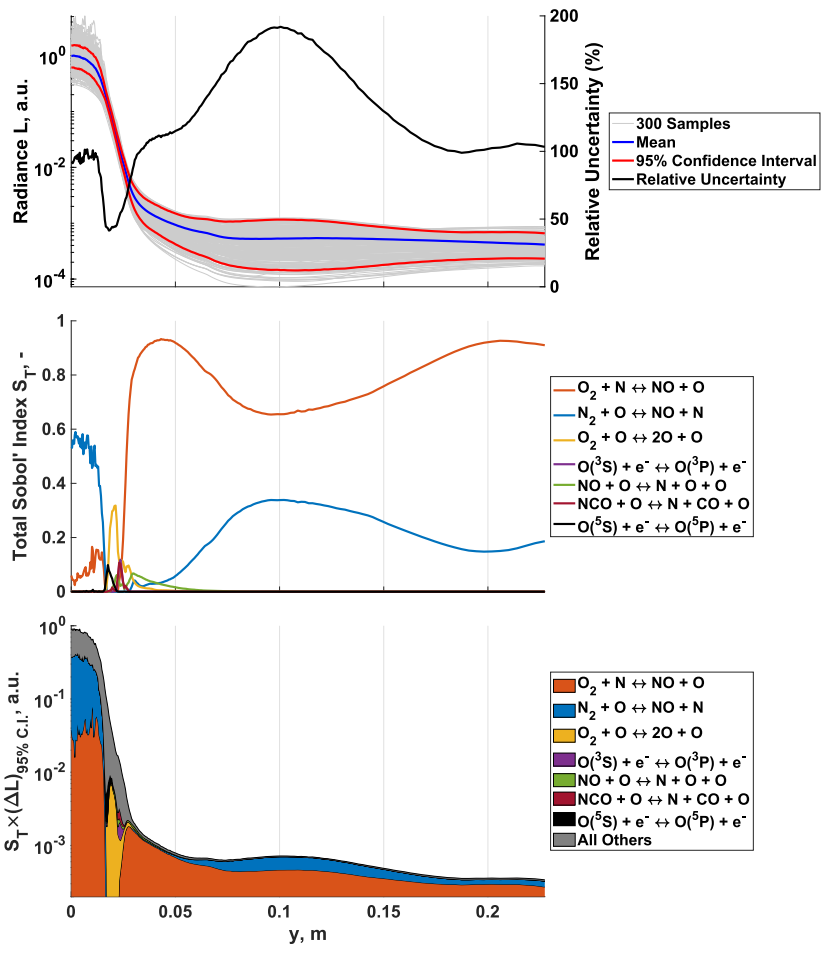
Radiance L, a.u.
Relative Uncertainty (%)
300 Samples
Mean
95% Confidence Interval
Relative Uncertainty
Total Sobol' Index S_T, -
$O_2 + N \leftrightarrow NO + O$
$N_2 + O \leftrightarrow NO + N$
$O_2 + O \leftrightarrow 2O + O$
$O(^3S) + e^- \leftrightarrow O(^3P) + e^-$
$NO + O \leftrightarrow N + O + O$
$NCO + O \leftrightarrow N + CO + O$
$O(^5S) + e^- \leftrightarrow O(^5P) + e^-$
$S_T \times (\Delta L)_{95\%\ c.i.}$, a.u.
All Others
y, m

b)

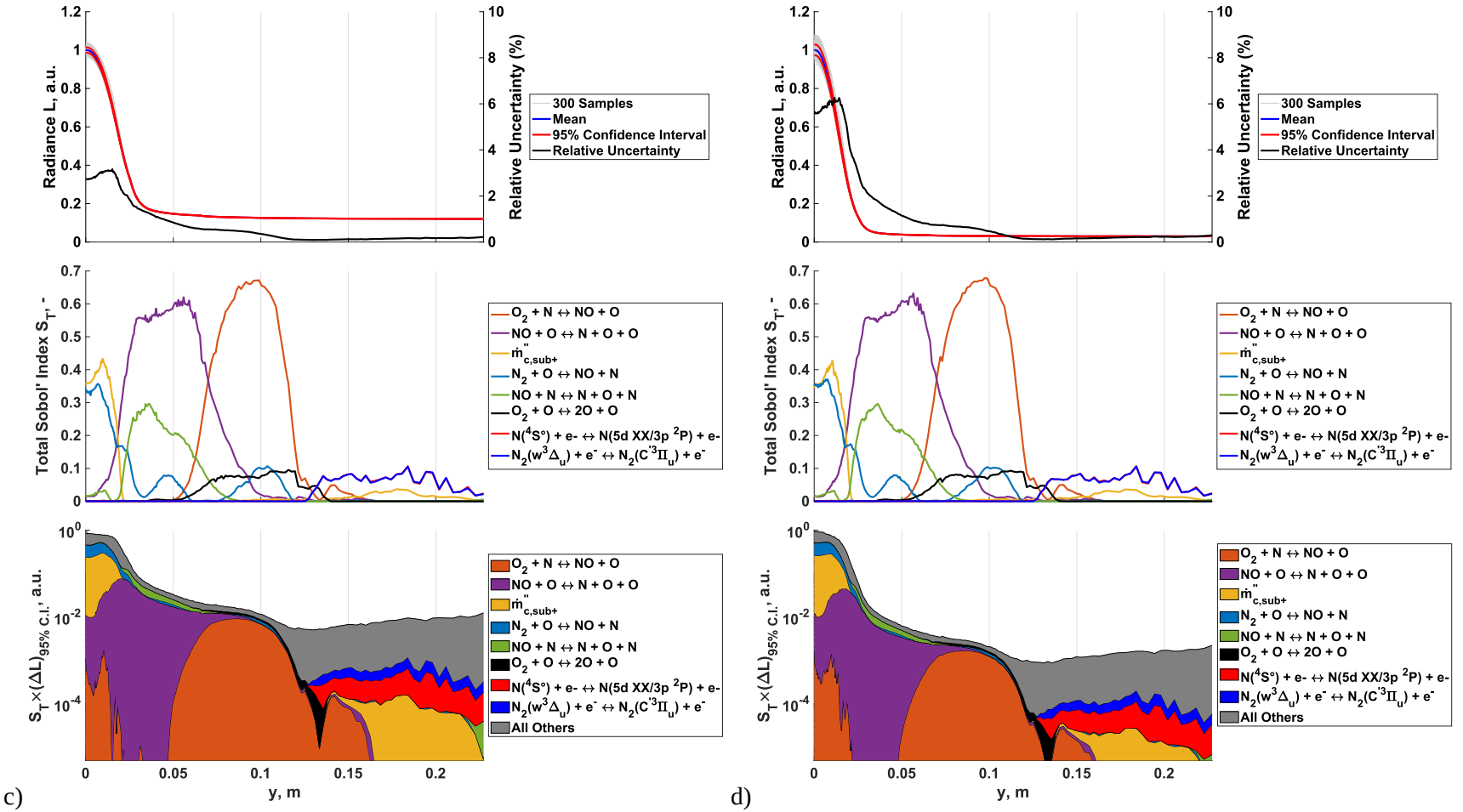

Figure 7.19: TP02 Normalized uncertainty bounds, Sobol' indices, and scaled Sobol' indices for black body and PM (a) IR-A (0.78-1.4 μm), (b) IR-B (1.4-3.0 μm), (c) IR-C (3.0-20.0 μm) and (d) IR-T (0.78-20.0 μm) bands. 'All others' category defined as less than 5% variance or scaled variance contribution integrated over the QoI range.

TP02 PM only radiance results are depicted in Figure 7.21. Relative uncertainty values follow similar trends over the IRV-2 body with a maximum of 145% at the vehicle shoulder in the IR-A band. Significantly less parameter sparsity is present across all bands near the nose, indicating smaller variance contributions from a larger number of parameters when compared to TP01. Figure 7.21(a) depicts results for IR-A, where Zel'dovich mechanism reaction variance contributes most to PM only radiance in the nose region, but E-CIE O and N rate influences are also present at the nose and shoulder. The increases in O, N and e^- species number densities along the stagnation LOS and subsequent increases in PM radiance contributions in the IR-A bands are shown in Figure 7.9. These increased densities at TP02 lead to increased atomic E-CIE. Some E-CIE influences are direct via radiative depopulation of the specific states after collisional excitation. Other E-CIE transitions influence IR radiance indirectly via changing the coupled state population rate system such that increased IR radiance occurs via different state transitions. Figure 7.20 illustrates the impacts of E-CIE for N and O excited state population changes at the stagnation LOS and at a maximum T_{ve} LOS point location. The collisional excitation reaction rate $O(^5P) + e^- \rightleftharpoons O(^5D) + e^-$ represents the transition from 6th to 9th aggregate electronic states at $8.66x10^6 m^{-1}$ and $9.74x10^6 m^{-1}$, respectively. The net population rates of change at this LOS point location indicate large E-CIE populating and subsequently high net radiative depopulating for $O(^5D)$. Similar collisional to radiative exchange of electronic state populations occurs for E-CIE from the 10th to 16th aggregate electronic states of N at $1.05x10^7 m^{-1}$ and $1.12x10^7 m^{-1}$, respectively. An interesting observation is that although the majority of the sensitive atomic oxygen and nitrogen E-CIE transitions emit directly within the IR-A band, a few of the atomic transitions with higher variance contributions have lines outside of the IR band. Specifically, the $N(^4S) + e^- \rightleftharpoons N(^2D) + e^-$ has a very low probability of emitting at a 520.1 nm visible line, but instead indirectly affects multiple state populations whose transition energy differences lead to longer wavelength emissions within the IR-A band. The coupled nature of every state population rate of change for given categories make pinpointing specific pathways where variance of a particular collisional excitation might affect aggregate IR radiance quantities extremely difficult for large numbers of population states. However,

the general trends of the increased variance contributions from E-CIE of oxygen and nitrogen for IR-A at TP02 are consistent with the higher ionization present around the IRV-2 nose and shoulder.

Moving to LOSs further aft along the vehicle, IR-A PM sensitivities shift to oxygen recombination and $CN - CO$ and $CN - NO$ exchange reactions with atomic oxygen. Interestingly, direct sublimation variance is not a primary driver of IR-A PM radiation uncertainty just past the shoulder region like in TP01. This is most likely due to the increased sublimation rates at TP02 no longer being a limiting factor for IR-A PM radiation while rates that produce major radiative species like CN in this band (see Figure 7.10) are limiting. Lastly, similar IR-A PM sensitivities to TP01 are present in the downstream region for TP01 and include Zel'dovich mechanisms affecting N_2 concentrations as well as N_2 HP-CIE rates affecting N_2 PM radiation.

IR-B and IR-C PM radiation GSA/UQ results in Figure 7.21(b-c) for TP02 include similar Zel'dovich mechanism influences at the nose and downstream locations, while differences mainly reside near the shoulder region. Variance contributions from atomic oxygen E-CIE rates involve line transitions in the visible spectrum for both IR PM bands and therefore, variations in these collisional rates most likely have an indirect influences on populations that affect O line transitions in the IR-B and IR-C wavelengths. As with the majority of other trajectory point and radiation type combinations, NO and O_2 dissociation influences are present at the shoulder for both bands as well. Similar to TP01, small variance contributions from sublimation rates are present in the IR-C band just past the shoulder for TP02.

Overall, the IR PM radiance sensitivities presented in Figure 7.21(d) illustrate the increased influences of collisional excitation near the nose and shoulder of the IRV-2 vehicle in the higher density TP02 flow. This increased complexity also depicts an increase in smaller variance contributions (<5%) from many parameters in the nose and shoulder regions. The maximum relative uncertainty in this region of over 90% and the rapid local change in Sobol' indices along these LOSs also attests to a more complex region marked by high degrees of chemical and radiative nonequilibrium.

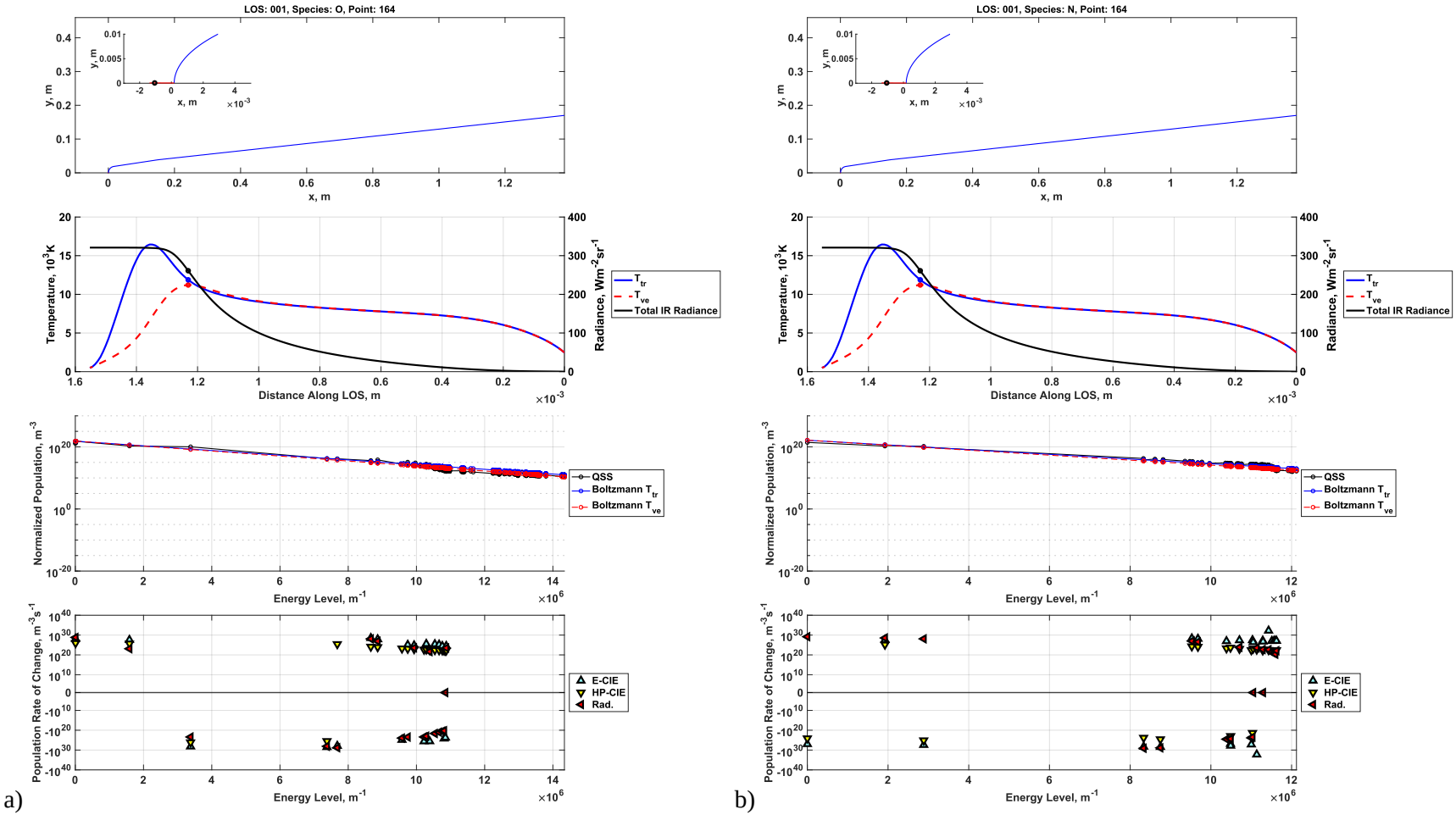

Figure 7.20: Atomic (a) oxygen and (b) nitrogen E-CIE rate influences on stagnation PM IR radiance.

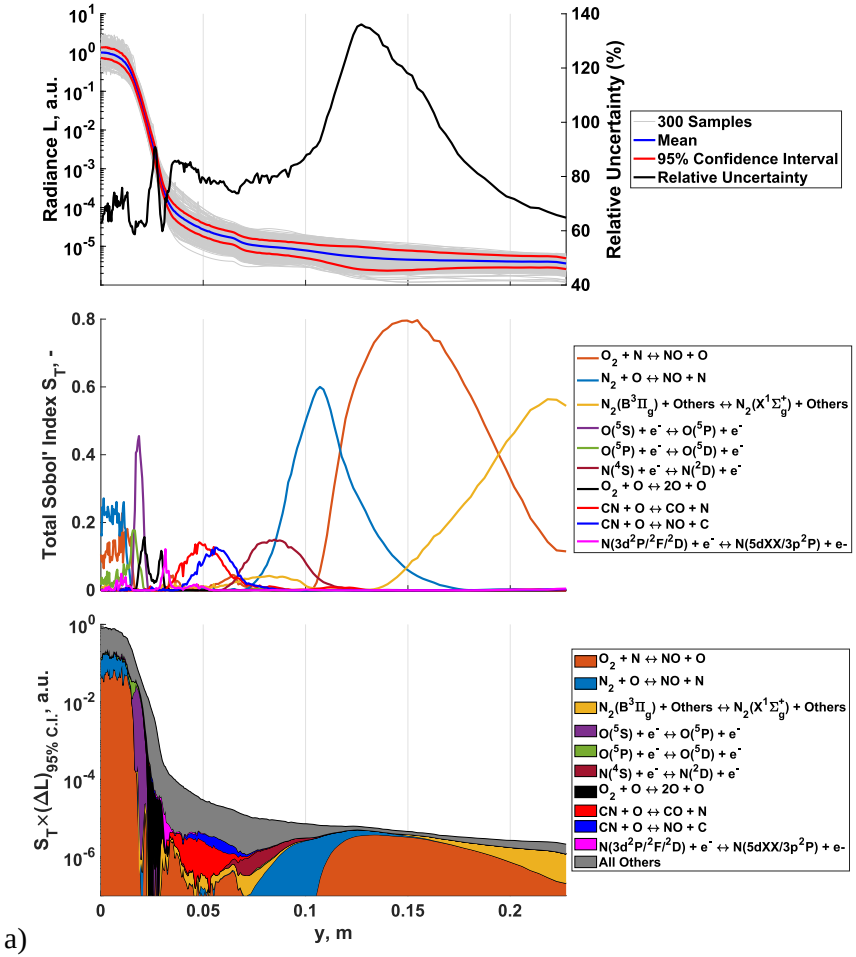
Radiance L, a.u.
Relative Uncertainty (%)
300 Samples
Mean
95% Confidence Interval
Relative Uncertainty
Total Sobol' Index S_T, -
$O_2 + N \leftrightarrow NO + O$
$N_2 + O \leftrightarrow NO + N$
$N_2(B^3\Pi_g) + Others \leftrightarrow N_2(X^1\Sigma_g^+) + Others$
$O(^5S) + e^- \leftrightarrow O(^5P) + e^-$
$O(^5P) + e^- \leftrightarrow O(^5D) + e^-$
$N(^4S) + e^- \leftrightarrow N(^2D) + e^-$
$O_2 + O \leftrightarrow 2O + O$
$CN + O \leftrightarrow CO + N$
$CN + O \leftrightarrow NO + C$
$N(3d^2P/^2F/^2D) + e^- \leftrightarrow N(5dXX/3p^2P) + e-$
$S_T \times (\Delta L)_{95\%\ c.i.}$, a.u.
All Others
y, m

a)

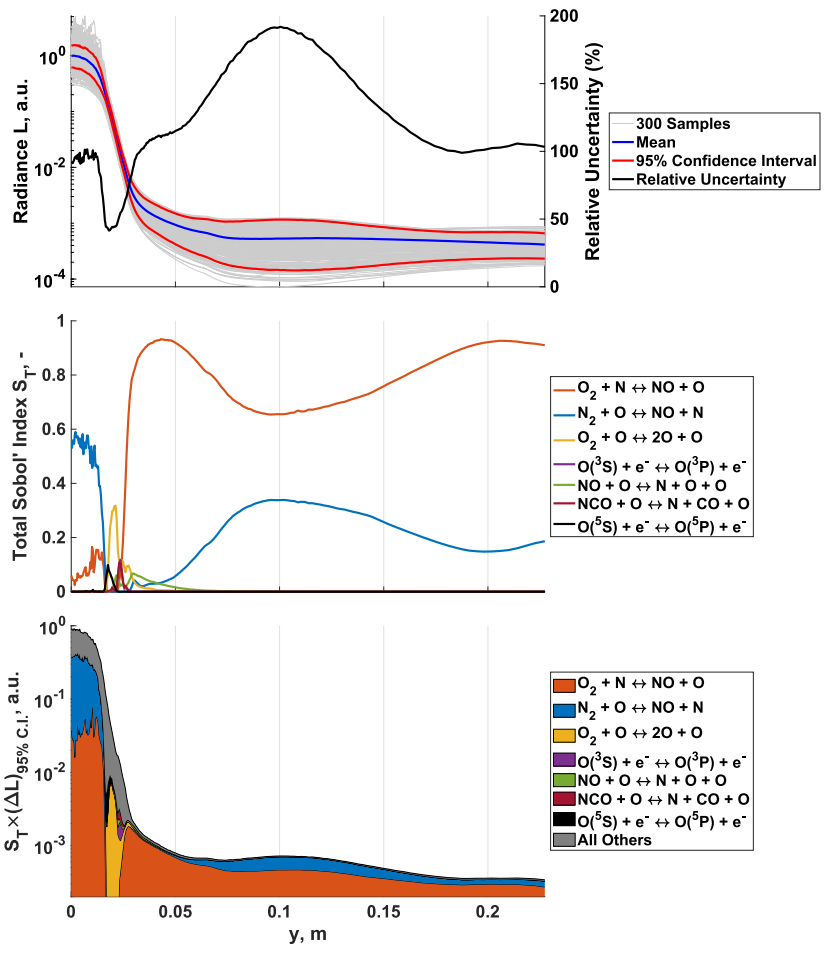
Radiance L, a.u.
Relative Uncertainty (%)
300 Samples
Mean
95% Confidence Interval
Relative Uncertainty
Total Sobol' Index S_T, -
$O_2 + N \leftrightarrow NO + O$
$N_2 + O \leftrightarrow NO + N$
$O_2 + O \leftrightarrow 2O + O$
$O(^3S) + e^- \leftrightarrow O(^3P) + e^-$
$NO + O \leftrightarrow N + O + O$
$NCO + O \leftrightarrow N + CO + O$
$O(^5S) + e^- \leftrightarrow O(^5P) + e^-$
$S_T \times (\Delta L)_{95\%\ c.i.}$, a.u.
All Others
y, m

b)

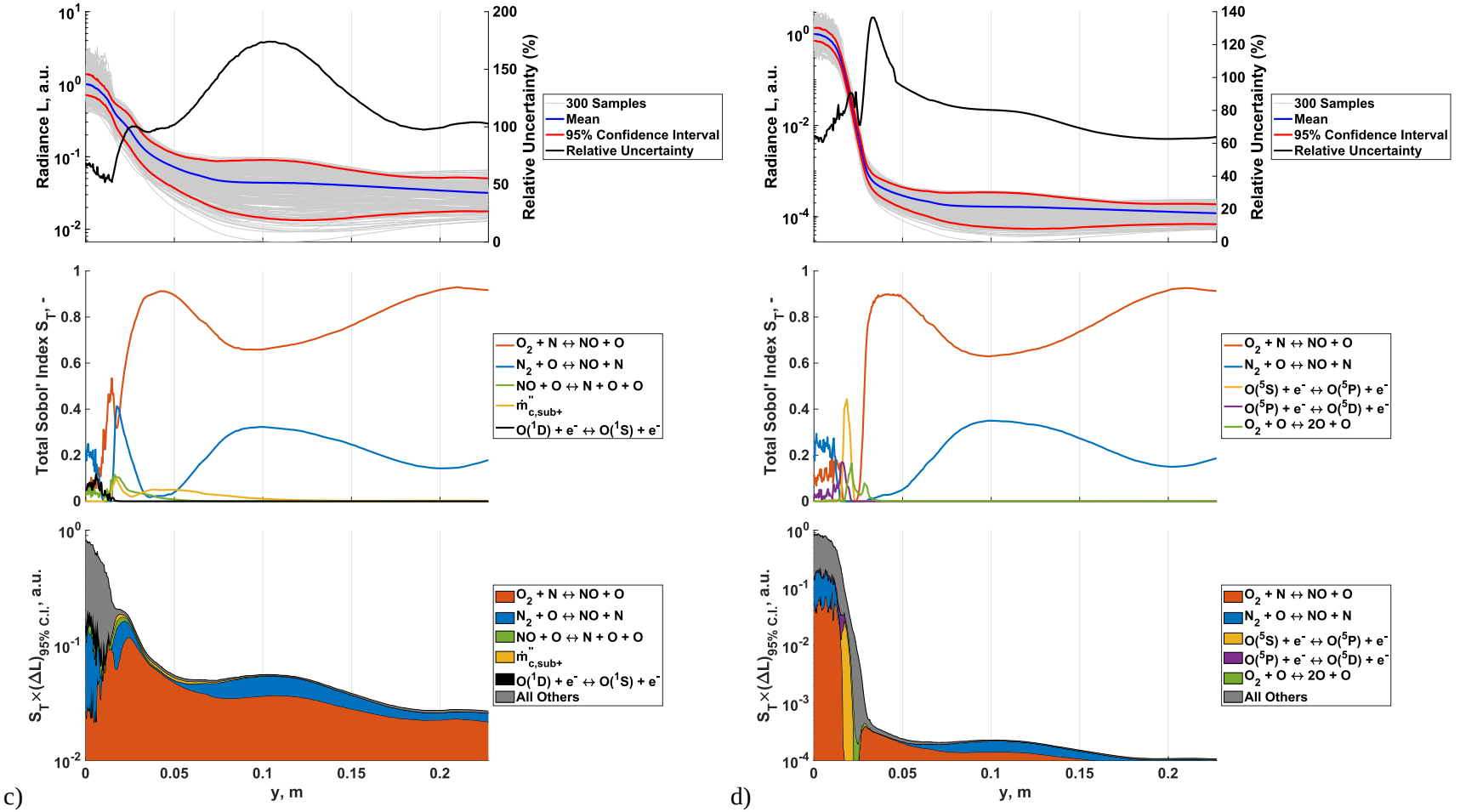

Figure 7.21: TP02 Normalized uncertainty bounds, Sobol' indices, and scaled Sobol' indices for PM only (a) IR-A (0.78-1.4 μm), (b) IR-B (1.4-3.0 μm), (c) IR-C (3.0-20.0 μm) and (d) IR-T (0.78-20.0 μm) bands. 'All others' category defined as less than 5% variance or scaled variance contribution integrated over the QoI range.

7.5 Discussion and Summary

7.5.1 Aggregated Results and General Trends

The global sensitivity analysis and uncertainty quantification results in this case study included 612 log-uniformly distributed parameters sampled into parameter sets for 200 wall-normal LOSs distributed over the entire vehicle at two IRV-2 trajectory points, two radiance types, and 4 IR band combinations totaling 3,200 QoIs. Table 7.3 depicts these combinations, regions of interest, local relative uncertainty bounds and major contributing variance parameters for those regions of interest. Trends for all combinations include the reoccurring importance of nitrogen dissociation and recombination via Zel'dovich exchange reactions. For BB+PM radiance, the reason for this dependency is due to these reactions' influence on surface temperature, which contributes to the majority of the grey body and overall radiance. For PM only radiance, Zel'dovich mechanism variance contributions directly affect N_2 and NO concentrations which in turn, influence IR radiation across all bands.

Additionally, NO dissociation and recombination with atomic oxygen and nitrogen are major contributors to IR radiation of almost all trajectory points, LOS locations, and IR bands. Again, the reasons for these reactions' influence depend upon the combination of conditions. Generally, NO dissociation and recombination rate coefficients indirectly affects N_2 populations for PM only radiance and directly affects wall temperature for BB+PM radiance at the nose.

Moreover, the increase in the "All Others" category provided insight as to which combinations of conditions and locations might lead to a lack of parameter sparsity and/or numerical instabilities in the hypersonic flow, material response and radiation codes. Specifically, the BB+PM radiance relative uncertainties decrease to low values in the downstream region of the vehicle for both trajectory points and across all bands. This low uncertainty leads to a breakdown of the sparsity assumption inherent in the normalized regression algorithm, wherein a larger number of parameters contribute small amounts of variance to ever-decreasing QoI uncertainties.

For numerical instabilities, the nose region of TP02 PM only radiance displayed an increase in the "All Others" category for all bands. In this region and conditions, a small fraction of samples show increased variability between LOS radiance values. Looking further into the output files of these samples, it was determined that approximately 1-3% of the LOS points near the nose and shoulder exhibited QSS convergence failures related to calculating the state populations for select species and LOS points in lower temperature regions. NEQAIR accounts for these instabilities by trying multiple QSS solution algorithms when a solution is not converged for a species/LOS point combination. When all methods fail, NEQAIR reverts the LOS point/species combination state population to a Boltzmann distribution. Although these individual LOS point/species combination electronic state population changes along the LOS do not necessarily change overall LOS radiance significantly, the cumulative effect on GSA/UQ results is a larger number of smaller variance contributions seen in the nose and shoulder regions of Figure 7.21.

The trajectory point differences for both radiance types and across all bands include increased influences from finite rate surface chemistry and collisional excitation and quenching on radiance. Variation in the FRSC sublimation approximation via Equations 97 and 98 greatly influences how quickly the normalized carbon mass flux B_C' increases to the CO diffusion limit of 0.175 for a given wall temperature and mass conductance. At TP02, these influences become more apparent for all IR radiance bands and types, particularly in the nose and shoulder regions. Additionally, TP02 experienced increased variance contributions from collisional excitation from heavy particles and electrons in the case of N_2, and O and N, respectively. The HP-CIE of N_2 in downstream locations was determined to be a function of state population increase via collisions to $N_2(B)$ followed by direct subsequent emission from that state population. For atomic nitrogen and oxygen E-CIE variance contributors, more complicated and indirect paths to increases in state populations that lead to IR radiation occurred. In other words, E-CIE reactions rates for O and N that contribute most to IR radiance uncertainty may not necessarily correspond to radiative transitions that emit in the IR spectrum but instead influence other state population combinations.

Table 7.3: Summary of the full IRV-2 case study GSA/UQ results.

Conditions	Radiance Type	Bands	LOS Region	Local Relative Uncertainty	Major Contributing Variance Parameters
TP01 56 km 6.8 km/s 4.25 s	BB + PM	IR-A	Nose	12.5-12.8%	$N_2 + O \rightleftharpoons NO + N$ $O_2 + N \rightleftharpoons NO + O$ $NO + N \rightleftharpoons N + O + N$ $NO + O \rightleftharpoons N + O + O$ $O_2 + O \rightleftharpoons 2O + O$
			Shoulder		
			Downstream	0.12-12.5%	All Others
		IR-B	Nose	6.7-7.2%	$N_2 + O \rightleftharpoons NO + N$ $O_2 + N \rightleftharpoons NO + O$ $NO + N \rightleftharpoons N + O + N$ $NO + O \rightleftharpoons N + O + O$ $O_2 + O \rightleftharpoons 2O + O$
			Shoulder		
			Downstream	0.07-4.1%	All Others
		IR-C	Nose	3.5-4.0%	$N_2 + O \rightleftharpoons NO + N$ $O_2 + N \rightleftharpoons NO + O$ $NO + N \rightleftharpoons N + O + N$ $NO + O \rightleftharpoons N + O + O$ $O_2 + O \rightleftharpoons 2O + O$
			Shoulder		
			Downstream	0.0-3.5%	All Others
		IR-T	Nose	12.1-13.0%	$N_2 + O \rightleftharpoons NO + N$ $O_2 + N \rightleftharpoons NO + O$ $NO + N \rightleftharpoons N + O + N$ $NO + O \rightleftharpoons N + O + O$ $O_2 + O \rightleftharpoons 2O + O$
			Shoulder		
			Downstream	0.12-12.1%	All Others
	PM Only	IR-A	Nose	47.1-129%	$N_2 + O \rightleftharpoons NO + N$ $O_2 + N \rightleftharpoons NO + O$
			Shoulder	47.1-139%	$O_2 + O \rightleftharpoons 2O + O$ $N_2(B^3\Pi_g)$ + Others $\rightleftharpoons N_2(X^1\Sigma_g^+)$ + Others $NO + O \rightleftharpoons N + O + O$
			Downstream	68.2-139%	$CN + O \rightleftharpoons CO + N$ $\dot{m}''_{c,sub+}$ $N_2 + O \rightleftharpoons NO + N$ $O_2 + N \rightleftharpoons NO + O$ $N_2(B^3\Pi_g) + O_2 \rightleftharpoons N_2(X^1\Sigma_g^+) + O_2$ $N_2(B^3\Pi_g)$ + Others $\rightleftharpoons N_2(X^1\Sigma_g^+)$ + Others
		IR-B	Nose	42.1-137%	$N_2 + O \rightleftharpoons NO + N$ $O_2 + N \rightleftharpoons NO + O$
			Shoulder	42.1-124%	$\dot{m}''_{c,sub+}$ $O_2 + O \rightleftharpoons 2O + O$ $N_2(B^3\Pi_g)$ + Others $\rightleftharpoons N_2(X^1\Sigma_g^+)$ + Others $NO + O \rightleftharpoons N + O + O$ $CN + O \rightleftharpoons CO + N$
			Downstream	101-163%	$O_2 + N \rightleftharpoons NO + O$ $N_2 + O \rightleftharpoons NO + N$
		IR-C	Nose	63.2-88.6%	$N_2 + O \rightleftharpoons NO + N$ $O_2 + N \rightleftharpoons NO + O$ $\dot{m}''_{c,sub+}$ $NO + O \rightleftharpoons N + O + O$

			Shoulder	63.2-108%	$O_2 + N \rightleftharpoons NO + O$ $\dot{m}''_{c,sub+}$ $N_2 + O \rightleftharpoons NO + N$ $NO + O \rightleftharpoons N + O + O$
			Downstream	108-156%	$O_2 + N \rightleftharpoons NO + O$ $N_2 + O \rightleftharpoons NO + N$
		IR-T	Nose	45.9-130%	$N_2 + O \rightleftharpoons NO + N$ $O_2 + N \rightleftharpoons NO + O$
			Shoulder	46.9-110%	$O_2 + O \rightleftharpoons 2O + O$ $\dot{m}''_{c,sub+}$ $CN + O \rightleftharpoons CO + N$ $N_2(B^3\Pi_g) + \text{Others} \rightleftharpoons N_2(X^1\Sigma_g^+) + \text{Others}$ $NO + O \rightleftharpoons N + O + O$
			Downstream	96.5-151%	$O_2 + N \rightleftharpoons NO + O$ $N_2 + O \rightleftharpoons NO + N$
TP02 49 km 6.8 km/s 6.75 s	BB + PM	IR-A	Nose / Shoulder	8.1-9.8%	$N_2 + O \rightleftharpoons NO + N$ $\dot{m}''_{c,sub+}$ $NO + O \rightleftharpoons N + O + O$ $NO + N \rightleftharpoons N + O + N$
			Downstream	0.30-9.8%	$O_2 + N \rightleftharpoons NO + O$ $N_2 + O \rightleftharpoons NO + N$ $NO + N \rightleftharpoons N + O + N$ $O_2 + O \rightleftharpoons 2O + O$ $NO + O \rightleftharpoons N + O + O$ All Others
		IR-B	Nose / Shoulder	4.7-5.6%	$\dot{m}''_{c,sub+}$ $N_2 + O \rightleftharpoons NO + N$ $NO + O \rightleftharpoons N + O + O$ $NO + N \rightleftharpoons N + O + N$
			Downstream	0.21-5.6%	$O_2 + N \rightleftharpoons NO + O$ $NO + O \rightleftharpoons N + O + O$ $NO + N \rightleftharpoons N + O + N$ $O_2 + O \rightleftharpoons 2O + O$ $N_2 + O \rightleftharpoons NO + N$ All Others
		IR-C	Nose / Shoulder	2.7-3.1%	$\dot{m}''_{c,sub+}$ $N_2 + O \rightleftharpoons NO + N$ $NO + O \rightleftharpoons N + O + O$ $NO + N \rightleftharpoons N + O + N$
			Downstream	0.11-3.1%	$O_2 + N \rightleftharpoons NO + O$ $NO + O \rightleftharpoons N + O + O$ $NO + N \rightleftharpoons N + O + N$ $O_2 + O \rightleftharpoons 2O + O$ $N_2 + O \rightleftharpoons NO + N$ All Others
		IR-T	Nose / Shoulder	5.6-6.3%	$\dot{m}''_{c,sub+}$ $N_2 + O \rightleftharpoons NO + N$ $NO + O \rightleftharpoons N + O + O$ $NO + N \rightleftharpoons N + O + N$
			Downstream	0.13-6.3%	$O_2 + N \rightleftharpoons NO + O$ $NO + O \rightleftharpoons N + O + O$ $NO + N \rightleftharpoons N + O + N$ $O_2 + O \rightleftharpoons 2O + O$

				$N_2 + O \rightleftharpoons NO + N$ All Others
PM Only	IR-A	Nose	58.7-75.8%	$N_2 + O \rightleftharpoons NO + N$ $O_2 + N \rightleftharpoons NO + O$ $O(3p\ ^5P) + e^- \rightleftharpoons O(3d\ ^5D°/^3D°) + e^-$ $N(3d\ ^2P/^2F/^2D) + e^- \rightleftharpoons N(5d\ XX/3p\ ^2P) + e^-$
		Shoulder	58.7-91.1%	$O(3s\ ^5S°) + e^- \rightleftharpoons O(3p\ ^5P) + e^-$ $O_2 + O \rightleftharpoons 2O + O$ $O(3p\ ^5P) + e^- \rightleftharpoons O(3d\ ^5D°/^3D°) + e^-$ $CN + O \rightleftharpoons CO + N$ $CN + O \rightleftharpoons NO + C$ $N(3d\ ^2P/^2F/^2D) + e^- \rightleftharpoons N(5d\ XX/3p\ ^2P) + e^-$
		Downstream	59.8-136%	$O_2 + N \rightleftharpoons NO + O$ $N_2 + O \rightleftharpoons NO + N$ $N_2(B^3\Pi_g) + \text{Others} \rightleftharpoons N_2(X^1\Sigma_g^+) + \text{Others}$ $N(^4S°) + e^- \rightleftharpoons N(^2D°) + e^-$
	IR-B	Nose	41.8-102%	$N_2 + O \rightleftharpoons NO + N$ $O_2 + N \rightleftharpoons NO + O$
		Shoulder	102-110%	$O_2 + O \rightleftharpoons 2O + O$ $O(3s\ ^5S°) + e^- \rightleftharpoons O(3p\ ^5P) + e^-$ $NO + O \rightleftharpoons N + O + O$ $NCO + O \rightleftharpoons N + CO + O$ $O(3s\ ^3S°) + e^- \rightleftharpoons O(3p\ ^3P) + e^-$
		Downstream	98.9-191%	$O_2 + N \rightleftharpoons NO + O$ $N_2 + O \rightleftharpoons NO + N$
	IR-C	Nose	52.0-68.8%	$N_2 + O \rightleftharpoons NO + N$ $O_2 + N \rightleftharpoons NO + O$ All Others $O(^1D) + e^- \rightleftharpoons O(^1S) + e^-$ $NO + O \rightleftharpoons N + O + O$
		Shoulder	68.8-100%	$O_2 + N \rightleftharpoons NO + O$ $N_2 + O \rightleftharpoons NO + N$ $NO + O \rightleftharpoons N + O + O$ $\dot{m}''_{c,sub+}$
		Downstream	100-174%	$N_2 + O \rightleftharpoons NO + N$ $O_2 + N \rightleftharpoons NO + O$ $\dot{m}''_{c,sub+}$
	IR-T	Nose	56.7-77.7%	$N_2 + O \rightleftharpoons NO + N$ $O_2 + N \rightleftharpoons NO + O$ $O(3p\ ^5P) + e^- \rightleftharpoons O(3d\ ^5D°/^3D°) + e^-$
		Shoulder	77.7-98.7%	$O(3s\ ^5S°) + e^- \rightleftharpoons O(3p\ ^5P) + e^-$ $O(3p\ ^5P) + e^- \rightleftharpoons O(3d\ ^5D°/^3D°) + e^-$ $O_2 + O \rightleftharpoons 2O + O$
		Downstream	98.7-171%	$O_2 + N \rightleftharpoons NO + O$ $N_2 + O \rightleftharpoons NO + N$

7.5.2 Parameter Implications

This case study investigated multiple scenarios and conditions involving hundreds of parameters. Over these scenarios, the 17 parameters depicted in Table 7.4 contributed to more than 95% of overall IR radiance variance. The listed uncertainty bound multipliers were extensively reviewed in Chapter 3. Many of these parameters have been well studied via experiments over multiple decades. However, many of these parameters were not performed at temperatures relevant to the conditions of the case studies. This discrepancy leads to increased uncertainty from extrapolations that's necessitated to study realistic hypersonic flows [113]. More accurate predictions of IR radiance can be obtained by allocating resources for reducing both experimental and computational uncertainty with these parameters over a wider range of hypersonic flight conditions. Incorporating more refined thermochemical models that account for the coupling of internal energy variations with the dissociation and exchange reactions could greatly increase the accuracy of remote observation predictions in environments with high degrees of nonequilibrium. Further pairing these higher-fidelity models with ground and flight test campaigns that can replicate these conditions can further provide a feedback loop for further model improvement. By identifying those parameters that most affect remote observation prediction, this work significantly reduces the amount of resources required to conduct this feedback loop.

Examples of thermochemical model improvements for parameters 1-4 in Table 7.4 include estimating internal energy influences on state-resolved kinetics of NO stemming from empirical potential energy surfaces (PESs) via quasi-classical trajectory (QCT) methods. Additionally, work on approximating oxygen dissociation (parameter 5) analyses via similar PES/QCT methods alongside chemical models like MMT have come far in improving physical fidelity while balancing computational cost for vehicle scale simulation. Additionally, further investigations to increasing fidelity for oxygen dissociation are ongoing and include other internal energy processes like electronic excitation [182,222,223].

Carbon exchange parameters 6-7 have also been studied in a similar manner, where PESs and trajectory theory were used in approximating reaction rates [197,224]. Although more computationally expensive, these higher fidelity simulations and models rely upon less semiempirical data while maintaining

accuracy; an advantage when conducting simulations under a wide range of conditions that cannot currently be replicated in ground test facilities or flight test without considerable expense. By filtering the gas phase reaction rate parameters for IR radiance, this case study pinpoints reactions whose thermochemical model improvements can have the most impact for accurate IR remote observation prediction.

Moreover, FRSC sublimation rate parameter 8 can be further refined by adding in physical processes and fidelity. As previously mentioned, the FRSC processes modeled throughout this work rely upon simplified assumptions for the purposes of incorporating FRSC informed B'_C tables for efficient and stable evaluations during GSA/UQ analyses. Further improvements to reduce FRSC rate uncertainty could incorporate processes and features like adsorption/desorption, gas phase dependent reactions, Eley–Rideal and Langmuir–Hinshelwood reactions, the inclusion of active site densities, and for sublimation, the inclusion of carbon species thermochemical data beyond C_3 [2,26,28,33,37,80,81]. The current FRSC model implementation allows for applying this increased fidelity with minimal changes to the underlying LeMANS-MOPAR code. The results from this case study pinpoint where both spectrally and spatially these model improvements can have the most impact on IR radiance uncertainty.

Lastly, parameters 9-17 incorporate collision induced state excitation rates on those atoms and molecules that most influence IR radiance under weakly ionized conditions. The most immediate implication of this case study is that it filtered those collisional excitations that require a more detailed uncertainty bound review. Additionally, the incorporation of all excitation and quenching rates within NEQAIR for the GSA/UQ scenarios found transitions that absorb and emit radiation outside of the IR band (parameters 9-11 and 16) influence IR radiance prediction uncertainty via indirect effects on electronic state populations. These results motivate further investigations into higher fidelity collisional-radiative models involving electronic state populations of N_2, N, and O that relax any QSS assumptions made within NEQAIR [99].

Additionally, the increased fraction of direct IR-C radiance from NO vibrational state transitions found in this analysis motivate increased study into the influence of rovibrational states of NO. Recent analyses by Thirani et al. (2025) [225] utilizing DSMC simulations for Mach 7 flow over a cylinder found

significant variations in IR radiance stemming from PES/QCT derived relaxation times of NO affecting vibrational temperatures in "regions of the flow characterized by strong coupling of thermochemistry and flow transport properties, such as in expansion and wake regions." Further comparisons of both DSMC, QSS, Boltzmann, and CR models were made on the vibrational state populations of NO, where significant variation was found on the spectral radiance in the fundamental band of NO at 5.0-5.5 μm in these expansion regions.

Table 7.4: Most sensitive parameters for all scenarios.

No.	Parameter Category	Major Contributing Variance Parameters	Uncertainty Bound Multipliers
1	Neutral Exchange	N_2 + O ⇌ NO + N	0.1, 7.0
2	Neutral Exchange	O_2 + N ⇌ NO + O	0.1, 10
3	Dissociation	NO + N ⇌ N + O + N	0.2, 2.5
4	Dissociation	NO + O ⇌ N + O + O	0.2, 2.5
5	Dissociation	O_2 + O ⇌ 2O + O	0.3, 2.1
6	Neutral Exchange	CN + O ⇌ CO + N	0.1, 10
7	Neutral Exchange	CN + O ⇌ NO + C	0.1, 6.0
8	FRSC	$\dot{m}''_{c,sub+}$	0.7, 2.8
9	HP-CIE	$N_2\, B^3\Pi_g \rightarrow X^1\Sigma_g^+$ M = O_2 (164.0-168.5 nm)	0.1, 10
10		$N_2\, B^3\Pi_g \rightarrow X^1\Sigma_g^+$ M = Others (164.0-168.5 nm)	
11	E-CIE	O 2→3 (557.9 nm)	0.1, 10
12		O 4→6 (777.5 nm)	
13		O 5→7 (844.9 nm)	
14		O 6→9 (924.6 nm)	
15		O 10→12 (2802.7 nm)	
16	E-CIE	N 1→2 (520.1 nm)	0.1, 10
17		N 10→16 (1258.0 nm)	

7.5.3 Quantity of Interest and Other Implications

The GSA/UQ results extend beyond identifying which parameters most influence a particular QoI. Specifically, these results provide a roadmap for improving both the fidelity of computational models and the design of physical systems. By quantifying the propagation of uncertainty through complex hypersonic flow and radiative models, engineers can prioritize efforts on reducing uncertainty in critical chemical reactions that substantially affect wall temperatures and, consequently, IR radiance near the vehicle. This

targeted approach can lead to more robust thermal protection systems and better remote observation approximations of ablative vehicles under weakly ionized conditions by ensuring that the most influential reaction pathways are modeled and measured with higher precision.

One practical application lies in the realm of sensor and diagnostic system design. The spatial and spectral mapping of uncertainty along the vehicle enables a more focused allocation of measurement resources. If uncertainty is localized within specific IR bands or vehicle regions, instrumentation can be calibrated and optimized to capture those critical data points, improving the accuracy of real-time diagnostic systems during high-speed flight. This enhanced data quality can then feed back into the UQ framework, further refining model predictions. For example, onboard diagnostics, particularly those looking back into the vehicle wake, can benefit from these results by focusing on those fundamental and overtone IR-C bands in the wake where NO and CO PM radiance dominate and provide validation data to reduce parameter uncertainties.

Another possible application includes utilizing these IR radiance uncertainties for the detection of species and ablative contaminants via radiative spectroscopy in ground test experiments. By incorporating these GSA/UQ results, specific spatial and spectral regions can be narrowed for detecting particular species that most affect IR radiance. Specifically, the influences of sublimation and carbon exchange parameters on IR PM radiance were found to be primarily localized downstream of the IRV-2 shoulder approximately 0.04 m from the original stagnation point datum. Detecting IR influences of the carbon species in this region should therefore focus on CN and CO features in the IR-A and IR-B bands.

Moreover, these UQ/GSA outcomes have significant implications for computational efficiency and model improvement. By identifying regions where the “All Others” category dominates variance, analysts can determine where the assumption of parameter sparsity breaks down. This insight informs developers that additional model complexity or more robust numerical schemes might be required in those regions to capture the subtle yet cumulative effects of numerous small contributors. In essence, the results guide both the refinement of current simulation codes and the strategic deployment of computational resources, ensuring that efforts are concentrated on the aspects of the model that most impact predictive capability. A

particular example for model improvements includes developing electronic state distribution population models in NEQAIR that are more robust to regions of extreme flow variable gradients as well as low temperatures along particular LOSs or incorporating CR frameworks within NEQAIR similar to those proposed by Thirani et al. and others [225,226].

These results highlight the complex nature of global sensitivity analyses and uncertainty quantification within high-fidelity multidisciplinary codes. By breaking down these codes into lists of uncertain input parameters, conditions, radiance types, radiance bands, and spatial locations along the entire IRV-2 body, insights into both overall relative uncertainties and parameter contributions to those uncertainties were revealed. Additionally, these analyses exposed where certain conditions and locations can cause numerical instabilities in codes that might otherwise go unnoticed in more simplified parameterization studies. Overall, this case study points to parameters filtered by their influence on IR radiance QoIs in different scenarios. These parameters should be further investigated and refined to help narrow IR radiance uncertainties in both ground based and in remote observation settings. Other applications and conclusions to this and other case studies, as well as suggestions for future efforts are outlined in the next chapter.

Chapter 8

Conclusions and Recommendations

This chapter summarizes the work completed throughout this thesis in Section 8.1, the major contributions to the research community in Section 8.2, and recommendations for future work in Section 8.3. Each of these sections includes subsections highlighting major conclusions and ramifications.

8.1 Summary of Completed Work

8.1.1 Parameter Baseline and Uncertainty Bound Literature Review

A comprehensive literature review of past hypersonic flow GSA/UA analyses and all parameters utilized in this work was conducted. This includes 612 thermochemical gas, energy relaxation, excitation/deexcitation, and surface chemistry rate parameters. For gas-phase thermochemical rate parameters alone, this included 238 experiments, 134 meta-studies, and 40 numerical and theory references. For each parameter category, baseline and uncertainty bounds were determined. Additionally, calculated uncertainty bounds for gas phase reaction rate coefficients were compared with past literature reviews. Each parameter category was described in detail, with explanations for trends, outliers, and comparisons with previous uncertainty bounds where applicable.

Variations in these baseline and uncertainty bounds were found to notably impact key QoIs under weakly ionized hypersonic flow scenarios. The compiled data, analysis results, and synthesized uncertainty bounds offer a significant resource to the hypersonic flow community, extending beyond the immediate case studies. In some instances, sufficient data were amassed to support probability density functions beyond uniform distributions, including potential multivariate distributions for temperature and reaction rates. Where large uncertainties are driven by sparse data sources, the gathered findings point to areas needing additional experimentation or data reconsideration. Nonetheless, care must be taken not to artificially reduce uncertainty without proper justification. In parameters requiring extensive data post-

processing—such as temperature extrapolation, reverse reaction calculations, and reaction pathway uncertainties—consideration of larger uncertainty bounds might be warranted.

For those parameters where minimal or no experimental data existed beyond standard references, this review helped highlight areas in which further inquiry might be beneficial for specific QoIs. While imposing uncertainty bounds of one or two orders of magnitude on excitation and quenching rates might be defensible based on expert opinions, more in-depth uncertainty analyses could refine sensitivities and propagated errors under certain conditions.

8.1.2 Global Sensitivity Analysis and Uncertainty Quantification Tool Development

Analyses in Chapter 4, 5, and 7 involved significant development of custom drivers capable of integrating with GSA/UQ wrapper tools like Dakota and UQLab. This includes the processes described in Figure 4.4, Figure 5.1, and Figure 7.1. These custom codes and processes decreased the wall-clock times to conduct GSA/UQ analyses by orders of magnitude by leveraging embarrassingly parallel frameworks. The tools developed made higher dimension scenarios more computationally tractable in this work and provide a valuable means for current and future hypersonic modeling efforts.

8.1.3 Global Sensitivity Analysis and Uncertainty Quantification of Plasma Formation

GSA/UQ was conducted for gas-phase rate coefficient variance contributions on plasma formation around a slender hypersonic vehicle under weakly-ionized, suborbital flow conditions. The case study integrated simulations with advanced GSA/UQ techniques, comparing 2D axisymmetric plasma formation sensitivity and uncertainty metrics with those from previous 1D post-shock investigations. Nonintrusive point collocation with polynomial chaos expansions was employed to construct surrogate models for every CFD point within the flowfield around a spherical nose-cone representation of the IRV-2 nose tip. A point collocation oversampling ratio of 2 was applied for freestream flow conditions of 5, 7, and 9 km/s at 60 km, which resulted in 3,540 simulations per condition to evaluate 33,775 electron number density quantities of interest in the domain. For each simulation, input bounds for multiple parameters were sampled using Latin hypercube sampling in log-space to build the surrogates.

For the 5 and 7 km/s cases, the major reaction rate sensitivities on electron number density along the stagnation line in the 2D model were found to be associative ionization and dissociative recombination of nitrogen and oxygen. In addition, reactions producing N and O via dissociation of oxygen and nitrogen via Zel'dovich exchange contributed significantly to variance, trends that aligned with the sensitivities observed in previous 1D analyses. Differences between the models were observed near the shock, where contributions to electron number density variance from associative ionization forming O_2^+ were smaller, and near the wall, where those from associative ionization forming NO^+ were also reduced. These differences arose from 1D model assumptions of a shock discontinuity and the 2D model's inclusion of plasma catalytic wall boundary conditions. For the 9 km/s condition, the sensitivities along the stagnation line initially depended on associative ionization forming O_2^+, followed by the charge exchange reaction $O_2^+ + N \rightleftharpoons \mathrm{N}^+ + O_2$ and Zel'dovich exchange. Electron impact ionization sensitivities that appeared in the 1D model were absent in the 2D stagnation line due to wall influences that affect the flow conditions before their development. These sensitivity differences highlighted how 2D viscous effects and surface boundary conditions influenced plasma evolution in axisymmetric nonequilibrium flows.

The findings in this case study held several implications for the study of plasma formation in weakly-ionized flow regimes. Comparisons between 1D inviscid and 2D axisymmetric models demonstrated differences in GSA/UQ results due to higher fidelity, i.e., shock diffusion, multidimensional energy relief, and wall boundary effects. The case studies identified where these phenomena affected simulated electron number densities under baseline conditions and how they influenced relative uncertainty bounds and variance contributions. This effect was particularly pronounced for flows around slender vehicles like the IRV-2, especially at 9 km/s, where the influence of the 2D model and vehicle geometry led to significant discrepancies in predicted plasma formation and associated uncertainty due to decreased shock standoff distances. Moreover, the multidimensional uncertainty bounds and corresponding variance contribution field results provided insights into how variations in thermochemistry and energy exchange semiempirical relations affected plasma formation at different spatial locations. These findings have

implications for vehicle design and experimental studies on plasma formation, offering a valuable framework for refining uncertainty assessments in location-specific applications.

8.1.4 Modeling and Sensitivity Analysis of Finite Rate Surface Chemistry

The FRSC model developed in Section 2.4 and assessed in Chapter 6 enabled the stable and efficient incorporation of surface chemistry rates in GSA/UQ analyses. Major uncertain surface kinetics parameters, including basic models that approximated oxidation and sublimation processes, were introduced. The methodology for implementing these parameters within the FRSC model's framework includes a novel approach. In this method, surface kinetics rates along with boundary layer edge mass conductance were utilized together with precomputed 4D lookup tables to generate FRSC informed B_C' values. This process offloads the majority of the computational time for FRSC process integration to the initial 4D tables, thereby allowing for more efficient and stable computation of carbon ablation updates in a tightly coupled flow-material response algorithm.

Comparisons were then made between the new FRSC model, the equilibrium CEA2 model, and experimental observations obtained from both subsonic and supersonic/hypersonic experiments. The FRSC model was determined to better approximate experimental results at lower temperatures, where the CEA2 model overpredicted B_C' values compared to ATJ carbon ablation experiments. However, both the FRSC and CEA2 models overpredict experiment results above 3,000 K. A global sensitivity and uncertainty analysis for the uncertain surface kinetics parameters at atmospheric conditions revealed that the reaction probability for oxidation of O_2 and the sublimation mass flux rate kinetics were the major contributors to the variance in B_C' uncertainty below and above 1,800 K, respectively. Baseline comparisons between finite rate surface and equilibrium chemistry parameter sets for the IRV-2 initial trajectory points identified differences in surface parameters, particularly affecting ablation mass fluxes and surface recession, which influenced the coupled flow species mole fractions near the vehicle surface.

The development, implementation and assessment of the FRSC framework directly addressed the limitations of equilibrium models in predicting carbon ablation during hypersonic flight. By accounting for

finite rate oxidation and sublimation kinetics, the FRSC model improved the accuracy of ablation predictions when compared to experiments. A key innovation was the integration of four-dimensional lookup tables for the molecular oxygen dissociation fraction and Damköhler number, which captured the dependencies of reaction rates on wall temperature, pressure, mass conductance, and kinetic parameters while dramatically reducing computational overhead and inherent instabilities. Finally, detailed GSA/UQ results identified the oxidation probability for atomic oxygen and the sublimation mass flux rate as the dominant sources of uncertainty in the predicted carbon mass blowing rate. Comparative studies with both theoretical equilibrium models and experimental data underscored the practical advantages of the FRSC approach for improving the design and analysis of hypersonic vehicles.

8.1.5 Global Sensitivity Analysis and Uncertainty Quantification of Black Body and Participating Medium Radiation

This case study aggregated GSA/UQ results from 612 log-uniformly distributed parameters that were sampled and input to produce 200 wall-normal LOSs across the entire vehicle. These analyses involved two IRV-2 trajectory points, two radiance types, and four IR band combinations, which together generated 3,200 QoIs. Nitrogen dissociation and recombination rates via the Zel'dovich exchange reactions were major variance contributors across all QoI combinations. For BB+PM radiance, these reactions influenced surface temperatures and overall grey-body radiance. For PM only radiance, Zel'dovich exchange reactions affected N_2 and NO concentrations that influenced IR radiation. Additional trends revealed that the importance of other parameters increased in regions where decreased uncertainties or numerical instabilities led to a breakdown of the parameter sparsity assumption inherent in the normalized PCE regression algorithms.

The case study results further determined that variations in the FRSC sublimation and collisional excitation processes greatly affect radiance predictions. At the second trajectory point, these effects became more pronounced in the nose and shoulder regions. The scenarios also identified increases in contributions from heavy-particle and electron collision induced excitation in generating IR emissions, and it detailed

how atomic species influenced state populations both directly and indirectly through several collisional-radiative reaction pathways. Additionally, the study recognized that a small percentage of LOS points near the nose and shoulder exhibited quasi-steady state convergence failures, which were managed by NEQAIR through multiple solution algorithms and a fallback to a Boltzmann distribution for certain species.

Overall, the case study filtered hundreds of input parameters to highlight those that most influenced IR radiance outcomes, thereby establishing a roadmap for improving computational models and physical system designs. The results indicated that reducing uncertainty in critical chemical reactions could lead to more robust thermal protection systems and more accurate remote observations of ablative vehicles under suborbital, weakly-ionized conditions. Practical applications of these findings included guiding sensor and diagnostic system designs to focus on high-uncertainty regions and spectral bands, as well as refining model components to address numerical instabilities. This comprehensive analysis ultimately underscored the complex interplay among various physical and chemical processes in high-fidelity multidisciplinary simulations and motivates further research into enhanced thermochemical and collisional-radiative models for improved predictive accuracy.

8.2 Contributions

- **Comprehensive review and assessment of 612 gas-phase thermochemical reaction rates, relaxation parameters, FRSC rates, and state specific collision induced excitation and quenching rates.** The extensive literature review of the variation in these parameters helped inform more robust analyses for the case studies in this work. Additionally, the review provided insights into the state of experimental, numerical, and aggregate study for each parameter category. This context provided both a qualitative and quantitative background for GSA/UQ implementation and informs why certain input parameters variances might impact results. Furthermore, these input parameter references, baselines and uncertainty bounds can be used in future GSA/UQ analyses for a multitude of different conditions and QoIs.

- **Development of multiple sensitivity analysis wrapper tools for efficient integration of high-fidelity hypersonic, material response, and radiation simulations.** GSA/UQ investigations into hypersonic flow, material response, and radiation phenomena required hundreds to thousands of computationally expensive simulations. Frameworks and methods were built to address these limitations by parallelizing both within each subcode simulation and the overall evaluations of multiple codes, allowing for an order of magnitude speedup for GSA/UQ evaluation sets. These codes are now being utilized for different applications for multiple hypersonic GSA/UQ applications.
- **Identified sensitive parameters influencing ionization uncertainty throughout a 2D axisymmetric flowfield under weakly ionized flow conditions.** GSA/UQ considering 58 gas-phase rate coefficients and relaxation parameters were conducted to assess overall plasma formation uncertainty and variance apportionment via quantifying converged Sobol' index metrics. Dominant pathways toward ionization in a 2D axisymmetric flowfield were identified and compared with 1D shock GSA/UQ analyses at the stagnation line. Multiple weakly ionized flight conditions were examined, and uncertainties and sensitivities were quantified for each CFD point in the flowfield. Streamlines and field plots were used to better quantify spatial variations in primary ionization pathways at these flight conditions.
- **Development of a nonintrusive FRSC model using nondimensional table integration within LeMANS-MOPAR-MD.** A new FRSC model was developed, tested, and implemented with the goal of incorporating a more efficient and stable way to implement GSA/UQ analyses that involve surface chemistry rate effects. This included utilizing a variant of the Damköhler number as a ratio of surface kinetics rates to mass conductance to generate 4D tables that are then used to generate FRSC informed B_C' tables for carbon ablation. The model outputs were compared to experiment and equilibrium surface chemistry methods and GSA/UQ analyses were conducted. Gas phase ablative products, surface conditions and recession rates at trajectory point conditions were also

compared between models. The methods employed also allow for integration of future high-fidelity models while maintaining the advantages of lookup table nondimensional blowing rates.

- **Identified sensitive parameters influencing black body and participating medium IR radiation uncertainty throughout a 2D axisymmetric flowfield.** Identified 17 influential parameters from a set of 612 that included gas phase reaction rate coefficients, FRSC rates and collision induced excitation and quenching rates coefficients for over 3,200 QoI combinations involving IR radiation. These combinations included different trajectory points, radiance types, IR band categories, and LOS locations along the entire IRV-2 vehicle body. Mechanisms explaining GSA/UQ results were rigorously investigated. Implications involving parameters and QoIs as well as applications for modeling and experimentation were identified.

8.3 Recommendations for Future Work

8.3.1 Higher Fidelity Modeling and Experimental Feedback and Integration for Sensitive Parameters

As previously mentioned throughout this work, one of the main benefits of these model assessments is the ability to identify those uncertain input parameters whose increased study would most impact both simulation and experimental QoIs. By narrowing these input parameter uncertainties, the larger portions of the QoI uncertainty can also be reduced. These parameter uncertainties can be reduced via computational and experimental methods. Examples highlighted at the end of Chapter 7 include the incorporation of computational chemistry techniques involving PES/QCT numerical methods for estimating the most sensitive gas-phase chemical reaction rate coefficients. Frameworks could be built to leverage the increased model fidelity of these techniques for only those parameters that are most sensitive to QoIs. This would allow for a balance between computational expense and increased QoI accuracy by focusing on increased fidelity where it most matters. Quantum chemistry to full vehicle CFD bridging chemical models like MMT are well-suited for higher fidelity parameter integration. Other model fidelity increases involving relaxing

the QSS assumption, particularly for N and O can be made to better predict QoIs under certain conditions and locations.

Moreover, using these GSA/UQ results within experiments under hypersonic flight conditions would better focus where to isolate the observation of certain reactions for better rate prediction. For example, field ionization sensitivity and uncertainty results can be used to inform spatial boundaries where certain ionization pathways most influence ion creation. This would allow for more targeted experimental campaigns under various flight conditions. Other field GSA/UQ to experiment applications include spatially varying QoIs like contaminant detection or instrument calibration. Insights found from these experimental campaigns can then be fed back into better inform further GSA/UQ simulations.

8.3.2 FRSC Model Improvements

The FRSC model developed in Section 2.4 and evaluated in Chapter 6 includes many simplifying assumptions and excludes many surface chemical processes. Despite its accuracy relative to equilibrium surface chemistry models, there is much room for improvement to better characterize ablation phenomena. These include the incorporation of higher fidelity models derived alongside molecular beam experiments like those mentioned in Section 2.4.1 and Chapter 6 [2,26,28,80,81]. Additionally, the current model does not compare well to experiment at temperatures above 3,000 K. Although out of the scope of this work, better carbon sublimation modeling in this regime is necessary for both accurate recession and ablative product prediction at lower trajectory points where surface heating further increases. These more accurate ablation models could then be incorporated into the Damköhler FRSC integrated B_C' table framework for both efficient and numerically stable integration.

8.3.3 Effects of Three-Dimensional Radiation, Atmospheric Absorbance, and Narrow-band Spectral QoIs

The GSA/UQ results in this work motivate further simulation of more aggregate radiation predictions involving 3D simulations of integrated irradiance while accounting for atmospheric attenuation as viewed from an observer. Previous studies involving the Hayabusa 2 have been conducted with both

NEQAIR and other nonequilibrium radiation codes [12,213]. Incorporation of 3D integrated radiation QoIs and vehicle wakes would greatly increase computational expense, but the methods included in these studies allow for the formation of reduced dimensional GSA/UQ analyses by only including those parameters that are most sensitive to PM IR radiance at different flight conditions.

Additionally, investigations into spectral radiance QoIs over narrow band regions of interest would allow for identifying parameters that most influence sensor specific results. This would better inform how model parameters would affect the prediction uncertainty of what a particular multispectral sensor could detect. Particularly, uncertainties associated with scan input options within NEQAIR could be investigated for given sensor specifications. Applications for this process include onboard diagnostics, ground test, and remote observation of flight tests.

Bibliography

[1] Park, C., “Nonequilibrium Hypersonic Aerothermodynamics,” Wiley, New York, 1990.

[2] Candler, G. V., “Rate Effects in Hypersonic Flows,” *Annual Review of Fluid Mechanics*, Vol. 51, No. 1, 2019, pp. 379–402. https://doi.org/10.1146/annurev-fluid-010518-040258

[3] Sundberg, R., Duff, J., and Bernstein, L., “Nonequilibrium Infrared Emission Model for Reentry Vehicles,” presented at the 27th Thermophysics Conference, Nashville,TN,U.S.A., 1992. https://doi.org/10.2514/6.1992-2916

[4] Winter, M., “Airborne Observation of Re-Entries - Lessons Learned and Future Perspectives (Invited),” presented at the 19th AIAA International Space Planes and Hypersonic Systems and Technologies Conference, Atlanta, GA, 2014. https://doi.org/10.2514/6.2014-2806

[5] Chen, C., Cunfeng, G., Yaqian, L., Ruiheng, L., and Shuwen Wang, S. W., “The Analysis on Infrared Radiant Properties of Hypersonic Vehicle,” presented at the IET International Radar Conference 2015, Hangzhou, China, 2015. https://doi.org/10.1049/cp.2015.1003

[6] Niu, Q., Yuan, Z., Chen, B., and Dong, S., “Infrared Radiation Characteristics of a Hypersonic Vehicle under Time-Varying Angles of Attack,” *Chinese Journal of Aeronautics*, Vol. 32, No. 4, 2019, pp. 861–874. https://doi.org/10.1016/j.cja.2019.01.003

[7] Sahai, A., Johnston, C. O., Lopez, B., and Panesi, M., “Flow-Radiation Coupling in CO 2 Hypersonic Wakes Using Reduced-Order Non-Boltzmann Models,” *Physical Review Fluids*, Vol. 4, No. 9, 2019, p. 093401. https://doi.org/10.1103/PhysRevFluids.4.093401

[8] Bao, C., Li, N., Gong, G., Tian, C., and Lu, Y., “A Fast Calculation and Rendering Method for Infrared Characteristics of Hypersonic Vehicle,” *Journal of Physics: Conference Series*, Vol. 1584, No. 1, 2020, p. 012067. https://doi.org/10.1088/1742-6596/1584/1/012067

[9] Hu, S., Tan, J., Li, X., Ye, Q., and Liu, Z., “A Review of Studies on the Infrared Remote Sensing Characteristics of Hypersonic Cruise Vehicles,” presented at the Conference on Optical Sensing and Imaging Technology, Beijing, China, 2020. https://doi.org/10.1117/12.2580355

[10] Candler, G. V., and Leyva, I. A., “Computational Fluid Dynamics Analysis of the Infrared Emission From a Generic Hypersonic Glide Vehicle,” *Science & Global Security*, Vol. 30, No. 3, 2022, pp. 117–130. https://doi.org/10.1080/08929882.2022.2145777

[11] Du, Y., Li, X., Shi, L., Li, F., and Yuan, S., “Optimizing Spectral Waveband Selection for Spectral Radiation Detection of Hypersonic Vehicle,” *IEEE Transactions on Plasma Science*, Vol. 50, No. 11, 2022, pp. 4683–4692. https://doi.org/10.1109/TPS.2022.3208925

[12] Prabhu, D. K., Saunders, D., Cruden, B. A., and Grinstead, J. H., “Simulations of Hayabusa2 Atmospheric Entry and Comparisons with Data from the Imaging Campaign,” presented at the AIAA AVIATION 2022 Forum, Chicago, IL & Virtual, 2022. https://doi.org/10.2514/6.2022-3800

[13] Grosso Ferreira, R., Carvalho, B. B., Alves, L. L., Gonçalves, B., Villace, V. F., Marraffa, L., and Lino Da Silva, M., “VUV to IR Emission Spectroscopy and Interferometry Diagnostics for the European Shock Tube for High-Enthalpy Research,” *Sensors*, Vol. 23, No. 13, 2023, p. 6027. https://doi.org/10.3390/s23136027

[14] Song, X.-X., Zhang, S., Zhang, J.-F., and Zheng, Y., "Study on the Variation of Gas Radiation Characteristics of Hypersonic Reentry Vehicles," *AIAA Journal*, Vol. 61, No. 12, 2023, pp. 5277–5287. https://doi.org/10.2514/1.J063001

[15] Yuan, S., Shi, L., Zhai, Y., Yao, B., Li, F., and Du, Y., "An Unsupervised Classification Method of Flight States for Hypersonic Targets Based on Hyperspectral Features," *Chinese Journal of Aeronautics*, Vol. 36, No. 5, 2023, pp. 434–446. https://doi.org/10.1016/j.cja.2022.11.028

[16] Bian, X., Liu, M., Wang, Y., Liu, H., and Liu, Z., "Analysis of Infrared Radiation Characteristics and Detection Technology of Near-Space Hypersonic Vehicles," presented at the Application of Imaging Technologies in Space, Remote Sensing, Surveying, and Mapping, Security, Etc., Nanjing, China, 2024. https://doi.org/10.1117/12.3017890

[17] Du, X., Yang, Q., Yang, H., Bai, J., and Shi, Y., "Infrared Radiation Characteristics of Dagger-Type Hypersonic Missile," *Chinese Journal of Aeronautics*, Vol. 37, No. 4, 2024, pp. 137–150. https://doi.org/10.1016/j.cja.2023.12.010

[18] Mattes, M. P. W., "What, Exactly, Is an Integrated Air Defense System?," *Michell Forum*, Vol. 26, 2019.

[19] "Defense Budget Overview: United States Department of Defense Fiscal Year 2025 Budget Request," Office of the Under Secretary of Defense Chief Financial Officer, 2024.

[20] Bertin, J., "Hypersonic Aerothermodynamics," American Institute of Aeronautics and Astronautics, Inc., Washington, DC, 1994. https://doi.org/10.2514/4.470363

[21] Braun, R. D., "Thermal Protection Systems," Georgia Institute of Technology, 2022.

[22] Anderson, J. D., "Hypersonic and High-Temperature Gas Dynamics, Third Edition," American Institute of Aeronautics and Astronautics, Inc., Reston, VA, 2019. https://doi.org/10.2514/4.105142

[23] Sawicki, P., Chaudhry, R. S., and Boyd, I. D., "Influence of Chemical Kinetics Models on Plasma Generation in Hypersonic Flight," *AIAA Journal*, 2021, pp. 1–10. https://doi.org/10.2514/1.J060615

[24] Sawicki, S., "Numerical Assessment of Plasma Formation and Potential Mitigation Approaches for Hypersonic Blackout," PhD. University of Colorado Boulder, Boulder, Colorado, 2022.

[25] Liu, Z., Shi, L., Yao, B., Teng, Z., Wang, Y., Li, F., and Chen, Z., "Skywave Ionosphere Communication Channel Characteristics for Hypersonic Vehicles at a Typical Frequency of 14 MHz," *Remote Sensing*, Vol. 17, No. 5, 2025, p. 909. https://doi.org/10.3390/rs17050909

[26] Prata, K. S., Schwartzentruber, T. E., and Minton, T. K., "Air–Carbon Ablation Model for Hypersonic Flight from Molecular-Beam Data," *AIAA Journal*, Vol. 60, No. 2, 2022, pp. 627–640. https://doi.org/10.2514/1.J060516

[27] Cross, P. G., and Boyd, I. D., "Conjugate Analyses of Ablation in Rocket Nozzles," *Journal of Spacecraft and Rockets*, Vol. 56, No. 5, 2019, pp. 1593–1610. https://doi.org/10.2514/1.A34311

[28] Swaminathan-Gopalan, K., Borner, A., Murray, V. J., Poovathingal, S., Minton, T. K., Mansour, N. N., and Stephani, K. A., "Development and Validation of a Finite-Rate Model for Carbon Oxidation

by Atomic Oxygen," *Carbon*, Vol. 137, 2018, pp. 313–332. https://doi.org/10.1016/j.carbon.2018.04.088

[29] Cross, P. G., "Conjugate Analysis of Two-Dimensional Ablation and Pyrolysis in Rocket Nozzles," PhD. The University of Michigan, 2017.

[30] Banerji, N., "The Effects of Radiation on Ablative Heat Shields during Atmospheric Entry," PhD. École Polytechnique Fédérale de Lausanne, 2017.

[31] Martin, A., Cozmuta, I., Wright, M. J., and Boyd, I. D., "Kinetic Rates for Gas-Phase Chemistry of Phenolic-Based Carbon Ablator in Atmospheric Air," *Journal of Thermophysics and Heat Transfer*, Vol. 29, No. 2, 2015, pp. 222–240. https://doi.org/10.2514/1.T4184

[32] Anna, A., and Boyd, I. D., "Numerical Analysis of Surface Chemistry in High-Enthalpy Flows," *Journal of Thermophysics and Heat Transfer*, Vol. 29, No. 4, 2015, pp. 653–670. https://doi.org/10.2514/1.T4530

[33] Alba, C. R., "A Nonequilibrium Finite-Rate Carbon Ablation Model for Radiating Earth Re-Entry Flows," PhD. Air Force Institute of Technology, Wright-Patterson Air Force Base, Ohio, 2015.

[34] Wiebenga, J. E., "High-Fidelity Material Response Modeling as Part of an Aerothermoelastic Framework for Hypersonic Flows," PhD. The University of Michigan, 2014.

[35] Farbar, E. D., Alkandry, H., Wiebenga, J., and Boyd, I. D., "Simulation of Ablating Hypersonic Vehicles with Finite-Rate Surface Chemistry," presented at the 11th AIAA/ASME Joint Thermophysics and Heat Transfer Conference, Atlanta, GA, 2014. https://doi.org/10.2514/6.2014-2124

[36] Martin, A., Scalabrin, L. C., and Boyd, I. D., "High Performance Modeling of Atmospheric Re-Entry Vehicles," *Journal of Physics: Conference Series*, Vol. 341, 2012, p. 012002. https://doi.org/10.1088/1742-6596/341/1/012002

[37] Gosse, R., Gogineni, S., and Roy, S., "Graphite Ablation Experiments in the LHEML Laser Facility," presented at the 43rd AIAA Thermophysics Conference, New Orleans, Louisiana, 2012. https://doi.org/10.2514/6.2012-2745

[38] Marschall, J., and MacLean, M., "A Finite-Rate Surface Reaction Model for the Data-Parallel Line Relaxation (DPLR) Computational Fluid Dynamics Code," Manual, 2011.

[39] Modest, M. F., "Radiative Heat Transfer," Academic Press, New York, 2013.

[40] Bohren, C. F., and Huffman, D. R., "Absorption and Scattering of Light by Small Particles," Wiley, New York, 1983.

[41] Beier, K., "Infrared Radiation Model For Aircraft And Reentry Vehicle," presented at the 32nd Annual Technical Symposium, San Diego, CA, United States, 1988. https://doi.org/10.1117/12.948320

[42] Plastinin, Yu., Vlasov, V., Gorshkov, A., Kovalev, R., and Kuznetsova, L., "Analysis of Nonequilibrium Radiation for Low Density Hypersonic Flows at Low to Moderate Velocities,"

presented at the 7th AIAA/ASME Joint Thermophysics and Heat Transfer Conference, Albuquerque,NM,U.S.A., 1998. https://doi.org/10.2514/6.1998-2466

[43] Boyd, I. D., and Jenniskens, P., "Modeling of Stardust Entry at High Altitude, Part 2: Radiation Analysis," *Journal of Spacecraft and Rockets*, Vol. 47, No. 6, 2010, pp. 901–909. https://doi.org/10.2514/1.37357

[44] Palmer, G. E., White, T., and Pace, A., "Direct Coupling of the NEQAIR Radiation and DPLR CFD Codes," *Journal of Spacecraft and Rockets*, Vol. 48, No. 5, 2011, pp. 836–845. https://doi.org/10.2514/1.52043

[45] Brandis, A., Johnston, C., Cruden, B., Prabhu, D., and Bose, D., "Validation of High Speed Earth Atmospheric Entry Radiative Heating from 9.5 to 15.5 Km/s," presented at the 43rd AIAA Thermophysics Conference, New Orleans, Louisiana, 2012. https://doi.org/10.2514/6.2012-2865

[46] Boyd, I. D., Martin, A., Wiebenga, J. E., and Jenniskens, P., "Hypersonic Flow and Radiation Analysis of the Automated Transfer Vehicle Jules Verne," *Journal of Spacecraft and Rockets*, Vol. 50, No. 1, 2013, pp. 124–136. https://doi.org/10.2514/1.A32208

[47] West, T. K., Johnston, C. O., and Hosder, S., "Uncertainty and Sensitivity Analysis of Afterbody Radiative Heating Predictions for Earth Entry," *Journal of Thermophysics and Heat Transfer*, Vol. 31, No. 2, 2017, pp. 294–306. https://doi.org/10.2514/1.T4948

[48] Johnston, C. O., West, T. K., and Brandis, A. M., "Features of Afterbody Radiative Heating for Titan Entry," 2019. https://doi.org/10.2514/6.2019-3010

[49] Hansson, K., and Boyd, I. D., "Modeling Requirements for Accurate Prediction of Radiative Transfer in Particle Laden Flow," presented at the AIAA Scitech 2020 Forum, Orlando, FL, 2020. https://doi.org/10.2514/6.2020-0734

[50] Saad, A. A., Martinez, C., and Trice, R. W., "Radiation Heat Transfer during Hypersonic Flight: A Review of Emissivity Measurement and Enhancement Approaches of Ultra-high Temperature Ceramics," *International Journal of Ceramic Engineering & Science*, Vol. 5, No. 2, 2023. https://doi.org/10.1002/ces2.10171

[51] Johnston, C. O., and Brandis, A. M., "Features of Afterbody Radiative Heating for Earth Entry," *Journal of Spacecraft and Rockets*, Vol. 52, No. 1, 2015, pp. 105–119. https://doi.org/10.2514/1.A33084

[52] Johnston, C. O., and Kleb, B., "Uncertainty Analysis of Air Radiation for Lunar-Return Shock Layers," *Journal of Spacecraft and Rockets*, Vol. 49, No. 3, 2012, pp. 425–434. https://doi.org/10.2514/1.A32161

[53] Johnston, C., Brandis, A., and Sutton, K., "Shock Layer Radiation Modeling and Uncertainty for Mars Entry," presented at the 43rd AIAA Thermophysics Conference, New Orleans, Louisiana, 2012. https://doi.org/10.2514/6.2012-2866

[54] West, T. K., and Johnston, C. O., "Efficient Parametric Uncertainty Analysis of an Earth Entry Vehicle Concept Using Least Angle Regression," 2023. https://doi.org/10.2514/6.2023-2430

[55] West, T. K., and Hosder, S., "Uncertainty Quantification of Hypersonic Reentry Flows with Sparse Sampling and Stochastic Expansions," *Journal of Spacecraft and Rockets*, Vol. 52, No. 1, 2015, pp. 120–133. https://doi.org/10.2514/1.A32947

[56] West, T. K., Brune, A. J., Hosder, S., and Johnston, C. O., "Uncertainty Analysis of Radiative Heating Predictions for Titan Entry," *Journal of Thermophysics and Heat Transfer*, Vol. 30, No. 2, 2016, pp. 438–451. https://doi.org/10.2514/1.T4620

[57] Brandis, A. M., Johnston, C. O., Cruden, B. A., Prabhu, D., and Bose, D., "Uncertainty Analysis and Validation of Radiation Measurements for Earth Reentry," *Journal of Thermophysics and Heat Transfer*, Vol. 29, No. 2, 2015, pp. 209–221. https://doi.org/10.2514/1.T4000

[58] Brandis, A., Cruden, B., Prabhu, D., Johnston, C., and Bose, D., "Uncertainty Analysis of NEQAIR and HARA Predictions of Air Radiation Measurements Obtained in the EAST Facility," presented at the 42nd AIAA Thermophysics Conference, Honolulu, Hawaii, 2011. https://doi.org/10.2514/6.2011-3478

[59] Cruden, B. A., and Brandis, A. M., "Measurement of Radiative Nonequilibrium for Air Shocks Between 7 and 9 Km/s," *Journal of Thermophysics and Heat Transfer*, Vol. 34, No. 1, 2020, pp. 154–180. https://doi.org/10.2514/1.T5735

[60] Wright, M. J., "Data Parallel Line Relaxation (DPLR) Code User Manual Acadia - Version 4.01.1," User Manual NASA/TM–2009-215388, National Aeronautics and Space Administration, Moffett Field, CA, 2009.

[61] Thompson, K. B., Hollis, B. R., Jonston, C. O., Kleb, B., Lessard, V. R., and Mazaheri, A., "LAURA Users Manual: 5.6," User Manual NASA/TM–2020–220566, National Aeronautics and Space Administration, Langley Research Center, Hampton, Virginia, 2020.

[62] Scalabrin, L. C., "Numerical Simulation of Weakly Ionized Hypersonic Flow Over Reentry Capsules," PhD. The University of Michigan, 2007.

[63] Farbar, E., Boyd, I. D., and Martin, A., "Numerical Prediction of Hypersonic Flowfields Including Effects of Electron Translational Nonequilibrium," *Journal of Thermophysics and Heat Transfer*, Vol. 27, No. 4, 2013, pp. 593–606. https://doi.org/10.2514/1.T3963

[64] Aiken, T. T., and Boyd, Iain. D., "Sensitivity Analysis of Ionization in Two-Temperature Models of Hypersonic Air Flows," *Journal of Thermophysics and Heat Transfer*, 2024, pp. 1–13. https://doi.org/10.2514/1.T6909

[65] McBride, B. J., Gordon, S., and Reno, M., A., "Coefficients for Calculating Thermodynamic and Transport Properties of Individual Species," NASA Technical Memorandum 4513, National Aeronautics and Space Administration, 1993.

[66] Linstrom, P. J., and Mallard, W. G., "The NIST Chemistry WebBook: A Chemical Data Resource on the Internet," *Journal of Chemical & Engineering Data*, Vol. 46, No. 5, 2001, pp. 1059–1063. https://doi.org/10.1021/je000236i

[67] Lee, J.-H., "Basic Governing Equations for the Flight Regimes of Aeroassisted Orbital Transfer Vehicles," presented at the 19th Thermophysics Conference, Snowmass,CO,U.S.A., 1984. https://doi.org/10.2514/6.1984-1729

[68] Vincenti, W. G., and Kruger, C. H., "Introduction to Physical Gas Dynamics," Krieger, Malabar (Fla.), 1986.

[69] Millikan, R. C., and White, D. R., "Systematics of Vibrational Relaxation," *The Journal of Chemical Physics*, Vol. 39, No. 12, 1963, pp. 3209–3213. https://doi.org/10.1063/1.1734182

[70] Gnoffo, A., Gupta, N., and Shinn, L., "Conservation Equations and Physical Models for Hypersonic Air Flows in Thermal and Chemical Nonequilibrium," NASA TP 2867, National Aeronautics and Space Administration, Langley Research Center, Hampton, Virginia, 1989.

[71] Martin, A., and Boyd, I. D., "Strongly Coupled Computation of Material Response and Nonequilibrium Flow for Hypersonic Ablation," *Journal of Spacecraft and Rockets*, Vol. 52, No. 1, 2015, pp. 89–104. https://doi.org/10.2514/1.A32847

[72] Amar, A. J., Blackwell, B. F., and Edwards, J. R., "Development and Verification of a One-Dimensional Ablation Code Including Pyrolysis Gas Flow," *Journal of Thermophysics and Heat Transfer*, Vol. 23, No. 1, 2009, pp. 59–71. https://doi.org/10.2514/1.36882

[73] McBride, B. J., and Gordon, S., "Computer Program for Calculation of Complex Chemical Equilibrium Compositions and Applications," 1311, National Aeronautics and Space Administration, Lewis Research Center, Cleveland, Ohio, 1996.

[74] Candler, G., "Nonequilibrium Processes in Hypervelocity Flows: An Analysis of Carbon Ablation Models," presented at the 50th AIAA Aerospace Sciences Meeting including the New Horizons Forum and Aerospace Exposition, Nashville, Tennessee, 2012. https://doi.org/10.2514/6.2012-724

[75] Scala, S. M., and Gilbert, L. M., "Sublimation of Graphite at Hypersonic Speeds," *AIAA Journal*, Vol. 3, No. 9, 1965, pp. 1635–1644. https://doi.org/10.2514/3.3220

[76] Welsh, W. E. J., "Experimental Results on the Combustion Rate of Graphite Exposed to a Plasma-Arc Flow:," Defense Technical Information Center, Fort Belvoir, VA, August 1963. https://doi.org/10.21236/AD0420941

[77] Miller, I. M., and Sutton, K., "An Experimental Study of the Oxidation of Graphite in High-Temperature Supersonic and Hypersonic Environments," Technical Note NASA TN D-3444, National Aeronautics and Space Administration, Langley Research Center, Hampton, Virginia, 1966.

[78] Perini, L., "Review of Graphite Ablation Theory and Experimental Data," ANSP-M--1, 4286220, December 1971, p. ANSP-M--1, 4286220. https://doi.org/10.2172/4286220

[79] Metzger, J. W., Engel, M. J., and Diaconis, N. S., "Oxidation and Sublimation of Graphite in Simulated Re-Entry Environments.," *AIAA Journal*, Vol. 5, No. 3, 1967, pp. 451–460. https://doi.org/10.2514/3.4001

[80] Zhluktov, S. V., and Abe, T., "Viscous Shock-Layer Simulation of Airflow Past Ablating Blunt Body with Carbon Surface," *Journal of Thermophysics and Heat Transfer*, Vol. 13, No. 1, 1999, pp. 50–59. https://doi.org/10.2514/2.6400

[81] Poovathingal, S., Schwartzentruber, T. E., Murray, V. J., Minton, T. K., and Candler, G. V., "Finite-Rate Oxidation Model for Carbon Surfaces from Molecular Beam Experiments," *AIAA Journal*, Vol. 55, No. 5, 2017, pp. 1644–1658. https://doi.org/10.2514/1.J055371

[82] Weiland, C., "Mechanics of Flow Similarities," Springer, Cham, 2020.

[83] "JANAF THERMOCHEMICAL TABLES Third Edition," *Analytical Chemistry*, Vol. 61, No. 24, 1989, pp. 1378A-1378A. https://doi.org/10.1021/ac00199a720

[84] Brandis, A. M., and Cruden, B. A., "NEQAIR V15.0 Release Notes Nonequilibrium and Equilibrium Radiative Transport and Spectra Program," 2023.

[85] Whiting, E., Park, C., Liu, Y., Arnold, J., and Paterson, J., "NEQAIR96, Nonequilibrium and Equilibrium Radiative Transport and Spectra Program: User's Manual," Manual 1389, National Aeronautics and Space Administration, 1996.

[86] Cruden, B. A., Shulz, J. C., Dean, T. M., Hill, J. P., and Brandis, A. M., "New Features of the NEQAIR Radiation Code," NASA Ames Research Center, 2022.

[87] Lemal, A., Jacobs, C. M., Perrin, M.-Y., Laux, C. O., Tran, P., and Raynaud, E., "Prediction of Nonequilibrium Air Plasma Radiation Behind a Shock Wave," *Journal of Thermophysics and Heat Transfer*, Vol. 30, No. 1, 2016, pp. 197–210. https://doi.org/10.2514/1.T4550

[88] Huo, W. M., Liu, Y., Panesi, M., Wray, A., and Carbon, D. F., "Electron-Impact Excitation Cross Sections for Modeling Non-Equilibrium Gas," presented at the 53rd AIAA Aerospace Sciences Meeting, Kissimmee, Florida, 2015. https://doi.org/10.2514/6.2015-1896

[89] Cruden, B. A., and Brandis, A. M., "Measurement of Radiative Non-Equilibrium for Air Shocks Between 7-9 Km/s," presented at the 47th AIAA Thermophysics Conference, Denver, Colorado, 2017. https://doi.org/10.2514/6.2017-4535

[90] Cruden, B. A., and Brandis, A. M., "Updates to the Neqair Radiation Solver," Update Report, National Aeronautics and Space Administration, Moffett Field, CA, 2015.

[91] Dalbey, K. R., Eldred, M. S., Geraci, G., Jakeman, J. D., Maupin, K. A., Monschke, J. A., Seidl, D. T., Swiler, L. P., and Tran, A., "Dakota, A Multilevel Parallel Object-Oriented Framework for Design Optimization, Parameter Estimation, Uncertainty Quantification, and Sensitivity Analysis: Version 6.16 Theory Manual," Manual, Sandia National Laboratories, 2022.

[92] Adams, B. M., Bohnhoff, W. J., Dalbey, K. R., Ebeida, M. S., Eddy, J. P., Eldred, M. S., Hooper, R. W., Hough, P. D., Hu, K. T., Jakeman, J. D., Khalil, M., Maupin, K. A., Monschke, J. A., Ridgway, E. M., Rushdi, A. A., Seidl, D. T., Stephens, J. A., Swiler, L. P., Tran, A., and Winokur, J. G., "Dakota, A Multilevel Parallel Object-Oriented Framework for Design Optimization, Parameter Estimation, Uncertainty Quantification, and Sensitivity Analysis: Version 6.16 User's Manual," Manual, Sandia National Laboratories, 2022.

[93] Luthen, N., Marelli, S., and Sudret, B., "Sparse Polynomial Chaos Expansions: Solvers, Basis Adaptivity and Meta-Selection," RSUQ-2020-011, 2020.

[94] Marelli, S., Lüthen, N., and Sudret, B., "UQLab User Manual – Polynomial Chaos Expansions," UQLab-V2.0-104, Chair of Risk, Safety and Uncertainty Quantification, Zurich, Sqitzerland, 2022.

[95] Han, D., and Hosder, S., "Inherent and Model-Form Uncertainty Analysis for CFD Simulation of Synthetic Jet Actuators," presented at the 50th AIAA Aerospace Sciences Meeting including the New Horizons Forum and Aerospace Exposition, Nashville, Tennessee, 2012. https://doi.org/10.2514/6.2012-82

[96] West, T. K., Hosder, S., and Johnston, C. O., "Multistep Uncertainty Quantification Approach Applied to Hypersonic Reentry Flows," *Journal of Spacecraft and Rockets*, Vol. 51, No. 1, 2014, pp. 296–310. https://doi.org/10.2514/1.A32592

[97] Holloway, M. E., and Boyd, I. D., "Sensitivity Analysis of Thermochemical Kinetics Modeling for Hypersonic Air Flows," *Journal of Thermophysics and Heat Transfer*, Vol. 36, No. 3, 2022, pp. 584–593. https://doi.org/10.2514/1.T6427

[98] Kuppa, M., Rostkowski, P., Lee, T., Ghanem, R., and Panesi, M., "One Dimensional Modelling and Sensitivity Analysis for the ACT-II Facility," presented at the AIAA AVIATION 2022 Forum, Chicago, IL & Virtual, 2022. https://doi.org/10.2514/6.2022-3502

[99] Aiken, T. T., and Boyd, I. D., "Analysis of Critical Rate Processes for Ionization in Shock-Heated Air," 2023. https://doi.org/10.2514/6.2023-3330

[100] Sudret, B., "Global Sensitivity Analysis Using Polynomial Chaos Expansions," *Reliability Engineering & System Safety*, Vol. 93, No. 7, 2008, pp. 964–979. https://doi.org/10.1016/j.ress.2007.04.002

[101] Crestaux, T., Le Maıˆtre, O., and Martinez, J.-M., "Polynomial Chaos Expansion for Sensitivity Analysis," *Reliability Engineering & System Safety*, Vol. 94, No. 7, 2009, pp. 1161–1172. https://doi.org/10.1016/j.ress.2008.10.008

[102] Askey, R., and Wilson, J. A., "Some Basic Hypergeometric Orthogonal Polynomials That Generalize Jacobi Polynomials," American Mathematical Society, Providence, R.I., U.S.A, 1985.

[103] Hosder, S., Walters, R., and Balch, M., "Efficient Sampling for Non-Intrusive Polynomial Chaos Applications with Multiple Uncertain Input Variables," presented at the 48th AIAA/ASME/ASCE/AHS/ASC Structures, Structural Dynamics, and Materials Conference, Honolulu, Hawaii, 2007. https://doi.org/10.2514/6.2007-1939

[104] Hosder, S., Walters, R. W., and Balch, M., "Point-Collocation Nonintrusive Polynomial Chaos Method for Stochastic Computational Fluid Dynamics," *AIAA Journal*, Vol. 48, No. 12, 2010, pp. 2721–2730. https://doi.org/10.2514/1.39389

[105] Saltelli, A., Aleksankina, K., Becker, W., Fennell, P., Ferretti, F., Holst, N., Li, S., and Wu, Q., "Why so Many Published Sensitivity Analyses Are False: A Systematic Review of Sensitivity Analysis Practices," *Environmental Modelling & Software*, Vol. 114, 2019, pp. 29–39. https://doi.org/10.1016/j.envsoft.2019.01.012

[106] Pianosi, F., Beven, K., Freer, J., Hall, J. W., Rougier, J., Stephenson, D. B., and Wagener, T., "Sensitivity Analysis of Environmental Models: A Systematic Review with Practical Workflow," *Environmental Modelling & Software*, Vol. 79, 2016, pp. 214–232. https://doi.org/10.1016/j.envsoft.2016.02.008

[107] Bose, D., Wright, M. J., and Palmer, G. E., "Uncertainty Analysis of Laminar Aeroheating Predictions for Mars Entries," *Journal of Thermophysics and Heat Transfer*, Vol. 20, No. 4, 2006, pp. 652–662. https://doi.org/10.2514/1.20993

[108] Strand, J., and Goldstein, D., "Sensitivity Analysis for DSMC Simulations of High-Temperature Air Chemistry," presented at the 49th AIAA Aerospace Sciences Meeting including the New Horizons Forum and Aerospace Exposition, Orlando, Florida, 2011. https://doi.org/10.2514/6.2011-535

[109] Strand, J. S., and Goldstein, D. B., "Global Sensitivity Analysis for DSMC Simulations of Hypersonic Shocks," *Journal of Computational Physics*, Vol. 246, 2013, pp. 184–206. https://doi.org/10.1016/j.jcp.2013.03.035

[110] Higdon, K. J., Goldstein, D. B., and Varghese, P. L., "Sensitivity Analysis of Direct Simulation Monte Carlo Parameters for Ionizing Hypersonic Flows," *Journal of Thermophysics and Heat Transfer*, Vol. 32, No. 1, 2018, pp. 90–102. https://doi.org/10.2514/1.T5094

[111] Holloway, M. E., "Detailed Analysis of Thermochemistry Modeling for Hypersonic Air Flows," PhD. The University of Michigan, 2021.

[112] Aiken, T. T., "Detailed Modeling and Sensitivity Analysis of Nonequilibrium Thermochemistry in Shock-Heated Gases," PhD. University of Colorado Boulder, Boulder, Colorado, 2023.

[113] Aiken, T. T., Carter, N. A., and Boyd, I. D., "Sensitivity Analysis and Uncertainty Quantification of Ionization Kinetics in an Electronic State-Resolved Model," presented at the AIAA SciTech Forum, Orlando, Florida, 2025. https://doi.org/10.2514/6.2025-0212

[114] Carter, N. A., and Boyd, I. D., "Sensitivity Analyses of Thermochemical Kinetics for Radiating Ablative Nonequilibrium Hypersonic Flows," presented at the AIAA AVIATION 2024 FORUM, Las Vegas, NV, 2024. https://doi.org/10.2514/6.2024-3948

[115] Carter, N. A., Aiken, T. T., and Boyd, I. D., "Sensitivity Analysis and Uncertainty Quantification of Plasma Formation in Nonequilibrium Hypersonic Airflows," presented at the AIAA SciTech 2025, Orlando, FL, 2025. https://doi.org/10.2514/6.2025-0950

[116] Rataczak, J. A., Boyd, I. D., and McMahon, J. W., "Parametric Sensitivity Analysis and Uncertainty Quantification of Ice Giant Aerocapture Aerothermodynamics," presented at the AIAA AVIATION Conference, Las Vegas, NV, 2024. https://doi.org/10.2514/6.2024-4472

[117] Dunn, M. G., and Kang, S.-W., "Theoretical and Experimental Studies of Reentry Plasmas," NASA CR-2232, National Aeronautics and Space Administration, Washington, DC, 1973.

[118] Gupta, R. N., Yos, J. M., Thompson, R. A., and Lee, K. P., "A Review of Reaction Rates and Thermodynamic and Transport Properties for an 11-Species Air Model for Chemical and Thermal Nonequilibrium Calculations to 30 000k," 1232, National Aeronautics and Space Administration, 1990.

[119] Park, C., Jaffe, R. L., and Partridge, H., "Chemical-Kinetic Parameters of Hyperbolic Earth Entry," *Journal of Thermophysics and Heat Transfer*, Vol. 15, No. 1, 2001, pp. 76–90. https://doi.org/10.2514/2.6582

[120] Sharma, S. P., and Gillespie, W., "Nonequilibrium and Equilibrium Shock Front Radiation Measurements," *Journal of Thermophysics and Heat Transfer*, Vol. 5, No. 3, 1991, pp. 257–265. https://doi.org/10.2514/3.259

[121] Bourdon, A., and Vervisch, P., "Study of a Low-Pressure Nitrogen Plasma Boundary Layer over a Metallic Plate," *Physics of Plasmas*, Vol. 4, No. 11, 1997, pp. 4144–4157. https://doi.org/10.1063/1.872535

[122] Teulet, P., Sarrette, J. P., and Gomes, A. M., "Calculation of Electron Impact Inelastic Cross Sections and Rate Coe$cients for Diatomic Molecules. Application to Air Molecules," 1999. https://doi.org/10.1016/s0022-4073(98)00129-0

[123] Yu, L., Pierrot, L., Laux, C. O., and Kruger, C. H., "Effects of Vibrational Nonequilibrium on the Chemistry of Two-Temperature Nitrogen Plasmas," *Plasma Chemistry and Plasma Processing*, Vol. 21, No. 4, 2001, pp. 483–503. https://doi.org/10.1023/A:1012073800284

[124] Majeed, T., and Strickland, D. J., "New Survey of Electron Impact Cross Sections for Photoelectron and Auroral Electron Energy Loss Calculations," *Journal of Physical and Chemical Reference Data*, Vol. 26, No. 2, 1997, pp. 335–349. https://doi.org/10.1063/1.556008

[125] Itikawa, Y., "Cross Sections for Electron Collisions with Nitrogen Molecules," *Journal of Physical and Chemical Reference Data*, Vol. 35, No. 1, 2006, pp. 31–53. https://doi.org/10.1063/1.1937426

[126] Mertens, J. D., and Hanson, R. K., "A Shock Tube Study of H+HNCO→H2+NCO and the Thermal Decomposition of NCO," *Symposium (International) on Combustion*, Vol. 26, No. 1, 1996, pp. 551–555. https://doi.org/10.1016/S0082-0784(96)80259-1

[127] Baulch, D. L., Bowman, C. T., Cobos, C. J., Cox, R. A., Just, Th., Kerr, J. A., Pilling, M. J., Stocker, D., Troe, J., Tsang, W., Walker, R. W., and Warnatz, J., "Evaluated Kinetic Data for Combustion Modeling: Supplement II," *Journal of Physical and Chemical Reference Data*, Vol. 34, No. 3, 2005, pp. 757–1397. https://doi.org/10.1063/1.1748524

[128] Fujita, K., Yamada, T., and Ishii, N., "Impact of Ablation Gas Kinetics on Hyperbolic Entry Radiative Heating," presented at the 44th AIAA Aerospace Sciences Meeting and Exhibit, Reno, Nevada, 2006. https://doi.org/10.2514/6.2006-1185

[129] Haynes, B. S., Iverach, D., and Kirov, N. Y., "The Behavior of Nitrogen Species in Fuel Rich Hydrocarbon Flames," *Symposium (International) on Combustion*, Vol. 15, No. 1, 1975, pp. 1103–1112. https://doi.org/10.1016/S0082-0784(75)80375-4

[130] Jacobs, A., Wahl, M., Weller, R., and Wolfrum, J., "Measurements of Absolute Rate Coefficients for the Reactions of CN Radicals with H2O, H2, and CO2 in the Temperature Range 295 K≤T≤1027 K," *Symposium (International) on Combustion*, Vol. 22, No. 1, 1989, pp. 1093–1100. https://doi.org/10.1016/S0082-0784(89)80119-5

[131] Balla, R. J., and Casleton, K. H., "Kinetic Study of the Reactions of Cyanyl Radical with Oxygen and Carbon Dioxide from 292 to 1500 K Using High-Temperature Photochemistry," *The Journal of Physical Chemistry*, Vol. 95, No. 6, 1991, pp. 2344–2351. https://doi.org/10.1021/j100159a042

[132] Wang, N. S., Yang, D. L., Lin, M. C., and Melius, C. F., "Kinetics of CN Reactions with N_2O and CO_2," *International Journal of Chemical Kinetics*, Vol. 23, No. 2, 1991, pp. 151–160. https://doi.org/10.1002/kin.550230206

[133] Lindackers, D., Burmeister, M., and Roth, P., "High-Temperature Kinetics of the Reaction CN + CO2," *Combustion and Flame*, Vol. 81, Nos. 3–4, 1990, pp. 251–259. https://doi.org/10.1016/0010-2180(90)90023-K

[134] Tsang, W., "Chemical Kinetic Data Base for Propellant Combustion. II. Reactions Involving CN, NCO, and HNCO," *Journal of Physical and Chemical Reference Data*, Vol. 21, No. 4, 1992, pp. 753–791. https://doi.org/10.1063/1.555914

[135] Zhao, R., Gao, D., Pan, X., Song, L., Yu, H., Yu, S., and Yao, L., "Anharmonic Effect of the Reactions Related to Cyano Radical as Reactant in Fuel Combustion Mechanism," *Chemical Physics*, Vol. 516, 2019, pp. 38–47. https://doi.org/10.1016/j.chemphys.2018.08.035

[136] Bose, D., and Candler, G. V., "Thermal Rate Constants of the O2+N→NO+O Reaction Based on the A2′and A4′ Potential-Energy Surfaces," *The Journal of Chemical Physics*, Vol. 107, No. 16, 1997, pp. 6136–6145. https://doi.org/10.1063/1.475132

[137] Park, C., Howe, J. T., Jaffe, R. L., and Candler, G. V., "Review of Chemical-Kinetic Problems of Future NASA Missions. II - Mars Entries," *Journal of Thermophysics and Heat Transfer*, Vol. 8, No. 1, 1994, pp. 9–23. https://doi.org/10.2514/3.496

[138] Boyd, I. D., and Josyula, E., "Analysis of Associative Ionization Rates for Hypersonic Flows," *Journal of Thermophysics and Heat Transfer*, Vol. 35, No. 3, 2021, pp. 484–493. https://doi.org/10.2514/1.T6109

[139] Padellec, A. L., "Partial Near Threshold Cross Sections for the Associative Ionization to Form CO^+, NO^+ and O^{2+}," *Physica Scripta*, Vol. 71, No. 6, 2005, pp. 621–626. https://doi.org/10.1088/0031-8949/71/6/008

[140] Yang, D., and Guo, H., "A Time-Dependent Quantum Approach to Dissociative Recombination, Associative Ionization, and Penning Ionization," *The Journal of Chemical Physics*, Vol. 159, No. 4, 2023, p. 044105. https://doi.org/10.1063/5.0156998

[141] Gokcen, T., "N2-CH4-Ar Chemical Kinetic Model for Simulations of Atmospheric Entry to Titan," *Journal of Thermophysics and Heat Transfer*, Vol. 21, No. 1, 2007, pp. 9–18. https://doi.org/10.2514/1.22095

[142] Kim, J. G., "Expansion of the Equilibrium Constants for the Temperature Range of 300K to 20,000K," *International Journal of Aeronautical and Space Sciences*, Vol. 17, No. 4, 2016, pp. 455–466. https://doi.org/10.5139/IJASS.2016.17.4.455

[143] Hierl, P. M., Dotan, I., Seeley, J. V., Van Doren, J. M., Morris, R. A., and Viggiano, A. A., "Rate Constants for the Reactions of O+ with N2 and O2 as a Function of Temperature (300–1800 K)," *The Journal of Chemical Physics*, Vol. 106, No. 9, 1997, pp. 3540–3544. https://doi.org/10.1063/1.473450

[144] Levandier, D. J., Dressler, R. A., Chiu, Y., and Murad, E., "The Reaction of O+(4S) and N2(X 1Σg+) Revisited: Recoil Velocity Analysis of the NO+ Product," *The Journal of Chemical Physics*, Vol. 111, No. 9, 1999, pp. 3954–3960. https://doi.org/10.1063/1.479697

[145] Dunn, M. G., and Lordi, J. A., "Measurement of N2/plus/ plus e/-/ Dissociative Recombination in Expanding Nitrogen Flows," *AIAA Journal*, Vol. 8, No. 2, 1970, pp. 339–345. https://doi.org/10.2514/3.5666

[146] Liechty, D. S., and Lewis, M. J., "Extension of a Kinetic-Theory Approach for Computing Chemical-Reaction Rates to Reactions with Charged Particles," presented at the 27TH INTERNATIONAL SYMPOSIUM ON RAREFIED GAS DYNAMICS, Pacific Grove, California, (USA), 2011. https://doi.org/10.1063/1.3562813

[147] Phelps, A. V., "Cross Sections and Swarm Coefficients for Nitrogen Ions and Neutrals in N2 and Argon Ions and Neutrals in Ar for Energies from 0.1 eV to 10 keV," *Journal of Physical and Chemical Reference Data*, Vol. 20, No. 3, 1991, pp. 557–573. https://doi.org/10.1063/1.555889

[148] Bird, G., "Nonequilibrium Radiation during Re-Entry at 10 Km/s," presented at the 22nd Thermophysics Conference, Honolulu,HI,U.S.A., 1987. https://doi.org/10.2514/6.1987-1543

[149] Fangman, A. J., and Andrienko, D. A., "Vibrational-Specific Model of Simultaneous N2−N and N2−N2 Relaxation Under Postshock Conditions," *Journal of Thermophysics and Heat Transfer*, Vol. 36, No. 3, 2022, pp. 568–583. https://doi.org/10.2514/1.T6441

[150] Torres, E., Geistfeld, E. C., and Schwartzentruber, T. E., "Direct Molecular Simulation of Rovibrational Relaxation and Chemical Reactions in Air Mixtures," presented at the AIAA SCITECH 2022 Forum, San Diego, CA & Virtual, 2022. https://doi.org/10.2514/6.2022-1010

[151] Streicher, J. W., Krish, A., and Hanson, R. K., "Coupled Vibration-Dissociation Time-Histories and Rate Measurements in Shock-Heated, Nondilute O2 and O2–Ar Mixtures from 6000 to 14 000 K," *Physics of Fluids*, Vol. 33, No. 5, 2021, p. 056107. https://doi.org/10.1063/5.0048059

[152] Grover, M. S., Schwartzentruber, T. E., Varga, Z., and Truhlar, D. G., "Vibrational Energy Transfer and Collision-Induced Dissociation in O+O2 Collisions," *Journal of Thermophysics and Heat Transfer*, Vol. 33, No. 3, 2019, pp. 797–807. https://doi.org/10.2514/1.T5551

[153] Hao, J., Wang, J., and Lee, C., "Modeling of Electron Impact Ionization for Hypersonic Nonequilibrium Simulations," *Journal of Thermophysics and Heat Transfer*, Vol. 32, No. 1, 2018, pp. 262–268. https://doi.org/10.2514/1.T5193

[154] Johnston, C. O., Hollis, B. R., and Sutton, K., "Non-Boltzmann Modeling for Air Shock-Layer Radiation at Lunar-Return Conditions," *Journal of Spacecraft and Rockets*, Vol. 45, No. 5, 2008, pp. 879–890. https://doi.org/10.2514/1.33006

[155] Marsh, H., O'Hair, T. E., and Wynne-Jones, Lord, "The Carbon-Atomic Oxygen Reaction—Surface-Oxide Formation on Paracrystalline Carbon and Graphite," *Carbon*, Vol. 7, No. 5, 1969, pp. 555–566. https://doi.org/10.1016/0008-6223(69)90028-1

[156] Rosner, D. E., and Allendorf, H. D., "Kinetics of the Attack of Refractory Materials by Dissociated Gases," *Heterogeneous Kinetics at Elevated Temperatures*, edited by G. R. Belton and W. L.

Worrell, Springer US, Boston, MA, 1970, pp. 231–251. https://doi.org/10.1007/978-1-4684-8065-8_9

[157] Rosner, D. E., and Allendorf, H. D., "Comparative Studies of the Attack of Pyrolytic and Isotropic Graphite by Atomic and Molecular Oxygen at High Temperatures.," *AIAA Journal*, Vol. 6, No. 4, 1968, pp. 650–654. https://doi.org/10.2514/3.4558

[158] Liu, G. N.-K., "High Temperature Oxidation of Graphite by a Dissociated Oxygen Beam:," Defense Technical Information Center, Fort Belvoir, VA, August 1973. https://doi.org/10.21236/AD0779949

[159] Berkowitz-Mattuck, J. B., "Research to Determine the Effects of Surface Catalycity on Materials Behavior in Dissociated Gas Streams - ATJ Graphite," AFML-TR-70-172, Arthur D. Little, Inc., Cambridge, Massachusetts, 1970.

[160] Maahs, H. G., "Ablation Performance of Glasslike Carbons, Pyrolytic Graphite, and ARtificial Graphite in the Stagnation Pressure Range 0.035 to 15 Atmospheres," Technical Note NASA TN D-7005, National Aeronautics and Space Administration, Langley Research Center, Hampton, Virginia, 1970.

[161] Lundell, J. H., and Dickey, R. R., "Ablation of ATJ Graphite at High Temperatures," *AIAA Journal*, Vol. 11, No. 2, 1973, pp. 216–222. https://doi.org/10.2514/3.50451

[162] Park, C., "Effects of Atomic Oxygen on Graphite Ablation," *AIAA Journal*, 1976. https://doi.org/10.2514/3.7267

[163] Thomas, J. M., "Microscopic Studies of Graphite Oxidation," *Chemistry and Physics of Carbon*, edited by P. L. Walker, Vol. 1, Marcel Dekker, New York, 1965, pp. 122–202.

[164] Olander, D. R., Jones, R. H., Schwarz, J. A., and Siekhaus, W. J., "Reactions of Modulated Molecular Beams with Pyrolytic Graphite. II Oxidation of the Prism Plane," *The Journal of Chemical Physics*, Vol. 57, No. 1, 1972, pp. 421–433. https://doi.org/10.1063/1.1677981

[165] Knight, D., and Knechtel, E. D., "Graphite Oxidation at Low Temperature in Subsonic Air," presented at the 8th Thermophysics Conference, Palm Springs,CA,U.S.A., 1973. https://doi.org/10.2514/6.1973-735

[166] Okada, J., and Ikegawa, T., "Combustion Rate of Artificial Graphites from 700°C to 2000°C in Air," *Journal of Applied Physics*, Vol. 24, No. 9, 1953, pp. 1249–1250. https://doi.org/10.1063/1.1721483

[167] Nagle, J., and Strickland-Constable, R. F., "Oxidation of Carbon Between 1000–2000°C," *Proceedings of the Fifth Conference on Carbon*, Elsevier, 1962, pp. 154–164. https://doi.org/10.1016/B978-0-08-009707-7.50026-1

[168] Golovina, E. S., and Khaustovich, G. P., "The Interaction of Carbon with Carbon Dioxide and Oxygen at Temperatures up to 3000°k," *Symposium (International) on Combustion*, Vol. 8, No. 1, 1961, pp. 784–792. https://doi.org/10.1016/S0082-0784(06)80573-4

[169] Stern, J. H., and Gregory, N. W., "The Condensation Coefficient of Iodine," *The Journal of Physical Chemistry*, Vol. 61, No. 9, 1957, pp. 1226–1232. https://doi.org/10.1021/j150555a021

[170] Palmer, H. B., and Shelf, M., "Vaporization of Carbon," *Chemistry and Physics of Carbon*, edited by P. L. Walker, Vol. 4, Marcel Dekker, New York, 1968.

[171] Dolton, T., Goldstein, H., and Maurer, R., "Thermodynamic Performance of Carbon in Hyperthermal Environments," presented at the 3rd Thermophysics Conference, Los Angeles,CA,U.S.A., 1968. https://doi.org/10.2514/6.1968-754

[172] Park, C., "Review of Chemical-Kinetic Problems of Future NASA Missions. I - Earth Entries," *Journal of Thermophysics and Heat Transfer*, Vol. 7, No. 3, 1993, pp. 385–398. https://doi.org/10.2514/3.431

[173] Streicher, J. W., Krish, A., and Hanson, R. K., "High-Temperature Vibrational Relaxation and Decomposition of Shock-Heated Nitric Oxide. I. Argon Dilution from 2200 to 8700 K," *Physics of Fluids*, Vol. 34, No. 11, 2022, p. 116122. https://doi.org/10.1063/5.0109109

[174] Kim, J. G., and Boyd, I. D., "Thermochemical Nonequilibrium Analysis of O2+Ar Based on State-Resolved Kinetics," *Chemical Physics*, Vol. 446, 2015, pp. 76–85. https://doi.org/10.1016/j.chemphys.2014.11.009

[175] Starik, A. M., Titova, N. S., and Arsentiev, I. V., "Comprehensive Analysis of the Effect of Atomic and Molecular Metastable State Excitation on Air Plasma Composition behind Strong Shock Waves," *Plasma Sources Science and Technology*, Vol. 19, No. 1, 2010, p. 015007. https://doi.org/10.1088/0963-0252/19/1/015007

[176] Henriques, J., Tatarova, E., and Ferreira, C. M., "Microwave N2–Ar Plasma Torch. I. Modeling," *Journal of Applied Physics*, Vol. 109, No. 2, 2011, p. 023301. https://doi.org/10.1063/1.3532055

[177] Ma, G., Suto, M., and Lee, L. C., "NO (γ) Emission by Energy Transfer from NO+ (a) to NO," *Chemical Physics Letters*, Vol. 176, No. 1, 1991, pp. 141–145. https://doi.org/10.1016/0009-2614(91)90024-4

[178] Park, C., "Assessment of a Two-Temperature Kinetic Model for Dissociating and Weakly Ionizing Nitrogen," *Journal of Thermophysics and Heat Transfer*, Vol. 2, No. 1, 1988, pp. 8–16. https://doi.org/10.2514/3.55

[179] Kuntz, D. W., Hassan, B., and Potter, D. L., "Predictions of Ablating Hypersonic Vehicles Using an Iterative Coupled Fluid/Thermal Approach," *Journal of Thermophysics and Heat Transfer*, Vol. 15, No. 2, 2001, pp. 129–139. https://doi.org/10.2514/2.6594

[180] Carter, N. A., and Boyd, I. D., "Sensitivity Analyses of Thermochemical Kinetics for Radiating Ablative Nonequilibrium Hypersonic Flows," *Journal of Thermophysics and Heat Transfer*, 2025, pp. 1–18. https://doi.org/10.2514/1.t7119

[181] Carter, N. A., and Boyd, I. D., "Sensitivity Analyses of Thermochemical Kinetics for Radiating Ablative Nonequilibrium Hypersonic Flows," *Journal of Thermophysics and Heat Transfer (to be published)*, 2025.

[182] Chaudhry, R. S., Bender, J. D., Schwartzentruber, T. E., and Candler, G. V., "Quasiclassical Trajectory Analysis of Nitrogen for High-Temperature Chemical Kinetics," *Journal of Thermophysics and Heat Transfer*, Vol. 32, No. 4, 2018, pp. 833–845. https://doi.org/10.2514/1.T5484

[183] Adams, B. M., Bohnhoff, W. J., Canfield, R. A., Coomber, W. P., Dalbey, K. R., Eddy, J. P., Eldred, M. S., Geraci, G., Hooper, R. W., Hough, P. D., Hu, K. T., Jakeman, J. D., Kent, C., Khalil, M., Maupin, K. A., Monschke, J. A., Portone, T., Ridgway, M., Rushdi, A. A., Seidl, D. T., Stephens, J. A., Swiler, L. P., Tran, A., Vigil, D. M., Wildey, T. M., Winokur, J. G., and Zeng, X., "Dakota, A Multilevel Parallel Object-Oriented Framework for Design Optimization, Parameter Estimation, Uncertainty Quantification, and Sensitivity Analysis: Version 6.16 Reference Manual," Manual, Sandia National Laboratories, 2022.

[184] "Optics and Photonics - Spectral Bands," ISO 20473:2007, International Organization for Standardization, 2007.

[185] Davis, G., Mallat, S., and Avellaneda, M., "Adaptive Greedy Approximations," *Constructive Approximation*, Vol. 13, 1997, pp. 57–98.

[186] Efron, B., Hastie, T., Johnstone, I., and Tibshirani, R., "Least Angle Regression," *The Annals of Statistics*, Vol. 32, No. 2, 2004, pp. 407–499.

[187] Tibshirani, R., "Regression Shrinkage and Selection Via the Lasso," *Journal of the Royal Statistical Society: Series B (Methodological)*, Vol. 58, No. 1, 1996, pp. 267–288. https://doi.org/10.1111/j.2517-6161.1996.tb02080.x

[188] Diaz, P., Doostan, A., and Hampton, J., "Sparse Polynomial Chaos Expansions via Compressed Sensing and D-Optimal Design," *Computer Methods in Applied Mechanics and Engineering*, Vol. 336, 2018, pp. 640–666. https://doi.org/10.1016/j.cma.2018.03.020

[189] Babacan, S. D., Molina, R., and Katsaggelos, A. K., "Bayesian Compressive Sensing Using Laplace Priors," *IEEE Transactions on Image Processing, Image Processing, IEEE Transactions on, IEEE Trans. on Image Process.*, Vol. 19, No. 1, 2010, pp. 53–63. https://doi.org/10.1109/TIP.2009.2032894

[190] Park, C., "Two-Temperature Interpretation of Dissociation Rate Data for N2 and O2," presented at the 26th Aerospace Sciences Meeting, Reno,NV,U.S.A., 1988. https://doi.org/10.2514/6.1988-458

[191] Koshi, M., Bando, S., Saito, M., and Asaba, T., "Dissociation of Nitric Oxide in Shock Waves," *Symposium (International) on Combustion*, Vol. 17, No. 1, 1979, pp. 553–562. https://doi.org/10.1016/S0082-0784(79)80056-9

[192] Wray, K. L., and Teare, J. D., "Shock-Tube Study of the Kinetics of Nitric Oxide at High Temperatures," *The Journal of Chemical Physics*, Vol. 36, No. 10, 1962, pp. 2582–2596. https://doi.org/10.1063/1.1732338

[193] Nelson, H. F., Park, C., and Whiting, E. E., "Titan Atmospheric Composition by Hypervelocity Shock-Layer Analysis," *Journal of Thermophysics and Heat Transfer*, Vol. 5, No. 2, 1991, pp. 157–165. https://doi.org/10.2514/3.243

[194] Johnston, C. O., and Brandis, A. M., "Modeling of Nonequilibrium CO Fourth-Positive and CN Violet Emission in CO2–N2 Gases," *Journal of Quantitative Spectroscopy and Radiative Transfer*, Vol. 149, 2014, pp. 303–317. https://doi.org/10.1016/j.jqsrt.2014.08.025

[195] Ebrahim, N. A., and Sandeman, R. J., “Interferometric Studies of Carbon Dioxide Dissociation in a Free-Piston Shock Tube,” *The Journal of Chemical Physics*, Vol. 65, No. 9, 1976, pp. 3446–3453. https://doi.org/10.1063/1.433598

[196] Thorne, L. R., Branch, M. C., Chandler, D. W., Kee, R. J., and Miller, J. A., “Hydrocarbon/Nitric Oxide Interactions in Low-Pressure Flames,” *Symposium (International) on Combustion*, Vol. 21, No. 1, 1988, pp. 965–977. https://doi.org/10.1016/S0082-0784(88)80328-X

[197] Kroupnov, A. A., and Pogosbekian, M. Ju., “Detailed Mechanism of Exchange Reactions CO + N, CN + O and NO + C on the 4A″ Potential Energy Surface at High Temperature,” *Chemical Physics*, Vol. 523, 2019, pp. 172–178. https://doi.org/10.1016/j.chemphys.2019.04.026

[198] Geppert, W. D., Reignier, D., Stoecklin, T., Naulin, C., Costes, M., Chastaing, D., Le Picard, S. D., Sims, I. R., and Smith, I. W. M., “Comparison of the Cross-Sections and Thermal Rate Constants for the Reactions of C(3PJ) Atoms with O2 and NO,” *Physical Chemistry Chemical Physics*, Vol. 2, No. 13, 2000, pp. 2873–2881. https://doi.org/10.1039/b002583f

[199] Luo, H., Kulakhmetov, M., and Alexeenko, A., “*Ab Initio* State-Specific N2 + O Dissociation and Exchange Modeling for Molecular Simulations,” *The Journal of Chemical Physics*, Vol. 146, No. 7, 2017, p. 074303. https://doi.org/10.1063/1.4975770

[200] Slack, M. W., “Kinetics and Thermodynamics of the CN Molecule. III. Shock Tube Measurement of CN Dissociation Rates,” *The Journal of Chemical Physics*, Vol. 64, No. 1, 1976, pp. 228–236. https://doi.org/10.1063/1.431955

[201] Louge, M. Y., and Hanson, R. K., “Shock Tube Study of Cyanogen Oxidation Kinetics,” *International Journal of Chemical Kinetics*, Vol. 16, No. 3, 1984, pp. 231–250. https://doi.org/10.1002/kin.550160306

[202] Natarajan, K., Woiki, D., and Roth, P., “N-Atom Measurements in High Temperature C2N2/NO/Ar Reaction Systems,” *International Journal of Chemical Kinetics*, Vol. 29, No. 1, 1997, pp. 35–41. https://doi.org/10.1002/(SICI)1097-4601(1997)29:1<35::AID-KIN5>3.0.CO;2-M

[203] Baulch, D. L., Cobos, C. J., Cox, R. A., Frank, P., Hayman, G., Just, Th., Kerr, J. A., Murrells, T., Pilling, M. J., Troe, J., Walker, R. W., and Warnatz, J., “Evaluated Kinetic Data for Combustion Modeling. Supplement I,” *Journal of Physical and Chemical Reference Data*, Vol. 23, No. 6, 1994, pp. 847–848. https://doi.org/10.1063/1.555953

[204] Park, C. S., “Studies of Radiation Emission from the Simulated Shock Layer of the Huygens Probe,” PhD. Stanford University, 1991.

[205] Ibragimova, L. B., *Zhurnal Fizicheskoi Khimii*, Vol. 10, 1991, pp. 307–310.

[206] Avramenko, L. I., and Krasnen’kov, V. M., “Reactions of Nitrogen Atoms Communication 6. Rate Constant and Mechanism of the Elementary Reaction of Nitrogen Atoms with Carbon Dioxide,” *Institute of Chemical Physics, Academy of Sciences of the USSR*, Vol. 3, 1967, pp. 516–519.

[207] Becker, K. H., Kurtenbach, R., Schmidt, F., and Wiesen, P., “Kinetics of the Reactions of NCO Radicals with NO and NH_3,” *Berichte der Bunsengesellschaft für physikalische Chemie*, Vol. 101, No. 1, 1997, pp. 128–133. https://doi.org/10.1002/bbpc.19971010117

[208] Becker, K. H., Kurtenbach, R., Schmidt, F., and Wiesen, P., "Kinetics of the NCO Radical Reacting with Atoms and Selected Molecules," *Combustion and Flame*, Vol. 120, No. 4, 2000, pp. 570–577. https://doi.org/10.1016/S0010-2180(99)00108-X

[209] Park, C., "Assessment of Two-Temperature Kinetic Model for Ionizing Air," *Journal of Thermophysics and Heat Transfer*, Vol. 3, No. 3, 1989, pp. 233–244. https://doi.org/10.2514/3.28771

[210] Lüthen, N., Marelli, S., and Sudret, B., "Sparse Polynomial Chaos Expansions: Literature Survey and Benchmark," *SIAM/ASA J. Uncertainty Quantification (2021), 9(2), 593-649*, 2020. https://doi.org/10.1137/20M1315774

[211] Van Den Berg, E., and Friedlander, M. P., "Probing the Pareto Frontier for Basis Pursuit Solutions.," *SIAM Journal on Scientific Computing*, Vol. 31, No. 2, 2009, pp. 890–912. https://doi.org/10.1137/080714488

[212] Keck, J. C., Camm, J. C., Kivel, B., and Wentink, T., "Radiation from Hot Air," *Annals of Physics*, Vol. 7, 1959, pp. 1–38.

[213] Johnston, C. O., "Comparison between Hayabusa 2 Spectral Measurements and Simulations," presented at the AIAA AVIATION 2022 Forum, Chicago, IL & Virtual, 2022. https://doi.org/10.2514/6.2022-3799

[214] Diaconis, N. S., Gorsuch, P. D., and Sheridan, R. A., "The Ablation of Graphite in Dissociated Air Part Ii: Experimental Investigation," AD 290051, Space Sciences Laboratory, Los Angeles, California, 1962.

[215] Milos, F., Chen, Y.-K., Milos, F., and Chen, Y.-K., "Comprehensive Model for Multicomponent Ablation Thermochemistry," presented at the 35th Aerospace Sciences Meeting and Exhibit, Reno,NV,U.S.A., 1997. https://doi.org/10.2514/6.1997-141

[216] Milos, F. S., and Chen, Y.-K., "Ablation, Thermal Response, and Chemistry Program for Analysis of Thermal Protection Systems," *Journal of Spacecraft and Rockets*, Vol. 50, No. 1, 2013, pp. 137–149. https://doi.org/10.2514/1.A32302

[217] Hunter, L. W., Perini, L. L., Conn, D. W., and Brenza, P. T., "Calculation of Carbon Ablation on a Re-Entry Body during Supersonic/Subsonic Flight," *Journal of Spacecraft and Rockets*, Vol. 23, No. 5, 1986, pp. 487–491. https://doi.org/10.2514/3.25834

[218] King, H. H. C., Muramoto, K. K., Murray, A. L., and Pronchick, S. W., "ABRES Shape Change Code (ASCC86)," Technical Report and User's Manual BMO TR-87-57, Acruex Corp., Aerotherm Div., Mountain View, CA, 1986.

[219] Hampton, J., and Doostan, A., "Coherence Motivated Sampling and Convergence Analysis of Least Squares Polynomial Chaos Regression," *Computer Methods in Applied Mechanics and Engineering*, Vol. 290, 2015, pp. 73–97. https://doi.org/10.1016/j.cma.2015.02.006

[220] Hampton, J., and Doostan, A., "Compressive Sampling of Polynomial Chaos Expansions: Convergence Analysis and Sampling Strategies," *Journal of Computational Physics*, Vol. 280, 2015, pp. 363–386. https://doi.org/10.1016/j.jcp.2014.09.019

[221] Hampton, J., and Doostan, A., “Basis Adaptive Sample Efficient Polynomial Chaos (BASE-PC),” *Journal of Computational Physics*, Vol. 371, 2018, pp. 20–49. https://doi.org/10.1016/j.jcp.2018.03.035

[222] Chaudhry, R. S., and Candler, G. V., “Statistical Analyses of Quasiclassical Trajectory Data for Air Dissociation,” presented at the AIAA Scitech 2019 Forum, San Diego, California, 2019. https://doi.org/10.2514/6.2019-0789

[223] Chaudhry, R. S., Boyd, I. D., and Candler, G. V., “Vehicle-Scale Simulations of Hypersonic Flows Using the MMT Chemical Kinetics Model,” presented at the AIAA AVIATION 2020 FORUM, VIRTUAL EVENT, 2020. https://doi.org/10.2514/6.2020-3272

[224] Pogosbekian, J., and Losev, S. A., “Investigation of the Reaction of CO + N -> CN + O by the Quasiclassical Trajectories Method Using MD Trajectory Software,” *Chemical Physics*, Vol. 22, 2003, pp. 38–46.

[225] Thirani, S., Karpuzcu, I. T., and Levin, D. A., “Modeling of Nitric Oxide Vibrational Level Populations for High Mach Number Flows,” *Journal of Thermophysics and Heat Transfer*, 2025, pp. 1–15. https://doi.org/10.2514/1.T7111

[226] Karpuzcu, I. T., Thirani, S., Levin, D. A., and Andrienko, D., “Nitric Oxide Infrared Radiation Modeling from a Hypersonic Flow,” presented at the AIAA AVIATION 2022 Forum, Chicago, IL & Virtual, 2022. https://doi.org/10.2514/6.2022-3501

[227] Appleton, J. P., Steinberg, M., and Liquornik, D. J., “Shock-Tube Study of Nitrogen Dissociation Using Vacuum-Ultraviolet Light Absorption,” *The Journal of Chemical Physics*, Vol. 48, No. 2, 1968, pp. 599–608. https://doi.org/10.1063/1.1668690

[228] Jerig, L., Thielen, K., and Roth, P., “High-Temperature Dissociation of Oxygen Diluted in Argon or Nitrogen,” *AIAA Journal*, Vol. 29, No. 7, 1991, pp. 1136–1139. https://doi.org/10.2514/3.10714

[229] Bortner, M. H., “A Review of Rate Constants of Selected Reactions of Interest in Re-Entry Flow Fields in the Atmosphere,” NBS TN 484, National Bureau of Standards, Gaithersburg, MD, 1969, p. NBS TN 484. https://doi.org/10.6028/NBS.TN.484

[230] Appleton, J. P., Steinberg, M., and Liquornik, D. J., “Shock-Tube Study of Carbon Monoxide Dissociation Using Vacuum-Ultraviolet Absorption,” *The Journal of Chemical Physics*, Vol. 52, No. 5, 1970, pp. 2205–2221. https://doi.org/10.1063/1.1673286

[231] Husain, D., and Young, A. N., “Kinetic Investigation of Ground State Carbon Atoms, C(2’Ps),” *Journal of the Chemical Society, Faraday Transactions 2*, Vol. 71, 1975.

[232] Klippenstein, S. J., and Kim, Y.-W., “Variational Statistical Study of the CN+O2 Reaction Employing *Ab Initio* Determined Properties for the Transition State,” *The Journal of Chemical Physics*, Vol. 99, No. 8, 1993, pp. 5790–5799. https://doi.org/10.1063/1.465930

[233] Dunkin, D. B., Fehsenfeld, F. C., Schmeltekopf, A. L., and Ferguson, E. E., “Ion–Molecule Reaction Studies from 300° to 600°K in a Temperature-Controlled Flowing Afterglow System,” *The Journal of Chemical Physics*, Vol. 49, No. 3, 1968, pp. 1365–1371. https://doi.org/10.1063/1.1670232

[234] Schmeltekopf, A. L., Fehsenfeld, F. C., Oilman, G. I., and Ferguson, E. E., "Reaction of Atomic Oxygen Ions with Vibrationally Excited Nitrogen Molecules," *Planetary and Space Science*, Vol. 15, No. 3, 1967, pp. 401–406. https://doi.org/10.1016/0032-0633(67)90152-3

[235] Neynaber, R. H., Rutherford, J. A., and Vroom, D. A., "Report on Electronic and Ionic Reactions in Atmospheric Gases," AD-752582, Defense Nuclear Agency, Springfield, VA, 1972.

[236] Lindinger, W., Fehsenfeld, F. C., Schmeltekopf, A. L., and Ferguson, E. E., "Temperature Dependence of Some Ionospheric Ion-Neutral Reactions from 300°-900°K," *Journal of Geophysical Research*, Vol. 79, No. 31, 1974, pp. 4753–4756. https://doi.org/10.1029/JA079i031p04753

[237] Park, C., and Menees, G. P., "Odd Nitrogen Production by Meteoroids," *Journal of Geophysical Research: Oceans*, Vol. 83, No. C8, 1978, pp. 4029–4035. https://doi.org/10.1029/JC083iC08p04029

[238] Batey, P. H., Court, G. R., and Sayers, J., "Afterglow Measurements of the Rate Coefficients for the Reactions O+ + O2 → O2+ + O and O+ + N2 → NO+ + N," *Planetary and Space Science*, Vol. 13, No. 9, 1965, pp. 911–917. https://doi.org/10.1016/0032-0633(65)90176-5

[239] Espy, P. J., and Pendleton, W. R., "N 2 + Meinel Band Quenching Coefficients for Vibrational Levels 0 and 1," *The Journal of Chemical Physics*, Vol. 161, No. 10, 2024, p. 104302. https://doi.org/10.1063/5.0223913

[240] Piper, L. G., Green, B. D., Blumberg, W. A. M., and Wolnik, S. J., "N2+ Meinel Band Quenching," *The Journal of Chemical Physics*, Vol. 82, No. 7, 1985, pp. 3139–3145. https://doi.org/10.1063/1.448211

[241] Dilecce, G., Ambrico, P. F., and De Benedictis, S., "On the Collision Quenching of {\rm N}_2^+(B\,^2\Sigma_{\rm U}^+, V=0) by N_2 and O_2 and Its Influence on the Measurement of *E* / *N* by Intensity Ratio of Nitrogen Spectral Bands," *Journal of Physics D: Applied Physics*, Vol. 43, No. 19, 2010, p. 195201. https://doi.org/10.1088/0022-3727/43/19/195201

[242] Piper, L. G., "The Excitation of O(1 *S*) in the Reaction between N2(*A* 3Σ+ *u*) and O(3 *P*)," *The Journal of Chemical Physics*, Vol. 77, No. 5, 1982, pp. 2373–2377. https://doi.org/10.1063/1.444158

[243] Souza, A. R. D., Gousset, G., Touzeau, M., and Khiet, T., "Note on the Determination of the Efficiency of the Reaction N_2 (A^3 Σ)+O(^{3} P) to N_2 +O(^{1} S)," *Journal of Physics B: Atomic and Molecular Physics*, Vol. 18, No. 18, 1985, pp. L661–L666. https://doi.org/10.1088/0022-3700/18/18/005

[244] Capitelli, M., Ed., "Plasma Kinetics in Atmospheric Gases," Springer, Berlin ; New York, 2000.

[245] Gilmore, F. R., Bauer, E., and McGowan, J. W., "A Review of Atomic and Molecular Excitation Mechanisms in Nonequilibrium Gases up to 20 000°K," *Journal of Quantitative Spectroscopy and Radiative Transfer*, Vol. 9, No. 2, 1969, pp. 157–183. https://doi.org/10.1016/0022-4073(69)90084-3

[246] Flagan, R. C., and Appleton, J. P., "Excitation Mechanisms of the Nitrogen Frist-Positive and First-Negative Radiation at High Temperature," *The Journal of Chemical Physics*, Vol. 56, No. 3, 1972, pp. 1163–1173. https://doi.org/10.1063/1.1677339

[247] Golde, M. F., and Moyle, A. M., “Study of the Products of the Reactions of N2(A3Σu+): The Effect of Vibrational Energy in N2(A),” *Chemical Physics Letters*, Vol. 117, No. 4, 1985, pp. 375–380. https://doi.org/10.1016/0009-2614(85)85247-7

[248] Piper, L. G., “The Excitation of N(2 *P*) by N2(*A* 3∑+ *u* , *v* ′=0,1),” *The Journal of Chemical Physics*, Vol. 90, No. 12, 1989, pp. 7087–7095. https://doi.org/10.1063/1.456237

[249] Callear, A. B., and Wood, P. M., “Rates of Energy Transfer from N2 A 3? + u to Various Molecules. Initial and Final Quantum States in the Transfer to NOX 2? And Hg(61 S 0), and Vibrational Relaxation of N2 A 3? + u (v= 1) in Helium,” *Transactions of the Faraday Society*, Vol. 67, 1971, p. 272. https://doi.org/10.1039/tf9716700272

[250] Iannuzi, M. P., Jeffries, J. B., and Kaufman, F., “Product Channels of the N2 (A3Σ+u) + O2 Interaction,” *Chemical Physics Letters*, Vol. 87, No. 6, 1982, pp. 570–574. https://doi.org/10.1016/0009-2614(82)83180-1

[251] De Sousa, A. R., Touzeau, M., and Petitdidier, M., “Quenching Reactions of Metastable N2(A 3Σ, Y= 0, 1, 2) Molecules by O2,” *Chemical Physics Letters*, Vol. 121, Nos. 4–5, 1985, pp. 423–428. https://doi.org/10.1016/0009-2614(85)87207-9

[252] Fraser, M. E., and Piper, L. G., “Product Branching Ratios from the Nitrogen (A3.SIGMA.U+) + Oxygen Interaction,” *The Journal of Physical Chemistry*, Vol. 93, No. 3, 1989, pp. 1107–1111. https://doi.org/10.1021/j100340a017

[253] Clark, W. G., and Setser, D. W., “Energy Transfer Reactions of N2(A3.SIGMA.U+). 5. Quenching by Hydrogen Halides, Methyl Halides, and Other Molecules,” *The Journal of Physical Chemistry*, Vol. 84, No. 18, 1980, pp. 2225–2233. https://doi.org/10.1021/j100455a003

[254] Cao, D. Z., and Setser, D. W., “Energy-Transfer Reaction of Nitrogen (A3.SIGMA.U+) to Sulfur Monoxide and Other Diatomic and Polyatomic Molecules,” *The Journal of Physical Chemistry*, Vol. 92, No. 5, 1988, pp. 1169–1178. https://doi.org/10.1021/j100316a034

[255] Bak, M. S., Kim, W., and Cappelli, M. A., “On the Quenching of Excited Electronic States of Molecular Nitrogen in Nanosecond Pulsed Discharges in Atmospheric Pressure Air,” *Applied Physics Letters*, Vol. 98, No. 1, 2011, p. 011502. https://doi.org/10.1063/1.3535986

[256] Heidner, R. F., Sutton, D. G., and Suchard, S. N., “Kinetic Study of N2(B3Πg, υ) Quenching by Laser-Induced Fluorescence,” *Chemical Physics Letters*, Vol. 37, No. 2, 1976, pp. 243–248. https://doi.org/10.1016/0009-2614(76)80207-2

[257] Young, R. A., Black, G., and Slanger, T. G., “Vacuum-Ultraviolet Photolysis of N2O. II. Deactivation of N2(A 3Σu+*rpar; and N2(B 3Πg),” *The Journal of Chemical Physics*, Vol. 50, No. 1, 1969, pp. 303–308. https://doi.org/10.1063/1.1670792

[258] Piper, L. G., “Quenching Rate Coefficients for N2(*a* ′ 1Σ− *u*),” *The Journal of Chemical Physics*, Vol. 87, No. 3, 1987, pp. 1625–1629. https://doi.org/10.1063/1.453223

[259] Dreyer, J. W., and Perner, D., “The Deactivation of N2B3Πg, ν = 0–2 and N2a′1Σ−u, ν = 0 by Nitrogen,” *Chemical Physics Letters*, Vol. 16, No. 1, 1972, pp. 169–173. https://doi.org/10.1016/0009-2614(72)80483-4

[260] Dilecce, G., “Optical Spectroscopy Diagnostics of Discharges at Atmospheric Pressure,” *Plasma Sources Science and Technology*, Vol. 23, No. 1, 2014, p. 015011. https://doi.org/10.1088/0963-0252/23/1/015011

[261] Cartry, G., Magne, L., and Cernogora, G., “Experimental Study and Modelling of a Low-Pressure N_2 -O_2 Time Afterglow,” *Journal of Physics D: Applied Physics*, Vol. 32, No. 15, 1999, pp. 1894–1907. https://doi.org/10.1088/0022-3727/32/15/318

[262] Thoman, J. W., Gray, J. A., Durant, J. L., and Paul, P. H., “Temperature Dependence of NO (A2∑+) Electronic Quenching by Combustion Species,” presented at the OSA Annual Meeting, Albuquerque, New Mexico, 1992. https://doi.org/10.1364/OAM.1992.WL7

[263] Asscher, M., and Haas, Y., “The Quenching Mechanism of Electronically Excited Rydberg States of Nitric Oxide,” *The Journal of Chemical Physics*, Vol. 76, No. 5, 1982, pp. 2115–2126. https://doi.org/10.1063/1.443306

[264] Laux, C. O., “Optical Diagnostics and Radiative Emission of Air Plasmas,” PhD. Stanford University, Stanford, CA, 1993.

[265] Magin, T. E., Caillault, L., Bourdon, A., and Laux, C. O., “Nonequilibrium Radiative Heat Flux Modeling for the Huygens Entry Probe,” *Journal of Geophysical Research: Planets*, Vol. 111, No. E7, 2006, p. 2005JE002616. https://doi.org/10.1029/2005JE002616

[266] Wysong, I. J., “Measurement of Quenching Rates of CO(a3Π,V=0) Using Laser Pump-and-Probe Technique,” *Chemical Physics Letters*, Vol. 329, Nos. 1–2, 2000, pp. 42–46. https://doi.org/10.1016/S0009-2614(00)00967-2

[267] Kuranov, A. L., “Study of the Ionization, Excitation, and Deactivation of the Electronic States of Carbon Monoxide Molecules in Mixtureswith Helium, Xenon, and Oxygen,” *Vestnik Leningradskogo Universiteta, Seriya 4: Fizika, Khimiya*, Vol. 3, No. 18, 1988, pp. 25–30.

[268] Comes, F. J., and Fink, E. H., “Deactivation of CO(A1Π) in Individual Vibrational Levels,” *Chemical Physics Letters*, Vol. 14, No. 4, 1972, pp. 433–437. https://doi.org/10.1016/0009-2614(72)80231-8

[269] Melton, L. A., and Yiin, K.-C., “Energy Transfer in CO *A* 1Π, *v* ′=9. I. Quenching and Isotope Effects,” *The Journal of Chemical Physics*, Vol. 62, No. 7, 1975, pp. 2860–2868. https://doi.org/10.1063/1.430824

[270] Crandall, D. H., Kauppila, W. E., Phaneuf, R. A., Taylor, P. O., and Dunn, G. H., “Absolute Cross Sections for Electron-Impact Excitation of N 2 +,” *Physical Review A*, Vol. 9, No. 6, 1974, pp. 2545–2551. https://doi.org/10.1103/PhysRevA.9.2545

[271] Park, C., “Rate Parameters for Electronic Excitation of Diatomic Molecules II. Heavy Particle-Impact Processes,” presented at the 46th AIAA Aerospace Sciences Meeting and Exhibit, Reno, Nevada, 2008. https://doi.org/10.2514/6.2008-1446

[272] Skubenich, V. V., Povch, M. M., and Zapesochnyl, I. P., “Excitation of Diatomic-Molecules by Collisions with Monoenergetic Electrons. 3. Nitrogen and Nitric-Oxide (Vibrational Levels and Electronic States),” *High Energy Chemistry*, Vol. 11, No. 2, 1977, pp. 92–95.

[273] Brunger, M. J., Campbell, L., Cartwright, D. C., Middleton, A. G., Mojarrabi, B., and Teubner, P. J. O., "Electron-Impact Excitation of Rydberg and Valence Electronic States of Nitric Oxide: II. Integral Cross Sections," *Journal of Physics B: Atomic, Molecular and Optical Physics*, Vol. 33, No. 4, 2000, pp. 809–819. https://doi.org/10.1088/0953-4075/33/4/315

[274] Suzuki, Y.-I., Horio, T., Fuji, T., and Suzuki, T., "Publisher's Note: 'Time-Resolved Photoelectron Imaging of S2 → S1 Internal Conversion in Benzene and Toluene' [J. Chem. Phys. 134, 184313 (2011)]," *The Journal of Chemical Physics*, Vol. 135, No. 9, 2011, p. 099901. https://doi.org/10.1063/1.3633259

[275] Harrison, S., and Tennyson, J., "Electron Collisions with the CN Radical: Bound States and Resonances," *Journal of Physics B: Atomic, Molecular and Optical Physics*, Vol. 45, No. 3, 2012, p. 035204. https://doi.org/10.1088/0953-4075/45/3/035204

[276] Hyun, S., "Spradian07: Radiation Code Spradian07 and Its Applications," PhD. Korea Advanced Institute of Science & Technology, Daejeon, South Korea, 2009.

[277] Camac, M., Feinberg, R. M., and Teare, J. D., "The Production of Nitric Oxide in Shock-Heated Air," 245, AVCO Corporation, AVCO Everett Research Laboratory, 1966.

[278] Treanor, C. E., and Williams, M. J., "Kinetics of Nitric Oxide Formation Behind 3 to 4 KM/S Shock Waves," 1993.

[279] Treanor, C., Adamovich, I., Williams, M., and Rich, J., "Kinetics of NO Formation behind Strong Shock Waves," presented at the 30th Thermophysics Conference, San Diego,CA,U.S.A., 1995. https://doi.org/10.2514/6.1995-2061

[280] Gorelov, V. A., Gladyshev, M. K., Kireev, A. Y., Yegorov, I. V., Plastinin, Y. A., and Karabadzhak, G. F., "Experimental and Numerical Study of Nonequilibrium Ultraviolet NO and N Emission in Shock Layer," *Journal of Thermophysics and Heat Transfer*, Vol. 12, No. 2, 1998, pp. 172–179. https://doi.org/10.2514/2.6342

[281] Cary, B., "Shock-Tube Study of the Termal Dissociation of Nitrogen," *The Physics of Fluids*, Vol. 8, No. 1, 1965, pp. 26–35. https://doi.org/10.1063/1.1761099

[282] Hanson, R. K., and Baganoff, D., "Shock-Tube Study of Nitrogen Dissociation Rates Using Pressure Measurements," *AIAA Journal*, Vol. 10, No. 2, 1972, pp. 211–215. https://doi.org/10.2514/3.50082

[283] Baulch, D. L., Drysdale, D. D., Horne, D. G., and Lloyd, A. C., "Evaluated Kinetic Data for High Temperature Reactions. Vol. 2: Homogeneous Gas Phase Reactions of the H2 – N2 – O2 System.," Butterworths, London, 1973.

[284] Byron, S., "Shock-Tube Measurement of the Rate of Dissociation of Nitrogen," *The Journal of Chemical Physics*, Vol. 44, No. 4, 1966, pp. 1378–1388. https://doi.org/10.1063/1.1726870

[285] Bender, J. D., "Multiscale Computational Analysis of Nitrogen and Oxygen Gas-Phase Thermochemistry in Hypersonic Flows," PhD. University of Minnesota, 2016.

[286] Grover, M. S., Josyula, E., Suchyta, C. J., and Vogiatzis, K., "Effect of Low and High-Fidelity Thermochemical Models on Hypersonic Nonequilibrium Flows," presented at the AIAA Scitech 2019 Forum, San Diego, California, 2019. https://doi.org/10.2514/6.2019-0790

[287] Losev, S. A., Makarov, V. N., Pogosbekyan, M.J., Shatalov, O. P., and Nikol'sky, V. S., "Thermochemical Nonequilibrium Kinetic Models in Strong Shock Waves in Air," 1994.

[288] Boyd, I., and Gokcen, T., "Computation of Axisymmetric and Ionized Flows Using Particle and Continuum Methods," presented at the 31st Aerospace Sciences Meeting, Reno,NV,U.S.A., 1993. https://doi.org/10.2514/6.1993-729

[289] Wray, K. L., Teare, J. D., Kivel, B., and Hammerling, P., "Relaxation Processes and Reaction Rates behind Shock Fronts in Air and Component Gases," *Symposium (International) on Combustion*, Vol. 8, No. 1, 1961, pp. 328–339. https://doi.org/10.1016/S0082-0784(06)80520-5

[290] Mozzhukhin, E., Burmeister, M., and Roth, P., "High Temperature Dissociation of CN," *Berichte der Bunsengesellschaft für physikalische Chemie*, Vol. 93, No. 1, 1989, pp. 70–75. https://doi.org/10.1002/bbpc.19890930114

[291] Farbar, E., and Boyd, I., "Simulation of Reactions Involving Charged Particles in Hypersonic Rarefied Flows," presented at the 47th AIAA Aerospace Sciences Meeting including The New Horizons Forum and Aerospace Exposition, Orlando, Florida, 2009. https://doi.org/10.2514/6.2009-267

[292] Mathews, D. L., "Interferometric Measurement in the Shock Tube of the Dissociation Rate of Oxygen," *The Physics of Fluids*, Vol. 2, No. 2, 1959, pp. 170–178. https://doi.org/10.1063/1.1705908

[293] Byron, S. R., "Measurement of the Rate of Dissociation of Oxygen," *The Journal of Chemical Physics*, Vol. 30, No. 6, 1959, pp. 1380–1392. https://doi.org/10.1063/1.1730209

[294] Camac, M., and Vaughan, A., "O 2 Dissociation Rates O2-Ar Mixtures," *The Journal of Chemical Physics*, Vol. 34, No. 2, 1961, pp. 460–470. https://doi.org/10.1063/1.4757209

[295] Rink, J. P., Knight, H. T., and Duff, R. E., "Shock Tube Determination of Dissociation Rates of Oxygen," *The Journal of Chemical Physics*, Vol. 34, No. 6, 1961, pp. 1942–1947. https://doi.org/10.1063/1.1731797

[296] Ibraguimova, L. B., Sergievskaya, A. L., and Shatalov, O. P., "Dissociation Rate Constants for Oxygen at Temperatures up to 11000 K," *Fluid Dynamics*, Vol. 48, No. 4, 2013, pp. 550–555. https://doi.org/10.1134/S0015462813040145

[297] Eckerman, J., "The Measurement of the Rate of Dissociation of Oxygen at High Temperatures," PhD. The Catholic University of America, Washington, DC, 1958.

[298] Schexnayder, C. J., and Evans, J. S., "Measurements of the Dissociation Rate of Molecular Oxygen," R-108, National Aeronautics and Space Administration, 1961.

[299] Generalov, N. A., and Losev, S. A., "Vibrational Excitation and Molecular Dissociation of Gaseous Oxygen and Carbon Dioxide in a Shock Wave," *Journal of Quantitative Spectroscopy and Radiative Transfer*, Vol. 6, No. 1, 1966, pp. 101–125.

[300] Johnston, H. S., "Gas Phase Reaction Kinetics of Neutral Oxygen Species," NSRDS-NBS20, United States Department of Commerce, 1968.

[301] Shatalov, O. P., “Molecular Dissociation of Oxygen in the Absence of Vibrational Equilibrium,” *Combustion, Explosion, and Shock Waves*, Vol. 9, No. 5, 1975, pp. 610–613. https://doi.org/10.1007/BF00742888

[302] Kim, J. G., and Park, G., “Thermochemical Nonequilibrium Parameter Modification of Oxygen for a Two-Temperature Model,” *Physics of Fluids*, Vol. 30, No. 1, 2018, p. 016101. https://doi.org/10.1063/1.4996799

[303] Hall, J. G., Eschenroeder, A. Q., and Marrone, P. V., “Blunt-Nose Inviscid Airflows With Coupled Nonequilibrium Processes,” *Journal of the Aerospace Sciences*, Vol. 29, No. 9, 1962, pp. 1038–1051. https://doi.org/10.2514/8.9690

[304] Lifshitz, A., and Frenklach, M., “Oxidation of Cyanogen. II. The Mechanism of the Oxidation,” *International Journal of Chemical Kinetics*, Vol. 12, No. 3, 1980, pp. 159–168. https://doi.org/10.1002/kin.550120303

[305] Park, C., and Ahn, H.-K., “Stagnation-Point Heat Transfer Rates for Pioneer-Venus Probes,” *Journal of Thermophysics and Heat Transfer*, Vol. 13, No. 1, 1999, pp. 33–41. https://doi.org/10.2514/2.6426

[306] Tsang, W., and Herron, J. T., “Chemical Kinetic Data Base for Propellant Combustion I. Reactions Involving NO, NO2, HNO, HNO2, HCN and N2O,” *Journal of Physical and Chemical Reference Data*, Vol. 20, No. 4, 1991, pp. 609–663. https://doi.org/10.1063/1.555890

[307] Freedman, E., and Daiber, J. W., “Decomposition Rate of Nitric Oxide between 3000 and 4300°K,” *The Journal of Chemical Physics*, Vol. 34, No. 4, 1961, pp. 1271–1278. https://doi.org/10.1063/1.1731731

[308] Myerson, A. L., “Shock-Tube Atom Kinetics of Nitric Oxide Decomposition,” *Symposium (International) on Combustion*, Vol. 14, No. 1, 1973, pp. 219–228. https://doi.org/10.1016/S0082-0784(73)80023-2

[309] Fairbairn, A. R., “The Dissociation of Carbon Monoxide,” *Proceedings of the Royal Society of London*, Vol. A, No. 312, 1969, pp. 207–227.

[310] Beck, W. H., and Mackie, J. C., “Formation and Dissociation of C2 from High Temperature Pyrolysis of Acetylene,” *Journal of the Chemical Society, Faraday Transactions 1: Physical Chemistry in Condensed Phases*, Vol. 71, No. 0, 1975, p. 1363. https://doi.org/10.1039/f19757101363

[311] Kruse, T., and Roth, P., “Kinetics of C_2 Reactions during High-Temperature Pyrolysis of Acetylene,” *The Journal of Physical Chemistry A*, Vol. 101, No. 11, 1997, pp. 2138–2146. https://doi.org/10.1021/jp963373o

[312] Baulch, D. L., Duxbury, J., Grant, S. J., and Montague, D. C., “Evaluated Kinetic Data for High Temperature Reactions Volume 4 - Homogeneous Gas Phase Reactions of Halogen and Cyanidecontainina Species,” *Journal of Physical and Chemical Reference Data*, Vol. 10, No. 1, 1981.

[313] Tasaka, K., “Dissociation of CN,” M.Sc. Osaka University, Osaka, Japan, 1975.

[314] Mick, H.-J., Burmeister, M., and Roth, P., "Atomic Resonance Absorption Spectroscopy Measurements on High-Temperature CO Dissociation Kinetics," *AIAA Journal*, Vol. 31, No. 4, 1993, pp. 671–676. https://doi.org/10.2514/3.11602

[315] Chackerian, Jr., C., "The Dissociation of Shock Heated Carbon Monoxide Studied by Two Wavelength Infrared Emission," *Shock Tube Research, Imperial College, London*, 1971.

[316] Hanson, R. K., "Shock-Tube Study of Carbon Monoxide Dissociation Kinetics," *The Journal of Chemical Physics*, Vol. 60, No. 12, 1974, pp. 4970–4976. https://doi.org/10.1063/1.1681010

[317] Baulch, D. L., Drysdale, D. D., Duxbury, J., and Grant, S. J., "Evaluated Kinetic Data for High Temperature Reactions, Volume 3. Homogeneous Gas Phase Reactions of the O2-O3 System, the CO-O2-H2 System, and the Sulphur-Containing Species.," Butterworths, Lonton-Boston, 1976.

[318] Brabbs, T. A., Belles, F. E., and Zlatarich, S. A., "Shock-Tube Study of Carbon Dioxide Dissociation Rate," *The Journal of Chemical Physics*, Vol. 38, No. 8, 1963, pp. 1939–1944. https://doi.org/10.1063/1.1733900

[319] Davies, W. O., "Carbon Dioxide Dissociation at 3500° to 6000°K," *The Journal of Chemical Physics*, Vol. 41, No. 6, 1964, pp. 1846–1852. https://doi.org/10.1063/1.1726165

[320] Michel, K. W., Olschewski, H. A., Richtering, H., and Wagner, H. Gg., "Untersuchung des thermischen Zerfalls von CO_2 in Stoßwellen," *Zeitschrift für Physikalische Chemie*, Vol. 44, No. 3_4, 1965, pp. 160–172. https://doi.org/10.1524/zpch.1965.44.3_4.160

[321] Fishburne, E. S., Bilwakesh, K. R., and Edse, R., "Gaseous Reaction Rates at High Temperature. I. The Dissociation of Carbon Dioxide," *The Journal of Chemical Physics*, Vol. 45, No. 1, 1966, pp. 160–166. https://doi.org/10.1063/1.1727301

[322] Olschewski, H. A., Troe, J., and Wagner, H. Gg., "Studies of Unimolecular Reactions of Triatomic Molecules," *Symposium (International) on Combustion*, Vol. 11, No. 1, 1967, pp. 155–161. https://doi.org/10.1016/S0082-0784(67)80143-7

[323] Dean, A. M., "Dissociation of Carbon Dioxide behind Reflected Shock Waves," *The Journal of Chemical Physics*, Vol. 58, No. 12, 1973, pp. 5202–5208. https://doi.org/10.1063/1.1679131

[324] Hardy, W. A., Vasatko, H., Wagner, H. Gg., and Zabel, F., "Neuere Untersuchungen zum thermischen Zerfall von CO_2 1. Teil," *Berichte der Bunsengesellschaft für physikalische Chemie*, Vol. 78, No. 1, 1974, pp. 76–82. https://doi.org/10.1002/bbpc.19740780113

[325] Kiefer, J. H., "Densitometric Measurements of the Rate of Carbon Dioxide Dissociation in Shock Waves," *The Journal of Chemical Physics*, Vol. 61, No. 1, 1974, pp. 244–248. https://doi.org/10.1063/1.1681628

[326] Wagner, H. Gg., and Zabel, F., "Neuere Untersuchungen zum thermischen Zerfall von CO_2 . Teil II," *Berichte der Bunsengesellschaft für physikalische Chemie*, Vol. 78, No. 7, 1974, pp. 705–712. https://doi.org/10.1002/bbpc.19740780717

[327] Fujii, N., Sagawai, S., Sato, T., Nosaka, Y., and Miyama, H., "Study of the Thermal Dissociation of Nitrous Oxide and Carbon Dioxide Using Oxygen(3P) Atomic Resonance Absorption

Spectroscopy," *The Journal of Physical Chemistry*, Vol. 93, No. 14, 1989, pp. 5474–5478. https://doi.org/10.1021/j100351a031

[328] Burmeister, M., and Roth, P., "ARAS Measurements on the Thermal Decomposition of CO2 behind Shock Waves," *AIAA Journal*, Vol. 28, No. 3, 1990, pp. 402–405. https://doi.org/10.2514/3.10406

[329] Eremin, A. V., Ziborov, V. S., Shumova, V. V., Voiki, D., and Roth, P., "Formation of O(1d) Atoms in Thermal Decomposition of Co_2," *Kinetics and Catalysis*, Vol. 38, 1997, pp. 1–7.

[330] Higashihara, T., Kuroda, H., Saito, K., and Murakami, I., "Oxidation of BrCN in Shock Waves and Formation of NO," *Combustion and Flame*, Vol. 61, No. 2, 1985, pp. 167–175. https://doi.org/10.1016/0010-2180(85)90162-2

[331] Baulch, D. L., Cobos, C. J., Cox, R. A., Esser, C., Frank, P., Just, Th., Kerr, J. A., Pilling, M. J., Troe, J., Walker, R. W., and Warnatz, J., "Evaluated Kinetic Data for Combustion Modelling," *Journal of Physical and Chemical Reference Data*, Vol. 21, No. 3, 1992, p. 411. https://doi.org/10.1063/1.555908

[332] Sommer, T., Kruse, T., Roth, P., and Hippler, H., "Perturbation Study on the Reaction of C_2 with N_2 in High-Temperature C_{60} /Ar + N_2 Mixtures," *The Journal of Physical Chemistry A*, Vol. 101, No. 20, 1997, pp. 3720–3725. https://doi.org/10.1021/jp962779y

[333] Dean, A. J., Hanson, R. K., and Bowman, C. T., "High Temperature Shock Tube Study of Reactions of CH and C-Atoms with N2," *Symposium (International) on Combustion*, Vol. 23, No. 1, 1991, pp. 259–265. https://doi.org/10.1016/S0082-0784(06)80268-7

[334] Moskaleva, L. V., and Lin, M. C., "Computational Study on the Energetics of NCN Isomers and the Kinetics of the C + N_2 ⇄ N + CN Reaction," *The Journal of Physical Chemistry A*, Vol. 105, No. 16, 2001, pp. 4156–4163. https://doi.org/10.1021/jp0044328

[335] Andersson, S., Marković, N., and Nyman, G., "Computational Studies of the Kinetics of the C + NO and O + CN Reactions," *The Journal of Physical Chemistry A*, Vol. 107, No. 28, 2003, pp. 5439–5447. https://doi.org/10.1021/jp0222604

[336] Dorthe, G., Caubet, P., Vias, T., Barrere, B., and Marchais, J., "Fast Flow Studies of Atomic Carbon Kinetics at Room Temperature," *The Journal of Physical Chemistry*, Vol. 95, No. 13, 1991, pp. 5109–5116. https://doi.org/10.1021/j100166a038

[337] Martinotti, F. F., Welch, M. J., and Wolf, A. P., "The Reactivity of Thermal Carbon Atoms in the Gas Phase," *Chemical Communications (London)*, No. 3, 1968, p. 115. https://doi.org/10.1039/c19680000115

[338] Braun, W., Bass, A. M., Davis, D. D., and Simmons, J. D., "Flash Photolysis of Carbon Suboxide: Absolute Rate Constants for Reactions of C(P) and C(D) with H,, Na, CO, NO, 0, and CH," *Proceedings of the Royal Society A*, Vol. 312, 1969, pp. 417–434.

[339] Husain, D., and Kirsch, L. J., "Reactions of Atomic Carbon C(23Ps) by Kinetic Absorption Spectroscopy in the Vacuum Ultra-Violet," *Journal of the Chemical Society, Faraday Transactions 2*, Vol. 67, 1971.

[340] Becker, K. H., Brockmann, K. J., and Wiesen, P., "Halogenomethane H Flame Systems and Measurements of C(' P) Reaction Rate Constants by Two-Photon Laser-Induced Fluorescence," *Journal of the Chemical Society, Faraday Transactions 2*, Vol. 2, 1988, pp. 455–461.

[341] Husain, D., and Young, A. N., "Kinetic Investigation of Ground State Carbon Atoms, C(23 P J)," *Journal of the Chemical Society, Faraday Transactions 2*, Vol. 71, 1975, p. 525. https://doi.org/10.1039/f29757100525

[342] Sommer, T., Kruse, T., and Roth, P., "C2 Formation during High-Temperature Pyrolysis of Fullerene C60 in Shock Waves," *The Journal of Physical Chemistry*, Vol. 99, No. 36, 1995, pp. 13509–13512. https://doi.org/10.1021/j100036a030

[343] Patterson, W. L., and Greene, E. F., "Kinetic Study of the Formation and Reaction of CN Molecules in Shock Waves," *The Journal of Chemical Physics*, Vol. 36, No. 5, 1962, pp. 1146–1151. https://doi.org/10.1063/1.1732706

[344] Abian, M., Alzueta, M. U., and Glarborg, P., "Formation of NO from N_2/O_2 Mixtures in a Flow Reactor: Toward an Accurate Prediction of Thermal NO," *International Journal of Chemical Kinetics*, Vol. 47, No. 8, 2015, pp. 518–532. https://doi.org/10.1002/kin.20929

[345] Thielen, K., and Roth, P., "Resonance Absorption Measurements of N and O Atoms in High Temperature No Dissociation and Formation Kinetics," *Symposium (International) on Combustion*, Vol. 20, No. 1, 1985, pp. 685–693. https://doi.org/10.1016/S0082-0784(85)80558-0

[346] Kaufman, F., and Decker, L. J., "Nitric Oxide at High Temperatures," In *Symposium (International) on Combustion Proceedings*, Vol. 7, 1958.

[347] Baulch, D. L., Drysdale, D. D., Horne, D. G., and Lloyd, A. C., "High Temperature Reaction Rate Data," 4, Department of Physical Chemistry, Leeds, England, 1969.

[348] Fenimore, C. P., "Formation of Nitric Oxide in Premixed Hydrocarbon Flames," *Symposium (International) on Combustion*, Vol. 13, No. 1, 1971, pp. 373–380. https://doi.org/10.1016/S0082-0784(71)80040-1

[349] Bachmaier, F., Eberius, K. H., and Just, Th., "The Formation of Nitric Oxide and the Detection of HCN in Premixed Hydrocarbon-Air Flames at 1 Atmosphere," *Combustion Science and Technology*, Vol. 7, No. 2, 1973, pp. 77–84. https://doi.org/10.1080/00102207308952345

[350] Iverach, D., Basden, K. S., and Kirov, N. Y., "Formation of Nitric Oxide in Fuel-Lean and Fuel-Rich Flames," *Symposium (International) on Combustion*, Vol. 14, No. 1, 1973, pp. 767–775. https://doi.org/10.1016/S0082-0784(73)80071-2

[351] Harris, R. J., Nasralla, M., and Williams, A., "The Formation of Oxides of Nitrogen in High Temperature CH_4-O_2-N_2 Flames," *Combustion Science and Technology*, Vol. 14, Nos. 1–3, 1976, pp. 85–94. https://doi.org/10.1080/00102207608946749

[352] Heberling, P. V., "'Prompt No' Measurements at High Pressures," *Symposium (International) on Combustion*, Vol. 16, No. 1, 1977, pp. 159–168. https://doi.org/10.1016/S0082-0784(77)80321-4

[353] Blauwens, J., Smets, B., and Peeters, J., “Mechanism of ‘Prompt’ No Formation in Hydrocarbon Flames,” *Symposium (International) on Combustion*, Vol. 16, No. 1, 1977, pp. 1055–1064. https://doi.org/10.1016/S0082-0784(77)80395-0

[354] Monat, J. P., Hanson, R. K., and Kruger, C. H., “Shock Tube Determination of the Rate Coefficient for the Reaction N2+O→NO+N,” *Symposium (International) on Combustion*, Vol. 17, No. 1, 1979, pp. 543–552. https://doi.org/10.1016/S0082-0784(79)80055-7

[355] Seery, D. J., and Zabielski, M. F., “Laser Probes for Combustion Chemistry,” AMERICAN CHEMICAL SOCIETY, WASHINGTON, D. C., 1980. https://doi.org/10.1021/bk-1980-0134

[356] Hanson, R. K., and Salimian, S., “Combustion Chemistry,” Springer New York, New York, NY, 1984. https://doi.org/10.1007/978-1-4684-0186-8

[357] Zabielski, M. F., and Seery, D. J., “The Direct Measurement of the Rate of Nitric Oxide Formation in a High Temperature, Oxygen Enriched Methane Flame,” In *Fossil Fuels Combustion Symposium*, Vol. 25, Houston, TX, 1989, pp. 91–94.

[358] Davidson, D. F., and Hanson, R. K., “High Temperature Reaction Rate Coefficients Derived from N-atom ARAS Measurements and Excimer Photolysis of NO,” *International Journal of Chemical Kinetics*, Vol. 22, No. 8, 1990, pp. 843–861. https://doi.org/10.1002/kin.550220805

[359] Koshi, M., Yoshimura, M., Fukuda, K., Matsui, H., Saito, K., Watanabe, M., Imamura, A., and Chen, C., “Reactions of N(4 *S*) Atoms with NO and H2,” *The Journal of Chemical Physics*, Vol. 93, No. 12, 1990, pp. 8703–8708. https://doi.org/10.1063/1.459257

[360] Michael, J. V., and Lim, K. P., “Rate Constants for the N2O Reaction System: Thermal Decomposition of N2O; N+NO→N2+O; and Implications for O+N2→NO+N,” *The Journal of Chemical Physics*, Vol. 97, No. 5, 1992, pp. 3228–3234. https://doi.org/10.1063/1.463009

[361] Bose, D., and Candler, G. V., “Thermal Rate Constants of the N2+O→NO+N Reaction Using *Ab Initio* 3 *A* ″ and 3 *A* ′ Potential Energy Surfaces,” *The Journal of Chemical Physics*, Vol. 104, No. 8, 1996, pp. 2825–2833. https://doi.org/10.1063/1.471106

[362] Suzzi Valli, G., Orrú, R., Clementi, E., Laganà, A., and Crocchianti, S., “Rate Coefficients for the N+O2 Reaction Computed on an *Ab Initio* Potential Energy Surface,” *The Journal of Chemical Physics*, Vol. 102, No. 7, 1995, pp. 2825–2832. https://doi.org/10.1063/1.468660

[363] Fernandez, A., Goumri, A., and Fontijn, A., “Kinetics of the Reactions of N(^{4} S) Atoms with O_2 and CO_2 over Wide Temperatures Ranges,” *The Journal of Physical Chemistry A*, Vol. 102, No. 1, 1998, pp. 168–172. https://doi.org/10.1021/jp972365k

[364] Kaufman, F., and Kelso, J. R., “Thermal Decomposition of Nitric Oxide,” *The Journal of Chemical Physics*, Vol. 23, No. 9, 1955, pp. 1702–1707. https://doi.org/10.1063/1.1742415

[365] Vetter, K., “Kinetik der thermischen Zersetzung und Bildung von Stickoxyd. II. Teil,” *Zeitschrift für Elektrochemie und angewandte physikalische Chemie*, Vol. 53, No. 6, 1949, pp. 376–380. https://doi.org/10.1002/bbpc.19490530610

[366] Ludwig, C. B., and Sulzmann, K. G. P., “Chemical Kinetics in Shock-Heated Air,” Zph-082, General Dynamics Corporation, San Diego, CA, United States, 1961.

[367] Wurster, W. H., Treanor, C. E., and Williams, M. J., "Non-Equilibrium Radiation from Shock-Heated Air," AD-A244905, Calspan-UB Research Center, Buffalo, NY, 1991.

[368] Livesey, J. B., Roberts, A. L., and Williams, A., "The Formation of Oxides of Nitrogen in Some Oxy-Propane Flames," *Combustion Science and Technology*, Vol. 4, No. 1, 1971, pp. 9–15. https://doi.org/10.1080/00102207108952467

[369] Miller, J. A., Branch, M. C., Smooke, M. D., Kee, R. J., McLean, W. J., and Chandler, D. W., "The Conversion of HCN to NO and N2 in H2-O2-HCN-Ar Flames at Low Pressure," presented at the Twentieth Symposium (International) on Combustion, 1985. https://doi.org/10.1016/s0082-0784(85)80557-9

[370] Miller, J. A., and Bowman, C. T., "Mechanism and Modeling of Nitrogen Chemistry in Combustion," *Progress in Energy and Combustion Science*, Vol. 15, No. 4, 1989, pp. 287–338. https://doi.org/10.1016/0360-1285(89)90017-8

[371] Basevich, V. Ya., "Chemical Kinetics in the Combustion Processes: A Detailed Kinetics Mechanism and Its Implementation," *Progress in Energy and Combustion Science*, Vol. 13, No. 3, 1987, pp. 199–248. https://doi.org/10.1016/0360-1285(87)90011-6

[372] Slack, M. W., and Fishburne, E. S., "Kinetics and Thermodynamics of the CN Molecule. I. Decomposition Mechanism for CN Molecules," *The Journal of Chemical Physics*, Vol. 52, No. 11, 1970, pp. 5830–5833. https://doi.org/10.1063/1.1672865

[373] Atakan, B., Jacobs, A., Wahl, M., Weller, R., and Wolfrum, J., "Kinetic Studies of the Gas-Phase Reactions of CN with O2 and H2 from 294 to 1000 K," *Chemical Physics Letters*, Vol. 154, No. 5, 1989, pp. 449–453. https://doi.org/10.1016/0009-2614(89)87129-5

[374] Colket, M. B., "Cyanogen Pyrolysis and the CN + NO Reaction behind Incident Shock Waves," *International Journal of Chemical Kinetics*, Vol. 16, No. 4, 1984, pp. 353–369. https://doi.org/10.1002/kin.550160406

[375] Natarajan, K., and Roth, P., "A Shock Tube Study of CN Radical Reactions with H2 and NO Verified by H, N and O Atom Measurements," *Symposium (International) on Combustion*, Vol. 21, No. 1, 1988, pp. 729–737. https://doi.org/10.1016/S0082-0784(88)80305-9

[376] Davidson, D. F., Dean, A. J., Dirosa, M. D., and Hanson, R. K., "Shock Tube Measurements of the Reactions of CN with O and O_2," *International Journal of Chemical Kinetics*, Vol. 23, No. 11, 1991, pp. 1035–1050. https://doi.org/10.1002/kin.550231107

[377] Boden, J. C., and Thrush, B. A., "Study of the Reactions of Cn by Electronic Absorption Spectroscopy," *Proceedings of the Royal Society A*, Vol. 305, 1968, pp. 107–123.

[378] Kondratiev, V. N., "Rate Constants of Gas Phase Reactions," National Bureau of Standards, Washington, DC, 1972.

[379] Schmatjko, K. J., and Wolfrum, J., "Direct Determination of the Product Energy Distribution in the Reaction of O-Atoms with CN Radicals," *Symposium (International) on Combustion*, Vol. 16, No. 1, 1977, pp. 819–827. https://doi.org/10.1016/S0082-0784(77)80375-5

[380] Ibragimova, L. B., and Kuznetsova, L., "Kinetics of the CO + N -> CN + O Reaction at High Temperatures," *Chemical Physics*, Vol. 23, 2004, pp. 82–89.

[381] Bullock, G. E., and Cooper, R., "Reactions of Cyanogen Radicals," *Journal of the Chemical Society, Faraday Transactions 1*, Vol. 68, 1972.

[382] Albers, E. A., Hoyermann, K., Schacke, H., Schmatjko, K. J., Wagner, H. Gg., and Wolfrum, J., "Absolute Rate Coefficients for the Reaction of H-Atoms with N2O and Some Reactions of CN Radicals," *Symposium (International) on Combustion*, Vol. 15, No. 1, 1975, pp. 765–773. https://doi.org/10.1016/S0082-0784(75)80345-6

[383] Sims, I. R., and Smith, I. W. M., "Pulsed Laser Photolysis-Laser-Induced Fluorescence Measurements on the Kinetics of CN(v = 0) and CN(v = 1) with O2, NH3, and NO Between 294 and 761 K," *Journal of the Chemical Society, Faraday Transactions 2*, Vol. 84, No. 5, 1988, pp. 527–539.

[384] Burmeister, M., Gulati, S. K., Natarajan, K., Thielen, K., Mozzhukin, E., and Roth, P., "Fachgebiet Verbrennung Und Gasdynamik Universitdt Duisburg 4100 Duisburg, West Germany," 1989.

[385] Myers, B. F., Sulzmann, K. G. P., and Bartle, E. R., "Oxidation of CO. II. Influence of H2 on the Induction Period Preceding Rapid CO2 Formation in Shock-Heated CO–O2–Ar Mixtures," *The Journal of Chemical Physics*, Vol. 43, No. 4, 1965, pp. 1220–1228. https://doi.org/10.1063/1.1696908

[386] Clark, T. C., Garnett, S. H., and Kistiakowsky, G. B., "Reaction of Carbon Dioxide with Atomic Oxygen and the Dissociation of Carbon Dioxide in Shock Waves," *The Journal of Chemical Physics*, Vol. 51, No. 7, 1969, pp. 2885–2891. https://doi.org/10.1063/1.1672428

[387] Baber, S. C., and Dean, A. M., "Reaction of Atomic Oxygen with Carbon Dioxide behind Reflected Shock Waves," *The Journal of Chemical Physics*, Vol. 60, No. 1, 1974, pp. 307–313. https://doi.org/10.1063/1.1680785

[388] Korovkina, T. D., "Rate of Dissociation of Co2 Molecules in Collisions with Oxygen Atoms," *High Energy Chemistry*, Vol. 10, 1976, pp. 75–76.

[389] Warnatz, J., "Rate Coefficients in the C/H/O/System," *Combustion Chemistry*, Springer New York, New York, NY, 1984. https://doi.org/10.1007/978-1-4684-0186-8

[390] Tsang, W., and Hampson, R. F., "Chemical Kinetic Data Base for Combustion Chemistry. Part I. Methane and Related Compounds," *Journal of Physical and Chemical Reference Data*, Vol. 15, No. 3, 1986, pp. 1087–1279. https://doi.org/10.1063/1.555759

[391] Thielen, K., and Roth, P., "Stoßtwellenuntersuchungen zum Start der Reaktion CO + O2," *Berichte der Bunsengesellschaft für physikalische Chemie*, Vol. 87, No. 10, 1983, pp. 920–925. https://doi.org/10.1002/bbpc.19830871017

[392] Teulet, P., Gonzalez, J. J., Mercado-Cabrera, A., Cressault, Y., and Gleizes, A., "One-Dimensional Hydro-Kinetic Modelling of the Decaying Arc in AIR–PA66–Copper Mixtures: I. Chemical Kinetics, Thermodynamics, Transport and Radiative Properties," *Journal of Physics D: Applied Physics*, Vol. 42, No. 17, 2009, p. 175201. https://doi.org/10.1088/0022-3727/42/17/175201

[393] Brownsword, R. A., Hancock, G., and Heard, D. E., "Kinetics of the N+NCO Reaction at 298 K," *Journal of the Chemical Society, Faraday Transactions*, Vol. 93, No. 15, 1997, pp. 2473–2475. https://doi.org/10.1039/a702542d

[394] Cooper, W. F., Park, J., and Hershberger, J. F., "Product Channel Dynamics of the Cyanato Radical + Nitric Oxide Reaction," *The Journal of Physical Chemistry*, Vol. 97, No. 13, 1993, pp. 3283–3290. https://doi.org/10.1021/j100115a033

[395] Atakan, B., and Wolfrum, J., "Kinetic Studies of the Reactions of CN Radicals with Alkanes in the Temperature Range between 294 and 1260 K," *Chemical Physics Letters*, Vol. 186, No. 6, 1991, pp. 547–552. https://doi.org/10.1016/0009-2614(91)90465-L

[396] Fifer, R. A., and Holmes, H. E., "Kinetics of the Hydrogen Cyanide + Nitrogen Dioxide Reaction behind Shock Waves," *The Journal of Physical Chemistry*, Vol. 86, No. 15, 1982, pp. 2935–2944. https://doi.org/10.1021/j100212a026

[397] Perry, R. A., "Kinetics of the Reactions of NCO Radicals with H2 and NO Using Laser Photolysis–Laser Induced Fluorescence," *The Journal of Chemical Physics*, Vol. 82, No. 12, 1985, pp. 5485–5488. https://doi.org/10.1063/1.448583

[398] Mertens, J. D., Dean, A. J., Hanson, R. K., and Bowman, C. T., "A Shock Tube Study of Reactions of NCO with O and NO Using NCO Laser Absorption," *Symposium (International) on Combustion*, Vol. 24, No. 1, 1992, pp. 701–710. https://doi.org/10.1016/S0082-0784(06)80086-X

[399] Cooper, W. F., and Hershberger, J. F., "Measurement of Product Branching Ratios of the Cyanato + Nitric Oxide Reaction," *The Journal of Physical Chemistry*, Vol. 96, No. 2, 1992, pp. 771–775. https://doi.org/10.1021/j100181a046

[400] Lin, M. C., He, Y., and Melius, C. F., "Theoretical Aspects of Product Formatino from the NCO + NO Reaction," *Journal of Physical Chemistry*, Vol. 97, No. 36, 1993, pp. 9124–9128.

[401] Juang, D. Y., Lee, J., and Wang, N. S., "Kinetics of the Reactions of NCO with NO and NO_2," *International Journal of Chemical Kinetics*, Vol. 27, No. 11, 1995, pp. 1111–1120. https://doi.org/10.1002/kin.550271108

[402] Schacke, H., Schmatjko, K. J., and Wolfrum, J., "Reaktionen von CN-Radikalen Im H-C-N-O-System," *Archiwum Procesów Spalania*, Vol. 5, 1974.

[403] Mulvihill, J. N., and Phillips, L. F., "Breakdown of Cyanogen in Fuel-Rich H2/N2/O2 Flames," *Symposium (International) on Combustion*, Vol. 15, No. 1, 1975, pp. 1113–1122. https://doi.org/10.1016/S0082-0784(75)80376-6

[404] Higashihara, T., Saito, K., and Murakami, I., "Oxidation of Hydrogen Cyanide in Shock Waves. Formation of Nitrogen Monoxide," *The Journal of Physical Chemistry*, Vol. 87, No. 19, 1983, pp. 3707–3712. https://doi.org/10.1021/j100242a026

[405] Louge, M. Y., and Hanson, R. K., "Shock Tube Study of NCO Kinetics," *Symposium (International) on Combustion*, Vol. 20, No. 1, 1985, pp. 665–672. https://doi.org/10.1016/S0082-0784(85)80556-7

[406] Perry, R. A., "Kinetics of the Reaction of NCO with Ethene and Oxygen over the Temperature Range 295–662K*," *Symposium (International) on Combustion*, Vol. 21, No. 1, 1988, pp. 913–918. https://doi.org/10.1016/S0082-0784(88)80323-0

[407] Losev, S., Makarov, V., and Nikolsky, V., "Thermochemical Nonequilibrium Kinetic Models in Strong Shock Waves on Air," presented at the 6th Joint Thermophysics and Heat Transfer Conference, Colorado Springs,CO,U.S.A., 1994. https://doi.org/10.2514/6.1994-1990

[408] Mul, P. M., and McGowan, J. W., "Merged Electron-Ion Beam Experiments 111% Temperature Dependence of Dissociative Recombination for Atmospheric Ions NO*, 0; and N;," *Journal of Physics B: Atomic and Molecular Physics*, Vol. 12, 1979, p. 1591.

[409] Walls, F. L., and Dunn, G. H., "Measurement of Total Cross Sections for Electron Recombination with NO^+ and O_2^+ Using Ion Storage Techniques," *Journal of Geophysical Research*, Vol. 79, No. 13, 1974, pp. 1911–1915. https://doi.org/10.1029/JA079i013p01911

[410] Lin, S. C., "Research Report 33," 33, AVCO Research Laboratory, 1958.

[411] Lin, S.-C., and Teare, J. D., "Rate of Ionization Behind Shock Waves in Air. II. Theoretical Interpretations," *The Physics of Fluids*, Vol. 6, No. 3, 1963, pp. 355–375. https://doi.org/10.1063/1.1706741

[412] Bascombe, K., Jenkins, D., Schiff, H. I., and Sugden, T. M., Chicago, IL, 1961.

[413] Stein, R. P., Scheibe, M., Syverson, M. W., Shaw, T. M., and Gunton, R. C., "Recombination Coefficient of Electrons with NO+ Ions in Shock-Heated Air," *The Physics of Fluids*, Vol. 7, No. 10, 1964, pp. 1641–1650. https://doi.org/10.1063/1.1711070

[414] Dunn, M. G., and Lordi, J. A., "Measurement of Electron Temperature and Number Density in Shock-Tunnel Flows. II," *AIAA Journal*, Vol. 7, No. 11, 1969, pp. 2099–2104. https://doi.org/10.2514/3.5563

[415] Bardsley, J. N., "Temperature Dependence of Dissociative Recombination," *Physical Review A*, Vol. 2, No. 4, 1970, pp. 1359–1365. https://doi.org/10.1103/PhysRevA.2.1359

[416] Huang, C.-M., Biondi, M. A., and Johnsen, R., "Variation of Electron-N O + -Ion Recombination Coefficient with Electron Temperature," *Physical Review A*, Vol. 11, No. 3, 1975, pp. 901–905. https://doi.org/10.1103/PhysRevA.11.901

[417] Torr, R., and Torr, D. G., "Associative Ionization of N(‘d) and 0," *Planes Space Science*, Vol. 27, 1979, pp. 1233–1237.

[418] Fite, W. L., Rutherford, J. A., Snow, W. R., and Van Lint, V. A. J., "Ion-Neutral Collisions in Afterglows," *Discussions of the Faraday Society*, Vol. 33, 1962, p. 264. https://doi.org/10.1039/df9623300264

[419] Fehsenfeld, F. C., Schmel'Iekopf, A. L., and Ferguson, E. E., "Some Measured Rates for Oxygen and Nitrogen Ion-Molecule Reactions of Atmospheric Importance, Including O+ + N2 = No+ + N," *Planet and Space Science*, Vol. 13, No. 9, 1965, pp. 219–223.

[420] Stebbings, R. F., Turner, B. R., and Rutherford, J. A., "Low-Energy Collisions between Some Atmospheric Ions and Neutral Particles," *Journal of Geophysical Research*, Vol. 71, No. 3, 1966, pp. 771–784. https://doi.org/10.1029/JZ071i003p00771

[421] Aquilanti, V., and Volpi, G. G., "Some Ionic Processes of Interest in the Upper Atmospher," *Ricerca Scientifica*, Vol. 36, 1966, pp. 359–364.

[422] Warneck, P., "Studies of Ion—Neutral Reactions by a Photoionization Mass-Spectrometer Technique. IV. Reactions of He+ with N2 and O2," *The Journal of Chemical Physics*, Vol. 47, No. 10, 1967, pp. 4279–4281. https://doi.org/10.1063/1.1701624

[423] Golden, D. E., Sinnott, G., and Varney, R. N., "Charge-Transfer Cross Sections for the Reaction N 2 + + O 2 → O 2 + + N 2 at Very Low Energies," *Physical Review Letters*, Vol. 20, No. 6, 1968, pp. 239–241. https://doi.org/10.1103/PhysRevLett.20.239

[424] Ferguson, E. E., Bohme, D. K., Fehsenfeld, F. C., and Dunkin, D. B., "Temperature Dependence of Slow Ion–Atom Interchange Reactions," *The Journal of Chemical Physics*, Vol. 50, No. 11, 1969, pp. 5039–5040. https://doi.org/10.1063/1.1671008

[425] Johnsen, R., Brown, H. L., and Biondi, M. A., "Ion–Molecule Reactions Involving N2+, N+, O2+, and O+ Ions from 300°K to ∼1 eV," *The Journal of Chemical Physics*, Vol. 52, No. 10, 1970, pp. 5080–5084. https://doi.org/10.1063/1.1672745

[426] McFarland, M., Albritton, D. L., Fehsenfeld, F. C., Ferguson, E. E., and Schmeltekopf, A. L., "Flow-Drift Technique for Ion Mobility and Ion-Molecule Reaction Rate Constant Measurements. III. Negative Ion Reactions of O− with CO, NO, H2, and D2," *The Journal of Chemical Physics*, Vol. 59, No. 12, 1973, pp. 6629–6635. https://doi.org/10.1063/1.1680043

[427] Kobayashi, N., and Kaneko, Y., "Low Energy Ion-Neutral Reactions. V. O_2^+ +NO, N_2^+ +NO, CO^+ +NO, $N_2^+ + O_2$, $CO_2^+ + O_2$, $CO^+ + O_2$ and N_2^+ +CO," *Journal of the Physical Society of Japan*, Vol. 37, No. 4, 1974, pp. 1082–1088. https://doi.org/10.1143/JPSJ.37.1082

[428] Lindinger, W., Albritton, D. L., Fehsenfeld, F. C., and Ferguson, E. E., "Laboratory Measurements of the Ionospheric $O_2^+ (X\,^2\Pi_g)$ and $O_2^+ (a\,^4\Pi_u)$ Reactions With NO," *Journal of Geophysical Research*, Vol. 80, No. 25, 1975, pp. 3725–3726. https://doi.org/10.1029/JA080i025p03725

[429] Langstroth, G. F. O., and Hasted, J. B., "General Discussion," *Discussions of the Faraday Society*, Vol. 33, 1962, p. 298.

[430] Batey, P. H., Court, G. R., and Sayers, J., "Afterglow Measurements of the Rate Coefficients for the Reactions of O+ + O2 ->O2+ + O and O+ + N2 -> NO+ + N," *Planet and Space Science*, Vol. 13, No. 9, 1965, pp. 911–917.

[431] Fehsenfeld, F. C., Schmeltekopf, A. L., and Ferguson, E. E., "Correction in the Laboratory Measurement of the Rate Constant for N2+ + 02 -> N2 + O2+ at 300°K," *Planet and Space Science*, Vol. 13, No. 11, 1965, pp. 919–920.

[432] Giese, C. F., "The Reaction O+ + N2 --> NO+ + N, in Ion-Molecule Reactions in the Gas Phase," *American Chemical Society*, Vol. 58, 1966, pp. 20–27.

[433] Copsey, M. J., Smith, D., and Sayers, J., "Laboratory Afterglow Studies of O+ Ions in Helium-Oxygen and Helium-Oxygen-Nitrogen Mixtures," *Planet and Space Science*, Vol. 14, 1966, pp. 1047–1055.

[434] Ausloos, P. J., Ed., "Ion-Molecule Reactions in the Gas Phase," AMERICAN CHEMICAL SOCIETY, WASHINGTON, D.C., 1967. https://doi.org/10.1021/ba-1966-0058

[435] Bohme, D. K., Ong, P. P., and Hasted, J. B., "Energy Dependence of Reactions O+ with N2, 0,-I," *Planet and Space Science*, Vol. 15, 1967, pp. 1777–1780.

[436] Paulson, J. F., Dale, F., and Murad, E., "Laboratory Studies on Some Positive Ion-Neutral Reactions," presented at the DASA Symposium, University of Pittsburgh, 1967.

[437] Nakshbandi, M. M., and Hasted, J. B., "Energy Dependence of Reactions of 0+ with Na, 02-II," *Planet and Space Science*, Vol. 15, 1967, pp. 1781–1786.

[438] Schmeltekopf, A. L., Ferguson, E. E., and Fehsenfeld, F. C., "Afterglow Studies of the Reactions He+, He(23S), and O+ with Vibrationally Excited N2," *The Journal of Chemical Physics*, Vol. 48, No. 7, 1968, pp. 2966–2973. https://doi.org/10.1063/1.1669560

[439] Johnsen, R., and Biondi, M. A., "Measurements of the O+ + N2 and O+ + O2 Reaction Rates from 300°K to 2 eV," *The Journal of Chemical Physics*, Vol. 59, No. 7, 1973, pp. 3504–3509. https://doi.org/10.1063/1.1680511

[440] St.-Maurice, J. P., and Torr, D. G., "Nonthermal Rate Coefficients in the Ionosphere: The Reactions of O ⁺ with N ₂ , O ₂ , and No," *Journal of Geophysical Research: Space Physics*, Vol. 83, No. A3, 1978, pp. 969–977. https://doi.org/10.1029/JA083iA03p00969

[441] Ferguson, E. E., "Ionospheric Ion-molecule Reaction Rates," *Reviews of Geophysics*, Vol. 5, No. 3, 1967, pp. 305–327. https://doi.org/10.1029/RG005i003p00305

[442] Goldan, P. D., Schmeltekopf, A. L., Fehsenfeld, F. C., Schiff, H. I., and Ferguson, E. E., "Thermal Energy Ion—Neutral Reaction Rates. II. Some Reactions of Ionospheric Interest," *The Journal of Chemical Physics*, Vol. 44, No. 11, 1966, pp. 4095–4103. https://doi.org/10.1063/1.1726588

[443] Rutherford, J. A., and Vroom, D. A., "Effect of Metastable O+(2 *D*) on Reactions of O+ with Nitrogen Molecules," *The Journal of Chemical Physics*, Vol. 55, No. 12, 1971, pp. 5622–5624. https://doi.org/10.1063/1.1675729

[444] Fehsenfeld, F. C., Dunein, D. B., and Ferguson, E. E., "Rate Constants for the Reaction of CO2+ with O, O2, and NO; N2+ with O and NO; and O2+ with NO," *Planet and Space Science*, Vol. 18, 1970, pp. 1267–1269.

[445] McFarland, M., Albritton, D. L., Fehsenfeld, F. C., Ferguson, E. E., and Schmeltekopf, A. L., "Energy Dependence and Branching Ratio of the $N_2^+ + O$ Reaction," *Journal of Geophysical Research*, Vol. 79, No. 19, 1974, pp. 2925–2926. https://doi.org/10.1029/JA079i019p02925

[446] Richards, P. G., and Voglozin, D., "Reexamination of Ionospheric Photochemistry: IONOSPHERIC PHOTOCHEMISTRY," *Journal of Geophysical Research: Space Physics*, Vol. 116, No. A8, 2011, p. n/a-n/a. https://doi.org/10.1029/2011JA016613

[447] Boyd, I., "Modeling of Plasma Formation in Rarefied Hypersonic Entry Flows," presented at the 45th AIAA Aerospace Sciences Meeting and Exhibit, Reno, Nevada, 2007. https://doi.org/10.2514/6.2007-206

[448] Fehsenfeld, F. C., "The Reaction of O2+ with Atomic Nitrogen and NO+ H2O and NO2+ with Atomic Oxygen," *Planet and Space Science*, Vol. 25, 1977, pp. 195–196.

[449] Bortner, M. H., and Baurer, T., "Defense Nuclear Agency Reaction Rate Handbook," DNA1948H, General Electric Company, Santa Berbere, California, 1978.

[450] Freysinger, W., Khan, F. A., Armentrout, P. B., Tosi, P., Dmitriev, O., and Bassi, D., "Charge-Transfer Reaction of 14,15N+(3 *P J*)+N2(1Σ+ *g*) from Thermal to 100 eV. Crossed-Beam and Scattering-Cell Guided-Ion Beam Experiments," *The Journal of Chemical Physics*, Vol. 101, No. 5, 1994, pp. 3688–3695. https://doi.org/10.1063/1.467553

[451] Park, C., "Measurement of Ionic Recombination Rate of Nitrogen.," *AIAA Journal*, Vol. 6, No. 11, 1968, pp. 2090–2094. https://doi.org/10.2514/3.4937

[452] Ozawa, T., Zhong, J., and Levin, D. A., "Development of Kinetic-Based Energy Exchange Models for Noncontinuum, Ionized Hypersonic Flows," *Physics of Fluids*, Vol. 20, No. 4, 2008, p. 046102. https://doi.org/10.1063/1.2907198

[453] Maahs, H. G., "A Study of the Effect of Selected Material Properties on the Ablation Performance of Artificial Graphites," TN-D-6624, National Aeronautics and Space Administration, Langley Research Center, Hampton, Virginia, 1972.

Appendix A

Baseline Parameters and Uncertainty Bounds

Table A1: Chemical reaction rate baseline (BL) parameters and uncertainty bound (UB) multiplier intervals applied to preexponential factors.

$$k_f(T_f) = UC_f T_f^{\eta_f} exp(-\theta_f/T_f), \quad T_f = max\{T_{tr}^{A} T_{ve}^{B}, T_{min}\}, \quad k_b(T_b) = k_f(T_b)/K_{eq}(T_b), \quad T_b = max\{T_{tr}^{A'} T_{ve}^{B'}, T_{min}\}, T_{min} = 500K$$

No.	Reaction	C_f, $cm^3 mol^{-1} s^{-1}$	η_f	θ_f, K	A	B	A'	B'	U_{low}	U_{high}	BL Refs.	UB Refs.
1	$N_2 + N_2 \rightleftharpoons 2N + N_2$	$7.00x10^{21}$	-1.60	$1.132x10^{05}$	0.7	0.3	1.0	0.0	0.30	8.0	[1]	Figure B1(a)
2	$N_2 + O_2 \rightleftharpoons 2N + O_2$	$7.00x10^{21}$	-1.60	$1.132x10^{05}$	0.7	0.3	1.0	0.0	0.30	8.0	[1]	Figure B1(a)
3	$N_2 + NO \rightleftharpoons 2N + NO$	$7.00x10^{21}$	-1.60	$1.132x10^{05}$	0.7	0.3	1.0	0.0	0.30	8.0	[1]	Figure B1(a)
4	$N_2 + N \rightleftharpoons 2N + N$	$1.62x10^{22}$	-1.60	$1.132x10^{05}$	0.7	0.3	1.0	0.0	0.30	7.0	[227]	Figure B1(b)
5	$N_2 + O \rightleftharpoons 2N + O$	$1.62x10^{22}$	-1.60	$1.132x10^{05}$	0.7	0.3	1.0	0.0	0.30	7.0	[227]	Figure B1(b)
6	$N_2 + C \rightleftharpoons 2N + C$	$1.62x10^{22}$	-1.60	$1.132x10^{05}$	0.7	0.3	1.0	0.0	0.30	7.0	[227]	Figure B1(b)
7	$N_2 + NCO \rightleftharpoons 2N + NCO$	$7.00x10^{21}$	-1.60	$1.132x10^{05}$	0.7	0.3	1.0	0.0	0.30	8.0	[1]	Figure B1(a)
8	$N_2 + C_2 \rightleftharpoons 2N + C_2$	$7.00x10^{21}$	-1.60	$1.132x10^{05}$	0.7	0.3	1.0	0.0	0.30	8.0	[1]	Figure B1(a)
9	$N_2 + C_3 \rightleftharpoons 2N + C_3$	$7.00x10^{21}$	-1.60	$1.132x10^{05}$	0.7	0.3	1.0	0.0	0.30	8.0	[1]	Figure B1(a)
10	$N_2 + CO_2 \rightleftharpoons 2N + CO_2$	$7.00x10^{21}$	-1.60	$1.132x10^{05}$	0.7	0.3	1.0	0.0	0.30	8.0	[1]	Figure B1(a)
11	$N_2 + CO \rightleftharpoons 2N + CO$	$7.00x10^{21}$	-1.60	$1.132x10^{05}$	0.7	0.3	1.0	0.0	0.30	8.0	[1]	Figure B1(a)
12	$N_2 + CN \rightleftharpoons 2N + CN$	$7.00x10^{21}$	-1.60	$1.132x10^{05}$	0.7	0.3	1.0	0.0	0.30	8.0	[1]	Figure B1(a)
13	$N_2 + NO^+ \rightleftharpoons 2N + NO^+$	$7.00x10^{21}$	-1.60	$1.132x10^{05}$	0.7	0.3	1.0	0.0	0.30	8.0	[1]	Figure B1(a)
14	$N_2 + N_2^+ \rightleftharpoons 2N + N_2^+$	$7.00x10^{21}$	-1.60	$1.132x10^{05}$	0.7	0.3	1.0	0.0	0.30	8.0	[1]	Figure B1(a)
15	$N_2 + O_2^+ \rightleftharpoons 2N + O_2^+$	$7.00x10^{21}$	-1.60	$1.132x10^{05}$	0.7	0.3	1.0	0.0	0.30	8.0	[1]	Figure B1(a)
16	$N_2 + CO^+ \rightleftharpoons 2N + CO^+$	$7.00x10^{21}$	-1.60	$1.132x10^{05}$	0.7	0.3	1.0	0.0	0.30	8.0	[1]	Figure B1(a)
17	$N_2 + C^+ \rightleftharpoons 2N + C^+$	$1.62x10^{22}$	-1.60	$1.132x10^{05}$	0.7	0.3	1.0	0.0	0.30	7.0	[227]	Figure B1(b)
18	$N_2 + N^+ \rightleftharpoons 2N + N^+$	$1.62x10^{22}$	-1.60	$1.132x10^{05}$	0.7	0.3	1.0	0.0	0.30	7.0	[227]	Figure B1(b)
19	$N_2 + O^+ \rightleftharpoons 2N + O^+$	$1.62x10^{22}$	-1.60	$1.132x10^{05}$	0.7	0.3	1.0	0.0	0.30	7.0	[227]	Figure B1(b)
20	$N_2 + e^- \rightleftharpoons 2N + e^-$	$3.00x10^{24}$	-1.00	$5.938x10^{04}$	0.0	1.0	0.0	1.0	0.03	10.0	[1]	Figure B1(c)
21	$O_2 + N_2 \rightleftharpoons 2O + N_2$	$3.40x10^{18}$	-1.00	$5.938x10^{04}$	0.7	0.3	1.0	0.0	0.20	5.0	[228]	Figure B2(a)
22	$O_2 + O_2 \rightleftharpoons 2O + O_2$	$2.00x10^{21}$	-1.50	$5.950x10^{04}$	0.7	0.3	1.0	0.0	0.20	5.0	[190]	Figure B2(b)
23	$O_2 + NO \rightleftharpoons 2O + NO$	$2.00x10^{21}$	-1.50	$5.950x10^{04}$	0.7	0.3	1.0	0.0	0.20	5.0	[190]	Figure B2(b)

24	$O_2 + N \rightleftharpoons 2O + N$	$9.00x10^{19}$	-1.00	$5.950x10^{04}$	0.7	0.3	1.0	0.0	0.30	2.1	[229]	Figure B2(c)
25	$O_2 + O \rightleftharpoons 2O + O$	$9.00x10^{19}$	-1.00	$5.950x10^{04}$	0.7	0.3	1.0	0.0	0.30	2.1	[229]	Figure B2(c)
26	$O_2 + C \rightleftharpoons 2O + C$	$9.00x10^{19}$	-1.00	$5.950x10^{04}$	0.7	0.3	1.0	0.0	0.30	2.1	[229]	Figure B2(c)
27	$O_2 + NCO \rightleftharpoons 2O + NCO$	$2.00x10^{21}$	-1.50	$5.950x10^{04}$	0.7	0.3	1.0	0.0	0.20	5.0	[190]	Figure B2(b)
28	$O_2 + C_2 \rightleftharpoons 2O + C_2$	$2.00x10^{21}$	-1.50	$5.950x10^{04}$	0.7	0.3	1.0	0.0	0.20	5.0	[190]	Figure B2(b)
29	$O_2 + C_3 \rightleftharpoons 2O + C_3$	$2.00x10^{21}$	-1.50	$5.950x10^{04}$	0.7	0.3	1.0	0.0	0.20	5.0	[190]	Figure B2(b)
30	$O_2 + CO_2 \rightleftharpoons 2O + CO_2$	$2.00x10^{21}$	-1.50	$5.950x10^{04}$	0.7	0.3	1.0	0.0	0.20	5.0	[190]	Figure B2(b)
31	$O_2 + CO \rightleftharpoons 2O + CO$	$2.00x10^{21}$	-1.50	$5.950x10^{04}$	0.7	0.3	1.0	0.0	0.20	5.0	[190]	Figure B2(b)
32	$O_2 + CN \rightleftharpoons 2O + CN$	$2.00x10^{21}$	-1.50	$5.950x10^{04}$	0.7	0.3	1.0	0.0	0.20	5.0	[190]	Figure B2(b)
33	$O_2 + NO^+ \rightleftharpoons 2O + NO^+$	$2.00x10^{21}$	-1.50	$5.950x10^{04}$	0.7	0.3	1.0	0.0	0.20	5.0	[190]	Figure B2(b)
34	$O_2 + N_2^+ \rightleftharpoons 2O + N_2^+$	$2.00x10^{21}$	-1.50	$5.950x10^{04}$	0.7	0.3	1.0	0.0	0.20	5.0	[190]	Figure B2(b)
35	$O_2 + O_2^+ \rightleftharpoons 2O + O_2^+$	$2.00x10^{21}$	-1.50	$5.950x10^{04}$	0.7	0.3	1.0	0.0	0.20	5.0	[190]	Figure B2(b)
36	$O_2 + CO^+ \rightleftharpoons 2O + CO^+$	$2.00x10^{21}$	-1.50	$5.950x10^{04}$	0.7	0.3	1.0	0.0	0.20	5.0	[190]	Figure B2(b)
37	$O_2 + C^+ \rightleftharpoons 2O + C^+$	$9.00x10^{19}$	-1.00	$5.950x10^{04}$	0.7	0.3	1.0	0.0	0.30	2.1	[229]	Figure B2(c)
38	$O_2 + N^+ \rightleftharpoons 2O + N^+$	$9.00x10^{19}$	-1.00	$5.950x10^{04}$	0.7	0.3	1.0	0.0	0.30	2.1	[229]	Figure B2(c)
39	$O_2 + O^+ \rightleftharpoons 2O + O^+$	$9.00x10^{19}$	-1.00	$5.950x10^{04}$	0.7	0.3	1.0	0.0	0.30	2.1	[229]	Figure B2(c)
40	$NO + N_2 \rightleftharpoons N + O + N_2$	$2.00x10^{15}$	0.00	$7.457x10^{04}$	0.7	0.3	1.0	0.0	0.20	3.0	[194]	Figure B3(a)
41	$NO + O_2 \rightleftharpoons N + O + O_2$	$2.00x10^{15}$	0.00	$7.457x10^{04}$	0.7	0.3	1.0	0.0	0.20	3.0	[194]	Figure B3(a)
42	$NO + NO \rightleftharpoons N + O + NO$	$4.40x10^{16}$	0.00	$7.457x10^{04}$	0.7	0.3	1.0	0.0	0.20	2.5	[194]	Figure B3(b)
43	$NO + N \rightleftharpoons N + O + N$	$4.40x10^{16}$	0.00	$7.457x10^{04}$	0.7	0.3	1.0	0.0	0.20	2.5	[194]	Figure B3(b)
44	$NO + O \rightleftharpoons N + O + O$	$4.40x10^{16}$	0.00	$7.457x10^{04}$	0.7	0.3	1.0	0.0	0.20	2.5	[194]	Figure B3(b)
45	$NO + C \rightleftharpoons N + O + C$	$4.40x10^{16}$	0.00	$7.457x10^{04}$	0.7	0.3	1.0	0.0	0.20	2.5	[194]	Figure B3(b)
46	$NO + NCO \rightleftharpoons N + O + NCO$	$2.00x10^{15}$	0.00	$7.457x10^{04}$	0.7	0.3	1.0	0.0	0.20	3.0	[194]	Figure B3(a)
47	$NO + C_2 \rightleftharpoons N + O + C_2$	$2.00x10^{15}$	0.00	$7.457x10^{04}$	0.7	0.3	1.0	0.0	0.20	3.0	[194]	Figure B3(a)
48	$NO + C_3 \rightleftharpoons N + O + C_3$	$2.00x10^{15}$	0.00	$7.457x10^{04}$	0.7	0.3	1.0	0.0	0.20	3.0	[194]	Figure B3(a)
49	$NO + CO_2 \rightleftharpoons N + O + CO_2$	$4.40x10^{16}$	0.00	$7.457x10^{04}$	0.7	0.3	1.0	0.0	0.20	2.5	[194]	Figure B3(b)
50	$NO + CO \rightleftharpoons N + O + CO$	$2.00x10^{15}$	0.00	$7.457x10^{04}$	0.7	0.3	1.0	0.0	0.20	3.0	[194]	Figure B3(a)
51	$NO + CN \rightleftharpoons N + O + CN$	$2.00x10^{15}$	0.00	$7.457x10^{04}$	0.7	0.3	1.0	0.0	0.20	3.0	[194]	Figure B3(a)

52	$NO + NO^+ \rightleftharpoons N + O + NO^+$	$4.40x10^{16}$	0.00	$7.457x10^{04}$	0.7	0.3	1.0	0.0	0.20	2.5	[194]	Figure B3(b)
53	$NO + N_2^+ \rightleftharpoons N + O + N_2^+$	$2.00x10^{15}$	0.00	$7.457x10^{04}$	0.7	0.3	1.0	0.0	0.20	3.0	[194]	Figure B3(a)
54	$NO + O_2^+ \rightleftharpoons N + O + O_2^+$	$2.00x10^{15}$	0.00	$7.457x10^{04}$	0.7	0.3	1.0	0.0	0.20	3.0	[86]	Figure B3(a)
55	$NO + CO^+ \rightleftharpoons N + O + CO^+$	$2.00x10^{15}$	0.00	$7.457x10^{04}$	0.7	0.3	1.0	0.0	0.20	3.0	[194]	Figure B3(a)
56	$NO + C^+ \rightleftharpoons N + O + C^+$	$4.40x10^{16}$	0.00	$7.457x10^{04}$	0.7	0.3	1.0	0.0	0.20	2.5	[194]	Figure B3(b)
57	$NO + N^+ \rightleftharpoons N + O + N^+$	$4.40x10^{16}$	0.00	$7.457x10^{04}$	0.7	0.3	1.0	0.0	0.20	2.5	[194]	Figure B3(b)
58	$NO + O^+ \rightleftharpoons N + O + O^+$	$4.40x10^{16}$	0.00	$7.457x10^{04}$	0.7	0.3	1.0	0.0	0.20	2.5	[194]	Figure B3(b)
59	$C_2 + N_2 \rightleftharpoons 2C + N_2$	$9.68x10^{22}$	-2.00	$7.100x10^{04}$	0.5	0.5	1.0	0.0	0.10	4.0	[193]	Figure B4
60	$C_2 + O_2 \rightleftharpoons 2C + O_2$	$9.68x10^{22}$	-2.00	$7.100x10^{04}$	0.5	0.5	1.0	0.0	0.10	4.0	[193]	Figure B4
61	$C_2 + NO \rightleftharpoons 2C + NO$	$9.68x10^{22}$	-2.00	$7.100x10^{04}$	0.5	0.5	1.0	0.0	0.10	4.0	[193]	Figure B4
62	$C_2 + N \rightleftharpoons 2C + N$	$9.68x10^{22}$	-2.00	$7.100x10^{04}$	0.5	0.5	1.0	0.0	0.10	4.0	[193]	Figure B4
63	$C_2 + O \rightleftharpoons 2C + O$	$9.68x10^{22}$	-2.00	$7.100x10^{04}$	0.5	0.5	1.0	0.0	0.10	4.0	[193]	Figure B4
64	$C_2 + C \rightleftharpoons 2C + C$	$9.68x10^{22}$	-2.00	$7.100x10^{04}$	0.5	0.5	1.0	0.0	0.10	4.0	[193]	Figure B4
65	$C_2 + NCO \rightleftharpoons 2C + NCO$	$9.68x10^{22}$	-2.00	$7.100x10^{04}$	0.5	0.5	1.0	0.0	0.10	4.0	[193]	Figure B4
66	$C_2 + C_2 \rightleftharpoons 2C + C_2$	$9.68x10^{22}$	-2.00	$7.100x10^{04}$	0.5	0.5	1.0	0.0	0.10	4.0	[193]	Figure B4
67	$C_2 + C_3 \rightleftharpoons 2C + C_3$	$9.68x10^{22}$	-2.00	$7.100x10^{04}$	0.5	0.5	1.0	0.0	0.10	4.0	[193]	Figure B4
68	$C_2 + CO_2 \rightleftharpoons 2C + CO_2$	$9.68x10^{22}$	-2.00	$7.100x10^{04}$	0.5	0.5	1.0	0.0	0.10	4.0	[193]	Figure B4
69	$C_2 + CO \rightleftharpoons 2C + CO$	$9.68x10^{22}$	-2.00	$7.100x10^{04}$	0.5	0.5	1.0	0.0	0.10	4.0	[193]	Figure B4
70	$C_2 + CN \rightleftharpoons 2C + CN$	$9.68x10^{22}$	-2.00	$7.100x10^{04}$	0.5	0.5	1.0	0.0	0.10	4.0	[193]	Figure B4
71	$C_2 + NO^+ \rightleftharpoons 2C + NO^+$	$9.68x10^{22}$	-2.00	$7.100x10^{04}$	0.5	0.5	1.0	0.0	0.10	4.0	[193]	Figure B4
72	$C_2 + N_2^+ \rightleftharpoons 2C + N_2^+$	$9.68x10^{22}$	-2.00	$7.100x10^{04}$	0.5	0.5	1.0	0.0	0.10	4.0	[193]	Figure B4
73	$C_2 + O_2^+ \rightleftharpoons 2C + O_2+$	$9.68x10^{22}$	-2.00	$7.100x10^{04}$	0.5	0.5	1.0	0.0	0.10	4.0	[193]	Figure B4
74	$C_2 + CO^+ \rightleftharpoons 2C + CO^+$	$9.68x10^{22}$	-2.00	$7.100x10^{04}$	0.5	0.5	1.0	0.0	0.10	4.0	[193]	Figure B4
75	$C_2 + C^+ \rightleftharpoons 2C + C^+$	$9.68x10^{22}$	-2.00	$7.100x10^{04}$	0.5	0.5	1.0	0.0	0.10	4.0	[193]	Figure B4
76	$C_2 + N^+ \rightleftharpoons 2C + N^+$	$9.68x10^{22}$	-2.00	$7.100x10^{04}$	0.5	0.5	1.0	0.0	0.10	4.0	[193]	Figure B4
77	$C_2 + O^+ \rightleftharpoons 2C + O^+$	$9.68x10^{22}$	-2.00	$7.100x10^{04}$	0.5	0.5	1.0	0.0	0.10	4.0	[193]	Figure B4
78	$CN + N_2 \rightleftharpoons C + N + N_2$	$6.00x10^{15}$	-0.40	$7.100x10^{04}$	0.5	0.5	1.0	0.0	0.20	4.0	[128]	Figure B5
79	$CN + O_2 \rightleftharpoons C + N + O_2$	$6.00x10^{15}$	-0.40	$7.100x10^{04}$	0.5	0.5	1.0	0.0	0.20	4.0	[128]	Figure B5

80	$CN + NO \rightleftharpoons C + N + NO$	$6.00x10^{15}$	-0.40	$7.100x10^{04}$	0.5	0.5	1.0	0.0	0.20	4.0	[128]	Figure B5
81	$CN + N \rightleftharpoons C + N + N$	$6.00x10^{15}$	-0.40	$7.100x10^{04}$	0.5	0.5	1.0	0.0	0.20	4.0	[128]	Figure B5
82	$CN + O \rightleftharpoons C + N + O$	$6.00x10^{15}$	-0.40	$7.100x10^{04}$	0.5	0.5	1.0	0.0	0.20	4.0	[128]	Figure B5
83	$CN + C \rightleftharpoons C + N + C$	$6.00x10^{15}$	-0.40	$7.100x10^{04}$	0.5	0.5	1.0	0.0	0.20	4.0	[128]	Figure B5
84	$CN + NCO \rightleftharpoons C + N + NCO$	$6.00x10^{15}$	-0.40	$7.100x10^{04}$	0.5	0.5	1.0	0.0	0.20	4.0	[128]	Figure B5
85	$CN + C_2 \rightleftharpoons C + N + C_2$	$6.00x10^{15}$	-0.40	$7.100x10^{04}$	0.5	0.5	1.0	0.0	0.20	4.0	[128]	Figure B5
86	$CN + C_3 \rightleftharpoons C + N + C_3$	$6.00x10^{15}$	-0.40	$7.100x10^{04}$	0.5	0.5	1.0	0.0	0.20	4.0	[128]	Figure B5
87	$CN + CO_2 \rightleftharpoons C + N + CO_2$	$6.00x10^{15}$	-0.40	$7.100x10^{04}$	0.5	0.5	1.0	0.0	0.20	4.0	[128]	Figure B5
88	$CN + CO \rightleftharpoons C + N + CO$	$6.00x10^{15}$	-0.40	$7.100x10^{04}$	0.5	0.5	1.0	0.0	0.20	4.0	[128]	Figure B5
89	$CN + CN \rightleftharpoons C + N + CN$	$6.00x10^{15}$	-0.40	$7.100x10^{04}$	0.5	0.5	1.0	0.0	0.20	4.0	[128]	Figure B5
90	$CN + NO^+ \rightleftharpoons C + N + NO^+$	$6.00x10^{15}$	-0.40	$7.100x10^{04}$	0.5	0.5	1.0	0.0	0.20	4.0	[128]	Figure B5
91	$CN + N_2^+ \rightleftharpoons C + N + N_2^+$	$6.00x10^{15}$	-0.40	$7.100x10^{04}$	0.5	0.5	1.0	0.0	0.20	4.0	[128]	Figure B5
92	$CN + O_2^+ \rightleftharpoons C + N + O_2^+$	$6.00x10^{15}$	-0.40	$7.100x10^{04}$	0.5	0.5	1.0	0.0	0.20	4.0	[128]	Figure B5
93	$CN + CO^+ \rightleftharpoons C + N + CO^+$	$6.00x10^{15}$	-0.40	$7.100x10^{04}$	0.5	0.5	1.0	0.0	0.20	4.0	[128]	Figure B5
94	$CN + C^+ \rightleftharpoons C + N + C^+$	$6.00x10^{15}$	-0.40	$7.100x10^{04}$	0.5	0.5	1.0	0.0	0.20	4.0	[128]	Figure B5
95	$CN + N^+ \rightleftharpoons C + N + N^+$	$6.00x10^{15}$	-0.40	$7.100x10^{04}$	0.5	0.5	1.0	0.0	0.20	4.0	[128]	Figure B5
96	$CN + O^+ \rightleftharpoons C + N + O^+$	$6.00x10^{15}$	-0.40	$7.100x10^{04}$	0.5	0.5	1.0	0.0	0.20	4.0	[128]	Figure B5
97	$CO + N_2 \rightleftharpoons O + C + N_2$	$2.30x10^{20}$	-1.00	$1.290x10^{05}$	0.5	0.5	1.0	0.0	0.10	8.0	[137]	Figure B6(b)
98	$CO + O_2 \rightleftharpoons O + C + O_2$	$2.30x10^{20}$	-1.00	$1.290x10^{05}$	0.5	0.5	1.0	0.0	0.10	8.0	[137]	Figure B6(b)
99	$CO + NO \rightleftharpoons O + C + NO$	$2.30x10^{20}$	-1.00	$1.290x10^{05}$	0.5	0.5	1.0	0.0	0.10	8.0	[137]	Figure B6(b)
100	$CO + N \rightleftharpoons O + C + N$	$4.13x10^{15}$	0.00	$1.028x10^{05}$	0.5	0.5	1.0	0.0	0.20	8.0	[230]	Figure B6(a)
101	$CO + O \rightleftharpoons O + C + O$	$4.13x10^{15}$	0.00	$1.028x10^{05}$	0.5	0.5	1.0	0.0	0.20	8.0	[230]	Figure B6(a)
102	$CO + C \rightleftharpoons O + C + C$	$4.13x10^{15}$	0.00	$1.028x10^{05}$	0.5	0.5	1.0	0.0	0.20	8.0	[230]	Figure B6(a)
103	$CO + NCO \rightleftharpoons O + C + NCO$	$2.30x10^{20}$	-1.00	$1.290x10^{05}$	0.5	0.5	1.0	0.0	0.10	8.0	[137]	Figure B6(b)
104	$CO + C_2 \rightleftharpoons O + C + C_2$	$2.30x10^{20}$	-1.00	$1.290x10^{05}$	0.5	0.5	1.0	0.0	0.10	8.0	[137]	Figure B6(b)
105	$CO + C_3 \rightleftharpoons O + C + C_3$	$2.30x10^{20}$	-1.00	$1.290x10^{05}$	0.5	0.5	1.0	0.0	0.10	8.0	[137]	Figure B6(b)
106	$CO + CO_2 \rightleftharpoons O + C + CO_2$	$2.30x10^{20}$	-1.00	$1.290x10^{05}$	0.5	0.5	1.0	0.0	0.10	8.0	[137]	Figure B6(b)
107	$CO + CO \rightleftharpoons O + C + CO$	$2.30x10^{20}$	-1.00	$1.290x10^{05}$	0.5	0.5	1.0	0.0	0.10	8.0	[137]	Figure B6(b)

108	$CO + CN \rightleftharpoons O + C + CN$	2.30×10^{20}	-1.00	1.290×10^{05}	0.5	0.5	1.0	0.0	0.10	8.0	[137]	Figure B6(b)
109	$CO + NO^+ \rightleftharpoons O + C + NO^+$	2.30×10^{20}	-1.00	1.290×10^{05}	0.5	0.5	1.0	0.0	0.10	8.0	[137]	Figure B6(b)
110	$CO + N_2^+ \rightleftharpoons O + C + N_2^+$	2.30×10^{20}	-1.00	1.290×10^{05}	0.5	0.5	1.0	0.0	0.10	8.0	[137]	Figure B6(b)
111	$CO + O_2^+ \rightleftharpoons O + C + O_2^+$	2.30×10^{20}	-1.00	1.290×10^{05}	0.5	0.5	1.0	0.0	0.10	8.0	[137]	Figure B6(b)
112	$CO + CO^+ \rightleftharpoons O + C + CO^+$	2.30×10^{20}	-1.00	1.290×10^{05}	0.5	0.5	1.0	0.0	0.10	8.0	[137]	Figure B6(b)
113	$CO + C^+ \rightleftharpoons O + C + C^+$	4.13×10^{15}	0.00	1.028×10^{05}	0.5	0.5	1.0	0.0	0.20	8.0	[230]	Figure B6(a)
114	$CO + N^+ \rightleftharpoons O + C + N^+$	4.13×10^{15}	0.00	1.028×10^{05}	0.5	0.5	1.0	0.0	0.20	8.0	[230]	Figure B6(a)
115	$CO + O^+ \rightleftharpoons O + C + O^+$	4.13×10^{15}	0.00	1.028×10^{05}	0.5	0.5	1.0	0.0	0.20	8.0	[230]	Figure B6(a)
116	$CO_2 + N_2 \rightleftharpoons O + CO + N_2$	7.47×10^{12}	0.50	5.232×10^{04}	0.5	0.5	1.0	0.0	0.20	8.0	[195]	Figure B7(b)
117	$CO_2 + O_2 \rightleftharpoons O + CO + O_2$	7.47×10^{12}	0.50	5.232×10^{04}	0.5	0.5	1.0	0.0	0.20	8.0	[195]	Figure B7(b)
118	$CO_2 + NO \rightleftharpoons O + CO + NO$	7.47×10^{12}	0.50	5.232×10^{04}	0.5	0.5	1.0	0.0	0.20	8.0	[195]	Figure B7(b)
119	$CO_2 + N \rightleftharpoons O + CO + N$	1.19×10^{22}	-1.50	6.328×10^{04}	0.5	0.5	1.0	0.0	0.20	1.3	[47]	Figure B7(a)
120	$CO_2 + O \rightleftharpoons O + CO + O$	1.19×10^{22}	-1.50	6.328×10^{04}	0.5	0.5	1.0	0.0	0.20	1.3	[47]	Figure B7(a)
121	$CO_2 + C \rightleftharpoons O + CO + C$	1.19×10^{22}	-1.50	6.328×10^{04}	0.5	0.5	1.0	0.0	0.20	1.3	[47]	Figure B7(a)
122	$CO_2 + NCO \rightleftharpoons O + CO + NCO$	7.47×10^{12}	0.50	5.232×10^{04}	0.5	0.5	1.0	0.0	0.20	8.0	[195]	Figure B7(b)
123	$CO_2 + C_2 \rightleftharpoons O + CO + C_2$	7.47×10^{12}	0.50	5.232×10^{04}	0.5	0.5	1.0	0.0	0.20	8.0	[195]	Figure B7(b)
124	$CO_2 + C_3 \rightleftharpoons O + CO + C_3$	7.47×10^{12}	0.50	5.232×10^{04}	0.5	0.5	1.0	0.0	0.20	8.0	[195]	Figure B7(b)
125	$CO_2 + CO_2 \rightleftharpoons O + CO + CO_2$	7.47×10^{12}	0.50	5.232×10^{04}	0.5	0.5	1.0	0.0	0.20	8.0	[195]	Figure B7(b)
126	$CO_2 + CO \rightleftharpoons O + CO + CO$	7.47×10^{12}	0.50	5.232×10^{04}	0.5	0.5	1.0	0.0	0.20	8.0	[195]	Figure B7(b)
127	$CO_2 + CN \rightleftharpoons O + CO + CN$	7.47×10^{12}	0.50	5.232×10^{04}	0.5	0.5	1.0	0.0	0.20	8.0	[195]	Figure B7(b)
128	$CO_2 + NO^+ \rightleftharpoons O + CO + NO^+$	7.47×10^{12}	0.50	5.232×10^{04}	0.5	0.5	1.0	0.0	0.20	8.0	[195]	Figure B7(b)
129	$CO_2 + N_2^+ \rightleftharpoons O + CO + N_2^+$	7.47×10^{12}	0.50	5.232×10^{04}	0.5	0.5	1.0	0.0	0.20	8.0	[195]	Figure B7(b)
130	$CO_2 + O_2^+ \rightleftharpoons O + CO + O_2^+$	7.47×10^{12}	0.50	5.232×10^{04}	0.5	0.5	1.0	0.0	0.20	8.0	[195]	Figure B7(b)
131	$CO_2 + CO^+ \rightleftharpoons O + CO + CO^+$	7.47×10^{12}	0.50	5.232×10^{04}	0.5	0.5	1.0	0.0	0.20	8.0	[195]	Figure B7(b)
132	$CO_2 + C^+ \rightleftharpoons O + CO + C^+$	1.19×10^{22}	-1.50	6.328×10^{04}	0.5	0.5	1.0	0.0	0.20	1.3	[47]	Figure B7(a)
133	$CO_2 + N^+ \rightleftharpoons O + CO + N^+$	1.19×10^{22}	-1.50	6.328×10^{04}	0.5	0.5	1.0	0.0	0.20	1.3	[47]	Figure B7(a)
134	$CO_2 + O^+ \rightleftharpoons O + CO + O^+$	1.19×10^{22}	-1.50	6.328×10^{04}	0.5	0.5	1.0	0.0	0.20	1.3	[47]	Figure B7(a)
135	$NCO + N_2 \rightleftharpoons N + CO + N_2$	3.10×10^{16}	-0.50	2.400×10^{04}	0.5	0.5	1.0	0.0	0.05	10.0	[196]	Figure B8

136	$NCO + O_2 \rightleftharpoons N + CO + O_2$	$3.10x10^{16}$	-0.50	$2.400x10^{04}$	0.5	0.5	1.0	0.0	0.05	10.0	[196]	Figure B8
137	$NCO + NO \rightleftharpoons N + CO + NO$	$3.10x10^{16}$	-0.50	$2.400x10^{04}$	0.5	0.5	1.0	0.0	0.05	10.0	[196]	Figure B8
138	$NCO + N \rightleftharpoons N + CO + N$	$3.10x10^{16}$	-0.50	$2.400x10^{04}$	0.5	0.5	1.0	0.0	0.05	10.0	[196]	Figure B8
139	$NCO + O \rightleftharpoons N + CO + O$	$3.10x10^{16}$	-0.50	$2.400x10^{04}$	0.5	0.5	1.0	0.0	0.05	10.0	[196]	Figure B8
140	$NCO + C \rightleftharpoons N + CO + C$	$3.10x10^{16}$	-0.50	$2.400x10^{04}$	0.5	0.5	1.0	0.0	0.05	10.0	[196]	Figure B8
141	$NCO + NCO \rightleftharpoons N + CO + NCO$	$3.10x10^{16}$	-0.50	$2.400x10^{04}$	0.5	0.5	1.0	0.0	0.05	10.0	[196]	Figure B8
142	$NCO + C_2 \rightleftharpoons N + CO + C_2$	$3.10x10^{16}$	-0.50	$2.400x10^{04}$	0.5	0.5	1.0	0.0	0.05	10.0	[196]	Figure B8
143	$NCO + C_3 \rightleftharpoons N + CO + C_3$	$3.10x10^{16}$	-0.50	$2.400x10^{04}$	0.5	0.5	1.0	0.0	0.05	10.0	[196]	Figure B8
144	$NCO + CO_2 \rightleftharpoons N + CO + CO_2$	$3.10x10^{16}$	-0.50	$2.400x10^{04}$	0.5	0.5	1.0	0.0	0.05	10.0	[196]	Figure B8
145	$NCO + CO \rightleftharpoons N + CO + CO$	$3.10x10^{16}$	-0.50	$2.400x10^{04}$	0.5	0.5	1.0	0.0	0.05	10.0	[196]	Figure B8
146	$NCO + CN \rightleftharpoons N + CO + CN$	$3.10x10^{16}$	-0.50	$2.400x10^{04}$	0.5	0.5	1.0	0.0	0.05	10.0	[196]	Figure B8
147	$NCO + NO^+ \rightleftharpoons N + CO + NO^+$	$3.10x10^{16}$	-0.50	$2.400x10^{04}$	0.5	0.5	1.0	0.0	0.05	10.0	[196]	Figure B8
148	$NCO + N_2^+ \rightleftharpoons N + CO + N_2^+$	$3.10x10^{16}$	-0.50	$2.400x10^{04}$	0.5	0.5	1.0	0.0	0.05	10.0	[196]	Figure B8
149	$NCO + O_2^+ \rightleftharpoons N + CO + O_2^+$	$3.10x10^{16}$	-0.50	$2.400x10^{04}$	0.5	0.5	1.0	0.0	0.05	10.0	[196]	Figure B8
150	$NCO + CO^+ \rightleftharpoons N + CO + CO^+$	$3.10x10^{16}$	-0.50	$2.400x10^{04}$	0.5	0.5	1.0	0.0	0.05	10.0	[196]	Figure B8
151	$NCO + C^+ \rightleftharpoons N + CO + C^+$	$3.10x10^{16}$	-0.50	$2.400x10^{04}$	0.5	0.5	1.0	0.0	0.05	10.0	[196]	Figure B8
152	$NCO + N^+ \rightleftharpoons N + CO + N^+$	$3.10x10^{16}$	-0.50	$2.400x10^{04}$	0.5	0.5	1.0	0.0	0.05	10.0	[196]	Figure B8
153	$NCO + O^+ \rightleftharpoons N + CO + O^+$	$3.10x10^{16}$	-0.50	$2.400x10^{04}$	0.5	0.5	1.0	0.0	0.05	10.0	[196]	Figure B8
154	$N_2 + C \rightleftharpoons CN + N$	$5.24x10^{13}$	0.00	$2.260x10^{04}$	1.0	0.0	1.0	0.0	0.50	1.3	[127]	Figure B9
155	$CN + O \rightleftharpoons NO + C$	$1.60x10^{13}$	0.10	$1.460x10^{04}$	1.0	0.0	1.0	0.0	0.10	6.0	[133]	Figure B10
156	$CO + N \rightleftharpoons NO + C$	$1.10x10^{14}$	0.07	$5.350x10^{04}$	1.0	0.0	1.0	0.0	0.50	8.0	[128]	Figure B11
157	$CO + O \rightleftharpoons C + O_2$	$9.79x10^{11}$	0.42	$6.920x10^{04}$	1.0	0.0	1.0	0.0	0.10	15.0	[231]	Figure B12
158	$C_3 + C \rightleftharpoons C_2 + C_2$	$6.00x10^{11}$	1.07	$1.650x10^{04}$	1.0	0.0	1.0	0.0	0.30	3.0	[128]	Figure B13
159	$C_2 + N_2 \rightleftharpoons CN + CN$	$7.10x10^{13}$	0.00	$2.100x10^{04}$	1.0	0.0	1.0	0.0	0.20	12.0	[193]	Figure B14
160	$N_2 + O \rightleftharpoons NO + N$	$2.97x10^{10}$	0.98	$3.789x10^{04}$	1.0	0.0	1.0	0.0	0.10	7.0	[199]	Figure B15
161	$O_2 + N \rightleftharpoons NO + O$	$2.49x10^{09}$	1.18	$4.005x10^{03}$	1.0	0.0	1.0	0.0	0.10	10.0	[136]	Figure B16
162	$CN + C \rightleftharpoons C_2 + N$	$3.00x10^{14}$	0.00	$1.812x10^{04}$	1.0	0.0	1.0	0.0	0.30	10.0	[200]	Figure B17
163	$CN + CO \rightleftharpoons C + NCO$	$1.50x10^{16}$	-0.49	$6.580x10^{04}$	1.0	0.0	1.0	0.0	0.10	10.0	[201]	Figure B18

164	$CN + CO_2 \rightleftharpoons CO + NCO$	$3.68x10^{06}$	2.16	$1.353x10^{04}$	1.0	0.0	1.0	0.0	0.10	10.0	[132]	Figure B19
165	$CN + NO \rightleftharpoons N + NCO$	$9.64x10^{13}$	0.00	$2.117x10^{04}$	1.0	0.0	1.0	0.0	0.50	2.0	[202]	Figure B20
166	$CN + O \rightleftharpoons CO + N$	$3.53x10^{11}$	0.72	$3.860x10^{04}$	1.0	0.0	1.0	0.0	0.10	10.0	[127]	Figure B21
167	$NCO + O \rightleftharpoons CN + O_2$	$4.74x10^{16}$	-0.99	$7.390x10^{03}$	1.0	0.0	1.0	0.0	0.10	40.0	[232]	Figure B22
168	$CO_2 + O \rightleftharpoons CO + O_2$	$2.71x10^{14}$	0.00	$3.380x10^{04}$	1.0	0.0	1.0	0.0	0.30	10.0	[205]	Figure B23
169	$CO_2 + N \rightleftharpoons NO + CO$	$1.93x10^{11}$	0.00	$1.710x10^{03}$	1.0	0.0	1.0	0.0	0.10	5.0	[206]	Figure B24
170	$NCO + N \rightleftharpoons N_2 + CO$	$1.39x10^{14}$	-0.25	$0.000x10^{00}$	1.0	0.0	1.0	0.0	0.30	3.2	[127]	Figure B25
171	$NCO + NO \rightleftharpoons N_2 + CO_2$	$6.09x10^{17}$	-1.73	$3.800x10^{02}$	1.0	0.0	1.0	0.0	0.20	2.5	[203]	Figure B26
172	$NCO + O \rightleftharpoons NO + CO$	$2.00x10^{13}$	0.00	$0.000x10^{00}$	1.0	0.0	1.0	0.0	0.40	3.0	[196]	Figure B27
173	$NCO + O2 \rightleftharpoons NO + CO_2$	$1.32x10^{10}$	0.00	$0.000x10^{00}$	1.0	0.0	1.0	0.0	0.20	2.0	[208]	Figure B28
174	$C + O \rightleftharpoons CO^+ + e^-$	$2.05x10^{10}$	0.60	$3.499x10^{04}$	1.0	0.0	0.0	1.0	0.10	5.0	[138]	Figure B29
175	$N + O \rightleftharpoons NO^+ + e^-$	$1.09x10^{12}$	0.15	$3.459x10^{04}$	1.0	0.0	0.0	1.0	0.30	4.0	[138]	Figure B30
176	$N + N \rightleftharpoons N_2^+ + e^-$	$3.49x10^{11}$	0.51	$7.121x10^{04}$	1.0	0.0	0.0	1.0	0.50	10.0	[99]	Figure B31
177	$O + O \rightleftharpoons O_2^+ + e^-$	$1.82x10^{10}$	0.68	$8.068x10^{04}$	1.0	0.0	1.0	0.0	0.10	6.0	[138]	Figure B32
178	$N_2 + O_2^+ \rightleftharpoons N_2^+ + O_2$	$2.01x10^{10}$	0.98	$4.070x10^{04}$	1.0	0.0	1.0	0.0	0.05	10.0	[233]	Figure B33
179	$NO^+ + N \rightleftharpoons O^+ + N_2$	$2.54x10^{12}$	-0.17	$1.280x10^{04}$	1.0	0.0	1.0	0.0	0.05	20.0	[234]	Figure B34
180	$NO^+ + O \rightleftharpoons N^+ + O_2$	$1.34x10^{13}$	0.31	$7.727x10^{04}$	1.0	0.0	1.0	0.0	0.30	5.0	[117]	Figure B35
181	$NO^+ + O_2 \rightleftharpoons O_2^+ + NO$	$3.73x10^{15}$	-0.06	$3.260x10^{04}$	1.0	0.0	1.0	0.0	0.20	5.0	[229]	Figure B36
182	$NO^+ + N \rightleftharpoons N_2^+ + O$	$7.20x10^{13}$	0.00	$3.550x10^{04}$	1.0	0.0	1.0	0.0	0.50	9.0	[1]	Figure B37
183	$O_2^+ + N \rightleftharpoons N^+ + O_2$	$5.81x10^{14}$	0.03	$2.860x10^{04}$	1.0	0.0	1.0	0.0	0.30	2.5	[235]	Figure B38
184	$NO + O+ \rightleftharpoons N^+ + O_2$	$1.04x10^{12}$	0.33	$2.660x10^{04}$	1.0	0.0	1.0	0.0	0.01	5.0	[236]	Figure B39
185	$NO^+ + O \rightleftharpoons O_2^+ + N$	$7.20x10^{12}$	0.29	$4.860x10^{04}$	1.0	0.0	1.0	0.0	0.70	2.0	[1]	Figure B40
186	$O^+ + N_2 \rightleftharpoons N_2^+ + O$	$3.46x10^{12}$	0.11	$2.280x10^{04}$	1.0	0.0	1.0	0.0	0.03	8.0	[237]	Figure B41
187	$NO^+ + C \rightleftharpoons NO + C^+$	$1.00x10^{13}$	0.00	$2.320x10^{04}$	1.0	0.0	1.0	0.0	0.10	10.0	[137]	Figure B42
188	$O_2 + C+ \rightleftharpoons O_2^+ + C$	$1.00x10^{13}$	0.00	$9.400x10^{03}$	1.0	0.0	1.0	0.0	0.10	10.0	[137]	Figure B42
189	$CO + C+ \rightleftharpoons CO^+ + C$	$1.00x10^{13}$	0.00	$3.140x10^{04}$	1.0	0.0	1.0	0.0	0.10	10.0	[137]	Figure B42
190	$N_2 + C^+ \rightleftharpoons N_2^+ + C$	$1.11x10^{14}$	-0.11	$5.000x10^{04}$	1.0	0.0	1.0	0.0	0.10	10.0	[193]	Figure B42
191	$N_2 + N^+ \rightleftharpoons N_2^+ + N$	$3.30x10^{07}$	1.43	$1.220x10^{04}$	1.0	0.0	1.0	0.0	0.10	30.0	[145]	Figure B43

192	$O_2^+ + O \rightleftharpoons O^+ + O_2$	3.26×10^{11}	0.31	1.800×10^{04}	1.0	0.0	1.0	0.0	0.10	12.0	[238]	Figure B44
193	$C + e^- \rightleftharpoons C^+ + e^- + e^-$	3.90×10^{33}	-3.78	1.307×10^{05}	0.0	1.0	0.0	1.0	0.10	15.0	[137]	Figure B45
194	$N + e^- \rightleftharpoons N^+ + e^- + e^-$	2.50×10^{34}	-3.82	1.682×10^{05}	0.0	1.0	0.0	1.0	0.03	15.0	[178]	Figure B46
195	$O + e^- \rightleftharpoons O^+ + e^- + e^-$	3.90×10^{33}	-3.78	1.585×10^{05}	0.0	1.0	0.0	1.0	0.04	50.0	[1]	Figure B47

Table A2: Vibrational-translational, electron-heavy particle, and electron impact ionization translational energy transfer baseline (BL) and uncertainty multiplier intervals.

No.	Energy Exchange Parameter	Baseline Expression	U_{low}	U_{high}	UB Refs.
196	$\boldsymbol{\tau}_{vt}$, $N_2 + N_2$	$\tau_{sr} = U\frac{101{,}325}{p}\exp\left[A_{sr}\left(T_{tr}^{-\frac{1}{3}} - B_{sr}\right) - 18.42\right]$	0.30	1.5	[64,149]
197	$\boldsymbol{\tau}_{vt}$, $N_2 + N$		0.50	2.0	[64,149]
198	$\boldsymbol{\tau}_{vt}$, $N_2 + O_2$	$A_{sr} = 1.16x10^{-3}\mu_{sr}^{\frac{1}{2}}\theta_{v_s}^{\frac{4}{3}}$	0.10	10.0	[64,150]
199	$\boldsymbol{\tau}_{vt}$, $N_2 + O$		0.10	10.0	[64,150]
200	$\boldsymbol{\tau}_{vt}$, $O_2 + O_2$	$B_{sr} = 0.015\,\mu_{sr}^{\frac{1}{4}}$	0.50	2.0	[64,151]
201	$\boldsymbol{\tau}_{vt}$, $O_2 + O$		0.50	4.0	[64,150,152]
202	$\boldsymbol{\tau}_{vt}$, $O_2 + N_2$	$\mu_{sr} = \frac{M_s M_r}{M_s + M_r}$	0.10	5.0	[64,150]
203	$\boldsymbol{\tau}_{vt}$, $O_2 + N$		0.30	2.0	[64,150]
204	$\boldsymbol{\sigma}_{er}$, N	$S_{h-e} = 3UR_u\rho_e(T_{tr} - T_{ve})\sqrt{\frac{8R_uT_{ve}}{\pi M_e}}\sum_{s\neq e}\frac{\rho_s N_a}{M_s^2}\sigma_{er}$	0.10	10.0	[54,64]
205	$\boldsymbol{\sigma}_{er}$, O		0.10	10.0	
206	$\boldsymbol{\alpha}_{EII}$	$S_{e-i} = \alpha_{EII}\left(\dot{w}_{N,EII}M_N I_N + \dot{w}_{O,EII}M_O I_O\right)$	0.33	3.3	[64,70,153]

Table A3: Atomic nitrogen electron impact excitation rate transition baseline (BL) and uncertainty multiplier intervals applied to preexponential factors.

$$k_f^{el}(l,u) = UC_{el}\left(\frac{T_{ve}}{10{,}000}\right)^{\eta_{el}} exp[-\Delta E_{el}/(k_B T_{ve})], \quad U_{low} = 0.1, U_{high} = 10 \text{ [47,52,154]}$$

No.	Reaction*	l	u	C_{el}, cm$^3 s^{-1}$	η_{el}	ΔE_{el}, cm^{-1}	λ, nm	BL Refs.
207	N(^{4}S°) + e$^-$ ⇌ N(^{2}D°) + e$^-$	1	2	1.10x10^{-08}	0.20	1.923x10^{04}	520.1	[66,84,88,89]
208	N(^{4}S°) + e$^-$ ⇌ N(^{2}P°) + e$^-$	1	3	3.50x10^{-09}	0.21	2.884x10^{04}	346.7	[66,84,88,89]
209	N(^{4}S°) + e$^-$ ⇌ N(^{4}P) + e$^-$	1	4	5.40x10^{-10}	0.26	8.334x10^{04}	120.0	[66,84,88,89]
210	N(^{4}S°) + e$^-$ ⇌ N(2p^4 ^{4}P/3s ^{2}P) + e$^-$	1	5	1.00x10^{-09}	-0.12	8.749x10^{04}	114.3	[66,84,88,89]
211	N(^{4}S°) + e$^-$ ⇌ N(3p ^{4}D°/^{4}P/^{4}S) + e$^-$	1	6	4.00x10^{-09}	0.82	9.528x10^{04}	105.0	[66,84,88,89]
212	N(^{4}S°) + e$^-$ ⇌ N(3p ^{2}S/^{2}D/^{2}P) + e$^-$	1	7	1.00x10^{-30}	0.00	9.679x10^{04}	103.3	[66,84,88,89]
213	N(^{4}S°) + e$^-$ ⇌ N(4s ^{4}P/^{2}P) + e$^-$	1	8	3.50x10^{-10}	-0.13	1.039x10^{05}	96.3	[66,84,88,89]
214	N(^{4}S°) + e$^-$ ⇌ N(3d ^{4}F/^{4}P/^{4}D) + e$^-$	1	9	1.50x10^{-09}	-0.21	1.049x10^{05}	95.4	[66,84,88,89]
215	N(^{4}S°) + e$^-$ ⇌ N(3d ^{2}P/^{2}F/^{2}D) + e$^-$	1	10	1.40x10^{-09}	-0.22	1.049x10^{05}	95.3	[66,84,88,89]
216	N(^{4}S°) + e$^-$ ⇌ N(4p XX) + e$^-$	1	11	5.90x10^{-09}	0.82	1.071x10^{05}	93.4	[66,84,88,89]
217	N(^{4}S°) + e$^-$ ⇌ N(5s XX) + e$^-$	1	12	1.80x10^{-10}	-0.11	1.100x10^{05}	90.9	[66,84,88,89]
218	N(^{4}S°) + e$^-$ ⇌ N(4d XX) + e$^-$	1	13	1.60x10^{-09}	-0.19	1.103x10^{05}	90.6	[66,84,88,89]
219	N(^{4}S°) + e$^-$ ⇌ N(4f XX) + e$^-$	1	14	1.00x10^{-30}	0.00	1.105x10^{05}	90.5	[66,84,88,89]
220	N(^{4}S°) + e$^-$ ⇌ N(5p XX) + e$^-$	1	15	1.00x10^{-30}	0.00	1.114x10^{05}	89.8	[66,84,88,89]
221	N(^{4}S°) + e$^-$ ⇌ N(5d XX/3p ^{2}P) + e$^-$	1	16	3.90x10^{-11}	0.30	1.129x10^{05}	88.6	[66,84,88,89]
222	N(^{4}S°) + e$^-$ ⇌ N(5f XX/5g XX) + e$^-$	1	17	1.00x10^{-30}	0.00	1.129x10^{05}	88.6	[66,84,88,89]
223	N(^{4}S°) + e$^-$ ⇌ N(6) + e$^-$	1	18	1.10x10^{-11}	0.17	1.143x10^{05}	87.5	[66,84,88,89]
224	N(^{4}S°) + e$^-$ ⇌ N(7) + e$^-$	1	19	1.90x10^{-05}	-2.09	1.151x10^{05}	86.9	[66,84,88,89]
225	N(^{4}S°) + e$^-$ ⇌ N(8) + e$^-$	1	20	2.10x10^{-05}	-2.09	1.156x10^{05}	86.5	[66,84,88,89]
226	N(^{4}S°) + e$^-$ ⇌ N(9) + e$^-$	1	21	2.20x10^{-05}	-2.09	1.160x10^{05}	86.2	[66,84,88,89]
227	N(^{4}S°) + e$^-$ ⇌ N(10) + e$^-$	1	22	1.00x10^{-30}	0.00	1.162x10^{05}	86.0	[66,84,88,89]
228	N(^{2}D°) + e$^-$ ⇌ N(^{2}P°) + e$^-$	2	3	5.40x10^{-09}	0.27	9.612x10^{03}	1040.4	[66,84,88,89]
229	N(^{2}D°) + e$^-$ ⇌ N(^{4}P) + e$^-$	2	4	1.00x10^{-30}	0.00	6.411x10^{04}	156.0	[66,84,88,89]

230	$N(^2D°) + e^- \rightleftharpoons N(2p^4\ ^4P/3s\ ^2P) + e^-$	2	5	$2.80x10^{-09}$	-0.10	$6.826x10^{04}$	146.5	[66,84,88,89]
231	$N(^2D°) + e^- \rightleftharpoons N(3p\ ^4D°/^4P/^4S) + e^-$	2	6	$1.00x10^{-30}$	0.00	$7.605x10^{04}$	131.5	[66,84,88,89]
232	$N(^2D°) + e^- \rightleftharpoons N(3p\ ^2S/^2D/^2P) + e^-$	2	7	$6.80x10^{-09}$	0.62	$7.757x10^{04}$	128.9	[66,84,88,89]
233	$N(^2D°) + e^- \rightleftharpoons N(4s\ ^4P/^2P) + e^-$	2	8	$5.70x10^{-10}$	-0.22	$8.463x10^{04}$	118.2	[66,84,88,89]
234	$N(^2D°) + e^- \rightleftharpoons N(3d\ ^4F/^4P/^4D) + e^-$	2	9	$2.00x10^{-09}$	-0.24	$8.563x10^{04}$	116.8	[66,84,88,89]
235	$N(^2D°) + e^- \rightleftharpoons N(3d\ ^2P/^2F/^2D) + e^-$	2	10	$7.90x10^{-10}$	-0.04	$8.567x10^{04}$	116.7	[66,84,88,89]
236	$N(^2D°) + e^- \rightleftharpoons N(4p\ XX) + e^-$	2	11	$3.30x10^{-09}$	0.79	$8.785x10^{04}$	113.8	[66,84,88,89]
237	$N(^2D°) + e^- \rightleftharpoons N(5s\ XX) + e^-$	2	12	$2.60x10^{-10}$	-0.28	$9.079x10^{04}$	110.1	[66,84,88,89]
238	$N(^2D°) + e^- \rightleftharpoons N(4d\ XX) + e^-$	2	13	$1.80x10^{-09}$	-0.22	$9.109x10^{04}$	109.8	[66,84,88,89]
239	$N(^2D°) + e^- \rightleftharpoons N(4f\ XX) + e^-$	2	14	$1.00x10^{-30}$	0.00	$9.126x10^{04}$	109.6	[66,84,88,89]
240	$N(^2D°) + e^- \rightleftharpoons N(5p\ XX) + e^-$	2	15	$1.00x10^{-30}$	0.00	$9.214x10^{04}$	108.5	[66,84,88,89]
241	$N(^2D°) + e^- \rightleftharpoons N(5d\ XX/3p\ ^2P) + e^-$	2	16	$3.40x10^{-10}$	0.26	$9.362x10^{04}$	106.8	[66,84,88,89]
242	$N(^2D°) + e^- \rightleftharpoons N(5f\ XX/5g\ XX) + e^-$	2	17	$1.00x10^{-30}$	0.00	$9.370x10^{04}$	106.7	[66,84,88,89]
243	$N(^2D°) + e^- \rightleftharpoons N(6) + e^-$	2	18	$5.70x10^{-06}$	-2.07	$9.507x10^{04}$	105.2	[66,84,88,89]
244	$N(^2D°) + e^- \rightleftharpoons N(7) + e^-$	2	19	$6.30x10^{-06}$	-2.07	$9.588x10^{04}$	104.3	[66,84,88,89]
245	$N(^2D°) + e^- \rightleftharpoons N(8) + e^-$	2	20	$7.00x10^{-06}$	-2.07	$9.640x10^{04}$	103.7	[66,84,88,89]
246	$N(^2D°) + e^- \rightleftharpoons N(9) + e^-$	2	21	$7.60x10^{-06}$	-2.07	$9.676x10^{04}$	103.3	[66,84,88,89]
247	$N(^2D°) + e^- \rightleftharpoons N(10) + e^-$	2	22	$8.10x10^{-06}$	-2.07	$9.702x10^{04}$	103.1	[66,84,88,89]
248	$N(^2P°) + e^- \rightleftharpoons N(^4P) + e^-$	3	4	$1.00x10^{-30}$	0.00	$5.450x10^{04}$	183.5	[66,84,88,89]
249	$N(^2P°) + e^- \rightleftharpoons N(2p^4\ ^4P/3s\ ^2P) + e^-$	3	5	$4.90x10^{-09}$	-0.10	$5.865x10^{04}$	170.5	[66,84,88,89]
250	$N(^2P°) + e^- \rightleftharpoons N(3p\ ^4D°/^4P/^4S) + e^-$	3	6	$1.00x10^{-30}$	0.00	$6.644x10^{04}$	150.5	[66,84,88,89]
251	$N(^2P°) + e^- \rightleftharpoons N(3p\ ^2S/^2D/^2P) + e^-$	3	7	$7.10x10^{-09}$	0.59	$6.795x10^{04}$	147.2	[66,84,88,89]
252	$N(^2P°) + e^- \rightleftharpoons N(4s\ ^4P/^2P) + e^-$	3	8	$9.40x10^{-10}$	-0.33	$7.502x10^{04}$	133.3	[66,84,88,89]
253	$N(^2P°) + e^- \rightleftharpoons N(3d\ ^4F/^4P/^4D) + e^-$	3	9	$5.60x10^{-09}$	-0.25	$7.602x10^{04}$	131.5	[66,84,88,89]
254	$N(^2P°) + e^- \rightleftharpoons N(3d\ ^2P/^2F/^2D) + e^-$	3	10	$3.90x10^{-09}$	-0.14	$7.606x10^{04}$	131.5	[66,84,88,89]
255	$N(^2P°) + e^- \rightleftharpoons N(4p\ XX) + e^-$	3	11	$3.60x10^{-09}$	0.76	$7.824x10^{04}$	127.8	[66,84,88,89]
256	$N(^2P°) + e^- \rightleftharpoons N(5s\ XX) + e^-$	3	12	$7.30x10^{-06}$	-1.88	$8.118x10^{04}$	123.2	[66,84,88,89]
257	$N(^2P°) + e^- \rightleftharpoons N(4d\ XX) + e^-$	3	13	$4.40x10^{-09}$	-0.20	$8.148x10^{04}$	122.7	[66,84,88,89]

258	$N(^2P°) + e^- \rightleftharpoons N(4f\ XX) + e^-$	3	14	$1.00x10^{-30}$	0.00	$8.165x10^{04}$	122.5	[66,84,88,89]
259	$N(^2P°) + e^- \rightleftharpoons N(5p\ XX) + e^-$	3	15	$1.00x10^{-30}$	0.00	$8.252x10^{04}$	121.2	[66,84,88,89]
260	$N(^2P°) + e^- \rightleftharpoons N(5d\ XX/3p\ ^2P) + e^-$	3	16	$8.40x10^{-10}$	0.00	$8.401x10^{04}$	119.0	[66,84,88,89]
261	$N(^2P°) + e^- \rightleftharpoons N(5f\ XX/5g\ XX) + e^-$	3	17	$1.00x10^{-30}$	0.00	$8.409x10^{04}$	118.9	[66,84,88,89]
262	$N(^2P°) + e^- \rightleftharpoons N(6) + e^-$	3	18	$4.50x10^{-06}$	-2.06	$8.546x10^{04}$	117.0	[66,84,88,89]
263	$N(^2P°) + e^- \rightleftharpoons N(7) + e^-$	3	19	$5.10x10^{-06}$	-2.07	$8.627x10^{04}$	115.9	[66,84,88,89]
264	$N(^2P°) + e^- \rightleftharpoons N(8) + e^-$	3	20	$5.60x10^{-06}$	-2.07	$8.679x10^{04}$	115.2	[66,84,88,89]
265	$N(^2P°) + e^- \rightleftharpoons N(9) + e^-$	3	21	$6.10x10^{-06}$	-2.07	$8.715x10^{04}$	114.7	[66,84,88,89]
266	$N(^2P°) + e^- \rightleftharpoons N(10) + e^-$	3	22	$6.60x10^{-06}$	-2.07	$8.741x10^{04}$	114.4	[66,84,88,89]
267	$N(^4P) + e^- \rightleftharpoons N(2p^4\ ^4P/3s\ ^2P) + e^-$	4	5	$7.30x10^{-12}$	-0.43	$4.151x10^{03}$	2409.1	[66,84,88,89]
268	$N(^4P) + e^- \rightleftharpoons N(3p\ ^4D°/^4P/^4S) + e^-$	4	6	$9.20x10^{-07}$	-0.15	$1.194x10^{04}$	837.6	[66,84,88,89]
269	$N(^4P) + e^- \rightleftharpoons N(3p\ ^2S/^2D/^2P) + e^-$	4	7	$2.40x10^{-08}$	-0.38	$1.346x10^{04}$	743.2	[66,84,88,89]
270	$N(^4P) + e^- \rightleftharpoons N(4s\ ^4P/^2P) + e^-$	4	8	$6.60x10^{-08}$	-0.12	$2.053x10^{04}$	487.2	[66,84,88,89]
271	$N(^4P) + e^- \rightleftharpoons N(3d\ ^4F/^4P/^4D) + e^-$	4	9	$1.10x10^{-07}$	-0.16	$2.152x10^{04}$	464.7	[66,84,88,89]
272	$N(^4P) + e^- \rightleftharpoons N(3d\ ^2P/^2F/^2D) + e^-$	4	10	$3.50x10^{-09}$	-0.72	$2.157x10^{04}$	463.7	[66,84,88,89]
273	$N(^4P) + e^- \rightleftharpoons N(4p\ XX) + e^-$	4	11	$2.00x10^{-08}$	-0.41	$2.375x10^{04}$	421.1	[66,84,88,89]
274	$N(^4P) + e^- \rightleftharpoons N(5s\ XX) + e^-$	4	12	$1.80x10^{-07}$	-0.11	$2.668x10^{04}$	374.8	[66,84,88,89]
275	$N(^4P) + e^- \rightleftharpoons N(4d\ XX) + e^-$	4	13	$1.20x10^{-07}$	-0.22	$2.698x10^{04}$	370.7	[66,84,88,89]
276	$N(^4P) + e^- \rightleftharpoons N(4f\ XX) + e^-$	4	14	$4.20x10^{-08}$	-0.23	$2.715x10^{04}$	368.3	[66,84,88,89]
277	$N(^4P) + e^- \rightleftharpoons N(5p\ XX) + e^-$	4	15	$7.80x10^{-08}$	-0.30	$2.803x10^{04}$	356.8	[66,84,88,89]
278	$N(^4P) + e^- \rightleftharpoons N(5d\ XX/3p\ ^2P) + e^-$	4	16	$1.70x10^{-07}$	-0.26	$2.951x10^{04}$	338.8	[66,84,88,89]
279	$N(^4P) + e^- \rightleftharpoons N(5f\ XX/5g\ XX) + e^-$	4	17	$1.10x10^{-07}$	-0.28	$2.959x10^{04}$	337.9	[66,84,88,89]
280	$N(^4P) + e^- \rightleftharpoons N(6) + e^-$	4	18	$2.10x10^{-07}$	-0.32	$3.096x10^{04}$	323.0	[66,84,88,89]
281	$N(^4P) + e^- \rightleftharpoons N(7) + e^-$	4	19	$2.50x10^{-07}$	-0.33	$3.177x10^{04}$	314.8	[66,84,88,89]
282	$N(^4P) + e^- \rightleftharpoons N(8) + e^-$	4	20	$2.90x10^{-07}$	-0.33	$3.229x10^{04}$	309.7	[66,84,88,89]
283	$N(^4P) + e^- \rightleftharpoons N(9) + e^-$	4	21	$3.20x10^{-07}$	-0.33	$3.265x10^{04}$	306.2	[66,84,88,89]
284	$N(^4P) + e^- \rightleftharpoons N(10) + e^-$	4	22	$3.60x10^{-07}$	-0.33	$3.291x10^{04}$	303.8	[66,84,88,89]
285	$N(2p^4\ ^4P/3s\ ^2P) + e^- \rightleftharpoons N(3p\ ^4D°/^4P/^4S) + e^-$	5	6	$2.20x10^{-07}$	-0.21	$7.788x10^{03}$	1284.0	[66,84,88,89]

286	$N(2p^4\ ^4P/3s\ ^2P) + e^- \rightleftharpoons N(3p\ ^2S/^2D/^2P) + e^-$	5	7	$5.60x10^{-07}$	-0.18	$9.305x10^{03}$	1074.7	[66,84,88,89]
287	$N(2p^4\ ^4P/3s\ ^2P) + e^- \rightleftharpoons N(4s\ ^4P/^2P) + e^-$	5	8	$7.20x10^{-08}$	-0.14	$1.637x10^{04}$	610.7	[66,84,88,89]
288	$N(2p^4\ ^4P/3s\ ^2P) + e^- \rightleftharpoons N(3d\ ^4F/^4P/^4D) + e^-$	5	9	$8.00x10^{-09}$	-0.71	$1.737x10^{04}$	575.7	[66,84,88,89]
289	$N(2p^4\ ^4P/3s\ ^2P) + e^- \rightleftharpoons N(3d\ ^2P/^2F/^2D) + e^-$	5	10	$2.30x10^{-07}$	-0.18	$1.741x10^{04}$	574.3	[66,84,88,89]
290	$N(2p^4\ ^4P/3s\ ^2P) + e^- \rightleftharpoons N(4p\ XX) + e^-$	5	11	$1.90x10^{-08}$	-0.43	$1.959x10^{04}$	510.4	[66,84,88,89]
291	$N(2p^4\ ^4P/3s\ ^2P) + e^- \rightleftharpoons N(5s\ XX) + e^-$	5	12	$1.40x10^{-07}$	-0.10	$2.253x10^{04}$	443.8	[66,84,88,89]
292	$N(2p^4\ ^4P/3s\ ^2P) + e^- \rightleftharpoons N(4d\ XX) + e^-$	5	13	$1.40x10^{-07}$	-0.25	$2.283x10^{04}$	438.1	[66,84,88,89]
293	$N(2p^4\ ^4P/3s\ ^2P) + e^- \rightleftharpoons N(4f\ XX) + e^-$	5	14	$4.80x10^{-08}$	-0.28	$2.300x10^{04}$	434.8	[66,84,88,89]
294	$N(2p^4\ ^4P/3s\ ^2P) + e^- \rightleftharpoons N(5p\ XX) + e^-$	5	15	$1.10x10^{-08}$	-0.45	$2.388x10^{04}$	418.8	[66,84,88,89]
295	$N(2p^4\ ^4P/3s\ ^2P) + e^- \rightleftharpoons N(5d\ XX/3p\ ^2P) + e^-$	5	16	$2.10x10^{-07}$	-0.27	$2.536x10^{04}$	394.3	[66,84,88,89]
296	$N(2p^4\ ^4P/3s\ ^2P) + e^- \rightleftharpoons N(5f\ XX/5g\ XX) + e^-$	5	17	$1.30x10^{-07}$	-0.32	$2.544x10^{04}$	393.1	[66,84,88,89]
297	$N(2p^4\ ^4P/3s\ ^2P) + e^- \rightleftharpoons N(6) + e^-$	5	18	$2.70x10^{-07}$	-0.35	$2.681x10^{04}$	373.0	[66,84,88,89]
298	$N(2p^4\ ^4P/3s\ ^2P) + e^- \rightleftharpoons N(7) + e^-$	5	19	$3.30x10^{-07}$	-0.35	$2.762x10^{04}$	362.1	[66,84,88,89]
299	$N(2p^4\ ^4P/3s\ ^2P) + e^- \rightleftharpoons N(8) + e^-$	5	20	$3.70x10^{-07}$	-0.36	$2.814x10^{04}$	355.3	[66,84,88,89]
300	$N(2p^4\ ^4P/3s\ ^2P) + e^- \rightleftharpoons N(9) + e^-$	5	21	$4.20x10^{-07}$	-0.36	$2.850x10^{04}$	350.8	[66,84,88,89]
301	$N(2p^4\ ^4P/3s\ ^2P) + e^- \rightleftharpoons N(10) + e^-$	5	22	$4.70x10^{-07}$	-0.36	$2.876x10^{04}$	347.7	[66,84,88,89]
302	$N(3p\ ^4D°/^4P/^4S) + e^- \rightleftharpoons N(3p\ ^2S/^2D/^2P) + e^-$	6	7	$2.20x10^{-12}$	-1.09	$1.517x10^{03}$	6592.0	[66,84,88,89]
303	$N(3p\ ^4D°/^4P/^4S) + e^- \rightleftharpoons N(4s\ ^4P/^2P) + e^-$	6	8	$7.60x10^{-07}$	-0.35	$8.586x10^{03}$	1164.7	[66,84,88,89]
304	$N(3p\ ^4D°/^4P/^4S) + e^- \rightleftharpoons N(3d\ ^4F/^4P/^4D) + e^-$	6	9	$1.30x10^{-05}$	-0.45	$9.581x10^{03}$	1043.7	[66,84,88,89]
305	$N(3p\ ^4D°/^4P/^4S) + e^- \rightleftharpoons N(3d\ ^2P/^2F/^2D) + e^-$	6	10	$1.70x10^{-05}$	-0.50	$9.626x10^{03}$	1038.9	[66,84,88,89]
306	$N(3p\ ^4D°/^4P/^4S) + e^- \rightleftharpoons N(4p\ XX) + e^-$	6	11	$1.40x10^{-08}$	-0.17	$1.181x10^{04}$	847.0	[66,84,88,89]
307	$N(3p\ ^4D°/^4P/^4S) + e^- \rightleftharpoons N(5s\ XX) + e^-$	6	12	$3.40x10^{-07}$	-0.61	$1.475x10^{04}$	678.2	[66,84,88,89]
308	$N(3p\ ^4D°/^4P/^4S) + e^- \rightleftharpoons N(4d\ XX) + e^-$	6	13	$4.80x10^{-06}$	-0.51	$1.504x10^{04}$	664.9	[66,84,88,89]
309	$N(3p\ ^4D°/^4P/^4S) + e^- \rightleftharpoons N(4f\ XX) + e^-$	6	14	$1.90x10^{-08}$	-0.44	$1.521x10^{04}$	657.5	[66,84,88,89]
310	$N(3p\ ^4D°/^4P/^4S) + e^- \rightleftharpoons N(5p\ XX) + e^-$	6	15	$1.30x10^{-08}$	-0.27	$1.609x10^{04}$	621.6	[66,84,88,89]
311	$N(3p\ ^4D°/^4P/^4S) + e^- \rightleftharpoons N(5d\ XX/3p\ ^2P) + e^-$	6	16	$3.00x10^{-07}$	-0.49	$1.758x10^{04}$	569.0	[66,84,88,89]
312	$N(3p\ ^4D°/^4P/^4S) + e^- \rightleftharpoons N(5f\ XX/5g\ XX) + e^-$	6	17	$3.40x10^{-08}$	-0.43	$1.765x10^{04}$	566.5	[66,84,88,89]
313	$N(3p\ ^4D°/^4P/^4S) + e^- \rightleftharpoons N(6) + e^-$	6	18	$5.20x10^{-07}$	-0.65	$1.902x10^{04}$	525.7	[66,84,88,89]

314	$N(3p\ ^4D°/^4P/^4S) + e^- \rightleftharpoons N(7) + e^-$	6	19	$7.20x10^{-08}$	-0.33	$1.983x10^{04}$	504.3	[66,84,88,89]
315	$N(3p\ ^4D°/^4P/^4S) + e^- \rightleftharpoons N(8) + e^-$	6	20	$8.40x10^{-08}$	-0.34	$2.036x10^{04}$	491.3	[66,84,88,89]
316	$N(3p\ ^4D°/^4P/^4S) + e^- \rightleftharpoons N(9) + e^-$	6	21	$9.70x10^{-08}$	-0.35	$2.072x10^{04}$	482.7	[66,84,88,89]
317	$N(3p\ ^4D°/^4P/^4S) + e^- \rightleftharpoons N(10) + e^-$	6	22	$1.10x10^{-07}$	-0.35	$2.097x10^{04}$	476.8	[66,84,88,89]
318	$N(3p\ ^2S/^2D/^2P) + e^- \rightleftharpoons N(4s\ ^4P/^2P) + e^-$	7	8	$1.10x10^{-08}$	0.16	$7.069x10^{03}$	1414.6	[66,84,88,89]
319	$N(3p\ ^2S/^2D/^2P) + e^- \rightleftharpoons N(3d\ ^4F/^4P/^4D) + e^-$	7	9	$5.40x10^{-05}$	-0.48	$8.064x10^{03}$	1240.1	[66,84,88,89]
320	$N(3p\ ^2S/^2D/^2P) + e^- \rightleftharpoons N(3d\ ^2P/^2F/^2D) + e^-$	7	10	$2.30x10^{-05}$	-0.45	$8.109x10^{03}$	1233.2	[66,84,88,89]
321	$N(3p\ ^2S/^2D/^2P) + e^- \rightleftharpoons N(4p\ XX) + e^-$	7	11	$1.90x10^{-08}$	-0.25	$1.029x10^{04}$	971.9	[66,84,88,89]
322	$N(3p\ ^2S/^2D/^2P) + e^- \rightleftharpoons N(5s\ XX) + e^-$	7	12	$1.20x10^{-06}$	-0.62	$1.323x10^{04}$	756.0	[66,84,88,89]
323	$N(3p\ ^2S/^2D/^2P) + e^- \rightleftharpoons N(4d\ XX) + e^-$	7	13	$1.00x10^{-05}$	-0.51	$1.352x10^{04}$	739.5	[66,84,88,89]
324	$N(3p\ ^2S/^2D/^2P) + e^- \rightleftharpoons N(4f\ XX) + e^-$	7	14	$1.40x10^{-08}$	-0.52	$1.369x10^{04}$	730.3	[66,84,88,89]
325	$N(3p\ ^2S/^2D/^2P) + e^- \rightleftharpoons N(5p\ XX) + e^-$	7	15	$1.00x10^{-07}$	-0.25	$1.457x10^{04}$	686.3	[66,84,88,89]
326	$N(3p\ ^2S/^2D/^2P) + e^- \rightleftharpoons N(5d\ XX/3p\ ^2P) + e^-$	7	16	$1.30x10^{-06}$	-0.49	$1.606x10^{04}$	622.7	[66,84,88,89]
327	$N(3p\ ^2S/^2D/^2P) + e^- \rightleftharpoons N(5f\ XX/5g\ XX) + e^-$	7	17	$2.10x10^{-08}$	-0.46	$1.614x10^{04}$	619.7	[66,84,88,89]
328	$N(3p\ ^2S/^2D/^2P) + e^- \rightleftharpoons N(6) + e^-$	7	18	$1.00x10^{-07}$	-0.37	$1.751x10^{04}$	571.3	[66,84,88,89]
329	$N(3p\ ^2S/^2D/^2P) + e^- \rightleftharpoons N(7) + e^-$	7	19	$1.30x10^{-07}$	-0.39	$1.831x10^{04}$	546.0	[66,84,88,89]
330	$N(3p\ ^2S/^2D/^2P) + e^- \rightleftharpoons N(8) + e^-$	7	20	$1.50x10^{-07}$	-0.40	$1.884x10^{04}$	530.8	[66,84,88,89]
331	$N(3p\ ^2S/^2D/^2P) + e^- \rightleftharpoons N(9) + e^-$	7	21	$1.70x10^{-07}$	-0.40	$1.920x10^{04}$	520.9	[66,84,88,89]
332	$N(3p\ ^2S/^2D/^2P) + e^- \rightleftharpoons N(10) + e^-$	7	22	$2.00x10^{-07}$	-0.41	$1.946x10^{04}$	514.0	[66,84,88,89]
333	$N(4s\ ^4P/^2P) + e^- \rightleftharpoons N(3d\ ^4F/^4P/^4D) + e^-$	8	9	$4.50x10^{-11}$	-0.44	$9.950x10^{02}$	10050.3	[66,84,88,89]
334	$N(4s\ ^4P/^2P) + e^- \rightleftharpoons N(3d\ ^2P/^2F/^2D) + e^-$	8	10	$4.40x10^{-11}$	-0.49	$1.040x10^{03}$	9615.4	[66,84,88,89]
335	$N(4s\ ^4P/^2P) + e^- \rightleftharpoons N(4p\ XX) + e^-$	8	11	$2.30x10^{-05}$	-0.39	$3.220x10^{03}$	3105.6	[66,84,88,89]
336	$N(4s\ ^4P/^2P) + e^- \rightleftharpoons N(5s\ XX) + e^-$	8	12	$1.80x10^{-08}$	-0.05	$6.159x10^{03}$	1623.6	[66,84,88,89]
337	$N(4s\ ^4P/^2P) + e^- \rightleftharpoons N(4d\ XX) + e^-$	8	13	$6.50x10^{-08}$	0.07	$6.453x10^{03}$	1549.7	[66,84,88,89]
338	$N(4s\ ^4P/^2P) + e^- \rightleftharpoons N(4f\ XX) + e^-$	8	14	$1.80x10^{-08}$	0.13	$6.624x10^{03}$	1509.7	[66,84,88,89]
339	$N(4s\ ^4P/^2P) + e^- \rightleftharpoons N(5p\ XX) + e^-$	8	15	$8.60x10^{-06}$	-0.57	$7.501x10^{03}$	1333.2	[66,84,88,89]
340	$N(4s\ ^4P/^2P) + e^- \rightleftharpoons N(5d\ XX/3p\ ^2P) + e^-$	8	16	$1.50x10^{-07}$	-0.05	$8.989x10^{03}$	1112.5	[66,84,88,89]
341	$N(4s\ ^4P/^2P) + e^- \rightleftharpoons N(5f\ XX/5g\ XX) + e^-$	8	17	$6.80x10^{-08}$	-0.01	$9.067x10^{03}$	1102.9	[66,84,88,89]

342	$N(4s\ ^4P/^2P) + e^- \rightleftharpoons N(6) + e^-$	8	18	$4.50x10^{-07}$	-0.37	$1.044x10^{04}$	958.2	[66,84,88,89]
343	$N(4s\ ^4P/^2P) + e^- \rightleftharpoons N(7) + e^-$	8	19	$5.90x10^{-07}$	-0.43	$1.125x10^{04}$	889.3	[66,84,88,89]
344	$N(4s\ ^4P/^2P) + e^- \rightleftharpoons N(8) + e^-$	8	20	$7.20x10^{-07}$	-0.46	$1.177x10^{04}$	849.7	[66,84,88,89]
345	$N(4s\ ^4P/^2P) + e^- \rightleftharpoons N(9) + e^-$	8	21	$8.50x10^{-07}$	-0.48	$1.213x10^{04}$	824.5	[66,84,88,89]
346	$N(4s\ ^4P/^2P) + e^- \rightleftharpoons N(10) + e^-$	8	22	$9.80x10^{-07}$	-0.49	$1.239x10^{04}$	807.4	[66,84,88,89]
347	$N(3d\ ^4F/^4P/^4D) + e^- \rightleftharpoons N(3d\ ^2P/^2F/^2D) + e^-$	9	10	$6.50x10^{-18}$	-0.96	$4.500x10^{01}$	222,220	[66,84,88,89]
348	$N(3d\ ^4F/^4P/^4D) + e^- \rightleftharpoons N(4p\ XX) + e^-$	9	11	$6.00x10^{-04}$	-0.39	$2.225x10^{03}$	4494.4	[66,84,88,89]
349	$N(3d\ ^4F/^4P/^4D) + e^- \rightleftharpoons N(5s\ XX) + e^-$	9	12	$2.70x10^{-09}$	0.07	$5.164x10^{03}$	1936.5	[66,84,88,89]
350	$N(3d\ ^4F/^4P/^4D) + e^- \rightleftharpoons N(4d\ XX) + e^-$	9	13	$1.80x10^{-08}$	-0.10	$5.458x10^{03}$	1832.2	[66,84,88,89]
351	$N(3d\ ^4F/^4P/^4D) + e^- \rightleftharpoons N(4f\ XX) + e^-$	9	14	$1.10x10^{-07}$	0.08	$5.629x10^{03}$	1776.5	[66,84,88,89]
352	$N(3d\ ^4F/^4P/^4D) + e^- \rightleftharpoons N(5p\ XX) + e^-$	9	15	$1.30x10^{-03}$	-0.49	$6.506x10^{03}$	1537.0	[66,84,88,89]
353	$N(3d\ ^4F/^4P/^4D) + e^- \rightleftharpoons N(5d\ XX/3p\ ^2P) + e^-$	9	16	$4.60x10^{-08}$	-0.20	$7.994x10^{03}$	1250.9	[66,84,88,89]
354	$N(3d\ ^4F/^4P/^4D) + e^- \rightleftharpoons N(5f\ XX/5g\ XX) + e^-$	9	17	$1.40x10^{-07}$	0.04	$8.072x10^{03}$	1238.9	[66,84,88,89]
355	$N(3d\ ^4F/^4P/^4D) + e^- \rightleftharpoons N(6) + e^-$	9	18	$1.30x10^{-07}$	-0.20	$9.441x10^{03}$	1059.2	[66,84,88,89]
356	$N(3d\ ^4F/^4P/^4D) + e^- \rightleftharpoons N(7) + e^-$	9	19	$1.70x10^{-07}$	-0.27	$1.025x10^{04}$	975.6	[66,84,88,89]
357	$N(3d\ ^4F/^4P/^4D) + e^- \rightleftharpoons N(8) + e^-$	9	20	$2.10x10^{-07}$	-0.31	$1.077x10^{04}$	928.2	[66,84,88,89]
358	$N(3d\ ^4F/^4P/^4D) + e^- \rightleftharpoons N(9) + e^-$	9	21	$2.50x10^{-07}$	-0.33	$1.113x10^{04}$	898.1	[66,84,88,89]
359	$N(3d\ ^4F/^4P/^4D) + e^- \rightleftharpoons N(10) + e^-$	9	22	$2.80x10^{-07}$	-0.35	$1.139x10^{04}$	877.9	[66,84,88,89]
360	$N(3d\ ^2P/^2F/^2D) + e^- \rightleftharpoons N(4p\ XX) + e^-$	10	11	$1.40x10^{-03}$	-0.39	$2.180x10^{03}$	4587.2	[66,84,88,89]
361	$N(3d\ ^2P/^2F/^2D) + e^- \rightleftharpoons N(5s\ XX) + e^-$	10	12	$2.50x10^{-09}$	-0.39	$5.119x10^{03}$	1953.5	[66,84,88,89]
362	$N(3d\ ^2P/^2F/^2D) + e^- \rightleftharpoons N(4d\ XX) + e^-$	10	13	$1.60x10^{-08}$	-0.07	$5.413x10^{03}$	1847.4	[66,84,88,89]
363	$N(3d\ ^2P/^2F/^2D) + e^- \rightleftharpoons N(4f\ XX) + e^-$	10	14	$1.20x10^{-07}$	0.04	$5.584x10^{03}$	1790.8	[66,84,88,89]
364	$N(3d\ ^2P/^2F/^2D) + e^- \rightleftharpoons N(5p\ XX) + e^-$	10	15	$2.90x10^{-03}$	-0.49	$6.461x10^{03}$	1547.7	[66,84,88,89]
365	$N(3d\ ^2P/^2F/^2D) + e^- \rightleftharpoons N(5d\ XX/3p\ ^2P) + e^-$	10	16	$4.50x10^{-08}$	-0.19	$7.949x10^{03}$	1258.0	[66,84,88,89]
366	$N(3d\ ^2P/^2F/^2D) + e^- \rightleftharpoons N(5f\ XX/5g\ XX) + e^-$	10	17	$1.60x10^{-07}$	0.00	$8.027x10^{03}$	1245.8	[66,84,88,89]
367	$N(3d\ ^2P/^2F/^2D) + e^- \rightleftharpoons N(6) + e^-$	10	18	$1.60x10^{-07}$	-0.27	$9.396x10^{03}$	1064.3	[66,84,88,89]
368	$N(3d\ ^2P/^2F/^2D) + e^- \rightleftharpoons N(7) + e^-$	10	19	$2.10x10^{-07}$	-0.34	$1.021x10^{04}$	979.9	[66,84,88,89]
369	$N(3d\ ^2P/^2F/^2D) + e^- \rightleftharpoons N(8) + e^-$	10	20	$2.60x10^{-07}$	-0.38	$1.073x10^{04}$	932.1	[66,84,88,89]

370	$N(3d\ ^2P/^2F/^2D) + e^- \rightleftharpoons N(9) + e^-$	10	21	$3.10x10^{-07}$	-0.40	$1.109x10^{04}$	901.8	[66,84,88,89]
371	$N(3d\ ^2P/^2F/^2D) + e^- \rightleftharpoons N(10) + e^-$	10	22	$3.60x10^{-07}$	-0.42	$1.135x10^{04}$	881.4	[66,84,88,89]

*Select states are combined to match TOPBase b-f and LEVELS.dat within NEQAIR. A term of 'XX' signifies that all terms of a leading configuration are included. If configuration is numeric, all states of the principal quantum number n are included.

Table A4: Atomic oxygen electron impact excitation rate transition baseline (BL) and uncertainty multiplier intervals applied to preexponential factors.

$$k_f^{el}(l,u) = UC_{el}\left(\frac{T_{ve}}{10{,}000}\right)^{\eta_{el}} exp(-\Delta E_{th}/k_B T_{ve}), \quad U_{low} = 0.1, U_{high} = 10 \text{ [47,52,154]}$$

No.	Reaction*	l	u	C_{el}, $cm^3 s^{-1}$	η_{el}	ΔE_{th}, cm^{-1}	λ, nm	BL Refs.
372	$O(^3P) + e^- \rightleftharpoons O(^1D) + e^-$	1	2	2.30×10^{-09}	0.47	1.579×10^{04}	633.3	[66,84,88,89]
373	$O(^3P) + e^- \rightleftharpoons O(^1S) + e^-$	1	3	3.80×10^{-10}	0.24	3.371×10^{04}	296.6	[66,84,88,89]
374	$O(^3P) + e^- \rightleftharpoons O(3s\ ^5S°) + e^-$	1	4	8.80×10^{-15}	0.04	7.369×10^{04}	135.7	[66,84,88,89]
375	$O(^3P) + e^- \rightleftharpoons O(3s\ ^3S°) + e^-$	1	5	1.90×10^{-09}	0.04	7.672×10^{04}	130.3	[66,84,88,89]
376	$O(^3P) + e^- \rightleftharpoons O(3p\ ^5P) + e^-$	1	6	5.70×10^{-09}	0.07	8.655×10^{04}	115.5	[66,84,88,89]
377	$O(^3P) + e^- \rightleftharpoons O(3p\ ^3P) + e^-$	1	7	3.40×10^{-09}	0.81	8.855×10^{04}	112.9	[66,84,88,89]
378	$O(^3P) + e^- \rightleftharpoons O(4s\ ^5S°/^3S°) + e^-$	1	8	1.10×10^{-10}	0.22	9.568×10^{04}	104.5	[66,84,88,89]
379	$O(^3P) + e^- \rightleftharpoons O(3d\ ^5D°/^3D°) + e^-$	1	9	2.40×10^{-10}	0.13	9.737×10^{04}	102.7	[66,84,88,89]
380	$O(^3P) + e^- \rightleftharpoons O(4p\ ^5P/^3P) + e^-$	1	10	2.70×10^{-08}	0.17	9.924×10^{04}	100.8	[66,84,88,89]
381	$O(^3P) + e^- \rightleftharpoons O(5s\ ^5S°/^3S°) + e^-$	1	11	2.70×10^{-11}	0.19	1.021×10^{05}	97.9	[66,84,88,89]
382	$O(^3P) + e^- \rightleftharpoons O(4d\ ^5D°/^3D°, 4f\ ^5F/^3F) + e^-$	1	12	1.10×10^{-10}	0.16	1.028×10^{05}	97.3	[66,84,88,89]
383	$O(^3P) + e^- \rightleftharpoons O(5p\ ^5P/^3P) + e^-$	1	13	1.00×10^{-30}	0.00	1.038×10^{05}	96.3	[66,84,88,89]
384	$O(^3P) + e^- \rightleftharpoons O(5d\ ^5D°/^3D°, 5f\ ^5F/^3F, 5g\ ^5G/^3F) + e^-$	1	14	4.10×10^{-11}	0.17	1.053×10^{05}	95.0	[66,84,88,89]
385	$O(^3P) + e^- \rightleftharpoons O(6) + e^-$	1	15	3.40×10^{-11}	0.03	1.066×10^{05}	93.8	[66,84,88,89]
386	$O(^3P) + e^- \rightleftharpoons O(7) + e^-$	1	16	1.70×10^{-11}	0.11	1.075×10^{05}	93.0	[66,84,88,89]
387	$O(^3P) + e^- \rightleftharpoons O(8) + e^-$	1	17	1.00×10^{-11}	0.16	1.080×10^{05}	92.6	[66,84,88,89]
388	$O(^3P) + e^- \rightleftharpoons O(9) + e^-$	1	18	5.50×10^{-12}	0.26	1.084×10^{05}	92.3	[66,84,88,89]
389	$O(^3P) + e^- \rightleftharpoons O(10) + e^-$	1	19	3.70×10^{-12}	0.27	1.087×10^{05}	92.0	[66,84,88,89]
390	$O(^1D) + e^- \rightleftharpoons O(^1S) + e^-$	2	3	1.30×10^{-09}	-0.03	1.792×10^{04}	557.9	[66,84,88,89]
391	$O(^1D) + e^- \rightleftharpoons O(3s\ ^5S°) + e^-$	2	4	3.20×10^{-17}	0.01	5.790×10^{04}	172.7	[66,84,88,89]
392	$O(^1D) + e^- \rightleftharpoons O(3s\ ^3S°) + e^-$	2	5	1.90×10^{-14}	0.02	6.093×10^{04}	164.1	[66,84,88,89]
393	$O(^1D) + e^- \rightleftharpoons O(3p\ ^5P) + e^-$	2	6	1.00×10^{-30}	0.00	7.076×10^{04}	141.3	[66,84,88,89]
394	$O(^1D) + e^- \rightleftharpoons O(3p\ ^3P) + e^-$	2	7	1.00×10^{-30}	0.00	7.276×10^{04}	137.4	[66,84,88,89]

395	$O(^1D) + e^- \rightleftharpoons O(4s\ ^5S°/^3S°) + e^-$	2	8	$9.60x10^{-16}$	0.18	$7.989x10^{04}$	125.2	[66,84,88,89]
396	$O(^1D) + e^- \rightleftharpoons O(3d\ ^5D°/^3D°) + e^-$	2	9	$9.00x10^{-15}$	0.09	$8.158x10^{04}$	122.6	[66,84,88,89]
397	$O(^1D) + e^- \rightleftharpoons O(4p\ ^5P/^3P) + e^-$	2	10	$1.00x10^{-30}$	0.00	$8.345x10^{04}$	119.8	[66,84,88,89]
398	$O(^1D) + e^- \rightleftharpoons O(5s\ ^5S°/^3S°) + e^-$	2	11	$1.00x10^{-30}$	0.00	$8.636x10^{04}$	115.8	[66,84,88,89]
399	$O(^1D) + e^- \rightleftharpoons O(4d\ ^5D°/^3D°, 4f\ ^5F/^3F) + e^-$	2	12	$1.00x10^{-30}$	0.00	$8.701x10^{04}$	114.9	[66,84,88,89]
400	$O(^1D) + e^- \rightleftharpoons O(5p\ ^5P/^3P) + e^-$	2	13	$1.00x10^{-30}$	0.00	$8.800x10^{04}$	113.6	[66,84,88,89]
401	$O(^1D) + e^- \rightleftharpoons O(5d\ ^5D°/^3D°, 5f\ ^5F/^3F, 5g\ ^5G/^3F) + e^-$	2	14	$1.00x10^{-30}$	0.00	$8.953x10^{04}$	111.7	[66,84,88,89]
402	$O(^1S) + e^- \rightleftharpoons O(3s\ ^5S°) + e^-$	3	4	$1.00x10^{-30}$	0.00	$3.998x10^{04}$	250.2	[66,84,88,89]
403	$O(^1S) + e^- \rightleftharpoons O(3s\ ^3S°) + e^-$	3	5	$7.90x10^{-17}$	-0.01	$4.300x10^{04}$	232.5	[66,84,88,89]
404	$O(^1S) + e^- \rightleftharpoons O(3p\ ^5P) + e^-$	3	6	$1.00x10^{-30}$	0.00	$5.284x10^{04}$	189.3	[66,84,88,89]
405	$O(^1S) + e^- \rightleftharpoons O(3p\ ^3P) + e^-$	3	7	$1.00x10^{-30}$	0.00	$5.484x10^{04}$	182.4	[66,84,88,89]
406	$O(^1S) + e^- \rightleftharpoons O(4s\ ^5S°/^3S°) + e^-$	3	8	$1.00x10^{-17}$	0.16	$6.197x10^{04}$	161.4	[66,84,88,89]
407	$O(^1S) + e^- \rightleftharpoons O(3d\ ^5D°/^3D°) + e^-$	3	9	$6.00x10^{-14}$	0.06	$6.365x10^{04}$	157.1	[66,84,88,89]
408	$O(^1S) + e^- \rightleftharpoons O(4p\ ^5P/^3P) + e^-$	3	10	$1.00x10^{-30}$	0.00	$6.552x10^{04}$	152.6	[66,84,88,89]
409	$O(^1S) + e^- \rightleftharpoons O(5s\ ^5S°/^3S°) + e^-$	3	11	$1.00x10^{-30}$	0.00	$6.844x10^{04}$	146.1	[66,84,88,89]
410	$O(^1S) + e^- \rightleftharpoons O(4d\ ^5D°/^3D°, 4f\ ^5F/^3F) + e^-$	3	12	$1.00x10^{-30}$	0.00	$6.909x10^{04}$	144.7	[66,84,88,89]
411	$O(^1S) + e^- \rightleftharpoons O(5p\ ^5P/^3P) + e^-$	3	13	$1.00x10^{-30}$	0.00	$7.008x10^{04}$	142.7	[66,84,88,89]
412	$O(^1S) + e^- \rightleftharpoons O(5d\ ^5D°/^3D°, 5f\ ^5F/^3F, 5g\ ^5G/^3F) + e^-$	3	14	$1.00x10^{-30}$	0.00	$7.160x10^{04}$	139.7	[66,84,88,89]
413	$O(3s\ ^5S°) + e^- \rightleftharpoons O(3s\ ^3S°) + e^-$	4	5	$1.00x10^{-30}$	0.00	$3.027x10^{03}$	3303.6	[66,84,88,89]
414	$O(3s\ ^5S°) + e^- \rightleftharpoons O(3p\ ^5P) + e^-$	4	6	$6.70x10^{-07}$	-0.07	$1.286x10^{04}$	777.5	[66,84,88,89]
415	$O(3s\ ^5S°) + e^- \rightleftharpoons O(3p\ ^3P) + e^-$	4	7	$4.70x10^{-12}$	-0.05	$1.486x10^{04}$	672.8	[66,84,88,89]
416	$O(3s\ ^5S°) + e^- \rightleftharpoons O(4s\ ^5S°/^3S°) + e^-$	4	8	$1.00x10^{-30}$	0.00	$2.199x10^{04}$	454.8	[66,84,88,89]
417	$O(3s\ ^5S°) + e^- \rightleftharpoons O(3d\ ^5D°/^3D°) + e^-$	4	9	$1.00x10^{-30}$	0.00	$2.368x10^{04}$	422.4	[66,84,88,89]
418	$O(3s\ ^5S°) + e^- \rightleftharpoons O(4p\ ^5P/^3P) + e^-$	4	10	$4.60x10^{-10}$	0.00	$2.555x10^{04}$	391.5	[66,84,88,89]
419	$O(3s\ ^5S°) + e^- \rightleftharpoons O(5s\ ^5S°/^3S°) + e^-$	4	11	$1.00x10^{-30}$	0.00	$2.846x10^{04}$	351.4	[66,84,88,89]
420	$O(3s\ ^5S°) + e^- \rightleftharpoons O(4d\ ^5D°/^3D°, 4f\ ^5F/^3F) + e^-$	4	12	$1.00x10^{-30}$	0.00	$2.911x10^{04}$	343.5	[66,84,88,89]
421	$O(3s\ ^5S°) + e^- \rightleftharpoons O(5p\ ^5P/^3P) + e^-$	4	13	$5.20x10^{-12}$	0.07	$3.010x10^{04}$	332.2	[66,84,88,89]
422	$O(3s\ ^5S°) + e^- \rightleftharpoons O(5d\ ^5D°/^3D°, 5f\ ^5F/^3F, 5g\ ^5G/^3F) + e^-$	4	14	$1.00x10^{-30}$	0.00	$3.163x10^{04}$	316.2	[66,84,88,89]

423	$O(3s\ ^5S°) + e^- \rightleftharpoons O(6) + e^-$	4	15	9.90×10^{-15}	-0.03	3.287×10^{04}	304.2	[66,84,88,89]
424	$O(3s\ ^5S°) + e^- \rightleftharpoons O(7) + e^-$	4	16	2.60×10^{-13}	0.15	3.382×10^{04}	295.7	[66,84,88,89]
425	$O(3s\ ^5S°) + e^- \rightleftharpoons O(8) + e^-$	4	17	2.90×10^{-13}	0.22	3.435×10^{04}	291.1	[66,84,88,89]
426	$O(3s\ ^5S°) + e^- \rightleftharpoons O(9) + e^-$	4	18	2.40×10^{-13}	0.27	3.471×10^{04}	288.1	[66,84,88,89]
427	$O(3s\ ^5S°) + e^- \rightleftharpoons O(10) + e^-$	4	19	1.90×10^{-13}	0.30	3.497×10^{04}	286.0	[66,84,88,89]
428	$O(3s\ ^3S°) + e^- \rightleftharpoons O(3p\ ^5P) + e^-$	5	6	2.20×10^{-11}	-0.09	9.834×10^{03}	1016.9	[66,84,88,89]
429	$O(3s\ ^3S°) + e^- \rightleftharpoons O(3p\ ^3P) + e^-$	5	7	1.30×10^{-06}	-0.07	1.184×10^{04}	844.9	[66,84,88,89]
430	$O(3s\ ^3S°) + e^- \rightleftharpoons O(4s\ ^5S°/^3S°) + e^-$	5	8	1.00×10^{-30}	0.00	1.896×10^{04}	527.4	[66,84,88,89]
431	$O(3s\ ^3S°) + e^- \rightleftharpoons O(3d\ ^5D°/^3D°) + e^-$	5	9	1.00×10^{-30}	0.00	2.065×10^{04}	484.3	[66,84,88,89]
432	$O(3s\ ^3S°) + e^- \rightleftharpoons O(4p\ ^5P/^3P) + e^-$	5	10	1.50×10^{-09}	0.13	2.252×10^{04}	444.1	[66,84,88,89]
433	$O(3s\ ^3S°) + e^- \rightleftharpoons O(5s\ ^5S°/^3S°) + e^-$	5	11	1.00×10^{-30}	0.00	2.543×10^{04}	393.2	[66,84,88,89]
434	$O(3s\ ^3S°) + e^- \rightleftharpoons O(4d\ ^5D°/^3D°, 4f\ ^5F/^3F) + e^-$	5	12	1.00×10^{-30}	0.00	2.609×10^{04}	383.3	[66,84,88,89]
435	$O(3s\ ^3S°) + e^- \rightleftharpoons O(5p\ ^5P/^3P) + e^-$	5	13	7.70×10^{-11}	0.12	2.707×10^{04}	369.4	[66,84,88,89]
436	$O(3s\ ^3S°) + e^- \rightleftharpoons O(5d\ ^5D°/^3D°, 5f\ ^5F/^3F, 5g\ ^5G/^3F) + e^-$	5	14	1.00×10^{-30}	0.00	2.860×10^{04}	349.7	[66,84,88,89]
437	$O(3s\ ^3S°) + e^- \rightleftharpoons O(6) + e^-$	5	15	6.90×10^{-12}	0.00	2.984×10^{04}	335.1	[66,84,88,89]
438	$O(3s\ ^3S°) + e^- \rightleftharpoons O(7) + e^-$	5	16	4.50×10^{-13}	0.16	3.079×10^{04}	324.8	[66,84,88,89]
439	$O(3s\ ^3S°) + e^- \rightleftharpoons O(8) + e^-$	5	17	3.20×10^{-15}	0.23	3.132×10^{04}	319.3	[66,84,88,89]
440	$O(3s\ ^3S°) + e^- \rightleftharpoons O(9) + e^-$	5	18	2.80×10^{-14}	0.28	3.168×10^{04}	315.6	[66,84,88,89]
441	$O(3s\ ^3S°) + e^- \rightleftharpoons O(10) + e^-$	5	19	6.20×10^{-14}	0.31	3.194×10^{04}	313.1	[66,84,88,89]
442	$O(3p\ ^5P) + e^- \rightleftharpoons O(3p\ ^3P) + e^-$	6	7	4.60×10^{-12}	-1.19	2.002×10^{03}	4995.0	[66,84,88,89]
443	$O(3p\ ^5P) + e^- \rightleftharpoons O(4s\ ^5S°/^3S°) + e^-$	6	8	2.20×10^{-07}	-0.15	9.128×10^{03}	1095.5	[66,84,88,89]
444	$O(3p\ ^5P) + e^- \rightleftharpoons O(3d\ ^5D°/^3D°) + e^-$	6	9	7.30×10^{-07}	-0.06	1.082×10^{04}	924.6	[66,84,88,89]
445	$O(3p\ ^5P) + e^- \rightleftharpoons O(4p\ ^5P/^3P) + e^-$	6	10	2.50×10^{-09}	-0.19	1.268×10^{04}	788.4	[66,84,88,89]
446	$O(3p\ ^5P) + e^- \rightleftharpoons O(5s\ ^5S°/^3S°) + e^-$	6	11	5.20×10^{-09}	0.01	1.560×10^{04}	641.1	[66,84,88,89]
447	$O(3p\ ^5P) + e^- \rightleftharpoons O(4d\ ^5D°/^3D°, 4f\ ^5F/^3F) + e^-$	6	12	1.80×10^{-08}	0.05	1.625×10^{04}	615.3	[66,84,88,89]
448	$O(3p\ ^5P) + e^- \rightleftharpoons O(5p\ ^5P/^3P) + e^-$	6	13	1.60×10^{-08}	-0.05	1.724×10^{04}	580.0	[66,84,88,89]
449	$O(3p\ ^5P) + e^- \rightleftharpoons O(5d\ ^5D°/^3D°, 5f\ ^5F/^3F, 5g\ ^5G/^3F) + e^-$	6	14	2.90×10^{-09}	0.11	1.877×10^{04}	532.9	[66,84,88,89]
450	$O(3p\ ^5P) + e^- \rightleftharpoons O(6) + e^-$	6	15	2.20×10^{-09}	-0.12	2.001×10^{04}	499.8	[66,84,88,89]

451	$O(3p\ ^5P) + e^- \rightleftharpoons O(7) + e^-$	6	16	7.50×10^{-10}	0.03	2.095×10^{04}	477.2	[66,84,88,89]
452	$O(3p\ ^5P) + e^- \rightleftharpoons O(8) + e^-$	6	17	3.40×10^{-10}	0.13	2.149×10^{04}	465.4	[66,84,88,89]
453	$O(3p\ ^5P) + e^- \rightleftharpoons O(9) + e^-$	6	18	1.60×10^{-10}	0.27	2.185×10^{04}	457.7	[66,84,88,89]
454	$O(3p\ ^5P) + e^- \rightleftharpoons O(10) + e^-$	6	19	9.20×10^{-11}	0.31	2.211×10^{04}	452.4	[66,84,88,89]
455	$O(3p\ ^3P) + e^- \rightleftharpoons O(4s\ ^5S°/^3S°) + e^-$	7	8	3.60×10^{-07}	0.01	7.126×10^{03}	1403.3	[66,84,88,89]
456	$O(3p\ ^3P) + e^- \rightleftharpoons O(3d\ ^5D°/^3D°) + e^-$	7	9	1.60×10^{-06}	-0.06	8.814×10^{03}	1134.6	[66,84,88,89]
457	$O(3p\ ^3P) + e^- \rightleftharpoons O(4p\ ^5P/^3P) + e^-$	7	10	7.90×10^{-08}	-0.54	1.068×10^{04}	936.2	[66,84,88,89]
458	$O(3p\ ^3P) + e^- \rightleftharpoons O(5s\ ^5S°/^3S°) + e^-$	7	11	1.00×10^{-08}	0.07	1.360×10^{04}	735.5	[66,84,88,89]
459	$O(3p\ ^3P) + e^- \rightleftharpoons O(4d\ ^5D°/^3D°, 4f\ ^5F/^3F) + e^-$	7	12	2.30×10^{-08}	0.04	1.425×10^{04}	701.8	[66,84,88,89]
460	$O(3p\ ^3P) + e^- \rightleftharpoons O(5p\ ^5P/^3P) + e^-$	7	13	8.60×10^{-08}	-0.26	1.524×10^{04}	656.3	[66,84,88,89]
461	$O(3p\ ^3P) + e^- \rightleftharpoons O(5d\ ^5D°/^3D°, 5f\ ^5F/^3F, 5g\ ^5G/^3F) + e^-$	7	14	2.50×10^{-09}	0.10	1.676×10^{04}	596.6	[66,84,88,89]
462	$O(3p\ ^3P) + e^- \rightleftharpoons O(6) + e^-$	7	15	3.30×10^{-09}	-0.18	1.801×10^{04}	555.3	[66,84,88,89]
463	$O(3p\ ^3P) + e^- \rightleftharpoons O(7) + e^-$	7	16	1.00×10^{-09}	-0.02	1.895×10^{04}	527.6	[66,84,88,89]
464	$O(3p\ ^3P) + e^- \rightleftharpoons O(8) + e^-$	7	17	4.20×10^{-10}	0.08	1.949×10^{04}	513.2	[66,84,88,89]
465	$O(3p\ ^3P) + e^- \rightleftharpoons O(9) + e^-$	7	18	1.80×10^{-10}	0.23	1.985×10^{04}	503.9	[66,84,88,89]
466	$O(3p\ ^3P) + e^- \rightleftharpoons O(10) + e^-$	7	19	1.10×10^{-10}	0.28	2.010×10^{04}	497.4	[66,84,88,89]
467	$O(4s\ ^5S°/^3S°) + e^- \rightleftharpoons O(3d\ ^5D°/^3D°) + e^-$	8	9	1.00×10^{-30}	0.00	1.688×10^{03}	5924.2	[66,84,88,89]
468	$O(4s\ ^5S°/^3S°) + e^- \rightleftharpoons O(4p\ ^5P/^3P) + e^-$	8	10	8.80×10^{-06}	-0.13	3.556×10^{03}	2812.1	[66,84,88,89]
469	$O(4s\ ^5S°/^3S°) + e^- \rightleftharpoons O(5s\ ^5S°/^3S°) + e^-$	8	11	1.00×10^{-30}	0.00	6.470×10^{03}	1545.6	[66,84,88,89]
470	$O(4s\ ^5S°/^3S°) + e^- \rightleftharpoons O(4d\ ^5D°/^3D°, 4f\ ^5F/^3F) + e^-$	8	12	1.00×10^{-30}	0.00	7.124×10^{03}	1403.7	[66,84,88,89]
471	$O(4s\ ^5S°/^3S°) + e^- \rightleftharpoons O(5p\ ^5P/^3P) + e^-$	8	13	2.40×10^{-08}	-0.04	8.112×10^{03}	1232.7	[66,84,88,89]
472	$O(4s\ ^5S°/^3S°) + e^- \rightleftharpoons O(5d\ ^5D°/^3D°, 5f\ ^5F/^3F, 5g\ ^5G/^3F) + e^-$	8	14	1.00×10^{-30}	0.00	9.637×10^{03}	1037.7	[66,84,88,89]
473	$O(4s\ ^5S°/^3S°) + e^- \rightleftharpoons O(6) + e^-$	8	15	1.80×10^{-09}	-0.12	1.088×10^{04}	918.9	[66,84,88,89]
474	$O(4s\ ^5S°/^3S°) + e^- \rightleftharpoons O(7) + e^-$	8	16	2.60×10^{-10}	0.07	1.183×10^{04}	845.6	[66,84,88,89]
475	$O(4s\ ^5S°/^3S°) + e^- \rightleftharpoons O(8) + e^-$	8	17	6.60×10^{-11}	0.15	1.236×10^{04}	809.1	[66,84,88,89]
476	$O(4s\ ^5S°/^3S°) + e^- \rightleftharpoons O(9) + e^-$	8	18	2.30×10^{-11}	0.22	1.272×10^{04}	786.1	[66,84,88,89]
477	$O(4s\ ^5S°/^3S°) + e^- \rightleftharpoons O(10) + e^-$	8	19	9.80×10^{-12}	0.26	1.298×10^{04}	770.6	[66,84,88,89]
478	$O(3d\ ^5D°/^3D°) + e^- \rightleftharpoons O(4p\ ^5P/^3P) + e^-$	9	10	2.20×10^{-06}	-0.22	1.868×10^{03}	5353.3	[66,84,88,89]

479	$O(3d\ ^5D°/^3D°) + e^- \rightleftharpoons O(5s\ ^5S°/^3S°) + e^-$	9	11	1.00×10^{-30}	0.00	4.782×10^{03}	2091.2	[66,84,88,89]
480	$O(3d\ ^5D°/^3D°) + e^- \rightleftharpoons O(4d\ ^5D°/^3D°, 4f\ ^5F/^3F) + e^-$	9	12	1.90×10^{-06}	-0.06	5.436×10^{03}	1839.6	[66,84,88,89]
481	$O(3d\ ^5D°/^3D°) + e^- \rightleftharpoons O(5p\ ^5P/^3P) + e^-$	9	13	3.10×10^{-09}	-0.07	6.424×10^{03}	1556.7	[66,84,88,89]
482	$O(3d\ ^5D°/^3D°) + e^- \rightleftharpoons O(5d\ ^5D°/^3D°, 5f\ ^5F/^3F, 5g\ ^5G/^3F) + e^-$	9	14	1.30×10^{-07}	0.02	7.949×10^{03}	1258.0	[66,84,88,89]
483	$O(3d\ ^5D°/^3D°) + e^- \rightleftharpoons O(6) + e^-$	9	15	2.90×10^{-08}	0.09	9.194×10^{03}	1087.7	[66,84,88,89]
484	$O(3d\ ^5D°/^3D°) + e^- \rightleftharpoons O(7) + e^-$	9	16	1.10×10^{-08}	0.11	1.014×10^{04}	986.4	[66,84,88,89]
485	$O(3d\ ^5D°/^3D°) + e^- \rightleftharpoons O(8) + e^-$	9	17	4.10×10^{-09}	0.24	1.067×10^{04}	937.0	[66,84,88,89]
486	$O(3d\ ^5D°/^3D°) + e^- \rightleftharpoons O(9) + e^-$	9	18	2.20×10^{-09}	0.27	1.103×10^{04}	906.4	[66,84,88,89]
487	$O(3d\ ^5D°/^3D°) + e^- \rightleftharpoons O(10) + e^-$	9	19	1.30×10^{-09}	0.30	1.129×10^{04}	885.8	[66,84,88,89]
488	$O(5s\ ^5S°/^3S°) + e^- \rightleftharpoons O(5s\ ^5S°/^3S°) + e^-$	10	11	2.30×10^{-06}	-0.14	2.914×10^{03}	3431.7	[66,84,88,89]
489	$O(5s\ ^5S°/^3S°) + e^- \rightleftharpoons O(4d\ ^5D°/^3D°, 4f\ ^5F/^3F) + e^-$	10	12	6.30×10^{-06}	-0.13	3.568×10^{03}	2802.7	[66,84,88,89]
490	$O(5s\ ^5S°/^3S°) + e^- \rightleftharpoons O(5p\ ^5P/^3P) + e^-$	10	13	8.20×10^{-09}	-0.15	4.556×10^{03}	2194.9	[66,84,88,89]
491	$O(5s\ ^5S°/^3S°) + e^- \rightleftharpoons O(5d\ ^5D°/^3D°, 5f\ ^5F/^3F, 5g\ ^5G/^3F) + e^-$	10	14	1.90×10^{-07}	-0.03	6.081×10^{03}	1644.5	[66,84,88,89]
492	$O(5s\ ^5S°/^3S°) + e^- \rightleftharpoons O(6) + e^-$	10	15	1.10×10^{-07}	-0.29	7.326×10^{03}	1365.0	[66,84,88,89]
493	$O(5s\ ^5S°/^3S°) + e^- \rightleftharpoons O(7) + e^-$	10	16	2.20×10^{-08}	-0.09	8.270×10^{03}	1209.2	[66,84,88,89]
494	$O(5s\ ^5S°/^3S°) + e^- \rightleftharpoons O(8) + e^-$	10	17	7.90×10^{-09}	0.02	8.804×10^{03}	1135.8	[66,84,88,89]
495	$O(5s\ ^5S°/^3S°) + e^- \rightleftharpoons O(9) + e^-$	10	18	3.10×10^{-09}	0.18	9.165×10^{03}	1091.1	[66,84,88,89]
496	$O(5s\ ^5S°/^3S°) + e^- \rightleftharpoons O(10) + e^-$	10	19	1.70×10^{-09}	0.23	9.421×10^{03}	1061.5	[66,84,88,89]

*Select states are combined to match TOPBase b-f and LEVELS.dat within NEQAIR. A term of 'XX' signifies that all terms of a leading configuration are included. If configuration is numeric, all states of the principal quantum number n are included.

Table A5: Molecular heavy particle impact quenching rate transition baseline (BL) and uncertainty multiplier intervals applied to preexponential factors.

$$k_f^{hp}(T_{tr}) = U k_{q,0} \sqrt{\frac{T_{tr}}{300}} exp\left(-\theta_{hp}/T_{tr}\right)$$

No.	Transition	u	l	$k_{q,0}$, $cm^3 s^{-1}$	θ_{hp}, K	U_{low}	U_{high}	BL Refs.	UB Refs.
497	$N_2^+(A^2\Pi_u)$ + M ⇌ $N_2^+(X^2\Sigma_g^+)$ + M	2	1	7.00x10^{-10}	0	0.1	10	[239,240]	-
498	$N_2^+(B^2\Sigma_u^+/D^2\Pi_g)$ + M ⇌ N_2^+(Others) + M	3/4	Others	1.00x10^{-09}	0	0.1	*10*	[241]	-
499	N_2^+(Others) + M ⇌ N_2^+(Others) + M	Others	Others	1.00x10^{-09}	0	0.1	10	[241]	-
500	$N_2(A^3\Sigma_u^+)$ + O ⇌ $N_2(X^1\Sigma_g^+)$ + O	2	1	2.10x10^{-11}	0	0.1	10	[242–244]	-
501	$N_2(A^3\Sigma_u^+)$ + N ⇌ $N_2(X^1\Sigma_g^+)$ + N	2	1	2.00x10^{-12}	0	0.1	10	[244–248]	-
502	$N_2(A^3\Sigma_u^+)$ + O_2 ⇌ $N_2(X^1\Sigma_g^+)$ + O_2	2	1	2.10x10^{-12}	0	0.1	10	[244,249–252]	-
503	$N_2(A^3\Sigma_u^+)$ + N_2 ⇌ $N_2(X^1\Sigma_g^+)$ + N_2	2	1	3.00x10^{-16}	0	0.1	10	[244,253]	-
504	$N_2(A^3\Sigma_u^+)$ + NO ⇌ $N_2(X^1\Sigma_g^+)$ + NO	2	1	6.90x10^{-11}	0	0.1	10	[244,254]	-
505	$N_2(A^3\Sigma_u^+)$ + Others ⇌ $N_2(X^1\Sigma_g^+)$ + Others	2	1	1.00x10^{-11}	0	0.1	10	[84]	-
506	$N_2(B^3\Pi_g)$+ N_2 ⇌ $N_2(X^1\Sigma_g^+)$ + N_2	3	1	1.00x10^{-12}	0	0.1	10	[244,255,256]	-
507	$N_2(B^3\Pi_g)$ + O_2 ⇌ $N_2(X^1\Sigma_g^+)$ + O_2	3	1	4.00x10^{-11}	0	0.1	10	[255]	-
508	$N_2(B^3\Pi_g)$ + Others ⇌ $N_2(X^1\Sigma_g^+)$ + Others	3	1	1.00x10^{-10}	0	0.1	10	[84]	-
509	$N_2(B^3\Pi_g)$ + NO ⇌ $N_2(A^3\Sigma_u^+)$ + NO	3	2	2.40x10^{-10}	0	0.1	10	[244,257]	-
510	$N_2(B^3\Pi_g)$ + N_2 ⇌ $N_2(A^3\Sigma_u^+)$ + N_2	3	2	1.50x10^{-11}	0	0.1	10	[255]	-
511	$N_2(B^3\Pi_g)$ + Others ⇌ $N_2(A^3\Sigma_u^+)$ + Others	3	2	1.00x10^{-10}	0	0.1	10	[84]	-
512	$N_2(a^1\Pi_g)$ + O_2 ⇌ N_2(Others) + O_2	4	Others	2.80x10^{-11}	0	0.1	10	[244,258]	-
513	$N_2(a^1\Pi_g)$ + NO ⇌ N_2(Others) + NO	4	Others	3.60x10^{-10}	0	0.1	10	[244,258]	-
514	$N_2(a^1\Pi_g)$ + N_2 ⇌ N_2(Others) + N_2	4	Others	1.90x10^{-13}	0	0.1	10	[244,258,259]	-
515	$N_2(a^1\Pi_g)$ + Others ⇌ N_2(Others) + Others	4	Others	1.00x10^{-11}	0	0.1	10	[84]	-
516	$N_2(C^3\Pi_u/C'^3\Pi_u)$ + N_2 ⇌ N_2(Others) + N_2	5/6	Others	2.90x10^{-11}	0	0.1	10	[260]	-
517	$N_2(C^3\Pi_u/C'^3\Pi_u)$ + O_2 ⇌ N_2(Others) + O_2	5/6	Others	3.10x10^{-10}	0	0.1	10	[260]	-
518	$N_2(C^3\Pi_u/C'^3\Pi_u)$ + Others ⇌ N_2(Others) + Others	5/6	Others	1.00x10^{-10}	0	0.1	10	[260]	-

519	N_2(Others) + O_2 ⇌ N_2(Others) + O_2	Others	Others	1.00×10^{-10}	0	0.1	10	[84]	-
520	NO($a^4\Pi$) + N_2 ⇌ NO($X^2\Pi$) + N_2	2	1	1.19×10^{-11}	0	0.1	10	[261]	-
521	NO($a^4\Pi$) + O_2 ⇌ NO($X^2\Pi$) + O_2	2	1	4.27×10^{-11}	0	0.1	10	[261]	-
522	NO($a^4\Pi$) + NO ⇌ NO($X^2\Pi$) + NO	2	1	1.38×10^{-10}	0	0.1	10	[261]	-
523	NO($a^4\Pi$) + Others ⇌ NO($X^2\Pi$) + Others	2	1	1.00×10^{-10}	0	0.1	10	[84]	-
524	NO($A^2\Sigma^+$) + N_2 ⇌ NO(Others) + N_2	3	Others	2.99×10^{-10}	0	0.1	10	[262]	-
525	NO($A^2\Sigma^+$) + O_2 ⇌ NO(Others) + O_2	3	Others	1.50×10^{-10}	8.49×10^{03}	0.1	10	[262]	-
526	NO($A^2\Sigma^+$) + NO ⇌ NO(Others) + NO	3	Others	2.00×10^{-10}	0	0.1	10	[262]	-
527	NO($A^2\Sigma^+$) + Others ⇌ NO(Others) + Others	3	Others	1.00×10^{-10}	0	0.1	10	[84]	-
528	NO($B^2\Pi$) + N_2 ⇌ NO(Others) + N_2	4	Others	6.10×10^{-13}	0	0.1	10	[261]	-
529	NO($B^2\Pi$) + O_2 ⇌ NO(Others) + O_2	4	Others	1.50×10^{-10}	0	0.1	10	[261]	-
530	NO($B^2\Pi$) + NO ⇌ NO(Others) + NO	4	Others	2.00×10^{-10}	0	0.1	10	[261]	-
531	NO($B^2\Pi$) + Others ⇌ NO(Others)+ Others	4	Others	1.00×10^{-10}	0	0.1	10	[84]	-
532	NO($b^4\Sigma^-$) + N_2 ⇌ NO(Others) + N_2	5	Others	1.19×10^{-11}	0	0.1	10	[261]	-
533	NO($b^4\Sigma^-$) + O_2 ⇌ NO(Others) + O_2	5	Others	4.27×10^{-11}	0	0.1	10	[261]	-
534	NO($b^4\Sigma^-$) + NO ⇌ NO(Others) + NO	5	Others	1.38×10^{-10}	0	0.1	10	[261]	-
535	NO($b^4\Sigma^-$) + Others ⇌ NO(Others)+ Others	5	Others	1.00×10^{-10}	0	0.1	10	[84]	-
536	NO($C^2\Pi$) + N_2 ⇌ NO(Others) + N_2	6	Others	6.10×10^{-13}	0	0.1	10	[261]	-
537	NO($C^2\Pi$) + O_2 ⇌ NO(Others) + O_2	6	Others	1.50×10^{-11}	0	0.1	10	[261]	-
538	NO($C^2\Pi$) + NO ⇌ NO(Others) + NO	6	Others	2.00×10^{-10}	0	0.1	10	[261]	-
539	NO($C^2\Pi$+ Others ⇌ NO(Others)+ Others	6	Others	1.00×10^{-10}	0	0.1	10	[84]	-
540	NO($D^2\Sigma^+$) + N_2 ⇌ NO(Others) + N_2	7	Others	4.83×10^{-11}	0	0.1	10	[263]	-
541	NO($D^2\Sigma^+$) + O_2 ⇌ NO(Others) + O_2	7	Others	4.57×10^{-10}	0	0.1	10	[263]	-
542	NO($D^2\Sigma^+$) + NO ⇌ NO(Others) + NO	7	Others	3.31×10^{-10}	0	0.1	10	[263]	-
543	NO($D^2\Sigma^+$) + Others ⇌ NO(Others)+ Others	7	Others	1.00×10^{-10}	0	0.1	10	[84]	-
544	NO($D^2\Sigma^+$) + N ⇌ NO($C^2\Pi$) + N	7	6	2.49×10^{-10}	0	0.1	10	[264]	-
545	NO($D^2\Sigma^+$) + O ⇌ NO($C^2\Pi$) + O	7	6	2.49×10^{-10}	0	0.1	10	[264]	-
546	NO($D^2\Sigma^+$) + Others ⇌ NO(Others)+ Others	Others	Others	1.19×10^{-11}	0	0.1	10	[84]	-
547	CN($A^2\Pi$) + M ⇌ CN($X^2\Sigma^+$) + M	2	1	1.89×10^{-12}	0	0.1	10	[265]	[47]

548	$CN(B^2\Sigma^+)$ + M ⇌ CN(Others) + M	3	Others	$2.73x10^{-12}$	0	0.1	10	[265]	-
549	$CO(a^3\Pi)$ + O_2 ⇌ $CO(X^1\Sigma^+)$ + O_2	2	1	$6.20x10^{-11}$	0	0.1	10	[266]	[47]
550	$CO(a^3\Pi)$ + NO ⇌ $CO(X^1\Sigma^+)$ + NO	2	1	$1.70x10^{-10}$	0	0.1	10	[266]	[47]
551	$CO(a^3\Pi)$ + CO ⇌ $CO(X^1\Sigma^+)$ + CO	2	1	$5.70x10^{-11}$	0	0.1	10	[266]	[47]
552	$CO(a^3\Pi)$ + O ⇌ $CO(X^1\Sigma^+)$ + O	2	1	$9.80x10^{-11}$	0	0.1	10	[266]	[47]
553	$CO(a^3\Pi)$ + Others ⇌ $CO(X^1\Sigma^+)$ + Others	2	1	$5.00x10^{-11}$	0	0.1	10	[84]	[47]
554	$CO(a'^3\Sigma^+)$ + Others ⇌ CO(Others) + Others	3	Others	$1.00x10^{-09}$	0	0.1	10	[267]	[47]
555	$CO(A^1\Pi)$ + N_2 ⇌ CO(Others) + N_2	4	Others	$2.96x10^{-11}$	0	0.1	10	[268]	[47]
556	$CO(A^1\Pi)$ + CO ⇌ CO(Others) + CO	4	Others	$8.70x10^{-10}$	0	0.1	10	[269]	[47]
557	$CO(A^1\Pi)$ + Others ⇌ CO(Others)+ Others	4	Others	$5.00x10^{-11}$	0	0.1	10	[84]	[47]

Table A6: Molecular electron impact excitation transition cross section baselines (BL) and uncertainty bound (UB) multiplier intervals.

$$k_f^{el} = \left[\sum_{v,v'} S_{vv'} q_{vv'} exp\left(-\frac{E_v}{T_{ve}}\right)\right] / Q_{vr}, \quad S_{vv'} = 5.47x10^{-11} n_e \sqrt{T_{ve}} exp\left(-\frac{\Delta E_{ve}}{T_{ve}}\right) I,$$

$$I = \int_0^\infty (2J)^2 exp\left[-\left(\frac{B_e' - B_e}{T_{ve}} + \frac{B_e}{T_{tr}}\right) J^2\right] \left(C + B\frac{B_e' - B_e}{T_{ve}} J^2\right) dJ,$$

$$A = \int_0^\infty \frac{U\sigma(\xi T_{ve})}{\pi a_0^2} e^\xi \xi d\xi, \quad B = \int_0^\infty \frac{U\sigma(\xi T_{ve})}{\pi a_0^2} e^\xi d\xi, \quad C = \frac{\Delta E_{ve}}{T_{ve}} B + A$$

No.	Transition	l u	E_1, eV σ_1, cm^{-2}	E_2, eV σ_2, cm^{-2}	E_3, eV σ_3, cm^{-2}	E_4, eV σ_4, cm^{-2}	E_5, eV σ_5, cm^{-2}	E_6, eV σ_6, cm^{-2}	E_7, eV σ_7, cm^{-2}	E_8, eV σ_8, cm^{-2}	U_{low} U_{high}	BL Refs.	UB Refs.
558	$N_2^+(X^2\Sigma_g^+)$ + e$^-$ ⇌ $N_2^+(A^2\Pi_u)$ + e$^-$	1 2	1.118 2.95x10^{-16}	1.411 2.83x10^{-16}	2.116 2.38x10^{-16}	2.821 1.90x10^{-16}	3.527 1.55x10^{-16}	5.289 1.10x10^{-16}	7.053 0.89x10^{-16}	10.58 0.68x10^{-16}	0.1 10	[270]	-
559	$N_2^+(X^2\Sigma_g^+)$ + e$^-$ ⇌ $N_2^+(B^2\Sigma_u^+)$ + e$^-$	1 3	3.17 0.00x10^{-17}	3.40 2.93x10^{-16}	4.00 2.94x10^{-16}	6.00 2.33x10^{-16}	8.00 1.91x10^{-16}	10.0 1.62x10^{-16}	15.0 1.20x10^{-16}	20.0 9.63x10^{-17}	0.1 10	[270]	-
560	$N_2^+(X^2\Sigma_g^+)$ + e$^-$ ⇌ $N_2^+(D^2\Pi_g)$ + e$^-$	1 4	6.405 2.95x10^{-16}	8.083 2.83x10^{-16}	12.12 2.38x10^{-16}	16.17 1.90x10^{-16}	20.21 1.55x10^{-16}	30.31 1.10x10^{-16}	40.42 0.89x10^{-16}	60.62 0.68x10^{-16}	0.1 10	[270]	-
561	$N_2^+(A^2\Pi_u)$ + e$^-$ ⇌ $N_2^+(B^2\Sigma_u^+)$ + e$^-$	2 3	2.052 2.95x10^{-16}	2.589 2.83x10^{-16}	3.884 2.38x10^{-16}	5.179 1.90x10^{-16}	6.473 1.55x10^{-16}	9.709 1.10x10^{-16}	12.95 0.89x10^{-16}	19.42 0.68x10^{-16}	0.1 10	[270]	-
562	$N_2^+(A^2\Pi_u)$ + e$^-$ ⇌ $N_2^+(D^2\Pi_g)$ + e$^-$	2 4	5.287 2.95x10^{-16}	6.673 2.83x10^{-16}	10.01 2.38x10^{-16}	13.35 1.90x10^{-16}	16.68 1.55x10^{-16}	25.02 1.10x10^{-16}	33.36 0.89x10^{-16}	50.04 0.68x10^{-16}	0.1 10	[270]	-
563	$N_2^+(B^2\Sigma_u^+)$ + e$^-$ ⇌ $N_2^+(D^2\Pi_g)$ + e$^-$	3 4	3.235 2.95x10^{-16}	4.083 2.83x10^{-16}	6.125 2.38x10^{-16}	8.166 1.90x10^{-16}	10.21 1.55x10^{-16}	15.31 1.10x10^{-16}	20.42 0.89x10^{-16}	20.42 0.68x10^{-16}	0.1 10	[270]	-
564	$N_2(X^1\Sigma_g^+)$ + e$^-$ ⇌ $N_2(A^3\Sigma_u^+)$ + e$^-$	1 2	6.1693 0	7.65 0.05x10^{-17}	8.74 1.37x10^{-17}	10.4 1.68x10^{-17}	12.1 2.57x10^{-17}	15.0 1.60x10^{-17}	20.0 1.26x10^{-17}	30.0 0.78x10^{-17}	0.2 200	[125]	[113]
565	$N_2(X^1\Sigma_g^+)$ + e$^-$ ⇌ $N_2(B^3\Pi_g)$ + e$^-$	1 3	7.3529 0	8.55 0.02x10^{-17}	10.0 2.50x10^{-17}	12.5 3.39x10^{-17}	15.0 2.70x10^{-17}	20.0 1.44x10^{-17}	25.0 0.92x10^{-17}	35.0 0.49x10^{-17}	0.1 150	[125]	[113]
566	$N_2(X^1\Sigma_g^+)$ + e$^-$ ⇌ $N_2(a^1\Pi_g)$ + e$^-$	1 4	8.5489 0	9.00 0.38x10^{-17}	11.0 1.74x10^{-17}	15.0 4.43x10^{-17}	16.5 4.73x10^{-17}	18.0 4.46x10^{-17}	21.5 3.00x10^{-17}	30.0 2.04x10^{-17}	0.01 1.0	[125]	[113]
567	$N_2(A^3\Sigma_u^+)$ + e$^-$ ⇌ $N_2(B^3\Pi_g)$ + e$^-$	2 3	1.167 0	1.667 5.91x10^{-17}	2.667 4.41x10^{-17}	4.667 2.67x10^{-17}	9.667 1.47x10^{-17}	19.667 8.54x10^{-18}	29.667 6.32x10^{-18}	49.667 4.36x10^{-18}	1.0 25	[271]	[113]
568	$N_2(A^3\Sigma_u^+)$ + e$^-$ ⇌ $N_2(a^1\Pi_g)$ + e$^-$	2 4	2.366 0	2.866 5.91x10^{-17}	3.866 4.41x10^{-17}	5.866 2.67x10^{-17}	10.866 1.47x10^{-17}	20.866 8.54x10^{-18}	30.866 6.32x10^{-18}	50.866 4.36x10^{-18}	0.05 1.0	[271]	[113]
569	$N_2(B^3\Pi_g)$ + e$^-$ ⇌ $N_2(a^1\Pi_g)$ + e$^-$	3 4	1.198 0	1.698 5.91x10^{-17}	2.698 4.41x10^{-17}	4.698 2.67x10^{-17}	9.698 1.47x10^{-17}	19.698 8.54x10^{-18}	29.698 6.32x10^{-18}	49.698 4.36x10^{-18}	0.1 10	[271]	-

570	$N_2(X^1\Sigma_g^+)$ + e⁻ ⇌ $N_2(C^3\Pi_u)$ + e⁻	1 5	11.032 0	11.5 0.74×10^{-17}	12.5 2.29×10^{-17}	14.5 5.83×10^{-17}	18.0 2.76×10^{-17}	20.0 2.12×10^{-17}	30.0 0.77×10^{-17}	40.0 0.38×10^{-17}	0.05 10	[125]	[113]
571	$N_2(a^3\Sigma_u^+)$ + e⁻ ⇌ $N_2(C^3\Pi_u)$ + e⁻	2 5	4.827 0	5.327 5.91×10^{-17}	6.327 4.41×10^{-17}	8.327 2.67×10^{-17}	13.327 1.47×10^{-17}	23.327 8.54×10^{-18}	33.327 6.32×10^{-18}	53.327 4.36×10^{-18}	0.5 15	[271]	[113]
572	$N_2(B^3\Pi_g)$ + e⁻ ⇌ $N_2(C^3\Pi_u)$ + e⁻	3 5	3.66 0	4.16 5.91×10^{-17}	5.16 4.41×10^{-17}	7.16 2.67×10^{-17}	12.16 1.47×10^{-17}	22.16 8.54×10^{-18}	32.16 6.32×10^{-18}	52.16 4.36×10^{-18}	1.0 2.0		[113, 271]
573	$N_2(a^1\Pi_g)$ + e⁻ ⇌ $N_2(C^3\Pi_u)$ + e⁻	4 5	2.462 0	2.962 5.91×10^{-17}	3.962 4.41×10^{-17}	5.962 2.67×10^{-17}	10.962 1.47×10^{-17}	20.962 8.54×10^{-18}	30.962 6.32×10^{-18}	50.962 4.36×10^{-18}	0.1 10	[271]	[113]
574	$N_2(X^1\Sigma_g^+)$ + e⁻ ⇌ $N_2(C'^3\Pi_u)$ + e⁻	1 6	12.048 0	12.55 0.74×10^{-17}	13.55 2.29×10^{-17}	15.55 5.83×10^{-17}	19.55 2.76×10^{-17}	21.55 2.12×10^{-17}	31.55 0.77×10^{-17}	41.55 0.38×10^{-17}	0.1 10	[125]	-
575	$N_2(A^3\Sigma_u^+)$ + e⁻ ⇌ $N_2(C'^3\Pi_u)$ + e⁻	2 6	5.969 0	6.569 5.91×10^{-17}	7.469 4.41×10^{-17}	9.469 2.67×10^{-17}	14.469 1.47×10^{-17}	24.469 8.54×10^{-18}	34.469 6.32×10^{-18}	54.469 4.36×10^{-18}	0.1 10	[271]	-
576	$N_2(B^3\Pi_g)$ + e⁻ ⇌ $N_2(C'^3\Pi_u)$ + e⁻	3 6	4.802 0	5.302 5.91×10^{-17}	6.302 4.41×10^{-17}	8.302 2.67×10^{-17}	13.302 1.47×10^{-17}	23.302 8.54×10^{-18}	33.302 6.32×10^{-18}	53.302 4.36×10^{-18}	0.1 10	[271]	-
577	$N_2(w^3\Delta_u)$ + e⁻ ⇌ $N_2(C'^3\Pi_u)$ + e⁻	4 6	3.604 0	4.104 5.91×10^{-17}	5.104 4.41×10^{-17}	7.104 2.67×10^{-17}	12.104 1.47×10^{-17}	22.104 8.54×10^{-18}	32.104 6.32×10^{-18}	52.104 4.36×10^{-18}	0.1 10	[271]	-
578	$N_2(C^3\Pi_u)$ + e⁻ ⇌ $N_2(C'^3\Pi_u)$ + e⁻	5 6	1.142 0	1.642 5.91×10^{-17}	2.642 4.41×10^{-17}	4.642 2.67×10^{-17}	9.642 1.47×10^{-17}	19.642 8.54×10^{-18}	29.642 6.32×10^{-18}	49.642 4.36×10^{-18}	0.1 10	[271]	-
579	$NO(X^2\Pi)$ + e⁻ ⇌ $NO(B^2\Pi)$ + e⁻	1 4	5.693 0	6.00 1.90×10^{-19}	8.00 8.74×10^{-19}	9.70 9.50×10^{-19}	12.0 8.36×10^{-19}	15.0 1.21×10^{-18}	30.0 2.13×10^{-18}	50.0 2.96×10^{-18}	0.1 10	[272, 273]	-
580	$NO(X^2\Pi)$ + e⁻ ⇌ $NO(A^2\Sigma^+)$ + e⁻	1 3	5.450 0	6.00 2.44×10^{-19}	8.00 1.39×10^{-18}	9.60 1.53×10^{-18}	13.0 1.35×10^{-18}	15.0 1.46×10^{-18}	20.0 1.50×10^{-18}	50.0 2.51×10^{-18}	0.1 10	[272, 273]	-
581	$NO(X^2\Pi)$ + e⁻ ⇌ $NO(C^2\Pi)$ + e⁻	1 6	6.470 0	8.470 2.31×10^{-18}	10.0 2.31×10^{-18}	15.0 2.31×10^{-18}	20.0 3.27×10^{-18}	30.0 4.13×10^{-18}	40.0 4.68×10^{-18}	50.0 3.27×10^{-18}	0.1 10	[273]	-
582	$NO(X^2\Pi)$ + e⁻ ⇌ $NO(D^2\Sigma^+)$ + e⁻	1 7	6.580 0	8.580 1.44×10^{-18}	10.0 1.44×10^{-18}	15.0 1.44×10^{-18}	20.0 1.85×10^{-18}	30.0 2.54×10^{-18}	40.0 2.97×10^{-18}	50.0 2.20×10^{-18}	0.1 10	[273]	-
583	$NO(A^2\Sigma^+)$ + e⁻ ⇌ $NO(B^2\Pi)$ + e⁻	3 4	0.244 0	0.55 1.90×10^{-19}	2.55 8.74×10^{-19}	4.35 9.50×10^{-19}	6.55 8.36×10^{-19}	9.55 1.22×10^{-18}	25.0 2.13×10^{-18}	45.0 2.96×10^{-18}	0.1 10	[272, 273]	-
584	$NO(A^2\Sigma^+)$ + e⁻ ⇌ $NO(C^2\Pi)$ + e⁻	3 6	1.020 0	3.020 2.31×10^{-18}	10.0 2.31×10^{-18}	9.55 2.31×10^{-18}	14.55 3.27×10^{-18}	24.55 4.13×10^{-18}	34.55 4.68×10^{-18}	44.55 3.27×10^{-18}	0.1 10	[273]	-
585	$NO(A^2\Sigma^+)$ + e⁻ ⇌ $NO(D^2\Sigma^+)$ + e⁻	3 7	1.130 0	3.330 1.44×10^{-18}	4.55 1.44×10^{-18}	9.55 1.44×10^{-18}	14.55 1.85×10^{-18}	24.55 2.54×10^{-18}	34.55 2.97×10^{-18}	44.55 2.20×10^{-18}	0.1 10	[273]	-
586	$NO(B^2\Pi)$ + e⁻ ⇌ $NO(C^2\Pi)$ + e⁻	4 6	0.774 0	2.774 2.31×10^{-18}	4.31 2.31×10^{-18}	9.31 2.31×10^{-18}	14.31 3.27×10^{-18}	24.31 4.13×10^{-18}	34.31 4.68×10^{-18}	44.31 3.27×10^{-18}	0.1 10	[273]	-
587	$NO(B^2\Pi)$ + e⁻ ⇌ $NO(D^2\Sigma^+)$ + e⁻	4 7	0.887 0	2.887 1.44×10^{-18}	4.31 1.44×10^{-18}	9.31 1.44×10^{-18}	14.31 1.85×10^{-18}	24.31 2.54×10^{-18}	34.31 2.97×10^{-18}	44.31 2.20×10^{-18}	0.1 10	[273]	-
588	$NO(C^2\Pi)$ + e⁻ ⇌ $NO(D^2\Sigma^+)$ + e⁻	6 7	0.113 0	2.113 1.44×10^{-18}	2.52 1.44×10^{-18}	8.53 1.44×10^{-18}	13.53 1.85×10^{-18}	23.53 2.54×10^{-18}	33.53 2.97×10^{-18}	43.53 2.20×10^{-18}	0.1 10	[273]	-

589	$NO(X^2\Pi) + e^- \rightleftharpoons$ $NO(a^4\Pi) + e^-$	1 2	4.700 0	6.700 $7.63x10^{-19}$	10.0 $7.63x10^{-19}$	15.0 $7.63x10^{-19}$	20.0 $9.80x10^{-19}$	30.0 $13.5x10^{-19}$	40.0 $9.50x10^{-19}$	50.0 $6.70x10^{-19}$	0.1 10	[273]	-
590	$NO(a^4\Pi) + e^- \rightleftharpoons$ $NO(A^2\Sigma^+) + e^-$	2 3	0.769 0	2.113 $1.44x10^{-18}$	3.53 $1.44x10^{-18}$	8.53 $1.44x10^{-18}$	13.53 $1.85x10^{-18}$	23.53 $2.54x10^{-18}$	33.53 $2.97x10^{-18}$	43.53 $2.20x10^{-18}$	0.1 10	[84]	-
591	$NO(a^4\Pi) + e^- \rightleftharpoons$ $NO(B^2\Pi) + e^-$	2 4	0.930 0	2.113 $1.44x10^{-18}$	3.53 $1.44x10^{-18}$	8.53 $1.44x10^{-18}$	13.53 $1.85x10^{-18}$	23.53 $2.54x10^{-18}$	33.53 $2.97x10^{-18}$	43.53 $2.20x10^{-18}$	0.1 10	[84]	-
592	$NO(a^4\Pi) + e^- \rightleftharpoons$ $NO(b^4\Sigma^-) + e^-$	2 5	1.280 0	2.113 $1.44x10^{-18}$	3.53 $1.44x10^{-18}$	8.53 $1.44x10^{-18}$	13.53 $1.85x10^{-18}$	23.53 $2.54x10^{-18}$	33.53 $2.97x10^{-18}$	43.53 $2.20x10^{-18}$	0.1 10	[84]	-
593	$NO(a^4\Pi) + e^- \rightleftharpoons$ $NO(C^2\Pi) + e^-$	2 6	1.790 0	2.113 $1.44x10^{-18}$	3.53 $1.44x10^{-18}$	8.53 $1.44x10^{-18}$	13.53 $1.85x10^{-18}$	23.53 $2.54x10^{-18}$	33.53 $2.97x10^{-18}$	43.53 $2.20x10^{-18}$	0.1 10	[84]	-
594	$NO(a^4\Pi) + e^- \rightleftharpoons$ $NO(D^2\Sigma^+) + e^-$	2 7	1.900 0	2.113 $1.44x10^{-18}$	3.53 $1.44x10^{-18}$	8.53 $1.44x10^{-18}$	13.53 $1.85x10^{-18}$	23.53 $2.54x10^{-18}$	33.53 $2.97x10^{-18}$	43.53 $2.20x10^{-18}$	0.1 10	[84]	-
595	$NO(X^2\Pi) + e^- \rightleftharpoons$ $NO(b^4\Sigma^-) + e^-$	1 5	5.980 0	7.50 $1.33x10^{-17}$	9.00 $7.60x10^{-18}$	15.0 $4.71x10^{-18}$	20.0 $4.65x10^{-18}$	30.0 $4.14x10^{-18}$	40.0 $1.96x10^{-18}$	50.0 $9.40x10^{-18}$	0.1 10	[272, 273]	-
596	$NO(A^2\Sigma^+) + e^- \rightleftharpoons$ $NO(b^4\Sigma^-) + e^-$	3 5	0.512 0	2.113 $1.44x10^{-18}$	3.53 $1.44x10^{-18}$	8.53 $1.44x10^{-18}$	13.53 $1.85x10^{-18}$	23.53 $2.54x10^{-18}$	33.53 $2.97x10^{-18}$	43.53 $2.20x10^{-18}$	0.1 10	[84]	-
597	$NO(B^2\Pi) + e^- \rightleftharpoons$ $NO(b^4\Sigma^-) + e^-$	4 5	0.351 0	2.113 $1.44x10^{-18}$	3.53 $1.44x10^{-18}$	8.53 $1.44x10^{-18}$	13.53 $1.85x10^{-18}$	23.53 $2.54x10^{-18}$	33.53 $2.97x10^{-18}$	43.53 $2.20x10^{-18}$	0.1 10	[84]	-
598	$NO(b^4\Sigma^-) + e^- \rightleftharpoons$ $NO(C^2\Pi) + e^-$	5 6	0.506 0	2.113 $1.44x10^{-18}$	3.53 $1.44x10^{-18}$	8.53 $1.44x10^{-18}$	13.53 $1.85x10^{-18}$	23.53 $2.54x10^{-18}$	33.53 $2.97x10^{-18}$	43.53 $2.20x10^{-18}$	0.1 10	[84]	-
599	$NO(C^2\Pi) + e^- \rightleftharpoons$ $NO(D^2\Sigma^+) + e^-$	6 7	0.616 0	2.113 $1.44x10^{-18}$	3.53 $1.44x10^{-18}$	8.53 $1.44x10^{-18}$	13.53 $1.85x10^{-18}$	23.53 $2.54x10^{-18}$	33.53 $2.97x10^{-18}$	43.53 $2.20x10^{-18}$	0.1 10	[84]	-
600	$O_2(X^3\Sigma_g^-) + e^- \rightleftharpoons$ $O_2(B^3\Sigma_u^+) + e^-$	1 5	8.44 0	9.50 $21.5x10^{-18}$	11.0 $31.7x10^{-18}$	15.0 $44.0x10^{-18}$	20.0 $49.6x10^{-18}$	30.0 $51.3x10^{-18}$	50.0 $46.7x10^{-18}$	100.0 $35.1x10^{-18}$	0.0 50	[274]	[113]
601	$CN(X^2\Sigma^+) + e^- \rightleftharpoons$ $CN(A^2\Pi) + e^-$	1 2	1.515 0	1.5332 $1.30x10^{-17}$	1.6834 $9.70x10^{-17}$	2.0630 $1.97x10^{-16}$	3.4842 $3.33x10^{-16}$	4.4034 $3.59x10^{-16}$	5.1409 $3.25x10^{-16}$	9.9749 $2.55x10^{-16}$	0.1 10	[275]	[47]
602	$CN(X^2\Sigma^+) + e^- \rightleftharpoons$ $CN(B^2\Sigma^+) + e^-$	1 3	3.491 0	3.5270 $1.17x10^{-17}$	4.1675 $7.60x10^{-17}$	5.7697 $1.52x10^{-16}$	7.2330 $2.17x10^{-16}$	7.8318 $2.13x10^{-16}$	9.4778 $2.51x10^{-16}$	10.016 $2.57x10^{-16}$	0.1 10	[275]	[47]
603	$CN(A^2\Pi) + e^- \rightleftharpoons$ $CN(B^2\Sigma^+) + e^-$	2 3	1.976 0	2.0120 $1.17x10^{-17}$	2.6525 $7.60x10^{-17}$	4.2547 $1.52x10^{-16}$	5.7180 $2.17x10^{-16}$	6.3168 $2.13x10^{-16}$	7.9628 $2.51x10^{-16}$	8.5010 $2.57x10^{-16}$	0.01 100	[275]	[47]
604	$CO(X^2\Sigma^+) + e^- \rightleftharpoons$ $CO(A^3\Pi) + e^-$	1 2	6.035 0	6.20 $2.49x10^{-18}$	6.50 $5.80x10^{-18}$	7.00 $9.95x10^{-18}$	8.00 $1.57x10^{-17}$	8.50 $1.88x10^{-17}$	9.00 $1.99x10^{-17}$	10.0 $1.69x10^{-17}$	0.1 10	[276]	[47]
605	$CO(X^2\Sigma^+) + e^- \rightleftharpoons$ $CO(a'^3\Sigma^+) + e^-$	1 3	6.9260 $5.86x10^{-21}$	7.20 $1.64x10^{-18}$	7.50 $3.44x10^{-18}$	8.00 $8.33x10^{-18}$	9.00 $1.44x10^{-17}$	9.50 $1.33x10^{-17}$	10.0 $1.28x10^{-17}$	11.0 $1.30x10^{-17}$	0.1 10	[276]	[47]
606	$CO(X^2\Sigma^+) + e^- \rightleftharpoons$ $CO(A^1\Pi) + e^-$	1 4	8.0660 0	8.20 $1.37x10^{-18}$	8.50 $4.13x10^{-18}$	9.00 $7.83x10^{-18}$	10.0 $1.40x10^{-17}$	11.0 $1.91x10^{-17}$	12.0 $2.33x10^{-17}$	13.0 $2.65x10^{-17}$	0.1 10	[276]	[47]
607	$CO(A^3\Pi) + e^- \rightleftharpoons$ $CO(a'^3\Sigma^+) + e^-$	2 3	0.8845 0	0.962 $5.40x10^{-18}$	1.203 $2.25x10^{-17}$	1.444 $2.99x10^{-17}$	1.805 $2.41x10^{-17}$	2.406 $1.56x10^{-17}$	3.127 $1.20x10^{-17}$	4.331 $7.60x10^{-18}$	0.1 10	[276]	[47]

608	$CO(A^3\Pi) + e^- \rightleftharpoons$	2	2.0315	2.5315	3.0315	3.5315	4.0315	4.5315	5.0315	5.5315	0.01	[276]	[47]
	$CO(A^1\Pi) + e^-$	4	0	$3.94x10^{-17}$	$3.52x10^{-17}$	$2.94x10^{-17}$	$2.52x10^{-17}$	$2.20x10^{-17}$	$1.96x10^{-17}$	$1.78x10^{-17}$	100		
609	$CO(a'^3\Sigma^+) + e^- \rightleftharpoons$	3	1.1466	1.6466	2.1466	2.6466	3.1466	3.6466	4.1466	4.6466	0.01		[47,276]
	$CO(A^1\Pi) + e^-$	4	0	$3.94x10^{-17}$	$3.52x10^{-17}$	$2.94x10^{-17}$	$2.52x10^{-17}$	$2.20x10^{-17}$	$1.96x10^{-17}$	$1.78x10^{-17}$	100		

Table A7: Finite rate surface chemistry baseline (BL) and uncertainty multiplier intervals.

$$k_O(T_w) = U\epsilon_O F_O = U0.63exp\left(-\frac{1160}{T_w}\right)P_O\sqrt{\frac{8M_O}{\pi k_B T_w}}$$

$$k_{O_2}(T_w) = U\epsilon_{O_2}F_{O_2} = U\frac{1.43x10^{-3} + 0.01exp\left(-\frac{1450}{T_w}\right)}{1 + 2x10^{-4}exp\left(-\frac{13000}{T_w}\right)}P_{O_2}\sqrt{\frac{8M_{O_2}}{\pi k_B T_w}}$$

No.	Reaction	U_{low}	U_{high}	BL Refs.	UB Refs.
610	C(s) + O(a) ⇀ CO(a) ⇀ CO(g)	0.3	3.0	[155–162]	Figure B48
611	C(s) + O_2(a) ⇀ CO(a) + O(a)	0.1	50	[77,156–158,162–168]	Figure B49
612	$\dot{m}''_{c,sub+} = U\frac{\alpha M_{C_3} P_1 \exp\left[-\frac{E_1}{R_u}\left(\frac{1}{T_w} - \frac{1}{T_1}\right)\right]}{\sqrt{2\pi M_{C_3} R_u T_w}}$	0.7	2.8	[1]	[1,169–171]

Appendix B

Gas and Surface Forward Reaction Coefficient Literature Reviews

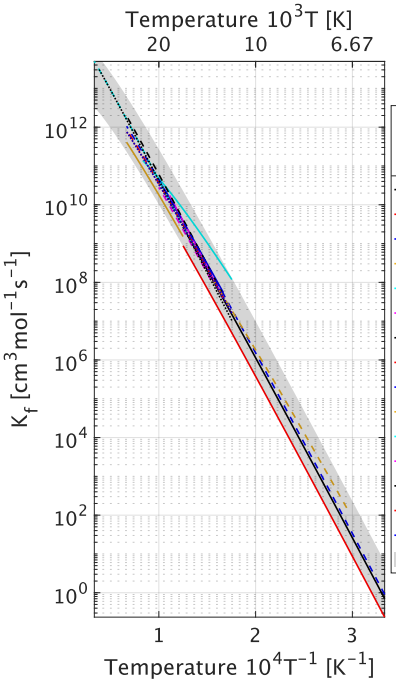

Dissociation
$N_2 + M \leftrightarrow 2N + M$
M = N_2

†¶Wray et al. (1961)	$T_a = T_{tr}^{1.0} T_{ve}^{0.0}$	$k_f = 4.93 \times 10^{21} T_a^{-1.57} e^{-113180/T_a}$
†¶Wray et al. (1961) M = $O_2/NO/Ar$	$T_a = T_{tr}^{1.0} T_{ve}^{0.0}$	$k_f = 1.64 \times 10^{21} T_a^{-1.57} e^{-113180/T_a}$
†Cary (1965)	$T_a = T_{tr}^{1.0} T_{ve}^{0.0}$	$k_f = 2.25 \times 10^{22} T_a^{-1.70} e^{-113210/T_a}$
†Appleton et al (1968)	$T_a = T_{tr}^{1.0} T_{ve}^{0.0}$	$k_f = 3.73 \times 10^{21} T_a^{-1.60} e^{-113200/T_a}$
†Hanson & Baganoff (1972)	$T_a = T_{tr}^{1.0} T_{ve}^{0.0}$	$k_f = 3.90 \times 10^{33} T_a^{-4.50} e^{-113100/T_a}$
†Byron (1966)	$T_a = T_{tr}^{1.0} T_{ve}^{0.0}$	$k_f = 4.80 \times 10^{17} T_a^{-0.50} e^{-113200/T_a}$
§Bortner (1969)	$T_a = T_{tr}^{1.0} T_{ve}^{0.0}$	$k_f = 5.00 \times 10^{18} T_a^{-0.75} e^{-113200/T_a}$
§Dunn & Lordi (1970)	$T_a = T_{tr}^{1.0} T_{ve}^{0.0}$	$k_f = 3.00 \times 10^{21} T_a^{-1.50} e^{-113200/T_a}$
§Baulch (1973)	$T_a = T_{tr}^{1.0} T_{ve}^{0.0}$	$k_f = 3.70 \times 10^{21} T_a^{-1.50} e^{-113260/T_a}$
†Thielen & Roth (1986) $k_{N_2} = 2.5 k_{Ar}$	$T_a = T_{tr}^{1.0} T_{ve}^{0.0}$	$k_f = 2.57 \times 10^{28} T_a^{-3.33} e^{-113220/T_a}$
‡Bender (2016)	$T_a = T_{tr}^{1.0} T_{ve}^{0.0}$	$k_f = 2.71 \times 10^{18} T_a^{-0.68} e^{-117000/T_a}$
‡Bender (2016) $M = O_2$	$T_a = T_{tr}^{1.0} T_{ve}^{0.0}$	$k_f = 1.02 \times 10^{23} T_a^{-1.87} e^{-117000/T_a}$
‡Grover (2019)	$T_a = T_{tr}^{1.0} T_{ve}^{0.0}$	$k_f = 1.87 \times 10^{17} T_a^{-0.43} e^{-113370/T_a}$
§Park (1988)	$T_a = T_{tr}^{0.5} T_{ve}^{0.5}$	$k_f = 7.00 \times 10^{21} T_a^{-1.60} e^{-113200/T_a}$
*§West & Johnston (2023)	$T_a = T_{tr}^{0.7} T_{ve}^{0.3}$	$k_f = 7.00 \times 10^{21} T_a^{-1.60} e^{-113200/T_a}$
Baseline Uncertainty Multiplier Bounds:	[0.3, 8]	

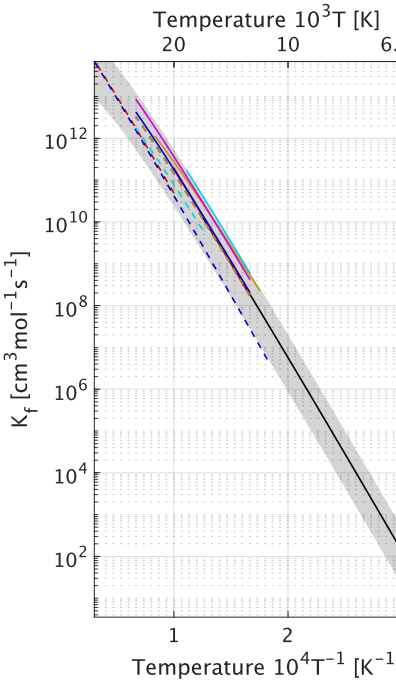

Dissociation
$N_2 + M \leftrightarrow 2N + M$
M = N

†¶Wray (1961)	$T_a = T_{tr}^{1.0} T_{ve}^{0.0}$	$k_f = 2.46 \times 10^{22} T_a^{-1.57} e^{-113180/T_a}$
†Cary (1965)	$T_a = T_{tr}^{1.0} T_{ve}^{0.0}$	$k_f = 1.63 \times 10^{20} T_a^{-1.00} e^{-113310/T_a}$
§Dunn & Lordi (1970)	$T_a = T_{tr}^{1.0} T_{ve}^{0.0}$	$k_f = 1.50 \times 10^{22} T_a^{-1.50} e^{-113260/T_a}$
†Hanson & Baganoff (1972)	$T_a = T_{tr}^{1.0} T_{ve}^{0.0}$	$k_f = 2.20 \times 10^{26} T_a^{-2.50} e^{-113000/T_a}$
†Byron (1966)	$T_a = T_{tr}^{1.0} T_{ve}^{0.0}$	$k_f = 4.30 \times 10^{22} T_a^{-1.50} e^{-113200/T_a}$
§Bortner (1969)	$T_a = T_{tr}^{1.0} T_{ve}^{0.0}$	$k_f = 3.01 \times 10^{22} T_a^{-1.50} e^{-113200/T_a}$
§Park (1988)	$T_a = T_{tr}^{0.5} T_{ve}^{0.5}$	$k_f = 3.01 \times 10^{22} T_a^{-1.60} e^{-113200/T_a}$
‡Bender (2016)	$T_a = T_{tr}^{1.0} T_{ve}^{0.0}$	$k_f = 4.05 \times 10^{17} T_a^{-0.50} e^{-113200/T_a}$
‡Grover (2019)	$T_a = T_{tr}^{1.0} T_{ve}^{0.0}$	$k_f = 1.87 \times 10^{17} T_a^{-0.43} e^{-113370/T_a}$
§West & Johnston (2023)	$T_a = T_{tr}^{0.7} T_{ve}^{0.3}$	$k_f = 3.01 \times 10^{22} T_a^{-1.60} e^{-113200/T_a}$
*†Appleton et al (1968)	$T_a = T_{tr}^{1.0} T_{ve}^{0.0}$	$k_f = 1.62 \times 10^{22} T_a^{-1.60} e^{-113200/T_a}$
Baseline Uncertainty Multiplier Bounds:	[0.3, 7]	

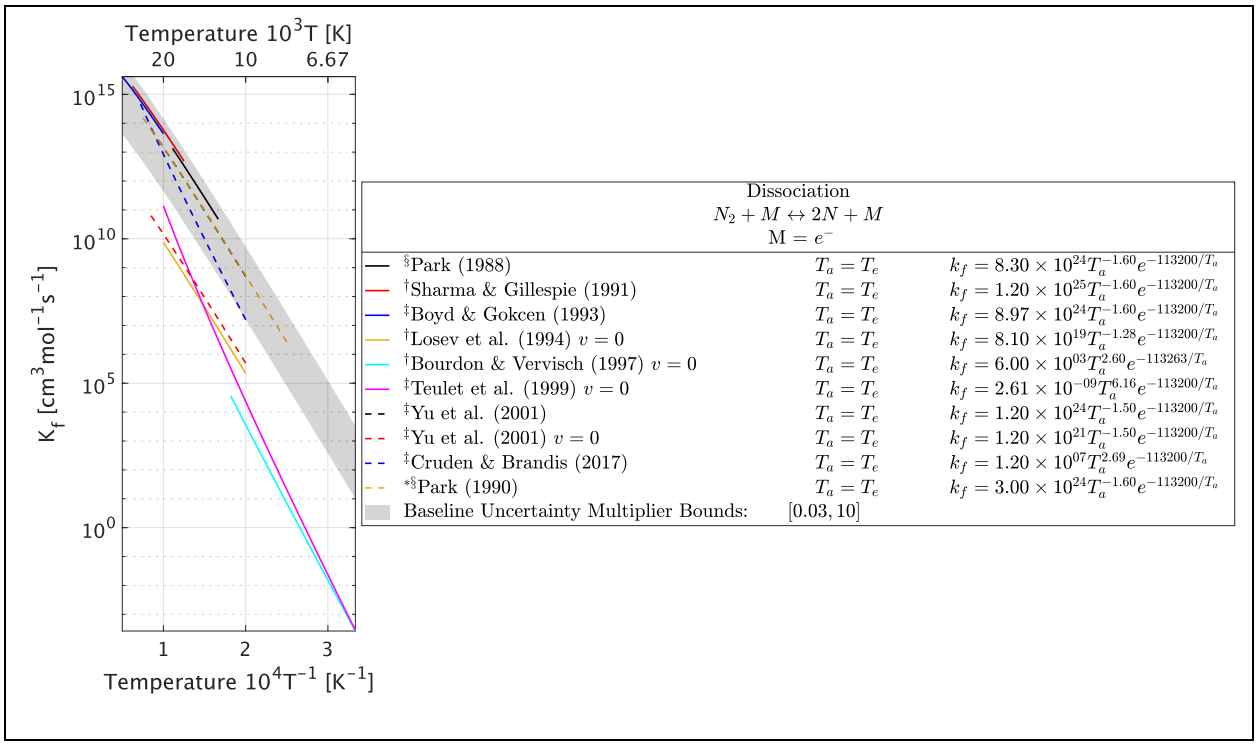

Figure B1: N_2 + M ⇌ 2N + M dissociation literature review.
(†Experiment, §Meta-study, ‡Numerical/Theory, ¶Converted reverse reaction, *Baseline)
[1,47,48,54,89,120–123,128,141,145,169–171,178,192–194,229,277–291]

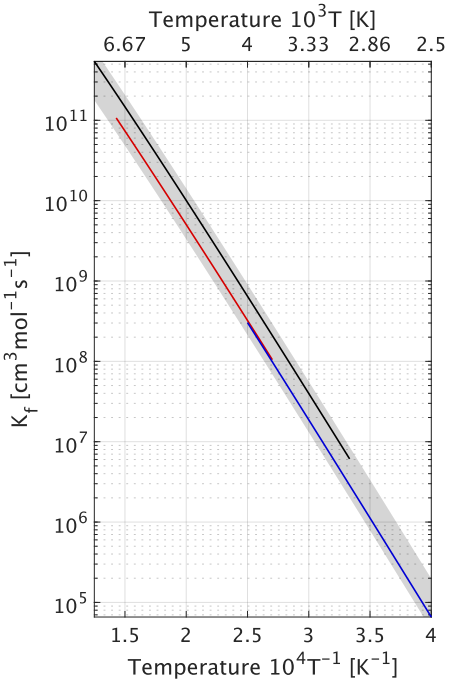

Dissociation $O_2 + M \leftrightarrow O + M$ M = N_2		
†Wray & Teare (1962)	$T_a = T_{tr}^{1.0} T_{ve}^{0.0}$	$k_f = 7.24 \times 10^{18} T_a^{-1.00} e^{-59383/T_a}$
†Generalov & Losev (1966)	$T_a = T_{tr}^{1.0} T_{ve}^{0.0}$	$k_f = 3.62 \times 10^{18} T_a^{-1.00} e^{-59383/T_a}$
*†Jerig et al. (1991)	$T_a = T_{tr}^{1.0} T_{ve}^{0.0}$	$k_f = 3.40 \times 10^{18} T_a^{-1.00} e^{-59380/T_a}$
Baseline Uncertainty Multiplier Bounds:	$[0.7, 3]$	

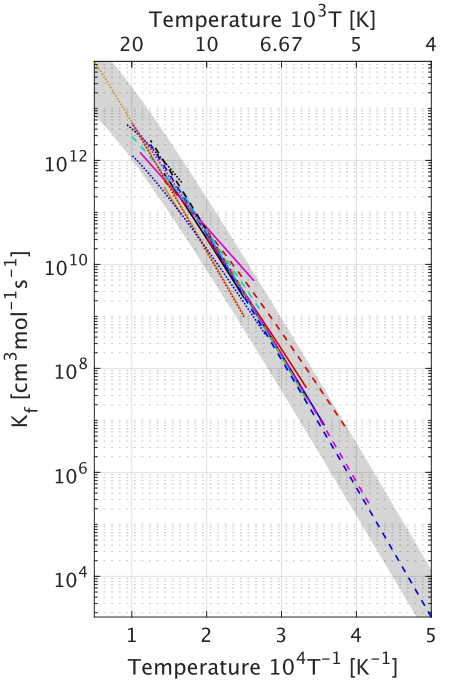

Dissociation $O_2 + M \leftrightarrow O + M$ M = O_2		
†Eckerman (1958)	$T_a = T_{tr}^{1.0} T_{ve}^{0.0}$	$k_f = 1.61 \times 10^{21} T_a^{-1.50} e^{-59396/T_a}$
†Mathews (1959)	$T_a = T_{tr}^{1.0} T_{ve}^{0.0}$	$k_f = 1.13 \times 10^{25} T_a^{-2.54} e^{-59380/T_a}$
†Byron (1959)	$T_a = T_{tr}^{1.0} T_{ve}^{0.0}$	$k_f = 1.92 \times 10^{21} T_a^{-1.50} e^{-59350/T_a}$
†Camac & Vaughan (1961)	$T_a = T_{tr}^{1.0} T_{ve}^{0.0}$	$k_f = 1.06 \times 10^{19} T_a^{-1.00} e^{-59369/T_a}$
†Rink et al. (1961)	$T_a = T_{tr}^{1.0} T_{ve}^{0.0}$	$k_f = 3.19 \times 10^{19} T_a^{-1.00} e^{-59578/T_a}$
†Schexnayder & Evans (1961)	$T_a = T_{tr}^{1.0} T_{ve}^{0.0}$	$k_f = 9.08 \times 10^{13} T_a^{0.00} e^{-37378/T_a}$
†Wray & Teare (1962)	$T_a = T_{tr}^{1.0} T_{ve}^{0.0}$	$k_f = 3.26 \times 10^{19} T_a^{-1.00} e^{-59383/T_a}$
†Generalov & Losev (1966)	$T_a = T_{tr}^{1.0} T_{ve}^{0.0}$	$k_f = 5.72 \times 10^{28} T_a^{-3.50} e^{-59383/T_a}$
§Johnston (1968)	$T_a = T_{tr}^{1.0} T_{ve}^{0.0}$	$k_f = 2.75 \times 10^{19} T_a^{-1.00} e^{-59500/T_a}$
§Bortner (1969)	$T_a = T_{tr}^{1.0} T_{ve}^{0.0}$	$k_f = 8.30 \times 10^{18} T_a^{-0.83} e^{-59500/T_a}$
†Shatalov (1973)	$T_a = T_{tr}^{1.0} T_{ve}^{0.0}$	$k_f = 1.09 \times 10^{25} T_a^{-2.50} e^{-59369/T_a}$
†Jerig et al. (1991)	$T_a = T_{tr}^{1.0} T_{ve}^{0.0}$	$k_f = 3.40 \times 10^{19} T_a^{-1.00} e^{-59380/T_a}$
‡Ibraguimova et al. (2013)	$T_a = T_{tr}^{0.5} T_{ve}^{0.5}$	$k_f = 3.87 \times 10^{27} T_a^{-3.10} e^{-59380/T_a}$
‡Chaudhry et al. (2018)	$T_a = T_{tr}^{1.0} T_{ve}^{0.0}$	$k_f = 5.58 \times 10^{16} T_a^{-0.36} e^{-59500/T_a}$
§Kim & Park (2018)	$T_a = T_{tr}^{0.5} T_{ve}^{0.5}$	$k_f = 1.12 \times 10^{25} T_a^{-2.59} e^{-59500/T_a}$
‡Grover et al. (2019)	$T_a = T_{tr}^{1.0} T_{ve}^{0.0}$	$k_f = 8.21 \times 10^{16} T_a^{-0.40} e^{-59383/T_a}$
§Park (1988)	$T_a = T_{tr}^{0.5} T_{ve}^{0.5}$	$k_f = 2.00 \times 10^{21} T_a^{-1.50} e^{-59500/T_a}$
*§West et al. (2023)	$T_a = T_{tr}^{0.7} T_{ve}^{0.3}$	$k_f = 2.00 \times 10^{21} T_a^{-1.50} e^{-59500/T_a}$
Baseline Uncertainty Multiplier Bounds:	$[0.2, 5]$	

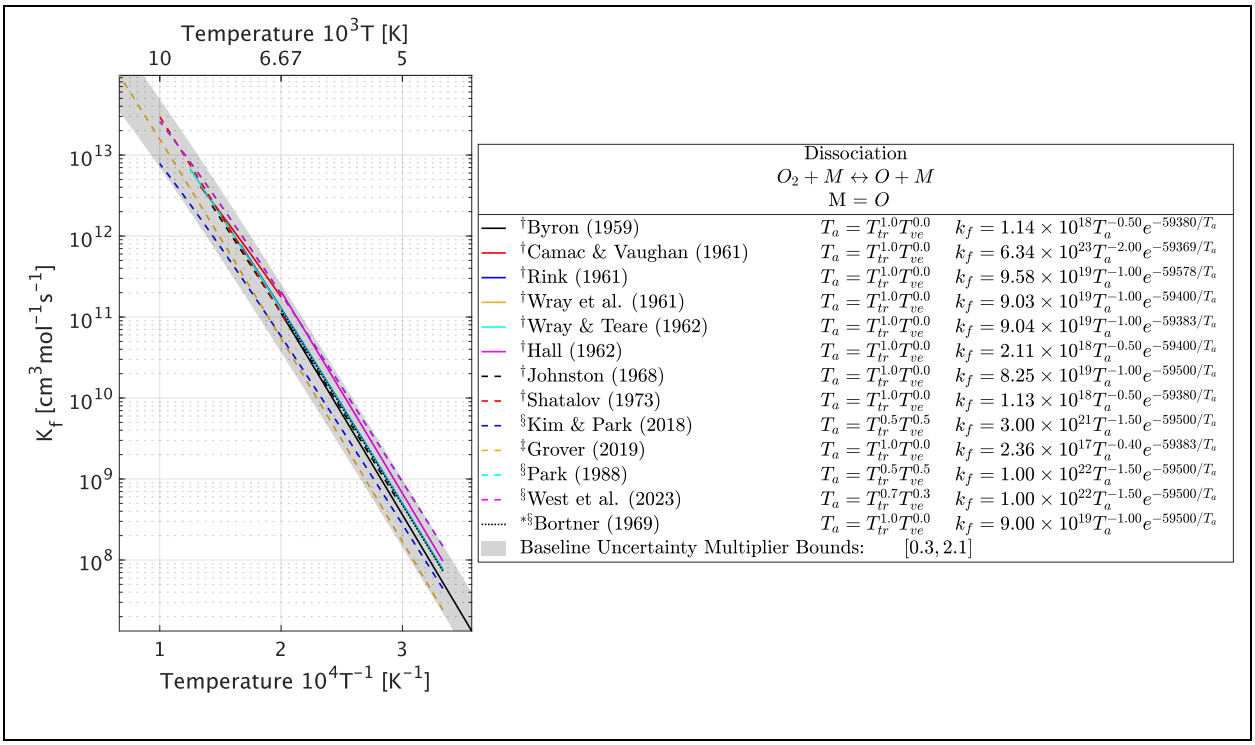

Figure B2: O_2 + M ⇌ 2O + M dissociation literature review.
(†Experiment, §Meta-study, ‡Numerical/Theory, ¶Converted reverse reaction, *Baseline)
[1,54,119,137,182,190,192,194,228,229,278–280,286,292–302,302–304]

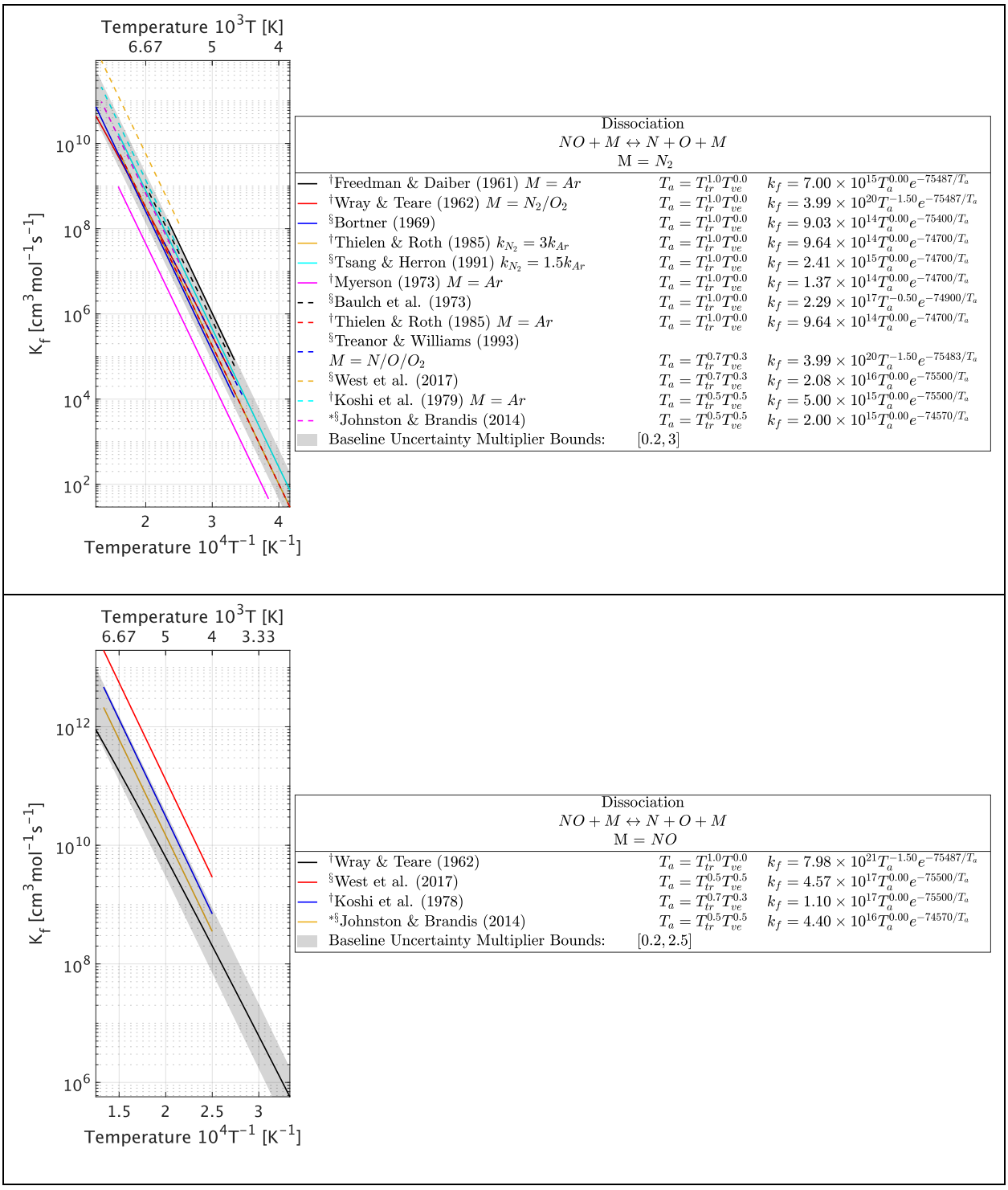

Figure B3: NO + M ⇌ N + O + M dissociation literature review.
(†Experiment, §Meta-study, ‡Numerical/Theory, ¶Converted reverse reaction, *Baseline)
[1,47,54,89,128,137,172,191,192,194,229,277–280,283,305–308]

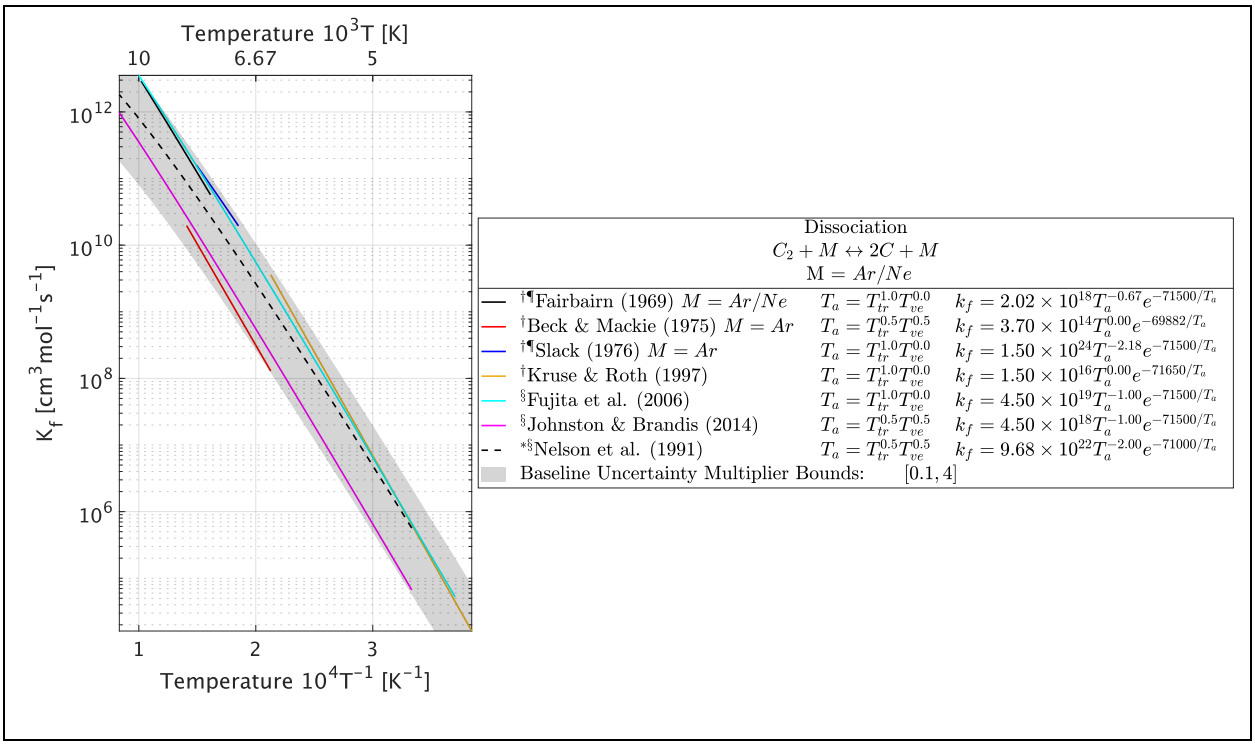

Figure B4: C_2 + M ⇌ 2C + M dissociation literature review.
(†Experiment, §Meta-study, ‡Numerical/Theory, ¶Converted reverse reaction, *Baseline)
[47,54,119,128,137,193,194,200,290,305,309–311]

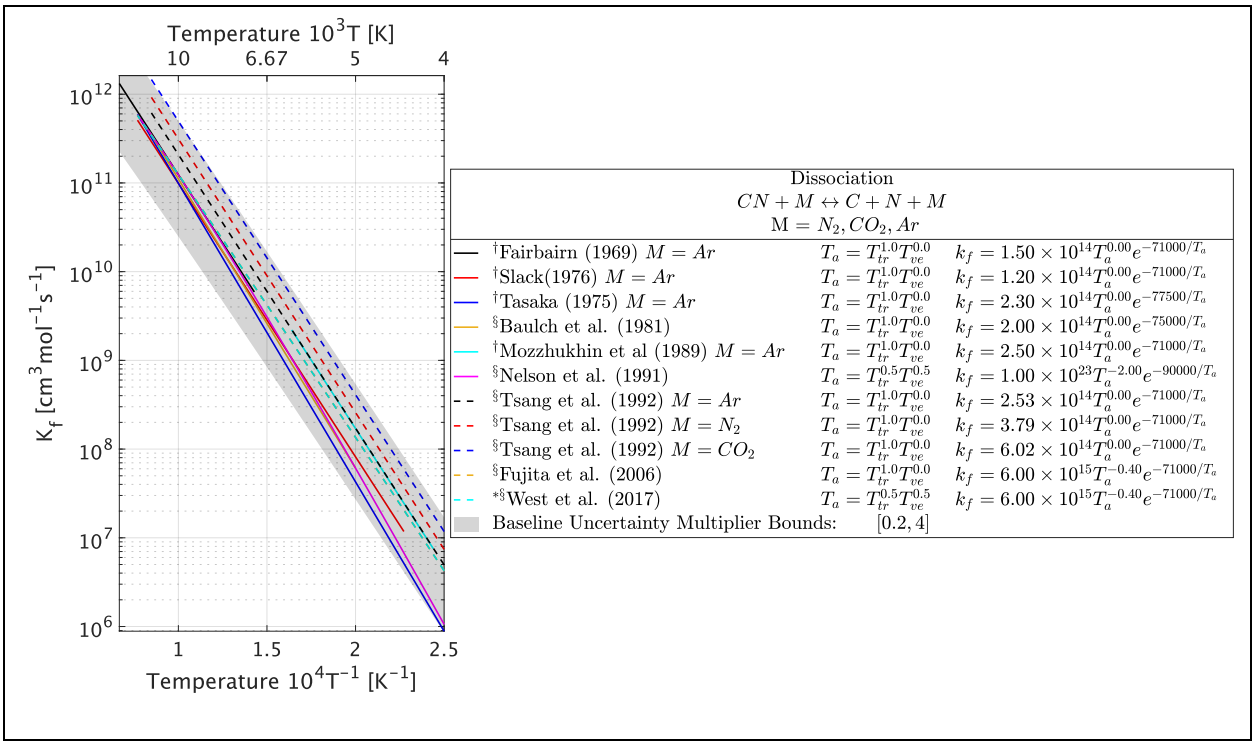

Figure B5: CN + M ⇌ C + N + M dissociation literature review.
(†Experiment, §Meta-study, ‡Numerical/Theory, ¶Converted reverse reaction, *Baseline)
[47,48,54,119,128,134,137,141,193,200,290,305,309,312,313]

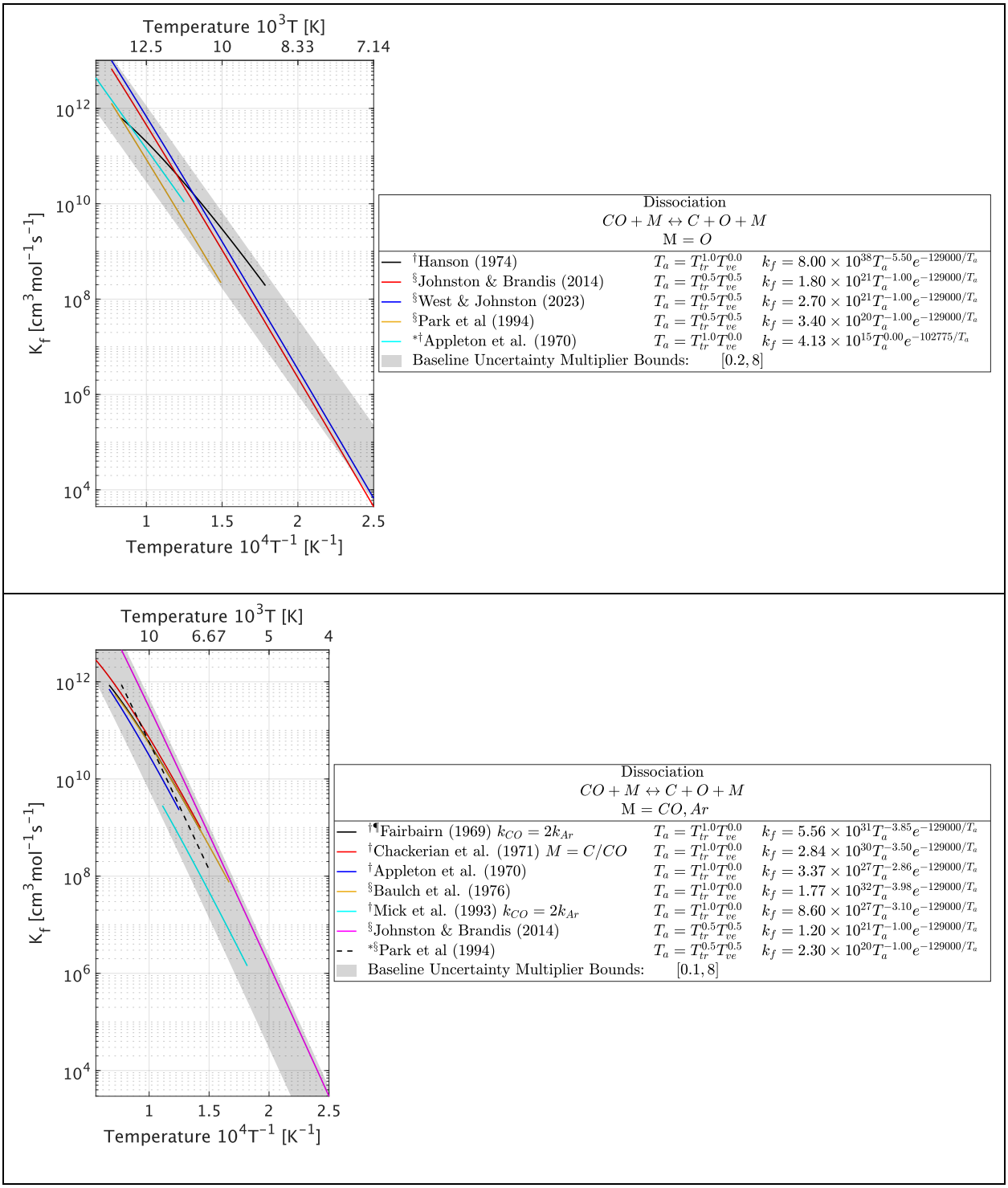

Figure B6: CO + M ⇌ C + O + M dissociation literature review.
(†Experiment, §Meta-study, ‡Numerical/Theory, ¶Converted reverse reaction, *Baseline)
[54,128,137,194,230,305,309,314–317]

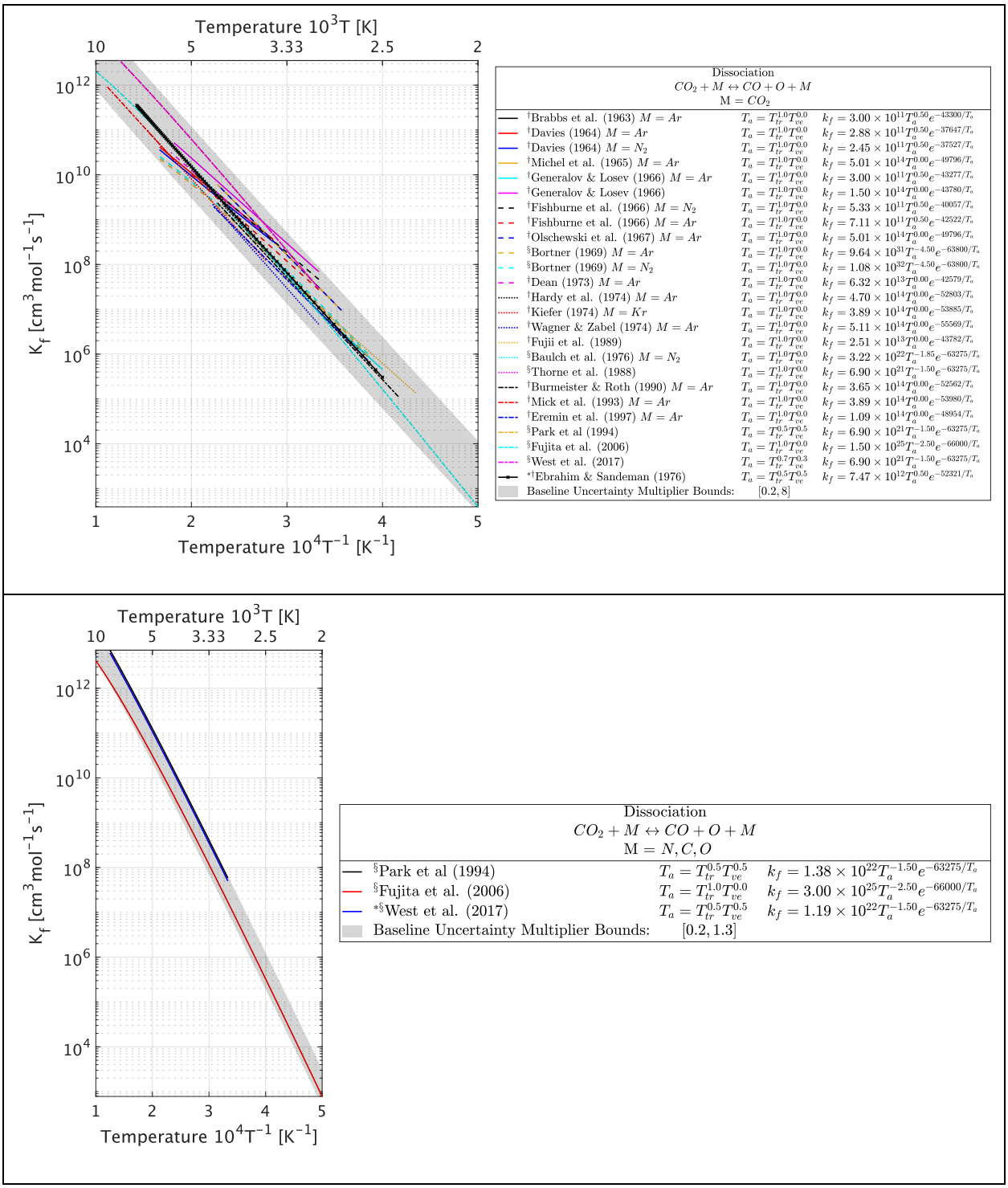

Figure B7: CO_2 + M ⇌ O + CO + M dissociation literature review.
(†Experiment, §Meta-study, ‡Numerical/Theory, ¶Converted reverse reaction, *Baseline)
[47,54,128,137,194–196,229,299,305,314,317–329]

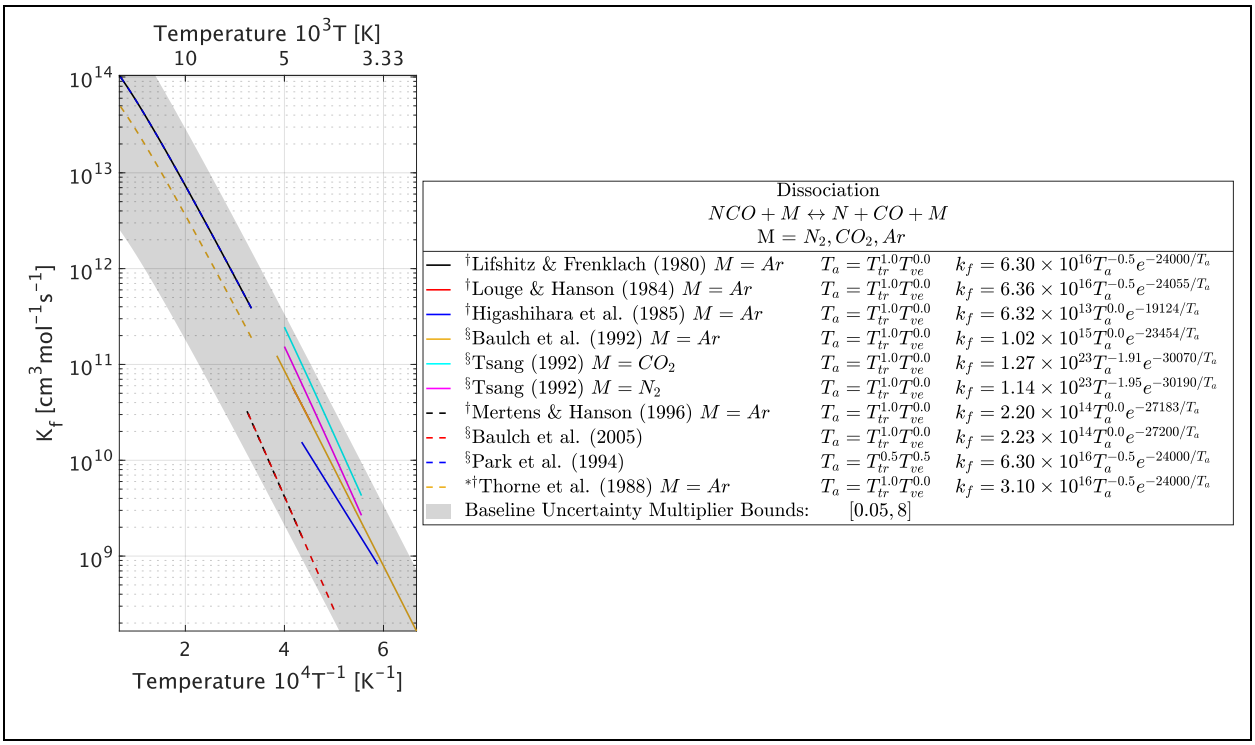

Figure B8: NCO + M ⇌ N + CO + M dissociation literature review.
(†Experiment, §Meta-study, ‡Numerical/Theory, ¶Converted reverse reaction, *Baseline)
[126,127,134,137,196,201,304,330,331]

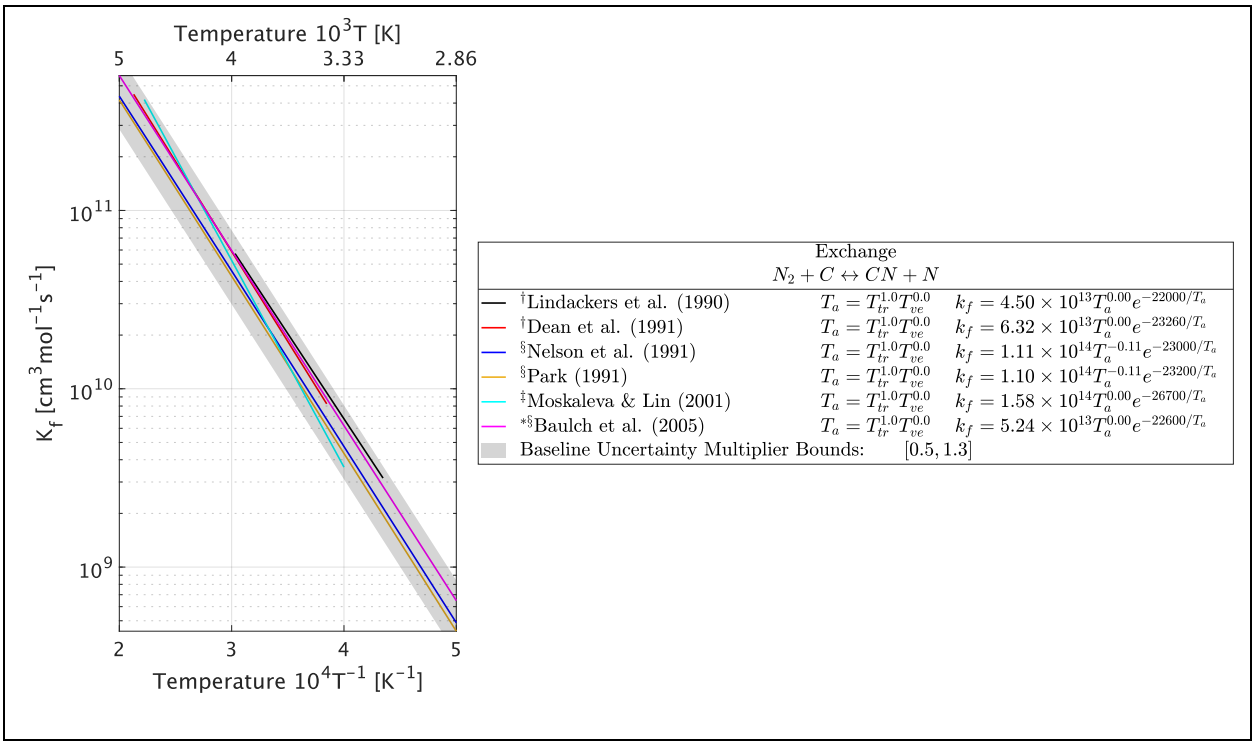

Figure B9: N_2 + C ⇌ CN + N exchange literature review.
(†Experiment, §Meta-study, ‡Numerical/Theory, ¶Converted reverse reaction, *Baseline)
[47,48,54,119,127,128,133,137,141,193,194,203,204,332–334]

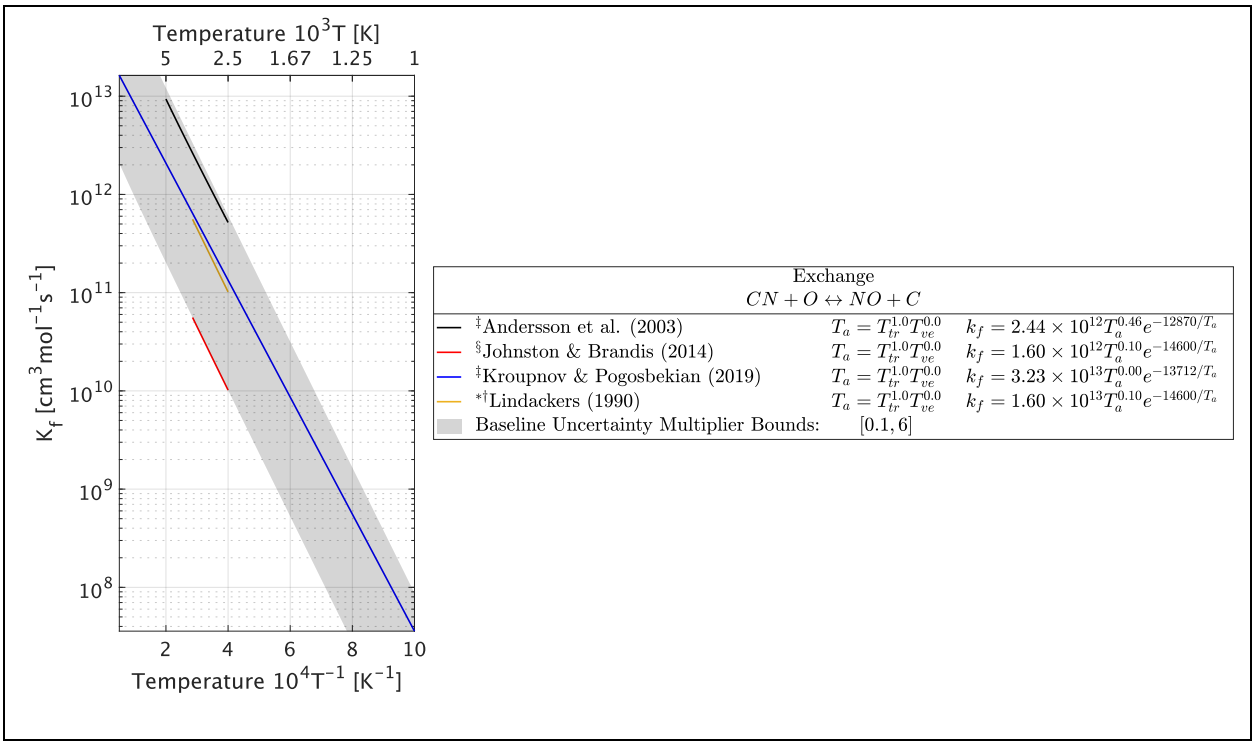

Figure B10: CN + O ⇌ NO + C exchange literature review.
(†Experiment, §Meta-study, ‡Numerical/Theory, ¶Converted reverse reaction, *Baseline)
[47,54,119,128,133,137,194,197,305,335]

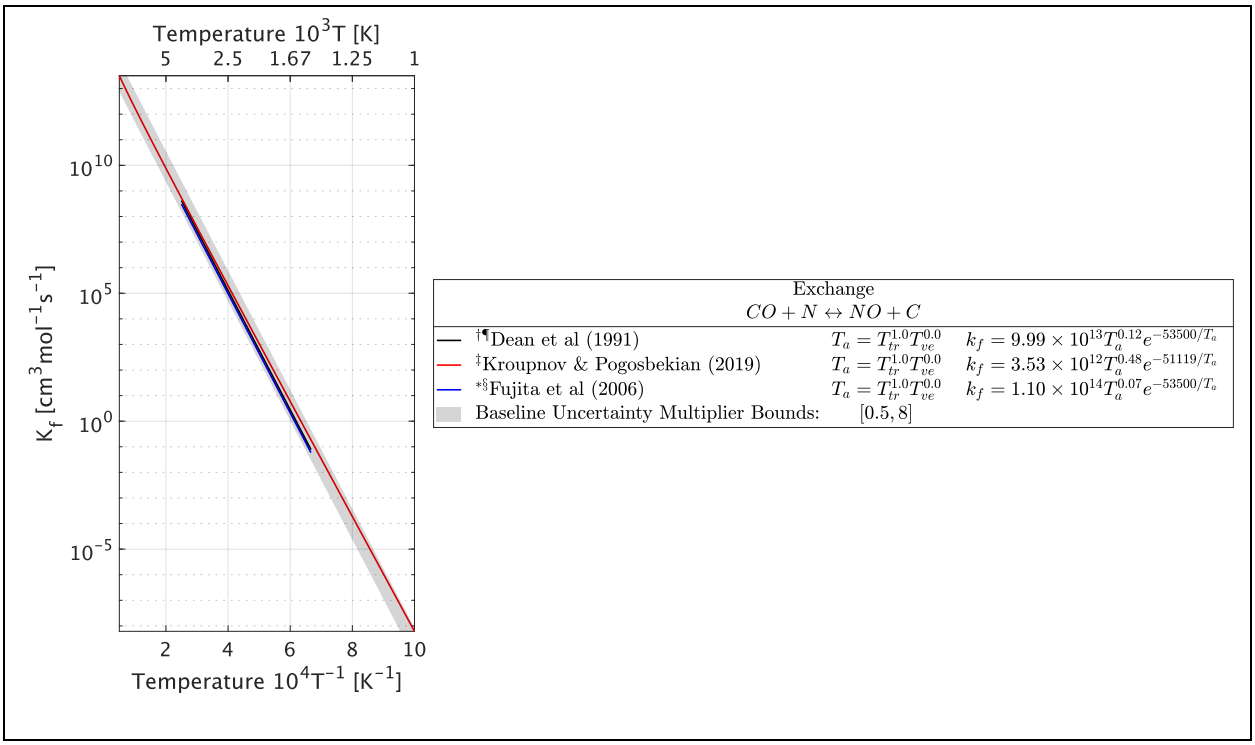

Figure B11: CO + N ⇌ NO + C exchange literature review.
(†Experiment, §Meta-study, ‡Numerical/Theory, ¶Converted reverse reaction, *Baseline)
[47,54,128,194,197,203,333,336]

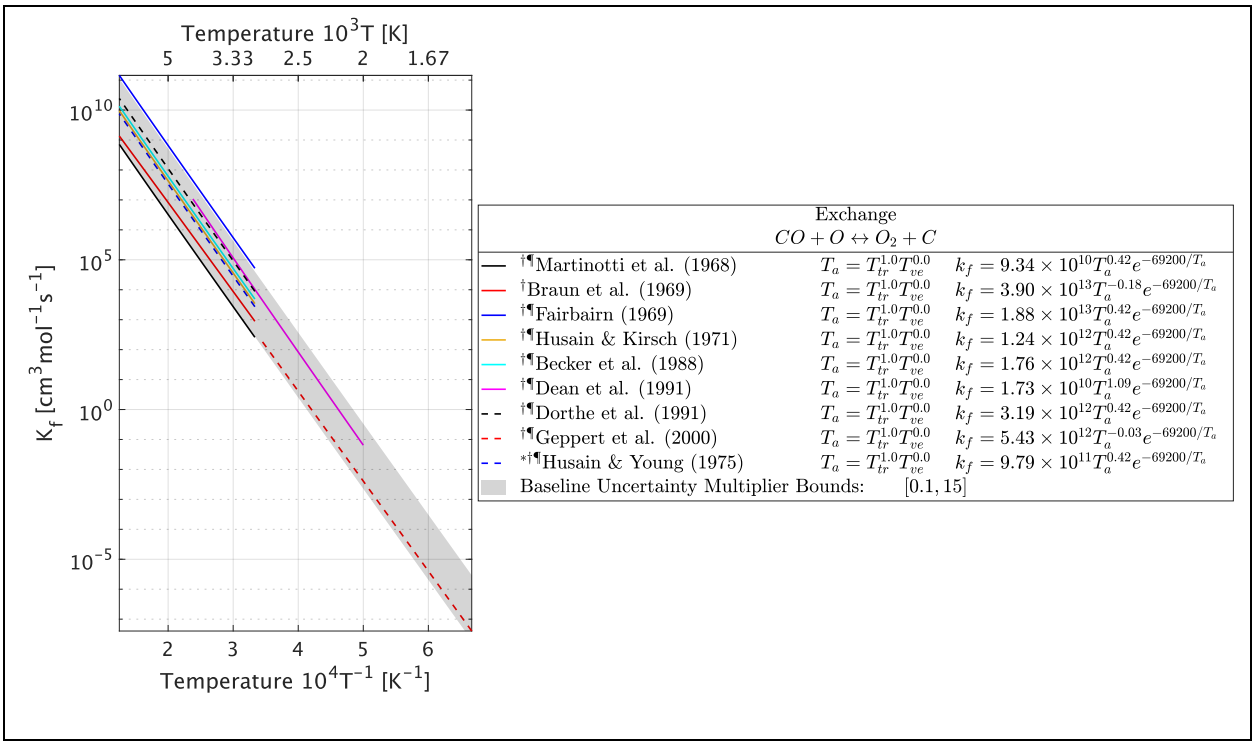

Figure B12: CO + O ⇌ O_2 + C exchange literature review.
(†Experiment, §Meta-study, ‡Numerical/Theory, ¶Converted reverse reaction, *Baseline)
[47,54,137,194,196,198,309,333,336–341]

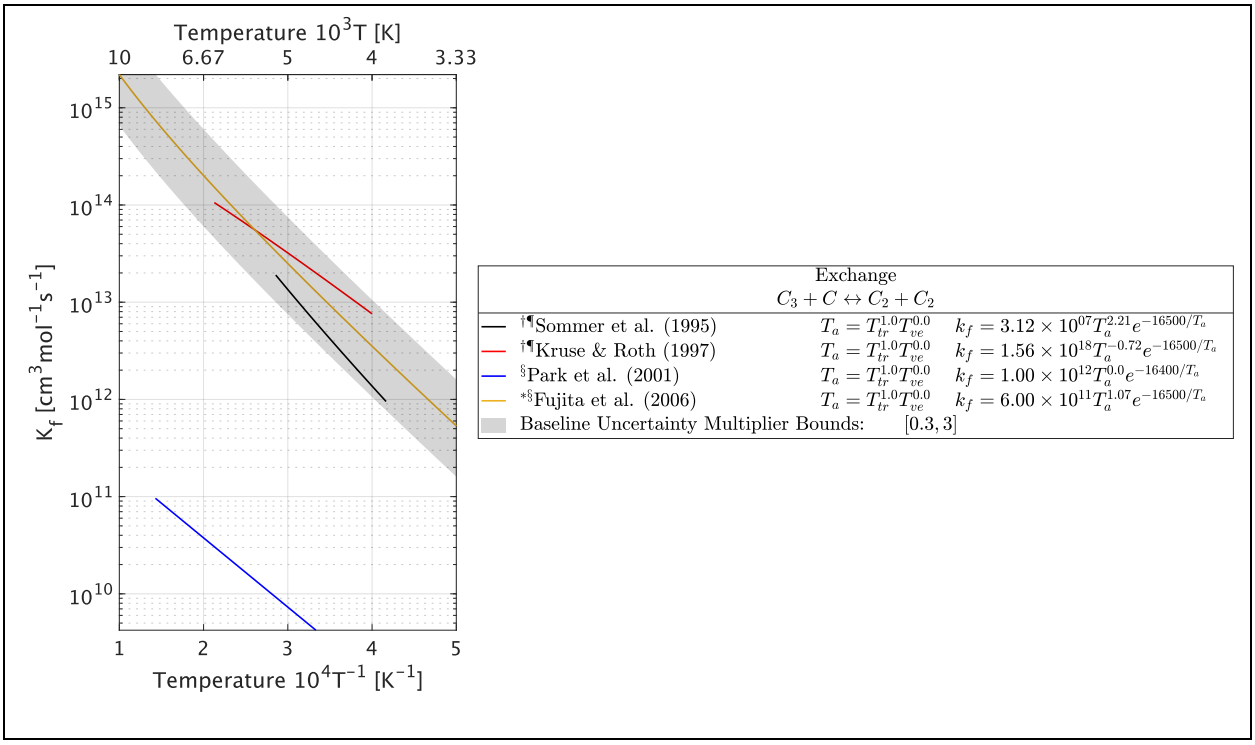

Figure B13: C_3 + C ⇌ C_2 + C_2 exchange literature review.
(†Experiment, §Meta-study, ‡Numerical/Theory, ¶Converted reverse reaction, *Baseline)
[47,48,54,119,128,141,311,332,342]

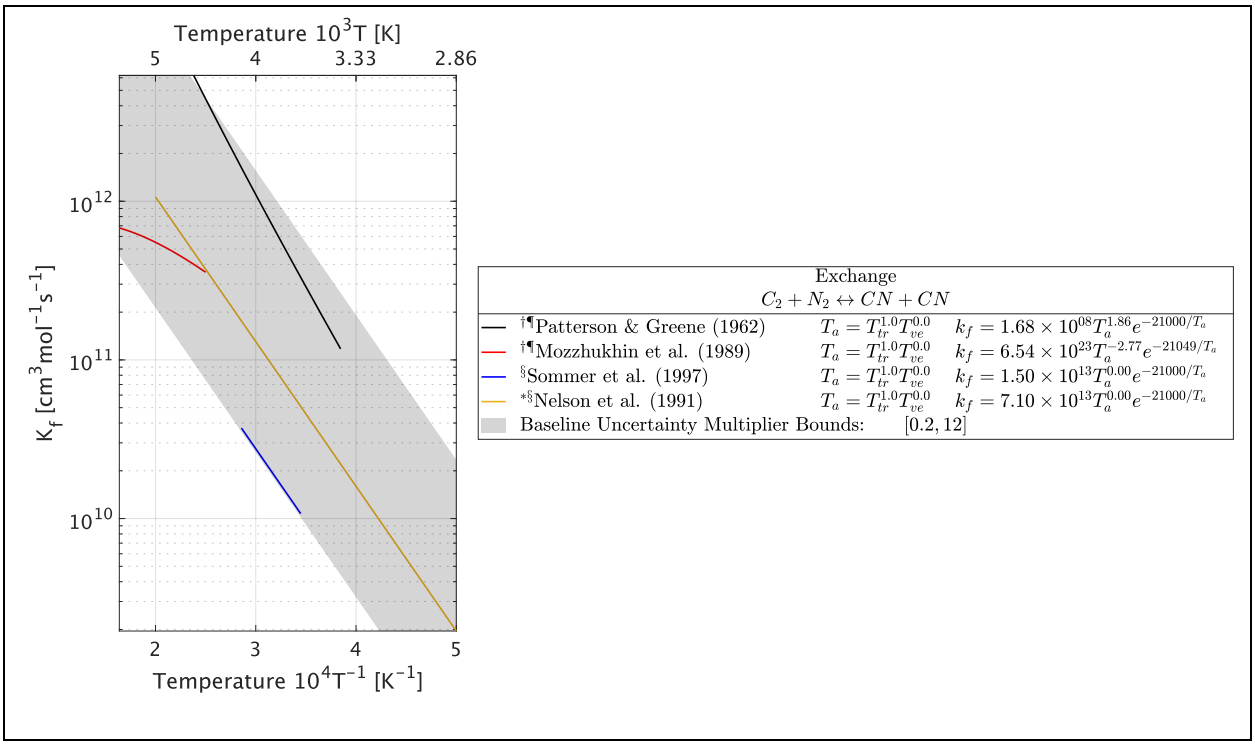

Figure B14: C_2 + N_2 ⇌ CN + CN exchange literature review.
(†Experiment, §Meta-study, ‡Numerical/Theory, ¶Converted reverse reaction, *Baseline)
[47,48,54,128,141,193,194,290,332,343]

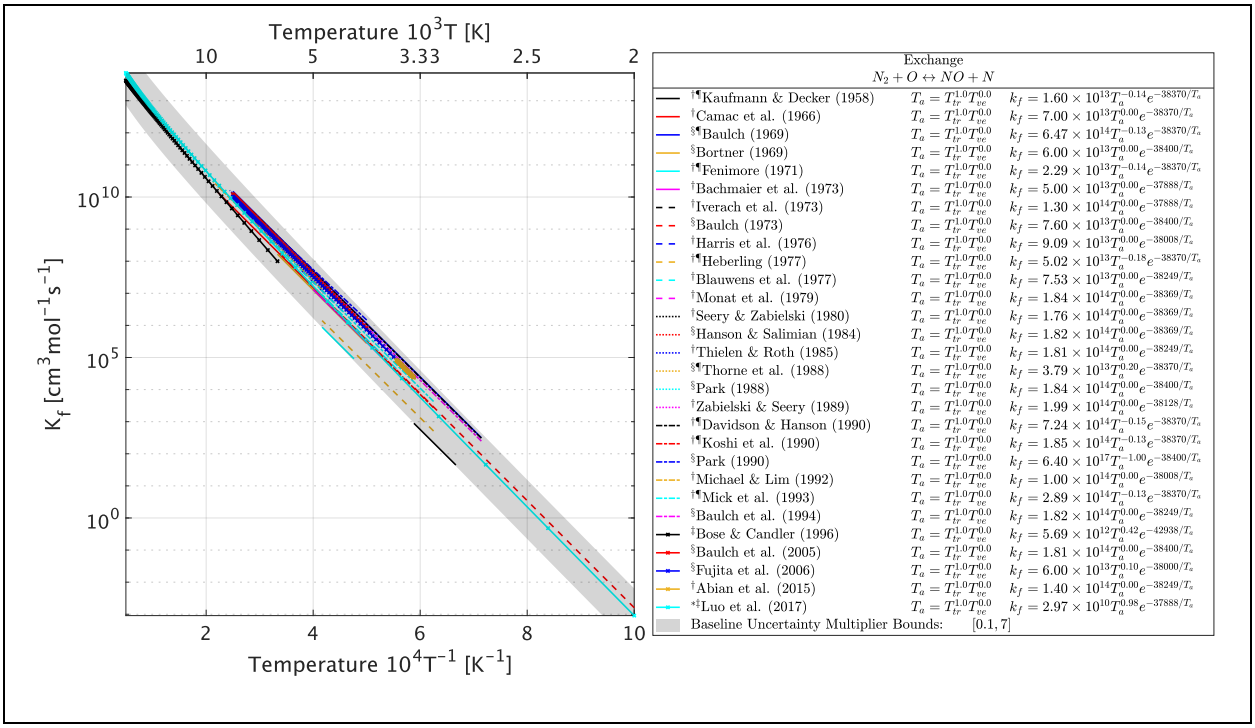

Figure B15: N_2 + O ⇌ NO + N exchange literature review.
(†Experiment, §Meta-study, ‡Numerical/Theory, ¶Converted reverse reaction, *Baseline)
[1,47,54,89,119,127,128,137,190,194,196,199,203,229,277,283,304,314,344–361]

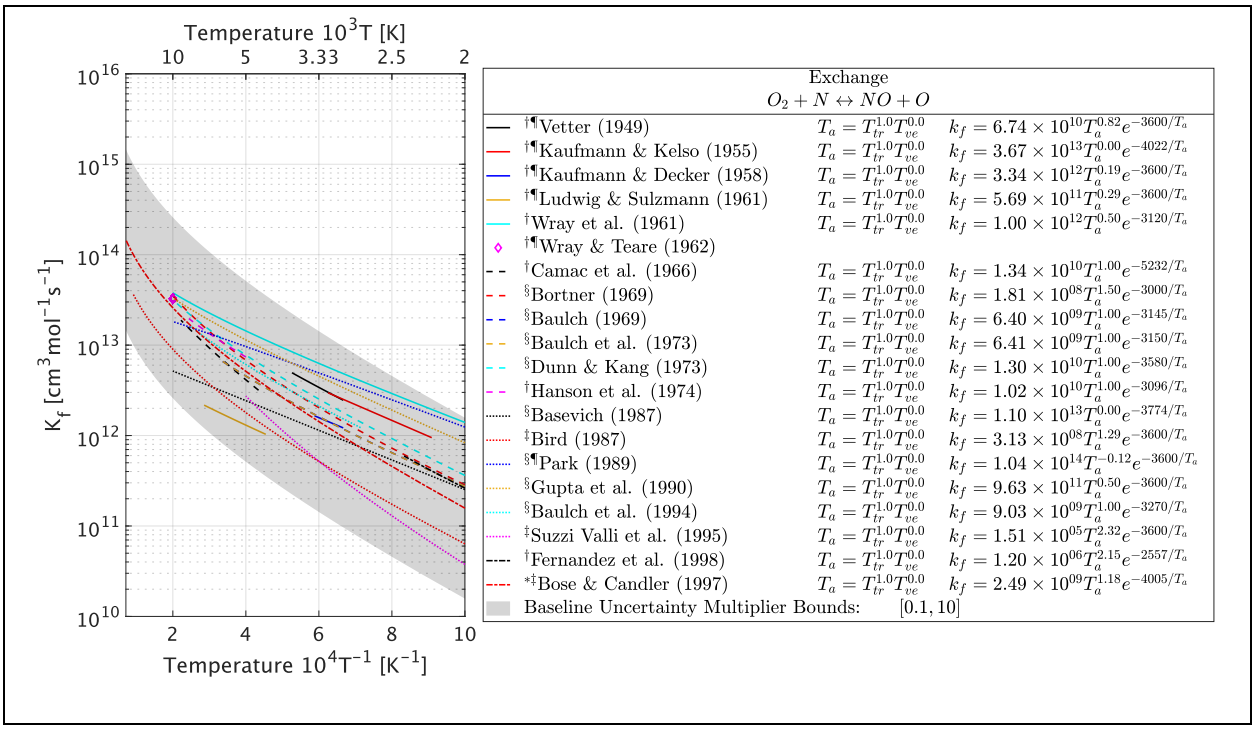

Figure B16: O_2 + N ⇌ NO + N exchange literature review.
(†Experiment, §Meta-study, ‡Numerical/Theory, ¶Converted reverse reaction, *Baseline)
[1,47,54,89,117,118,136,137,148,172,192,194,196,203,209,229,277–279,283,288,289,304,346,347,362–371]

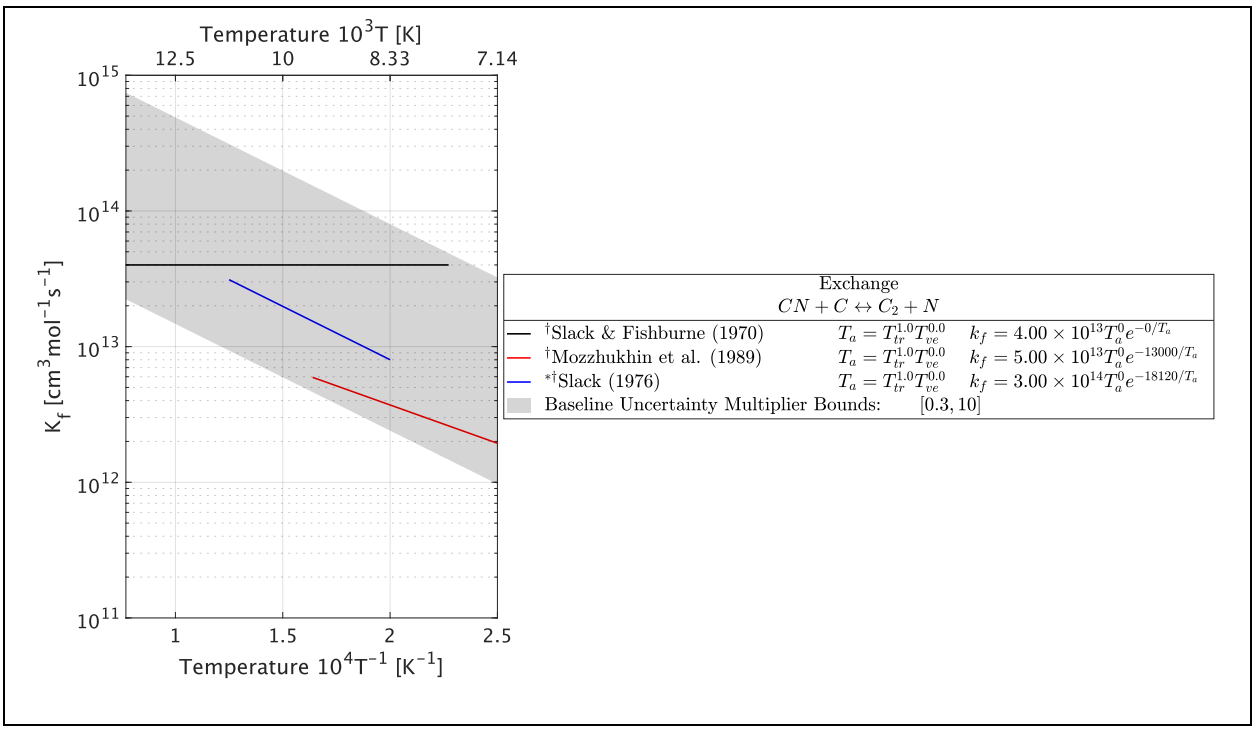

Figure B17: CN + C ⇌ C_2 + N exchange literature review.
(†Experiment, §Meta-study, ‡Numerical/Theory, ¶Converted reverse reaction, *Baseline)
[47,48,54,119,128,133,137,141,194,200,290,305,312,332,372]

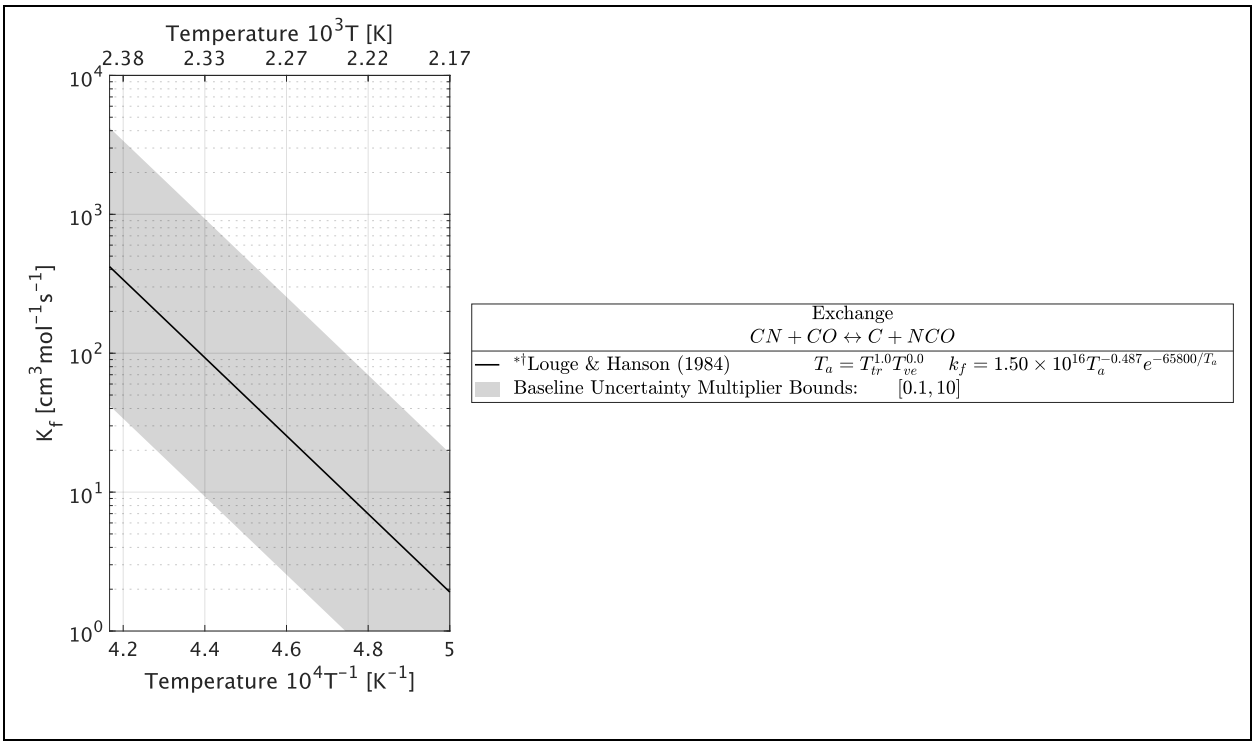

Figure B18: CN + CO ⇌ C + NCO exchange literature review.
(†Experiment, §Meta-study, ‡Numerical/Theory, ¶Converted reverse reaction, *Baseline)
[137,201]

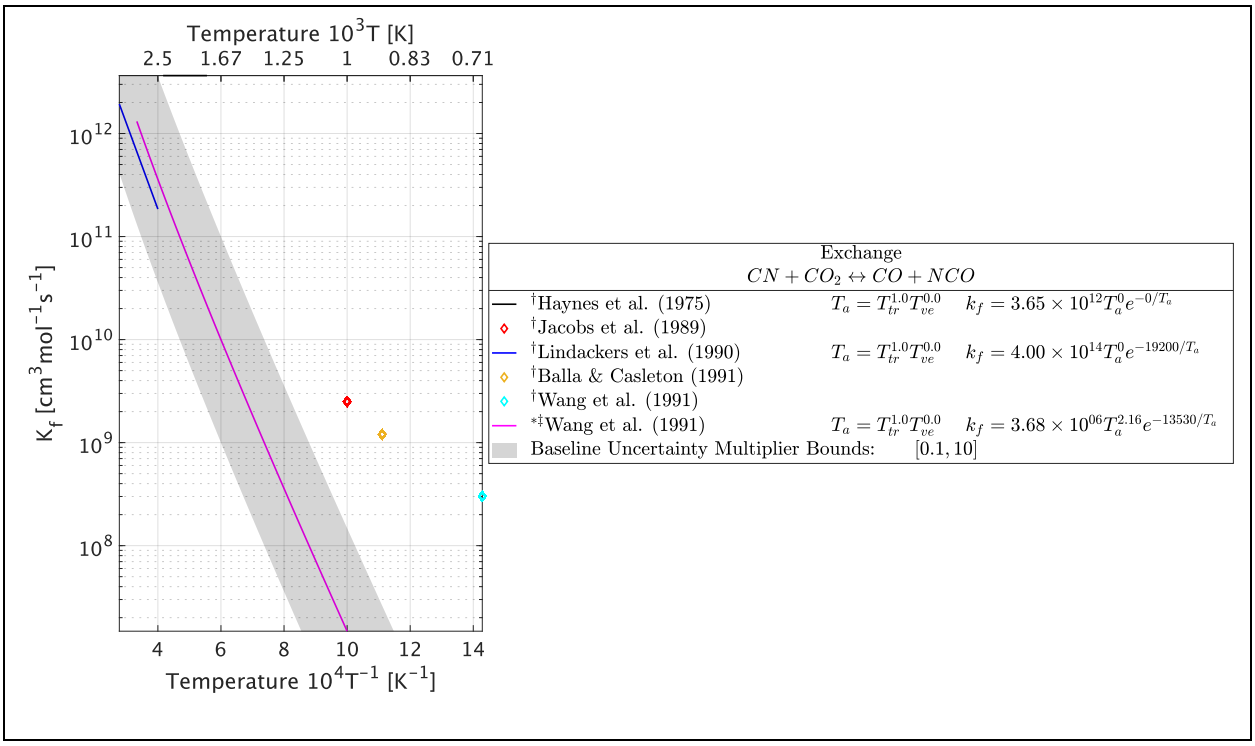

Figure B19: CN + CO_2 ⇌ CO + NCO exchange literature review.
(†Experiment, §Meta-study, ‡Numerical/Theory, ¶Converted reverse reaction, *Baseline)
[129,131–133,137,373]

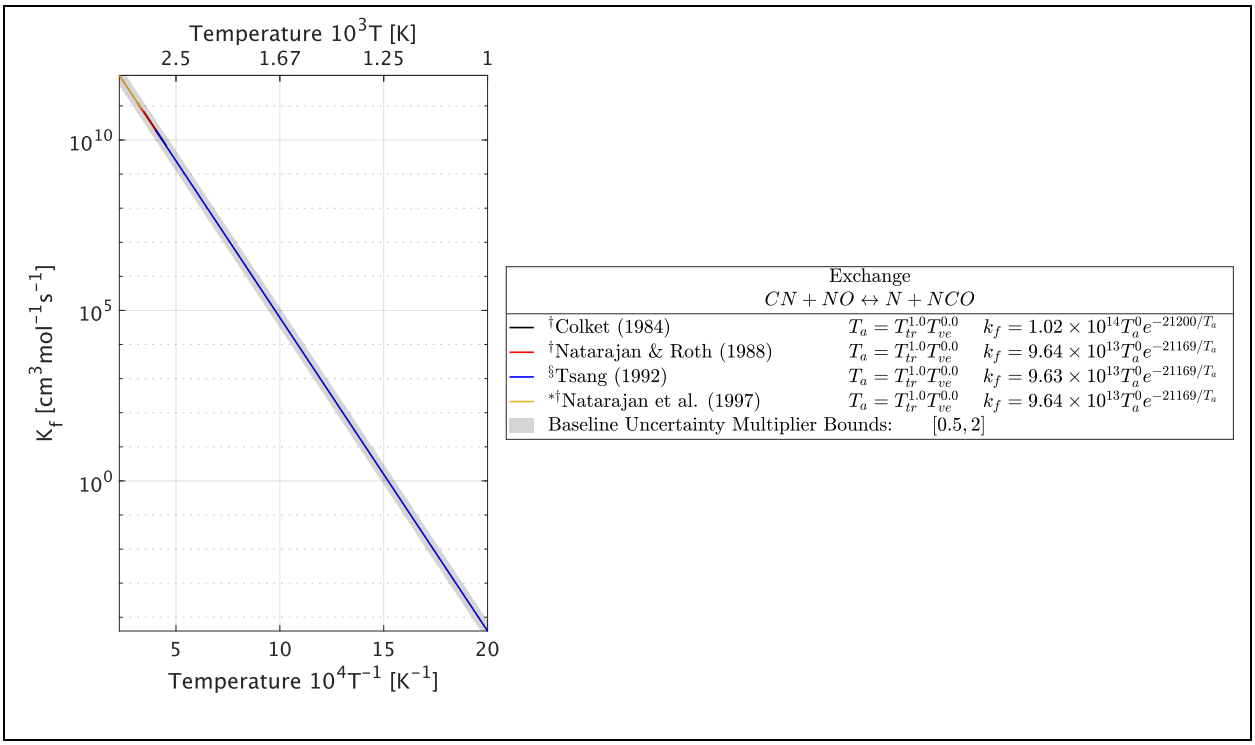

Figure B20: CN + NO ⇌ N + NCO exchange literature review.
(†Experiment, §Meta-study, ‡Numerical/Theory, ¶Converted reverse reaction, *Baseline)
[134,137,202,374,375]

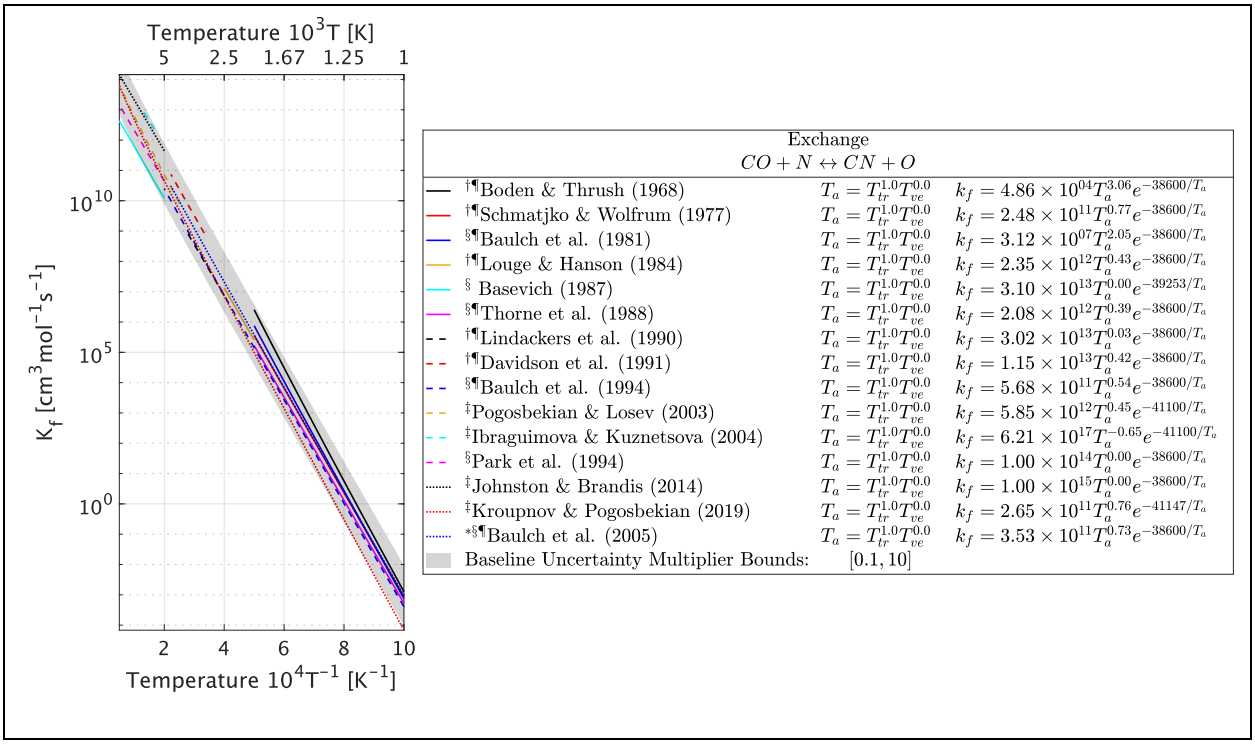

Figure B21: CO + N ⇌ CN + O exchange literature review.
(†Experiment, §Meta-study, ‡Numerical/Theory, ¶Converted reverse reaction, *Baseline)
[47,119,127,128,133,134,137,194,196,197,201,203,224,312,369–371,376–380]

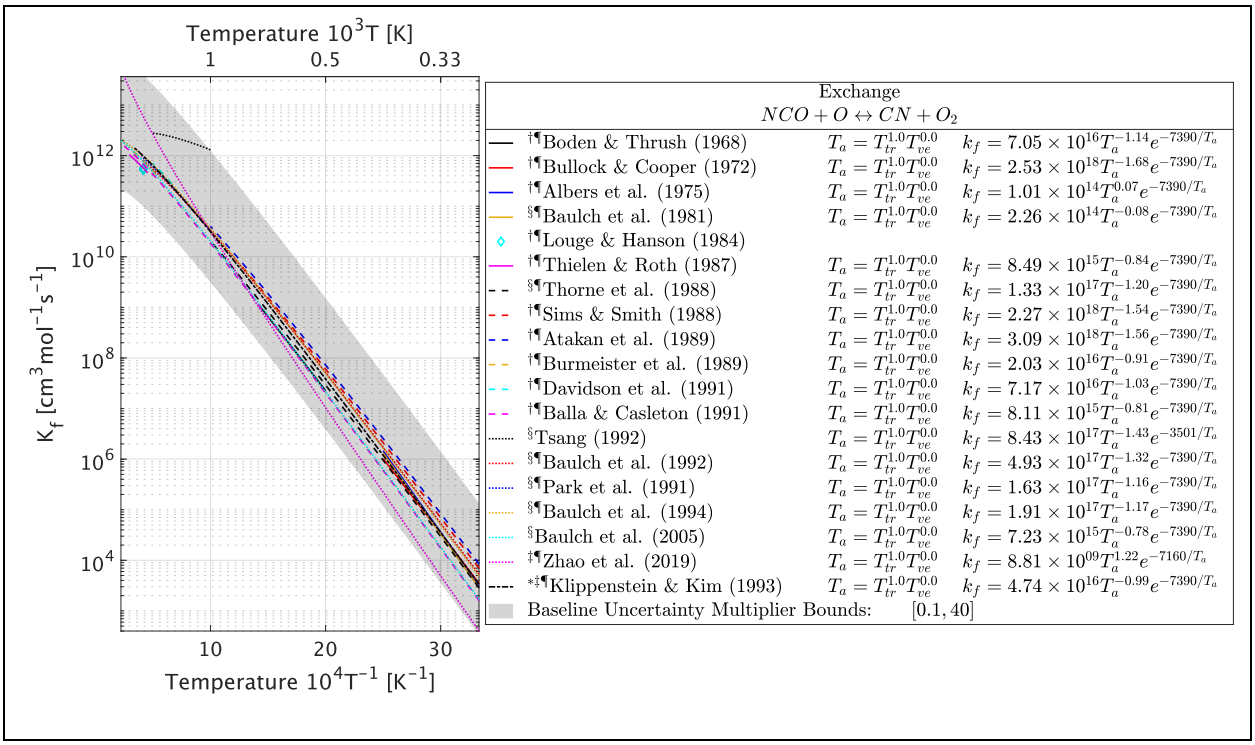

Figure B22: NCO + O ⇌ CN + O_2 exchange literature review.
(†Experiment, §Meta-study, ‡Numerical/Theory, ¶Converted reverse reaction, *Baseline)
[127,131,133–135,137,196,201,203,204,232,312,331,345,369,370,373,376,377,381–384]

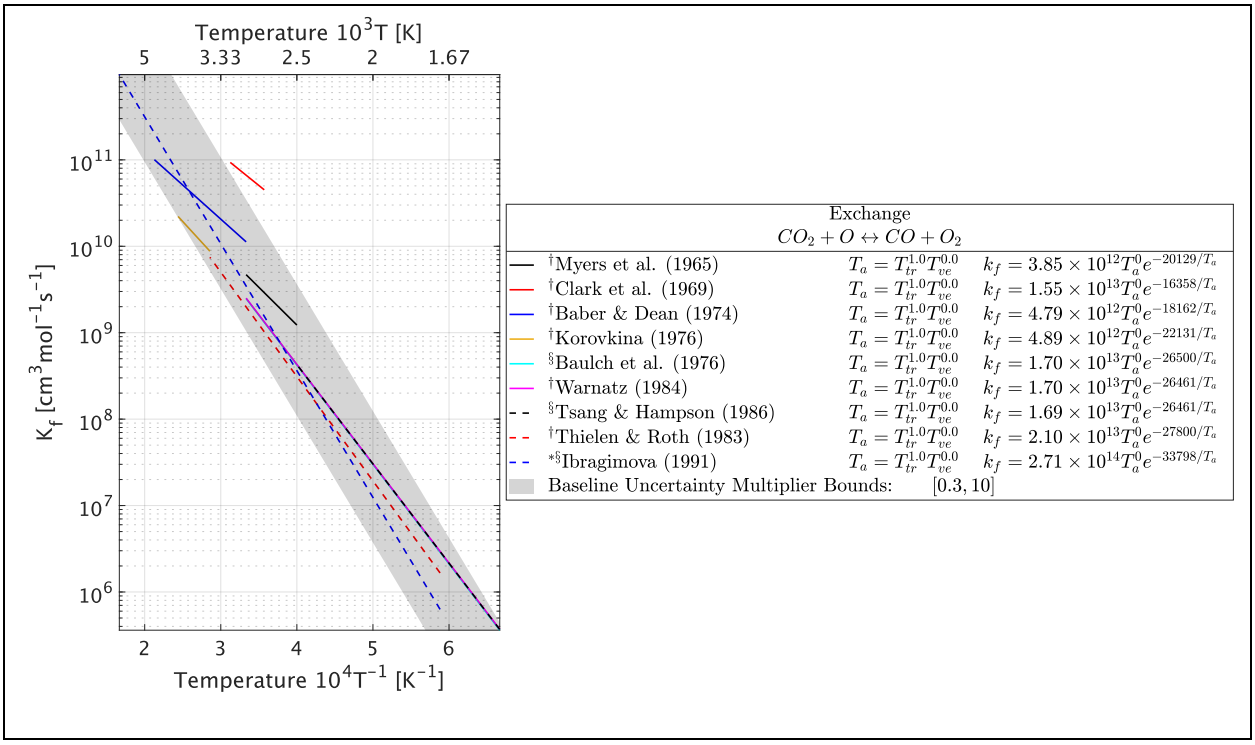

Figure B23: CO_2 + O ⇌ CO + O_2 exchange literature review.
(†Experiment, §Meta-study, ‡Numerical/Theory, ¶Converted reverse reaction, *Baseline)
[47,54,133,137,194,205,317,328,385–392]

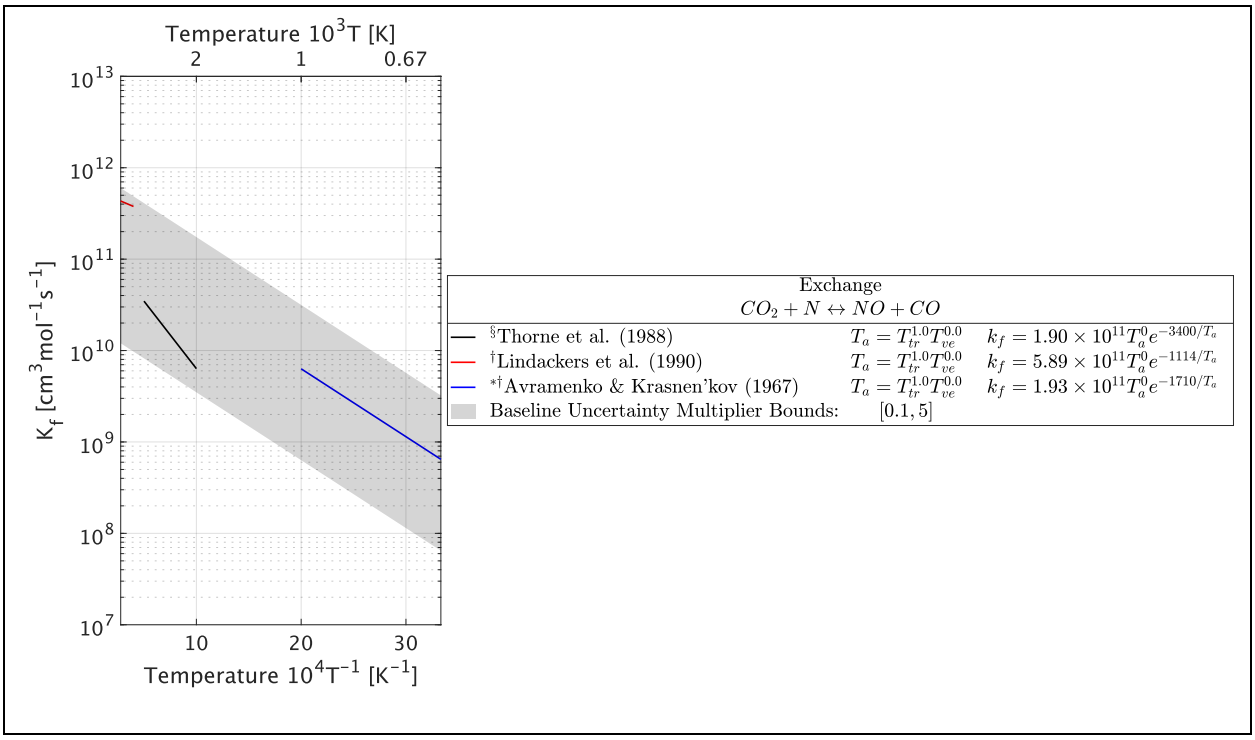

Figure B24: CO_2 + N ⇌ NO + CO exchange literature review.
(†Experiment, §Meta-study, ‡Numerical/Theory, ¶Converted reverse reaction, *Baseline)
[133,196,206,370]

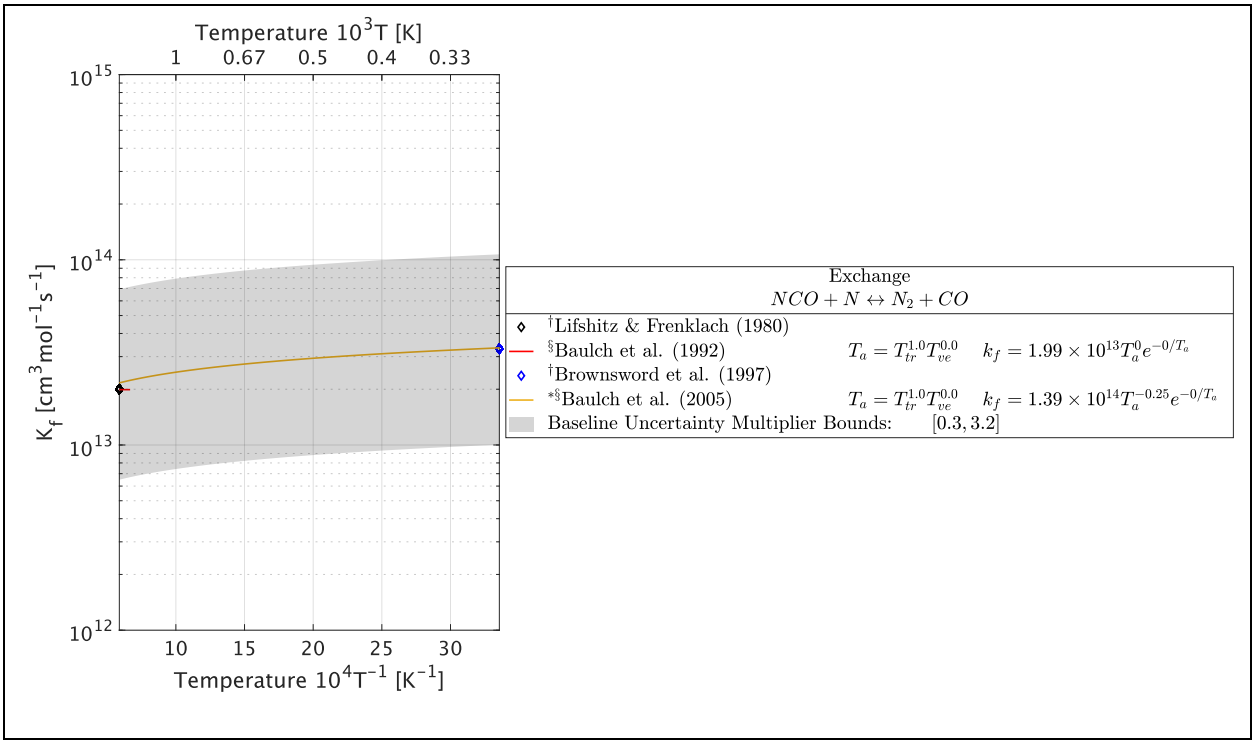

Figure B25: NCO + N ⇌ N_2 + CO exchange literature review.
(†Experiment, §Meta-study, ‡Numerical/Theory, ¶Converted reverse reaction, *Baseline)
[127,196,304,331,369,393]

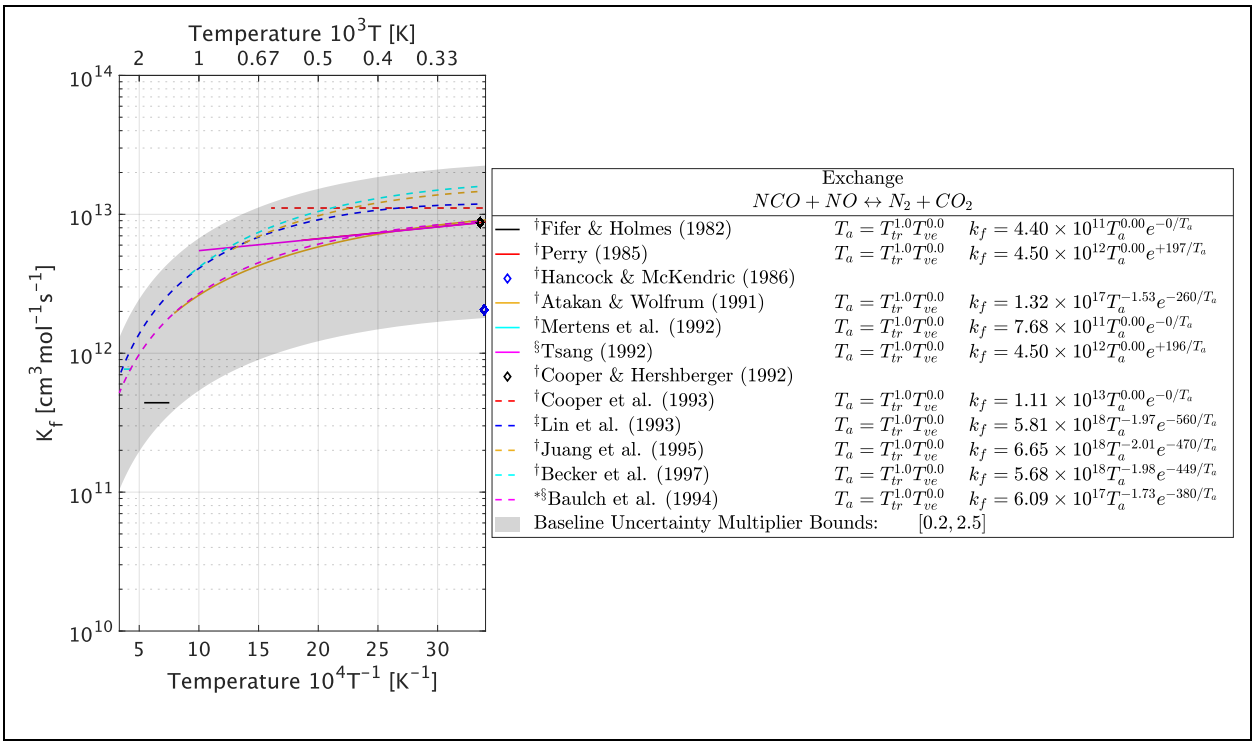

Figure B26: NCO + NO ⇌ N_2 + CO_2 exchange literature review.
(†Experiment, §Meta-study, ‡Numerical/Theory, ¶Converted reverse reaction, *Baseline)
[127,134,203,207,394–401]

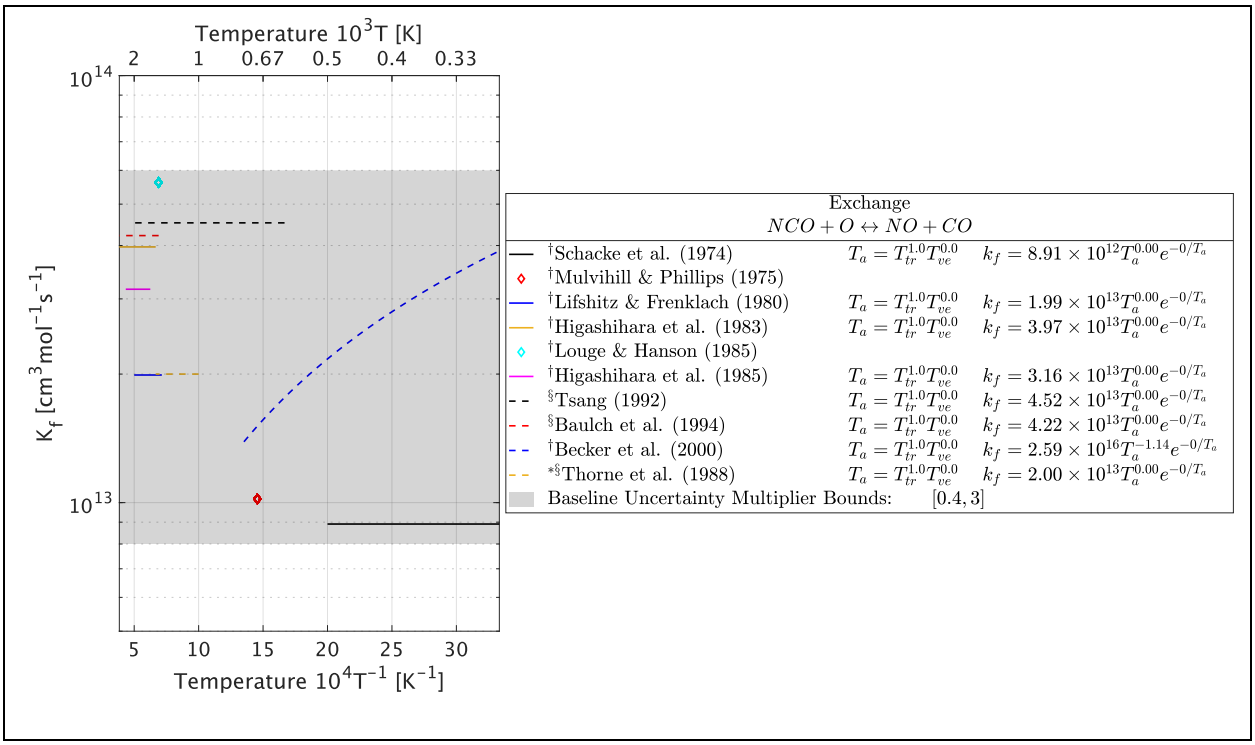

Figure B27: NCO + O ⇌ NO + CO exchange literature review.
(†Experiment, §Meta-study, ‡Numerical/Theory, ¶Converted reverse reaction, *Baseline)
[134,196,201,203,208,304,330,369,370,402–405]

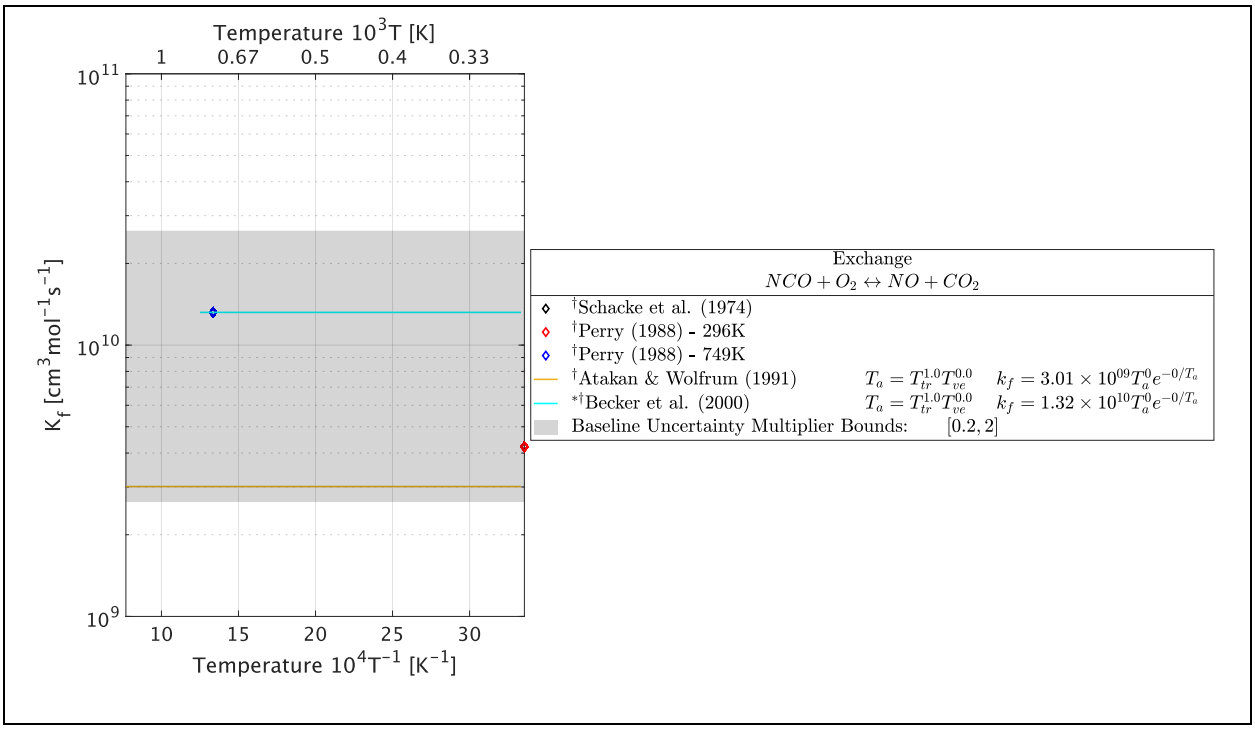

Figure B28: NCO + O_2 ⇌ NO + CO_2 exchange literature review.
(†Experiment, §Meta-study, ‡Numerical/Theory, ¶Converted reverse reaction, *Baseline)
[208,395,402,406]

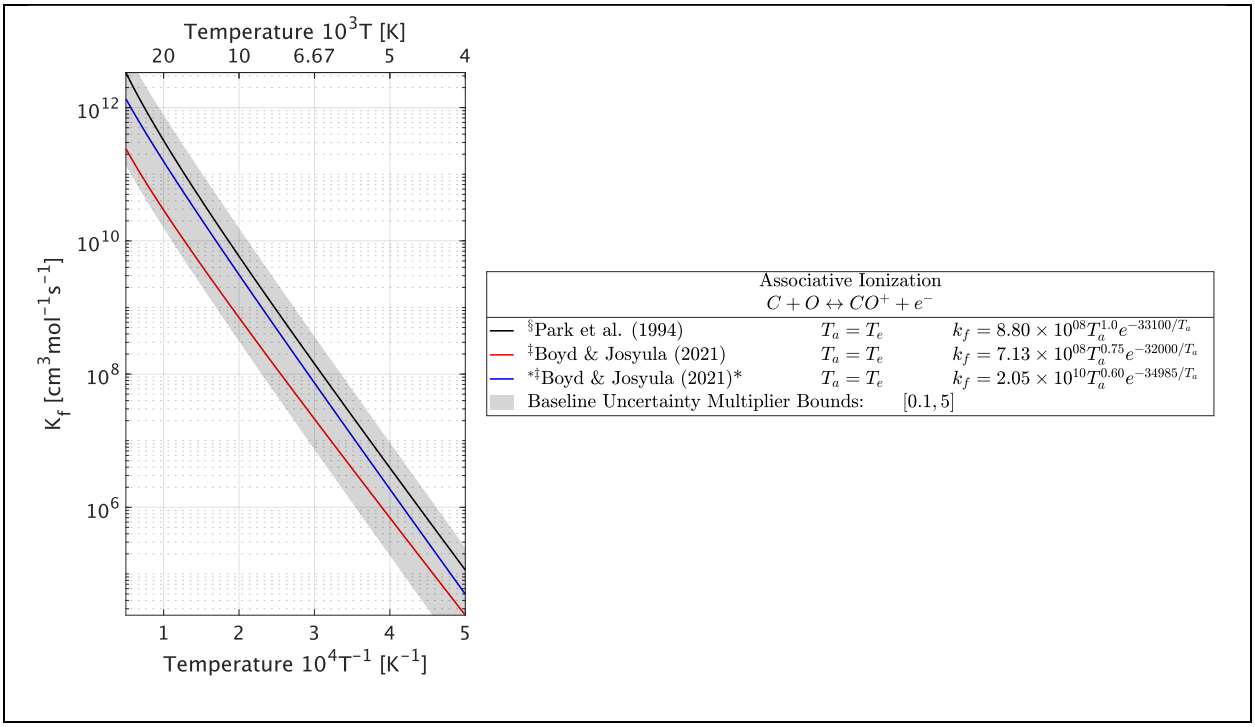

Figure B29: C + O ⇌ CO^+ + e^- associative ionization literature review.
(†Experiment, §Meta-study, ‡Numerical/Theory, ¶Converted reverse reaction, *Baseline / Corrected post publication)
[54,112,128,137,138,194]

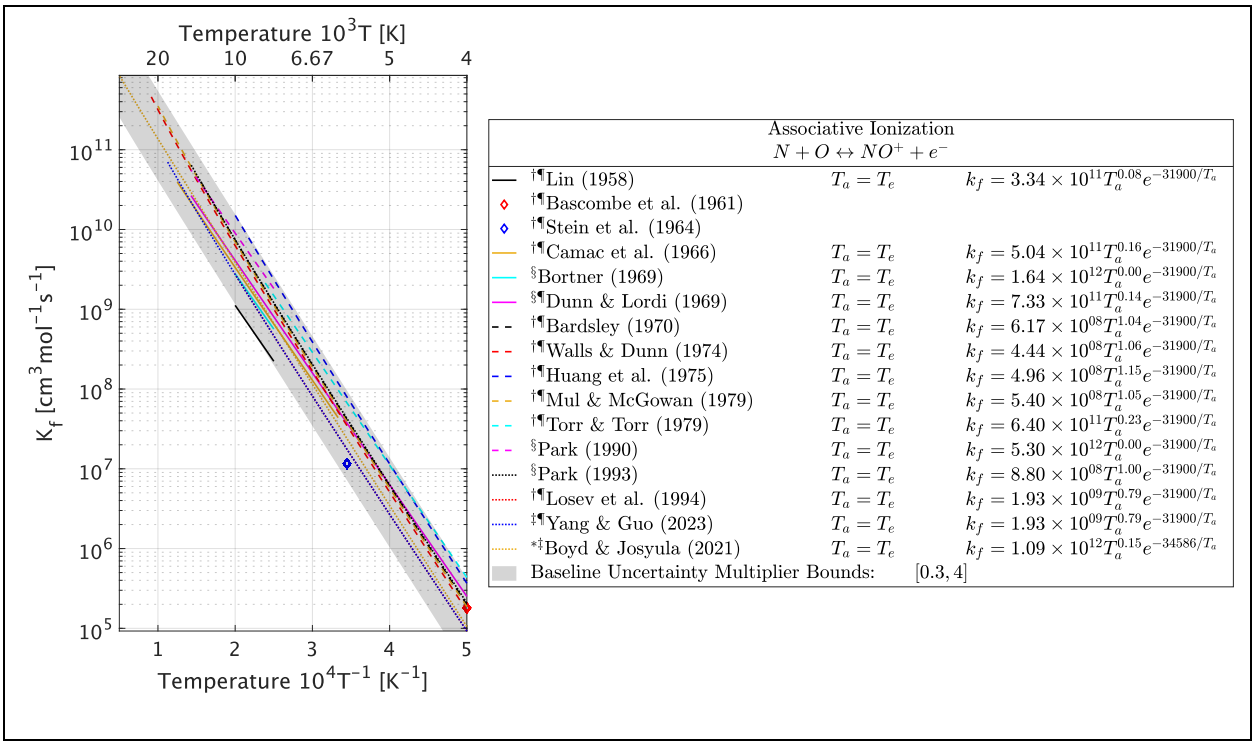

Figure B30: N + O ⇌ NO⁺ + e⁻ associative ionization literature review.
(†Experiment, §Meta-study, ‡Numerical/Theory, ¶Converted reverse reaction, *Baseline)
[1,47,54,89,112,119,128,137,138,140,172,194,229,277,278,280,289,305,367,407–417]

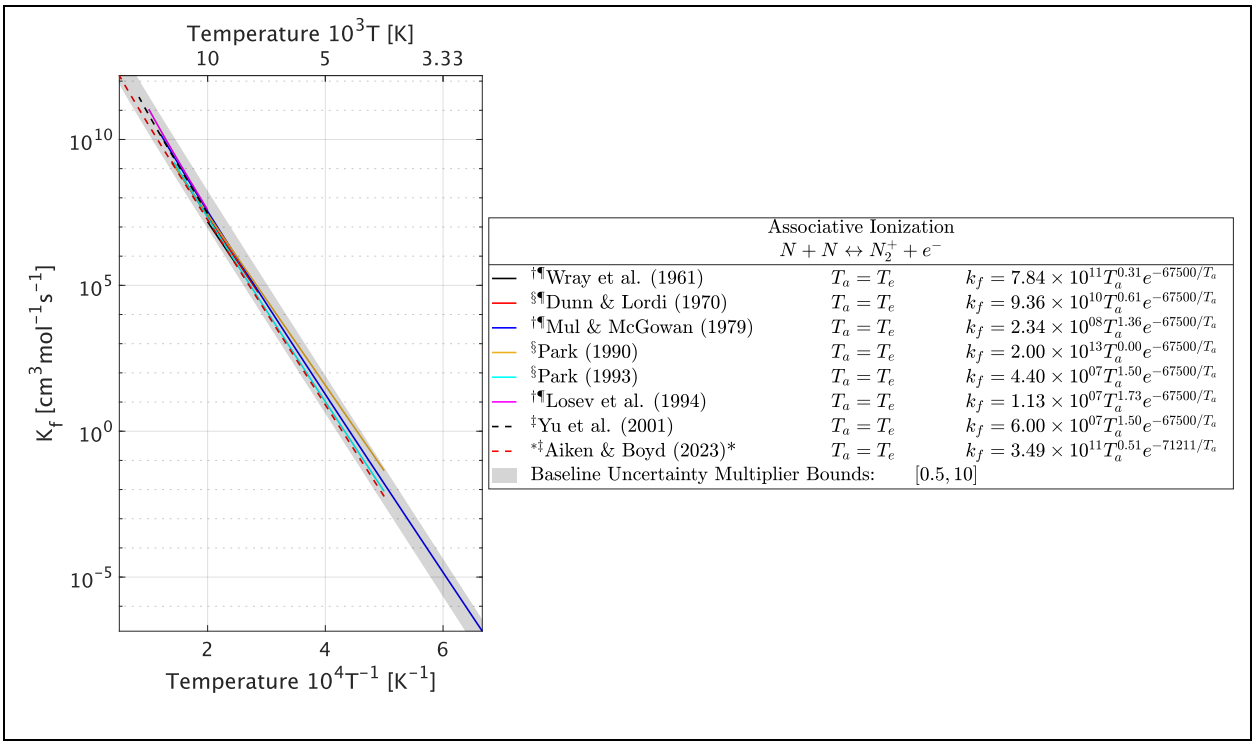

Figure B31: N + N ⇌ N₂⁺ + e⁻ associative ionization literature review.
(†Experiment, §Meta-study, ‡Numerical/Theory, ¶Converted reverse reaction, *Baseline)
[1,47,54,89,99,112,119,123,141,145,172,193,209,280,287,289,408]

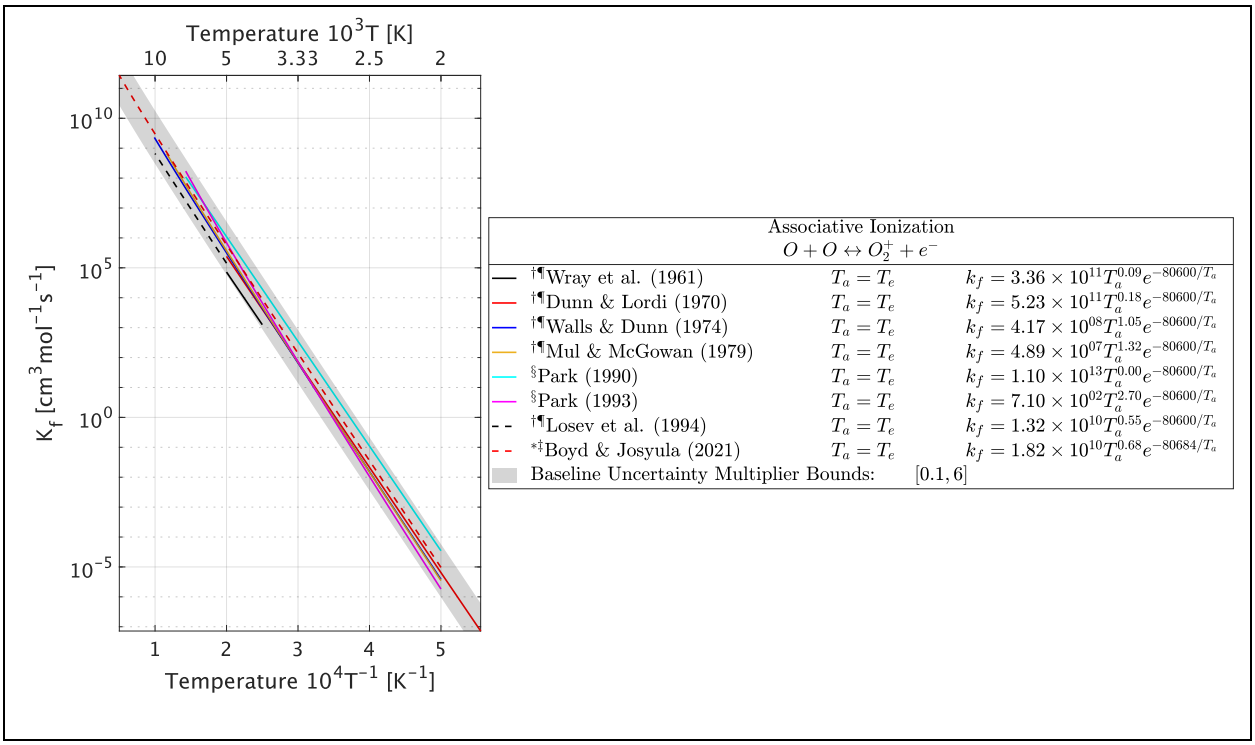

Figure B32: O + O ⇌ O_2^+ + e^- associative ionization literature review.
(†Experiment, §Meta-study, ‡Numerical/Theory, ¶Converted reverse reaction, *Baseline)
[1,47,54,89,112,128,137,138,145,172,194,209,280,287,289,302,408,409]

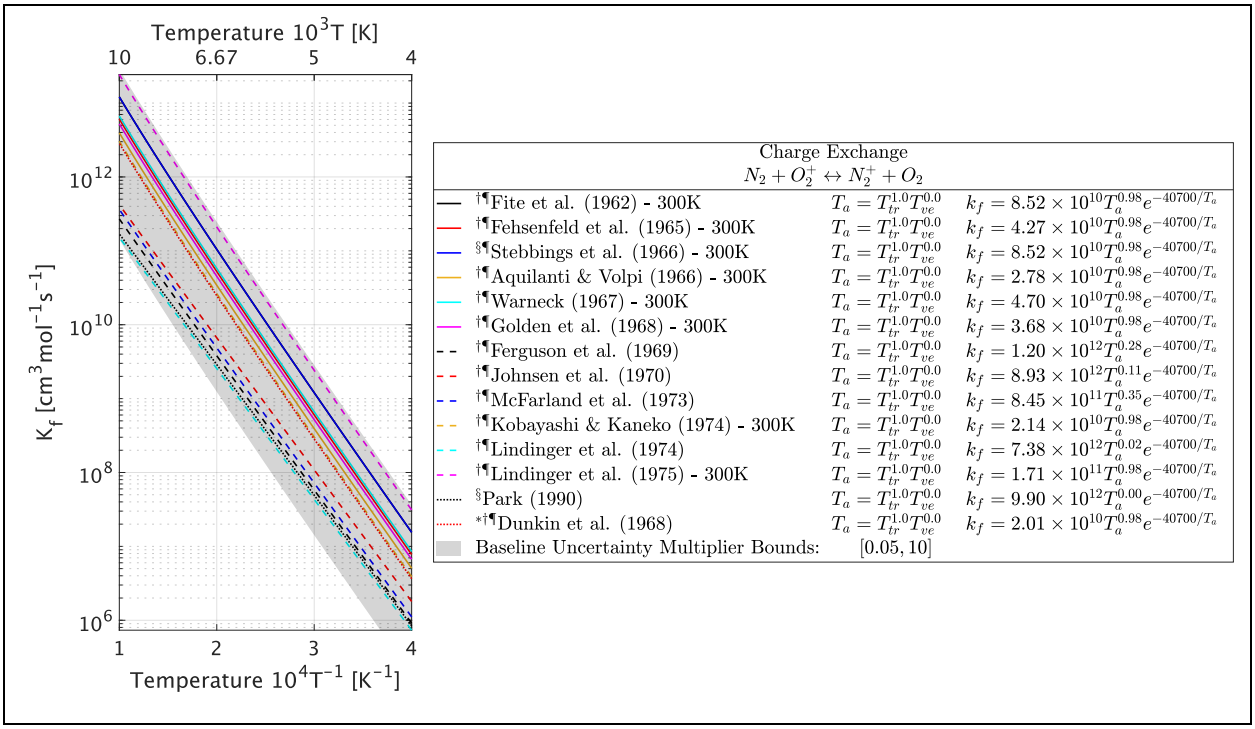

Figure B33: N_2 + O_2^+ ⇌ N_2^+ + O_2 charge exchange literature review.
(†Experiment, §Meta-study, ‡Numerical/Theory, ¶Converted reverse reaction, *Baseline)
[1,47,54,89,128,137,172,194,233,236,418–428]

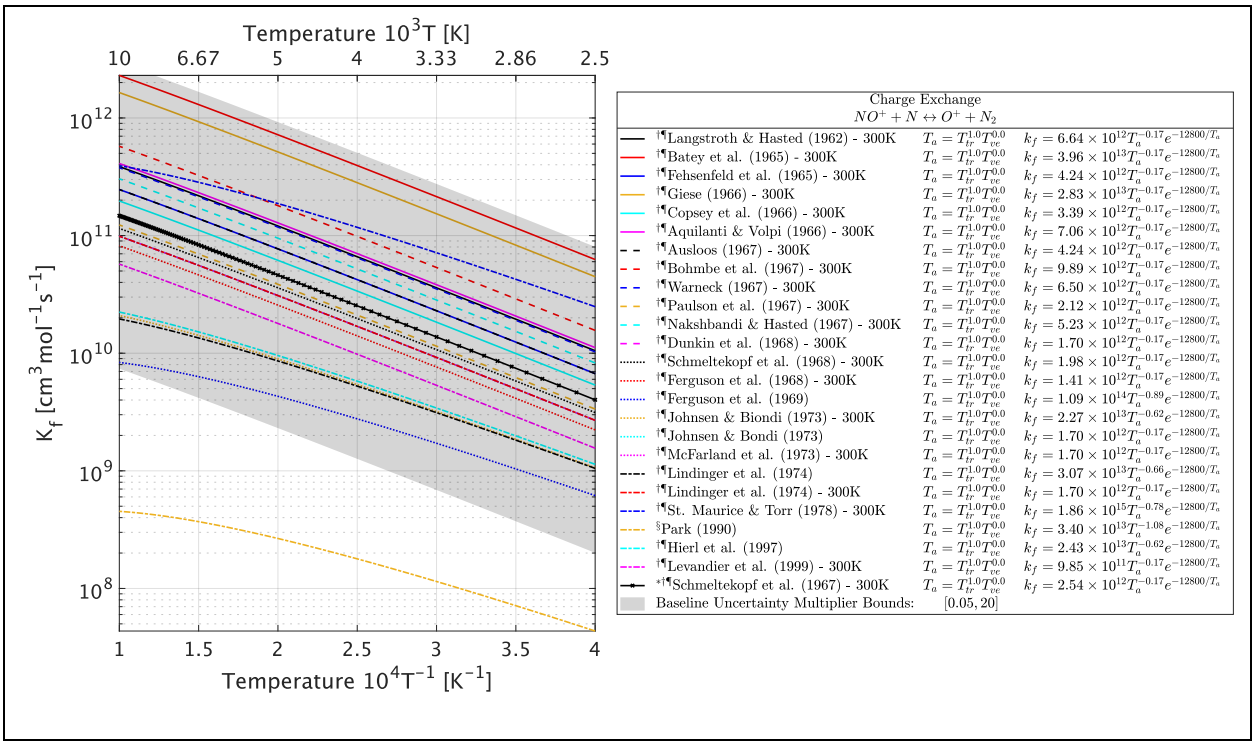

Figure B34: $NO^+ + N \rightleftharpoons O^+ + N_2$ charge exchange literature review.
(†Experiment, §Meta-study, ‡Numerical/Theory, ¶Converted reverse reaction, *Baseline)
[1,47,54,89,128,137,143,144,172,194,233,234,236,421,422,424,426,429–440]

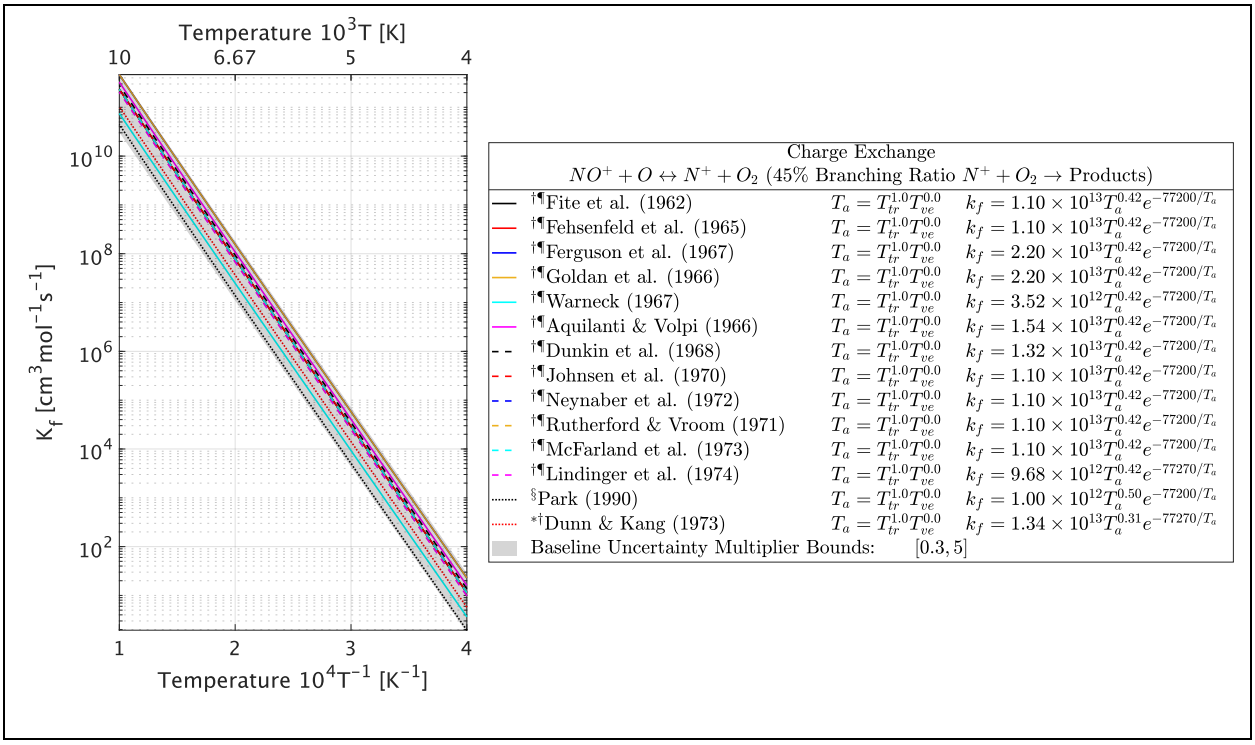

Figure B35: $NO^+ + O \rightleftharpoons N^+ + O_2$ charge exchange literature review.
(†Experiment, §Meta-study, ‡Numerical/Theory, ¶Converted reverse reaction, *Baseline)
[1,47,54,89,117,172,233,235,236,280,287,418,419,421,422,425,426,441–443]

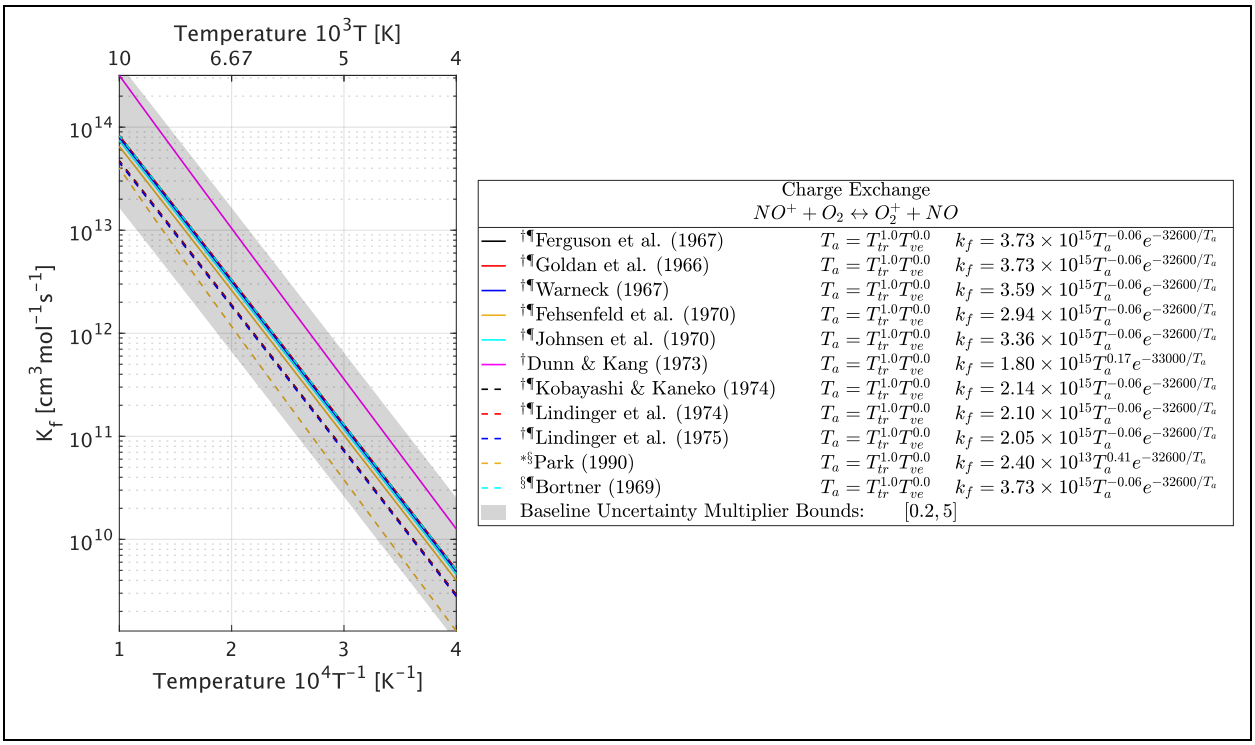

Figure B36: $NO^+ + O_2 \rightleftharpoons O_2^+ + NO$ charge exchange literature review.
(†Experiment, §Meta-study, ‡Numerical/Theory, ¶Converted reverse reaction, *Baseline)
[1,47,54,89,117,172,194,229,236,280,287,422,425,427,428,441,442,444]

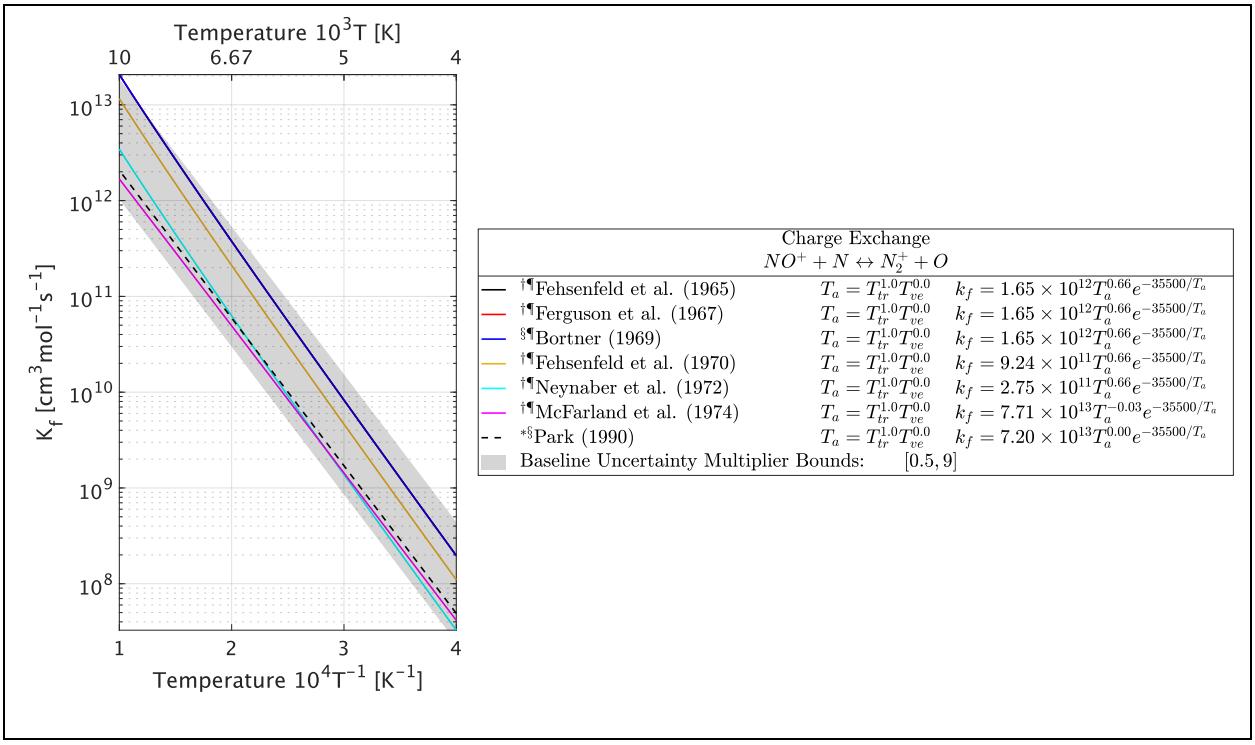

Figure B37: $NO^+ + N \rightleftharpoons N_2^+ + O$ charge exchange literature review.
(†Experiment, §Meta-study, ‡Numerical/Theory, ¶Converted reverse reaction, *Baseline)
[1,47,54,89,194,229,235,280,287,394,419,441,444,445]

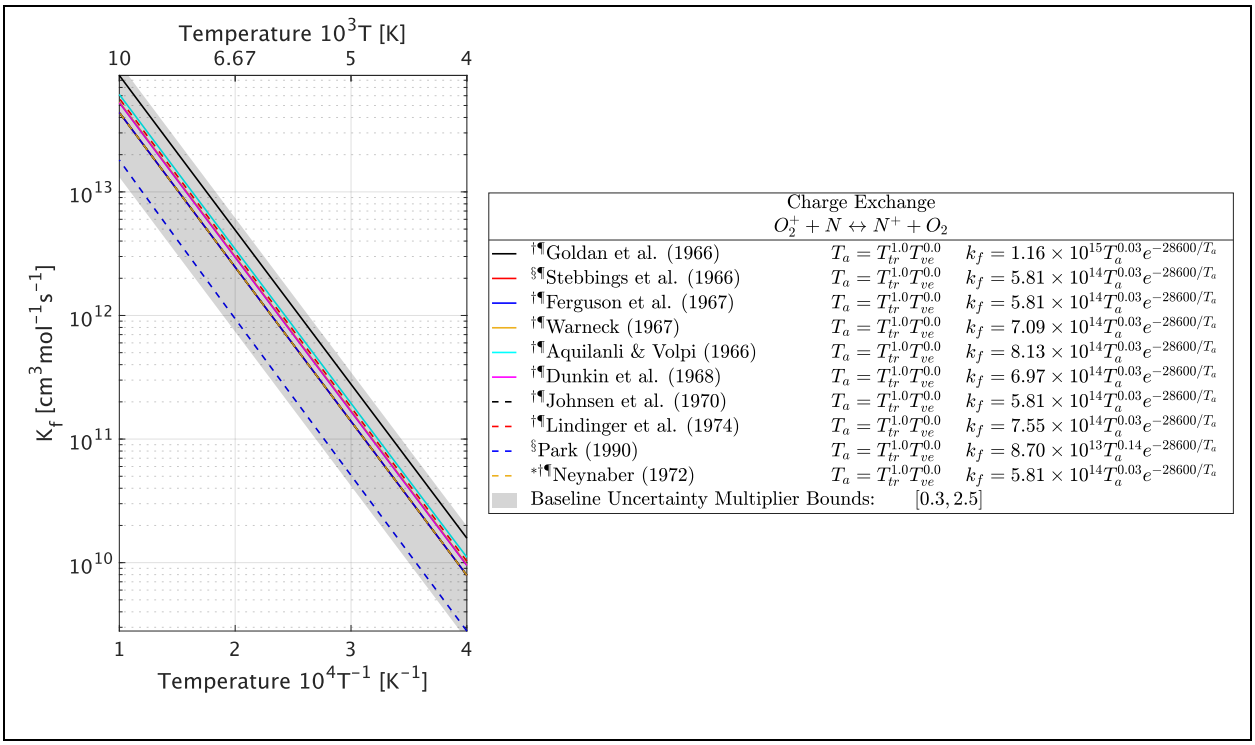

Figure B38: $O_2^+ + N \rightleftharpoons N^+ + O_2$ charge exchange literature review.
(†Experiment, §Meta-study, ‡Numerical/Theory, ¶Converted reverse reaction, *Baseline)
[1,47,54,89,172,194,233,235,236,280,287,420–422,425,441,442]

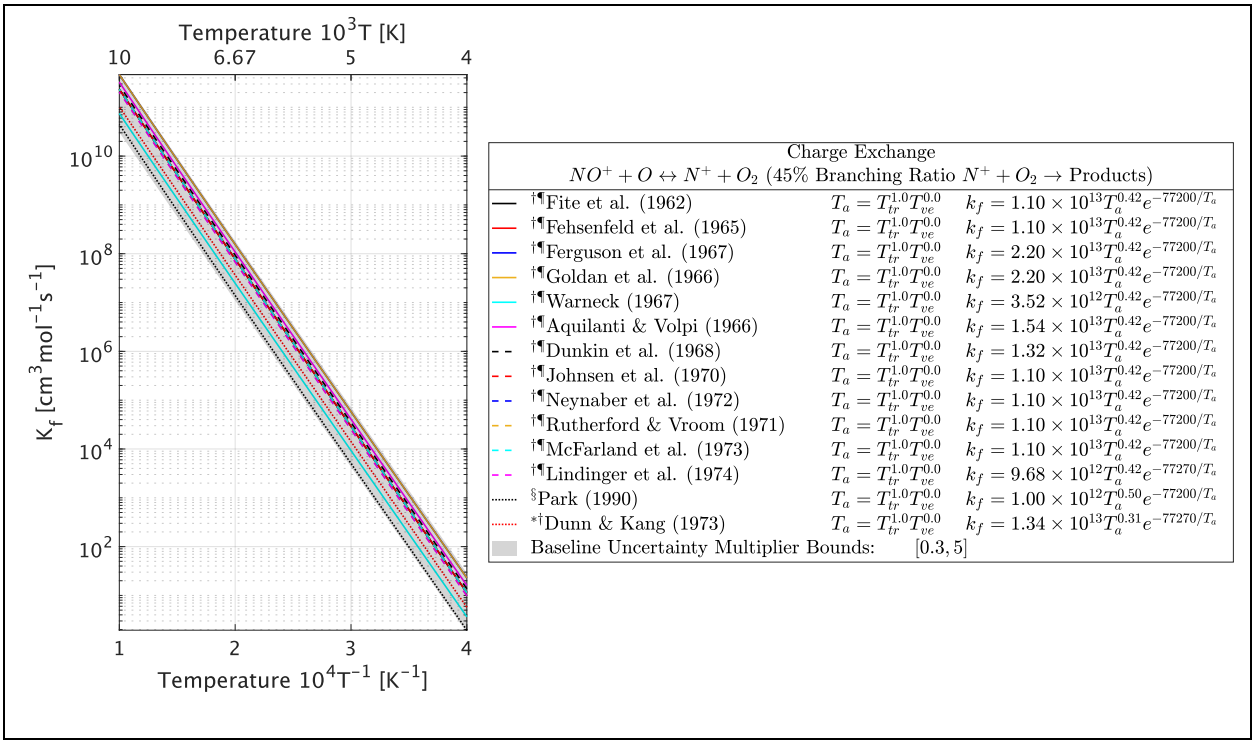

Figure B39: $NO + O^+ \rightleftharpoons N^+ + O_2$ charge exchange literature review.
(†Experiment, §Meta-study, ‡Numerical/Theory, ¶Converted reverse reaction, *Baseline)
[1,47,54,89,233,235,236,280,287,394,418,421,425,426,431,441–443,446,447]

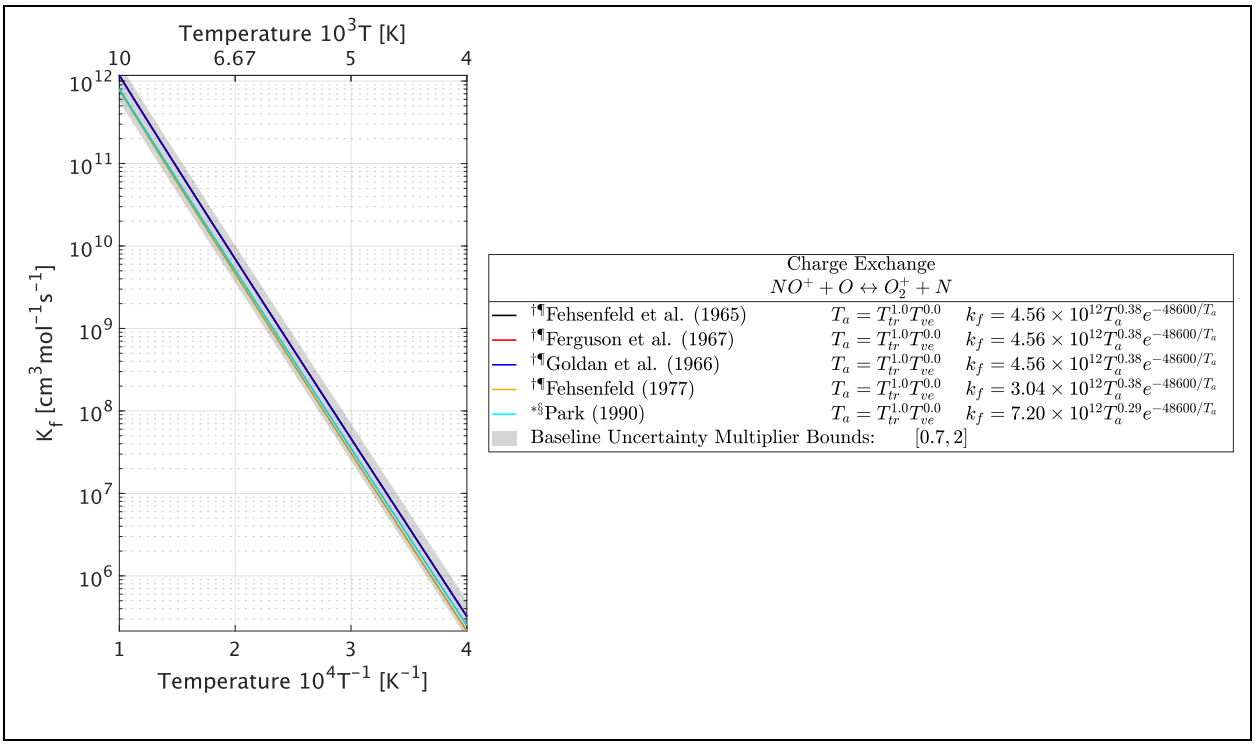

Figure B40: $NO^+ + O \rightleftharpoons O_2^+ + N$ charge exchange literature review.
(†Experiment, §Meta-study, ‡Numerical/Theory, ¶Converted reverse reaction, *Baseline)
[1,431,441,442,448]

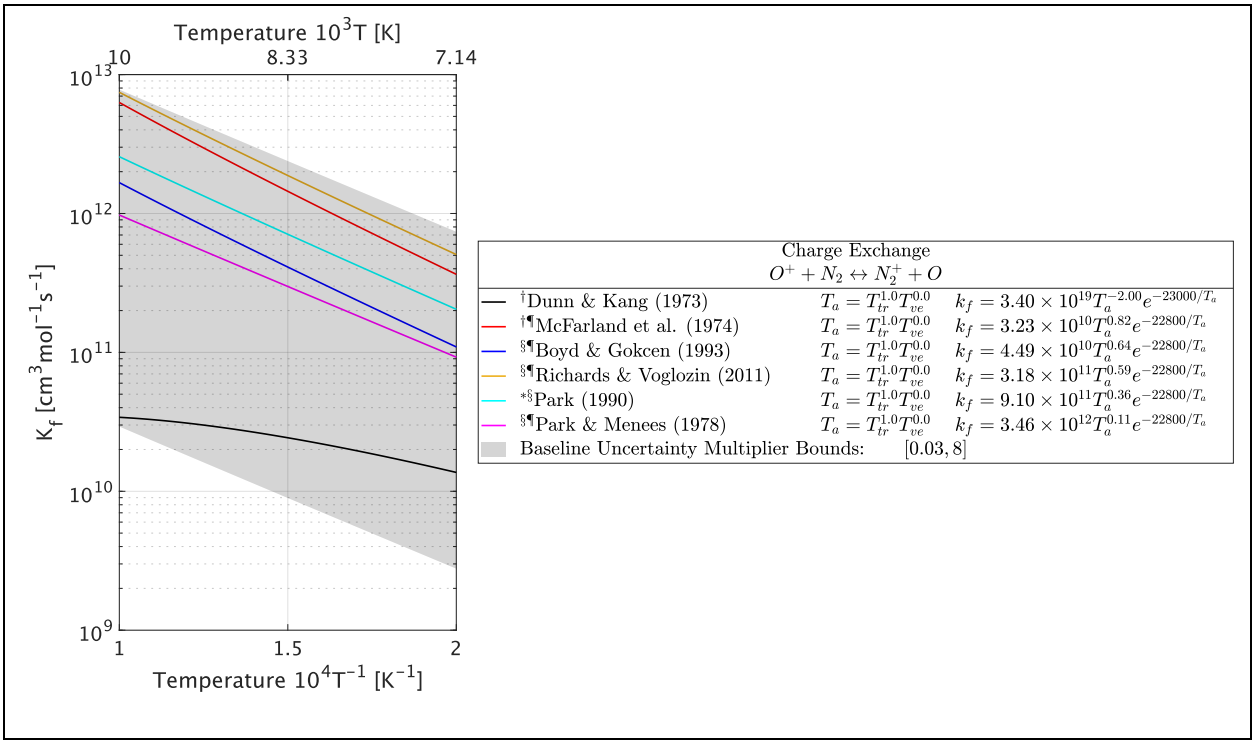

Figure B41: $O^+ + N_2 \rightleftharpoons N_2^+ + O$ charge exchange literature review.
(†Experiment, §Meta-study, ‡Numerical/Theory, ¶Converted reverse reaction, *Baseline)
[1,47,54,89,117,237,288,394,445,446]

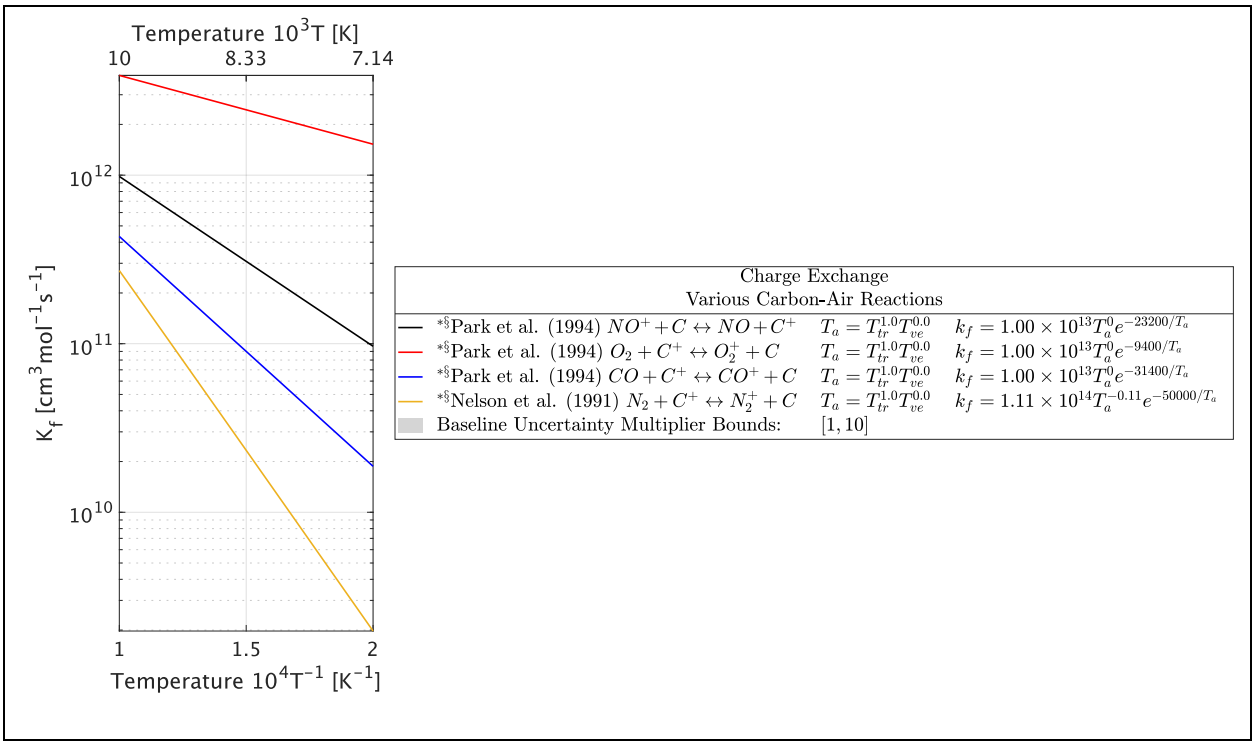

Figure B42: Various carbon-air charge exchange literature review.
(†Experiment, §Meta-study, ‡Numerical/Theory, ¶Converted reverse reaction, *Baseline)
[47,54,128,137,141,193,194]

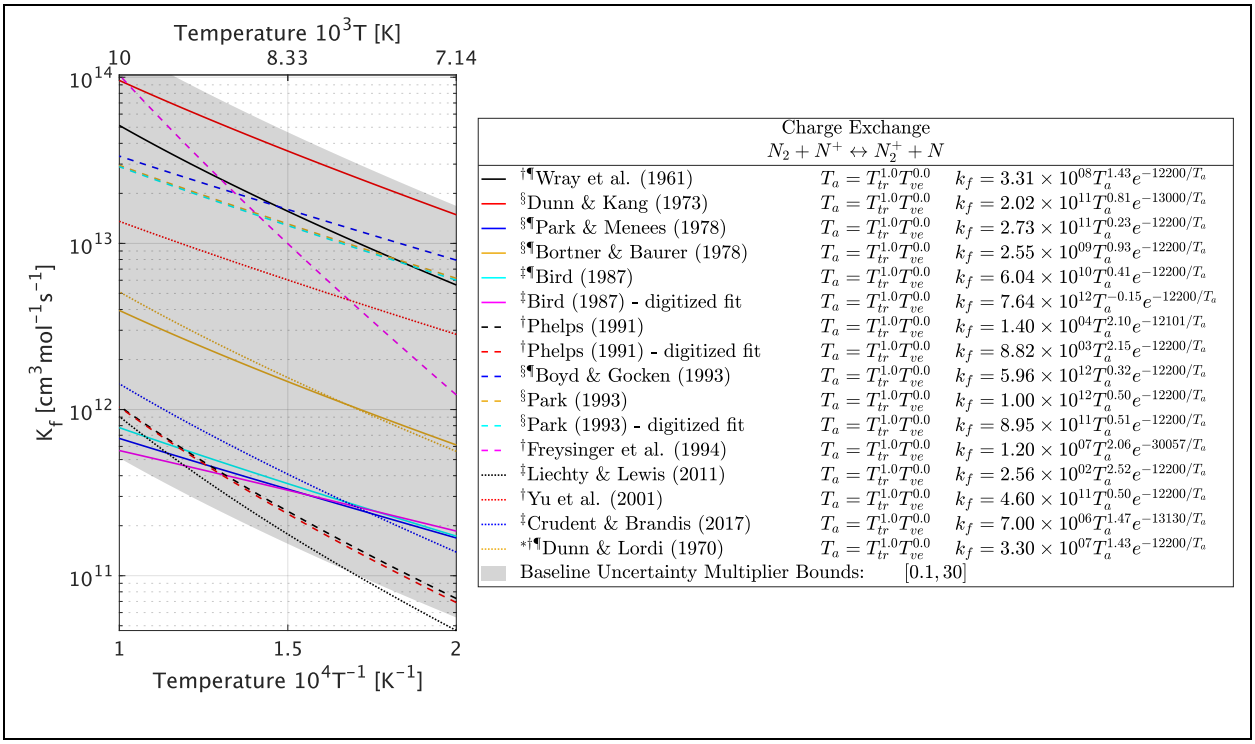

Figure B43: $N_2 + N^+ \rightleftharpoons N_2^+ + N$ charge exchange literature review.
(†Experiment, §Meta-study, ‡Numerical/Theory, ¶Converted reverse reaction, *Baseline)
[54,89,117,123,145–148,172,237,288,289,449,450]

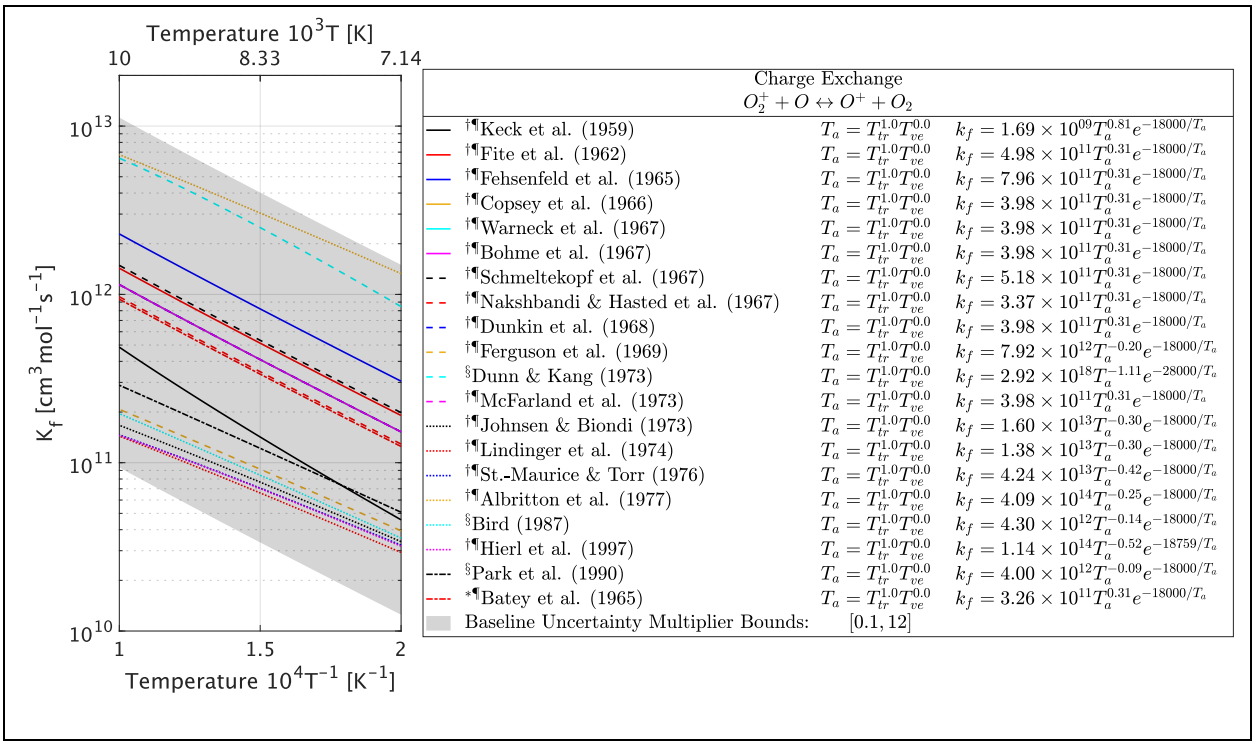

Figure B44: $O_2^+ + O \rightleftharpoons O^+ + O_2$ charge exchange literature review.
(†Experiment, §Meta-study, ‡Numerical/Theory, ¶Converted reverse reaction, *Baseline)
[1,54,117,137,143,148,172,212,233,234,236,418,422,424,426,430,431,433,435,437,439,440]

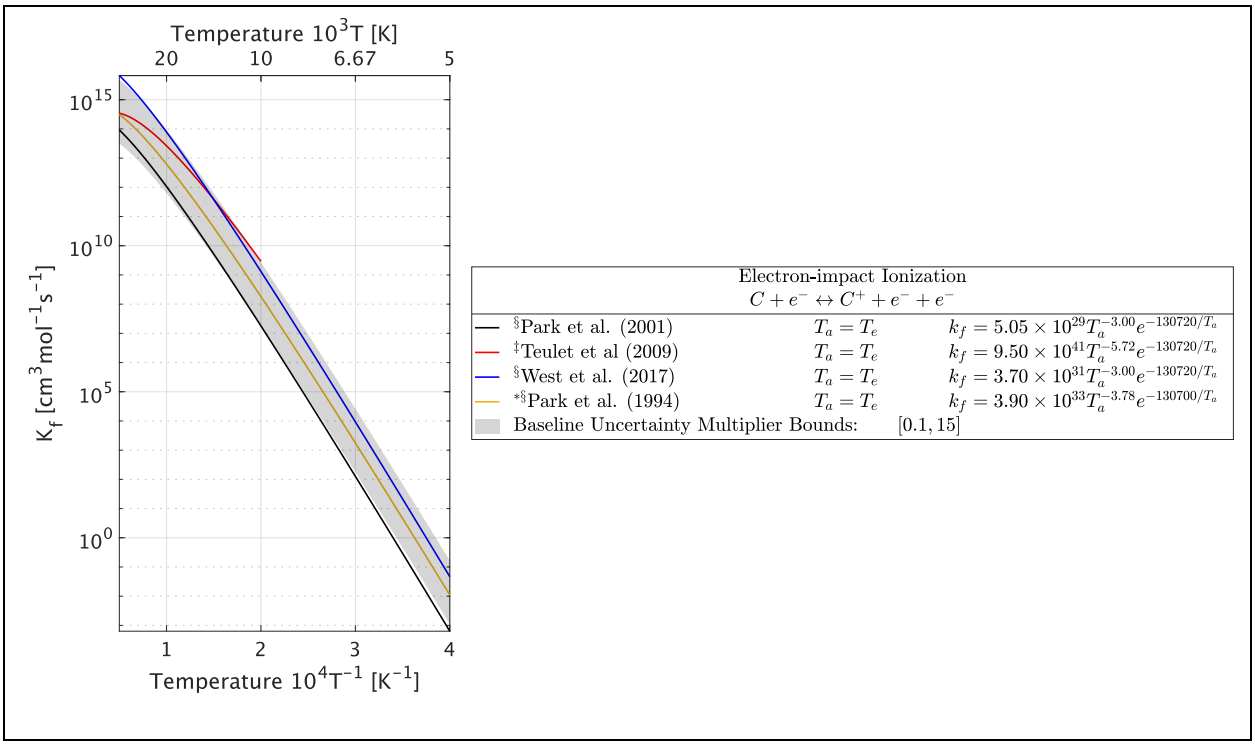

Figure B45: $C + e^- \rightleftharpoons C^+ + e^- + e^-$ electron impact ionization literature review.
(†Experiment, §Meta-study, ‡Numerical/Theory, ¶Converted reverse reaction, *Baseline)
[47,54,119,128,137,141,194,305,392]

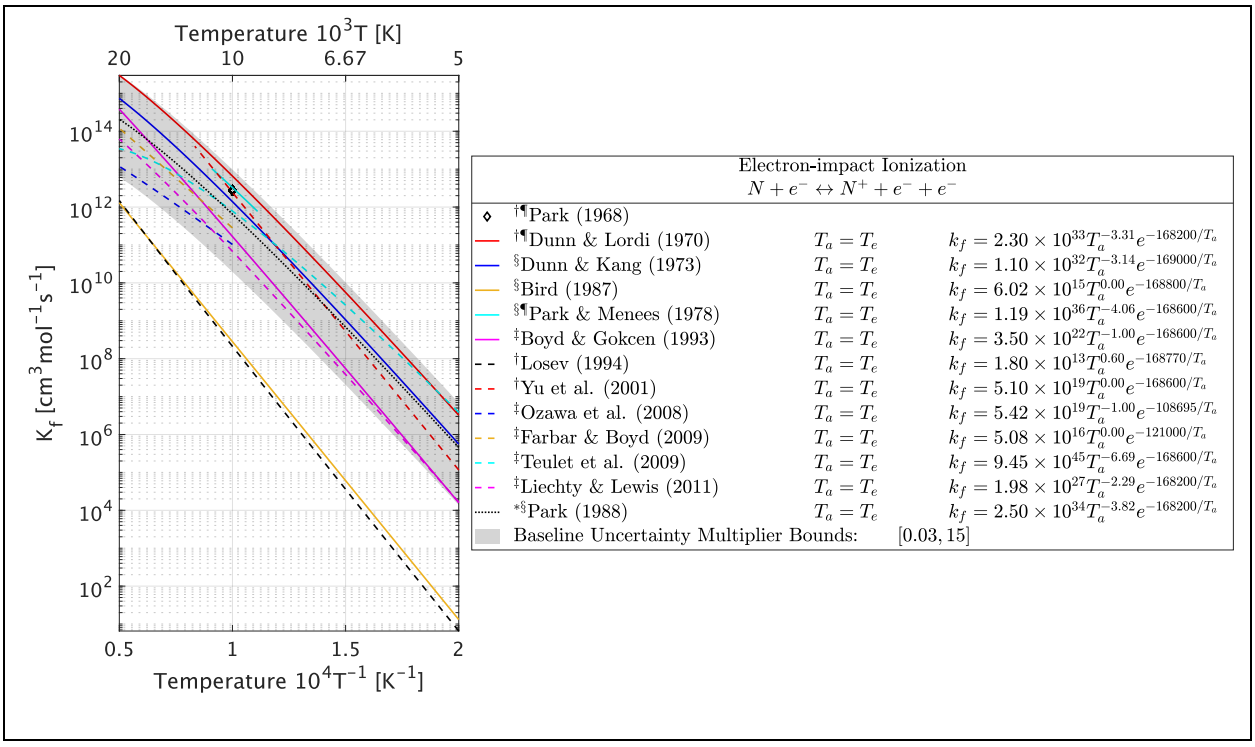

Figure B46: N + e⁻ ⇌ N⁺ + e⁻ + e⁻ electron impact ionization literature review. (†Experiment, §Meta-study, ‡Numerical/Theory, ¶Converted reverse reaction, *Baseline) [1,47,54,89,117–119,123,141,145,146,148,172,190,209,237,280,287,288,291,392,451,452]

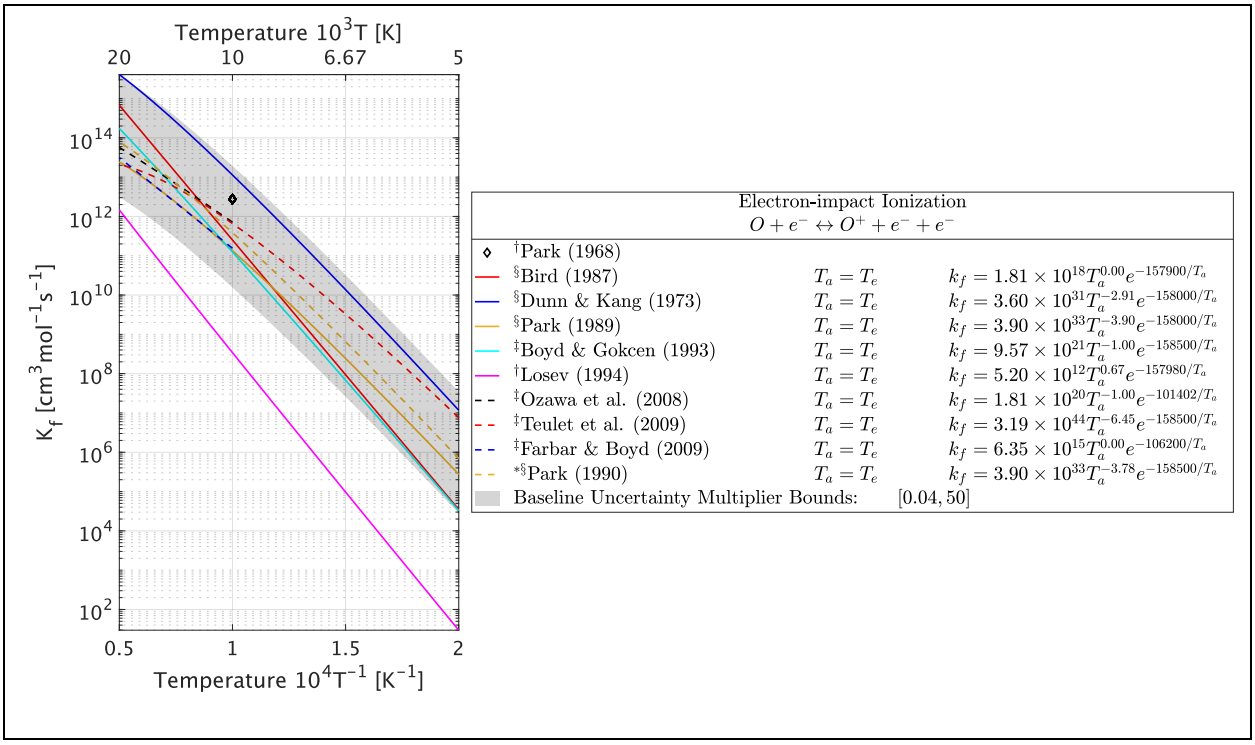

Figure B47: O + e⁻ ⇌ O⁺ + e⁻ + e⁻ electron impact ionization literature review. (†Experiment, §Meta-study, ‡Numerical/Theory, ¶Converted reverse reaction, *Baseline) [1,47,54,89,117–119,128,137,148,178,194,209,237,280,287,288,291,305,392,394,451,452]

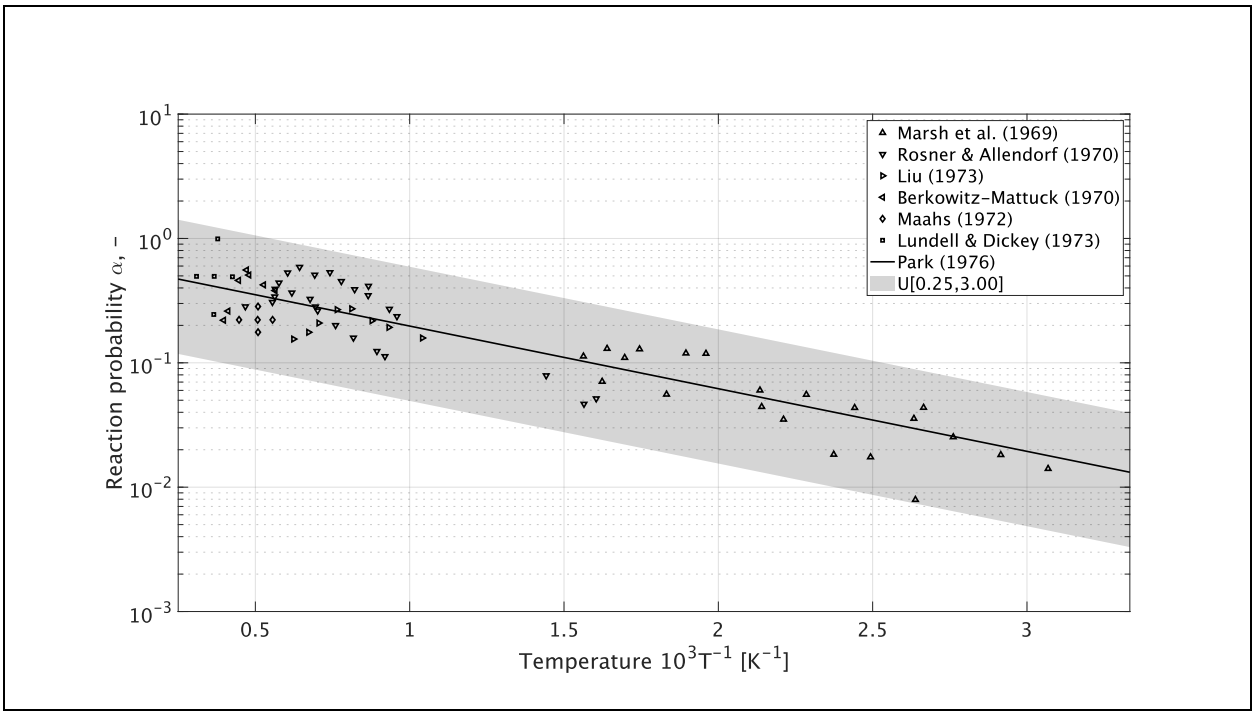

Figure B48: C(s) + O(a) ⇀ CO(a) + O(a) baseline and uncertainty bound literature review. [155–162,453]

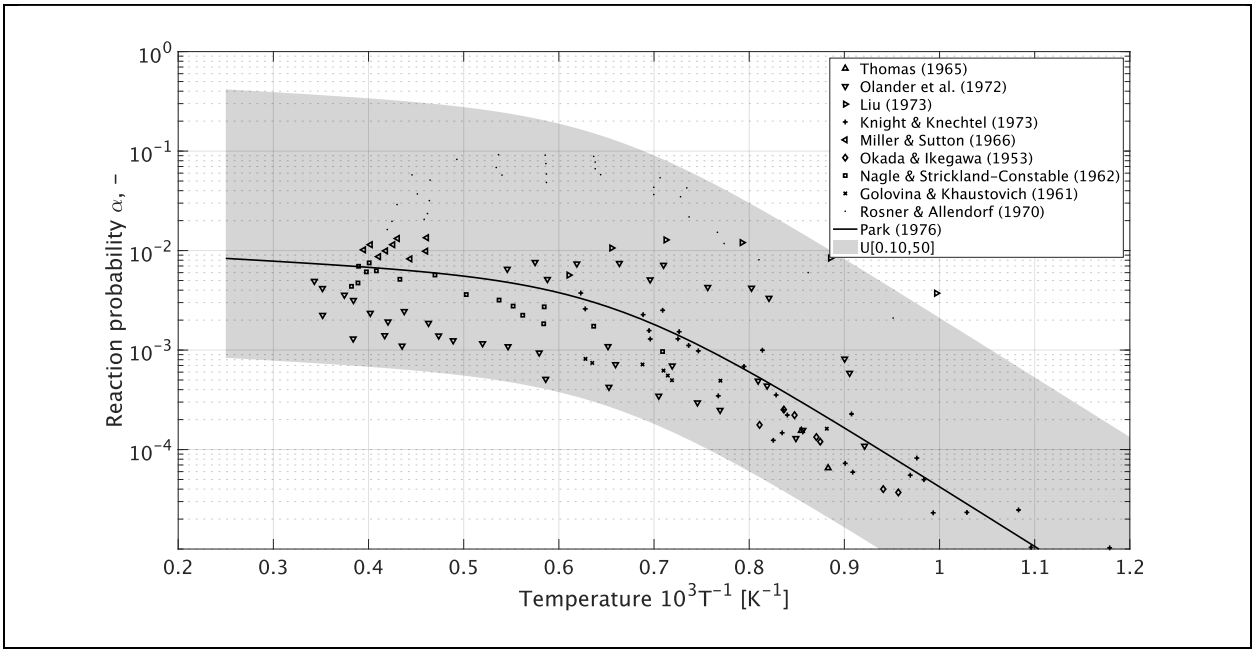

Figure B49: C(s) + O_2(a) ⇀ CO(a) ⇀ CO(g) baseline and uncertainty bound literature review. [77,156,158,163–168]

Appendix C

Gas Phase Reaction Rate Coefficient Uncertainty Bound Literature Review

Table C1: Dissociation reaction parameter uncertainty bound literature review and current work.

Reaction	Third Body, M	Uncertainty Bound Multipliers	References
$N_2 + M \rightleftharpoons 2N + M$	N_2	0.6, 1.5	[1,171,281]†
		0.7, 1.3	[227]†
		0.5, 2.0	[145]§
		0.5, 2.0	[282]†
		0.3, 3.2	[229]§
		0.6, 1.5	[178]§
		0.3, 3.0	[141]§
		0.1, 10	[47]§
		0.5, 4.0	[48,54]§
		0.3, 8.0	Figure B1(a)
	N	0.5, 2.0	[281]†
		0.6, 1.4	[227]†
		0.5, 2.0	[282]†
		0.5, 4.0	[229]§
		0.6, 1.5	[178]§
		0.2, 5.0	[141]§
		0.1, 10	[47]§
		0.2, 3.0	[48,54]§
		0.3, 7.0	Figure B1(b)
	e^-	0.1, 10	[47,48,54,141]§
		0.03, 10	Figure B1(c)
$O_2 + M \rightleftharpoons 2O + M$	O_2	0.6, 1.3	[292]†
		0.8, 1.3	[293]†
		0.1, 1.0	[294]†
		0.8, 1.2	[295]†
		0.5, 2.0	[283]§
		0.8, 1.3	[228]†
		0.5, 1.5	[296]†
		0.5, 2.0	[47]§
		0.3, 1.3	[54]§*
		0.2, 5.0	Figure B2(b)
	O	0.8, 1.3	[293]†
		0.5, 1.5	[294]†
		0.5, 2.0	[283]§
		0.5, 1.5	[47]§
		0.3, 1.3	[54]§*
		0.3, 2.1	Figure B2(c)
	N_2	0.7, 3.0	Figure B2(a)
$NO + M \rightleftharpoons N + O + M$	N_2	0.3, 3.6	[229]§
		0.5, 2.0	[306]§
		0.4, 2.5	[194]§
		0.1, 10	[47]§
		0.2, 2.5	[54]§*
		0.2, 3.0	Figure B3(a)
	NO	0.3, 4.0	[229]§
		0.1, 10	[47]§
		0.2, 2.5	[54]§
		0.2, 2.5	Figure B3(b)
$C_2 + M \rightleftharpoons 2C + M$	Ar, Ne	0.5, 1.5	[309]†
		0.5, 1.9	[310]†

		0.7, 1.3	[311]†
		0.5, 2.0	[141]§
		0.8, 1.3	[194]§
		0.1, 5.0	[47,54]§*
		0.1, 4.0	Figure B4
$CN + M \rightleftharpoons C + N + M$	N_2, CO_2, Ar	0.4, 1.6	[134,312]§
		0.5, 2.0	[134]§
		0.5, 2.0	[141]§
		0.1, 10	[47]§
		0.3, 1.9	[48,54]§
		0.2, 4.0	Figure B5
$CO + M \rightleftharpoons C + O + M$	O, Ar	0.8, 1.2	[230]†
		0.5, 1.5	[314]†
		0.3, 1.5	[47]§
		0.25, 1.5	[54]§
		0.2, 8.0	Figure B6(a)
	CO	0.8, 1.2	[230]†
		0.3, 1.5	[47]§
		0.25, 1.5	[54]§
		0.1, 8.0	Figure B6(b)
$CO_2 + M \rightleftharpoons CO + O + M$	N, C, O	0.1, 1.0	[47,54]§
		0.2, 1.3	Figure B7(a)
	CO_2	0.1, 1.0	[47,54]§
		0.2, 8.0	Figure B7(b)
$NCO + M \rightleftharpoons N + CO + M$	N_2, CO, Ar	0.3, 3.0	[134]§
		0.4, 1.6	[127]§
		0.05, 10	Figure B8

†Experimental/numerical uncertainty, §Meta-study uncertainty

Table C2: Neutral exchange reaction parameter uncertainty bound literature review and current work.

Reaction	Uncertainty Bound Multipliers	References
$N_2 + C \rightleftharpoons CN + N$	0.6, 1.4	[133]†
	0.7, 1.3	[333]†
	0.6, 1.4	[127,203]§
	0.5, 2.0	[141]§
	0.5, 1.5	[47,54]§
	0.5, 1.3	Figure B9
$CN + O \rightleftharpoons NO + C$	0.6, 1.0	[133]†
	1.0, 10	[47]§
	0.1, 10	[54]§
	0.1, 6.0	Figure B10
$CO + N \rightleftharpoons NO + C$	0.5, 2.0	[133]†
	0.1, 10	[47,54]§
	0.5, 8.0	Figure B11
$CO + O \rightleftharpoons O_2 + C$	0.1, 10	[47,54]§
	0.1, 15	Figure B12
$C_3 + C \rightleftharpoons C_2 + C_2$	0.1, 10	[47,54]§*
	0.3, 3.0	Figure B13
$C_2 + N_2 \rightleftharpoons CN + CN$	0.5, 1.5	[332]†
	0.5, 2.0	[141]§
	0.1, 10	[47]§
	0.5, 150	[48,54]§
	0.2, 12	Figure B14
$N_2 + O \rightleftharpoons NO + N$	0.5, 2.0	[229]§
	0.4, 1.6	[203]§
	0.6, 1.4	[127]§
	0.7, 1.3	[344]†
	0.5, 1.5	[47]§
	0.4, 1.3	[54]§
	0.1, 7.0	Figure B15
$O_2 + N \rightleftharpoons NO + O$	0.1, 10	[47,54]§*
	0.1, 10	Figure B16
$CN + C \rightleftharpoons C_2 + N$	0.8, 1.5	[200]†
	0.2, 5.0	[141]§
	0.5, 3.0	[48]§
	0.3, 10	Figure B17
$CN + CO \rightleftharpoons C + NCO$	0.1, 10	Figure B18
$CN + CO_2 \rightleftharpoons CO + NCO$	0.1, 10	Figure B19
$CN + NO \rightleftharpoons N + NCO$	0.5, 2.0	[134]§
	0.5, 2.0	Figure B20
$CO + N \rightleftharpoons CN + O$	0.5, 2.0	[312]§
	0.8, 2.2	[376]†
	0.5, 2.0	[134]§
	0.8, 2.3	[203]§
	0.1, 10	[54]§
	0.1, 10	Figure B21
$NCO + O \rightleftharpoons CN + O_2$	0.1, 40	Figure B22
$CO_2 + O \rightleftharpoons CO + O_2$	0.5, 2.0	[317]§
	0.2, 6.0	[194]§
	0.1, 10	[54]§

	0.3, 10	Figure B23
$CO_2 + N \rightleftharpoons NO + CO$	0.1, 5.0	Figure B24
$NCO + N \rightleftharpoons N_2 + CO$	0.3, 3.2	[127]§
	0.3, 3.2	Figure B25
$NCO + NO \rightleftharpoons N_2 + CO_2$	0.5, 2.0	[134]§
	0.7, 1.3	[203]§
	0.2, 2.5	Figure B26
$NCO + O \rightleftharpoons NO + CO$	0.5, 2.0	[134]§
	0.4, 2.3	[203]§
	0.4, 3.0	Figure B27
$NCO + O_2 \rightleftharpoons NO + CO_2$	0.2, 2.0	Figure B28

†Experimental/numerical uncertainty, §Meta-study uncertainty

Table C3: Associative ionization reaction parameter uncertainty bound literature review and current work.

Reaction	Uncertainty Bound Multipliers	References
$C + O \rightleftharpoons CO^+ + e^-$	0.1, 10 0.1, 5.0	[54]§* Figure B29
$N + O \rightleftharpoons NO^+ + e^-$	0.1, 10 0.3, 4.0	[47,54]§* Figure B30
$N + N \rightleftharpoons N_2^+ + e^-$	0.1, 10 0.3, 1.3 0.5, 10	[47,141]§ [54]§* Figure B31
$O + O \rightleftharpoons O_2^+ + e^-$	0.1, 10 0.1, 6.0	[47,54]§* Figure B32

†Experimental/numerical uncertainty, §Meta-study uncertainty

Table C4: Charge exchange parameter uncertainty bound literature review and current work.

Reaction	Uncertainty Bound Multipliers	References
$N_2 + O_2^+ \rightleftharpoons N_2^+ + O_2$	0.1, 10 0.05, 10	[47,141]§ Figure B33
$NO^+ + N \rightleftharpoons O^+ + N_2$	0.1, 10 0.05, 20	[47,54]§ Figure B34
$NO^+ + O \rightleftharpoons N^+ + O_2$	0.1, 10 0.3, 5.0	[47,54]§ Figure B35
$NO^+ + O_2 \rightleftharpoons O_2^+ + NO$	0.1, 10 0.2, 5.0	[47,54]§ Figure B36
$NO^+ + N \rightleftharpoons N_2^+ + O$	0.1, 10 0.5, 9.0	[47,54]§ Figure B37
$O_2^+ + N \rightleftharpoons N^+ + O_2$	0.1, 10 0.3, 2.5	[47,54]§ Figure B38
$NO + O^+ \rightleftharpoons N^+ + O_2$	0.1, 10 0.01, 5.0	[47,54]§ Figure B39
$NO^+ + O \rightleftharpoons O_2^+ + N$	0.1, 10 0.7, 2.0	[47,54]§ Figure B40
$O^+ + N_2 \rightleftharpoons N_2^+ + O$	0.1, 10 0.03, 8.0	[47,54]§ Figure B41
$O_2 + C^+ \rightleftharpoons O_2^+ + C$ $CO + C^+ \rightleftharpoons CO^+ + C$ $NO^+ + C \rightleftharpoons NO + C^+$ $N_2 + C^+ \rightleftharpoons N_2^+ + C$	0.1, 10	[47,54,141]§ Figure B42
$N_2 + N^+ \rightleftharpoons N_2^+ + N$	0.05, 1.7 0.1, 30	[54]§* Figure B43
$O_2^+ + O \rightleftharpoons O^+ + O_2$	0.1, 10 0.1, 12	[47,54]§ Figure B44

†Experimental/numerical uncertainty, §Meta-study uncertainty

Table C5: Electron impact ionization reaction parameter uncertainty bound literature review and current work.

Reaction	Uncertainty Bound Multipliers	References
$C + e^- \rightleftharpoons C^+ + e^- + e^-$	0.1, 10	[47,54,141]§*
	0.1, 15	Figure B45
$N + e^- \rightleftharpoons N^+ + e^- + e^-$	0.1, 10	[47,141]§
	0.5, 2.0	[54]§
	0.03,15	Figure B46
$O + e^- \rightleftharpoons O^+ + e^- + e^-$	0.1, 10	[47]§
	0.4, 3.0	[54]§
	0.04, 50	Figure B47

†Experimental/numerical uncertainty, §Meta-study uncertainty